Improved Lumped Parameter Thermal Modelling of Synchronous Generators

Carlos Mejuto

A thesis submitted for the degree of Doctor of Philosophy

The University of Edinburgh

2010

Abstract

Within the existing available mix of numerical and analytical thermal analysis options, lumped parameter thermal modelling is selected as the operational backbone to develop an improved novel synchronous generator thermal modelling package. The objective is for the creation of a user friendly quick feedback tool, which can serve as a means to make quick machine design thermal calculations and answer customer queries quickly and reliably. Furthermore, thermally improved generator designs will allow for inevitable operational losses to be channelled away from the machine more efficiently. As a result, machine component temperatures will be reduced, allowing lower generator thermal ratings. The end result will be smaller, longer lasting, more efficient generators, with the ability to be adapted with greater ease to particular applications.

With the contribution of selected numerical analysis techniques, mainly finite element analysis for the distribution of iron losses, the MySolver thermal modelling package is developed and presented in this thesis. It is this combination of numerical and analytical tools that improves synchronous generator thermal modelling accuracy, but ultimately it is the lumped parameter nature of the thermal models developed that makes MySolver succeed as a reliable quick feedback electrical machine thermal design tool, validated using experimental results for a wide range of operating conditions.

The initial part of the thesis analyses the electrical machine thermal modelling techniques available today, indicating advantages and disadvantages associated with each one, and providing a rationale for the selection of lumped parameter modelling to be used by MySolver. The development of the synchronous generator lumped parameter thermal models is detailed, with examples on its construction presented. Subsequently, finite element analysis is utilised to predict the distribution of machine iron losses across the rotor and stator laminations, with the findings applied to MySolver. Furthermore, a study is performed into the lumped parameter discretisation level needed to effectively represent machine windings. MySolver is experimentally verified using experimental data from a fully instrumented synchronous generator and this data is also used to obtain further insight into the temperature distribution within the generator. In the final part results are evaluated and the use of MySolver for modelling and optimising electrical machines is discussed. Finally, appropriate conclusions on the work presented are drawn.

Declaration

I declare that this thesis was composed by myself, that the work contained herein is my own except where explicitly stated otherwise in the text.

Carlos Mejuto

Acknowledgements

I would like to thank my University supervisor Dr Markus Mueller, second supervisor Dr Ewen Macpherson and Industry supervisor Dr Martin Shanel for their support and guidance throughout my PhD.

I would also like to express much gratitude to Dr Martin Reekie for his invaluable advice and support, particularly during the experimental stage of the project, and to Dr Dave Staton for his knowledge and expertise contributions.

Colleagues within the School of Engineering and Electronics at The University of Edinburgh have provided much moral support and companionship. In particular, the friendship and support of Douglas Carmichael, Jonathan Shek and Paul Stott is much appreciated.

Finally, I would like to thank my mum and dad, my brother Dani and my fiancée Gemma for their continued love and care, support, and encouragement. Without it, the completion of this work would not have been possible.

Quisiera agradecerles a mis padres, a mi hermano Dani y a mi prometida Gemma su continuo cariño, ánimo y motivación. Sin ellos, no me hubiese sido posible completar este trabajo.

Contents

Abbreviations

AVR	Automatic Voltage Regulator
CFD	Computational Fluid Dynamics
CGT	Cummins Generator Technologies
CO_2	Carbon dioxide
DAQ	Data Acquisition
DC	Direct Current
DE	Drive-End
Eff	Governmental energy standard (Eff1 = Efficiency standard number 1)
EU	European Union
FEA	Finite Element Analysis
GND	Electrical Ground
IC	Integrated Circuit
IEC	International Electrotechnical Commission
LCC	Lumped Circuit Coefficient
NDE	Non-Drive-End
PCB	Prototype Circuit Board
Rms	Root mean square
Rpm	Revolutions per minute
RTD	Resistance Temperature Detector
SR1	Slip-ring 1
SR2	Slip-ring 2
TC	Thermocouples
UK	United Kingdom
UL	Underwriters' Laboratories
VF	Vector Fields

Symbols

α	Empirical parameter for iron loss calculation
β	Fluid coefficient of cubical expansion
β	Empirical parameter for iron loss calculation
ΔT	Temperature difference
ε	Emissivity
θ	Temperature difference
ρ_{Cu}	Copper resistivity
ρ_{Cu_20}	Copper resistivity at 20 °C
ρ	Density
μ	Dynamic viscosity
σ	Stefan-Boltzmann constant
τ	Thermal time constant
Ω	Ohms
A	Area
A_1	Area of surface 1
A_2	Area of surface 2
B	Magnetic flux density
B_m	Peak magnetic flux density
C	Capacitance
C_m	Empirical parameter for iron loss calculation
c	Specific heat capacity
c_{int}	Graphical y-axis intercept point
$°C$	Degrees centigrade
D_h	Hydraulic diameter
dT/dx	Temperature gradient
F	Farads
F_{1-2}	View factor of surface 2 with respect to surface 1
f	Frequency
f_{coef}	Friction coefficient

g	Gravitational force of attraction
Gr	Grashof number
H	Magnetic field strength
H	Henrys
h	Heat transfer coefficient
h_c	Convection heat transfer coefficient
h_R	Radiation heat transfer coefficient
Hz	Hertz
I	Current
I_A	Armature current
I_F	Field current
J	Joules
K	Degrees Kelvin
k	Thermal conductivity
k_{air}	Air thermal conductivity
k	Iron loss calculation constants
k_h	Hysteresis iron loss calculation constant
k_e	Eddy-current iron loss calculation constant
k_f	Dimensionless fluid coefficient
kg	Kilograms
kVA	Kilovolt-ampere
kWh	Kilowatt hour
L	Inductance
L_A	Armature inductance
l	Length
m	Meters
m	Gradient
n	Iron loss coefficient
Nu	Nusselt number
Nu_D	Nusselt number related to the specific hydraulic diameter
P	Pressure
P_{Cu_length}	Copper losses per length

$P_{Cu\_endwinding}$	Endwinding copper losses
P_{Cu}	Copper losses
P_{Iron}	Iron losses
P_{Stray}	Stray losses
P_h	Hysteresis iron loss component
P_e	Eddy-current iron loss component
P_x	Excess iron loss component
Pr	Prandtl number
Q	Rate of heat transfer
$Q_{Conduction}$	Conduction rate of heat transfer
$Q_{Convection}$	Convection rate of heat transfer
$Q_{Radiation}$	Radiation rate of heat transfer
R	Resistance
$R_{x,y}$	Thermal resistance between lumped parameter nodes x and y
$R_{Conduction}$	Conduction thermal resistance
$R_{Convection}$	Convection thermal resistance
$R_{Radiation}$	Radiation thermal resistance
R_{Flow}	Airflow thermal resistance
R_F	Field winding resistance
R_A	Armature winding resistance
Re	Reynolds number
Re_D	Reynolds number related to the specific hydraulic diameter
S	Complex power
s	Seconds
T	Temperature
T_1	Temperature of surface 1
T_2	Temperature of surface 2
T	Tesla
TWh	Terawatt hour
V	Volume
V	Voltage
V_F	Field voltage

V_L	Line voltage
V_P	Phase voltage
V_t	Thermocouple voltage
V_{ac}	AC voltage
V_1	Voltage drop/offset through slip-ring 1
V_2	Voltage drop/offset through slip-ring 2
V_o	Output voltage
$V_{Ambient}$	PCB voltage resulting from thermocouple at ambient temperature
$V_{Junction\ Reference}$	PCB reference thermocouple voltage
V_{Rotor}	PCB rotor thermocouple voltage
V	Volts
v	Velocity
W	Watts
x	Graphical x-axis value
Xp	Phase load
y	Graphical y-axis value
Z	Impedance
€	Euros
%	Percentage

List of Figures

List of Tables

CHAPTER 1

Introduction

1.1 Introduction to Importance of Thermal Modelling

In the past, engineers have focused their efforts on the electromagnetic design of electrical machines, with thermal aspects only being dealt with at a very superficial level. However, today's requirements for smaller machines of an increased energy efficiency and reduced cost have added new topologies and materials to the designer's tool book [1]. It is fundamental for these to be thermally investigated together with the traditional electromagnetic analysis in an iterative way, in order for their real potential to be uncovered and deficiencies clearly identified [2]. Nowadays tighter weight and space limitations are imposed on newly developed aerospace, automotive and industrial applications, emphasising the need for thermal modelling. Examples of such highly regulated engineering products include the recently developed Thermo King refrigerator truck SLX-400 generator [3] with its low fuel consumption and minimal environmental impact, the Airbus A380 aeroplane [4] largest airliner in the world, and modern more efficient Hyundai Heavy Industries DWT bulk carriers [5], illustrated in Figure 1.1.

Figure 1.1: *Modern thermal modelling engineering applications [3]-[5].*

In addition to this, since 1997 European governmental energy efficiency standards (Eff1, Eff2 and Eff3 ratings) exist, offering incentives to the more efficient motor designs [6]. These have been voluntary to date, but have been signed by thirty-six manufacturers and have the potential of becoming mandatory in the near future. In North America and Australia a minimum motor efficiency standard exists and China is planning to introduce similar measures from 2010. A vast amount of the electrical energy used in industry is transferred back into mechanical energy and increasing the current average motor efficiency of 88 % to a technically possible 96 % would allow for annual savings of up to 5 TWh [6].

An example of the efforts made within the European Union is The Motor Challenge Programme, which was launched by the European Commission in February 2003 and has the support of the National Energy Agencies of fifteen European countries [7]. The aim of the programme is to aid industrial companies in improving the energy efficiency of their motor driven systems. It is estimated by the European Commission that energy efficient motor driven systems will allow Europe to save up to 202 billion kWh in electricity consumption every year. The appropriate thermal modelling of electric machines will play an important role in achieving these important savings, which will equate to a reduction of up to € 10 billion being spent each year on electricity generation. Savings of € 5 to € 10 billion per year in industry operations could be achieved, while environmental costs could decrease by € 6 billion a year. Table 1.1 presents the potential savings, broken down into three categories, which could be made in Europe and specific EU countries if high efficiency motors were introduced. For all of these, the thermal behaviour of electric machines is of crucial consideration.

	Savings potential (billion kWh / year)			
	EU - 15	EU - 25	Germany	UK
High efficiency motors	24	27	6	3
Variable speed drives	45	50	10	6
Application part of the motor systems	112	125	26	15
Total electricity savings potential	181	202	42	24

Table 1.1: *Energy savings potential for motor systems [7].*

Furthermore, in recent years there has been a growing awareness of the importance of reducing CO_2 emissions levels to the atmosphere. An estimated 79 million tonne of the 'greenhouse gas' could be saved by using more efficient machines. This accounts for a quarter of the European Union's Kyoto target, agreed in 1997. Aiming to achieve the agreed Kyoto target, emphasis is commonly on renewable energy sources and even on nuclear power, since they provide CO_2-free electricity, but making current electricity generation methods more efficient is just as important and is greatly overlooked. The worldwide competitiveness of Europe's manufacturing industry would be greatly enhanced by the application of these energy efficiency measures, allowing it to improve its position with respect to other regions in the world where such changes are already taking place. Countries such as the United States of America and Canada are also introducing similar policies and the American Department of Energy has launched the Energy Policy Act, making the importation of motors that do not meet a certain efficiency level illegal [7].

Accurate thermal modelling and optimisation of electrical machines is key to the improved engineering, energy savings and cleaner power possibilities described in this section, serving as the motivation for the work carried out in this thesis.

1.1.1 Importance of Electrical Machine Thermal Modelling

Progress in the thermal modelling area has revealed that the electrical machine's thermal rating is the main factor determining machine size, highlighting its importance [8]. The limiting machine temperature can be set by any component (wire insulation impregnation, bearings, magnet, plastic cover, encoder, housing, etc.) and the temperature exerted on it during operation can have a very significant effect on the machine's lifespan. Identification of temperature limiting components is therefore essential. Figure 1.2 shows the effect of temperature on the durability of different types of winding insulation [9].

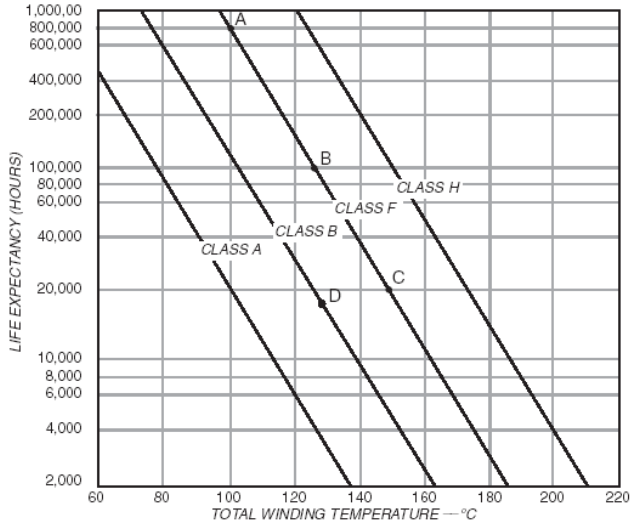

Figure 1.2: *Temperature vs. life curves for insulation systems [9].*

A clear life expectancy advantage is observed when operational winding temperature is kept low [10]. On these lines, according to Equation 1.1, increasing winding temperature, T, results in a rise in copper resistivity, ρ_{Cu}, where the copper resistivity at 20 °C, ρ_{Cu_20}, is 1.728×10^{-8} Ωm and constant α is 0.00393/°C.

$$\rho_{Cu} = \rho_{Cu\_20} \cdot [1 + \alpha \cdot (T - 20)] \tag{1.1}$$

Copper losses in an electric machine have been found to be proportional to resistance for a constant current, making the elevation in resistivity caused by the high temperatures very undesirable. In fact, a 50 °C rise results in a 20 % resistance increase, while a 140 °C increase causes resistance to be elevated by up to 55 % [10].

In addition to this, for example, in a permanent magnet motor torque is proportional to current. High currents lead to high I^2R copper losses and as magnet temperature increases, flux is lost and more current is needed to maintain the desired torque level. This will consequently result in further machine losses. Furthermore, machine lifetime is greatly dependant on the peak slot or endwinding temperature. Also, by limiting rotor temperatures, reductions in mechanical distortion and fatigue will be accomplished. In terms of machine integrity, in general, by achieving an accurate temperature distribution, damages such as the breakdown of stator winding insulation will be prevented [10]-[13].

Therefore, for all machine types and sizes, thermal analysis is a fundamental step in the design procedure and should be considered in an iterative manner with electromagnetic aspects. In depth analysis of electrical machine thermal modelling is covered in Chapter 2.

1.2 Initial Hypothesis

Following the evaluation of relevant literature and the thermal analysis work performed to date, it is clear that thermal modelling of electrical machines is an area that requires significant further work. Its benefits for machine manufacturers and customers alike are clear and research into imprecise thermal modelling areas can yield even more benefits. From the available range of thermal modelling techniques a novel everyday thermal modelling tool is required, for reliable thermal engineer new design consultations and immediate customer feedback. This needs to be an accurate, universal, user friendly, quick feedback, thermal modelling package. The hypothesis being assessed in this thesis is that:

Lumped parameter thermal modelling can effectively be implemented as the operational backbone of an accurate, universal, user friendly, quick feedback synchronous generator thermal modelling tool.

1.3 Aims and Objectives

The project has a number of clear objectives:

1. To critically review the electrical machine thermal modelling work executed to date, highlighting advantages and disadvantages linked with the techniques used, selecting the most appropriate methods for an accurate, universal, user friendly, quick feedback thermal modelling tool.

2. Following the selection of lumped parameter thermal modelling, to develop a truly representative synchronous generator thermal model, taking thermal resistances/capacitances, machine power losses and cooling airflow considerations into account.

3. To investigate the occurrence of iron losses in synchronous machine rotor and stator laminations utilising finite element analysis and experimental contributions. To apply these to the thermal models developed.

4. To obtain the complete thermal characteristic of an industrial commercialised Cummins Generator Technologies synchronous generator, using winding embedded TCs (thermocouples), thermal captures and additional external meters and sensors.

5. To validate the developed lumped parameter thermal modelling tool created utilising the experimental data obtained, highlighting strengths, deficiencies and areas where further work and research is required.

In order to successfully realise these objectives, the work carried out is segmented into three separate stages:

- Lumped parameter thermal model development: Utilise reliable synchronous machine geometric information and material property data to construct a representative thermal network. Employ spreadsheet and circuit analysis software to accommodate the thermal models, generating a user friendly reliable tool, capable of thermally analysing a wide range of electrical machines and yielding the required steady-state and transient results.

- Iron loss synchronous machine lamination distribution: Use of finite element analysis to investigate the challenge of predicting iron losses generated in electrical machine laminations. Application of synchronous machine results to the developed lumped parameter thermal networks, to re-distribute

lamination iron losses accurately, with the objective of achieving a more realistic alternator temperature representation.

- Experimental synchronous generator thermal analysis and thermal model verification: Test rig experimental thermal investigation and analysis of a Cummins Generator Technologies synchronous generator for a wide range of loadings scenarios and other external conditions. Make use of numerous winding embedded and additional thermocouples to obtain the required temperature data to validate the developed lumped parameter thermal modelling tool. Cover as wide a synchronous generator operational range as possible.

1.4 Contribution to Knowledge

Electrical machine designers have in the past concentrated efforts in the electromagnetic design, to the detriment of the design of the thermal performance of the machine. Nowadays this has been corrected to a certain extent, since it is clear that both design areas are interrelated. Even so, there are a number of electrical machine thermal modelling aspects requiring further research and the range of thermal modelling options available makes the selection of an ideal option, for a specific task, not trivial.

Lumped parameter thermal modelling has the potential of greatly aiding synchronous machine designers for fast thermal related consultations during the early machine development stage. It has proven to give accurate steady-state and transient synchronous machine temperature predictions for a wide range of operating conditions and serves as a user friendly method for non-experienced engineers to make quick reliable consultations of particular operational scenarios. Numerical thermal analysis methods will always provide higher levels of accuracy, at the expense of longer model set-up and computation times, but lumped parameter thermal models can be utilised to determine if detailed numerical thermal modelling

is necessary, potentially shortening design processes and speeding up customer feedback. The method presented in this thesis to create lumped parameter electrical machine thermal networks, from machine geometries, material properties and reliable power loss estimations and distributions, allows for this. This is presented through a newly developed lumped parameter thermal modelling tool named MySolver, which was fully developed throughout the performed work.

Overall, the research carried out increases understanding on how and when lumped parameter thermal modelling should be executed and utilised. Its virtues, along with current deficiencies, are uncovered by the work carried out, allowing for an informed evaluation of its role within the thermal modelling electrical machine design tool box.

In a broader context, the research evaluates the wide electrical machine thermal modelling picture available and demonstrates how lumped parameter thermal modelling has a clear place in electrical machine design, development and optimisation.

1.5 Thesis Outline

Chapter 2 presents modern thermal modelling techniques available today, after outlining traditional thermal modelling procedures. Pros and cons linked to each current thermal modelling method are covered, with examples on when each technique should be utilised given. Lumped parameter thermal modelling, selected as the most appropriate method to create the thermal modelling tool required, is covered in more detail, with all model development issues to be acknowledge outlined. Furthermore, synchronous machine loss issues and airflow related aspects of the thermal model are also discussed.

Chapter 3 explains how synchronous machine rotor and stator lumped parameter thermal networks should be developed. Numerous examples are given on the range

of thermal resistances constituting the thermal model, both in the radial and axial directions. The application of individual machine operating power losses to specific thermal model nodes is reasoned and the implications of the airflow on the model are covered. Finally, the addition of thermal capacitances to enable transient thermal simulations is explained.

Chapter 4 reviews the iron loss finite element analysis performed. Two-dimensional synchronous machine finite element model development and simulation settings are detailed. Iron loss information is extracted from the finite element solution and, in particular, the distribution of these losses across the rotor and stator laminations is revealed. Results are translated into iron loss re-distribution coefficients, which are implemented in the lumped parameter thermal models created. Limitations and deficiencies associated with the finite element analysis work executed are highlighted.

In Chapter 5 thermal model discretisation level issues are discussed. In particular, the importance of discretisation levels when modelling poor thermally conducting machine windings is analysed. MySolver's approach to winding discretisation, without the need for any experience based estimating formulas, is explained.

Chapter 6 presents the MySolver lumped parameter based thermal modelling tool. Its operation is overviewed and software components are stated.

Chapter 7 explains how the experimental verification stage is performed. The test rig and test bench components used to thermally analyse the synchronous generator are detailed. Specifically, the complications associated with reading k-type rotor winding embedded thermocouples are explained and a method to resolve the problematic unavoidable heat junctions is presented. The chapter emphasises the delicate considerations required when dealing with k-type thermocouples for any thermal investigation.

Chapter 8 analyses and assess the thermal data collected from the synchronous machine test rig for a wide range of operating conditions. All thermocouples are examined and the thermal characteristic of the synchronous generator is obtained. MySolver operation is validated against the experimental data collected and its ability to accurately model specific machine segments and the generator as a whole is discussed.

Chapter 9 evaluates and discusses the topics covered in the thesis, in order to objectively evaluate lumped parameter thermal modelling. MySolver specific issues related to the airflow, discretisation level and unclear thermal modelling areas are covered, together with MySolver overall limitations. Possible thermal modelling alternatives are also discussed. MySolver's use as an electrical machine thermal optimisation tool is assessed and illustrated. Finally, additional experiments providing further insight on the synchronous machine's thermal behaviour are presented and analysed.

To conclude, Chapter 10 summarises the main points from the work covered in this thesis and draws a final conclusion on MySolver's performance and lumped parameter thermal modelling in general. The thesis terminates with further work suggestions, which have the potential of enhancing the work carried out.

CHAPTER 2

Electrical Machine Thermal Modelling

2.1 Traditional Electrical Machine Thermal Modelling

The lack of attention received by thermal modelling in the past means that traditional electrical machine thermal design methods were mainly based on a single parameter, such as, thermal resistance, material heat transfer coefficients or winding current density. Material temperature indices were used to identify the lowest rated material, based on which the whole system was rated. This proved to be inaccurate in many cases, due to the fact that a single parameter fails to describe the complex nature of motor cooling. Furthermore, the insight provided by such techniques does not allow for machine thermal improvements to be made. The use of thermal data derived from tests on existing motors, competitor catalogue data and even from simple rules of thumb have also been a common ineffective practice. The problem is that published data of heat transfer coefficients for electric machines varies greatly, as illustrated in Figure 2.1 [11], [14] & [15].

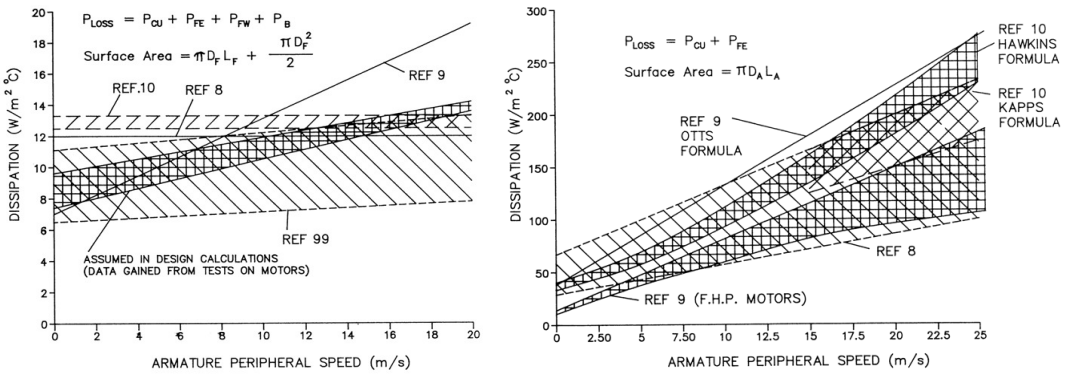

Figure 2.1: *Heat dissipated from frame surface of totally enclosed motor (left) and from armature surface of self ventilated motor (right) [11].*

Shown in Figure 2.1 is the information, provided by several sources, on the heat dissipated from the frame surface of a totally enclosed motor and from the armature surface of a self ventilated motor, with respect to armature peripheral speed. The difficulty in deciding which set of data to use is clear, with a wide range of contradicting information available. The electrical machine designer's decision at this point is of paramount importance, as it will determine the machine's size greatly. Size, in turn, will unquestionably limit the machine's application opportunities. As a result of this poor designing technique, there is a high chance of over-designing the electrical machine and, unfortunately, the user gains little insight on where future design efforts should be concentrated. More recently, the International Electrotechnical Commission (IEC) introduced improvements to these greatly limited modelling techniques, by adopting UL (Underwriters' Laboratories) Systems ratings [16] for electrical insulation, which take into account the synergistic effects between machine components. Although improving thermal design, completely satisfying thermal modelling did not result [11].

2.2 Modern Electrical Machine Thermal Modelling

Modern computer aided design packages can now be used to design the thermally relevant features of electric machines in an iterative manner with the electromagnetic design [17]-[19]. These software tools achieve a model which is true to the specific machine under investigation. Accurate characteristics, in terms of size, weight, output, efficiency, cost and lifetime can be achieved with them and development times and prototype costs greatly reduced as a consequence of this. Typical uses of thermal analysis today include design optimisation, sensitivity analysis, rapid response to customer enquiries, fast quantification of design changes and parameter estimation. By thermally optimising a particular design, in parallel with electromagnetic and mechanical design, the best possible machine can be developed and inevitable losses can be directed to the easiest route out of the machine [20]. For an electrical machine design and manufacturing company, these new techniques will

result in an increase in customer confidence and will inevitably lead to a rise in order numbers.

At first, a designer may not be aware of the most significant design variables affecting thermal performance and might be concentrating efforts on areas of the machine that have no significant thermal importance. Modern electrical machine thermal modelling tools have the potential of preventing this. Additionally, some modern tools allow customer wishes to be evaluated promptly, as the designer will immediately gain feedback on whether the electric machine analysed is suitable for the required task. In the same way, if a change in a machine component material or in the manufacturing procedure is suggested in order to improve performance or productivity, thermal analysis packages allow for a quick quantification of the implications that such changes could have. Advantages and deficiencies of the proposed alterations will be easily highlighted [21].

On the whole, it seems clear that it is fundamental for designers to be aware of the effect, if any, that machine parameters will have on thermal performance, and modern thermal analysis tools allow this. Today's thermal design techniques can be divided into two groups: analytical lumped circuit analysis and numerical analysis methods. The two numerical analysis methods available are finite element analysis (FEA) and computational fluid dynamics (CFD) [14].

In the last few years, there has been a growing awareness on the fact that thermal considerations are essential when designing more efficient physically smaller electric machines. Many papers have been published, mostly related to induction machines, discussing methods to improve understanding, modelling and approach to the thermal distribution within a machine [2], [9] & [22]-[24]. From the literature it is clear that both analytical and numerical methods provide thermal modelling benefits and should be carefully considered by machine designers. The flow diagram displayed in Figure 2.2 outlines the designing process that could lead to an ideal optimised machine. The iterative presence of analytical and numerical design steps in order to account for electromagnetic and thermal factors is presented as the correct

approach. The emphasis here is in proposing that analytical and numerical modelling techniques should not compete against each other, but be merged in to the same designing process. The speed calculation advantage characterising analytical tools should be combined with the greater accuracy provided by numerical methods. For example, CFD techniques are excellent for predicting flow in complex areas of the design [25], such as the open fin leakage. This method should be implemented to model difficult sections of the thermal design and develop functional relationships that can be used in the faster lumped circuit analysis. As a result of this effective combination, machine parameters optimisation will be possible and uncomplicated. In particular, a considerable reduction in machine size will be allowed [7] & [23].

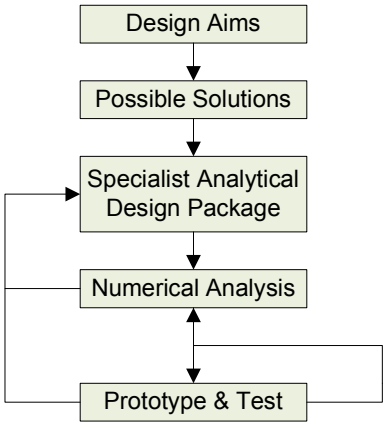

Figure 2.2: *Ideal thermal modelling design process [7].*

An important issue to consider, affecting both numerical and analytical modelling techniques, is the effect that the electrical machine manufacturing and assembly process has on thermal resistances, since this can be significant in some cases [1] & [26]. For example, the thermal resistance between the stator lamination and the machine housing can be influenced by the method utilised to place the stator in the machine housing. Therefore, extensive input by experienced electrical machine manufacturers is very important and irreplaceable [14].

2.2.1 Numerical Thermal Modelling Methods

Thermal modelling numerical analysis techniques have the potential of providing highly accurate solutions. Any electrical machine geometry can be modelled utilising numerical analysis, at the expense of complicated thermal model setup and extensive computational times [14]. Numerical thermal modelling can be segmented into two separate methods: FEA and CFD.

Finite Element Analysis

FEA is a widely used thermal modelling method, utilised to accurately model heat transfer through conduction along and across electrical machine sections, as well as perform electromagnetic analysis [27]-[29]. Limiting FEA, with respect to CFD, is its incapability to take fluid flow into account, which means that convection heat flow must be modelled using specific boundary conditions (heat transfer coefficient input for solid / fluid boundaries) [11]. Similarly to analytical lumped parameter thermal modelling, limited or inaccurate geometric or material properties knowledge can result in misleading FEA solutions and, therefore, reliable input information is very important [14].

The principle behind FEA is a system of partial differential equations [18] & [30]. Other than the work presented in Chapter 4, where FEA is utilised to predict synchronous generator iron loss lamination distributions and the related thermal effects, all other FEA considerations are out with the scope of this thesis.

The high degree of heat transfer conduction detail associated with FEA is illustrated in Figure 2.3, where the non-trivial slot copper conductor temperature distribution is clearly displayed [31]. Unfortunately, long execution times are FEA's greatest weakness, making it unsuitable to accomplish the project objectives established in Chapter 1. Furthermore, the inability to take cooling airflow into account greatly limits FEA as a universal stand alone thermal modelling tool and is, therefore, recommended exclusively for individual isolated thermal studies of machine

geometries too complex to model utilising lumped parameter thermal methods. In addition to this, the modelling of interface gaps between components proves complicated [1].

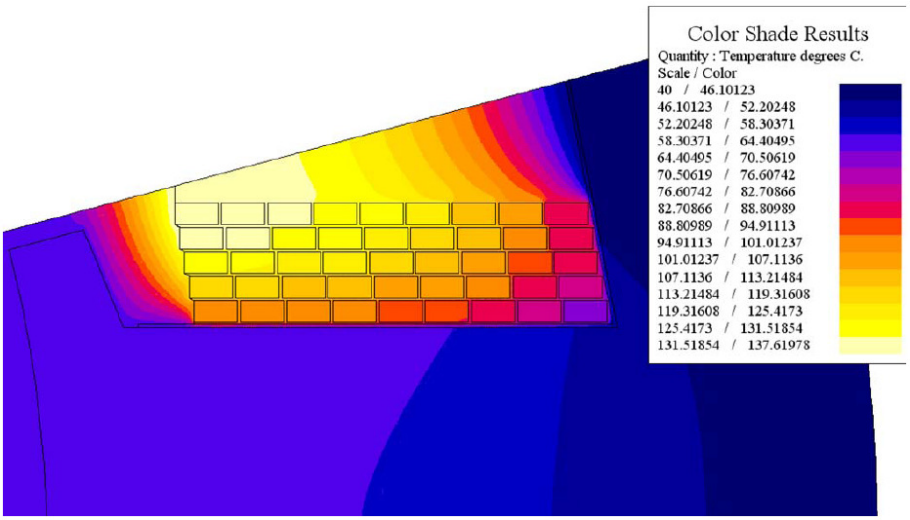

Figure 2.3: *FEA two-dimensional steady-state temperature rise in slot with rectangular copper conductors [31].*

Computational Fluid Dynamics

CFD is a numerical technique for the simulation of fluid flow and heat transfer. Similarly to FEA, it works on the basis of solving a series of coupled, non-linear, second order, partial differential equations known as the conservation equations, which correspond to velocity, pressure and temperature. Differently to FEA, CFD can model both conduction and convection, being a more popular appropriate option and a realistic competition for analytical methods as a single stand alone thermal modelling tool. The CFD machine model is subsequently subdivided into small finite elements or volumes and boundary conditions are applied, allowing flow and electrical machine temperatures to be determined [32].

There is a selection of CFD packages commercially available, although these are not trivial to use and require in-depth knowledge in order for representative machine

thermal models to be setup accurately [14]. Furthermore, the high computational requirements associated with CFD disregard it as a fast immediate feedback thermal modelling too. Typical CFD outputs, illustrating the highly detailed results, are pictured in Figure 2.4 for a totally enclosed fan cooled electrical machine.

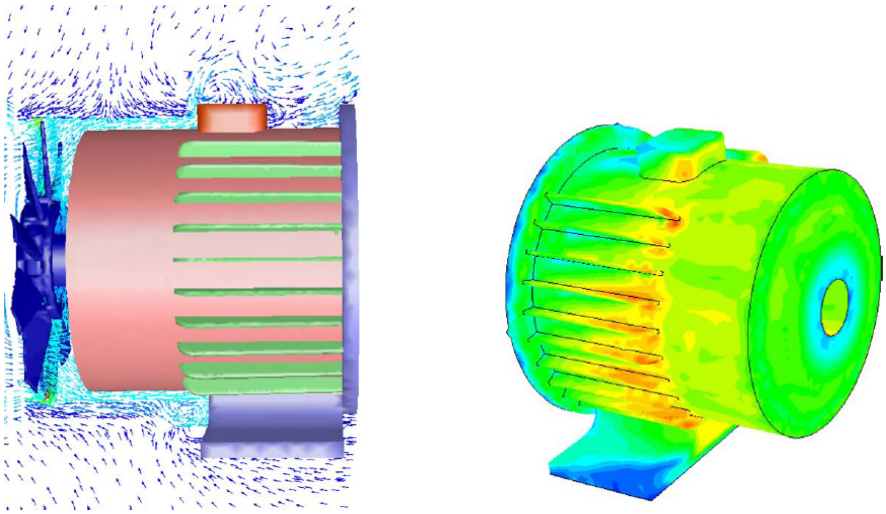

Figure 2.4: *TEFC synchronous generator CFD output example [20].*

Overall, CFD is an accurate technique, although as with the rest of thermal modelling techniques considered, special attention must be taken when implementing interface gaps, boundary conditions and different model types. Furthermore, turbulent flow is complicated to model with a high degree of accuracy. CFD's great incentive is that designers gain an immense insight as to where the thermal design of the machine might be compromised. Nevertheless, this high degree of detail comes at the expense of very extensive problem definition, execution and post-processing times, particularly when trying to model the complete electrical machine. These excessive time constraints are a decisive disadvantage for CFD, making an alternative method to achieve the project objectives essential. Therefore, this opens the door for less accurate analytical lumped parameter thermal modelling techniques [11].

2.2.2 Analytical Lumped Parameter Thermal Modelling Method

Analytical lumped parameter thermal modelling provides the very fast, user friendly, thermal design tool demanded in the project objectives and, hence, is identified and selected as the operational core of the thermal modelling tool to be developed. Short problem definition, execution and post-processing times are linked with lumped parameter thermal modelling, which are very attractive properties for a thermal modelling package. Since lumped parameter thermal modelling is based on a thermal arrangement very similar to an electrical layout, it is very easily comprehended. Lumped parameter thermal networks are made up of thermal resistances rather than electrical resistors, power sources instead of current sources, thermal capacitances in the place of electrical capacitors, nodal temperatures rather than voltages and power flow through resistances instead of current. The simplicity of the model helps the designer's understanding, particularly those with an electrical engineering background, and encourages thermal optimisation of the electrical machine analysed. The resulting nodal thermal network lumps electrical machine sections together, subject to the discretisation level established, with temperatures for the nodal segments computed. Extensive work has been carried out in this area of study, although recently analytical thermal analysis specific to synchronous generators has not been tackled in detail [33]-[39].

The thermal resistances on the circuit represent one of three heat transfer paths in the machine: conduction, convection and radiation. These are calculated utilising widely used heat transfer correlations, easily available from many literature sources and higher academic textbooks. Information from these sources is utilised throughout this chapter and thesis [40]-[44].

Conduction Heat Transfer

Conduction is the heat transfer mode in a solid due to temperature differences between different parts of a material. Conduction also occurs in liquids and gases, but convection is usually dominant in these cases. Heat transfer takes place from higher to lower temperature areas and is caused by the motion of molecules within the material. Good electrical conductors are also good thermal conductors.

Fourier's Law, in Equation 2.1, is behind conduction heat transfer, where $Q_{Conduction}$ is the rate of conduction heat transfer (W), k is the thermal conductivity of the material (W/m/°C), A is the cross-sectional heat transfer area (m^2) and dT/dx is the temperature gradient (°C/m).

$$Q_{Conduction} = -k \cdot A \cdot \frac{dT}{dx} \tag{2.1}$$

Metals have a high thermal conductivity, due to their crystalline structure, with k being in the range of 15 to 400 W/m/°C. On the other hand, insulators do not have a structure that favours thermal exchange, since they are often porous in nature, with k in the range of 0.1 to 1 W/m/°C [11].

Lumped parameter thermal circuit representation:

In lumped parameter thermal networks purely conductive thermal paths can be represented by the thermal resistance correlation illustrated in Equation 2.2, where $R_{Conduction}$ is the thermal resistance (°C/W), l the length of the conductive path, k is the conduction thermal conductivity of the material (W/m/°C) and A is the cross-sectional heat transfer area (m^2) [12] & [45].

$$R_{Conduction} = \frac{l}{k \cdot A} \tag{2.2}$$

Convection Heat Transfer

Heat is transferred by convection between a surface and a fluid. Energy exchange takes place between the surface and the fluid immediately adjacent to it. Fluid circulation, driven by the temperature gradient, takes place as a result of this and an automatic circulation system arises. There are two types of convection, natural convection, where fluid movements occur merely due to the change in density of the fluid itself, and forced convection, where fluid motion is caused, or enhanced, by an external force such as a fan. In practice, both of these mechanisms take place simultaneously and a mixed heat transfer coefficient of these two convection types occurs [46]. Within natural and forced convection two sub-divisions exist. Laminar flow, which is the streamline flow that exists at lower velocities and in the area bordering the high temperature surface, and turbulent flow [47], which describes the formation of eddies at higher speeds.

Newton's Law, shown in Equation 2.3, explains the mechanism behind convection heat transfer, where $Q_{Convection}$ is the rate of convection heat transfer (W), h_c is the convection heat transfer coefficient (W/m^2/°C), A is the cross-sectional heat transfer area (m^2) and $(T_1 - T_2)$ is the temperature difference between surface and fluid (°C).

$$Q_{Convection} = h_c \cdot A \cdot (T_1 - T_2) \tag{2.3}$$

A challenging difficulty arises in predicting the value of the heat transfer coefficient, h_c. It proves complicated to determine and can vary greatly depending on the convection type. The quantity of convection between a surface and fluid is affected by many issues. Factors like the shape and size of the solid-to-fluid boundary and the characteristics of fluid flow and fluid material have a key influence on the convection process. Convection is complex in nature and cannot be easily solved mathematically. An empirical technique of dimensional analysis, based on experimental data, is used instead. Many empirical dimensionless correlations exist in technical literature available to engineers, who can use these to analyse convection for particular geometric shapes [40], [41] & [48]. These correlations are used in a

process called dimensional analysis. The technique involves using a collection of dimensionless numbers to obtain a functional relationship for h_c and the relevant physical properties and fluid parameters of the air flow present. The set of dimensionless numbers available to thermal design engineers are presented in Table 2.1. The transition from laminar to turbulent flow is determined by Reynolds number (*Re*) in forced convection systems, while the product of Grashof's number and Prandtl's number (*Gr.Pr*) settles this shift in natural convection systems [46].

Dimensionless Number	Applicability	Formulation	
Reynolds number, *Re*	Inertia force / Viscous force	$Re = \rho v l / \mu$	(2.4)
Grashof number, *Gr*	Buoyancy force / Viscous force	$Gr = \beta g \theta \rho^2 l^3 / \mu^2$	(2.5)
Prandtl number, *Pr*	Momentum / Diffusivity for a fluid	$Pr = c_p \mu / k$	(2.6)
Nusselt number, *Nu*	Convection / Conduction heat transfer	$Nu = h L / k$	(2.7)

Table 2.1: *Dimensionless number formulations [46].*

where ρ is fluid density (kg/m^3), v is fluid velocity (m/s), l is the surface length (m), μ is fluid dynamic viscosity (kg/s.m), β is the fluid coefficient of cubical expansion (litres/°C), g is the gravitational force of attraction (m/s^2), θ is the temperature difference between surface and fluid (°C), c_p is the specific heat capacity of the fluid (kJ/kg/°C), k is the thermal conductivity of the fluid (W/m/°C) and h the heat transfer coefficient (W/m^2/°C).

The convection correlations for natural and forced heat transfers are illustrated in Equations 2.8 and 2.9 respectively, where a, b and c are constants [1].

$$Nu_{Natural} = a\,(Gr.Pr)^{b} \tag{2.8}$$

$$Nu_{Forced} = a\,.\,(Pr)^{c}.\,(Re)^{b} \tag{2.9}$$

Lumped parameter thermal circuit representation:

Within lumped parameter thermal modelling convection thermal resistances are represented by Equation 2.10 [49], where $R_{Convection}$ is the convection thermal resistance (°C/W), and h_c the heat transfer coefficient (W/m^2/°C) and A is the cross-

sectional heat transfer area (m^2). Additionally, h_c is obtained rearranging the Nusselt number correlation utilising Equation 2.11 [42], where Nu_D is the Nusselt number related to the specific hydraulic diameter, k_{air} is air thermal conductivity (W/m/°C) and D_h is the hydraulic diameter (m).

$$R_{Convection} = \frac{1}{h_c \cdot A} \tag{2.10}$$

$$h_c = Nu_D\left(\frac{k_{air}}{D_h}\right) \tag{2.11}$$

Two literature formulations for Nu_D are extracted from relevant literature (Equations 2.12 and 2.13) and utilised in the lumped parameter thermal modelling tool developed in this thesis. Equation 2.12 is a historically widely utilised correlation and Equation 2.13 a more modern formula, taking friction into account via friction coefficient, f_{coef}, obtained using Equation 2.14 [42].

$$Nu_D = 0.023 \cdot \mathrm{Pr}^{\frac{1}{3}} \cdot \mathrm{Re}_D^{0.8} \tag{2.12}$$

$$Nu_D = \frac{\frac{f_{coef}}{8} \cdot (\mathrm{Re}_D - 1000) \cdot \mathrm{Pr}}{1 + 12.7\sqrt{\frac{f_{coef}}{8}}\left(\mathrm{Pr}^{\frac{2}{3}} - 1\right)} \tag{2.13}$$

$$f_{coef} = \frac{1}{(1.82 \log_{10} \mathrm{Re}_D - 1.64)^2} \tag{2.14}$$

The equations presented in this section are utilised in Chapter 3, for the development of the lumped parameter thermal networks for the synchronous generator investigated and examples on their use are given.

Radiation Heat Transfer

Radiation is the process by which energy is transferred through electromagnetic waves from a surface. This is owed to the fact that electrons on the surface of the radiating material vibrate due to a high amount of energy being stored in them. Therefore, the absolute temperature of the body will determine how much radiation takes place.

The Stefan-Boltzmann's correlation, given in Equation 2.15, defines radiation heat transfer, where $Q_{Radiation}$ is the rate of radiation heat transfer (W), σ is the Stefan-Boltzmann constant (5.67×10^{-8} W/m^2/°C^4), A is the cross-sectional area (m^2) and T the absolute temperature of the surface (K) [22].

$$Q_{Radiation} = \sigma \cdot A \cdot T^4 \tag{2.15}$$

Equation 2.15 describes energy emission via radiation from a surface. This surface will normally be absorbing radiation at the same time it radiates heat. Equation 2.16 computes the resulting radiation exchange between two surfaces, A_1 and A_2. Where ε is the emissivity of the surface ($\varepsilon \leq 1$), $F_{1\text{-}2}$ the view factor of surface 2 with respect to surface 1 ($F_{1\text{-}2} \leq 1$) and T_1 and T_2 are the absolute temperatures of surfaces 1 and 2 respectively (K) [42].

$$Q_{Radiation} = \sigma \cdot A \cdot \varepsilon \cdot F_{1-2} \cdot (T_1^4 - T_2^4) \tag{2.16}$$

Lumped parameter thermal circuit representation:

For lumped parameter thermal modelling radiation thermal resistances are obtained using Equation 2.17, where $R_{Radiation}$ is the radiation thermal resistance (°C/W), and h_R the heat transfer coefficient (W/m^2/°C) and A is the cross-sectional heat transfer area (m^2). Furthermore, h_R is computed by Equation 2.18, leading to the final Equation 2.19. Specific information on the parameters comprising the presented equations is widely given in basic engineering textbooks [14], [22] & [50].

$$R_{Radiation} = \frac{1}{h_R \cdot A} \tag{2.17}$$

$$h_R = \frac{\sigma \cdot \varepsilon_1 \cdot F_{1-2} \cdot (T_1^4 - T_2^4)}{T_1 - T_2} \tag{2.18}$$

$$R_{Radiation} = \frac{T_1 - T_2}{\sigma \cdot A_1 \cdot \varepsilon_1 \cdot F_{1-2} \cdot (T_1^4 - T_2^4)} \tag{2.19}$$

Lumped Parameter Network Airflow Network Issues

The development of an electrical machine cooling airflow network is out with the scope of this thesis. Airflow information required to compute the convection thermal resistances heat transfer coefficients discussed in this chapter are provided by Cummins Generator Technologies, manufacturers of the synchronous generator investigation in this work. Extensive electrical machine airflow network work has been carried out to date [51]-[54] although, following the through ventilating airflow discoveries presented in this work (Chapter 8), additional detailed work is recommended. Details of this are given in the suggested further work section in Chapter 10.

Similarly to the thermal network heat transfer components described in this chapter, a flow network can be developed based on turbulent airflow Equation 2.20, and resembles an electrical circuit, with pressure (P (Pa)) being equivalent to voltage, volume flow rate (Q (m^3/s)) to current and flow resistance (R (kg/m^7)) to electrical resistance [46].

$$P = R \cdot Q^2 \tag{2.20}$$

Furthermore, within an airflow network, flow resistances (R) can be modelled using the relationship in Equation 2.21, where k_f is a dimensionless fluid coefficient

depending on the specific nature of the airflow resistance (obstruction, expansion, contraction, etc.), ρ is density (kg/m^3) and A is the cross-sectional heat transfer area (m^2). Numerous formulations for k_f are detailed in relevant literature [14], [55] & [56]. As stated, further airflow network related considerations are out with the scope of this work.

$$R = \frac{k_f \cdot \rho}{2 \cdot A^2} \tag{2.21}$$

An important flow related computation in the development of a lumped parameter thermal network is the heat flow picked up by the airflow as it travels along the axial length of the electrical machine, and the fluid temperature rise this causes. The air *Heat Flow* (W) is determined by Equation 2.22 [42], where R is the thermal resistance (°C/W) and ΔT is the temperature difference across the airflow resistance (°C) [57]-[59].

$$Heat\ Flow = \frac{\Delta T}{R} \tag{2.22}$$

Hence, using standard fluid temperature rise (ΔT) Equation 2.23 [11], where c_p is the specific heat capacity (J/kg/°C), results in the airflow heat pickup resistive correlation, shown in Equation 2.24. This resistive component is utilised as outlined in Chapter 3.

$$\Delta T = \frac{Power\ Dissipated\ (W)}{Volume\ Flow\ Rate\ (m^3/\mathrm{s}) \cdot Density(kg/m^3) \cdot c_p} \tag{2.23}$$

$$R_{Flow} = \frac{1}{Volume\ Flow\ Rate\ (m^3/\mathrm{s}) \cdot Density(kg/m^3) \cdot c_p} \tag{2.24}$$

Thermal Capacitances

In order to enable transient lumped parameter thermal modelling, thermal capacitances need to be added to the thermal network at each nodal point with a power loss input. Such thermal capacitances are computed using Equation 2.25 [22] and satisfy thermal time constant Equation 2.26. These are applied to the lumped parameter thermal network in Chapter 3.

$$C = \rho \cdot V \cdot c_p \tag{2.25}$$

$$\tau = R \cdot C \tag{2.26}$$

where C is the thermal capacitance (J/m^3/°C), ρ is density (kg/m^3), V is volume (m^3), c_p is the specific heat capacity (J/kg/°C), τ is the thermal time constant (s) and R is the thermal resistance (°C/W).

2.3 Synchronous Machine Power Losses

Understanding the power losses associated with an electrical machine, their behaviour and distribution is of paramount importance when evaluating machine performance and thermal distribution. In this thesis, this refers to power losses related to a synchronous generator. Machine operational power losses create heating effects in the electrical machinery and vice versa. For a designer it is essential to be aware of loss heat paths and source points in order to develop an effective electrical machine thermal model. As discussed in this chapter, losses have important implications in the size, initial cost and longevity of the electric machine [60]. Factors such as operating temperature, rotational speed, voltage and frequency can influence losses and should therefore be carefully considered. The power losses to be considered when thermal modelling a synchronous generator are listed below and outlined in this section. The calculation and application of these losses to the synchronous machine lumped parameter thermal model is detailed in Chapter 3.

Main synchronous machine losses:

- Copper losses.
- Iron losses.
- Mechanical losses: Friction and windage.
- Stray losses.

Copper Losses

Copper losses are straight forward to predict accurately, since they are calculated and quantified by measuring the rms currents flowing in the excitation and stator windings whilst under load, and calculating the product of square of this current and the resistance of the winding [60]. As shown in Chapter 3, these are winding lumped parameter nodal input power losses.

Iron Losses

Iron losses in synchronous machines are complicated to estimate, since they have a high frequency and magnetic flux dependency [61]. Iron losses are composed of hysteresis losses and eddy-current losses. Hysteresis losses are a function of frequency and of the maximum flux density per pole, given that the air-gap flux is mainly sinusoidal. On the other hand, eddy-current losses depend on the squared magnitude of frequency and maximum flux density [61]-[63]. The analysis of iron losses is an important part of this thesis and is, therefore, discussed in detail in Chapter 4. Iron losses are input into the lamination nodes of the electrical machine lumped parameter model.

Mechanical Losses

Mechanical losses are dependent on motor speed and relate to friction in bearings and windage. It is acceptable to assume that both of these losses remain at a constant level for a given machine rotational speed, regardless of the load [60] & [64]. Windage losses are located in rotor blades and in the cooling fan, with the latter being more significant in term of heat generation, but both prove complicated to remove without affecting the manufacturing process excessively. Mechanical losses can be experimentally estimated as outlined in Section 4.2.1. Further details on mechanical losses are outside the scope of this thesis.

Stray Losses

In general, stray losses are quantified as the mismatch between calculated and measured loss values. In an alternator, stray losses can be sub-divided into various categories, for example, eddy current losses in the stator conductors due to slot leakage flux or end region losses due to end leakage flux and pole face losses. Furthermore, stray losses include the losses linked with the damper bars present across the rotor laminations. Mainly, stray losses comprise of variations of known iron losses. They are considered to be any losses caused by non-sinusoidal, non-fundamental flux density variations [60] & [65].

A considerable amount of literature exists illustrating the difficult and ambiguous nature of stray losses [66]-[71]. In the synchronous generator lumped parameter thermal model developed in Chapter 3, stray losses are predicted utilising an estimation formula provided by the electrical machine manufacturer. Further stray losses discussions are out with the scope of this thesis.

2.4 Chapter Summary

Traditional and modern electrical machine thermal modelling techniques are presented and discussed in this chapter. Advantages and disadvantages of current thermal modelling methods are stated. In order to realise the objectives established in Chapter 1, analytical lumped parameter thermal modelling is selected as an ideal tool to construct the required precise, universal, user friendly, quick feedback, thermal modelling tool. The principles behind lumped parameter thermal modelling are covered, including the relevant thermal resistances, thermal capacitances and machine power losses. These modelling principles are subsequently expanded, explained in further detail and utilised to develop the synchronous generator thermal models in Chapter 3.

CHAPTER 3

Lumped Parameter Thermal Modelling

3.1 Introduction to Lumped Parameter Thermal Modelling

Utilising the thermal modelling principles presented in Chapter 2 and carefully weighing the advantages and disadvantages of each one of the electrical machine thermal modelling techniques outlined, lumped parameter models are identified as the ideal method for developing the operational core of the specific thermal modelling tool required, as reasoned in Chapter 2. The flexible nature of lumped parameter thermal modelling and, particularly, its fast computation time makes this method ideal to accommodate the thermal modelling additions covered in this thesis and generate a fast user friendly thermal modelling package.

In this chapter the rotor and stator lumped parameter thermal models are developed. The general process by which the rotor and stator geometries are translated into the relevant thermal networks is presented. Furthermore, the specific electrical machine analysed, the BCI184E Cummins Generator Technologies (CGT) synchronous generator specially modified prototype, is introduced. The specific thermal networks for this alternator are calculated in this chapter, but the principles outlined and the thermal network structures constructed are applicable to any electrical machine, once any minor modifications related to specific machine characteristics are accounted for. Finally, the important machine operational losses related to the synchronous generator, airflow issues and transient analysis network additions are discussed and their lumped parameter thermal mode implications stated.

It is important to note at this stage that the rotor and stator thermal resistances in the radial direction take into account the insulation present around individual copper

strands. For this reason, the thermal conductivity of the winding in the radial direction is greatly reduced. When modelling conduction thermal resistances in the preferential axial direction, standard copper thermal conductivities are utilised, since the mentioned copper conductor insulations have no effect. Similarly, when modelling lamination sections, the laminated nature of these affects thermal conduction in the axial direction, whilst it has no effect in the preferential radial direction. This has been taken into account in the thermal modelling performed.

As shown by the sensitivity analysis results presented in Table 3.1, slight variations (± 10 %) in the thermal conductivities utilised in the lumped parameter thermal modelling described, have a relatively small effect on the overall average rotor and stator temperatures predicted.

Parameter	Δ Parameter	Δ Average Temperature (°C)	
		Rotor	Stator
Rotor coil radial thermal conductivity	+ 10 %	- 0.79	-
	- 10 %	+ 0.94	-
Rotor coil axial thermal conductivity	+ 10 %	- 0.01	-
	- 10 %	+ 0.02	-
Rotor lamination radial thermal conductivity	+ 10 %	- 0.21	-
	- 10 %	+ 0.24	-
Rotor lamination axial thermal conductivity	+ 10 %	- 0.02	-
	- 10 %	+ 0.02	-
Stator coil radial thermal conductivity	+ 10 %	-	- 1.36
	- 10 %	-	+ 1.68
Stator coil axial thermal conductivity	+ 10 %	-	- 0.01
	- 10 %	-	+ 0.01
Stator lamination radial thermal conductivity	+ 10 %	-	- 0.39
	- 10 %	-	+ 0.46
Stator lamination axial thermal conductivity	+ 10 %	-	- 0.02
	- 10 %	-	+ 0.02
Rotor and stator winding insulation thermal conductivity	+ 10 %	- 0.10	- 0.25
	- 10 %	+ 0.11	+ 0.31
Rotor and stator lamination resin thermal conductivity	+ 10 %	- 0.04	- 0.07
	- 10 %	+ 0.06	+ 0.09

Table 3.1: *Rotor and stator thermal conductivity sensitivity analysis results.*

3.2 Cummins Generator Technologies BCI184E Synchronous Generator Prototype

The electrical machine utilised in the study is a specially modified 22.5 kVA CGT BCI184E, 50 Hz, 415 V, synchronous generator prototype, similar to the commercialised standard BCI184E electrical machine shown in Figure 3.1. The BCI184E generator is used in a wide range of low power application, due to its easy installation and maintenance, and typical uses of the alternator include combined heat and power supply, telecommunications, marine and offshore applications and as a standby power supply. The alternator is a standard 4-pole, self-excited (sustained short circuit capability), AVR (CGT, SX460 AVR) controlled electrical machine, which can be supplied with one or two sealed bearings. Machine windings are class 'H' insulated; with the armature wound to 2/3 pitch. Relevant electrical machine data sheets can be found in Appendix A [72].

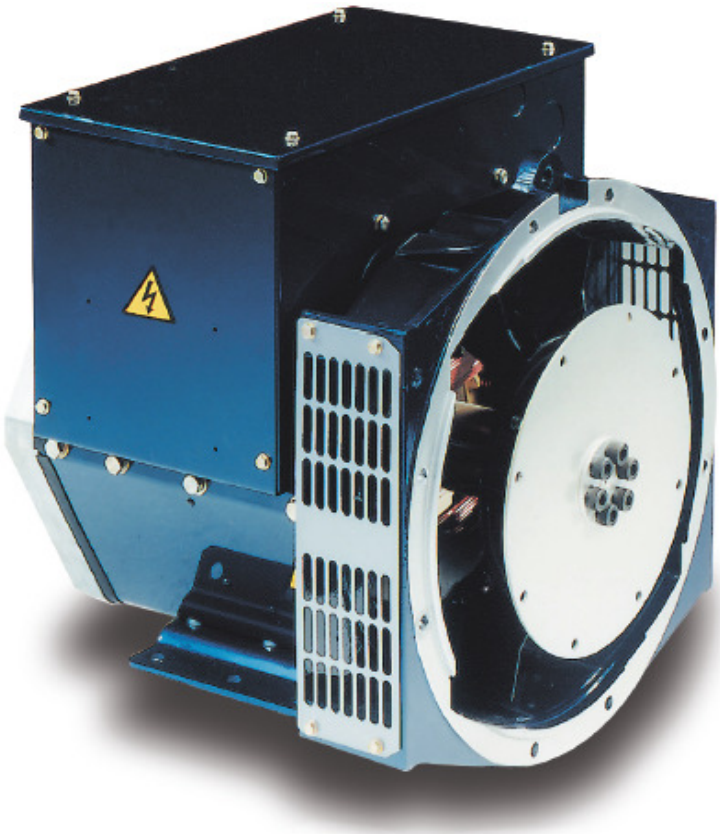

Figure 3.1: *Cummins Generator Technologies BCI184E synchronous generator.*

Lumped parameter thermal model implications for the BCI184E generator are discussed in Sections 3.3 and 3.4 for the rotor and stator respectively, with airflow implications presented in Section 3.6, thermal network machine losses discussed in Section 3.7 and the required transient analysis thermal network modifications outlined in Section 3.8. In addition, all aspects that affect the estimation of iron losses using finite element analysis, such as the stator winding pitch factor, are covered in Chapter 4.

3.3 Rotor Thermal Modelling

In order to create the rotor lumped parameter thermal network, the necessary electrical machine component information needs to be collected. Figure 3.2 indicates the electrical machine geometries that need to be obtained from detailed machine drawings or generator manufactures. Figure 3.2 is not to scale and the dimensions and shapes of rotor laminations and windings can vary significantly between electrical machines modelled. The geometric dimensions labelled illustrated over the rotor cross-section diagram are detailed in the table in Figure 3.2, with coil insulation and resin coat thicknesses also encapsulated. These values are also important to model the heat exchange between insulated rotor segments and from coated rotor sections to the surrounding airflow.

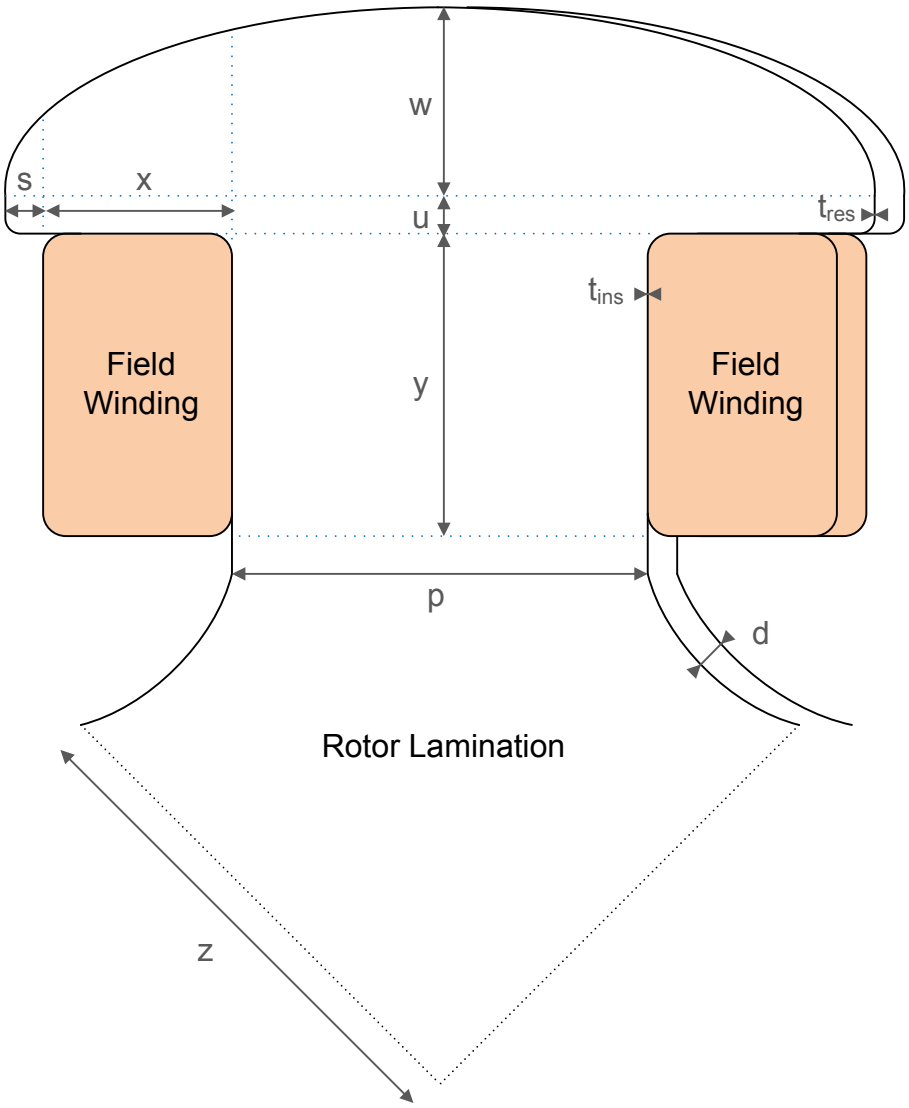

Rotor section	Section label	Rotor section	Section label
Coil width	x	Pole shoe middle height	w
Coil height	y	Inner lamination width	z
Pole middle width	p	Coil insulation thickness	t_{ins}
Pole shoe extension	s	Resin coat thickness	t_{res}
Pole shoe side height	u	Axial depth of model	d

Figure 3.2: *Rotor lamination and winding prototype parameters.*

The geometric data presented in Figure 3.2 can be translated into the required two-dimensional lumped parameter thermal resistance network. This network, superimposed on the rotor layout, is shown in Figure 3.3, with the rotor lamination and windings represented by a simple, easily understood, network of thermal

resistors. As indicated by the figure key, the internal network resistances, not in contact with the surrounding airflow (Ø), represent fully conductive heat transfer paths, whilst the resistances on the network edges, coloured in blue, correspond to the convection heat paths away from the rotor. The calculation of these resistances, using the principles presented in Chapter 2, is covered in this chapter.

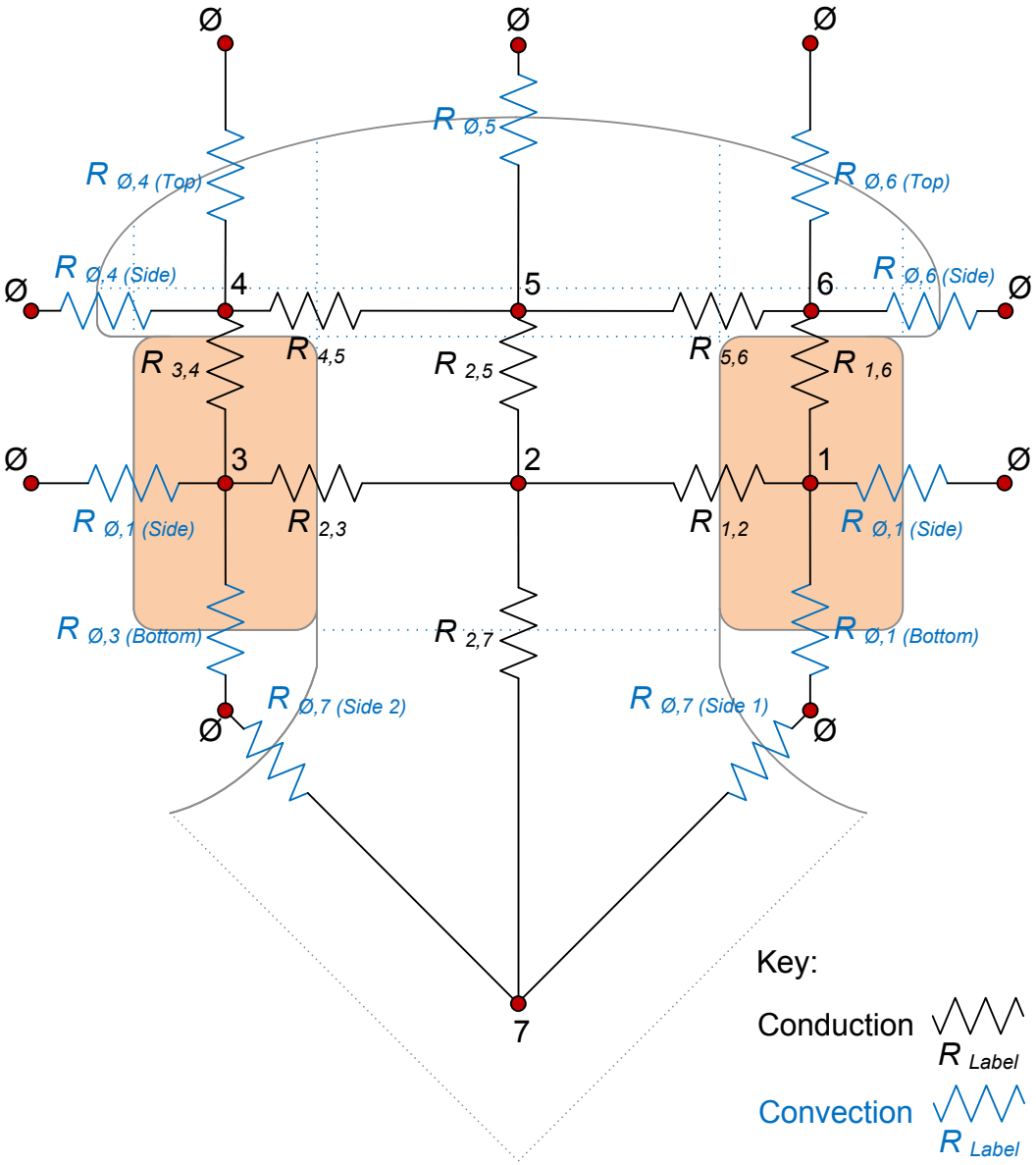

Figure 3.3: *Rotor lumped parameter thermal resistance network.*

In addition to the geometric data outlined in Figure 3.2, material conductivity (W/m/°C) for thermal conduction, and heat transfer coefficient values (W/m^2/°C) for thermal convection, are required in order to obtain the resistance values needed to generate the rotor lumped parameter thermal network presented in Figure 3.3. This data should be collected from machine manufacturers, material suppliers or experimentally, where possible. Detailed air flow analysis is out with the scope of this thesis and heat transfer coefficients are calculated using the well established equations presented in Chapter 2 and utilised in this chapter, in Section 3.6.

3.3.1 Rotor Lumped Parameter Network Calculations

Examples for the calculation for each type of thermal resistance illustrated in Figure 3.3 are presented in this section, along with the formulas required and the resulting resistances for the CGT machine prototype, which are collected at the end of each section and later used by the MySolver modelling tool to obtain the thermal results presented and analysed in Chapters 8 and 9.

Rotor Conduction Lumped Parameter Resistance

Using Equation 3.1, from Chapter 2, and the relevant geometric and thermal data, the values of the conductive resistances in the thermal network in Figure 3.3 are calculated and shown in Table 3.2. It should be noted that, as explained in Section 3.5, the core length of the electrical machine should be split into three equal axial sections, which are each modelled by individual rotor networks, such as the one shown in Figure 3.3, and connected together as outlined in Section 3.5. This corresponds to parameter *d* in Figure 3.2. The core length of the generator prototype analysed is 150 mm, hence the axial depth of each rotor thermal model plane, *d*, is 50 mm.

$$R_{Conduction} = \frac{l}{kA} \tag{3.1}$$

where $R_{Conduction}$ is the conductive thermal resistance (°C/W), l (m) represents the length of the conductive thermal path, A (m^2) the area through which the heat flows in the particular geometry being modelled and k the thermal conductivity of the material (W/m/°C).

The calculation to obtain the $R_{1,6}$, rotor winding to lamination thermal conduction resistance, shown in Figure 3.3, is outlined.

$R_{1,6}$ fully conductive thermal resistance calculation:

Using Equation 3.1, the thermal resistance of the fully conductive $R_{1,6}$ path in Figure 3.3 is determined. $R_{1,6}$ is divided into two separate thermal resistances, R_1 and R_2, corresponding to the winding and lamination segments, plus an additional resistive segment, R_3, accounting for the winding insulation, as shown in Figure 3.4.

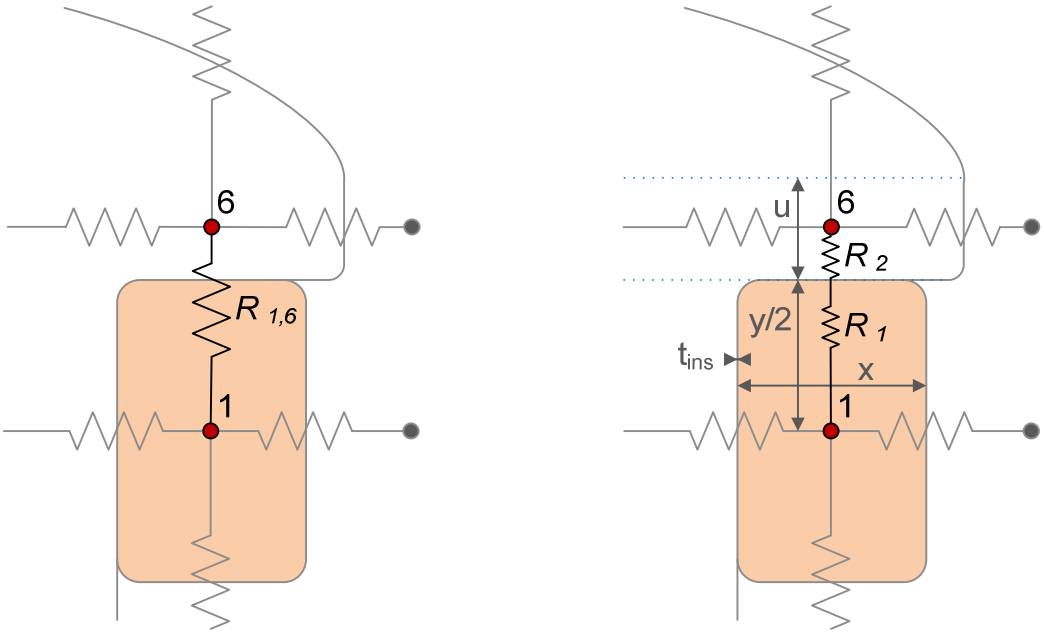

Figure 3.4: *$R_{1,6}$ rotor winding to lamination conduction resistance path.*

The calculation of the three individual resistances to yield $R_{1,6}$ is as follows:

$$R_{1,6} = \frac{l}{kA} = R_1 + R_2 + R_3 = \frac{\left(\frac{y}{2}\right)}{k_{coil}(x \times d)} + \frac{\left(\frac{u}{2}\right)}{k_{lam}(x \times d)} + \frac{t_{ins}}{k_{ins}(x \times d)}$$

where y, u, t_{ins}, x and d correspond to the geometrical dimensions presented in Figure 3.2 and k_{coil}, k_{lam} and k_{ins} are rotor coil, lamination and insulation thermal conductivities respectively and are 3.745 W/m/°C, 43 W/m/°C and 0.3 W/m/°C, collected from the electrical machine manufacturer. Thermal resistance k_{coil}, in the radial direction, is greatly reduced by insulation around the individual copper strands. Substituting this data into the equation above gives:

$$R_{1,6} = \frac{\left(\frac{0.023}{2}\right)}{3.745\,(0.0185 \times 0.05)} + \frac{\left(\frac{0.002}{2}\right)}{43\,(0.0185 \times 0.05)} + \frac{0.00025}{0.3\,(0.0185 \times 0.05)}$$

$$= 4.25\ ^{\circ}\text{C/W}$$

This example shows how a thermal conductive resistance going from the rotor winding, through the winding insulation, to the rotor lamination is determined. All other similar conduction thermal network resistances are calculated in this manner and the principles can be applied to other electrical machine parts and machine types.

The calculation outlined in Section 3.4, for a stator lamination internal fully conductive resistance, shows that the uniformity of the material through which the heat is transferred simplifies the calculation due to the absence of insulation/resin. Even so, the same approach should be taken to model any conductive heat transfer path across any material type and machine section.

The remaining purely conductive thermal resistances in the rotor thermal network are calculated in the same way. Table 3.2 shows the calculated values of the thermal resistances and the formulas used for the CGT alternator. The highest thermal resistances are exhibited by the thermal paths across the poorly thermally conducting rotor winding coil and insulation.

Thermal Resistance	R_{th} (°C/W)	Formula: $R_{x,x} = \left(\frac{l}{kA}\right)_1 + \left(\frac{l}{kA}\right)_2 + \left(\frac{l}{kA}\right)_3 = R_1 + R_2 + R_3$
$R_{1,2}$	3.48	$R_{1,2} = \frac{\left(\frac{x}{2}\right)}{k_{coil}(y \times d)} + \frac{\left(\frac{p}{2}\right)}{k_{lam}(y \times d)} + \frac{t_{ins}}{k_{ins}(y \times d)}$
$R_{1,6}$	4.25	$R_{1,6} = \frac{\left(\frac{y}{2}\right)}{k_{coil}(x \times d)} + \frac{\left(\frac{u}{2}\right)}{k_{lam}(x \times d)} + \frac{t_{ins}}{k_{ins}(x \times d)}$
$R_{2,3}$	3.48	$R_{2,3} = \frac{\left(\frac{p}{2}\right)}{k_{lam}(y \times d)} + \frac{\left(\frac{x}{2}\right)}{k_{coil}(y \times d)} + \frac{t_{ins}}{k_{ins}(y \times d)}$
$R_{2,5}$	0.10	$R_{2,5} = \frac{\left(\frac{y}{2}\right)}{k_{lam}(p \times d)} + \frac{\left(\frac{u}{2}\right)}{k_{lam}(p \times d)}$
$R_{2,7}$	0.91	$R_{2,7} = \frac{\left(\frac{y}{2}\right)}{k_{lam}(p \times d)} + \frac{z}{k_{lam}(p \times d)}$
$R_{3,4}$	4.25	$R_{3,4} = \frac{\left(\frac{y}{2}\right)}{k_{coil}(x \times d)} + \frac{\left(\frac{u}{2}\right)}{k_{lam}(x \times d)} + \frac{t_{ins}}{k_{ins}(x \times d)}$
$R_{4,5}$	1.47	$R_{4,5} = \frac{\left(\frac{x}{2}\right)}{k_{lam}((u + \left(\frac{2}{3}\right) \cdot w) \times d)} + \frac{\left(\frac{p}{2}\right)}{k_{lam}((u + \left(\frac{2}{3}\right) \cdot w) \times d)}$
$R_{5,6}$	1.47	$R_{5,6} = \frac{\left(\frac{p}{2}\right)}{k_{lam}((u + \left(\frac{2}{3}\right) \cdot w) \times d)} + \frac{\left(\frac{x}{2}\right)}{k_{lam}((u + \left(\frac{2}{3}\right) \cdot w) \times d)}$

Table 3.2: *Rotor conduction lumped parameter resistance values.*

Rotor Convection Lumped Parameter Resistance

The thermal convection heat transfer Equation 3.2, presented in Chapter 2, is required to compute the magnitude of the convection thermal resistances across the thermal network edges, shown in Figure 3.3. These electrical machine sections are in contact with the passing cooling airflow and convection thermal resistances are

required to represent the thermal heat transfer. Additionally, since part of the heat transfer path for these thermal resistances occurs fully within the rotor lamination, the conduction thermal resistance formulation (Equation 3.1), previously used to calculate thermal resistance $R_{1,6}$ is required. The process by which these thermal resistances are calculated is outlined in this section and the calculated values for the CGT generator prototype are tabulated in Table 3.3.

$$R_{Convection} = \frac{1}{h_c A} \tag{3.2}$$

where $R_{Convection}$ is the convective thermal resistance (°C/W), h_c the convection heat transfer coefficient (W/m^2/°C) and A the convective heat exchange area (m^2).

As an example, the calculation to obtain the $R_{Ø,6\ (Side)}$, rotor lamination to airflow, thermal convection resistance, shown in Figure 3.3, is presented.

$R_{Ø,6\ (Side)}$ convection thermal resistance calculation:

In order to account for the two heat transfer mechanisms that take place along the mentioned thermal path, resistance $R_{Ø,6\ (Side)}$ is divided into two independent thermal resistances, R_1 and R_2, corresponding to the rotor lamination conduction and convection to airflow segments respectively, as shown in Figure 3.5, plus an additional resistive sector, R_3, representing the lamination resin resistance.

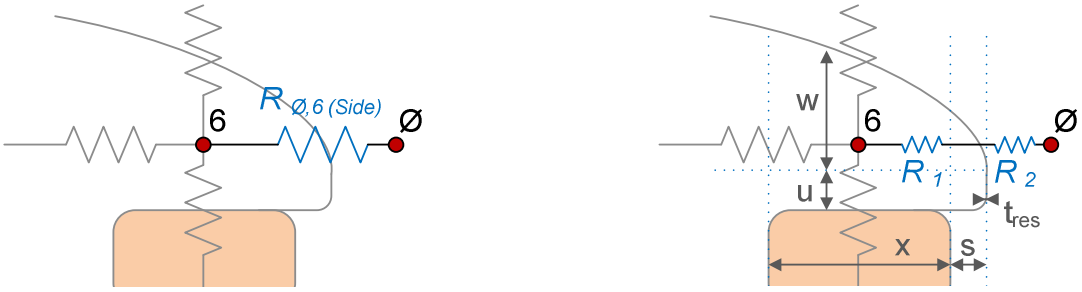

Figure 3.5: *$R_{Ø,6\ (Side)}$ rotor lamination to airflow convection resistance path.*

The calculation of the three individual resistances to yield $R_{Ø,6\,(Side)}$ is as follows:

$$R_{Ø,6\,(Side)} = R_1 + R_2 + R_3 = \frac{\left(\frac{x}{2} + s\right)}{k_{lam}(u \times d)} + \frac{1}{h_c(u \times d)} + \frac{t_{res}}{k_{res}(u \times d)}$$

where x, s, t_{res}, u and d relate to the geometries illustrated in Figure 3.2. k_{lam} and k_{res} are rotor lamination and resin insulation thermal conductivities, which are 43 W/m/°C and 0.22 W/m/°C respectively. h_c is the heat transfer coefficient linked with the airflow area adjacent to node 6 in Figure 3.3 (Section 3.3) and has a value of 70.95 W/m^2/°C.

Heat transfer coefficients are calculated as shown in Section 3.6, using the well established correlations presented and data provided by Cummins Generator Technologies. Substituting the above data into the presented equation gives:

$$R_{Ø,6\,(Side)} = \frac{\left(\frac{0.0185}{2} + 0.0015\right)}{43\,(0.002 \times 0.05)} + \frac{1}{70.95\,(0.002 \times 0.05)} + \frac{0.00006}{0.22\,(0.002 \times 0.05)}$$

$$= 146.17\ °C/W$$

As with the method utilised to calculate the fully resistive thermal network component, $R_{1,6}$, the calculations outlined for the heat convected away from the rotor lamination can also be adapted and applied to all other similar machine areas.

Convective lumped parameter thermal resistances for the synchronous machine investigated are presented in Table 3.3, along with the resistive formulas used. Due to the symmetrical nature of the rotor, some resistances, such as $R_{0,1\,(Side)}$ and $R_{0,3\,(Side)}$, are equal and, hence, collected together in the same row. From the results it can be seen that the areas near to the top of the rotor pole have a lower thermal resistance, due to the higher heat transfer coefficient values, indicating enhanced cooling, faster flowing air, around those areas of the rotor.

Thermal Resistance	R_{th} (°C/W)	Formula: $R_{x,x} = \left(\frac{l}{kA}\right)_1 + \left(\frac{1}{h_c A}\right)_2 + \left(\frac{l}{kA}\right)_3 = R_1 + R_2 + R_3$
$R_{Ø,1\ (Side)}$ & $R_{Ø,3\ (Side)}$	15.54	$R_{Ø,1(\text{Side})} = \frac{\left(\frac{x}{2}\right)}{k_{lam}(y \times d)} + \frac{1}{h_c(y \times d)} + \frac{t_{res}}{k_{res}(y \times d)}$
$R_{Ø,1\ (Bottom)}$ & $R_{Ø,3\ (Bottom)}$	19.84	$R_{Ø,1(\text{Bottom})} = \frac{\left(\frac{y}{2}\right)}{k_{lam}(x \times d)} + \frac{1}{h_c(x \times d)} + \frac{t_{res}}{k_{res}(x \times d)}$
$R_{Ø,4\ (Side)}$ & $R_{Ø,6\ (Side)}$	146.17	$R_{Ø,4(\text{Side})} = \frac{\left(\frac{x}{2} + s\right)}{k_{lam}(u \times d)} + \frac{1}{h_c(u \times d)} + \frac{t_{res}}{k_{res}(u \times d)}$
$R_{Ø,4\ (Top)}$ & $R_{Ø,6\ (Top)}$	14.57	$R_{Ø,4(\text{Top})} = \frac{\left(\frac{u}{2} + \frac{w}{2}\right)}{k_{lam}((x+s) \times d)} + \frac{1}{h_c((x+s) \times d)} + \frac{t_{res}}{k_{res}((x+s) \times d)}$
$R_{Ø,7\ (Side\ 1)}$ & $R_{Ø,7\ (Side\ 2)}$	6.23	$R_{Ø,7(\text{Side 1})} = \frac{z}{k_{lam}(z \times d)} + \frac{1}{h_c(z \times d)} + \frac{t_{res}}{k_{res}(z \times d)}$
$R_{Ø,5}$	4.92	$R_{Ø,5} = \frac{\left(\frac{u}{2} + w\right)}{k_{lam}(p \times d)} + \frac{1}{h_c(p \times d)} + \frac{t_{res}}{k_{res}(p \times d)}$

Table 3.3: *Rotor convective lumped parameter resistance values for first radial plane.*

3.4 Stator Thermal Modelling

Similarly to the development process of the rotor thermal model covered in the previous section, the required electrical machine geometric and thermal related information needed for the stator thermal model needs to be collected from the machine manufacturer or material supplier. The main stator parameters required to generate the thermal model are shown in Figure 3.6 (not drawn to scale).

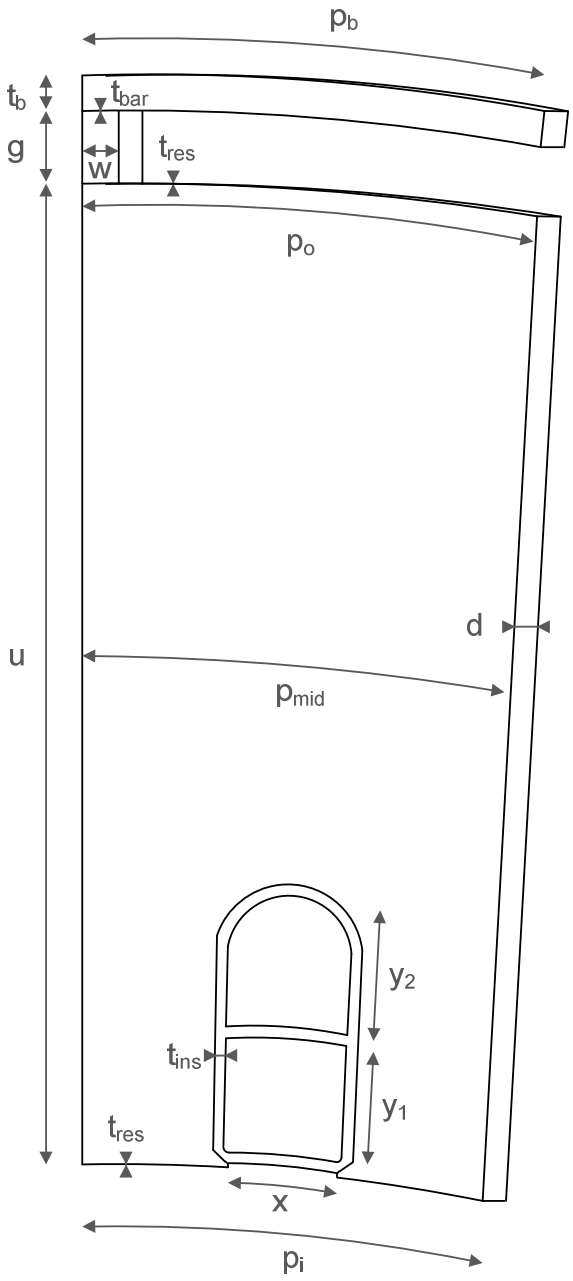

Rotor section	Label	Rotor section	Label
Slot width	x	Barrel gap	g
Lower coil height	y_1	Barrel to landbar contact width	w
Upper coil height	y_2	Lamination height	u
Internal perimeter per slot	p_i	Stator resin coating	t_{res}
Middle perimeter per slot	p_{mid}	Contact bars to barrel resin	t_{bar}
Outer perimeter per slot	p_o	Stator insulation thickness	t_{ins}
Barrel mean perimeter	p_b	Axial depth of model	d
Barrel thickness	t_b		

Figure 3.6: *Stator lamination and winding prototype parameters.*

The parameters outlined in Figure 3.6 are used to generate the stator two-dimensional lumped parameter thermal resistance network, displayed over the stator outline in Figure 3.7. As shown, the network is made up of conduction, convection and radiation/convection thermal resistances, which are colour coded black, blue and red respectively.

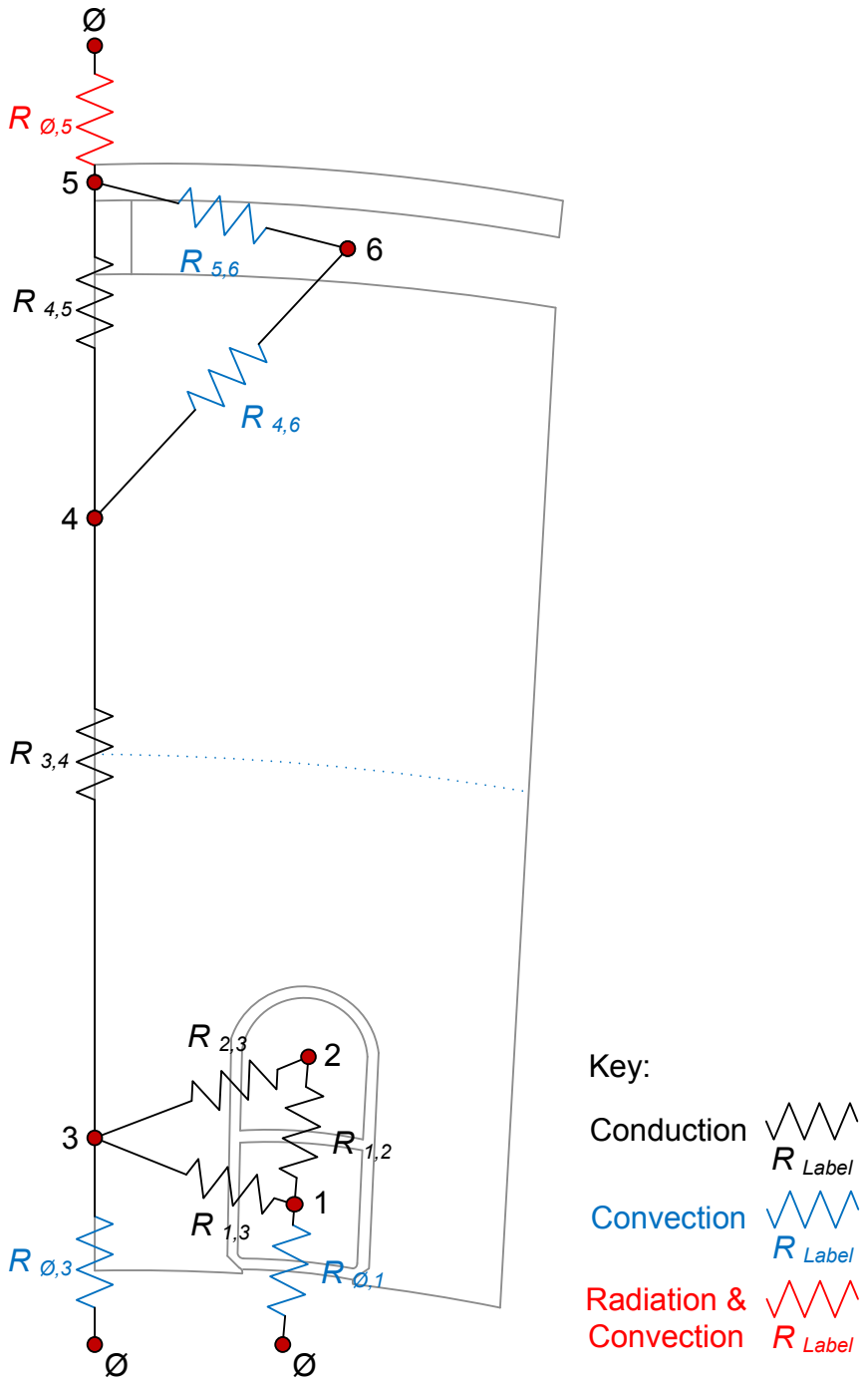

Figure 3.7: *Stator lumped parameter thermal resistance network.*

As well as the geometric parameters presented in Figure 3.6, thermal conductivity (W/m/°C) and heat transfer coefficient values (W/m^2/°C) are also required. Furthermore, the radiation thermal resistance information needs to be obtained and utilised as shown in next section for the calculation of $R_{Ø,5\ RAD}$.

3.4.1 Stator Lumped Parameter Network Calculations

The calculations to create the stator thermal network in Figure 3.7, with examples given for the three different types of thermal resistances are outlined in this section and the numerical data for the generator prototype analysed in the experimental stage is presented.

Stator Conduction Lumped Parameter Resistance

Thermal conduction resistances for the stator thermal network are calculated using the same method as outlined for the rotor thermal network in Section 3.3 and in accordance with the information introduced in Chapter 2 using Equation 3.1.

$$R_{Conduction} = \frac{l}{kA} \tag{3.1}$$

As an example, $R_{3,4}$, within the stator lamination, and $R_{1,3}$, stator winding to lamination are calculated.

$R_{3,4}$ fully conductive thermal resistance calculation:

The thermal resistance of the fully conductive path $R_{3,4}$ from Figure 3.8 is calculated using Equation 3.1. The paths being analysed are divided into two separate thermal resistances, R_1 and R_2. There is a lack of a third resistive segment, R_3, since there is no insulation or resin along the heat transfer path.

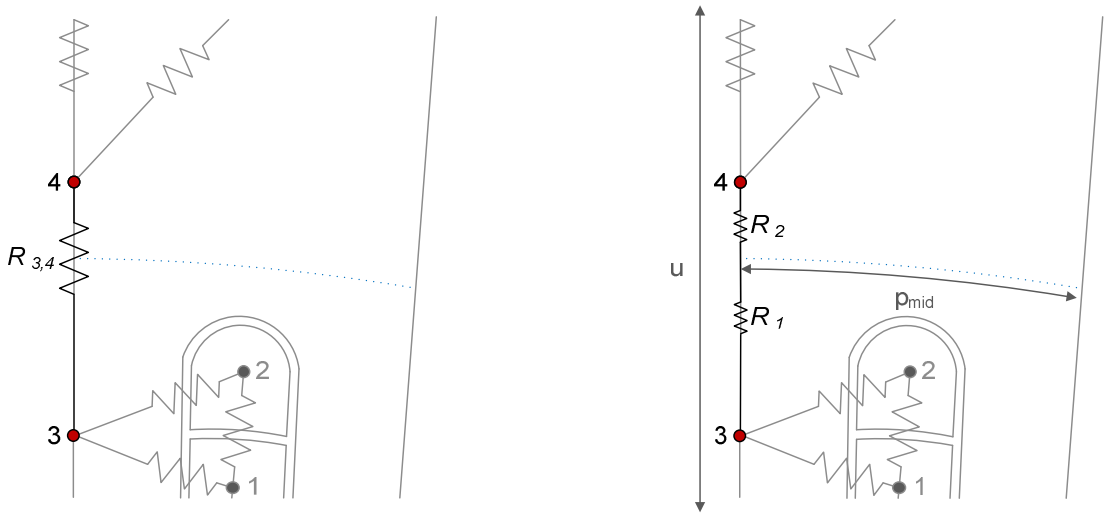

Figure 3.8: *$R_{3,4}$ stator conduction resistance path within generator lamination.*

$$R_{3,4} = \frac{l}{kA} = R_1 + R_2 = \frac{\left(\frac{u}{4}\right)}{k_{lam}(p_{mid} \times d)} + \frac{\left(\frac{u}{4}\right)}{k_{lam}(p_{mid} \times d)}$$

The calculations to obtain $R_{3,4}$ are presented, where u, p_{mid} and d represent the geometrical dimensions shown in Figure 3.6. k_{lam} is stator lamination thermal conductivity, which has a value of 43 W/m/°C provided by the generator manufacturer. Substituting the information above into the presented equation gives:

$$R_{3,4} = \frac{\left(\frac{0.0425}{4}\right)}{43\,(0.020289 \times 0.05)} + \frac{\left(\frac{0.0425}{4}\right)}{43\,(0.020289 \times 0.05)} = 0.49\ °C/W$$

This example illustrates the thermal fully conductive resistance that exists within the stator lamination. The uniformity of the material through which the heat is transferred, and the lack of any insulation and/or resin, simplifies the calculation and, as shown in Table 3.4, results in the lowest fully conductive thermal resistance in the stator thermal network. Conduction thermal network resistances within the same machine material are calculated in this manner for any machine part.

$R_{1,3}$ fully conductive thermal resistance calculation:

In a similar way to the calculation of the $R_{3,4}$, $R_{1,3}$ can be modelled as shown in Figure 3.9.

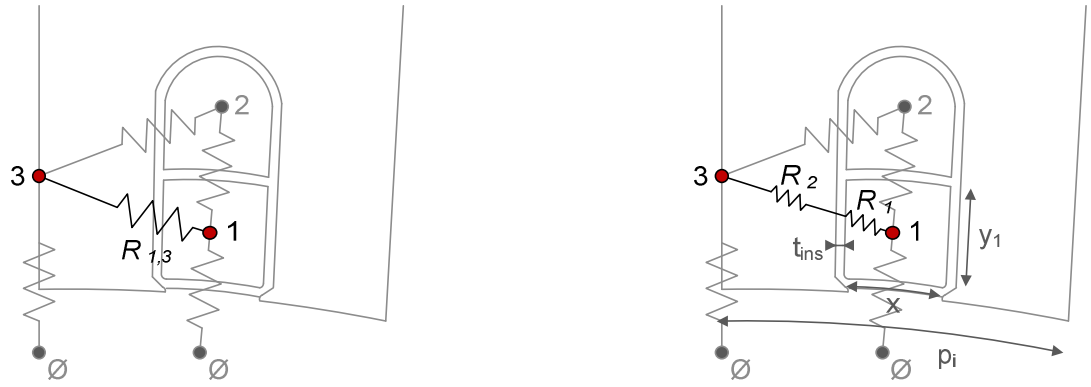

Figure 3.9: *$R_{1,3}$ stator winding to lamination conduction resistance path.*

Compared to $R_{3,4}$, resistance $R_{1,3}$ does include the lower thermally conducting winding insulation, which needs to be accounted for. Hence, the resistance formula presented for $R_{1,3}$ includes a third resistive component, R_3, which accounts for the heat transfer through the insulation between the stator winding and lamination.

$$R_{1,3} = \frac{l}{kA} = R_1 + R_2 + R_3 = \frac{\left(\frac{x}{2}\right)}{k_{coil}(y_1 \times d)} + \frac{\left(\frac{p_i - x}{2}\right)}{k_{lam}(y_1 \times d)} + \frac{t_{ins}}{k_{ins}(y_1 \times d)}$$

where x, p_i, y_1 and d are the geometrical dimensions illustrated in Figure 3.6. k_{coil}, k_{lam} and k_{ins} are stator coil, lamination and insulation thermal conductivities respectively and, as stated by the generator supplier, have values of 0.832 W/m/°C, 43 W/m/°C and 0.3 W/m/°C. Thermal resistance k_{coil}, in the radial direction, is greatly reduced by insulation around the individual copper strands.

Substituting the information given into the presented equation results in:

$$R_{1,3} = \frac{\left(\frac{0.0082}{2}\right)}{0.832\,(0.007\times 0.05)} + \frac{\left(\frac{0.01658-0.0082}{2}\right)}{43\,(0.007\times 0.05)} + \frac{0.0006}{0.3\,(0.007\times 0.05)}$$

$$= 20.06\ °C/W$$

The calculations outlined can be applied to other similar thermal resistance heat transfer paths, making the necessary adjustments to account for the geometric and thermal properties of the material along the thermal path.

Table 3.4 shows all the thermal resistances for the stator. The lowest stator fully conductive thermal resistance corresponds to $R_{3,4}$. As shown in the calculations presented in this chapter, this is due to the fact that heat travels only along the stator lamination, which has a high thermal conductivity, without the presence of any poor conducting insulation or resin.

Thermal Resistance	R_{th} (°C/W)	Formula: $R_{x,x} = \left(\frac{l}{kA}\right)_1 + \left(\frac{l}{kA}\right)_2 + \left(\frac{l}{kA}\right)_3 = R_1 + R_2 + R_3$
$R_{1,2}$	23.19	$R_{1,2} = \frac{\left(\frac{y_1}{2}\right)}{k_{coil}(x\times d)} + \frac{\left(\frac{y_2}{2}\right)}{k_{coil}(x\times d)} + \frac{t_{ins}}{k_{ins}(x\times d)}$
$R_{1,3}$	20.06	$R_{1,3} = \frac{\left(\frac{x}{2}\right)}{k_{coil}(y_1\times d)} + \frac{\left(\frac{p_i - x}{2}\right)}{k_{lam}(y_1\times d)} + \frac{t_{ins}}{k_{ins}(y_1\times d)}$
$R_{2,3}$	20.06	$R_{2,3} = \frac{\left(\frac{x}{2}\right)}{k_{coil}(y_2\times d)} + \frac{\left(\frac{p_i - x}{2}\right)}{k_{lam}(y_2\times d)} + \frac{t_{ins}}{k_{ins}(y_2\times d)}$
$R_{3,4}$	0.49	$R_{3,4} = \frac{\left(\frac{u}{4}\right)}{k_{lam}(p_{mid}\times d)} + \frac{\left(\frac{u}{4}\right)}{k_{lam}(p_{mid}\times d)}$
$R_{4,5}$	26.50	$R_{4,5} = \frac{\left(\frac{u}{4}+g\right)}{k_{coil}(w\times d)} + \frac{\left(\frac{t_b}{2}\right)}{k_{bar}(w\times d)} + \left(\frac{t_{res}}{k_{res}(w\times d)} + \frac{t_{bar}}{k_{bar}(w\times d)}\right)$

Table 3.4: *Stator conductive lumped parameter resistance values for first radial plane.*

Stator Convection Lumped Parameter Resistance

Similarly to the rotor convective resistance calculations in Section 3.3, Equation 3.2 is used to compute the stator thermal model convection thermal resistances. As with the rotor resistances, there is a fraction of the resistance which is obtained with the resistive thermal conduction Equation 3.1.

$$R_{Convection} = \frac{1}{h_c A} \tag{3.2}$$

where $R_{Convection}$ is the convective thermal resistance (°C/W), h_c the convection heat transfer coefficient (W/m^2/°C) and A the convective heat exchange area (m^2).

To illustrate this, the calculations of the stator lamination to airflow thermal convection resistances $R_{Ø,1}$ and $R_{Ø,5}$, shown in Figures 3.10 and 3.11 respectively, are presented in this section.

$R_{Ø,1}$ convection thermal resistance calculation:

Stator network thermal resistance, $R_{Ø,1}$, can be calculated using Equations 3.1 and 3.2. Since two heat transfer mechanism need to be considered and accounted for, the resistive path is segmented into two separate thermal resistances, R_1 and R_2, representing the stator lamination conduction and convection to airflow respectively, as illustrated in Figure 3.10. An extra resistive part, R_3, representing the lamination polyethylene insulation resistance is the third component of the overall thermal resistance $R_{Ø,1}$.

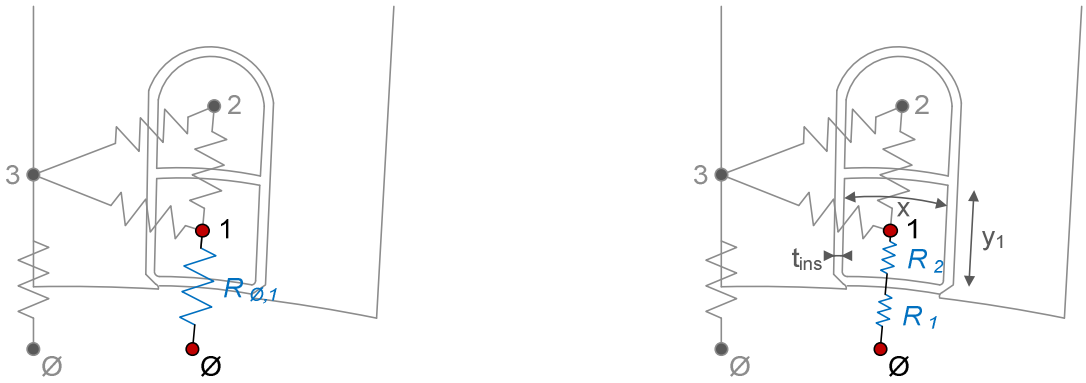

Figure 3.10: *$R_{Ø,1}$ stator winding to airflow thermal resistance path.*

The calculation of the three individual resistances to obtain $R_{Ø,1}$ is as follows:

$$R_{Ø,1} = R_1 + R_2 + R_3 = \frac{\left(\frac{y_1}{2}\right)}{k_{coil}(x \times d)} + \frac{1}{h_c(x \times d)} + \frac{t_{ins}}{k_{ins}(x \times d)}$$

where y_1, t_{ins}, x and d represent the geometries illustrated in Figure 3.6 (Section 3.4). k_{coil} and k_{ins} are stator coil and insulation thermal conductivities, which are 0.832 W/m/°C and 0.3 W/m/°C respectively. h_c is the heat transfer coefficient linked with the airflow area adjacent to stator node 1 in Figure 3.7 (Section 3.4) and has a value of 96.90 W/m^2/°C. Substituting this data into the equation above gives:

$$R_{Ø,1} = \frac{\left(\frac{0.007}{2}\right)}{0.832\,(0.0082 \times 0.05)} + \frac{1}{96.90\,(0.0082 \times 0.05)} + \frac{0.0006}{0.3\,(0.0082 \times 0.05)}$$

$$= 40.31\,°C/W$$

$R_{Ø,5}$ convection thermal resistance calculation:

The method to obtain the stator network thermal resistance, $R_{Ø,5}$, is as outlined:

$$R_{Ø,5} = R_1 + R_2 = \frac{\left(\frac{t_b}{2}\right)}{k_{bar}(p_b \times d)} + \frac{1}{h_c(p_b \times d)}$$

where t_b, p_b and d are the geometries shown in Figure 3.11. k_{bar} is the stator barrel thermal conductivity, 40 W/m/°C, and h_c is the heat transfer coefficient linked with the airflow around the machine barrel stator thermal network node 5 in Figure 3.11, which is 48.96 W/m^2/°C. This results in a thermal resistance of 15.43 °C/W for $R_{Ø,5}$:

$$R_{Ø,5} = \frac{\left(\frac{0.002}{2}\right)}{40\,(0.0265 \times 0.05)} + \frac{1}{48.96\,(0.0265 \times 0.05)} = 15.43\ °C/W$$

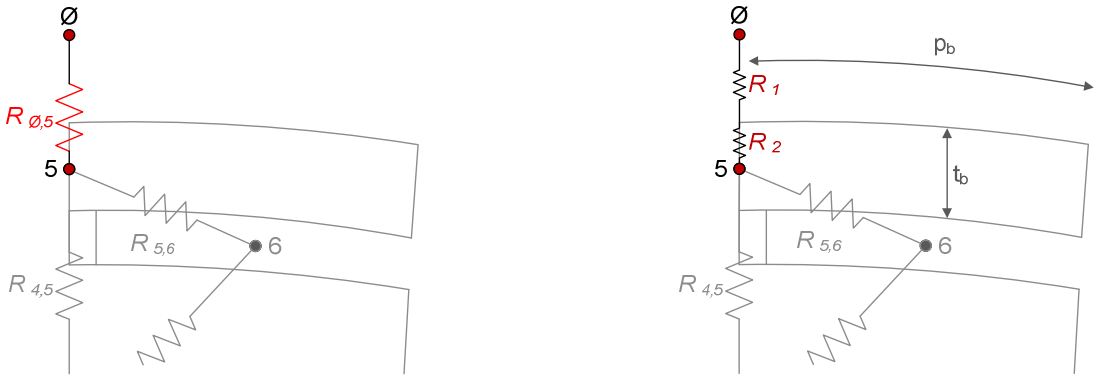

Figure 3.11: *$R_{Ø,5}$ frame barrel to airflow thermal resistance path.*

Stator lumped parameter convective resistances for the BCI184E CGT synchronous machine, with the necessary relevant formulations, are shown in Table 3.5.

Thermal Resistance	R_{th} (°C/W)	Formula: $R_{x,x} = \left(\frac{l}{kA}\right)_1 + \left(\frac{1}{h_c A}\right)_2 + \left(\frac{l}{kA}\right)_3 = R_1 + R_2 + R_3$
$R_{Ø,1}$	40.31	$R_{Ø,1} = \frac{\left(\frac{y_1}{2}\right)}{k_{coil}(x \times d)} + \frac{1}{h_c(x \times d)} + \frac{t_{ins}}{k_{ins}(x \times d)}$
$R_{Ø,3}$	21.56	$R_{Ø,3} = \frac{\left(\frac{u}{4}\right)}{k_{lam}((p_i - x) \times d)} + \frac{1}{h_c((p_i - x) \times d)} + \frac{t_{res}}{k_{res}((p_i - x) \times d)}$
$R_{4,6}$	9.61	$R_{4,6} = \frac{\left(\frac{u}{4}\right)}{k_{lam}((p_o - w) \times d)} + \frac{1}{h_c((p_o - w) \times d)} + \frac{t_{res}}{k_{res}((p_i - x) \times d)}$
$R_{5,6}$	8.26	$R_{5,6} = \frac{\left(\frac{t_b}{2}\right)}{k_{lam}((p_b - w) \times d)} + \frac{1}{h_c((p_b - w) \times d)}$
$R_{Ø,5}$	15.43	$R_{Ø,5} = \frac{\left(\frac{t_b}{2}\right)}{k_{bar}(p_b \times d)} + \frac{1}{h_c(p_b \times d)}$

Table 3.5: *Stator convective lumped parameter resistance values for first radial plane.*

Stator Radiation Lumped Parameter Resistance

As well as through conduction and convection heat transfer mechanisms, heat is also transferred away from the stator via radiation from the frame barrel. The concepts behind this heat transfer mechanism are introduced in Chapter 2, using Equations 3.3 and 3.4, which are utilised in this section. The radiation thermal resistance shown in Figure 3.7 can be calculated for the CGT synchronous machine prototype. Equations 3.3 to 3.5 are used to calculate the thermal radiation resistance

$$R_{Radiation} = \frac{1}{h_R A} \tag{3.3}$$

where $R_{Radiation}$ is the radiation thermal resistance (°C/W), h_R the radiation heat transfer coefficient (W/m^2/°C) and A the radiating heat exchange area (m^2).

$$h_R = \frac{\sigma \cdot \varepsilon_1 \cdot F_{1-2}\left(T_1^4 - T_2^4\right)}{T_1 - T_2} \tag{3.4}$$

where σ is Stefan-Boltzmann constant (5.6704x10^{-8} W/m^2/K^4), ε_1 the emissivity of the radiating surface, F_{1-2} the view factor of surface 2 with respect to surface 1, T_1 the absolute temperature of surface 1 (K) and T_2 the absolute temperature of surface 2.

Substituting Equation 3.4 into Equation 3.3, the radiation thermal resistance $R_{Ø,5\ RAD}$, shown in Figure 3.12, is obtained using Equation 3.5:

$$R_{Radiation} = \frac{T_1 - T_2}{\sigma \cdot A_1 \cdot \varepsilon_1 \cdot F_{1-2}\left(T_1^4 - T_2^4\right)} \tag{3.5}$$

$R_{Ø,5\ RAD}$ radiation thermal resistance calculation:

Radiation thermal resistance $R_{Ø,5\ RAD}$, shown in Figure 3.12 is calculated for the CGT generator prototype using Equation 3.5, where the radiating surface portion area is 0.001326 m^2, emissivity is 0.8, view factor is 0.8, the machine's barrel radiating temperature is 306.3 K and the radiating ambient is 290.9 K.

$$R_{Ø,5\ RAD} = \frac{306.3 - 290.9}{5.6704x10^{-8} \cdot 0.001326 \cdot 0.8 \cdot 0.8\left(306.3^4 - 290.9^4\right)} = 195.00\ °C/W$$

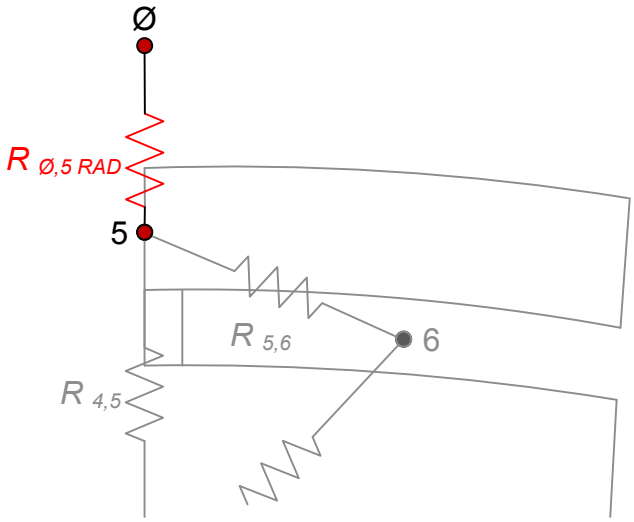

Figure 3.12: *$R_{Ø,5}$ frame barrel to airflow thermal radiation resistance path.*

The method outlined for the determination of a radiating thermal resistance can be applied to all external radiating machine surfaces in the same way.

3.5 Thermal Model Axial Length, Endwinding and Airflow Connections

In order to improve the synchronous machine rotor and stator lumped parameter thermal models presented in Sections 3.3 and 3.4, additional machine network planes are required to account for the range of axial lengths and for the two endwindings. To achieve this, connections in the axial direction between the different planes are made as shown in Figure 3.13. These modifications transform the initial two-dimensional nature of the models presented, into multi-plane three-dimensional thermal models. Planes A, B and C, such as the ones presented in Figure 3.3 for the rotor and Figure 3.7 for the stator, are used to build the multi-plane model. Furthermore, planes D and E are added in order to account for the non-drive-end and drive-end endwinding generator sections.

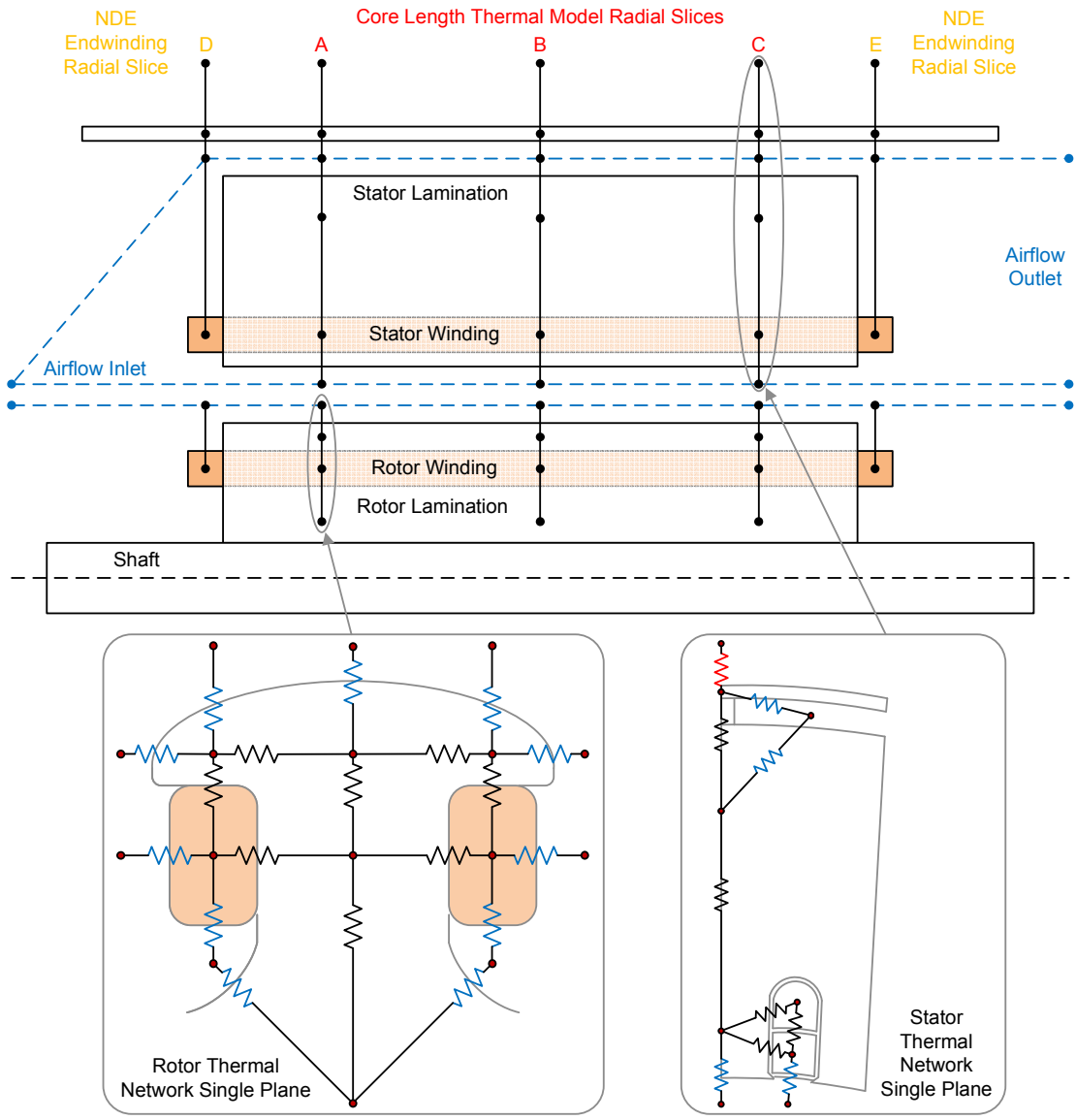

Figure 3.13: *Multi-plane lumped parameter rotor and stator thermal models.*

The multiple model planes are linked by adding inter-plane thermal resistance connections for the seven rotor network nodes, the six stator network nodes and for the airflow paths. In addition, connections from the outer core length planes to the corresponding endwindings are inserted. Finally, the thermal resistive airflow paths along the axial length of the rotor and stator are included in the thermal models, shown in blue in Figure 3.13. The connections made in the rotor and stator thermal models are outlined in the following sections.

3.5.1 Rotor Thermal Model Axial Length, Endwinding and Airflow Connections

The required inter-plane, endwinding and airflow rotor thermal resistances are illustrated in Figure 3.14, where the two-dimensional axial slice of the synchronous generator complete thermal model is shown. For simplicity and diagram clarity, rotor thermal nodes 2, 4 and 6 for the rotor lamination and node 3 for the rotor coil, presented in Figure 3.3 are omitted from Figure 3.14 and their inter-plane links are not shown. Rotor thermal nodes 2, 4 and 6 for the rotor lamination are connected in a similar way as nodes 5 and 7, which are shown in Figure 3.14. Node 3 for the rotor coil is connected in the same way as node 1. All endwinding thermal resistance connections are presented later in Figure 3.15. Note that, for example, thermal resistance R_{a1b1} in Figure 3.14 links rotor thermal network node 1 in Plane A, with node 1 in Plane B.

With regards to the thermal resistances comprising the rotor networks in Planes B and C, no modifications are applied to the fully resistive components shown in Figure 3.14 and presented in Section 3.3, which are calculated in the same way and have the same °C/W values. However, the convective thermal resistance, which are calculated as outlined in Section 3.3.1, have their heat transfer coefficients to the surrounding cooling airflow reduced by a factor of 0.9, which accounts for the reducing effectiveness of the airflow as it moves away from the cool inlet towards the hotter drive-end of the machine. The choice of this factor requires further work, as explained in the airflow considerations covered in Section 3.6. As a result of this addition, convective resistances increase in magnitude, due to the reduction in heat transfer coefficient, going from the non-drive-end of the machine to the drive-end of the synchronous machine modelled. For example, the value of convective thermal resistance $R_{0,5}$, presented in Table 3.3, goes from being 4.92 °C/W in Plane A, to 5.44 °C/W in Plane B, to 6.02 °C/W in Plane C.

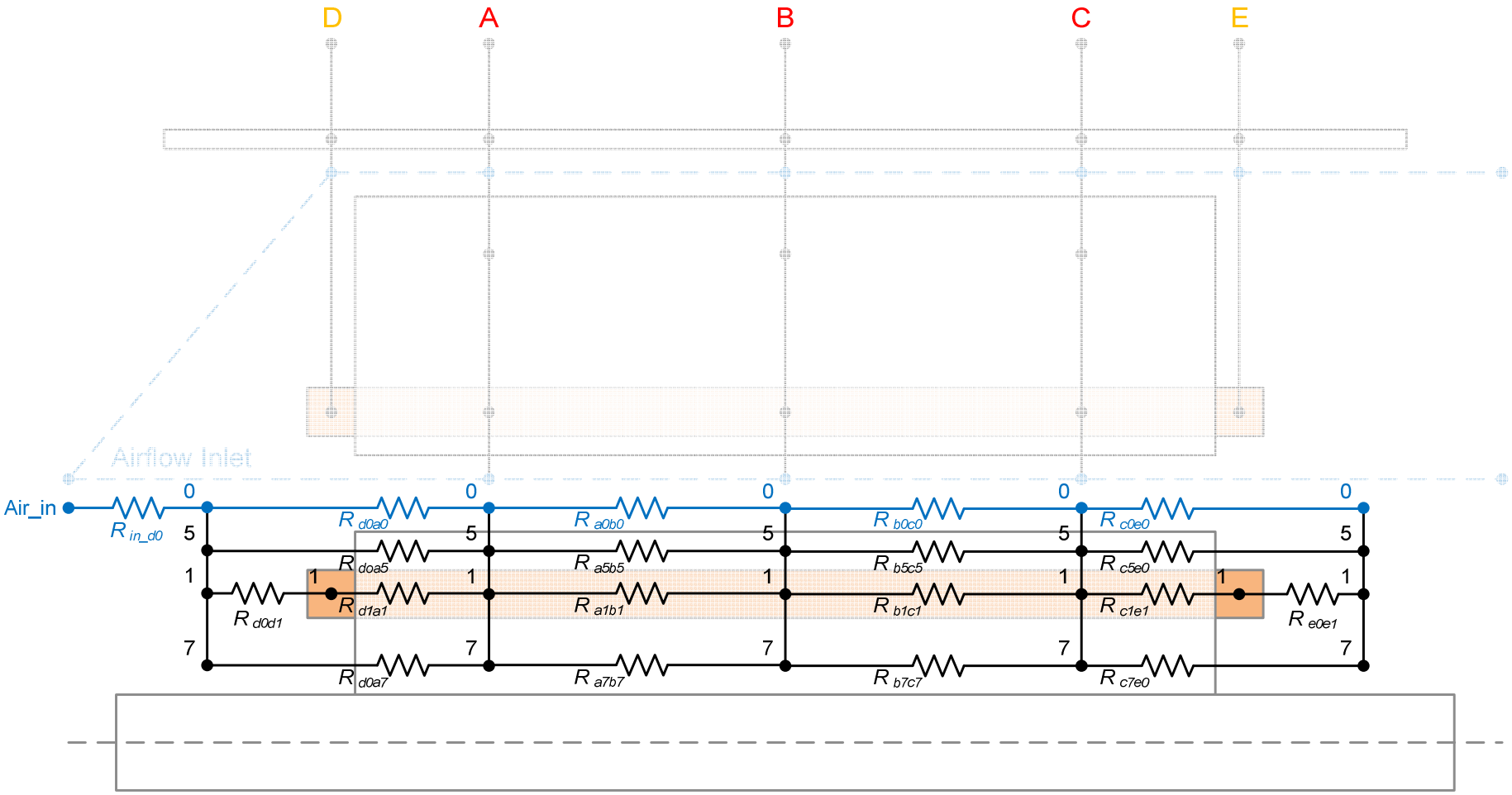

Figure 3.14: *Rotor thermal model axial length, endwinding and airflow connections.*

Rotor model inter-plane thermal conduction and endwinding thermal convection resistances, shown in black in Figure 3.14, are computed using the principles and examples presented in Sections 3.3 and 3.4. Tables 3.6 and 3.7 list and describe the thermal resistances required to complete the rotor thermal network.

Rotor Planes A & B * inter-plane links:

Thermal Resistance	Resistance Type: Description
R_{a1b1}	Conduction: Between lamination nodes 1 of planes A and B
R_{a2b2}	Conduction: Between lamination nodes 2 of planes A and B
R_{a3b3}	Conduction: Between lamination nodes 3 of planes A and B
R_{a4b4}	Conduction: Between lamination nodes 4 of planes A and B
R_{a5b5}	Conduction: Between lamination nodes 5 of planes A and B
R_{a6b6}	Conduction: Between lamination nodes 6 of planes A and B
R_{a7b7}	Conduction: Between lamination nodes 7 of planes A and B

* same inter-planes links between rotor Planes B & C are required.

Table 3.6: *Rotor inter-plane thermal resistances.*

Rotor Plane D^+ endwinding and A & D + inter-plane connections:

Thermal Resistance	Resistance Type: Description
R_{d1d0}	Convection: Rotor endwinding node 1 to surrounding airflow
R_{a1d1}	Conduction: Plane A rotor coil node 1 to endwinding node 1
R_{a2d0}	Convection: Plane A lamination node 2 to adjacent airflow
R_{a3d1}	Conduction: Plane A rotor coil node 3 to endwinding node 1
R_{a4d0}	Convection: Plane A lamination node 4 to adjacent airflow
R_{a5d0}	Convection: Plane A lamination node 5 to adjacent airflow
R_{a6d0}	Convection: Plane A lamination node 6 to adjacent airflow
R_{a7d0}	Convection: Plane A lamination node 7 to adjacent airflow

+ same inter-planes links for rotor Plane E and between Planes C & E are required.

Table 3.7: *Rotor endwinding thermal resistances.*

It should be noted that the rotor coil winding slot fill factor, typically 0.4 for CGT synchronous machines, is accounted for in the inter-plane conductive resistances. All the conduction areas (m^2) for the thermal resistances presented in Table 3.6 are multiplied by the slot fill factor, reducing the effective volume allowed for heat transfer along the windings axial direction, resulting in increased thermal resistances.

Thermal resistances presented in Table 3.7 are illustrated in Figure 3.15, showing the A and D plane rotor thermal model connections for the non-drive-end of the generator. Shown are the two fully conductive resistances connecting nodes 1 and 3

in Plane A with the endwinding node 1 in Plane D, and five of the six convective resistances from the lamination and the rotor coil to the surrounding airflow. The missing convective resistance in Figure 3.15, R_{a2d0}, is hidden behind the rotor endwinding turn and is therefore not shown. The same conductive/convective thermal resistance layout is created for the drive-end of the generator thermal model section, between Planes C and E.

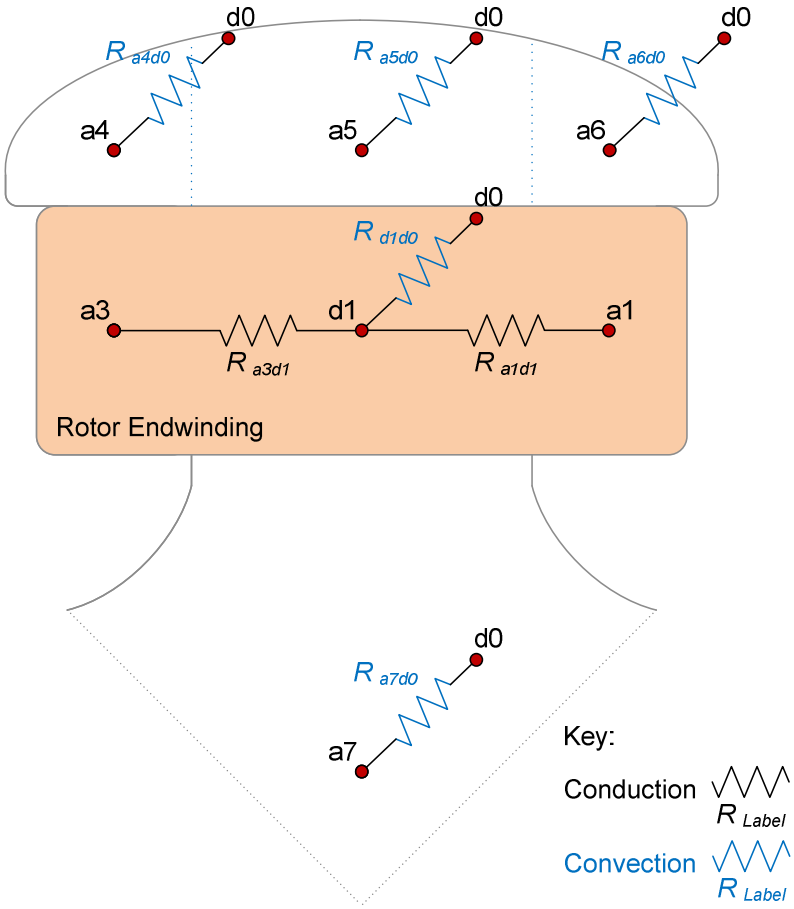

Figure 3.15: *Rotor thermal model endwinding thermal resistance connections.*

The remaining thermal resistances in Figure 3.14 correspond to the airflow path along the axial length of the rotor. Utilising Equation 3.6, introduced in Chapter 2, these thermal resistances are calculated and added to the rotor thermal network. In the simulations executed by MySolver, presented in Chapter 6, node Air_in in Figure 3.14 is set to 0 °C to calculate the temperature rise at the lumped parameter thermal network nodes. An alternative is to set node Air_in to the ambient temperature, in order to compute absolute temperature predictions.

$$\Delta T = \frac{Power\ Dissipated}{Volume\ Flow\ Rate \cdot Density \cdot c_p} \tag{3.6}$$

where ΔT is the temperature difference (°C) and c_p is specific heat capacity (J/kg/°C). The *Power Dissipated* is measured in W, airflow *Volume Flow Rate* in m^3/s and *Density* in kg/m^3. From Equation 3.6, the airflow heat flux thermal resistance results, as shown in Equation 3.7, and is used in the thermal model.

$$R_{Flow} = \frac{1}{X} \cdot \frac{1}{Volume\ Flow\ Rate \cdot Density \cdot c_p} \tag{3.7}$$

In Equation 3.7, used to calculate the thermal resistance along the axial length of the blue airflow path shown in Figure 3.14, dimensionless factor *X* determines the ratio of heat flow along the horizontal resistance in the axial direction, to the vertical resistance along the radial direction. As with other airflow related parameters and MySolver thermal modelling aspects, magnitudes for this *X* coefficient are estimated and, it is important to emphasise that future airflow analysis work should provide more accurate values. The rotor thermal network uses the *X* values presented in Figure 3.16, where a near-linear relationship is assumed. The *X* values illustrated in Figure 3.16 are rough estimates, guided by the experimentally obtained rotor winding temperature distribution along the axial core length of the generator, presented in Chapter 8. They are based on how machine component temperatures fall along the axial length of the electrical machine, from the non-drive-end to the drive-end. Such *X* values have proven to give good results when utilised by MySolver, as shown later in this thesis, but future airflow related fine tuning of *X* values will increase accuracy.

Axial Flow Thermal Resistance	*X* value
R_{In_d0}	5.0
R_{d0a0}	2.9
R_{a0b0}	2.1
R_{b0c0}	1.3
R_{c0e0}	1.0

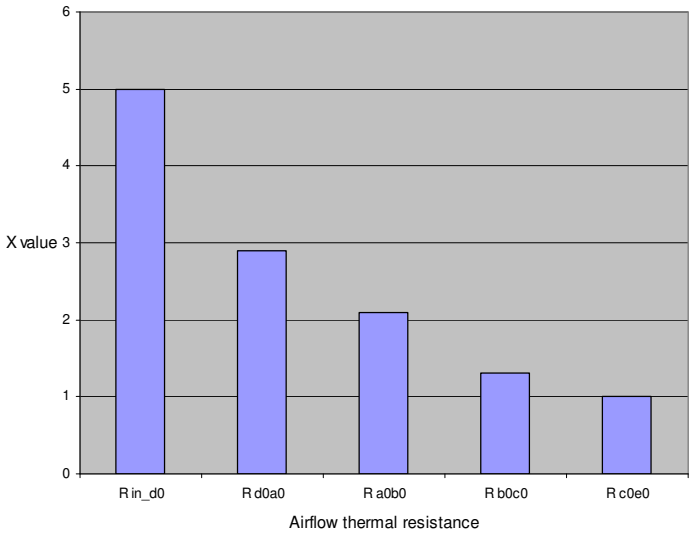

Figure 3.16: *Rotor thermal model X values for airflow thermal resistances.*

Essentially, the objective of factor *X* is to represent the decreasing effectiveness of the airflow cooling the rotor along the axial length of the generator, going from the airflow inlet to the outlet. As a consequence of this, the thermal resistance calculated by Equation 3.7 increases accordingly.

3.5.2 Stator Thermal Model Axial Length, Endwinding and Airflow Connections

In this section the necessary stator inter-plane axial length, endwinding and airflow thermal resistances, such as those presented for the rotor in the previous section, are outlined. The required additional thermal resistance connections are shown in Figure 3.17, transforming the single stator plane thermal network to a three-dimensional model representing the complete stator of the synchronous machine. As was the case with some rotor nodes in the rotor thermal model axial view in Figure 3.14, stator nodes 2 and 3 are excluded from Figure 3.17 to preserve the clarity of the diagram. Additional connections from stator node 2 can be treated in the same way as node 1, which is illustrated in Figure 3.17, and resistances along the path of node 3 are calculated like those for node 4, also in the stator lamination.

As with the rotor, the thermal resistances making up the stator thermal networks of Planes B and C see no differences with regards to Plane A. Hence, fully resistive components for Planes B and C are calculated in the same way and have the same °C/W values as those presented in Section 3.4 for Plane A. Similarly to the rotor, the convective resistances are modelled for each plane and, going towards the drive-end, heat transfer coefficients linked with the cooling airflow are reduced by a factor of 0.9. The stator typical coil winding slot fill factor of 0.4 is assumed and applied to the inter-plane conductive resistances, reducing the effective conduction stator coil area.

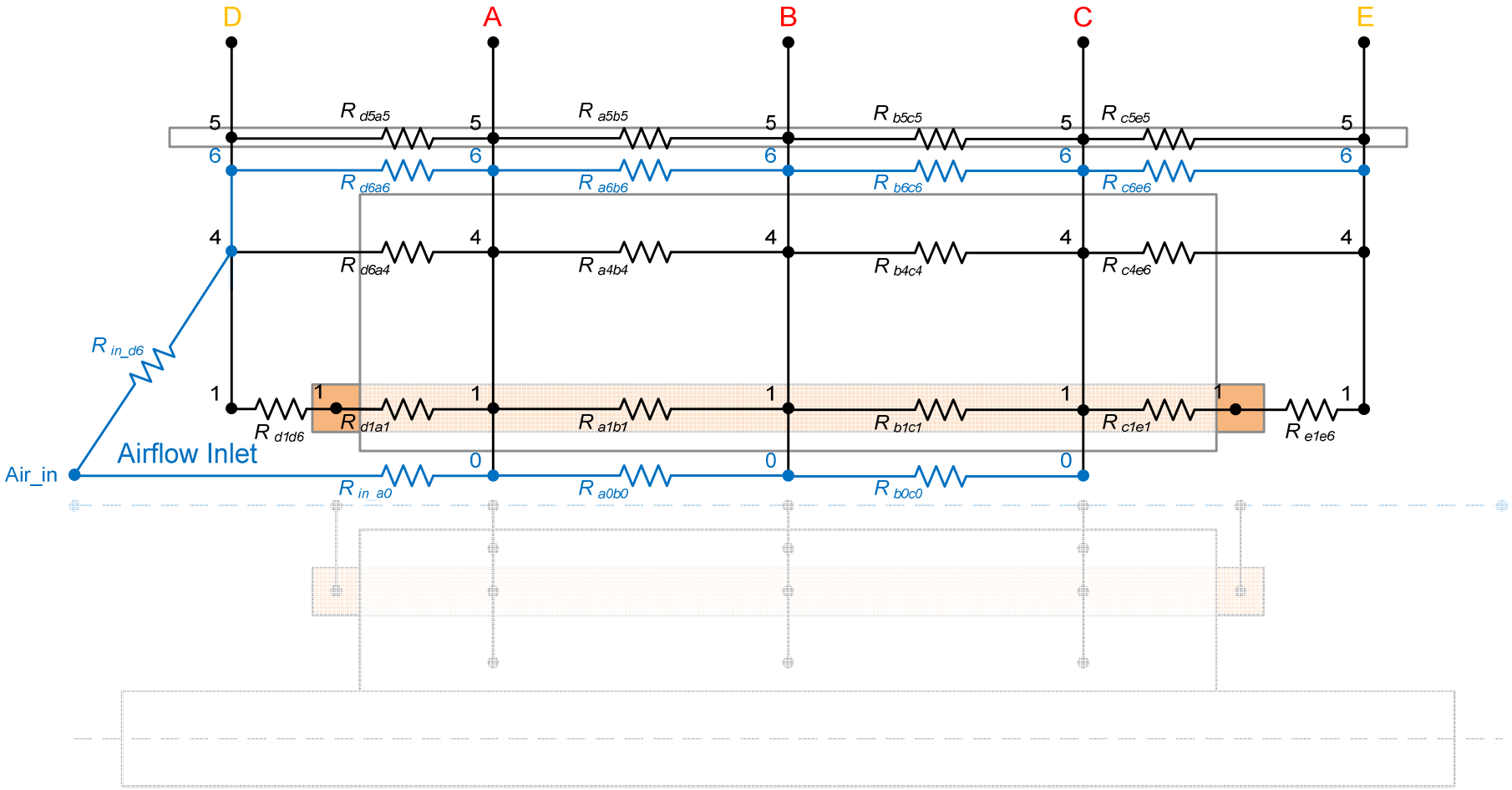

Figure 3.17: *Stator thermal model axial length, endwinding and airflow connections.*

Stator model inter-plane thermal conduction and endwinding thermal convection resistances, shown in black in Figure 3.17, are obtained using the techniques outlined in Sections 3.3 and 3.4. These thermal resistances are listed in Tables 3.8 and 3.9.

Stator Planes A & B * inter-plane links:

Thermal Resistance	Resistance Type: Description
R_{a1b1}	Conduction: Between lamination nodes 1 of planes A and B
R_{a2b2}	Conduction: Between lamination nodes 2 of planes A and B
R_{a3b3}	Conduction: Between lamination nodes 3 of planes A and B
R_{a4b4}	Conduction: Between lamination nodes 4 of planes A and B
R_{a5b5}	Conduction: Between lamination nodes 5 of planes A and B

* same inter-planes links between stator Planes B & C are required.

Table 3.8: *Stator inter-plane thermal resistances.*

Stator Plane D+ endwinding and A & D + inter-plane connections:

Thermal Resistance	Resistance Type: Description
R_{d1d6}	Convection: Stator endwinding node 1 to surrounding airflow
R_{d5d6}	Convection: Stator barrel node 5 to surrounding airflow
R_{a1d1}	Conduction: Plane A stator coil node 1 to endwinding node 1
R_{a2d1}	Conduction: Plane A stator coil node 2 to endwinding node 1
R_{a3d6}	Convection: Plane A lamination node 3 to adjacent airflow
R_{a4d6}	Convection: Plane A lamination node 4 to adjacent airflow
R_{a5d5}	Conduction: Plane A barrel node 5 to Plane D barrel node 5
R_{d5_AMB}	Convection: Plane D barrel node 5 to ambient
R_{d5_RAD}	Radiation: Plane D barrel node 5 to ambient

+ same inter-planes links for stator Plane E and between Planes C & E are required.

Table 3.9: *Stator endwinding thermal resistances.*

Table 3.9 presents the thermal resistances necessary to represent the stator non-drive-end and drive-end endwinding sections. These are illustrated in the two-dimensional endwinding radial view from the non-drive-end of the electrical machine thermal model in Figure 3.18, with the exception of R_{a5d5}, linking frame barrel nodes 5 between Planes A and D. The two fully conductive resistances connecting nodes 1 and 2 in Plane A with endwinding node 1 in Plane D, and the four convective resistances from the lamination and the stator coil to the surrounding airflow are shown. Conductive and convective thermal resistances for the drive-end side of the stator thermal model are constructed and calculated in the same way.

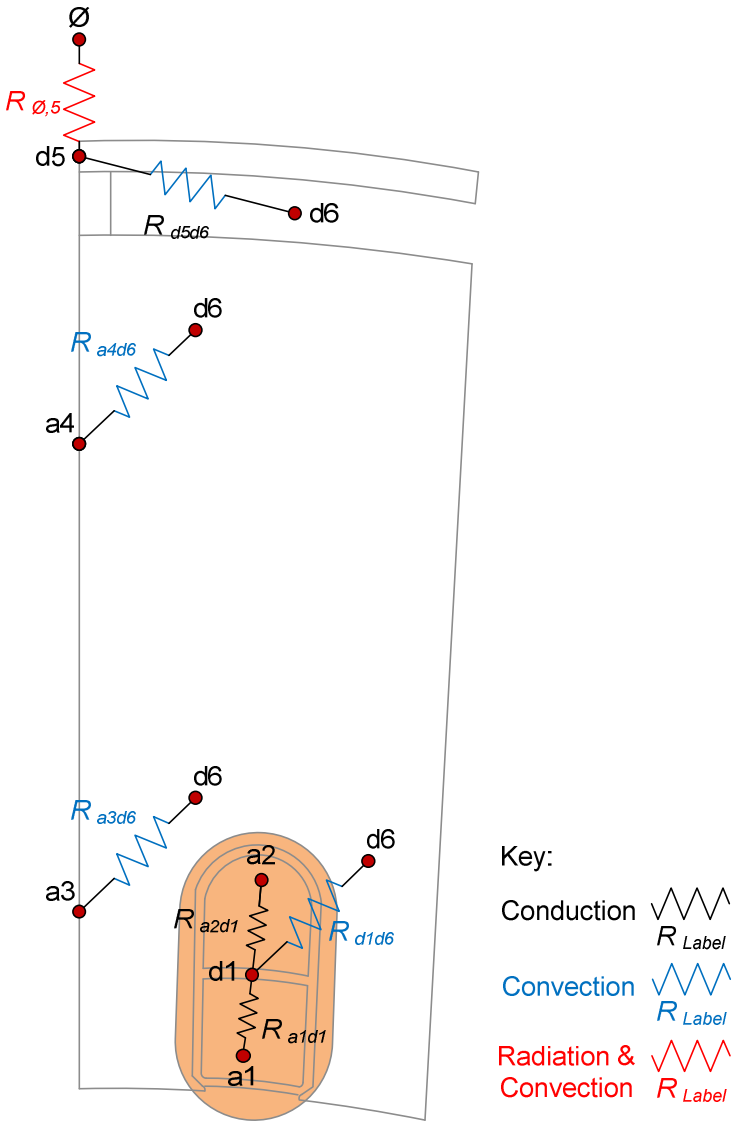

Figure 3.18: *Stator thermal model endwinding thermal resistance connections.*

The remaining thermal resistances in Figure 3.17 correspond to airflow paths along the axial length of the stator, along the barrel-frame gap and along the airgap of the machine. These thermal resistances are calculated using the same principles previously described in Section 3.5.1, using Equations 3.6 and 3.7.

$$\Delta T = \frac{Power\ Dissipated}{Volume\ Flow\ Rate \cdot Density \cdot c_p} \tag{3.6}$$

where ΔT is the temperature difference (°C) and c_p is specific heat capacity (J/kg/°C). The power dissipated is measured in W, airflow volume flow rate in m^3/s and density

in kg/m^3. From Equation 3.6, the airflow heat flux thermal resistance results, shown in Equation 3.7, and is used in the thermal model.

$$R_{Flow} = \frac{1}{X} \cdot \frac{1}{Volume\ Flow\ Rate \cdot Density \cdot c_p} \tag{3.7}$$

where dimensionless parameter *X*, determines the ratio of heat flow along the horizontal resistance in the axial direction, to the vertical resistance along the radial direction, is established and used as shown in the previous section for the rotor. As explained previously in Section 3.5.1, this airflow area requires further work in order to achieve an in depth understanding and accurate values for factor *X*.

Estimated *X* values for the two resistive airflow paths presented in Figure 3.17 (in blue) are shown in Figure 3.19. Slightly different *X* values for the stator barrel-frame gap airflow path are selected in an attempt to account for the slightly less effective cooling experienced along the barrel-frame stator airflow gap, in particular for the very first machine barrel stator segment which does not experience the full impact of the airflow, due to its location high up close to the machine frame. Apart from this minor alteration, a near-linear *X* value relationship is applied to the core length section of the resistive airflow path. Similarly to the rotor, near-linear *X* values for the airgap airflow path are selected and presented in Figure 3.19. As with the rotor thermal network values previously presented, the selected *X* values are based on the experimental thermocouple readings.

Barrel-Frame Axial Flow Resistance	*X* value
R_{In_d6}	3.5
R_{d6a6}	4.5
R_{a6b6}	3.5
R_{b6c6}	2.5
R_{c6e6}	1.0

Airgap Axial Flow Resistance	*X* value
R_{In_a0}	2.9
R_{a0b0}	2.1
R_{b0c0}	1.3

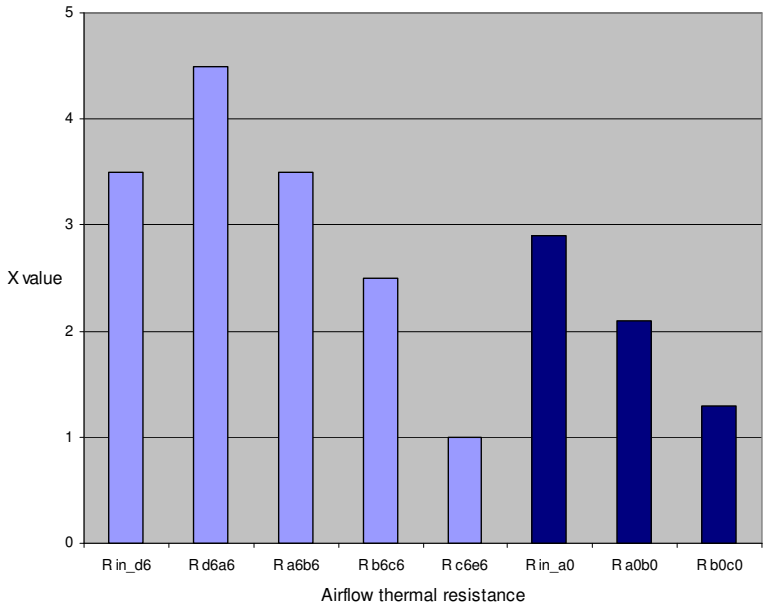

Figure 3.19: *Stator thermal model X values for barrel-frame gap airflow and airgap airflow thermal resistances.*

3.6 Airflow Heat Transfer Coefficient Calculation

In order to obtain the airflow convective heat transfer coefficients used in the previous sections for the rotor and stator models, the airflow paths along the synchronous machine, engulfing the rotor and the stator, need to be considered. As highlighted in the airflow related issues covered in the previous sections and detailed in Chapter 10, further airflow work is required in the future. Suggestions on how this future work should be executed are presented in Chapter 10. The CFD results provided by Cummins Generator Technologies shown in Figure 3.20 for a radial slice of an operating synchronous machine, illustrate the uneven airflow paths that exist around the electrical machine rotor and stator, and highlights the complications linked with this area of research.

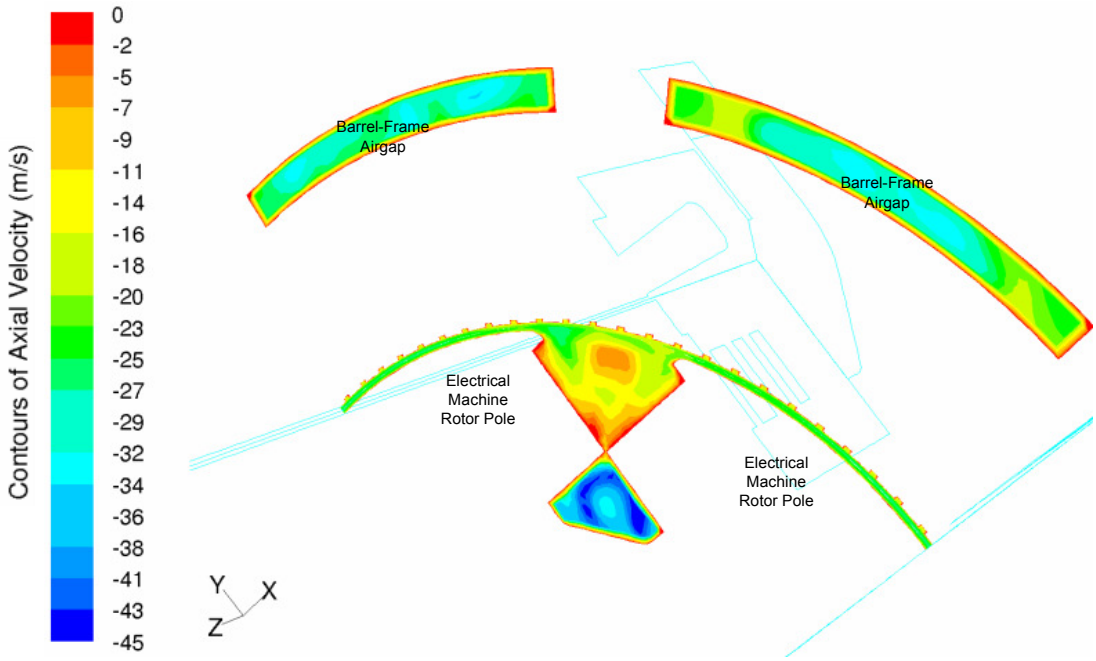

Figure 3.20: *Synchronous machine CFD radial slice airflow axial velocity results.*

The lumped parameter thermal models presented in this thesis and implemented in the thermal modelling tool MySolver, utilise the well established airflow correlations introduced in Chapter 2. These are used to obtain the heat transfer coefficients used by the rotor and stator thermal models as outlined in this section. Equation 3.8 is used to compute the specific convection heat transfer coefficients.

$$h_c = Nu_D\left(\frac{k_{air}}{D_h}\right) \tag{3.8}$$

where h_c is the convection heat transfer coefficient (W/m^2/°C), k_{air} is the thermal conductivity of air (W/m/°C), D_h is the hydraulic diameter (m) and Nu_D the dimensionless Nusselt number related to the specific hydraulic diameter considered.

Two literature formulations, Equations 3.9 and 3.10, for the Nusselt number, Nu_D, are utilised to obtain the value used in Equation 3.8. Both Nu_D equations presented apply to airflow along smooth pipes, with Equation 3.9 being a more historical Nusselt formulation and Equation 3.10 a more modern correlation that includes

friction considerations, introduced in Chapter 2. The average of both presented formulations is calculated and used as the input to Equation 3.8.

$$Nu_D = 0.023 \cdot \mathrm{Pr}^{\frac{1}{3}} \cdot \mathrm{Re}_D^{0.8} \tag{3.9}$$

where Pr and Re are the relevant Prandtl and Reynolds numbers and D is the hydraulic diameter (m).

$$Nu_D = \frac{\frac{f_{coef}}{8} \cdot (\mathrm{Re}_D - 1000) \cdot \mathrm{Pr}}{1 + 12.7\sqrt{\frac{f_{coef}}{8}}\left(\mathrm{Pr}^{\frac{2}{3}} - 1\right)} \tag{3.10}$$

where the smooth pipe friction factor, f_{coef}, is given by Equation 3.11. Pr values range between 0.5 and 200. A typical value of 0.7 is selected for Pr [42].

$$f_{coef} = \frac{1}{(1.82 \log_{10} \mathrm{Re}_D - 1.64)^2} \tag{3.11}$$

Finally, the formulation used to obtain the Reynolds number, Re_D, needed in Equations 3.9, 3.10 and 3.11 is shown in Equation 3.12 [42].

$$\mathrm{Re}_D = \frac{\rho \cdot v \cdot D_h}{\mu} \tag{3.12}$$

where ρ is the density (kg/m^3), v is the average axial velocity (m/s), D_h is the hydraulic diameter (m) and μ is the dynamic viscosity (kg/m.s).

Axial velocities (v) of the airflow flowing around the rotor and the stator required for Equation 3.12 are provided by Cummins Generator Technologies, utilising an

internal air flow modelling package. Further in depth airflow related implications are outside the scope of this thesis and are addressed in Chapters 9 and 10.

Finally, acknowledging the limitations linked with the method used to determine the necessary heat transfer coefficients described in this section, an additional h_c adjusting factor, X_{hc}, is introduced. The function of this factor is simply to calibrate the airflow aspects of the MySolver thermal modelling package presented in Chapter 6 after some initial verification heat-runs are executed. As a consequence heat transfer coefficients are adjusted by the magnitude of X_{hc}, as shown by Equation 3.13. An attempt should be made to try and maintain the X_{hc} adjusting coefficient as low as possible and a self-imposed limit of around 1.75 should not be exceeded. X_{hc} values utilised by MySolver are considerably lower than the mentioned limit (~ 1.5).

$$h_c = X_{hc} \cdot Nu_D \left(\frac{k_{air}}{D_h} \right) \tag{3.13}$$

Further work to better understand the airflow cooling the electrical machine will allow future versions of MySolver to account for the complex airflow nature without the need of an h_c overall adjusting factor, X_{hc}.

3.7 Synchronous Generator Operational Losses

Synchronous machine operational losses are the main input to the rotor and stator lumped parameter thermal models created in Sections 3.3 and 3.4. The different types of electrical machine power losses are introduced and explained in Chapter 2. Of the machine losses presented, those that are inputs to the rotor and stator thermal networks created are covered in this section.

3.7.1 Copper losses

Copper losses, P_{Cu}, associated with the rotor and stator winding can be quantified by experimentally measuring the field and armature currents flowing in the rotor and stator windings whilst under load, the relevant voltage and/or the associated winding resistance. P_{Cu} is calculated using Equation 3.14.

$$P_{Cu} = I \cdot V = I^2 \cdot R \tag{3.14}$$

where I is the winding current (A), V the winding voltage (V) and R the winding resistance (Ω). It is important to note that hot, experimentally obtained, thermal resistances are utilised. The experimental I, V and R measurements collected in Table 8.1, Section 8.1, are utilised for this.

Rotor copper loss inputs for each specific lumped parameter node, for the three core length planes (A, B and C), *Rotor* P_{Cu_length}, and for the two endwinding planes (D and E), *Rotor* $P_{Cu\_endwinding}$, are calculated using Equations 3.15 and 3.16. The axial length of a segment, d(m) is the total machine core length divided by the number of radial slices representing the electrical machine.

$$Rotor\ P_{Cu\_length} = \frac{Total\ P_{Cu}}{Number\ of\ poles} \cdot \frac{Axial\ length\ of\ segment,\ d\ (m)}{Total\ length\ of\ coil\ around\ pole} \tag{3.15}$$

$$Rotor\ P_{Cu\_endwinding} = \frac{Total\ P_{Cu}}{Number\ of\ poles} \cdot \frac{Coil\ endturn\ length}{Total\ length\ of\ coil\ around\ pole} \tag{3.16}$$

In a similar way, stator copper loss inputs for the three core length planes (A, B and C), *Stator* P_{Cu_length}, and for the two endwinding planes (D and E), *Stator* $P_{Cu\_endwinding}$, are calculated using Equations 3.17 to 3.18.

$$Stator\ P_{Cu\_length} = \frac{Total\ P_{Cu}}{Number\ stator\ slots} \cdot \frac{Axial\ length\ of\ segment,\ d\ (m)}{Total\ core\ length} \tag{3.17}$$

$$Stator\ P_{Cu\_endwinding} = \frac{Total\ P_{Cu}}{Number\ stator\ slots} \cdot \frac{Length\ of\ overhang\ winding}{Total\ core\ length} \quad (3.18)$$

The resulting copper losses are split accordingly and applied to rotor thermal network nodes 1 and 3, and stator thermal network nodes 1 and 2, shown in Figure 3.21, for each thermal model plane along the core length of the electrical machine. Endwinding copper losses are also added to the relevant winding nodes.

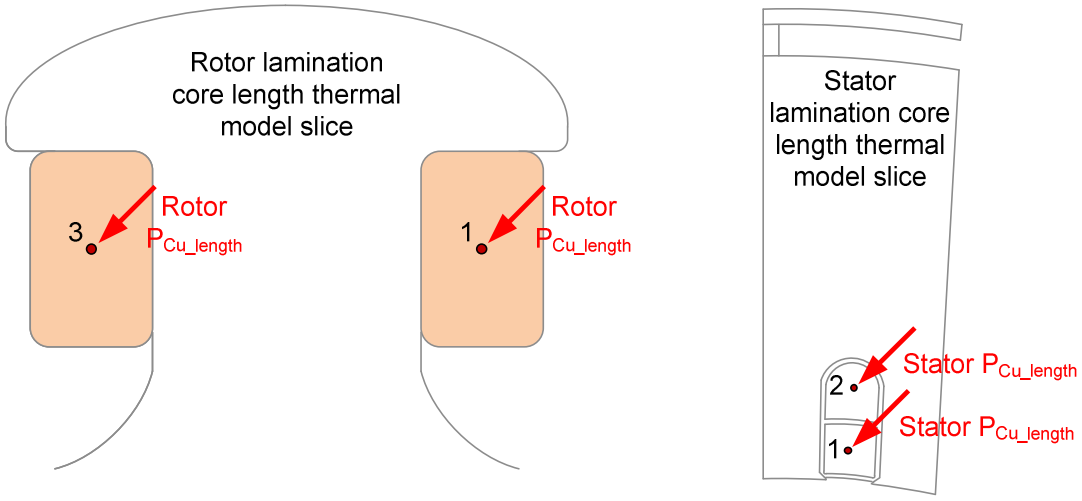

Figure 3.21: *Copper loss rotor and stator lumped parameter thermal network input nodes.*

For example, using the rotor field current and voltage readings (Table 8.1, Section 8.1) for the BCI184E CGT alternator, taken when supplying a 12.26 kW load, *Rotor* P_{Cu_length} equals 6.13 W and *Rotor* $P_{Cu\_endwinding}$ equals 14.85 W. Calculations are outlined using Equations 3.14, 3.15 and 3.16.

$$Total\ Rotor\ P_{Cu} = 18.2\ A \times 14.6\ V = 266\ W$$

$$Rotor\ P_{Cu\_length} = \frac{266\ W}{4\ poles} \cdot \frac{0.05\ m}{0.542\ m} = 6.13\ W$$

$$Rotor\ P_{Cu\_endwinding} = \frac{266\,W}{4\ poles} \cdot \frac{0.121\,m}{0.542\,m} = 14.85\,W$$

Rotor and stator copper losses for all machine loadings considered are calculated by the MySolver thermal modelling package introduced in Chapter 6.

3.7.2 Iron losses

Rotor and stator lamination iron losses are significantly more difficult to estimate than copper losses, due to their dependency on machine frequency and magnetic fluxes. Iron losses are introduced in detail in Chapter 4 and finite element analysis iron loss predictions, and their important distribution across the machine laminations, are covered. Once total machine iron losses, *Total* P_{Iron}, are obtained, these are added to the relevant rotor and stator thermal network nodes illustrated in Figure 3.22, using Equations 3.19 and 3.20. As shown, *Total* P_{Iron} is split between the rotor and the stator in a ratio of 15:85. This rotor to stator lamination iron loss split ratio is obtained from the finite element analysis results covered in Chapter 4 and is applicable to the complete synchronous generator loading range examined, supported by CGT's experience in the area.

$$Rotor\ P_{Iron} = \frac{Total\ P_{Iron} \times 0.15}{Number\ of\ poles} \cdot \frac{1}{No.\ axial\ planes \times No.\ plane\ nodes} \tag{3.19}$$

$$Stator\ P_{Iron} = \frac{Total\ P_{Iron} \times 0.85}{Number\ of\ stator\ slots} \cdot \frac{1}{No.\ axial\ planes \times No.\ plane\ nodes} \tag{3.20}$$

At this point, the iron loss LCCs presented in Chapter 4 are applied and lamination losses re-distributed according to the finite element analysis results obtained.

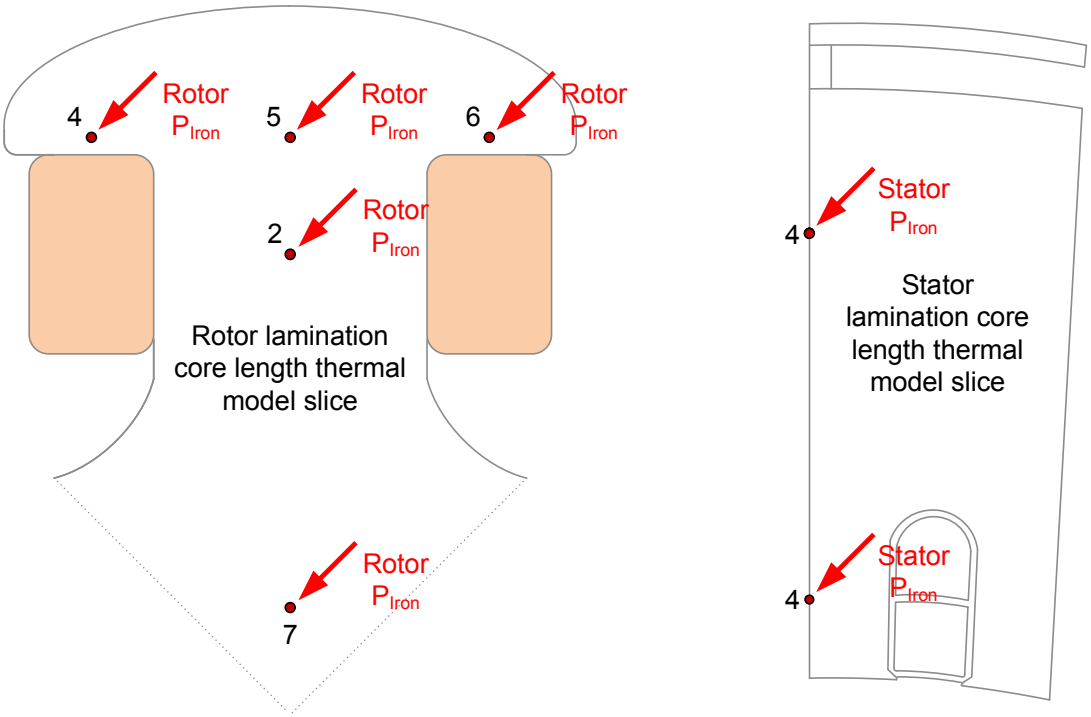

Figure 3.22: *Iron loss rotor and stator lumped parameter thermal network input nodes.*

As concluded from Chapter 4, a total iron loss, *Total* P_{Iron}, value of 505 W is obtained for the CGT electrical machine analysed, experimentally and through finite element analysis. Utilising this and assuming an even symmetrical distribution of iron losses across the laminations at this stage, rotor and stator iron loss thermal network power inputs are calculated, using Equations 3.19 and 3.20, as shown. Relatively low power values result, since this is the loss input to a single lamination lumped parameter network node, in one plane, for one pole. The slight modifications to the process introduced by the addition of the LCCs to increase accuracy are covered in Chapter 4, where LCCs are presented and their implementation is outlined.

$$Rotor\ P_{Iron} = \frac{505\,W \times 0.15}{4\ poles} \cdot \frac{1}{3\ planes \times 5\ nodes} = 1.26\,W$$

$$Stator\ P_{Iron} = \frac{505\,W \times 0.85}{36\ slots} \cdot \frac{1}{3\ planes \times 2\ nodes} = 1.99\ W$$

The method to distribute iron losses across the rotor and stator lamination thermal networks can be adapted to different thermal models, depending on the number of axial planes and plane nodes utilised to recreate the electrical machine analysed, but the presented principles should be applied to any lumped parameter network developed.

3.7.3 Stray losses

Stray losses are introduced in Chapter 2. Detailed stray loss magnitude estimations are out with the scope of the work presented. In the rotor and stator thermal models presented in the previous sections, stray losses, P_{Stray}(W), are quantified utilising Equation 3.21, a formulation fully elaborated by Cummins Generator Technologies from electrical machine designing and manufacturing experience.

$$P_{Stray} = (Load\ \ fraction)^{0.8} \cdot \left(Machine\ rating \times \left(\frac{50}{f} \right) \right)^{0.59} \cdot \left(\frac{f}{50} \right)^{1.5} \tag{3.21}$$

where the *Load fraction* ranges from 0 at no-load to 1 at full load, *Machine rating* is the specific nominal operational load rating related to the synchronous generator (W) and *f* is the frequency (Hz), which is 50 Hz for all simulations considered in Chapter 8.

For example, taking the 12.26 kW load test considered in Chapter 8, stray losses are quantified using Equation 3.12 for the 22.5 kVA BCI184E CGT alternator as shown:

$$P_{Stray} = (0.5449)^{0.8} \cdot \left(22500 \times \left(\frac{50}{50} \right) \right)^{0.59} \cdot \left(\frac{50}{50} \right)^{1.5} = 227.43\,W$$

The calculated P_{Stray} is then fractioned and applied to the relevant thermal network nodes in the same way that iron losses are in the previous section.

3.8 Thermal Network Additions for Transient Analysis

In order to enable the MySolver thermal modelling tool to produce transient results and perform duty-cycle simulations, thermal capacitances are added to the rotor and stator thermal networks in Figures 3.3 and 3.7, at every loss power input node, as illustrated in Figure 3.23. The capacitances shown in Figure 3.23 are added to all thermal model core length planes and to the two endwinding planes.

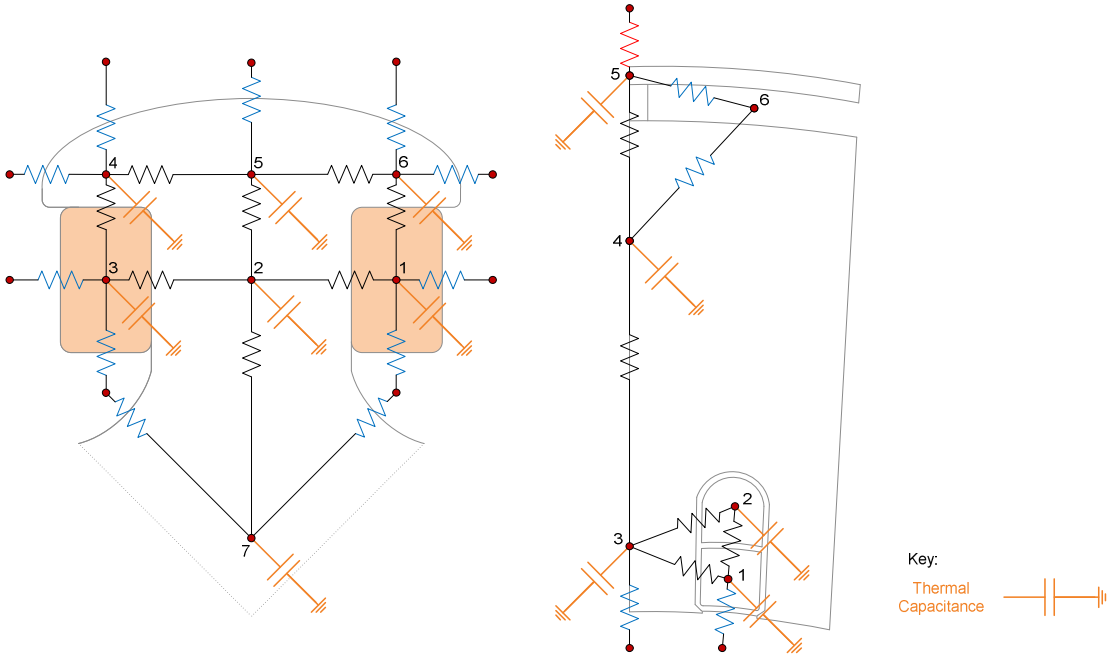

Figure 3.23: *Rotor and stator thermal network transient thermal capacitances.*

It has to be noted that the winding time constant, τ, is significantly smaller than the electrical machine's overall time constant, since a significant amount of heat is generated in the windings and it takes longer to transfer through to other machine sections. Hence, time constants for the rotor and stator winding need to be considered independently. For the CGT alternator analysed in this thesis, the rotor winding time

constant is identified as being 20 minutes and the stator winding time constant 12 minutes, as presented in Chapter 8.

The time constant, τ, is determine by the product of the thermal resistance, R, and capacitance, C, as indicated in Equation 3.22.

$$\tau = R \cdot C \tag{3.22}$$

where the thermal resistance, R, is obtained by Equation 3.1 (thermal conduction) or Equation 3.2 (thermal convection) depending on the heat transfer nature of the resistive path, as explained in this chapter. The capacitance, C, used in Equation 3.22 is obtained by Equation 3.23.

$$C = \rho \cdot V \cdot C_p \tag{3.23}$$

where ρ is the density (kg/m^3), V is the volume (kg/m^3) and Cp is the specific heat capacity of the material (J/kg/°C).

A density of 7800 kg/m^3 and a specific heat capacity of 500 J/kg/°C is utilised for the electrical machine lamination sections. With regards to the winding material proprieties used, copper has a density of 8900 kg/m^3 and a specific heat capacity of 390 J/kg/°C, but these have been modified to 7500 kg/m^3 and 460 J/kg/°C respectively to account for the presence of insulation within the windings. This information was provided by the electrical machine supplier.

To model the BCI184E CGT alternator, rotor and stator coil structure densities provided by the manufacturer are used. Accurate coil density information is not always easily available, even from material and machine suppliers, given the number of different materials comprising the windings and the difference between manufacturing processes. In addition to this, since rotor and stator windings are not constructed identically they can have different densities, but will remain within the

kg/m^3 range provided by the supplier. Furthermore, rotor and stator coil structure specific heat capacities, which are again subject to a limited accuracy, are utilised.

3.9 Chapter Summary

The principles by which the synchronous machine lumped parameter thermal modelling networks can be developed have been presented in this chapter, with individual thermal models for the rotor and the stator. Well proven formulations are employed and, backed with reliable geometric and physical electrical machine data, produce accurate thermal representations of the synchronous generators modelled, with examples for these provided. All considerations required to make the lumped parameter models representative of the complete electrical machine investigated are presented and discussed. Furthermore, airflow implications, necessary to determine the required heat transfer coefficients are presented, and the addition of thermal capacitances to enable transient thermal analysis is described. The reasonable assumptions made and the areas which require further work have been highlighted, with detailed reasons and suggested future plans of work outlined in Chapters 9 and 10. Lumped parameter thermal model limitations and assumptions outlined through out this chapter do not jeopardise accuracy excessively but, even so, it is very important to address the further work aspects collected in Chapter 10, in order to increase understanding and obtain an even higher accuracy.

CHAPTER 4

Finite Element Analysis – Iron Loss Distribution within Machine Lamination

4.1 Introduction

The prediction and exact distribution of iron losses under transient conditions across a synchronous machine's lamination has proven to be a challenging area [73]. In the past, several loss calculation methods have been applied in the frequency domain, but analysis in the time domain still requires significant work [74]-[76]. Therefore, utilising the more established frequency domain approach, the objective of the work presented in this section is to utilise Vector Fields (VF) Finite Element Analysis (FEA) [77] to determine the synchronous machine lamination iron loss distribution and to apply the results obtained to the lumped parameter thermal networks presented in Chapter 3. Given current demands for more efficient electrical machines, the prediction of iron losses has become increasingly important [78] and FEA proves to be a method suitable to achieve this.

FEA is a powerful design tool that allows mirroring electrical machine tests and extracting important electromagnetic and thermal information, with a high degree of accuracy. Once precise geometries of the machine under investigation have been established, feeding experimentally obtained data related to the field and armature of the machine allows for the determination of useful data such as the vector potential, current density, magnetic flux density and magnetic field strength distribution. Therefore, FEA provides a level of insight and detail of the machine's inner behaviour otherwise unattainable by experimental methods, at the expense of meticulous model calibration and extensive computing times.

The main machine characterising parameters required for a synchronous machine model relate to the rotor, where the field voltage and winding impedance are required as an input to the simulations. On the other hand, no voltage input settings are required for the armature winding, since these are generated by the simulation itself. Only the armature winding resistance and inductance are required for the stator settings. Magnetisation properties of the rotor and stator lamination materials, as well as the shaft, need to be accurately established. Furthermore, boundary conditions (fixed potential edges) around particular machine components need to be carefully considered [30].

4.2 Synchronous Generator Iron Losses

As presented in Chapter 2, iron losses are among the electrical machine operational losses that need to be considered during the thermal modelling of a synchronous generator, along with copper, mechanical and stray losses. The thermal modelling importance of iron losses varies with electrical machine types [79] & [80], but these are always significant and need to be accounted for [81]. Compared to copper losses, iron losses are significantly more challenging to predict, given their high frequency and magnetic flux dependency [61] & [82]. Iron losses are composed of hysteresis losses and eddy-current losses [60] & [63], but can also be affected by machine loading and by electrical and mechanical transients for particular electrical machine types [73]. Iron loss analysis work has been carried out for a wide range of machines, such as permanent magnet machines [79] & [83]-[87], induction machines [63] & [73] and linear DC motors [88], but this area of study still remains challenging for machine designers. Some iron loss investigations have been carried out on synchronous machines [81] & [89], but further work is required to fully understand their behaviour.

In order to predict iron losses, P_{Iron}, in an effective and reliable manner, harmonic evaluation of the flux density waveform in each FEA model element in the frequency domain, for the time cycle under investigation, is required. Hence, the end result is a

decomposition of the magnetic flux waveform per element into its constituent parts (fundamental, 1st order, 2nd order, 3rd order, etc.). For ferritic materials, such as the synchronous machine's lamination, this is then used to compute the loss per harmonic using the well-known Steinmetz formulae [74], shown in Equation 4.1.

$$P_{Iron} = C_m \cdot f^{\alpha} \cdot B_m^{\beta} \tag{4.1}$$

where P_{Iron} is the total iron loss, C_m, α and β are empirical parameters obtained from experimental measurement under sinusoidal condition. B_m represents the peak magnetic flux density and f the frequency.

As a more general approach, total iron loss is the sum of the hysteresis and eddy current components, with the addition of an excess loss component due to domain wall effects, which should be taken into account for non-ferrite materials, as shown in Equation 4.2 [63], [73], [74] & [90].

$$P_{Iron} = P_h + P_e + P_x = k_h \cdot f \cdot B_m^{\beta} + k_e \cdot \left(f \cdot B_m^{\beta}\right)^2 + k_x \cdot \left(f \cdot B_m^{\beta}\right)^{1.5} \tag{4.2}$$

where P_h is the hysteresis component, P_e the eddy-current component and P_x the excess loss. The k loss constants are determined as shown in Section 4.4.

4.2.1 Experimental Estimation of Iron Losses in Synchronous Generators

Iron losses can be experimentally estimated for the specific synchronous generator investigated. In comparison with the behaviour of iron losses in induction machines [73], where these vary significantly with machine loading, in synchronous generators iron losses remain constant with changing load and fluctuate with alterations in the armature voltage, as shown in Figure 4.1.

Given that a constant armature voltage of 415 V is considered in this thesis, iron losses are determined by subtracting windage and friction losses from the total no-load loss at the machine rated voltage [91]. Figure 4.1 illustrates how iron losses are experimentally predicted for the CGT BCI184E synchronous generator for a particular stator armature voltage. When the voltage is at 0 V, only windage and friction losses are present, which are fully supplied by and can be measured from the drive machine. Subsequently, these are utilised to calculate iron losses as shown.

Voltage (V)	Total Loss (kW)	Iron Loss (kW)
0.0	**0.260**	**0.0**
186.9	0.354	0.094
235.5	0.405	0.145
263.4	0.437	0.177
299.0	0.492	0.232
343.4	0.567	0.307
379.3	0.652	0.392
415.0	**0.765**	**0.505**
432.7	0.854	0.594
457.7	1.027	0.767
473.1	1.240	0.980
482.1	1.424	1.164
491.7	1.649	1.389
499.6	1.827	1.567

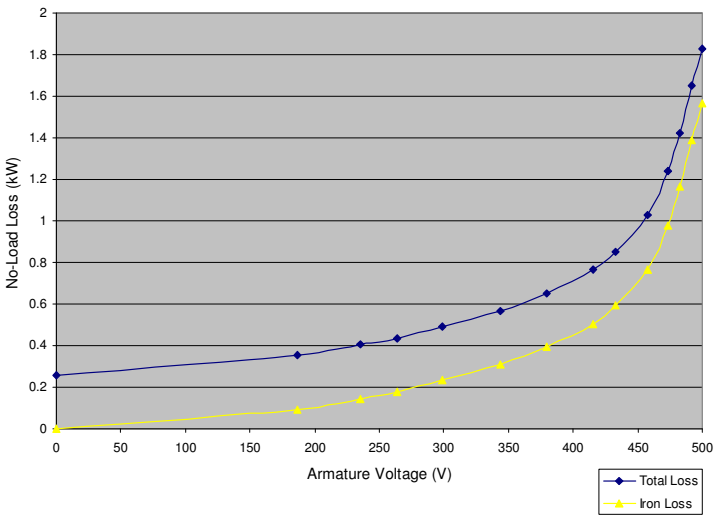

Figure 4.1: *Experimental total and iron loss no-load determination.*

As illustrated in Figure 4.1, windage and friction losses have a magnitude of 260 W when the armature voltage is 0 V. Hence, subtracting these from the 765 W for the rated voltage (415 V), yields an iron loss value of 505 W. This result serves as a method to evaluate the FEA simulations presented in this chapter. As shown later in Section 4.4, the results yielded by FEA are reasonably close to this experimentally obtained value, which indicates that the conclusions reached in this chapter are supported by data obtained experimentally from the synchronous machine analysed.

Search coils located in the stator of the test machine examined are utilised to further validate the non-variation of iron losses with machine loading. Shown in Figures 4.2 and 4.3 respectively are the search coil readings for the stator back iron and slot at no-load, 5 kW and 10 kW loadings. As illustrated in Figure 4.2, there is practically no change in the voltage readings for the stator back iron for the three loading scenarios considered. The stator slot search coil readings plotted in Figure 4.3 exhibit slight differences between loadings, but these are minor. Hence, the results presented confirm that iron losses do not vary significantly with loadings and can be assumed to be constant in synchronous machine lumped parameter thermal models.

No-Load:

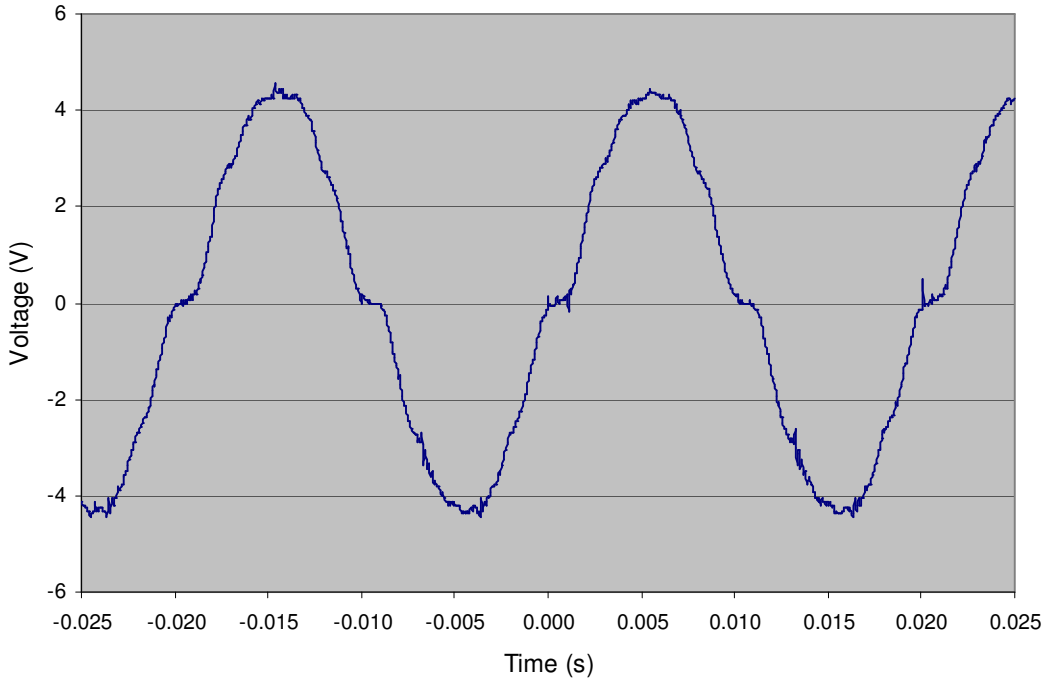

5 kW Loading:

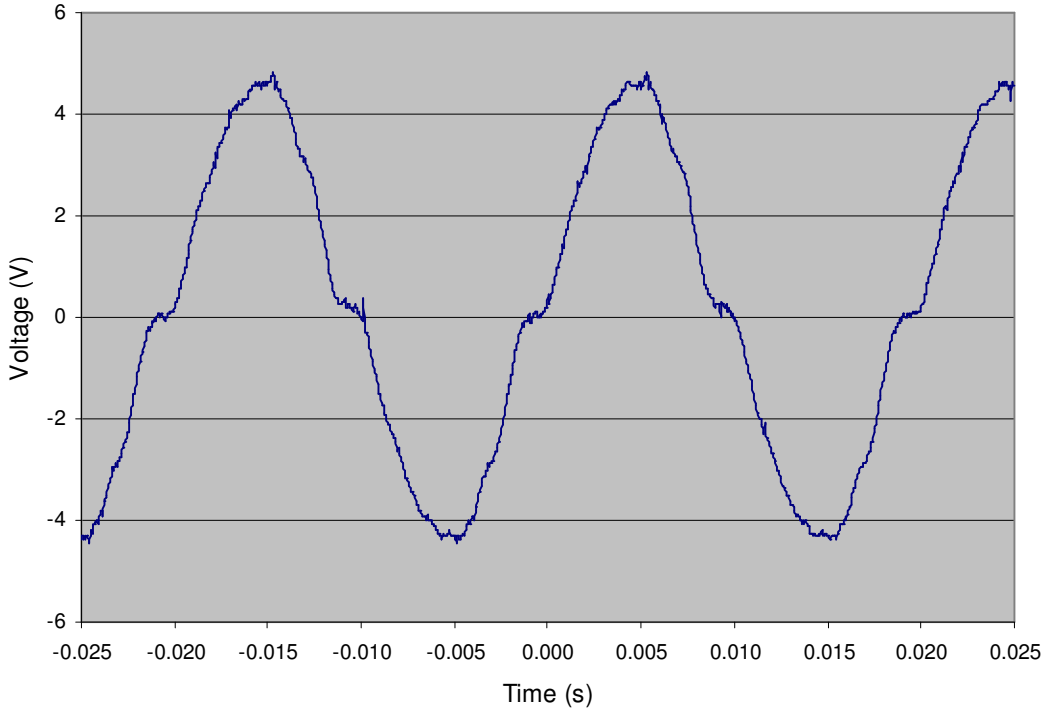

10 kW Loading:

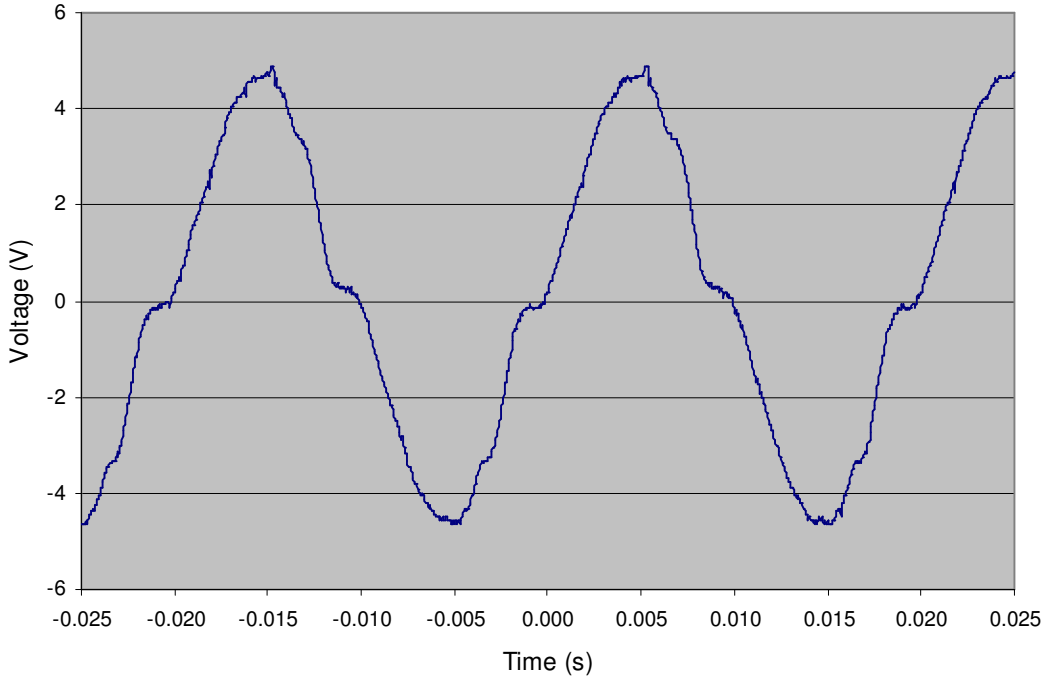

Figure 4.2: *Stator back iron search coil results for no-load, 5 kW and 10 kW loadings.*

No-Load:

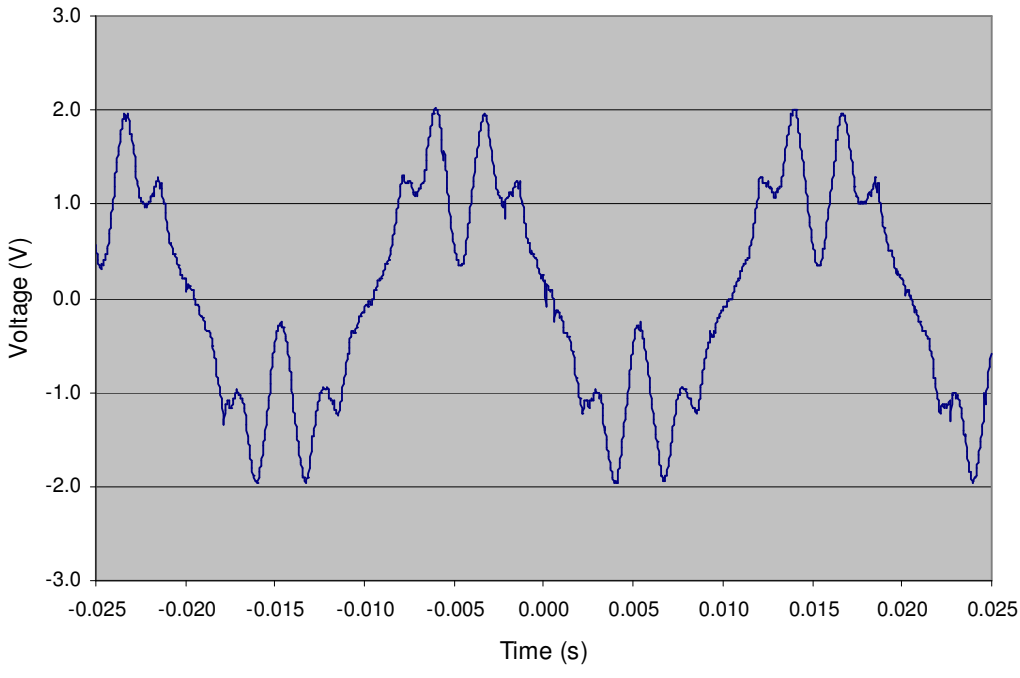

5 kW Loading:

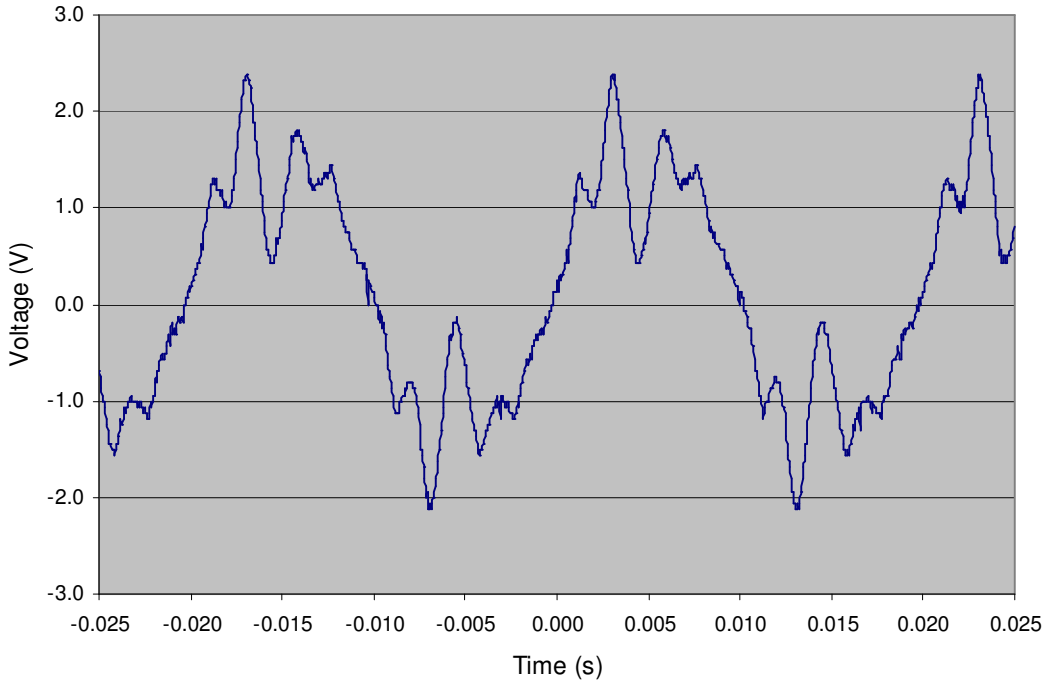

10 kW Loading:

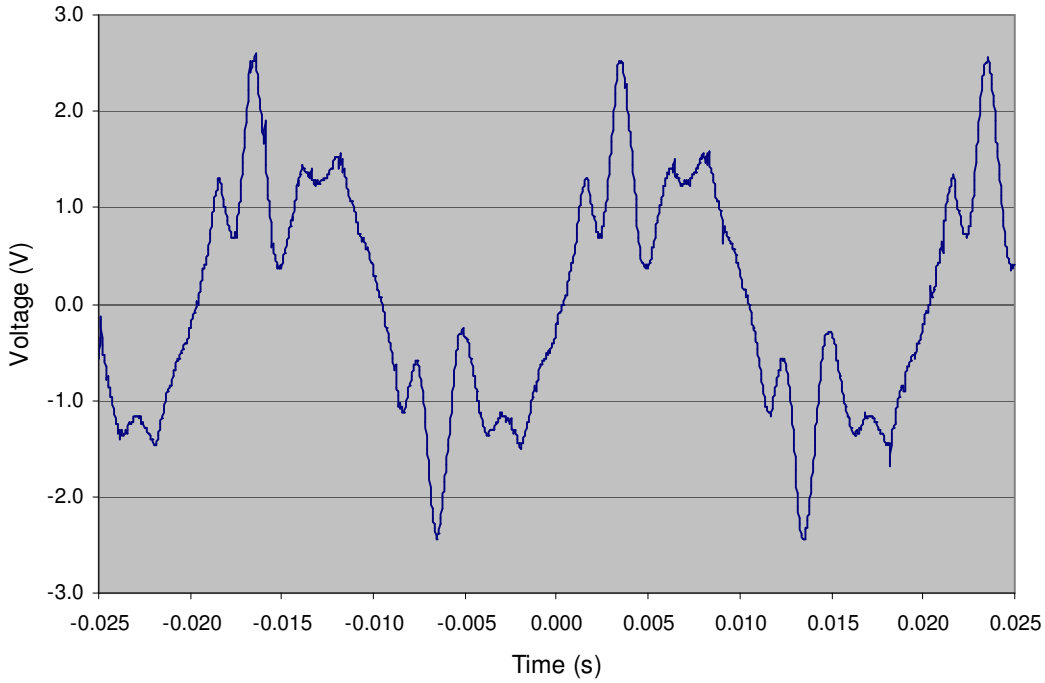

Figure 4.3: *Stator slot search coil results for no-load, 5 kW and 10 kW loadings.*

Finally, additionally to the results presented in Figures 4.2 and 4.3, sensitivity analysis was performed on the iron loss value utilised in the synchronous generator lumped parameter thermal models. Results show that an iron loss fluctuation of ± 100 W from the obtained 505 W value yields a rotor ± 1.5 °C and stator ± 3.0 °C steady-state average temperature swing. This finding means that the computed iron loss value of 505 W can be confidently fixed for the constant armature voltage lumped parameter model simulations. Even if iron losses do slightly change with loading, the effect on the resulting overall thermal model temperature predictions will not be significant enough to cause concern.

4.3 FEA Synchronous Generator Modelling

The FEA model of the CGT electrical machine presented in Section 3.2 is described in this section. The steps and method presented to create the FEA model for the synchronous machine are applicable to other machine sizes and machine types.

4.3.1 FEA Synchronous Generator Model Development

The geometries of the generator windings, shaft, laminations and other design components need to be precisely extracted from reliable machine drawings, from which, the two-dimensional cross-section of the alternator, shown in Figure 4.4, is created.

The model presented is that of the CGT BCI184E 4-pole synchronous generator. It is composed of 36 stator slots, in which a 2/3 pitched double layer concentric winding is used. There are 3 slots per pole per phase and 98 turns per phase. The generator's armature is series star wound and machine rotation is in the clockwise direction. It is important to note that for the synchronous generator model shown, fixed potential boundaries conditions are exclusively utilised around the stator lamination. Boundary conditions should be placed around particular machine components and are a useful tool in order to encapsulate the electrical machine model's field lines within the

desired section, but need to be accurate in order to not affect the simulation unrealistically [92]. For instance, a fixed potential boundary around a steel shaft would be an incorrect simplification, since the magnetic properties of the shaft's steel composition would be ignored. In the model illustrated in Figure 4.4, boundaries were placed around the stator lamination.

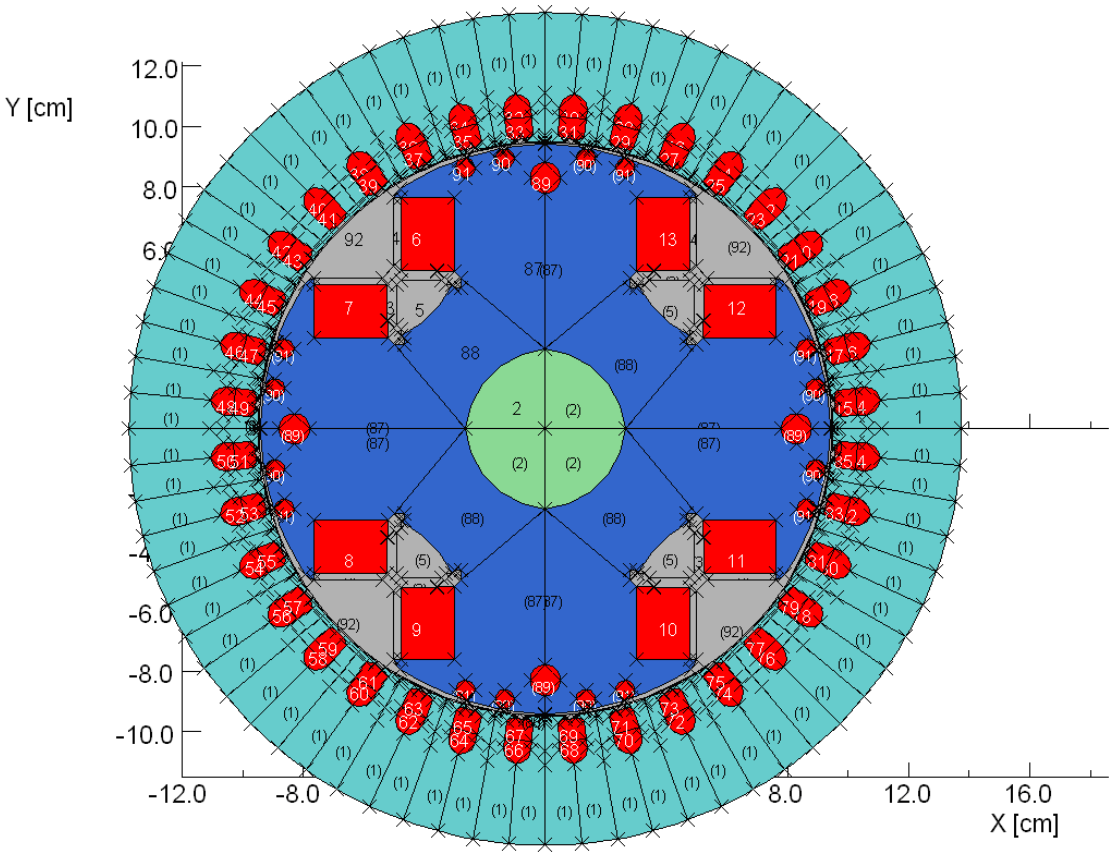

Figure 4.4: *Cummins Generator Technologies BCI184E 2-D FEA model.*

Magnetisation properties of the rotor and stator lamination materials, as well as the shaft, are very important and need to be accurately established. Critically, the rotor and stator lamination BH curves selected will determine the output armature current generated by the simulation. Hence, acquiring and selecting the appropriate rotational core loss affecting BH curves [93] from the generator material suppliers is a crucial task during the FEA model elaboration process. FEA model rotor and stator lamination properties are set in accordance with the material supplier's data. If the lamination suppliers are unable to provide certain material data for particular operating conditions, then reasonable approximations, from BH curves for similar

materials on comparable machines, need to be made. The most important sections of the BH curves are the point at which the 'knee' occurs and the saturation regions, shown in the BH curves in Figures 4.5 and 4.6. Points below the BH curve 'knee' are normally not critical for the simulation's outcome. The BH curves used for the BCI184E machine lamination and for the steel shaft are presented in Figures 4.5 and 4.6 respectively. These are extracted from data provided by material suppliers, but are slightly extrapolated due to limited information being available for the desired frequency and operating condition. The resulting BH curves presented in Figures 4.5 and 4.6 are validated by comparing them with other Cummins Generator Technologies BH curves of similar electrical machines.

After accounting for the lamination geometry and material properties, the winding arrangements needs to be defined in the FEA model. For the test machine, the stator is wound in a series star configuration, with a double layer concentric winding layout of 2/3 pitch and 98 turns per phase. Figure 4.7 displays the armature winding series star layout of the machine's 3 phases (U-V-W), whilst further armature winding details for each phase are presented in Appendix B.

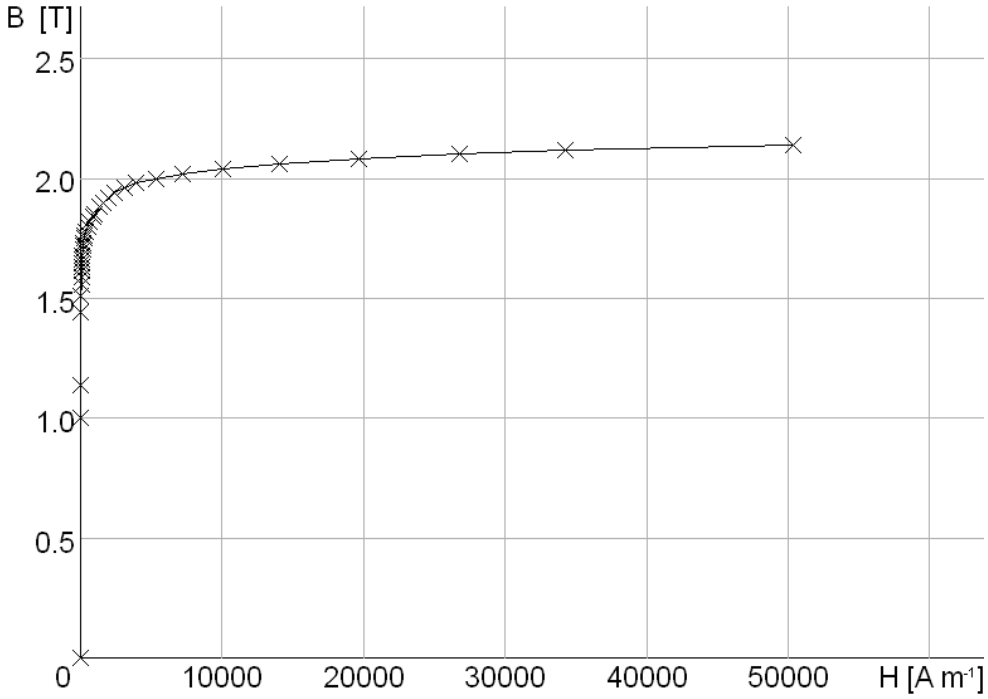

Figure 4.5: *BH curve for BCI184E synchronous generator's lamination.*

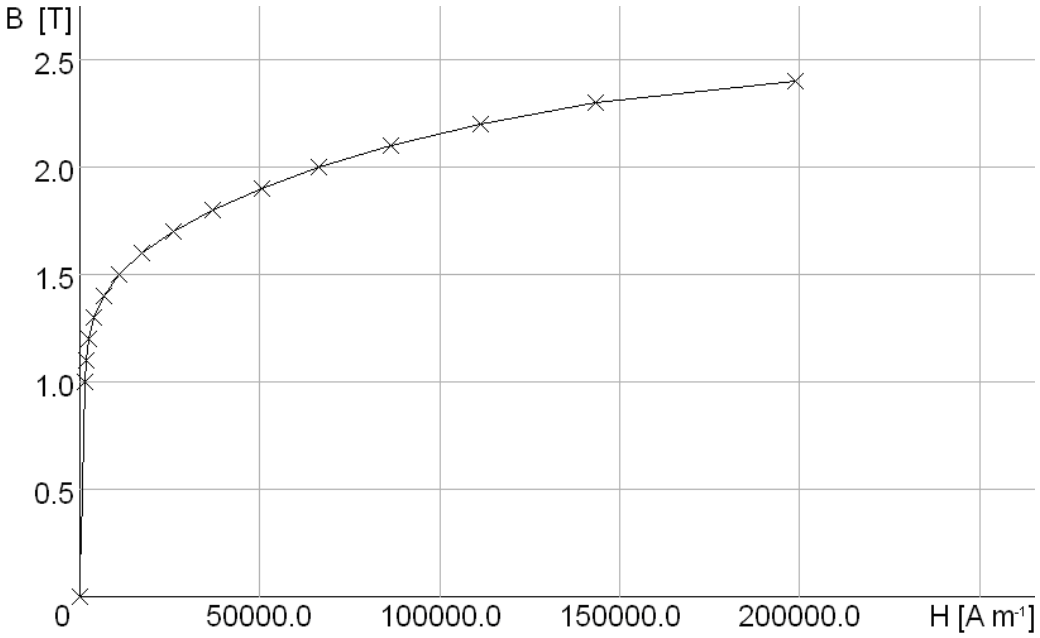

Figure 4.6: *BH curve for BCI184E synchronous generator's steel shaft.*

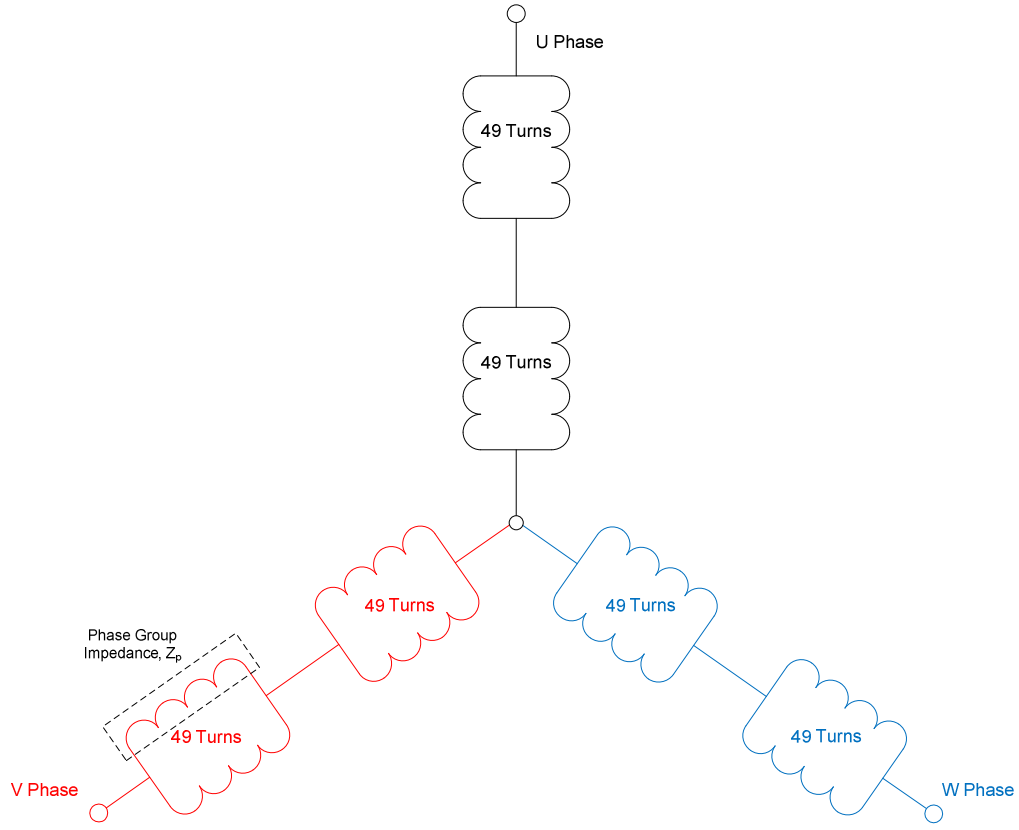

Figure 4.7: *BCI184E machine's series star armature winding configuration.*

Once electrical machine armature winding details are established, FEA external circuit simulation settings should be determined. External circuits are a convenient tool for the FEA model calibration process stage. They are effectively used by the FEA simulator to account for armature or field resistances, capacitances and inductances, with a resulting V(t) voltage. For example, armature external circuits are utilised by the Vector Fields FEA simulator as shown in Figure 4.8.

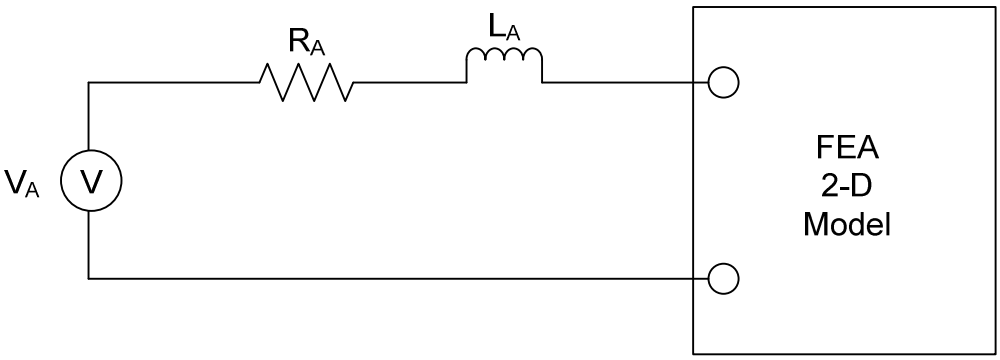

Figure 4.8: *External circuits utilised in FEA 2-dimensional model.*

For the specific test machine investigated six armature winding external circuits are used, with two external circuits per phase. This is illustrated in Figure 4.9, where the three armature phases are shown and V_p is the phase voltage, I_p the phase current and Z_p the phase group impedance in Figure 4.8.

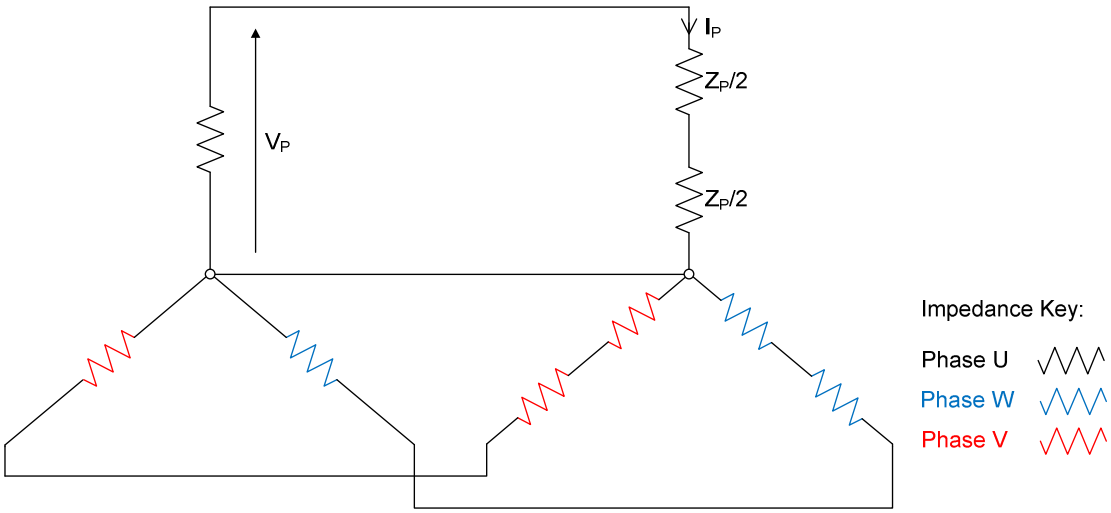

Figure 4.9: *BCI184E machine external circuit, equivalent circuit components.*

The FEA simulator input parameters for the synchronous generator investigated are the field voltage, field resistance, armature resistance and armature inductance, obtained as shown. External circuits are utilised for the armature, with the external resistance and inductance per external circuit being the inputs to the FEA software. The particular operating point considered for finite element analysis is: 22.5 kVA, 31.3 A, 415 V, 50 Hz. Data used, shown in Table 4.1, is extracted from the steady-state experimental test results for the operating point examined. It should be noted that armature and field measured resistance values are utilised in the calculations outlined.

Rpm	1500	Power Factor	0.8
Frequency (Hz)	50	Field Voltage (V)	32.3
Armature Voltage (V)	415	Field Current (I)	35.0
Armature Current (I)	31.3	Armature Resistance (Ω)	0.8896
kVA	22.5	Field Resistance (Ω)	0.863
kW	18.0		

Table 4.1: *FEA synchronous machine experimentally obtained operating point details.*

Rotor Field Settings:

Field current, $I_F = 35\ A$

Field winding measured resistance, $R_F = 0.863\ \Omega$

Field Voltage, $V_F = I_F \times R_F$

$V_F = 35 \times 0.863$

$V_F = 30.205\ V$

Stator Armature Settings:

Armature line voltage, $V_L = 415\ V\ (rms)$

Armature current, $I_A = 31.3\ A\ (rms)$

Armature winding measured resistance, $R_A = 0.8896\ \Omega$

$$Armature\ Phase\ Volatge,\quad V_P = \frac{V_L}{\sqrt{3}} = \frac{415\,V}{\sqrt{3}} = 239.6\,V\ (rms)$$

$$Armature\ Phase\ Load,\quad X_P = \frac{V_P}{I_A} = \frac{239.6\,V}{31.3\,A}\ at\ 0.8\ power\ factor$$
$$= 7.65496\cos(36.87) + j\ 7.65496\sin(36.87)$$
$$= 6.12397 + j\ 4.59298\ \Omega$$

$$External\ R = 6.12397\ \Omega + R_A = 6.12397\ \Omega + 0.8896\,\Omega = 7.01357\ \Omega$$

$$\Rightarrow External\ R\ \ per\ External\ Circuit = \frac{7.01357\ \Omega}{2} = 3.506785\ \Omega$$

$$External\ L = \frac{X_P\ \ j\ component}{2\pi \cdot frequency} = \frac{4.59298}{2\pi \cdot 50\ Hz} = 0.0146\ H$$

$$\Rightarrow External\ L\ \ per\ External\ Circuit = \frac{0.0146\ H}{2} = 7.30995\ mH$$

A reasonable FEA simulation tolerance and time step for the simulation are required. An adaptive time step should be ideally selected, since it manages the simulation computing time effectively, focusing on the most sensitive simulation segments. The desired output times, at which the simulator will subsequently generate data, also needs to be determined.

Once the simulation has terminated, the results need to be validated using experimental data before conclusions can be drawn. In particular, resulting field and armature currents from the FEA simulation need to be carefully examined. For the FEA simulation described, the resulting rotor field and stator armature currents show an acceptable percentage error agreement with experimentally obtained information. As shown in Figures 4.10 and 4.11 respectively, the FEA simulation yields a rotor

steady-state field current of 35 A and a peak stable state stator armature current of approximately 38 A, resulting in an rms current of ~ 27 A.

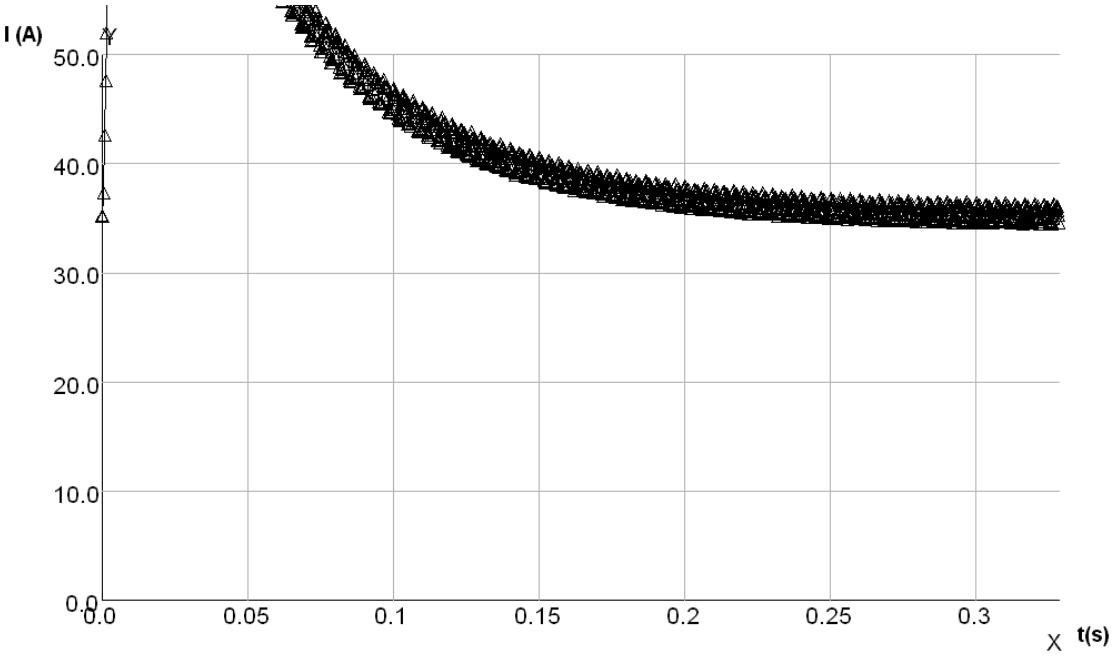

Figure 4.10: *Rotor field current variation with time (FEA result).*

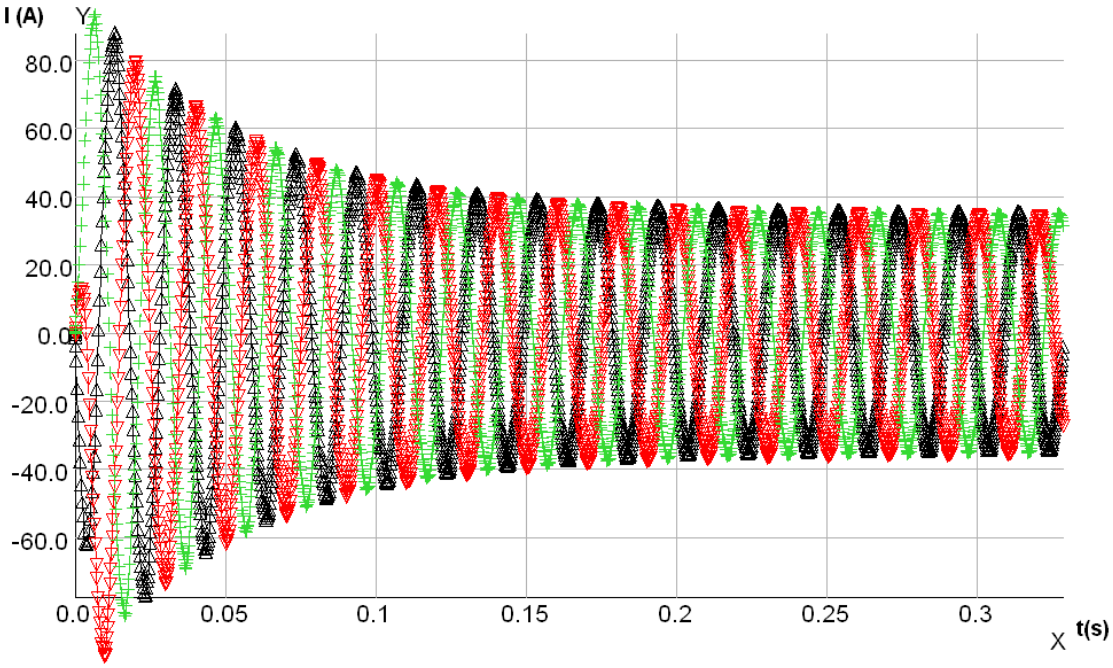

Figure 4.11: *Stator armature 3-phase current variation with time (FEA results).*

In comparison with the experimental data in Table 4.1, the rotor field current result fully agrees with the experimental readings. The simulation stator armature current result shows an error of under 10 % with respect to the test measurements. This is an acceptable mismatch given the enforced BH curve related assumptions made during the generator's model setup, outlined in this section. Furthermore, there are numerous other factors that could lead to a discrepancy between FEA simulation outputs and practical results. Apart from the mentioned material property related data, machine manufacturing techniques can have a significant effect on the resulting armature current, since the high pressures exerted on the laminations during the manufacturing process, or the machining they are subjected to, can considerably alter their electromagnetic behaviour [94] & [95].

4.3.2 FEA Synchronous Generator Model Lamination Dissection

The main objective of the FEA simulation work regards the prediction of iron losses and the distribution of these losses across the synchronous machine, in order for the findings to be accommodated by the lumped parameter thermal networks developed in Chapter 3. For this reason, the rotor and stator lamination sections of the FEA model have been dissected, as shown in Figure 4.12.

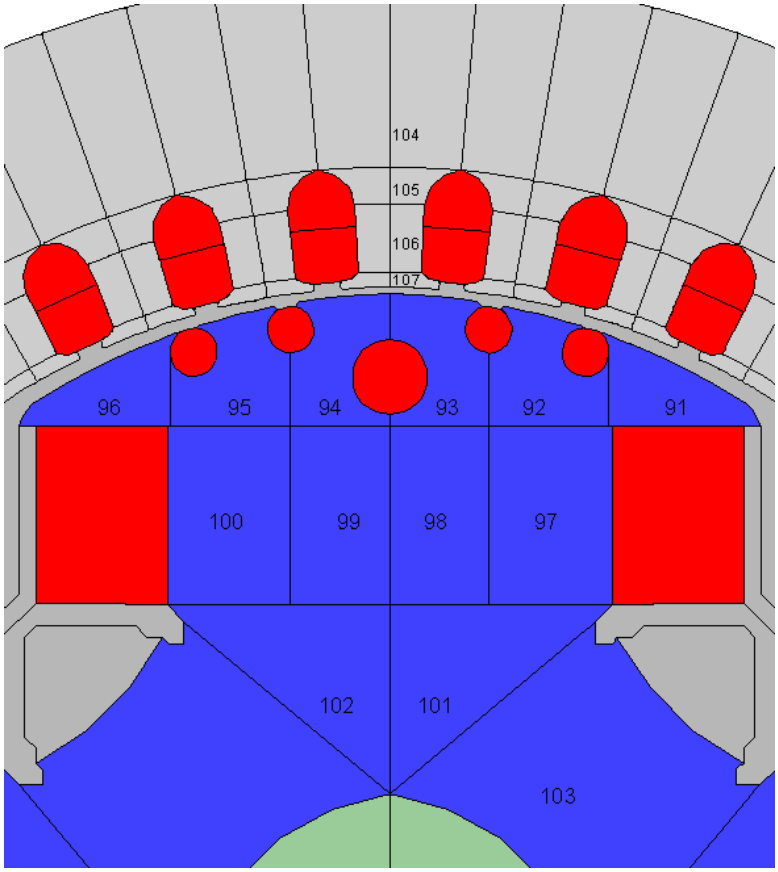

Figure 4.12: *BCI184E machine dissected rotor and stator lamination.*

Hence the iron loss distribution in each individual rotor and stator lamination section can be evaluated separately and subsequently transferred to the lumped circuit thermal network representation of the synchronous machine. The thermal model for 1/4 of the rotor is represented by up to thirteen individual segments (91 to 103). Smaller thermal networks can be elaborated simply by combining adjacent rotor sections together. Similarly, this applies to the stator, where a discretisation level of up to four sectors (104 to 107) is possible to represent 1/72 of the lamination. Table 4.2 displays the areas (mm^2) of the dissected rotor and stator lamination sections shown in Figure 4.12. Furthermore, the material properties utilised for the simulation are presented in Table 4.3.

Rotor lamination:

Section	Area (mm^2)
91	152.1
92	187.2
93	175.4
94	175.4
95	187.2
96	152.1
97	402.4

Section	Area (mm^2)
98	322.7
99	322.7
100	402.4
101	389.3
102	389.3
103	1058.0

Stator lamination:

Section	Area (mm^2)
104	285.5
105	30.3

Section	Area (mm^2)
106	41.1
107	11.9

Table 4.2: *Dissected BCI14E rotor and stator lamination section areas.*

	Rotor	Stator
Radial lamination thermal conductivity (W/m/°C)	43	43
Radial winding thermal conductivity (W/m/°C)	3.745	0.832
Lamination specific heat capacity (J/kg/°C)	500	500
Winding specific heat capacity (J/kg/°C)	460	460
Lamination mass density (kg/m^3)	7800	7800
Winding mass density (kg/m^3)	7500	7500

Table 4.3: *FEA analysis material properties.*

4.3.3 FEA Synchronous Generator Magnetic Flux Density Distribution Results

In order to correctly understand and predict the occurrence and allocation of power losses during synchronous generator operation, it is fundamental to understand and analyse the magnetic flux distribution across the electrical machine. This information is extracted from the FEA vector potential and magnetic flux density plots, shown in Figures 4.13 and 4.14 respectively. It is important to note that rotational direction of the machine simulated is clockwise.

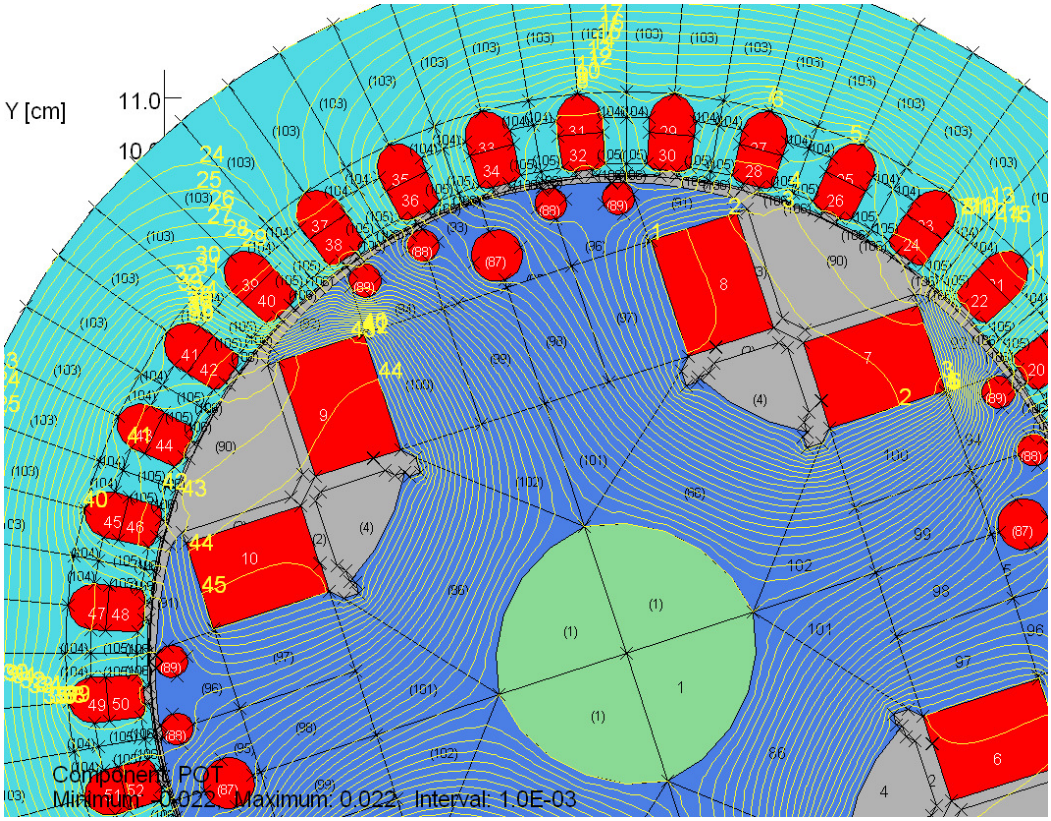

Figure 4.13: *BCI184E machine vector potential distribution.*

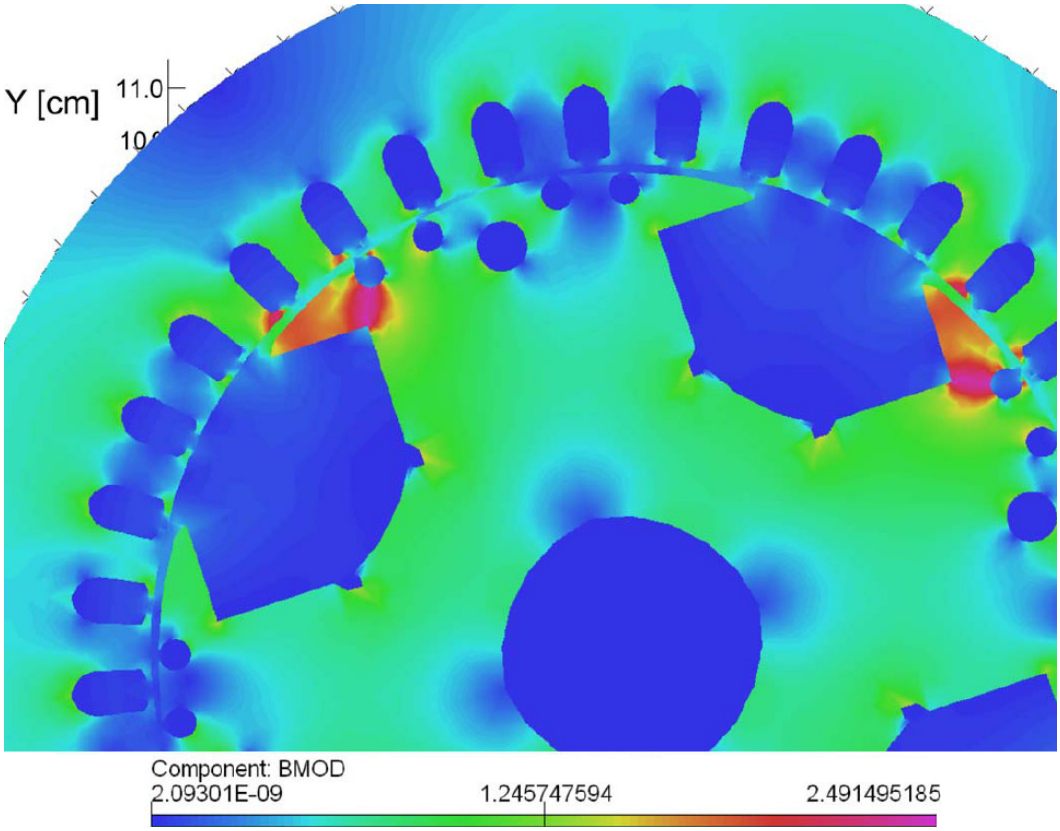

Figure 4.14: *BCI184E machine magnetic flux density (T) distribution.*

Figures 4.13 and 4.14 clearly illustrate the non-symmetrical nature of the operational power losses that occur during synchronous machine rotation. Noting rotational direction, the most concentrated lamination losses are situated at the 'lagging' half of the rotor pole, with flux densities of over 2 T in particular areas. Interestingly, a relatively low magnetic flux density is identified at the 'leading' half of the rotor pole. This is caused by a phenomenon known as armature reaction, which causes the existing flux to be distorted by the stator armature field, resulting in the weakening of the magnetic flux and increased field strength at the lamination tip.

4.4 FEA Synchronous Generator Iron Loss Lamination Distribution Calculation

Iron losses for each of the rotor and stator sections shown in Figure 4.12 (Section 4.3.2) are extracted from FEA results using a specially modified Vector Fields command file, presented in Appendix C. An iron loss calculating default command file was provided by FEA software supplier Vector Fields and modified to correctly model the CGT electrical machine analysed. The command file performs a harmonic evaluation of the flux density waveform in each FEA model element. Hence, the end result is a decomposition of the magnetic flux waveform per element into its constituent parts. It is important to note that the described method takes into account iron losses exclusively and excludes stray losses from consideration, since these are out with the scope of the study and should be dealt with independently. As presented in Section 4.2, Steinmetz formula Equation 4.1 is utilised to compute the loss per harmonic [74]. Equation 4.3, computing hysteresis and eddy current iron loss components, is used in the iron loss calculating FEA command file.

$$P_{Iron} = P_h + P_e = k_h \cdot f \cdot B^n + k_e \cdot (f \cdot B)^2 \tag{4.3}$$

where k_h and k_e represent hysteresis and eddy current iron loss coefficients respectively. B represents the magnetic flux density and f represents the frequency.

The calculation method to obtain the important hysteresis and eddy current iron loss coefficients, k_h and k_e, is outlined in Section 4.4.1. The n coefficients, used by the FEA simulator as a calibrating mechanism for the iron loss calculation are presented in Section 4.4.2. Finally, iron loss results for the CGT alternator are covered in Section 4.4.3.

4.4.1 Hysteresis and Eddy Current Iron Loss Coefficients

In order to calculate the essential hysteresis, k_h, and eddy current, k_e, iron loss coefficients the following technique should be employed. This technique, utilised by Vector Fields in loss calculations, has given good results in the past on a wide range of machines, including CGT electrical machines such as the one investigated.

The Steinmetz related Equation 4.4 together with the BCI184E synchronous machine PowerCore® M 800-65 A 0.65 mm ThyssenKrupp Stahl lamination material information, collected in Appendix D, are required.

$$P_{Iron} = P_h + P_e = k_h \cdot \frac{f}{density} \cdot B^n + k_e \cdot \frac{f^2}{density} \cdot B^2 \tag{4.4}$$

From the manufacturer supplied lamination material information in Appendix D, Table 4.3 is extracted. The case for B = 1 T, at 400 Hz and 500 Hz is highlighted. The BCI184E machine's lamination density is 7800 kg/m^3. When B is 1 T in Equation 4.4, Equation 4.5 results:

$$P_{Iron} = k_h \cdot \frac{f}{density} + k_e \cdot \frac{f^2}{density} \tag{4.5}$$

	f = 400 Hz				f = 500 Hz			
B (T)	H (A/m)	μ_a	P_{Iron} (W/kg)	S_s (VA/kg)	H (A/m)	μ_a	P_{Iron} (W/kg)	S_s (VA/kg)
0.6	**236**	**2023**	**19.64**	**23.03**	**259**	**1846**	**26.91**	**31.23**
0.7	278	2004	26.68	31.02	309	1804	36.96	42.63
0.8	326	1956	35.23	40.78	366	1740	49.28	56.68
0.9	379	1889	45.64	52.75	431	1664	64.33	73.91
1.0	**439**	**1813**	**57.85**	**66.85**	**503**	**1582**	**82.56**	**94.96**
1.1	503	1740	72.17	83.44	583	1503	103.89	119.77
1.2	576	1659	88.98	103.34	668	1430	128.34	148.45
1.3	653	1585	108.39	126.64	760	1362	156.92	182.51
1.4	**737**	**1514**	**130.23**	**154.30**	**859**	**1298**	**188.96**	**222.16**

Table 4.4: *PowerCore® M 800-65 A 0.65 mm ThyssenKrupp Stahl lamination information (f = 400 Hz and 500 Hz).*

Therefore, using Equation 4.5 and the information in Table 4.3, hysteresis, k_h, and eddy current, k_e, iron loss coefficients are computed as outlined:

$$\textit{At 400 Hz and 1 T:} \quad 57.85 = \frac{k_h \times 400}{7800} + \frac{k_e \times 400^2}{7800}$$

$$\textit{hence,} \quad 451230 = 400 \cdot k_h + 160000 \cdot k_e$$

$$\Rightarrow \quad k_h = 1128.075 - 400 \cdot k_e \tag{4.6}$$

$$\textit{At 500 Hz and 1 T:} \quad 82.56 = \frac{k_h \times 500}{7800} + \frac{k_e \times 500^2}{7800}$$

$$\textit{hence,} \quad 643968 = 500 \cdot k_h + 250000 \cdot k_e \tag{4.7}$$

Equation 4.6 for k_h is substituted into Equation 4.7 to obtain k_e as presented:

Substituting k_h into Equation 4.7:

$$643968 = 500 \cdot (1128.075 - 400 \cdot k_e) + 250000 \cdot k_e$$

$$643968 = 564037.5 - 200000 \cdot k_e + 250000 \cdot k_e$$

$$79930.5 = 50000 \cdot k_e$$

$$\Rightarrow k_e = 1.59861$$

The computed k_e value can now be substituted into Equation 4.6 to obtain k_h as shown:

Substituting k_e into Equation 4.6:

$$k_h = 1128.075 - 400 \cdot (1.59861)$$

$$\Rightarrow k_h = 488.631$$

Hence, from the presented calculations, values of 1.6 and 489 for k_e and k_h respectively are utilised in the Vector Fields code based iron loss calculating command file shown in Appendix C.

A couple of quick validation checks on the calculated k_h and k_e values are recommended at this stage, to ensure that these work acceptably for the magnetic flux density conditions considered. For this, cases B = 0.6 and B = 1.4, 400 Hz, highlighted in Table 4.3, are considered using Equation 4.4. It is important to note that Equation 4.8 (Section 4.4.2), developed by Vector Fields and introduced in the following section is utilised to obtain the n coefficient. P_{Iron} values calculated with the new coefficients and the tabulated actual magnitudes are compared.

Quick check # 1:

- *At B = 0.6, f = 400 Hz and n = 1.8*

$$P_{Iron} = k_h \cdot \frac{f}{density} \cdot B^n + k_e \cdot \frac{f^2}{density} \cdot B^2$$

$$= 488.631 \times \frac{400}{7800} \times 0.6^{1.8} + 1.59861 \times \frac{400^2}{7800} \times 0.6^2$$

$$= 21.796\ W/kg$$

Table 4.3 manufacturer data gives a P_{Iron} value of 19.64 W/kg.

- *At B = 1.4, f = 400 Hz and n = 2.3*

$$P_{Iron} = k_h \cdot \frac{f}{density} \cdot B^n + k_e \cdot \frac{f^2}{density} \cdot B^2$$

$$= 488.631 \times \frac{400}{7800} \times 1.4^{2.3} + 1.59861 \times \frac{400^2}{7800} \times 1.4^2$$

$$= 118.602\ W/kg$$

Table 4.3 manufacturer data gives a P_{Iron} value of 130.23 W/kg.

For both of the operating conditions considered a reasonably good agreement is observed between the calculated P_{Iron} values and the manufacturer provided information in Table 4.3. Even though the correlation is not perfect, since k_h and k_e values fluctuate with B [61], [94] & [95], it is close enough for the purpose of the FEA work executed, where the emphasis is in determining the distribution of iron losses across the machine laminations and not in highly precise iron loss magnitude predictions.

As a second quick k_h and k_e check, the calculated coefficients can be checked at another operational condition from the lamination material information in Appendix D. For example, at the B = 1 T, f = 1 kHz operating condition, again, using Equation 4.5 and the calculated k_h and k_e values, P_{Iron} (W/kg) for the mentioned operational condition is computed as shown.

Quick check # 2:

- *At B = 1.0 and f = 1 kHz*

$$P_{Iron} = k_h \cdot \frac{f}{density} + k_e \cdot \frac{f^2}{density}$$

$$= 488.631 \times \frac{1000}{7800} + 1.59861 \times \frac{1000^2}{7800}$$

$$= 267.595\ W/kg$$

As shown in Figure 4.15, the calculated P_{Iron} (W/kg) value agrees with manufacturer's lamination data for the f = 1 kHz operating condition, which indicates a successful check of the calculated k_h and k_e values.

	f = 1 kHz
B (T)	P_{Iron} (W/kg)
0.2	9.81
0.3	20.09
0.4	34.50
0.5	53.61
0.6	79.11
0.7	112.71
0.8	154.69
0.9	206.05
1.0	**267.60**

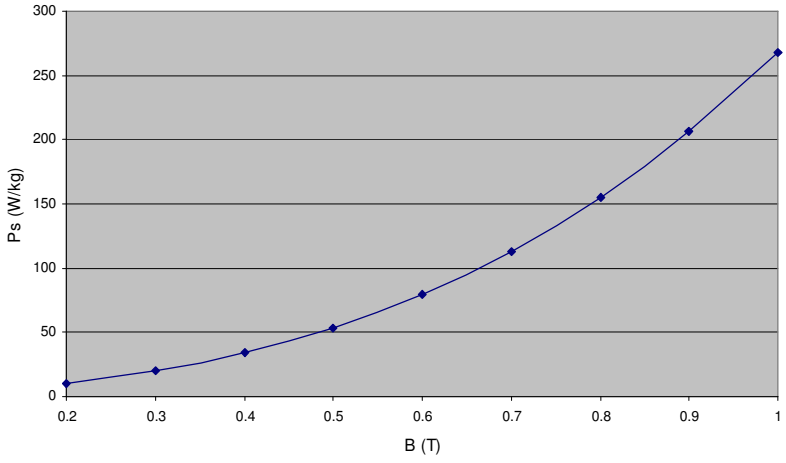

Figure 4.15: *PowerCore® M 800-65 A 0.65 mm ThyssenKrupp Stahl lamination information (f = 1 kHz).*

4.4.2 FEA Calibrating *n* Coefficient Calculation

As presented in the Vector Fields code based iron loss calculating command file, in Appendix C, n dimensionless coefficients (a, b and c) are used as a calibrating mechanism for the FEA simulator solution iron loss calculation process, to obtain the overall n coefficient in Equation 4.4 [96]. This allows for a more accurate characterisation of the electrical machine being modelled. The n coefficients selected need to agree with the relationship shown in Equation 4.8. This equation is provided by Vector Fields as a standard correlation to calculate n values in iron loss formulations.

$$n = a + b \cdot B + c \cdot B^2 \tag{4.8}$$

As a standard industry practical level, n should equal around 1.5 at $B = 0$ T and 2.5 at $B = 2$ T, but specific lamination material n values will vary. The n values presented and used in the command file collected in Appendix C are listed below. These have been used by Vector Fields and have given accurate results for CGT electrical machine FEA simulations in the past. Further n coefficient considerations are out with the scope of this thesis.

$$a = 1.31$$
$$b = 0.875$$
$$c = -0.205$$

4.4.3 FEA BCI184E Iron Loss Distribution Results

Tables 4.4 and 4.5 present the iron losses related to each rotor and stator section of the dissected FEA model of the CGT synchronous generator presented in Figure 4.12 (Section 4.3.2). For convenience, in Table 4.4, rotor sections are divided into three lamination sub-groups: top, middle and bottom rotor lamination sections. Lamination section areas used to compute the power loss per area (W/cm^2) for the generator rotor and stator laminations are extracted from Table 4.2 (Section 4.3.2). Results shown correspond to the operating condition: 22.5 kVA, 31.3 A, 415 V, 50 Hz. The presented results are utilised in Section 4.5 for the calculation of the Lumped Circuit Coefficients, which are later incorporated into the thermal networks utilised by the MySolver thermal modelling package. It should be noted that the rotor sections in Table 4.4 account for 1/4 of the total rotor lamination area and enclose 25 % of total rotor iron losses, whilst the stator sections presented in Table 4.5 account for 1/72 of the total stator lamination surface and encapsulate ~ 1.39 % of total stator iron losses.

Rotor lamination:

Top Sections	Iron Loss (W)	% of Rotor Iron Losses	W/cm^2
96	2.08	3.01	1.37
95	1.68	2.44	0.90
94	0.70	1.02	0.40
93	0.61	0.89	0.35
92	0.53	0.77	0.28
91	0.57	0.83	0.38

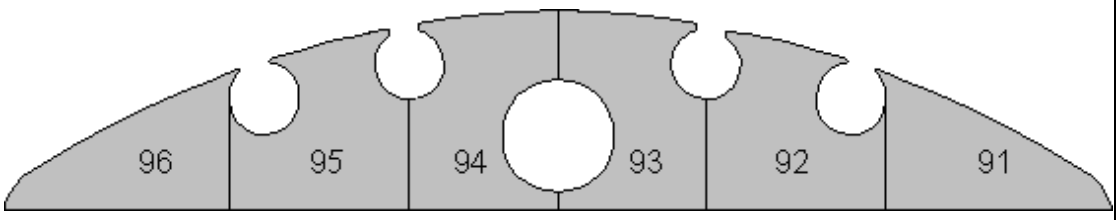

Middle Sections	Iron Loss (W)	% of Rotor Iron Losses	W/cm^2
100	2.26	3.27	0.56
99	1.10	1.60	0.34
98	0.83	1.20	0.26
97	1.05	1.52	0.26

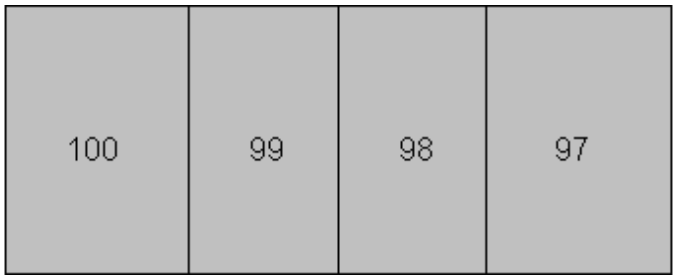

Bottom Sections	Iron Loss (W)	% of Rotor Iron Losses	W/cm^2
102	1.22	1.77	0.31
101	1.06	1.54	0.27
103	3.55	5.14	0.34

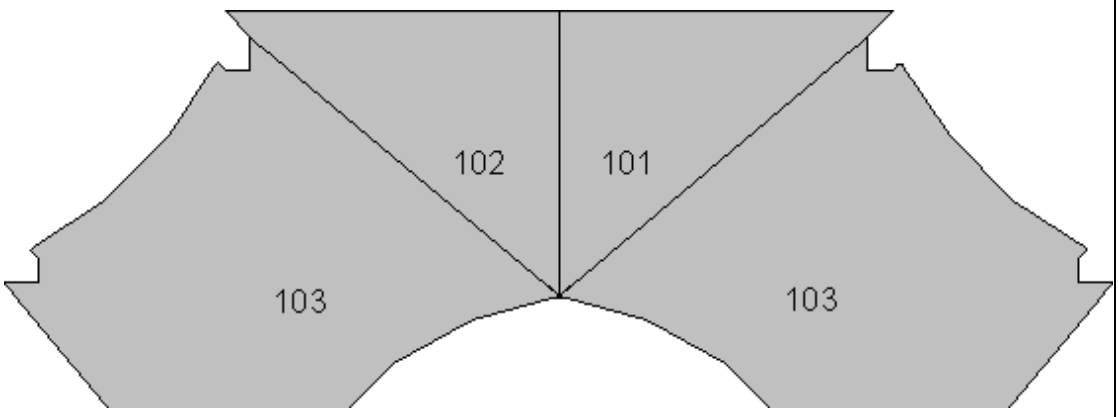

Table 4.5: *BCI184E iron loss rotor lamination distribution results.*

Stator Lamination:

Section	Iron Loss (W)	% of Stator Iron Losses	W/cm^2
104	3.76	0.96	1.32
105	0.59	0.15	1.94
106	0.74	0.19	1.81
107	0.35	0.09	2.96

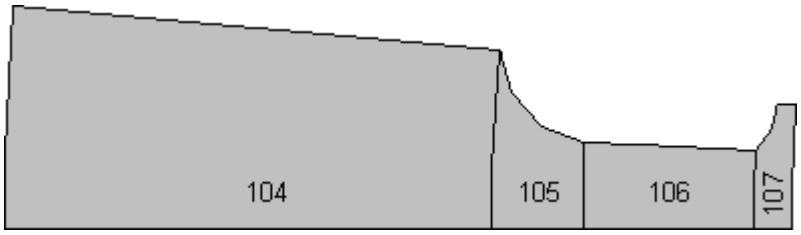

Table 4.6: *BCI184E iron loss stator lamination distribution results.*

Total synchronous generator iron losses of 460.3 W result from the FEA simulation described which, given the limitations associated with the analysis described in this chapter, agrees reasonably well with the 505 W obtained through experimental tests, as shown in Section 4.2.1.

From Table 4.4, the highest concentration of iron losses in the rotor lamination occurs at the top lamination section (96), followed by the adjacent section (95), with the remaining sections exhibiting significantly lower iron loss concentrations. Once again, this highlights the non-symmetrical distribution of iron losses across the rotor lamination during machine operation, with the highest iron loss concentration occurring at the 'lagging half' of the rotor lamination. This agrees with the magnetic flux density distribution illustrated in Figure 4.14 (Section 4.3.3). The stator iron loss concentrations are more uniform across the lamination, with only stator lamination Section 106 showing a higher loss concentration than the rest.

4.4.4 Rotor Lamination Eddy Current, Hysteresis and Total Iron Loss Temperature Distribution.

Given the significantly uneven iron loss distribution across the rotor lamination, the individual thermal effects on the rotor lamination of eddy current and hysteresis losses, along with the resulting overall thermal effect of the total iron losses, is

presented in this section. The rotor lamination temperature rise (°C), when only the eddy current component of iron losses is taken into account, for the operating condition considered in this chapter is shown in Figure 4.16. It should be noted that all other electrical machine operational losses, such as copper losses, are included in the FEA simulation.

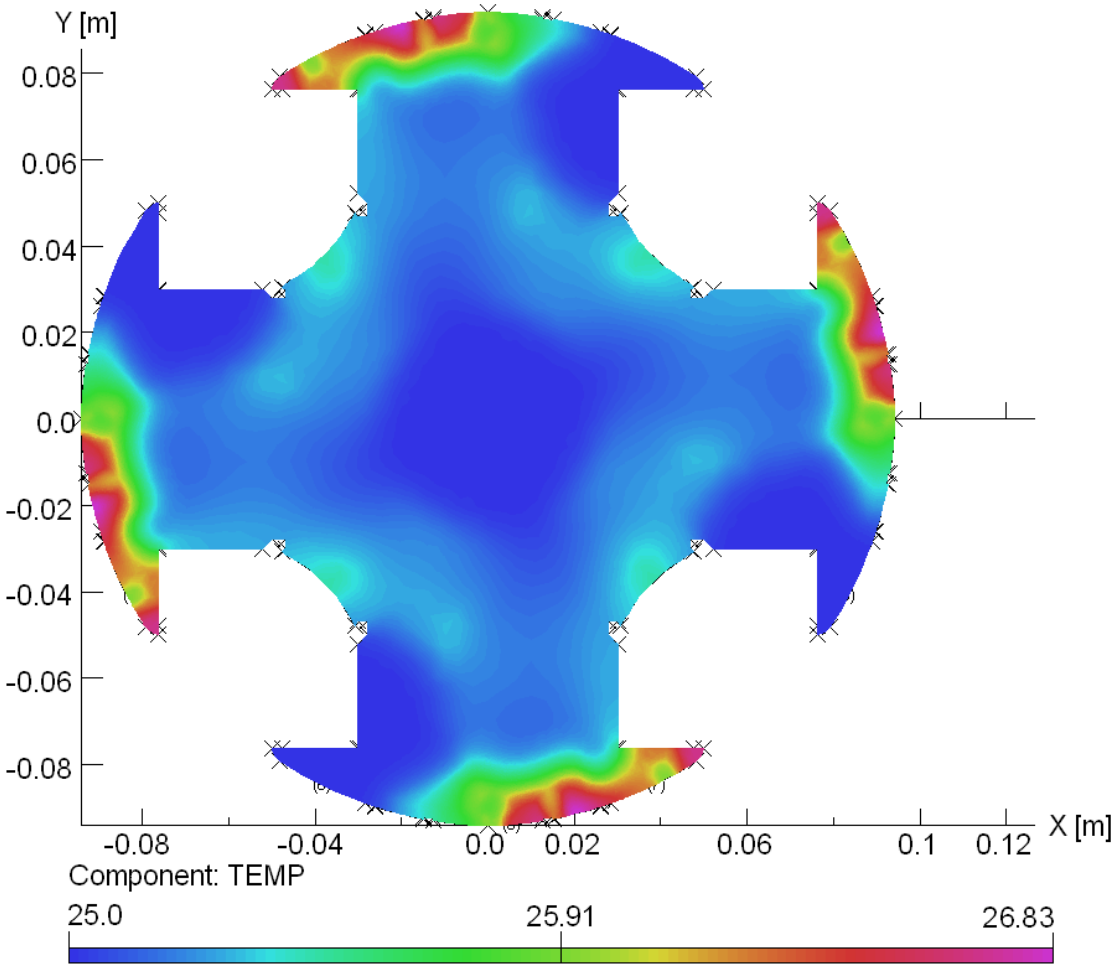

Figure 4.16: *Temperature rise when only eddy current losses of total iron losses are considered across the rotor lamination.*

Agreeing with the magnetic flux density distribution shown in Figure 4.14 (Section 4.3.3), eddy current losses are clearly concentrated in the 'lagging half' of the rotating rotor pole, resulting in the highest temperature spots of the rotor lamination.

The rotor lamination temperature rise (°C) enforced when only the hysteresis loss component of iron losses is considered is displayed in Figure 4.17.

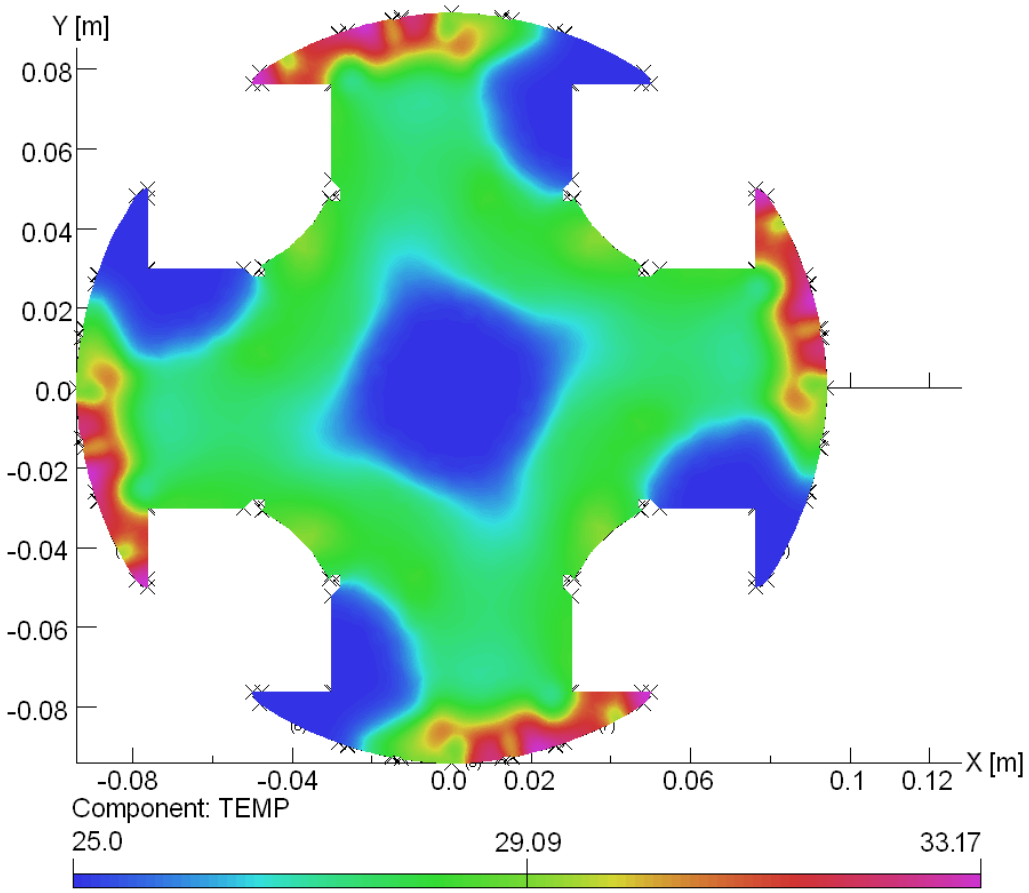

Figure 4.17: *Temperature rise when only hysteresis current losses of total iron losses are considered across the rotor lamination.*

In a similar way to eddy current losses, hysteresis losses concentrate their thermal effect on the 'lagging half' of the rotating rotor pole. As Figure 4.17 shows, they have a more general effect on the temperature of the whole rotor lamination cross-section. Furthermore, the magnitude of hysteresis losses is higher, as indicated by the higher overall temperature rise of the rotor lamination and of hot-spots present.

Finally, the combination of eddy current and hysteresis losses, together with all other operational losses, yields the temperature distribution presented in Figure 4.18. As expected, the iron loss related thermal distribution is dominated by the hysteresis loss, due to its higher magnitude and more uniform distribution, but both loss components contribute to the final rotor lamination thermal distribution.

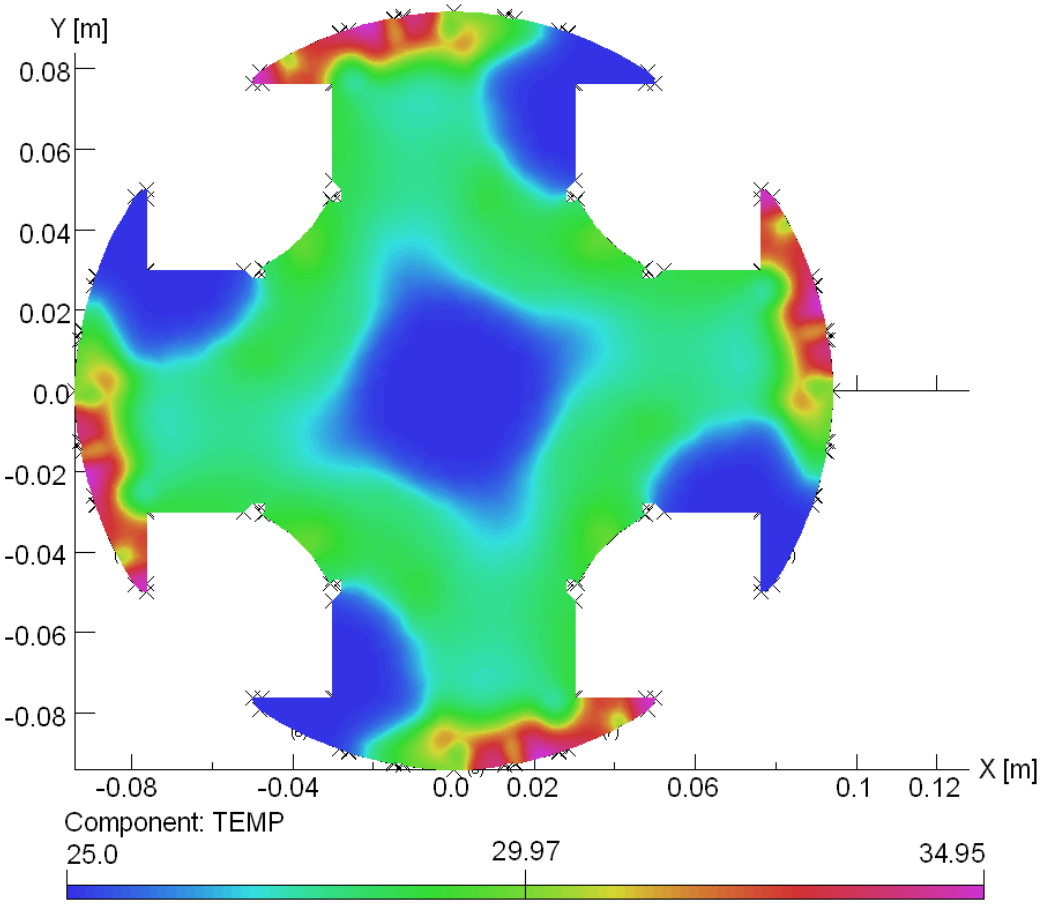

Figure 4.18: *Overall temperature rise thermal characteristic of total iron losses and all other operational losses across the rotor lamination.*

4.4.5 Iron Loss Stator:Rotor Split Ratio

The iron loss split ratio between the stator and the rotor is an important factor, since the fraction of the overall iron loss related to each machine part will greatly determine its thermal characterisation. Hence, it is very important for thermal modelling tools to distribute iron losses between the stator and the rotor as accurately as possible.

The FEA simulation outlined in this section indicates an approximately 85:15 stator to rotor iron loss split ratio, with 391.3 W of the FEA obtained total 460.3 W iron loss occurring in the stator and the remaining 69.0 W in the rotor lamination. Cummins Generator Technologies have historically assumed a 90:10 stator to rotor

iron loss split ratio for their complete range of alternators, which shows a close agreement with the FEA obtained ratio, but has been modified following the results presented.

4.5 Iron Loss Lumped Circuit Coefficients for Thermal Networks

Utilising the results presented in this chapter, lumped parameter thermal network coefficients can be derived. These coefficients are of benefit in generating a lumped circuit thermal model truly representative of the synchronous generator's rotor and stator iron loss distribution. These coefficients have been called Lumped Circuit Coefficients (LCCs) and they are derived as outlined in this section for the CGT test machine, but the method is applicable to other synchronous machine geometries.

4.5.1 Rotor Iron Loss Lumped Circuit Coefficients

Rotor iron loss LCCs are determined utilising the results presented in Section 4.4. The specific results and the LCCs related to each rotor lamination section are shown in Table 4.6. LCCs are obtained by comparing the iron loss concentration (W/cm^2) between the sections making up the rotor lamination. The lowest rotor lamination section W/cm^2 value is assigned an LCC value of one and the remaining section LCCs are derived from it. For example, in Table 4.6, middle rotor lamination Section 98 is assigned an LCC value of 1 and, from this the LCC value for top rotor lamination Section 96 is 1.37 / 0.26, giving an LCC value of five. The remaining LCCs are calculated in this manner. Rotor section numbers refer to the rotor laminations sections illustrated in Figure 4.12, in Section 4.3.2.

Rotor lamination:

Top Sections	W/cm^2	LCC Value
96	1.37	5
95	0.90	4
94	0.40	2
93	0.35	1
92	0.28	1
91	0.38	1
Middle Sections	W/cm^2	LCC Value
100	0.56	2
99	0.34	1
98	0.26	1
97	0.26	1
Bottom Sections	W/cm^2	LCC Value
102	0.31	1
101	0.27	1
103	0.34	1

Table 4.7: *Rotor Lumped Circuit Coefficients (LCCs) computation information.*

LCC values in Table 4.6 are illustrated in Figure 4.19 over the rotor lamination cross-section, linking each coefficient with the relevant rotor lamination segment.

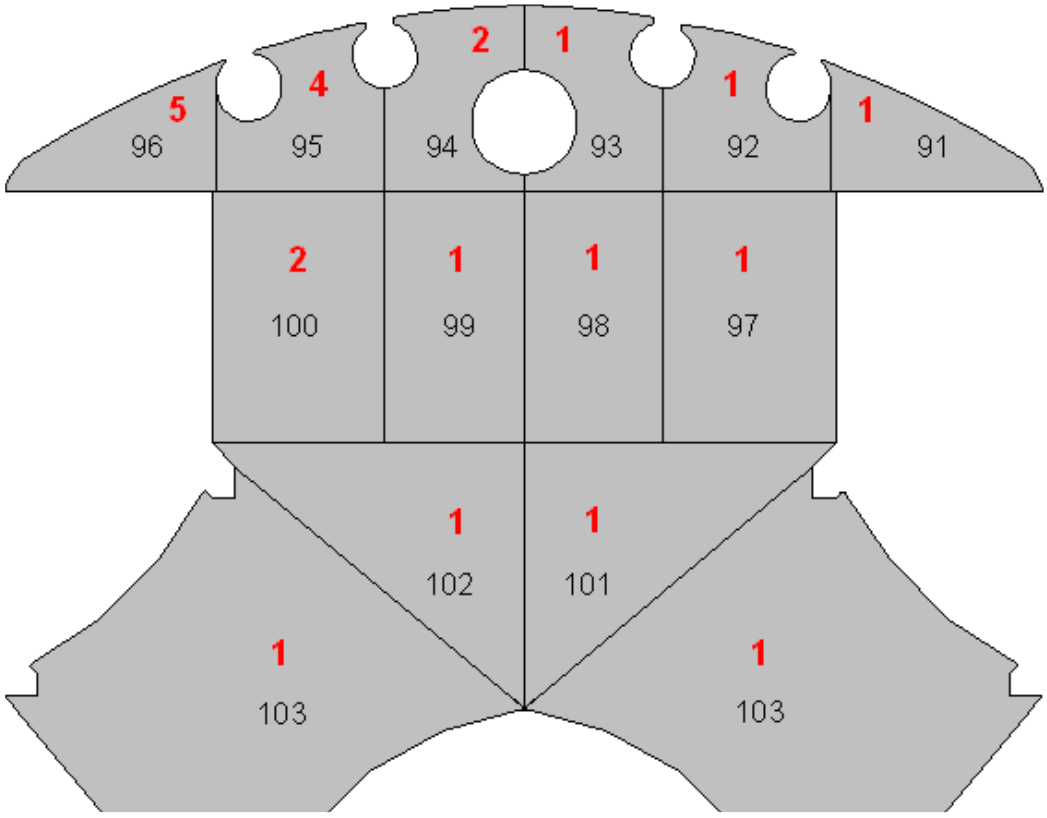

Figure 4.19: *Rotor Lumped Circuit Coefficients (LCCs) distribution.*

The rotor lamination LCC results presented in this section, shown in Figure 4.19, indicate that the highest thermal impact iron loss input sources in a lumped parameter rotor lamination thermal network should be concentrated at the top left corner (rotating 'lagging' half) of the rotor pole. LCC values of five and four for Sections 96 and 95 account for this. Adjacent rotor lamination Sections 94 and 100 also exhibit a higher than average iron loss concentration and hence receive an LCC value two. The remainder of the rotor lamination sections show a relatively uniform distribution of iron losses with respect to their area and have LCC values of one.

4.5.2 Stator Iron Loss Lumped Circuit Coefficients

Stator lamination iron loss LCCs are obtained utilising the same method presented in the previous section to calculate rotor LCCs. The resulting stator lamination LCCs are shown in Table 4.7 and are also presented in Figure 4.20, indicating their position within the stator lamination.

Stator Lamination:

Section	W/cm^2	LCC Value
104	1.32	1
105	1.94	1
106	1.81	1
107	2.96	2

Table 4.8: *Stator Lumped Circuit Coefficients (LCCs) computation information.*

As expected, the highest concentration of iron losses in the stator lamination, and hence highest LCC value, is located at the bottom of the stator lamination tooth. For this reason, the potentially hottest stator lamination Section 107 receives an LCC value of two, whilst the remaining stator lamination sections are applied an LCC value of one, due to their lower iron loss concentration.

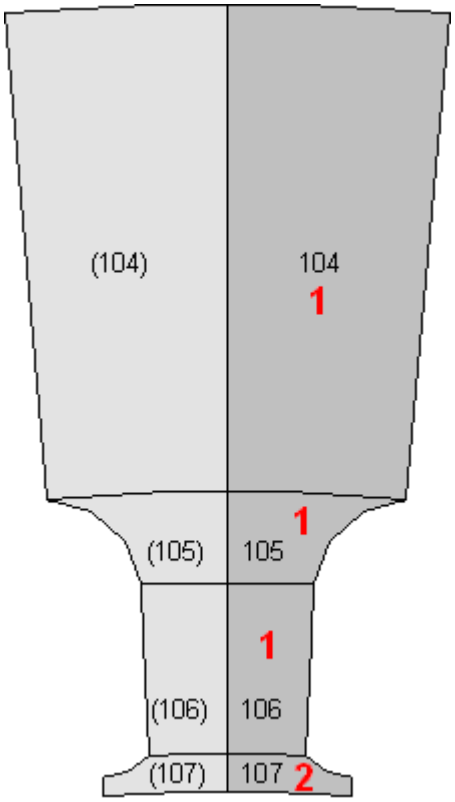

Figure 4.20: *Stator Lumped Circuit Coefficients (LCCs) distribution.*

4.6 LCC Lumped Parameter Thermal Network Application and Evaluation

By accommodating the LCCs in the rotor and stator synchronous machine thermal models, the true distribution of iron losses and their thermal effect can be recreated, resulting in more accurate thermal simulations. Rotor and stator thermal networks presented in Chapter 3 are illustrated in Figure 4.21. Input iron losses to the five rotor lamination nodes (rotor nodes 2, 4, 5, 6 and 7) and to the two stator lamination nodes (stator nodes 3 and 4) are re-distributed according to the LCC results obtained in this chapter.

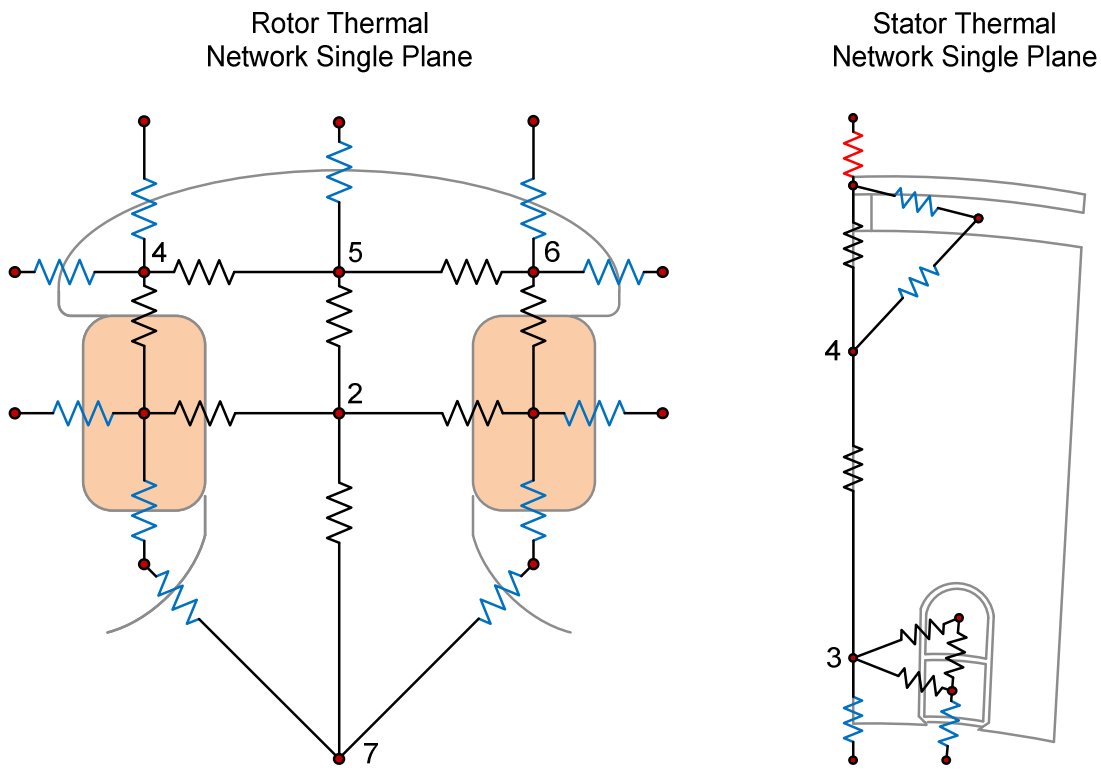

Figure 4.21: *MySolver rotor and stator lumped parameter thermal networks.*

The application of LCCs to the lumped parameter networks in Figure 4.21 results in improved synchronous generator thermal modelling, which mimics the true thermal distribution of the electrical machine in a more realistic manner, agreeing more closely with the thermal data (obtained via thermocouples) presented and analysed in Chapter 8. For example, after the application of LCCs to the rotor lumped parameter thermal network a more realistic temperature distribution between rotor lamination nodes four and six is achieved, as shown in Figure 4.22, when modelling the CGT synchronous generator. It should be noted that the temperatures shown in Figure 4.22 differ from those in Figure 4.18 (Section 4.4.4). This is due to the fact that Figure 4.22 illustrates absolute temperature, whilst Figure 4.18 shows temperature rise.

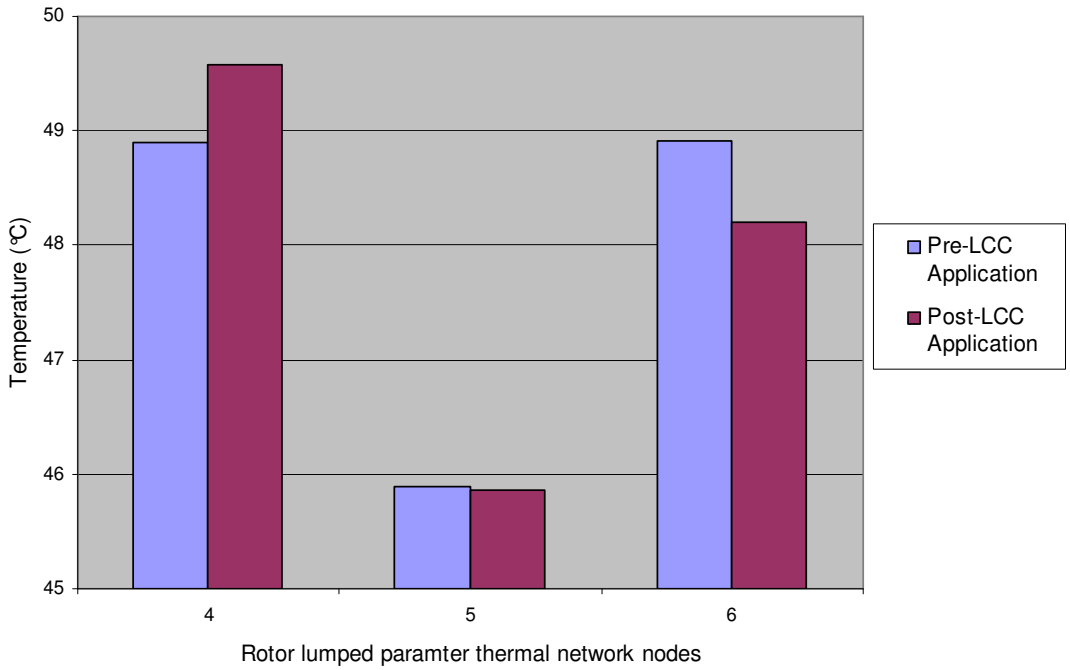

Figure 4.22: *Pre-LCC and post-LCC top rotor pole thermal distribution comparison.*

As shown, the initial unrealistic symmetrical temperature distribution between rotor lamination nodes four and six is now replaced with a temperature gradient between the two nodes. This simulates the real synchronous machine rotor lamination temperature distribution more accurately, as is indicated by the experimental results obtained, shown in Chapter 8, and the FEA data presented in this chapter.

These findings will be particularly significant in long generator heat-runs, due to the increase in nodal temperatures and, consequently, lamination hotspots. In addition to this, the rise in the temperature gradient across the rotor lamination's radial length is also an important electrical machine design consideration, as this will exert increased pressure on the lamination's operational lifetime. It is important to note that the simulation results presented relate to the CGT alternator. Appling the LCC method described to higher rated machines, with higher W/kg values, would accentuate the results obtained, as the magnitude of the node-to-node temperature difference would be increased, making their correct prediction more important.

4.7 Chapter Summary

In this chapter, the development of iron loss lumped parameter network redistribution factors, called Lumped Circuit Coefficients (LCCs), has been covered. It is important for modern generator design methods to take into account precise iron loss distributions and FEA is utilised to compute the LCCs related to each rotor and stator lamination section across a two-dimensional cross-section of the synchronous machine. The process by which the FEA model of the synchronous machine is developed is presented in this chapter, focusing on the setup of the required external circuits. As the results presented in this chapter show, the application of LCCs to the alternator's lumped parameter thermal network yields a more accurate representation of the electrical machine's lamination temperature distribution. The method described in this chapter is implemented on the CGT synchronous generator investigated with satisfactory results, with the presented method being applicable to other electrical machine types.

The emphasis of the work presented in this chapter is on the distribution of iron losses across the synchronous machine's laminations, in order to increase the accuracy of the lumped parameter thermal networks presented in Chapter 3. Due to the limitations associated with the use of FEA, covered in this chapter, to accurately predict the precise magnitude of iron losses in synchronous machines, the reasonable agreement between the FEA simulated iron losses and the experimental based reading is deemed as appropriate to extract the required iron loss lamination distribution desired.

CHAPTER 5

Lumped Parameter Modelling Winding Discretisation Level

5.1 Introduction to Winding Discretisation Level

A thermal model's discretisation level refers to the sections that are used to model the electrical machine as a whole, or some of the more critical components, both in the axial and radial directions. An excessively crude model with a too low discretisation level will prove simple to create and fast to analyse, but will lack accuracy. On the other hand, increasing the discretisation level unjustifiably will complicate the analysis without yielding better, more accurate results. Hence, it is key to identify an acceptable discretisation level, both in terms of accuracy and computing time. With regards to electrical machines, the main discretisation level concerns refer to the lamination and coil windings. Heat is transferred through these sections constantly during machine operation and the determination of an appropriate discretisation level across these machine parts is very important.

The most important material property to be considered when determining a thermal model's discretisation level is the individual component's overall thermal conductivity. Structures made exclusively from components such as copper or steel will require very low discretisations due to their high thermal conductivities (around 400 W/m/°C and 40 W/m/°C, respectively). This is because the high conductivities result in uniform temperature distributions across these relatively small sections. Therefore, for example, heavily discretising a machine's rotor lamination in the axial or radial direction will bring little benefit, since heat travels with little obstruction in this direction and thermal distributions are relatively uniform.

It is in the electrical machine's coil windings where conductivity is dramatically reduced by the presence of insulating resins (~ 0.25 W/m/°C) and inevitable trapped air pockets (~ 0.03 W/m/°C) which result in the overall winding thermal conductivities falling to around 2-3 W/m/°C, making the consideration of an appropriate discretisation level very important. Such low thermal conductivities across components result in significant temperature gradients which are essential to model and take into account.

5.2 Synchronous Generator Winding Discretisation Level Determination

A study is performed in order to determine reasonable discretisation levels for synchronous generator rotor and stator windings, since these are the low thermal conductivity areas previously identified. The investigation is performed using the system analysis tool Portunus developed by Adapted Solutions [97], which allows for the generation and analysis of thermal networks composed of thermal resistances, power sources and temperature meters. Individual networks are created for each one of the discretisation levels considered.

5.2.1 Isolated Winding Discretisation Level Study

Initially the scenario of an isolated standard coil winding is considered. A number of individual isolated winding models are used for this, ranging from a single node (1x1) winding representation, presented in Figure 5.1, to a coil winding represented by 100 smaller nodal sections (10x10), illustrated in Figure 5.2. Model thermal resistances are calculated from winding geometries and material thermal properties for each model created. Overall model input power source values are kept constant across the whole range of models considered, with individual power source parameters calculated for each model being dependant on particular model discretisation levels.

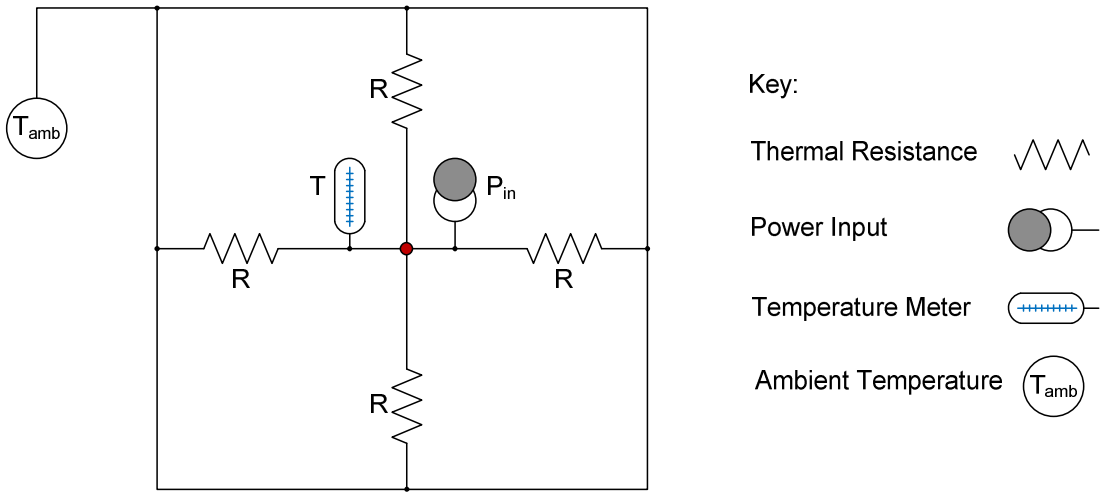

Figure 5.1: *Isolated machine winding single node (1x1) thermal network.*

In Figures 5.1 and 5.2, R represents thermal resistance paths, P_{in} the nodal input loss power fed into the model node, T the nodal temperature and T_{amb} the ambient temperature, which is set to 0 °C in order to compute temperature rise.

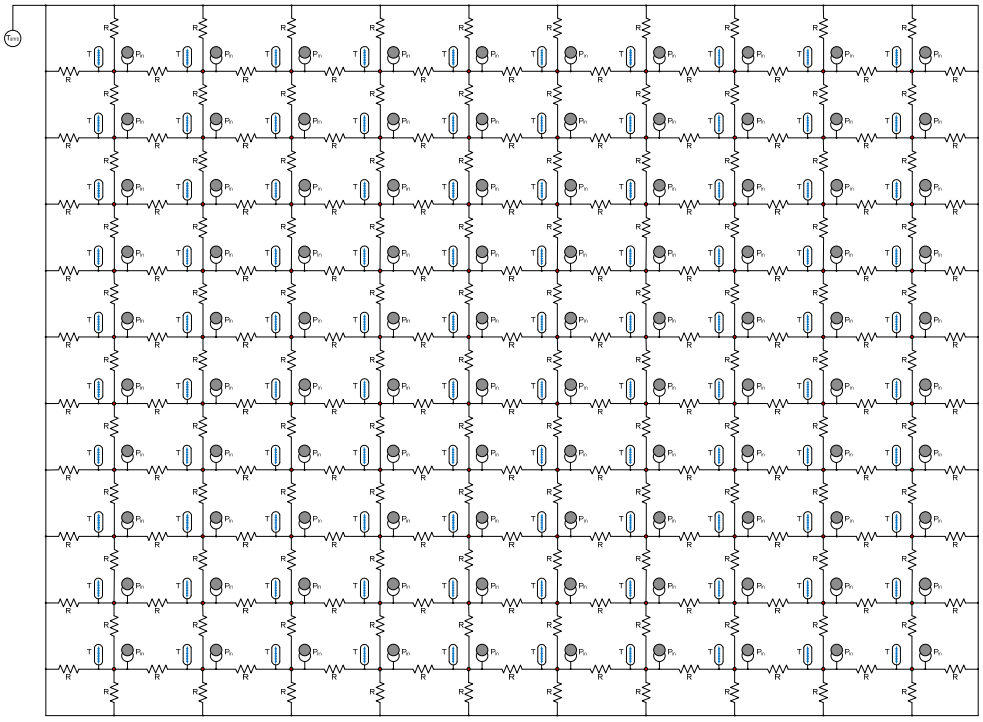

Figure 5.2: *Isolated machine winding 100 node (10x10) thermal network.*

Model networks of node arrays varying from 1x1 to 10x10 network are exposed to an identical loss scenario, with a 1.5 kW loss being divided between the input power

nodes comprising each model. Winding model average temperatures are calculated for all models considered in the study, under the conditions described, by averaging out all temperature meter readings.

Simultaneously to the work outlined and performed by Cummins Generator Technologies, finite element thermal analysis (using computational fluid dynamics tool Fluent) is utilised to analyse the same specific machine winding investigated under identical experimental conditions, with an equal 1.5 kW loss input. The finite element thermal analysis yields an average winding steady-state temperature of 17.07 °C. This result is combined with the thermal network multi-node study described to reach a winding discretisation level conclusion.

The combined lumped parameter thermal network and finite element results obtained are shown in Figure 5.3.

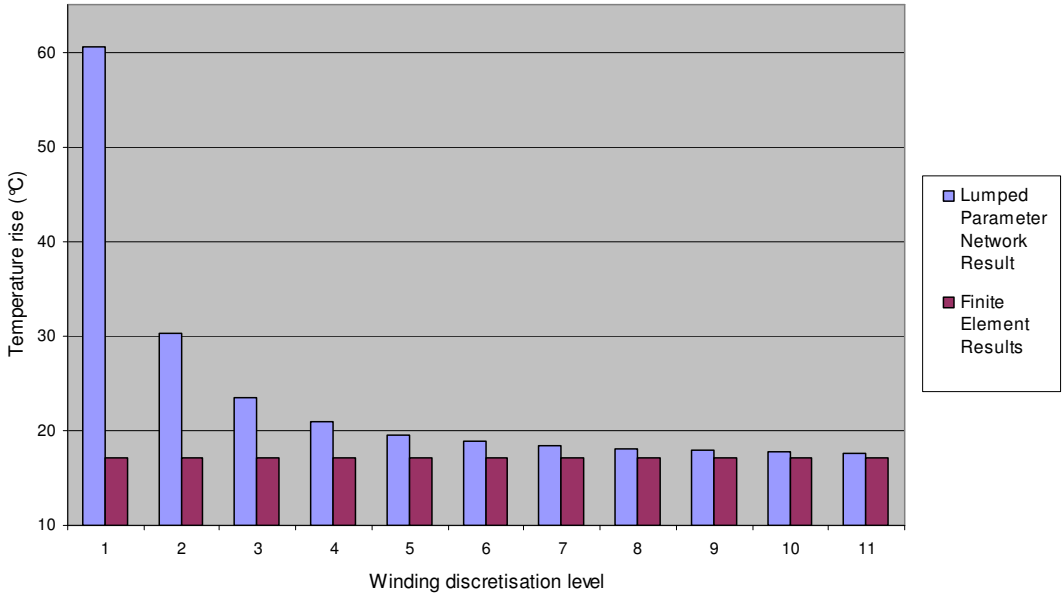

Figure 5.3: *Multi-node networks and FE winding discretisation results.*

In Figure 5.3, the x-axis winding discretisation level refers to the structure of the lumped parameter network, where a winding discretisation level of 1 refers to the 1x1 thermal network illustrated in Figure 5.1 and a winding discretisation level of 10 refers to the 10x10 thermal network shown in Figure 5.2. As presented in Figure 5.3,

the lumped parameter network results stabilise around winding discretisation level 10, generating an average winding temperature of 17.71 °C, compared to the finite element result of 17.07 °C.

As shown by the results presented a winding discretisation level of 10 yields very accurate results in comparison with the finite element results obtained. This result is validated against a wide range of input losses, winding thermal conductivities and winding geometries, all converging to a 10x10 array, as shown in Figure 5.3. Using lower discretisation levels reduces the accuracy of the results, jeopardising the machine's overall thermal model. On the other hand, increasing the winding discretisation level above the 10x10 thermal network is unnecessary and complicates the thermal model without a significant accuracy reward. Discretisation levels of up to 20x20 are simulated in the study, in order to increase confidence in the results presented and confirm that stabilisation of the lumped parameter network results illustrated in Figure 5.3.

5.2.2 Rotor Winding Discretisation Level Study

Once a winding discretisation level of 10 is identified as yielding reasonably accurate results when modelling an isolated coil winding, the model under investigation is extended to cover one pole of the CGT BCI184E alternator's rotor. The rotor thermal network developed and presented in Chapter 3 is utilised for the study, with the winding section modified to accommodate the range of winding discretisation levels tested, as shown in Figure 5.4.

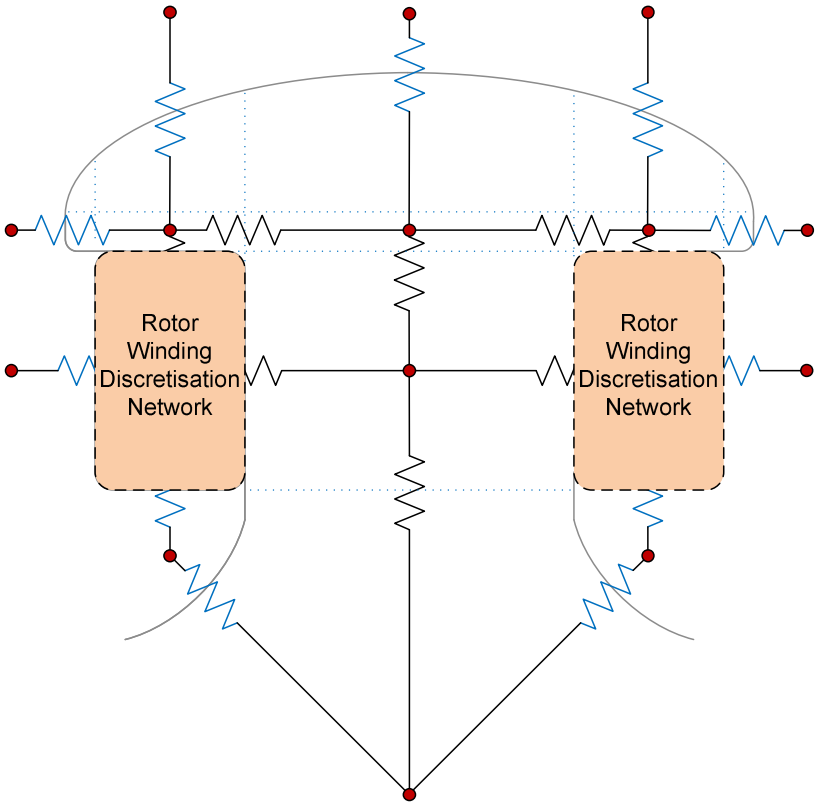

Figure 5.4: *Rotor winding discretisation level study thermal network.*

Model machine geometries and material thermal properties, such as the ones used for the CGT BCI184E synchronous machine models in Chapter 3, are selected to create a meaningful machine model and located as shown in Figure 5.4. In order to remain consistent with the previous isolated winding discretisation study, model losses are only added to the rotor winding section and, again for consistency, these have a magnitude of 1.5 kW. Once again, lumped parameter thermal network models are created for the range of rotor winding discretisation levels considered, from the 1x1 to the 10x10 discretisation level. The results obtained are presented in Figure 5.5.

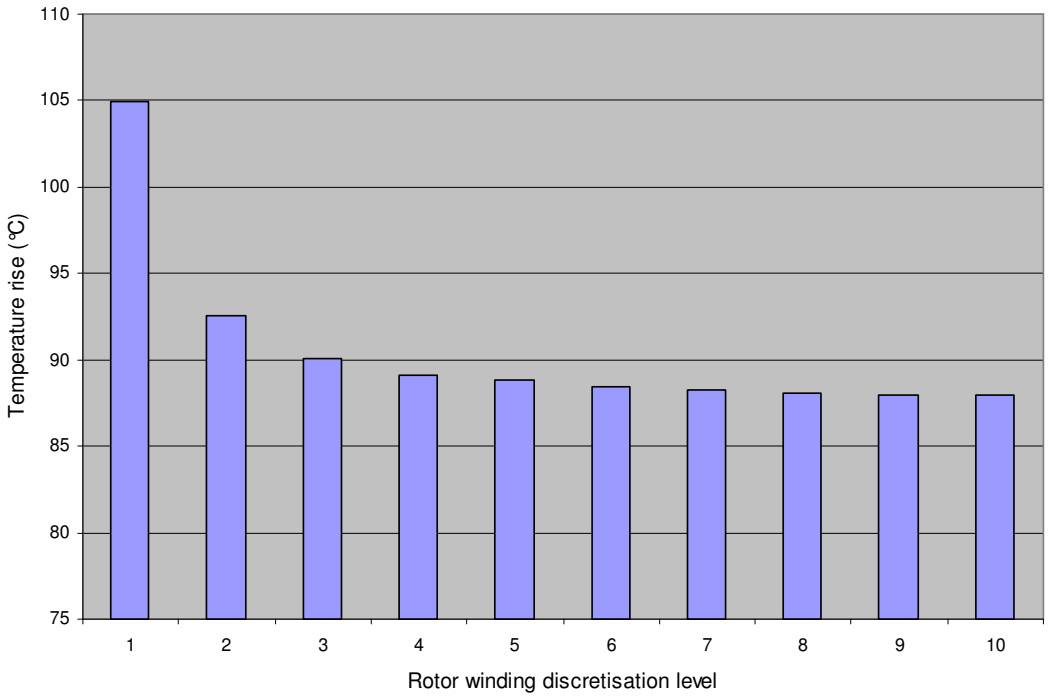

Figure 5.5: *Rotor winding discretisation results.*

As shown in Figure 5.5, similarly to the isolated winding study, a discretisation level of 10x10 is identified as providing an acceptable rotor coil winding discretisation level.

5.2.3 Stator Winding Discretisation Level Study

In order to confirm that the isolated winding and rotor winding results presented in the previous sections are also applicable to the stator winding a similar study is performed using the stator thermal network created in Chapter 3. Figure 5.6 displays the stator thermal network for the CGT alternator, with the location of the winding network under examination clearly marked.

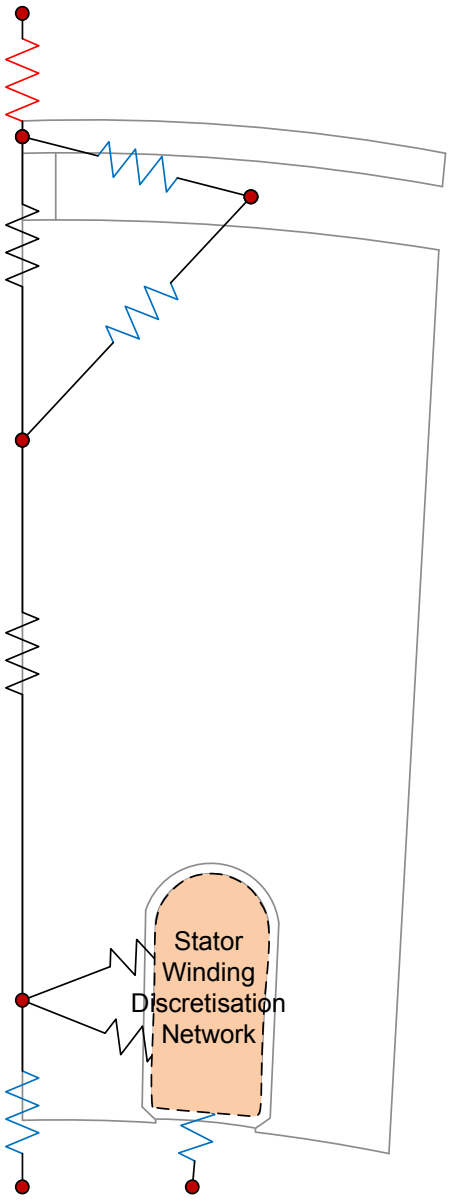

Figure 5.6: *Stator winding discretisation level study thermal network.*

As with the rotor winding study in the previous section, lumped parameter thermal network components are calculated from machine design data and a 1.5 kW loss is injected into the winding section. Again, discretisation levels ranging from a 1x1 stator winding thermal network to a 10x10 network are considered. The results obtained are presented in Figure 5.7. It should be noted that, as illustrated in Figure 3.6 in Section 3.4, the stator winding considered consists of two layers and that both of these stator winding layer sections are subjected to the winding discretisation described, with the overall effect monitored and shown in Figure 5.7.

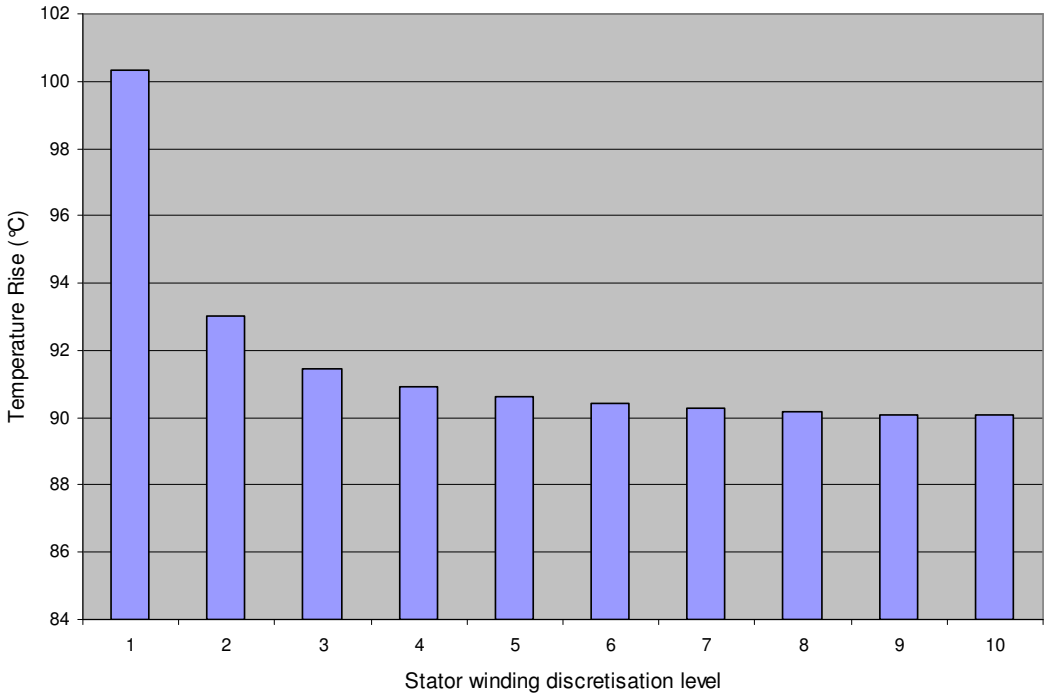

Figure 5.7: *Stator winding discretisation results.*

As illustrated in Figure 5.7, a level 10 (10x10), winding discretisation level is also identified as reasonably accurate to model the stator winding in lumped parameter thermal networks.

5.2.4 General Isolated Winding Discretisation Level Study

Finally, a more general isolated winding discretisation level solution, not exclusively applied to a CGT BCI184E synchronous generator, is achieved by considering electrical machine winding dimensions ranging from a 10 mm (winding height) by 10 mm (winding width) radial surface area winding to a 150 mm by 150 mm winding. In the study, winding geometries are increased in steps of 10 mm, between the two winding geometries stated. The winding analysis dimension range is selected because it covers the range of windings in synchronous generators manufactured by Cummins Generator Technologies examined in this thesis. The aspect ratio, winding height to width, is the main parameter in this study and so the results presented in this section are applicable to winding geometries outside the established winding

geometry range. Once again, to be consistent with the previous studies, a 1.5 kW loss is applied to all models and identical winding material properties are employed.

Results obtained are presented in Table 5.1, which indicates the winding discretisation levels at the point in which a further increase in discretisation level accuracy provides less than 0.5 °C accuracy benefit. At this point, the flat region seen in Figures 5.3 (Section 5.2.1), 5.5 (Section 5.2.2) and 5.7 is reached. Furthermore, in order to establish the level of accuracy linked with each one of the discretisation levels selected, the difference in °C temperature (ΔT) is included in Table 5.1 under each winding discretisation label. For example, a 6x6 winding discretisation level is recommend for a 0.02m x 0.08m winding and this has an error of 0.58 °C with respect to the solution a 10x10 winding model would yield.

Winding Width (m)	Winding Height (m)														
	0.01	0.02	0.03	0.04	0.05	0.06	0.07	0.08	0.09	0.1	0.11	0.12	0.13	0.14	0.15
0.01	7x7	7x7	6x6	6x6	5x5	5x5	5x5	5x5	4x4	4x4	4x4	4x4	4x4	4x4	4x4
ΔT (°C)	0.67	0.57	0.75	0.58	0.72	0.58	0.48	0.41	0.57	0.51	0.45	0.41	0.37	0.34	0.32
0.02	7x7	7x7	7x7	7x7	7x7	6x6	6x6	6x6	5x5	5x5	5x5	5x5	5x5	5x5	5x5
ΔT (°C)	0.57	0.67	0.64	0.57	0.51	0.75	0.66	0.58	0.81	0.72	0.65	0.58	0.53	0.48	0.44
0.03	6x6	7x7	7x7	7x7	7x7	7x7	7x7	7x7	6x6	6x6	6x6	6x6	6x6	5x5	5x5
ΔT (°C)	0.75	0.64	0.67	0.66	0.62	0.57	0.53	0.49	0.75	0.69	0.63	0.58	0.31	0.78	0.73
0.04	6x6	7x7	7x7	7x7	7x7	7x7	7x7	7x7	7x7	7x7	6x6	6x6	6x6	6x6	6x6
ΔT (°C)	0.58	0.57	0.66	0.67	0.66	0.64	0.61	0.57	0.54	0.51	0.8	0.75	0.7	0.66	0.62
0.05	5x5	7x7	7x7	7x7	7x7	7x7	7x7	7x7	7x7	7x7	7x7	7x7	7x7	6x6	6x6
ΔT (°C)	0.72	0.51	0.62	0.66	0.67	0.67	0.65	0.63	0.6	0.57	0.55	0.52	0.5	0.79	0.74
0.06	5x5	6x6	7x7	7x7	7x7	7x7	7x7	7x7	7x7	7x7	7x7	7x7	7x7	7x7	7x7
ΔT (°C)	0.58	0.75	0.57	0.64	0.67	0.67	0.67	0.66	0.64	0.62	0.6	0.57	0.55	0.53	0.51
0.07	5x5	6x6	7x7	7x7	7x7	7x7	7x7	7x7	7x7	7x7	7x7	7x7	7x7	7x7	7x7
ΔT (°C)	0.48	0.66	0.53	0.61	0.65	0.67	0.67	0.67	0.66	0.65	0.63	0.61	0.59	0.57	0.57
0.08	5x5	6x6	7x7	7x7	7x7	7x7	7x7	7x7	7x7	7x7	7x7	7x7	7x7	7x7	7x7
ΔT (°C)	0.41	0.58	0.49	0.57	0.63	0.66	0.67	0.67	0.67	0.66	0.65	0.64	0.62	0.61	0.59
0.09	4x4	5x5	6x6	7x7	7x7	7x7	7x7	7x7	7x7	7x7	7x7	7x7	7x7	7x7	7x7
ΔT (°C)	0.57	0.81	0.75	0.54	0.6	0.64	0.66	0.67	0.67	0.67	0.66	0.66	0.64	0.63	0.62
0.1	4x4	5x5	6x6	7x7	7x7	7x7	7x7	7x7	7x7	7x7	7x7	7x7	7x7	7x7	7x7
ΔT (°C)	0.51	0.72	0.69	0.51	0.57	0.62	0.65	0.66	0.67	0.67	0.67	0.67	0.66	0.65	0.64
0.11	4x4	5x5	6x6	6x6	7x7	7x7	7x7	7x7	7x7	7x7	7x7	7x7	7x7	7x7	7x7
ΔT (°C)	0.45	0.65	0.63	0.8	0.55	0.6	0.63	0.65	0.66	0.67	0.67	0.67	0.67	0.66	0.65
0.12	4x4	5x5	6x6	6x6	7x7	7x7	7x7	7x7	7x7	7x7	7x7	7x7	7x7	7x7	7x7
ΔT (°C)	0.41	0.58	0.58	0.75	0.52	0.57	0.61	0.64	0.66	0.67	0.67	0.67	0.67	0.67	0.66
0.13	4x4	5x5	6x6	6x6	7x7	7x7	7x7	7x7	7x7	7x7	7x7	7x7	7x7	7x7	7x7
ΔT (°C)	0.37	0.53	0.31	0.7	0.5	0.55	0.59	0.62	0.64	0.66	0.67	0.67	0.67	0.67	0.67
0.14	4x4	5x5	5x5	6x6	6x6	7x7	7x7	7x7	7x7	7x7	7x7	7x7	7x7	7x7	7x7
ΔT (°C)	0.34	0.48	0.78	0.66	0.79	0.53	0.57	0.61	0.63	0.65	0.66	0.67	0.67	0.67	0.67
0.15	4x4	5x5	5x5	6x6	6x6	7x7	7x7	7x7	7x7	7x7	7x7	7x7	7x7	7x7	7x7
ΔT (°C)	0.32	0.44	0.73	0.62	0.74	0.51	0.57	0.59	0.62	0.64	0.65	0.66	0.67	0.67	0.67

Table 5.1: *Minimum discretisation level required for specific winding geometry.*

As shown in Table 5.1, the most common minimum winding discretisation level allowed is a 7x7 array. Furthermore, windings with an aspect ratio at the extremes (i.e. much greater or less than one) can have a smaller nodal array. This is due to the fact the heat transfer through windings with these aspect ratios is easier to model, since a lower thermal resistance across the conducting path results. As presented in Table 5.1, the °C temperature magnitude errors linked to the winding discretisation levels selected are all under 1 °C.

To conclude the study, Table 5.2 presents a general overview of the results obtained in this chapter. As opposed to the minimum winding discretisation required presented in Table 5.1, the recommended winding discretisation level required to achieve high accuracy results for each winding geometry considered is stated in Table 5.2.

Winding Width (m) \ Winding Height (m)	0.01	0.02	0.03	0.04	0.05	0.06	0.07	0.08	0.09	0.1	0.11	0.12	0.13	0.14	0.15
0.01	9x9	8x8	7x7	6x6	6x6	5x5	5x5	5x5	4x4	4x4	4x4	4x4	4x4	4x4	4x4
0.02	8x8	9x9	8x8	7x7	7x7	7x7	7x7	6x6	6x6	6x6	6x6	5x5	5x5	5x5	5x5
0.03	7x7	8x8	9x9	8x8	8x8	7x7	7x7	7x7	7x7	7x7	7x7	6x6	6x6	6x6	6x6
0.04	6x6	7x7	8x8	9x9	8x8	8x8	8x8	7x7	7x7	7x7	7x7	7x7	7x7	7x7	7x7
0.05	6x6	7x7	8x8	8x8	10x10	9x9	8x8	8x8	8x8	7x7	7x7	7x7	7x7	7x7	7x7
0.06	5x5	7x7	7x7	8x8	9x9	10x10	9x9	8x8	8x8	8x8	8x8	7x7	7x7	7x7	7x7
0.07	5x5	7x7	7x7	8x8	8x8	9x9	10x10	9x9	8x8	8x8	8x8	8x8	7x7	7x7	7x7
0.08	5x5	6x6	7x7	7x7	8x8	8x8	9x9	10x10	9x9	8x8	8x8	8x8	8x8	8x8	7x7
0.09	4x4	6x6	7x7	7x7	8x8	8x8	8x8	9x9	10x10	9x9	8x8	8x8	8x8	8x8	8x8
0.1	4x4	6x6	7x7	7x7	7x7	8x8	8x8	8x8	9x9	10x10	9x9	9x9	8x8	8x8	8x8
0.11	4x4	6x6	7x7	7x7	7x7	8x8	8x8	8x8	8x8	9x9	10x10	9x9	9x9	8x8	8x8
0.12	4x4	5x5	6x6	7x7	7x7	7x7	8x8	8x8	8x8	9x9	9x9	10x10	9x9	9x9	8x8
0.13	4x4	5x5	6x6	7x7	7x7	7x7	7x7	8x8	8x8	8x8	9x9	9x9	10x10	9x9	9x9
0.14	4x4	5x5	6x6	7x7	7x7	7x7	7x7	8x8	8x8	8x8	8x8	9x9	9x9	10x10	9x9
0.15	4x4	5x5	6x6	7x7	7x7	7x7	7x7	7x7	8x8	8x8	8x8	8x8	9x9	9x9	10x10

Table 5.2: *Discretisation level required for specific winding geometry.*

The results presented in Table 5.2 can be used as a quick reference when developing electrical machine winding thermal models. As stated in the study, a discretisation level of 10x10 is required for the more complex coil windings. Simpler windings with longer, thinner coil windings, with significantly higher or lower than unity aspect ratios, can be successfully modelled with lower winding discretisation levels.

5.3 Winding Discretisation Level Application to Thermal Models and Evaluation

In order to avoid the use of experience based algorithms transforming thermal network nodal temperatures into actual temperatures, the winding discretisation levels stated in this chapter, mainly the 10x10 level, can be applied to electrical machine thermal networks by making the necessary thermal network adjustments to accommodate the highly discretised winding networks. This can significantly complicate the design of the thermal systems and make these considerably more difficult to analyse. For this reason, a curve fitting exercise is executed in order to generate a coefficient to translate single node 1x1 winding network temperatures to the desired 10x10 network temperature result. In order to achieve this, several input copper and iron loss operational conditions are applied to the rotor winding 1x1 and 10x10 thermal networks presented in Figure 5.4 (Section 5.2.2). The results to the tests performed are presented in Table 5.3.

Input Copper Loss (W)	Input Iron Loss (W)	1x1 Winding Temperature	10x10 Winding Temperature
100	50	9.2	8.1
500	500	56.8	51.3
1200	100	88.3	74.8
1200	300	97.1	83.5
1300	300	104.1	89.4
1200	500	105.8	92.3
1400	300	111.0	95.3
2000	500	161.8	139.2
2000	1000	183.6	161.1
3000	1500	275.4	241.7

Table 5.3: *Curve fitting integration study of 10x10 winding discretisation.*

The relationship between 1x1 and 10x10 winding temperature results presented in Table 5.3 is illustrated in Figure 5.8. From this, a graph gradient of 0.88 is extracted. Hence, this 0.88 coefficient can be utilised in lumped parameter electrical machine thermal models to translate single node winding network temperature results to the established accurate 10x10 network temperature prediction. This 1x1 to 10x10

winding temperature converting coefficient is utilised by the MySolver thermal modelling tool presented in Chapter 6.

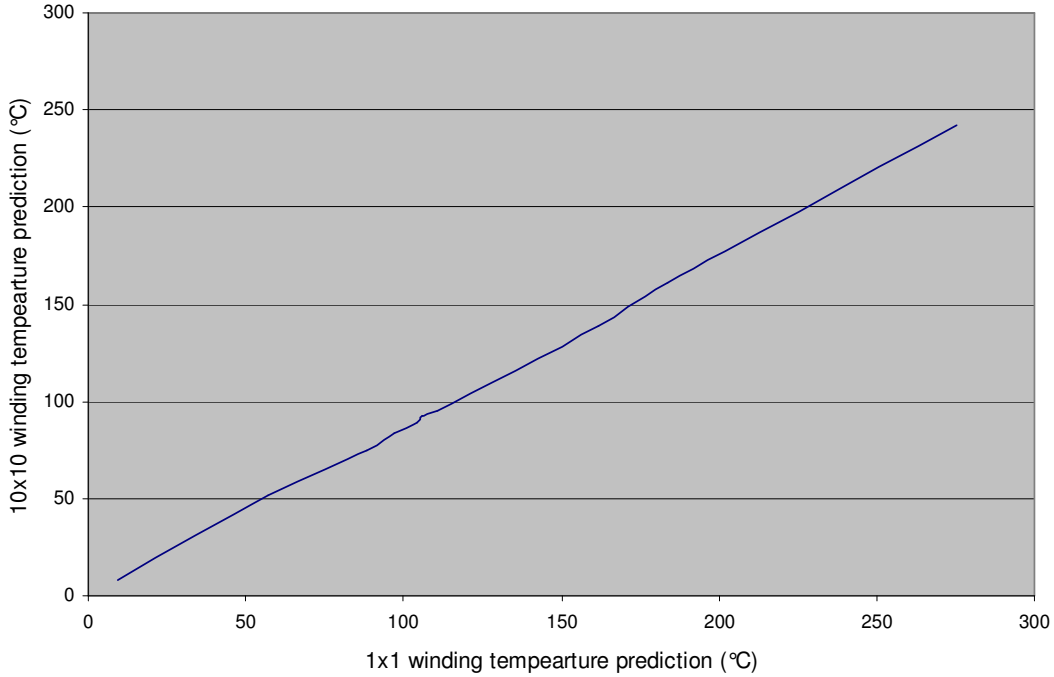

Figure 5.8: *Curve fitting integration of 10x10 winding discretisation.*

5.4 Chapter Summary

In this chapter the issues to be considered when selecting an appropriate winding discretisation level, to be accommodated within a lumped parameter thermal network of an electrical machine, are discussed. Discretisation studies are performed initially using an isolated winding model of the CGT BCI184E synchronous machine investigated in this thesis. The results of this investigation indicate that a lumped parameter thermal network made up of one hundred individual nodes, constructed in a 10x10 matrix structure, is ideal to correctly thermally model the machine winding and yield accurate winding average temperatures, which are validated using finite element simulation results. This result is subsequently validated with winding networks integrated into the rotor and stator thermal networks presented in Chapter 3, with the results confirming a reasonably accurate 10x10 winding discretisation level accuracy. Utilising this method, general tables, not related to the particular CGT alternator investigated in this thesis, are devised indicating the required winding discretisation levels needed for specific winding geometries. Finally, a curve fitting exercise is performed in ordered to translate the basic single node 1x1 winding temperature results to the desired 10x10 winding network generated temperatures. The resulting 1x1 to 10x10 winding temperature converting coefficient is subsequently used by the MySolver lumped parameter thermal modelling tool presented in Chapter 6.

CHAPTER 6

MySolver Lumped Parameter Thermal Modelling Tool

6.1 Introduction

Discoveries and lumped parameter thermal network developments covered in the preceding chapters are collected together and implemented into a novel thermal modelling tool, MySolver, presented in this chapter. This chapter outlines MySolver operation, highlighting its input requirements, the Excel and Portunus software implications and the generated outputs. Details of specific aspects covered in this chapter are tackled in the relevant thesis chapters and, hence, are not given in this chapter. In the subsequent Chapter 8, MySolver is utilised to thermally model the CGT BCI184E synchronous generator, presented in Chapter 3, with the results obtained analysed and its performance evaluated.

MySolver has been designed and subsequently tested for the thermal modelling of synchronous generators. The principles presented in this thesis are applicable to other machine types and MySolver can be modified to model them. Geometric alterations to MySolver can be executed as outlined in Chapter 3 and MySolver has the flexibility to change machine operational losses and airflow related issues. In this way, MySolver can be adapted to model the specific electrical machine type range of interest, from any manufacturer.

6.2 MySolver Thermal Modelling Operation

MySolver uses the rotor and stator lumped parameter thermal networks detailed and developed in Chapter 3. The necessary electrical machine geometric parameters and relevant material information data, outlined in Chapter 3, is fed in by the user via an Excel spreadsheet. Furthermore, armature and field winding voltage and current readings characterising the particular machine operation condition modelled, along with the power losses linked to this operational condition, are also an input to MySolver. These electrical machine operational losses are obtained as described in Chapter 3. The necessary airflow information to compute the important heat transfer coefficients, as explained in Chapter 3, need to be supplied by the user at this stage.
From the information supplied by the user tabulated in Excel, MySolver calculates all the lumped parameter thermal networks thermal resistance components comprising the rotor and stator networks, listed and explained in Sections 3.3, 3.4 and 3.5. In addition to this, input power loss nodal values, discussed in Section 3.7, and thermal capacitance magnitudes for transient simulations, covered in Section 3.8, are computed automatically. LCCs, presented in Section 4.5, come into effect at this point, as electrical machine lamination iron losses are redistributed accordingly across the rotor and stator thermal models. No additional FEA simulations are required by the user and MySolver is a stand alone thermal modelling package.

At this stage, the MySolver user can call for the thermal results to be generated via an ActiveX visual basic based link between Excel and system analysis tool Portunus. The information calculated in Excel is transferred to Portunus and fed into the developed rotor and stator lumped parameter thermal networks, outlined in the next section. The thermal network analysis is executed by the Portunus component of MySolver and, again via an ActiveX link, results are sent back to the MySolver's output spreadsheet page in Excel. Here, all nodal steady-state temperatures are presented and transient temperature rise graphs plotted. These are the thermal results subsequently validated, using experimentally obtained data, in Chapter 8. It is worth noting that in the Portunus to Excel final temperature data transfer, the winding

discretisation coefficient translating single node predictions to 10x10 winding network temperatures, elaborated in Chapter 5, is used.

MySolver requirements and operation are illustrated in Figure 6.1 and subsequently summarised.

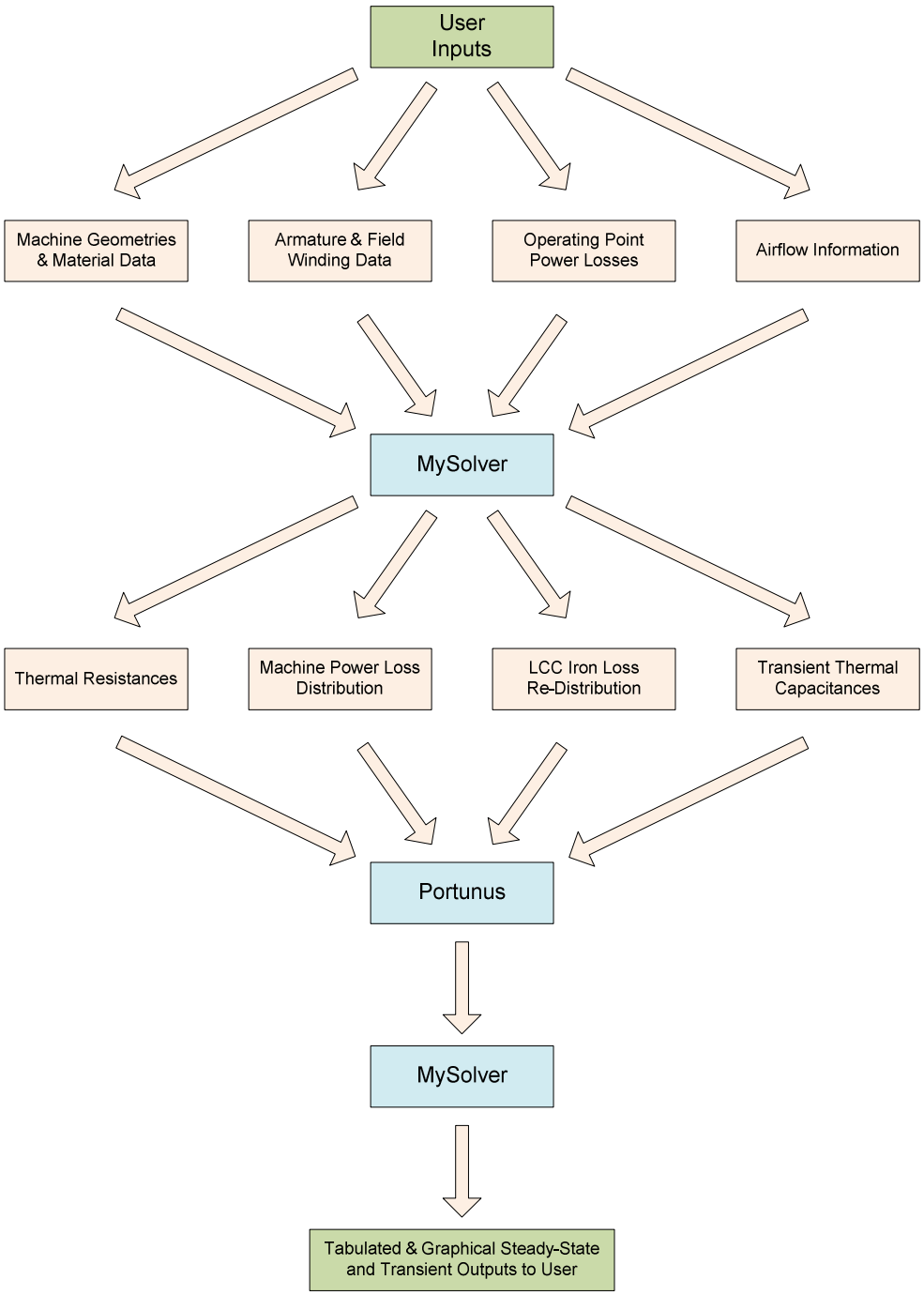

Figure 6.1: *MySolver operational flow diagram.*

Input requirements:

- Detailed geometries from machine drawings to include the parameters illustrated in Figures 3.2 and 3.6 (Sections 3.3 and 3.4 respectively).
- Material properties information provided by material suppliers added by user (utilised as described in Chapter 3).
- Experimental (if available), simulated or estimated armature and field winding information added. Current and voltage values to compute specific machine losses.
- Experimental (if available), simulated or estimated or simulated power losses, in particular iron losses, are added.
- Measured (if available) or estimated airflow related issues, such as the required heat transfer coefficients, are input.

Operation outline:

- All lumped parameter thermal network resistances computed utilising the geometric information supplied by the user.
- Input power losses injected at relevant thermal network nodes.
- LCCs (presented in Chapter 4) utilised to redistribute iron losses across rotor and stator laminations. The default stator:rotor iron loss split ratio of 85:15, explained in Section 4.4.5, is utilised by MySolver. No extra FEA simulations are required by the user to perform MySolver thermal consultations. The MySolver 85:15 iron loss split ratio can be modified by the user if required.
- Thermal capacitances for transient simulations calculated from material information supplied by the user and added to the thermal models.
- Electrical machine thermal network solved by system analysis tool, Portunus.
- Discretisation winding coefficient (presented in Chapter 5) used to obtain accurate winding temperatures.

Generated outputs:

- Steady-state and transient lumped parameter network nodal temperatures generated and relevant graphs plotted.

6.3 MySolver Portunus Thermal Models and Operation

The system analysis tool Portunus is used by MySolver to solve the rotor and stator lumped parameter thermal networks developed. Figures 6.2 and 6.3 overview the synchronous generator rotor and stator networks analysed by Portunus during MySolver operation. Values for each component shown in the figures are imported from Excel, where they are calculated from machine geometric and material information supplied by the user.

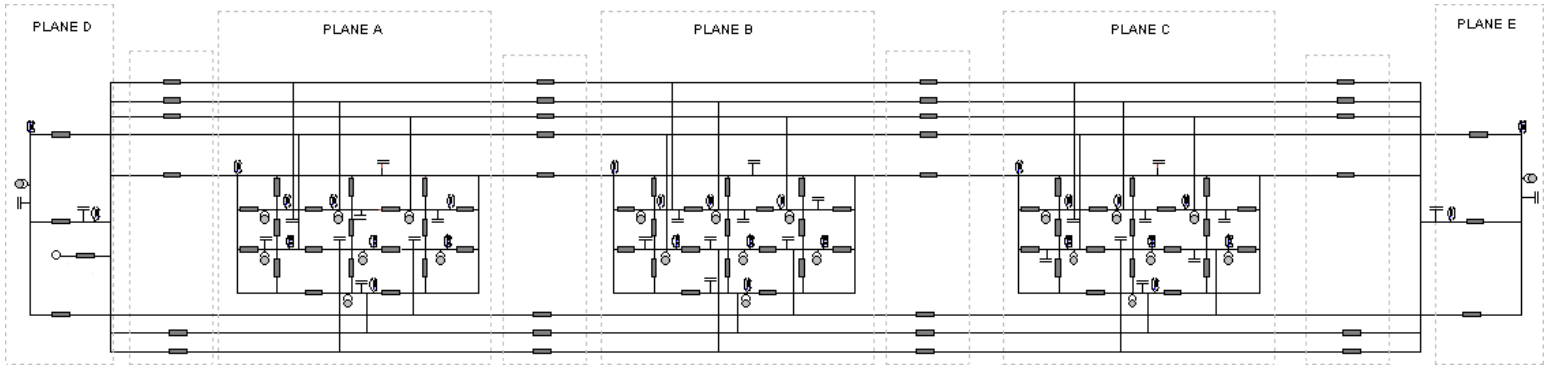

Figure 6.2: *Portunus rotor three axial plane lumped parameter thermal network.*

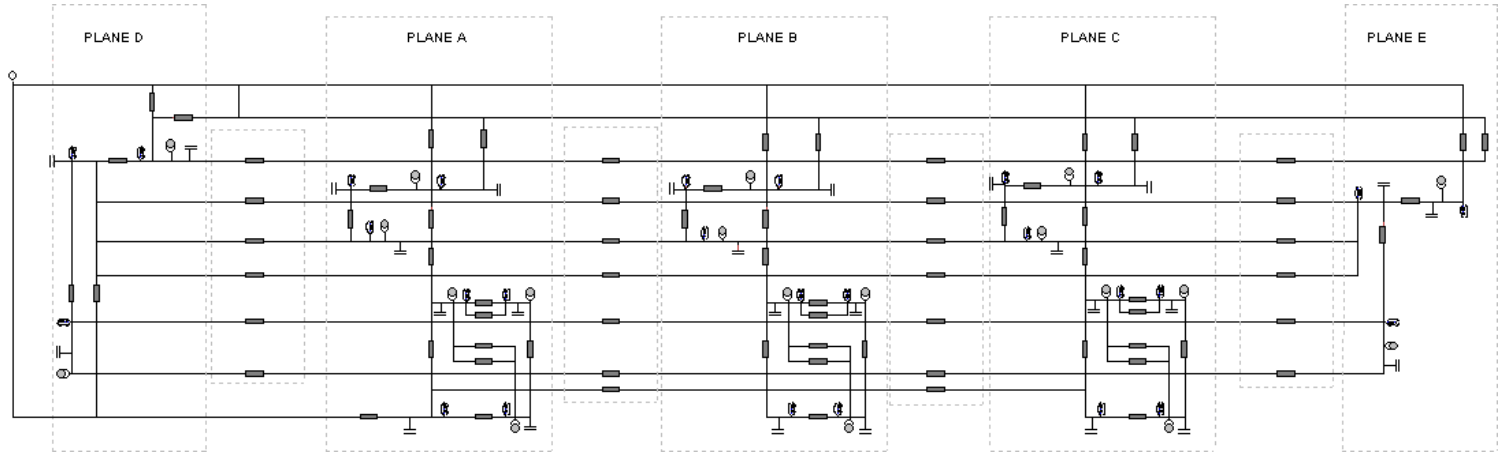

Figure 6.3: *Portunus stator three axial plane lumped parameter thermal network.*

Details of the rotor and stator thermal networks presented in Figures 6.2 and 6.3 are given in Chapter 3, where their development is explained in detail and each component making up the thermal networks is explained.

6.4 Evaluation of MySolver Use as a Thermal Modelling Tool

MySolver proves to be a user friendly reliable electrical machine thermal modelling tool, with a clear user interface. Using the diagrams presented in Chapter 3 the user can supply the geometric dimensions required to compute the thermal resistances making up the machine thermal networks for a wide range of machine size and types. After supplying experimentally obtained or estimated field and armature information, together with machine operational losses, nodal temperatures are returned to the user promptly. Very importantly, MySolver allows for future work to be easy accommodated. Its lumped parameter nature and the use of Portunus as the thermal network solver means that future alterations to the thermal networks or computing operations can be performed without major changes and implemented very quickly. MySolver provides both steady-state and transient thermal solutions, allowing the user to fully understand the electrical machine's thermal behaviour during the complete heat-run considered. Finally, as shown in Chapter 8, MySolver steady-state and transient temperature predictions for a wide range of load points agree closely with experimentally thermocouple obtained temperatures, which proves MySolver is a reliable thermal modelling tool that the user can trust.

6.5 Chapter Summary

The work presented in this thesis to this point is encapsulated in the MySolver thermal modelling tool, presented in this chapter. Outlined are the simple MySolver user instructions, with an overview of the inputs, outputs and operations executed listed. The Excel and Portunus usage in MySolver is explained and the rotor and stator lumped parameter thermal networks used by Portunus are presented. This chapter highlights the user friendly nature of MySolver and how future thermal modelling work, such as that described in Chapter 10, can easily be accommodate into the current MySolver version, due to its lumped parameter nature and thanks to the use of Portunus to compute the thermal network solution.

CHAPTER 7

Experimental Programme Procedure

7.1 Introduction to Experimental Validation

In order to effectively validate and evaluate the performance of the created electrical machine lumped parameter thermal models and to gain detailed insight on the thermal distribution across the machine's most important sections, an experimental verification stage was carried out. The experimental work carried out is described in this chapter, along with the design of the required test rig components and experimental limitations present. The resulting experimental results are presented and analysed in Chapter 8, with additional results presented in the Appendices.

7.2 Experimental Test Rig Setup

This chapter outlines the components required for the presented experimental validation stage. A schematic showing the main components of the system is shown in Figure 7.1.

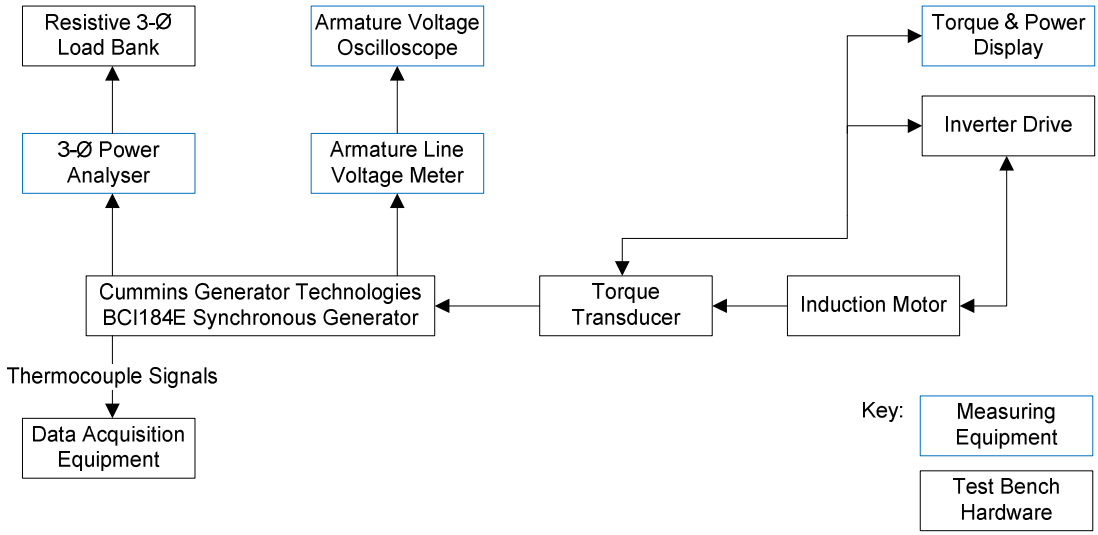

Figure 7.1: *Overview of experimental validation test rig layout.*

The synchronous generator test rig utilised consists of four main sections: the synchronous generator itself, an induction motor driving the generator, an inverter drive controlling the induction motor and a resistive load bank linked to the generator.

The synchronous generator is a 22.5 kVA CGT BCI184E electrical machine which is presented in Chapter 3. The motor is a conventional 22 kW induction machine, the inverter drive monitors the motor's rotational speed and the 3-phase resistive load bank can handle loads of up to 30 kW. The coupled synchronous generator and induction machine is shown in Figure 7.2.

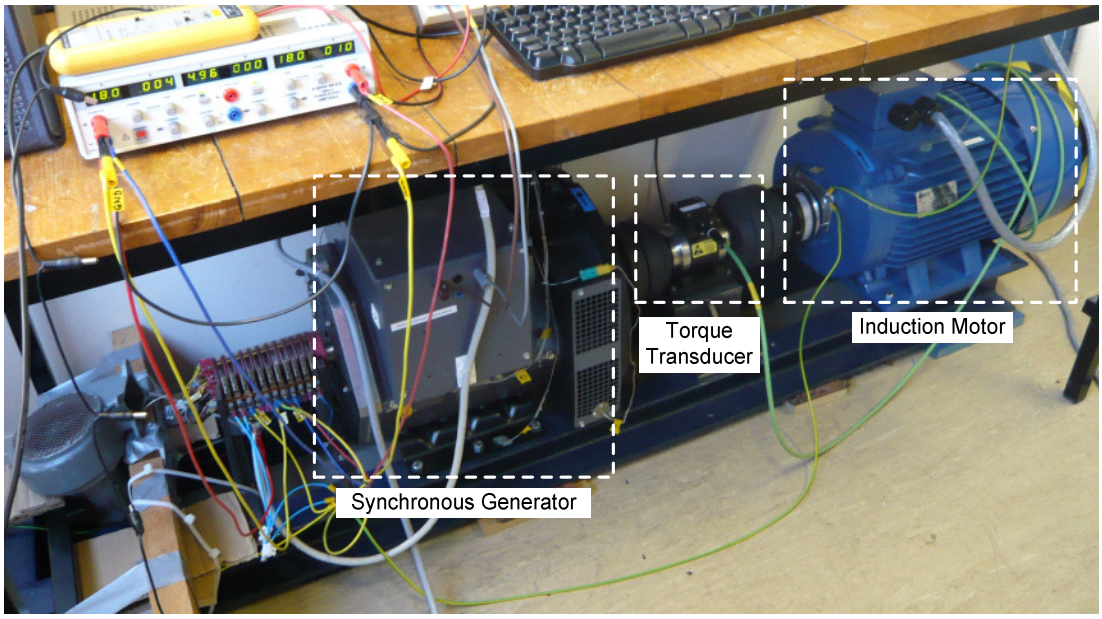

Figure 7.2: *Coupled synchronous generator, torque transducer and induction motor.*

For mechanical power to be transferred, the synchronous generator and induction motor are coupled as shown in Figure 7.2, with a torque transducer placed between the two electrical machines monitoring torque, power transferred and revolutions per minute. Additionally, a resolver provides the necessary feedback to the inverter drive for induction motor control. The power generated by the synchronous machine is passed through a 3-phase power analyser, to monitor armature voltage, current and power generated, before being transferred to the 3-phase resistive load bank.

7.2.1 Synchronous Generator k-Type Thermocouples

In order to monitor the temperature of the critical sections of the synchronous machine, k-type thermocouples are placed in a wide range of internal and external machine locations. The standard BCI184E machine was modified in order to collect the crucial information to validate the created lumped parameter models. The main modification areas during the assembly of the generator and the location of the thermocouples are discussed in this section.

Small k-type thermocouples are selected for this task in order not to obstruct the airflow and jeopardise the data collected. Other sensors, such as RTDs, provide clearer voltage signals, which are less susceptible to electrical noise, but their larger size makes them inappropriate for the task due to the potential to block the airflow. Wireless thermal sensors and transmission systems were considered, but the electrically and electromagnetically noisy environment makes wired systems a better option.

Internally, thermocouples are located at several positions in the stator and rotor windings. External thermocouples are utilised to monitor generator frame, feet and airflow temperatures at several positions.

Stator Winding Overhang and Slot Thermocouples

Thermocouples are placed both in the stator winding overhangs and along the axial length of a slot. The thermocouples placed in the stator winding overhang are located between overlapping coils of the same group. Twelve thermocouples, numbered S1 to S12, are placed both in the drive-end (DE) and in the non-drive-end (NDE). Stator winding overhang locations are illustrated in Figure 7.3.

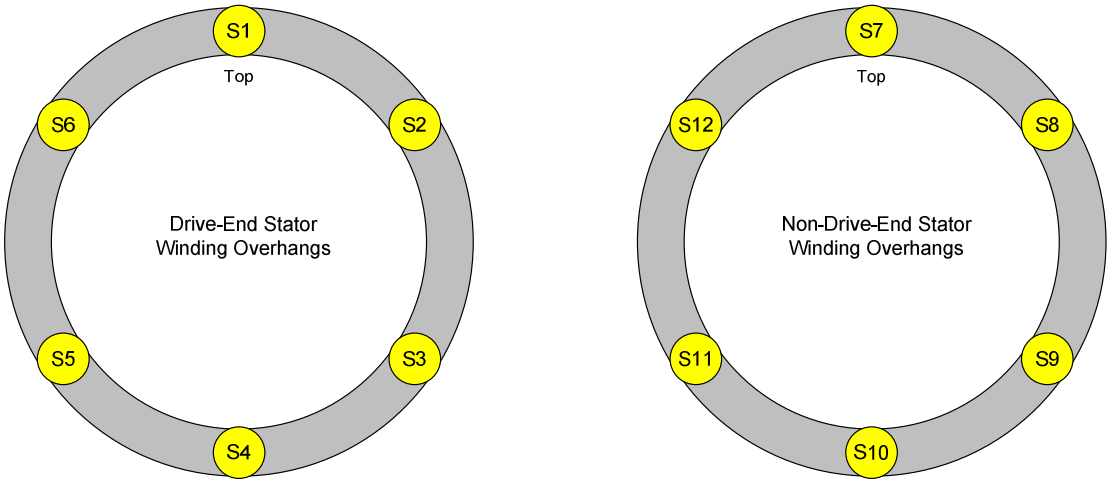

Figure 7.3: *Stator winding overhang thermocouple locations on DE and NDE.*

The synchronous machine's stator during the assembly process is shown in Figure 7.4. Illustrated is the presence of the specially placed overhang thermocouples, both on the NDE and DE overhangs.

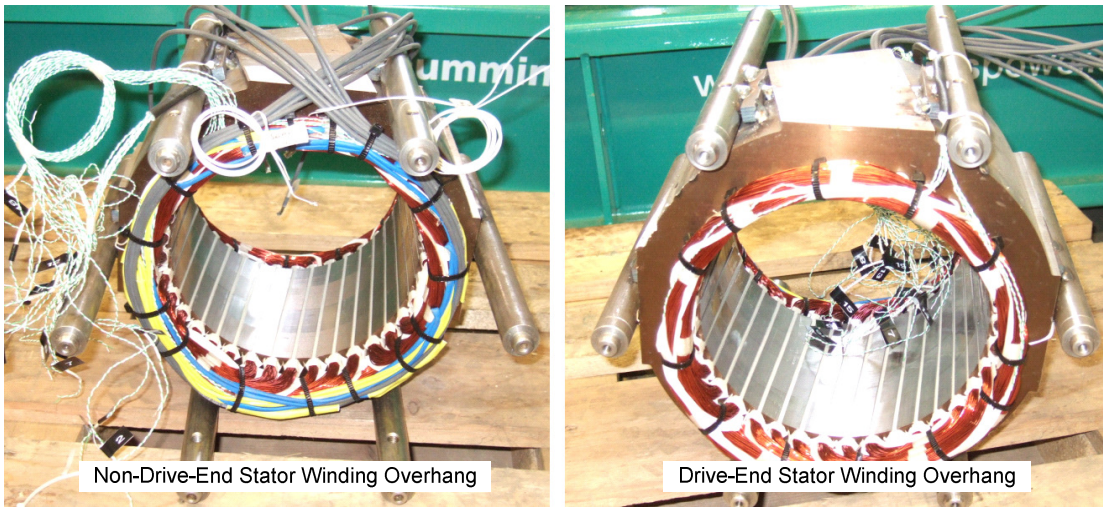

Figure 7.4: *Alternator stator NDE (left) and DE (right) winding overhangs.*

Additionally, five k-type thermocouples are placed axially equally spaced between armature coils, under the winding separator insulation, in the top slot of the stator lamination. These sensors are numbered S13 to S17, starting from the drive-end of the electrical machine, and their positions along the axial length of the stator lamination are shown in Figure 7.5. There is a gap of 25 mm between each of these thermocouples. Subsequently, three additional thermocouples are placed in slots 90 degrees apart, in the middle of the axial core length, numbered S18 to S20. Together with thermocouple S15, in Figure 7.5, these thermocouples monitor the winding temperature around the circumference of the machine at the middle of the core length, as shown in Figure 7.5.

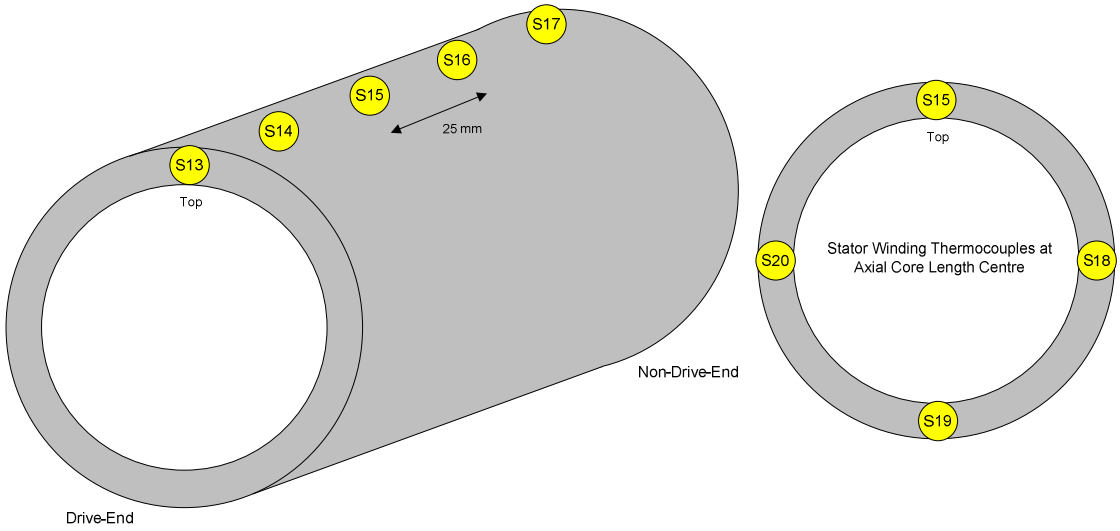

Figure 7.5: *Stator winding slot thermocouples placed along the machine core length.*

Rotor Winding Thermocouples

Fourteen thermocouples are placed in the rotor winding, all of which are located in one rotor pole, as shown in Figure 7.6.

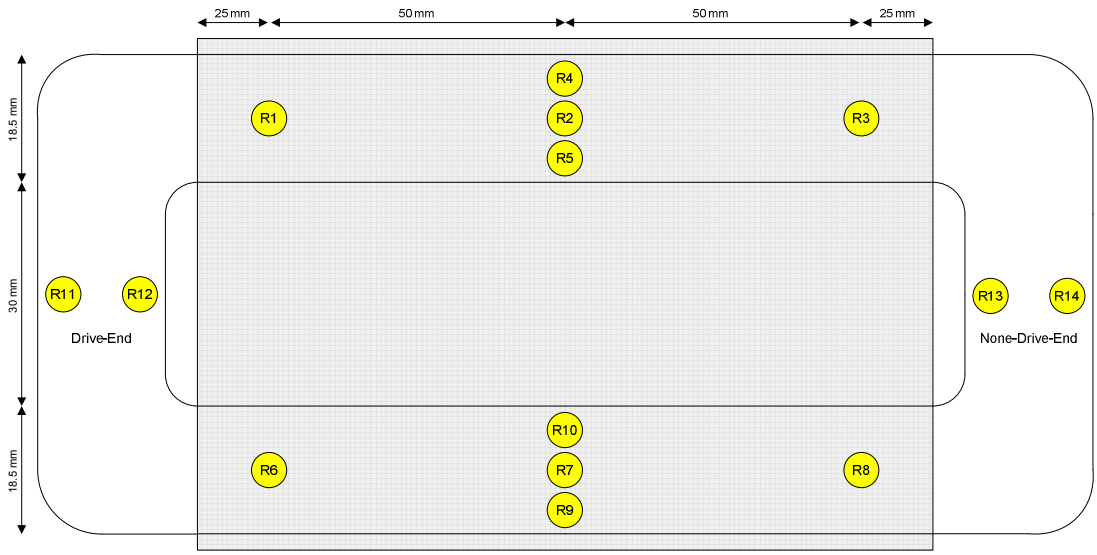

Figure 7.6: *Schematic location of rotor winding thermocouples.*

Rotor Design Modifications

In order to extract the information from the rotor thermocouples the rotor shaft had to be modified. The shaft was perforated and a duct running along its axial length created. All rotor thermocouple wires are collected and carried away from the rotor through this duct, as shown in Figure 7.7.

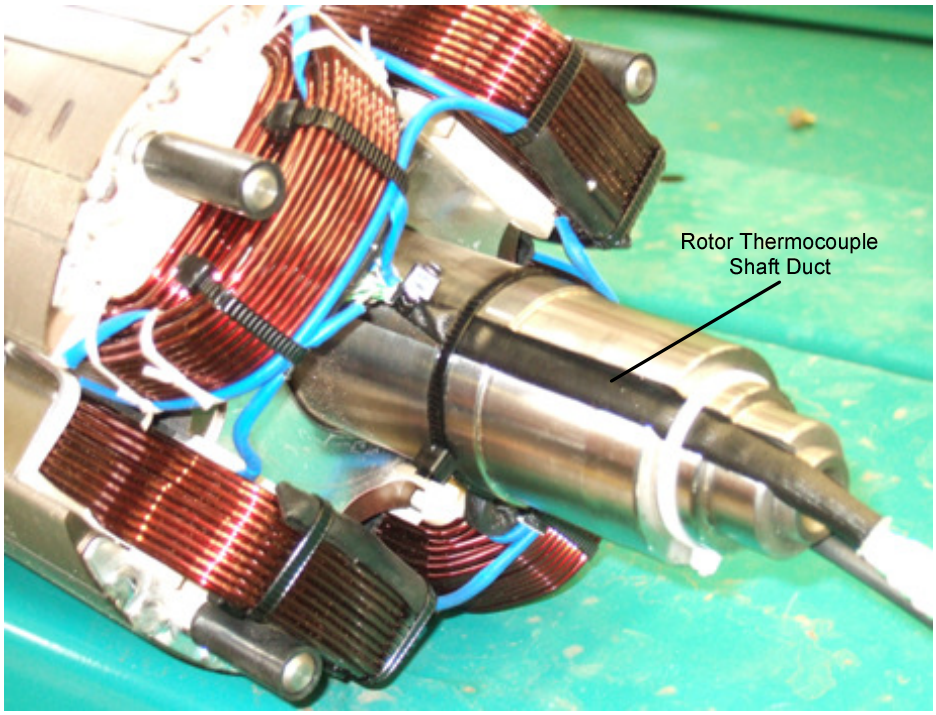

Figure 7.7: *Rotor shaft duct for thermocouple sensor extraction.*

External Synchronous Generator Thermocouples

In addition to the internal thermocouples, eight thermocouples are used to monitor external generator sections. As shown in Figure 7.8, four thermocouples (F1 to F4) are placed along the external length of the frame's core length. Single thermocouples are placed at the generator's feet (F5) and monitoring the AVR box temperature (F6). Finally, two thermocouples are used to measure the through ventilation air temperature increase (F7 and F8).

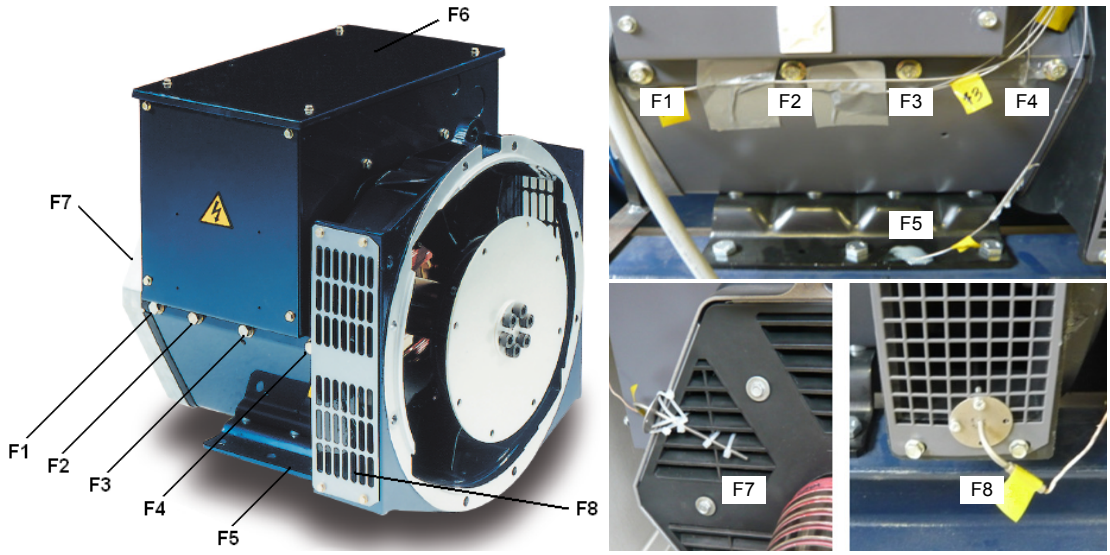

Figure 7.8: *Location of external synchronous machine thermocouples.*

7.2.2 Synchronous Generator Rotor Slip-Rings

In order to extract the thermal information collected by the rotor winding thermocouples, shaft mounted slip-rings are connected to the thermocouple wires ducted along the rotor shaft. The eleven brush bronze slip-rings presented in Figure 7.9 are utilised for this purpose. The conventional use of slip-rings to relay thermocouple information introduces problems in the shape of unpredictable thermal offsets and electrical noise interference. A description of these problems and how to tackle them is given in Section 7.3.

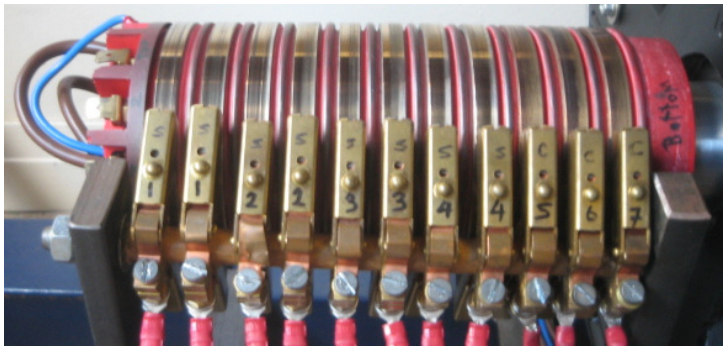

Figure 7.9: *Rotor shaft mounted bronze eleven brush slip-rings.*

7.2.3 Rotor Thermocouple Processing PCB

The rotor thermocouple processing PCB presented in this section, shown in Figure 7.10, is essential to guarantee the integrity of the recorded thermal signals. Essentially, the PCB removes the thermal offsets introduced by the use of the slip-rings; removes unwanted electrical and electromagnetic noise and amplifies the thermocouple signals. Details on its operation are given in Section 7.3.2.

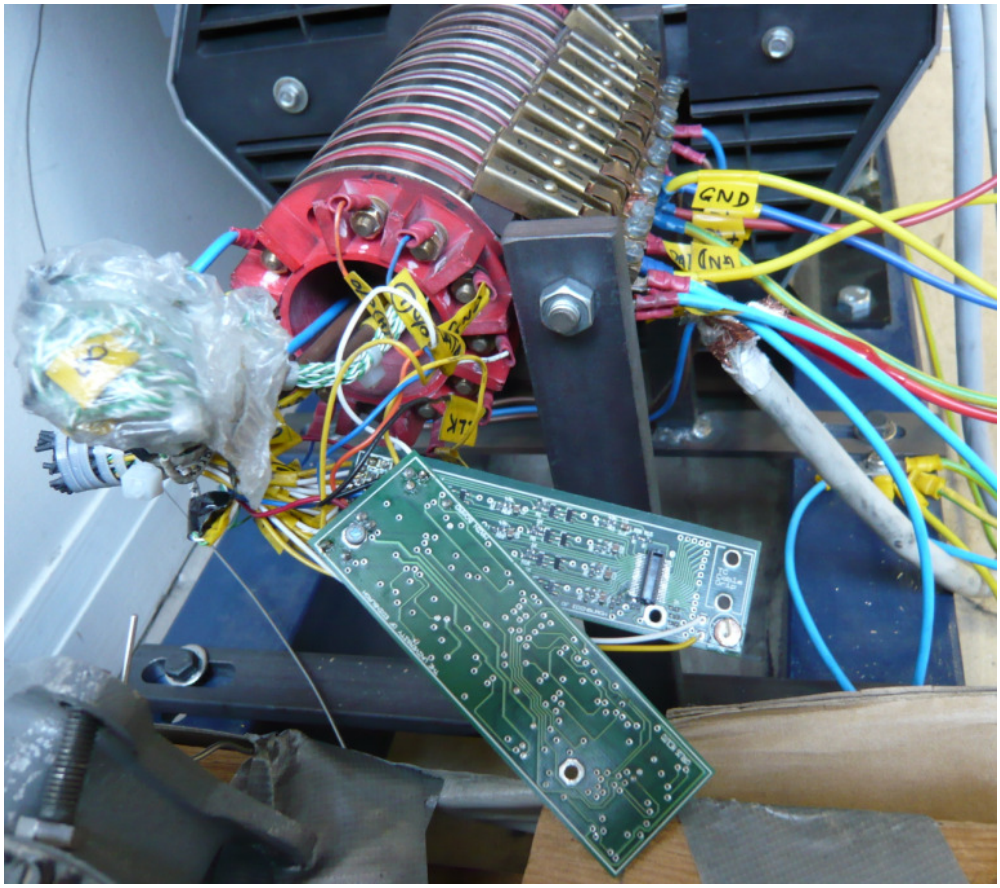

Figure 7.10: *Rotor thermocouple processing PCB.*

With the objective of keeping PCB temperatures as close to room temperature as possible a centrifugal fan was added to the experimental setup, as shown in Figure 7.11. A thermocouple was also placed between the fan and the PCB to monitor temperature. The importance and implications of the centrifugal fan are explained in Section 7.3.6.

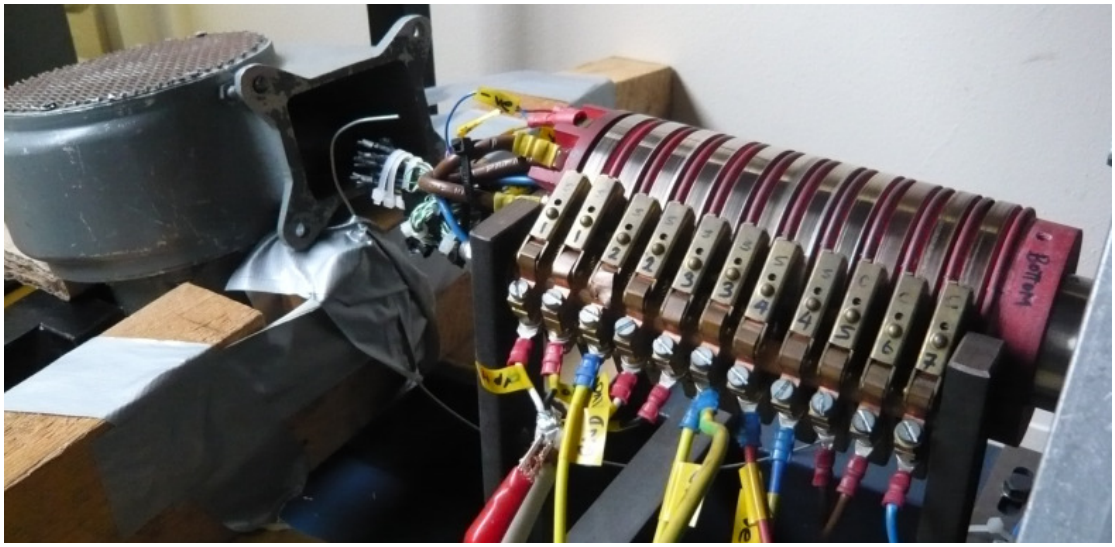

Figure 7.11: *PCB cooling centrifugal fan.*

7.2.4 Data Acquisition Equipment

All thermocouples are recorded using a Campbell Scientific CR1000 measurement and control system, shown in Figure 7.12. Additionally, a Campbell Scientific AM16/32A relay analogue multiplexer is used to increase the number of thermocouple input channels in order to accommodate for the numerous electrical machine thermocouples. Also utilised are the Agilent MSO6012A oscilloscope and the Voltech PM3000ACE power analyser presented in Figure 7.12. Furthermore, several voltage meters and ammeters are utilised to monitor the generator's field and armature windings.

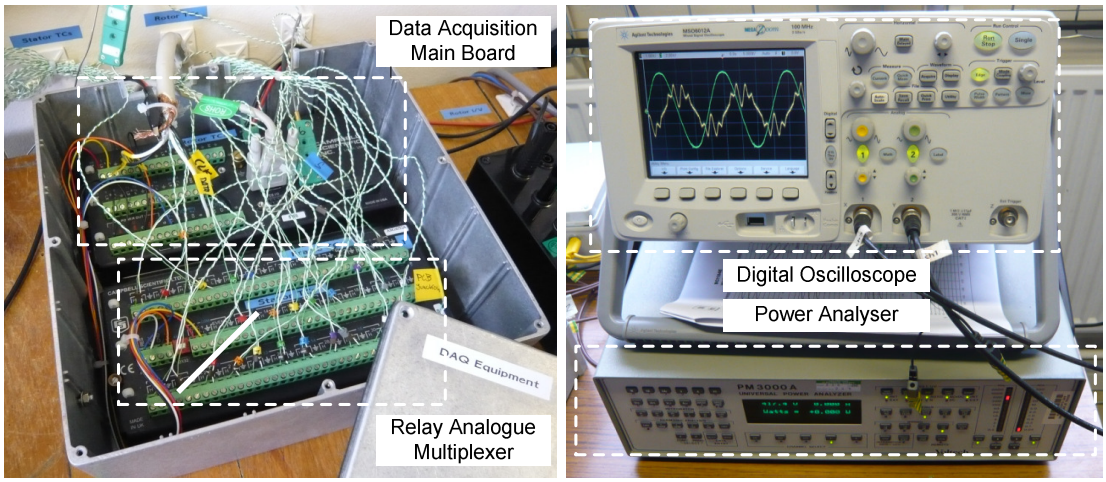

Figure 7.12: *Data acquisition main board, relay, digital oscilloscope and power analyser.*

7.2.5 Instrumentation

The instrumentation utilised during the experimental stage is presented in Table 7.1.

Instrument	Type	Accuracy
3-phase resistive load bank	Cressall, AC30, 230/400 V, 15/30 kW	-
Multimeter – Rotor voltage	Beckman, Tech 310	± 0.75 %
Multimeter – Stator voltage	Beckman, Tech 310	± 0.75 %
Ammeter – Rotor current	Sangamo Weston, Model 8103	± 0.2 A
Multimeter – Stator phase resistance	Beckman, Tech 310	± 0.5 %
Oscilloscope	Agilent MSO6012A 100 MHz	± 0.4 %
Power Analyser	Voltech, PM3000ACE	± 0.1 %
Data Acquisition System	Campbell Scientific, CR1000	± 0.06 %
Data Acquisition Relay Multiplexer	Campbell Scientific, AM16/32 A	-
Power supply – PCB	Hameg, HM7042-4	± 3 digits
Power supply – Data acquisition equipment	Iso-Tech, IPS-3610D	± 0.5 %
Torque transducer	Magtrol, TM312	± 0.1 %
Torque transducer indicator	Magtrol, Model 3410 Torque Display	± 0.01 %
Isolation transformer	SSE Ltd.	-
Thermal camera	Cedip, Titanium DCO19U-B	± 1 %

Table 7.1: *Instrumentation utilised during experimental validation stage.*

The complete test system is shown in Figure 7.13.

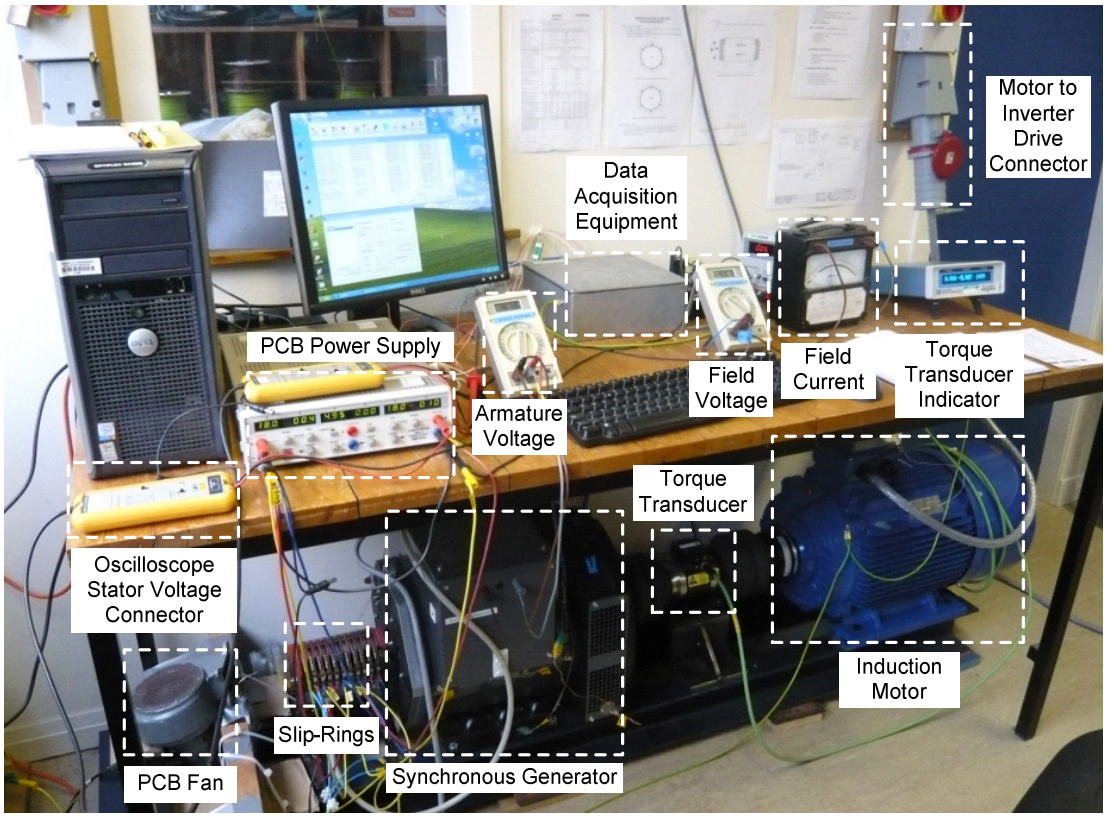

Figure 7.13: *Test rig layout of main instrumentation components.*

7.3 Reading Rotor k-Type Thermocouples

The most challenging experimental aspect involves reading and processing the data obtained from the rotor thermocouples via the shaft mounted slip-rings. The main difficulty arises in the form of unintended thermocouple junctions, which are created when the thermocouple k-type material path is broken by another conducting material, such as standard copper wiring. These junctions can be reduced by ensuring that the correct thermocouple material wiring, k-type in this case, is utilised between the thermocouple sensors and the data acquisition system, as is done for the stator and frame thermocouples. Unfortunately, the junction located between the k-type thermocouple wiring and the slip-ring connections cannot be removed and hence a

novel technique is required to tackle the problem. The high temperatures exhibited by the slip-rings during machine rotation accentuate the problem described. Furthermore, as the synchronous machine rotates at 1500rpm (50Hz), the low voltage thermocouple readings (~0.8mV at 20 °C) can easily be swamped by electrical and electromagnetic noise. Hence, it is vital that these signals are amplified as close to the thermocouple source as possible and certainly prior to the slip-rings.

7.3.1 Rotor k-Type Thermocouple Erroneous Operation

The initial main material junction problem is caused and accentuated by the frictional heat generated at the slip-rings as the machine rotates, which causes these to reach a temperature of approximately 60 °C, as shown by the Cepid Titanium DCO19U-B thermal camera capture displayed in Figure 7.14.

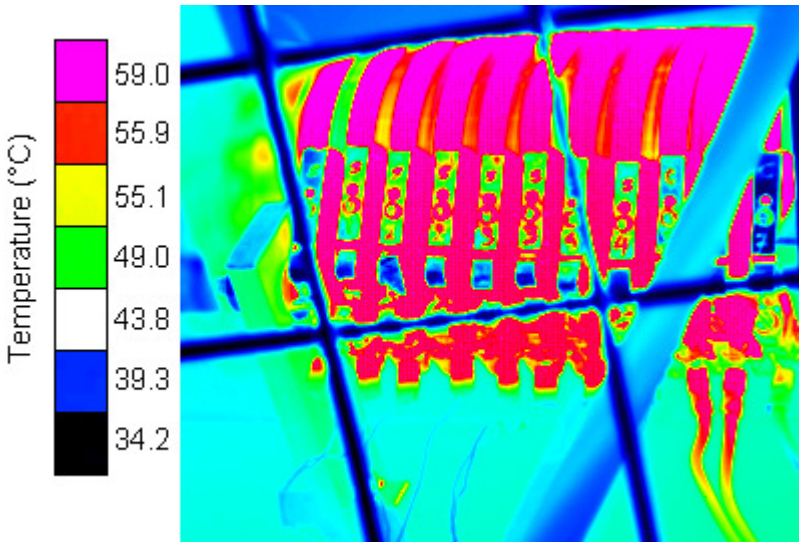

Figure 7.14: *Cepid thermal camera capture of slip-rings under machine operation.*

The temperature difference between this junction and the temperature at the data acquisition end results in inaccurate and unpredictable results being collected.

A couple of examples of this erroneous operation are shown in Figures 7.15 and 7.16. In Figure 7.15, the no-load heat curve for a rotor winding thermocouple is

incorrect, with an excessively high steady-state temperature and completely misleading cool down curve.

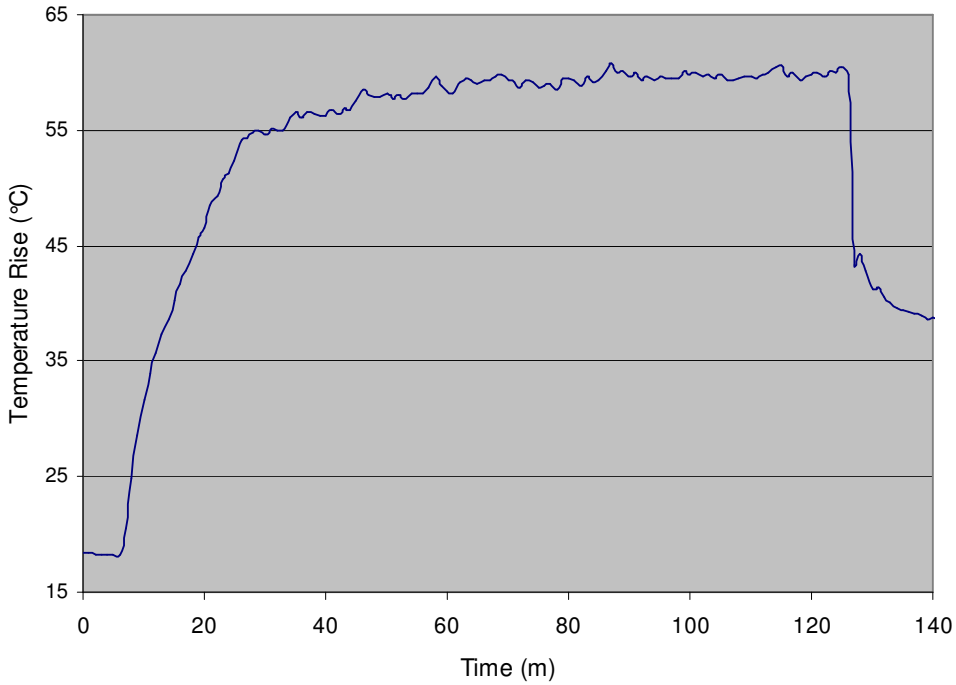

Figure 7.15: *Erroneous no-load heat curve for a rotor winding thermocouple.*

Figure 7.16 illustrates the effect on the rotor winding thermocouple readings when the electrical machine is turned off.

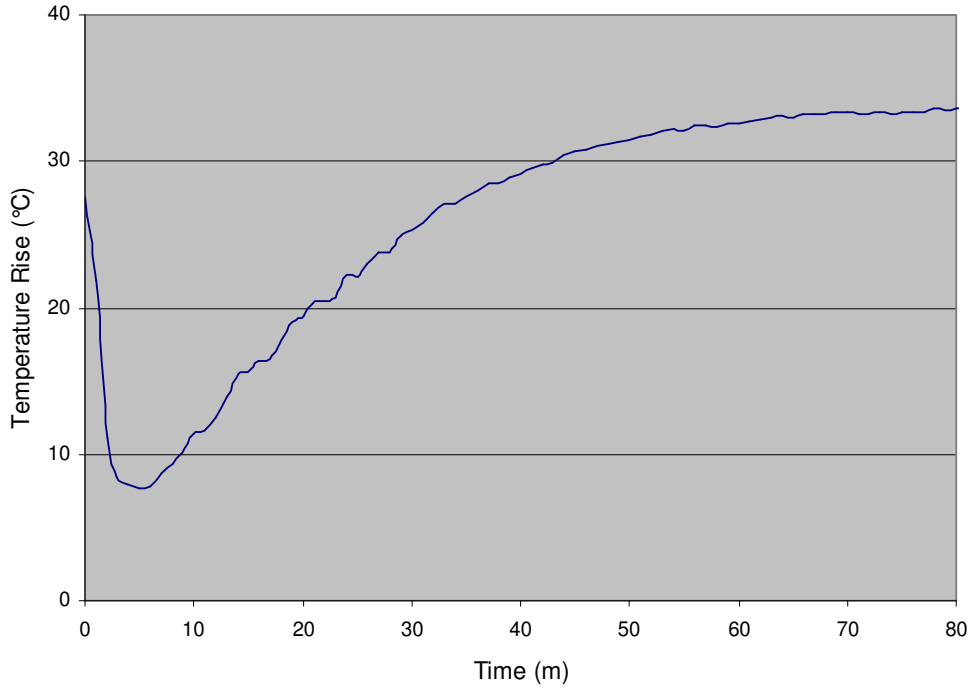

Figure 7.16: *Erroneous heat curve for a rotor winding thermocouple.*

In Figure 7.16, an unrealistic rotor winding temperature drop of nearly 20 °C is recorded. It is clear from this graph that as the temperature of the slip-rings goes down the readings start to become meaningful, due to the slip-ring temperature falling once the machine stops rotating. Once the slip-rings have cooled down, at the end of the presented heat curve, the problem seems to have nearly disappeared.

To simulate the thermocouple junction findings a very simple test can be carried out in which two k-type thermocouples are placed in a container of boiling water. Both thermocouples are recorded by the same data acquisition equipment via two separate identical k-type thermocouple connectors. One of the connectors is heated up using a heat-gun, whilst the other remains at room temperature. To validate the test, a third reading is taken using a standard mercury thermometer placed in the boiling water. The results show that whilst the thermocouple with the connector at ambient temperature and the mercury thermometer read an elevated water temperature (~ 85 °C), the thermocouple with the highly heated connector reads an unrealistic erroneous temperature (~ 10 °C). This test highlights the effect of the unevenly heated thermocouple junction along the thermocouple signal path. The test also

shows the effect as being very unpredictable, since the value recorded by the heated connector thermocouple fluctuates significantly even though the heat-gun is constantly placed at the same position and at an identical heat level setting.

Although the problematic junction cannot be removed, unless a radically different data acquisition approach and/or sensors are implemented, collecting, processing and amplifying the thermocouple voltages prior to the slip-rings diminishes the problem significantly, resulting in an improved acceptable level of accuracy. With the purpose of performing these actions a small PCB (4 cm x 10 cm), to be placed inside the hollow slip-ring shaft, was designed, manufactured, tested and accommodated within the set-up. Details of the PCB design are covered later in this chapter, in Section 7.3.3.

Another aspect that needs to be considered is the correct placement of the brushes on to the slip-rings themselves. It is fundamental that good smooth contact exists between the brushes and the slip-rings. For this, a good alignment is crucial, but so is the shaping on the actual brushes. Emery sandpaper, wrapped around the slip-rings against the brushes, can be used to shape every brush carefully, making sure they all have an equal and even contact surface with the slip-rings. The rotation of the slip-rings against the brushes with time also helps to achieve this. In order to minimise the effect that inevitable uneven slip-ring brushes can have on the rotor thermocouple signals, all thermocouple readings are multiplexed and made through one slip-ring brush pair, as detailed in this chapter.

Consideration was given to other data transmission systems, notably digitisation and radio transmission of the data, but that would still require a scheme very similar to that outlined here to perform the necessary signal conditioning before digitisation and transmission. As the available space was extremely limited, this simpler system was used and found to be entirely adequate.

7.3.2 Rotor Thermocouple Processing PCB Operation

In order to solve the thermocouple material junction problem described, a small electronics PCB is placed inside the slip-ring shaft, allowing a maximum PCB surface area of 4 cm x 10 cm. The PCB reads all 14 rotor winding thermocouples and processes them through several multiplexers. In addition to this, an amplification and noise filtering stage is also incorporated. A flow diagram of the electronic operations executed by the PCB is shown in Figure 7.17.

As shown in Figure 7.17, the multiplexers, controlled by the logic stage, read each of the 14 rotor thermocouples in turn, whilst the amplification stage increases the magnitude of the resulting multiplexer differential voltage before it is sent though the slip-ring to the data acquisition system. Though the output signal is still susceptible to noise, the signal to noise ratio is significantly increased. Protection circuitry stops voltage spikes from saturating or damaging the multiplexers, and the inevitable 50 Hz noise is cancelled and any remnants filtered out.

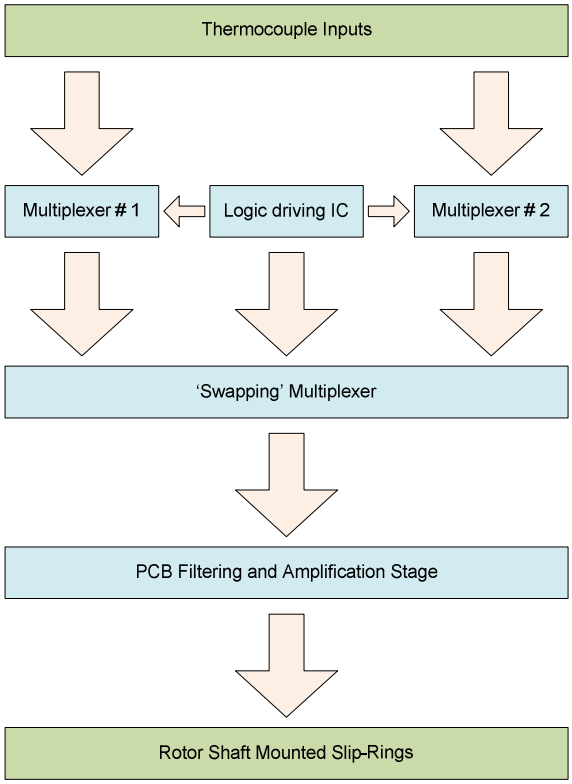

Figure 7.17: *Flow diagram of rotor TC reading electronics.*

A crucial function of the electronics stage is performed by the so-called 'swapping' multiplexer. In order to remove slip-ring related temperature offsets, the operation outlined in Figure 7.18 is performed for every thermocouple reading. Two of the fourteen slip-rings are allocated to the thermocouple data output. These remain unchanged through the experimental stage to avoid introducing further offsets by slightly different brush to slip-ring contacts.

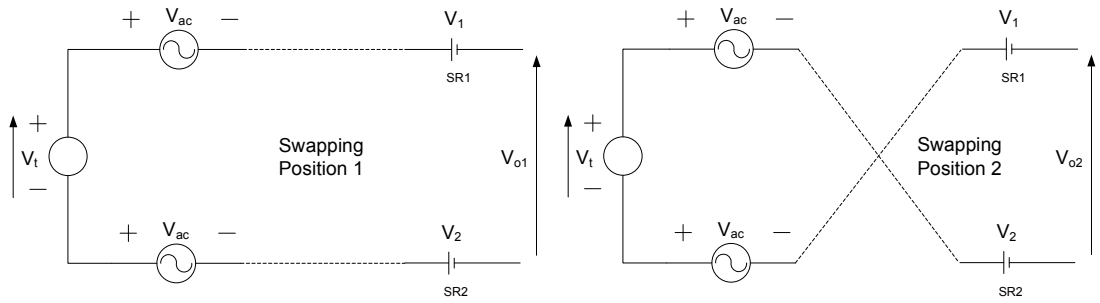

Figure 7.18: *Two positions of the 'swapping' multiplexer operation.*

In Figure 7.18, V_t is the thermocouple voltage, V_{ac} is the resulting interference ac voltage that is generated on the thermocouple wires, V_1 is the voltage drop/offset through slip-ring 1 (SR1), V_2 is the voltage drop/offset through slip-ring 2 (SR2) and V_o is the resulting output voltage.

The 'swapping' dotted lines represent the possible reading paths allowed by the 'swapping' multiplexer. The 'swapping' multiplexer takes one reading with position 1 and another with position 2 for every thermocouple measurement.

The analysis of the circuit diagrams presented in Figure 7.18 shows the 'swapping' procedure operation to be as shown in Equations 7.1 to 7.2.

$$V_o = V_2 + V_{ac} + V_t - V_{ac} - V_1 \tag{7.1}$$

$$V_o = (V_2 - V_1) + V_t \tag{7.2}$$

Hence, V_o is obtained by the 'swapping' multiplexer for the two positions shown in Figure 7.19. This yields V_{o1} and V_{o2} as shown:

$$V_{o1} = V_t + (V_2 - V_1) \tag{7.3}$$

$$V_{o2} = -V_t + (V_2 - V_1) \tag{7.4}$$

Therefore, a simple multiplexer subtraction removes the unwanted voltage offset introduced by the slip-rings:

$$V_{o1} - V_{o2} = 2V_t \tag{7.5}$$

7.3.3 Rotor Thermocouple Processing PCB Design

The PCB input and output information and operation outline is given in this section. Figure 7.19 illustrates the location within the PCB of the operational stages mentioned. The figure shows the final design model for the two separate PCBs before manufacture. Shown firstly is the input PCB and secondly the main processing PCB, where the multiplexing, amplifying and filtering takes place. The full circuit diagram for the rotor thermocouple processing PCB is presented in Appendix E.

PCB inputs and outputs:

- There are five input signals and two outputs to the PCB.
- The power is supplied via three slip-rings, supplying -18V, GND and +18V.
- The PCB driving digital logic data signals and clock signals are the other two inputs.
- The two outputs are the processed thermocouple leads.

PCB operation outline

The two PCBs shown are connected together via a plug/socket connection and held in place by two bolts, located at the two ends of the boards. Figure 7.19 shows the location of the different PCB stages mentioned in the operation outline.

Input PCB operation:

- The fourteen rotor thermocouples are input to the top PCB at the far left connections. There are two other reference thermocouple signals monitored. A reference short circuit channel and an additional thermocouple input, used for the Junction Reference thermocouple presented in Section 7.3.6.
- All thermocouples go through some initial filtering to remove some of the noise and the presence of Zener diodes prevents any possible voltage spikes from getting through and damaging any PCB components.
- After this, all sixteen thermocouple signals are transferred to the main (bottom) PCB, via a plug/socket placed at the right of the boards.

Main PCB operation:

- Three voltage regulators are present, converting the ±18V supplied to the PCB to the required -15V, +5V and +15V.
- Each one of the sixteen signals coming from the small input PCB is called by the two multiplexers in turn.
- The two multiplexer outputs are fed into a third multiplexer which performs the ‘swapping’ action outlined earlier and which allows for the necessary subtraction operation to take place.
- The three multiplexers are driven by the clock and logic data signals.
- The two swapped and subtracted resulting thermocouple voltages are then called upon by the filtering and amplification operational amplifiers.
- A multiple feedback low-pass filter is used to remove any unwanted 50Hz noise and its output is amplified by a sufficiently high gain of 300.

- The larger, cleaner voltage signals are then sent to the two allocated output slip-rings and to the data acquisition equipment via twisted pair, screened coaxial cable to further protect the integrity of the thermocouple signal against noise.

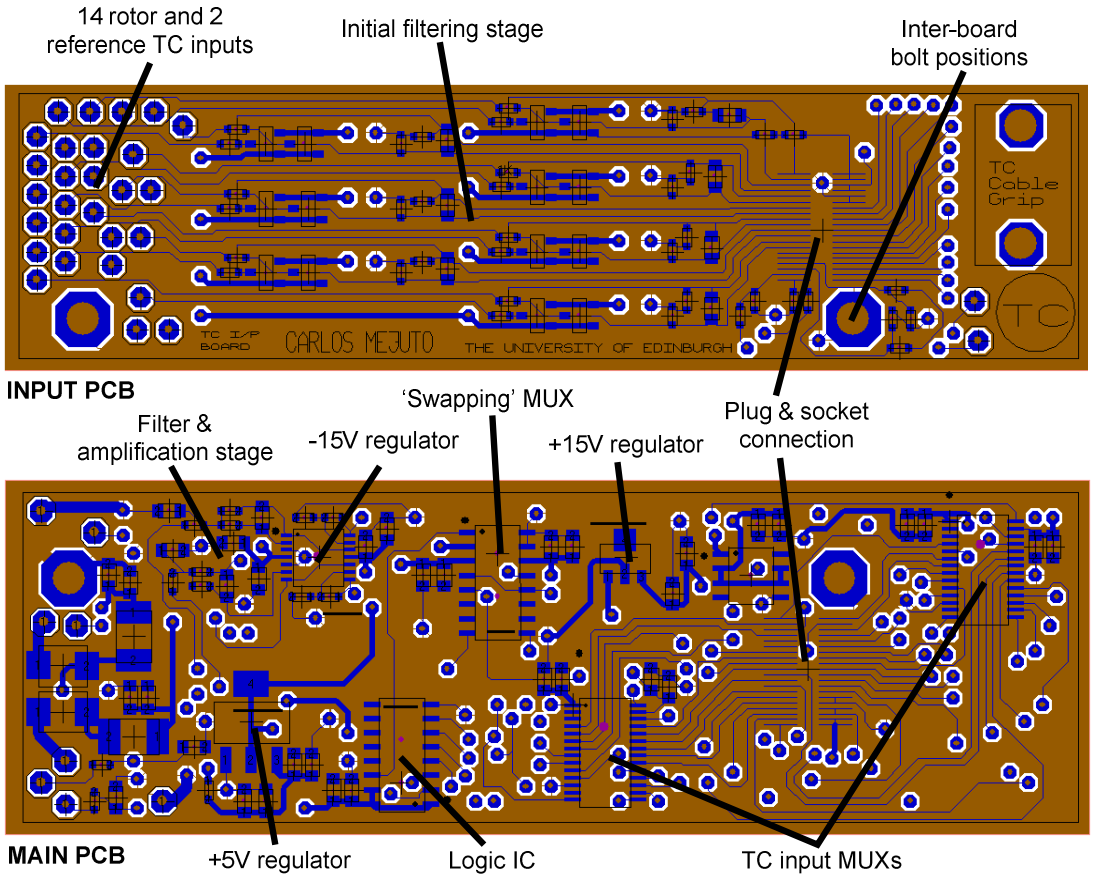

Figure 7.19: *Final design for thermocouple processing PCB.*

Once the outlined system was tested in isolation it was added to the system as shown in Figure 7.20. After the design, manufacture and implementation of the described PCB other minor, but critical, tasks and modifications were required in order to achieve an acceptable level of accuracy and consistency in the data recorded. These are presented in the following sections.

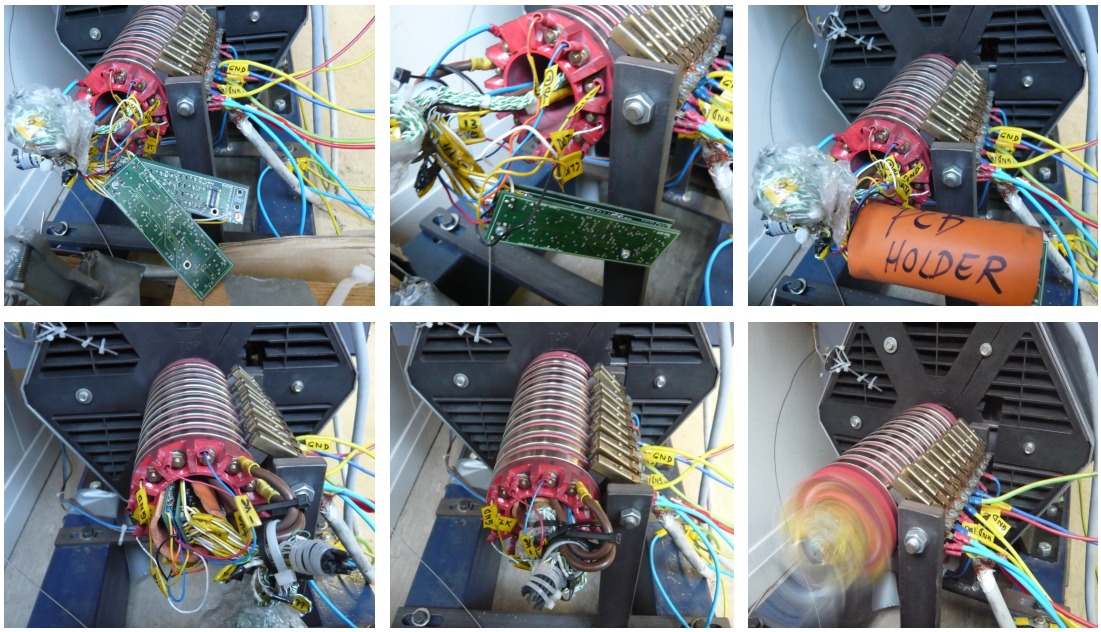

Figure 7.20: *Assembly and implementation of rotor thermocouple processing PCB.*

7.3.4 Data Acquisition Driving Code

The data acquisition equipment needs to be carefully configured in order for all thermocouples to be recorded and processed accurately. This is particularly important for the rotor thermocouples, since the PCB amplification and filtering stages need to be accounted for. This was accomplished by initially testing the PCB operation in isolation. In a number of tests a thermocouple was placed in boiling water and the cool down mV/°C characteristic recorded. One of the heat-runs performed is shown in Figure 7.21. From the results, a regression can be carried out to obtain the characteristics of a straight line presented in Equation 7.6, determining the gradient (m) and y-axis intercept (c) of the graphs.

$$y = mx + c_{int} \tag{7.6}$$

where m is the straight line gradient, c_{int} the y-axis intercept, x the PCB output voltage (mV) and y the temperature (°C) linked to that voltage.

Figure 7.21 gives a gradient of 12.18 and a y-axis intercept of -303. All PCB test runs performed agree with these values, showing a consistent PCB operation and proving that m and c_{int} values obtained can be implemented confidently in the data acquisition equipment code to compensate for the amplification stage and translate output mV values to °C temperatures. The complete data acquisition code utilised to drive the PCB and obtain the thermal data required is shown in Appendix F.

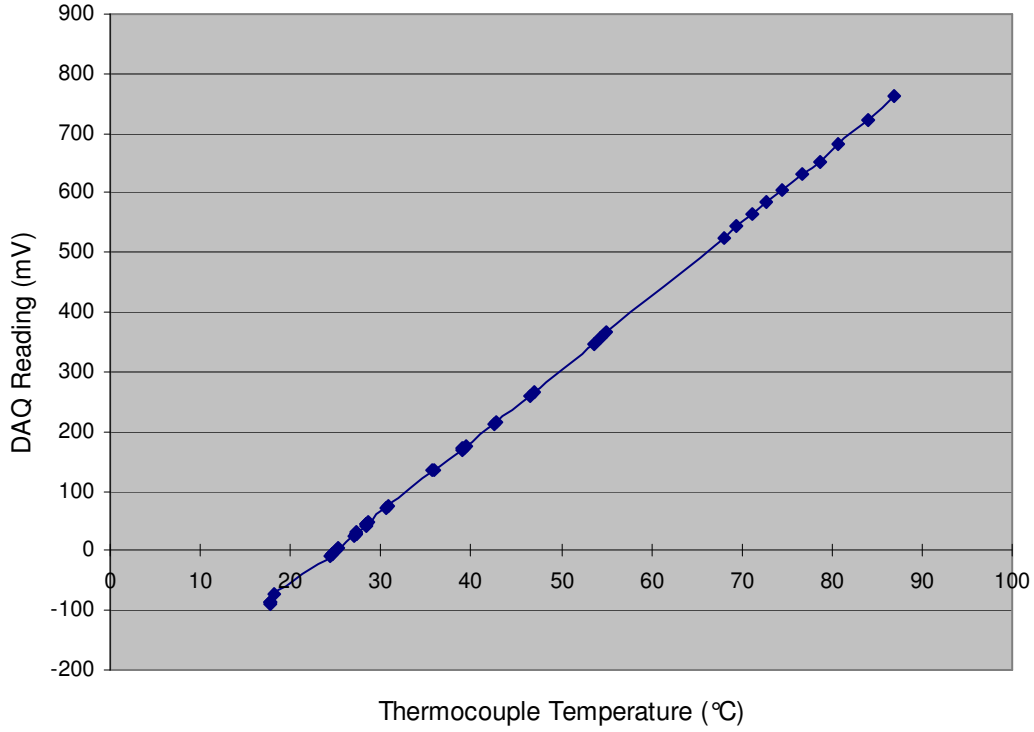

Figure 7.21: *PCB amplifier section characterisation.*

Furthermore, the rotor PCB running section of the data acquisition code sends in digital serial logic data and the required clock signal. This calls the binary address of each thermocouple multiplexer channel in turn. Each reading is sent to the third 'swapping' multiplexer, also controlled by the data acquisition code, and subsequently stored for post processing. As explained previously, two readings are taken, subtracted and divided by two. These calculations are performed by the data acquisition code. In addition, in order to increase accuracy, one hundred readings were taken and averaged for each thermocouple every minute. In addition to this, readings that are over or under 10 % of the average were removed and the average recalculated, in order to remove any possible erroneous readings.

Stator and frame thermocouples do not need to be amplified and multiplexed since they do not go through the slip-rings and see no material junctions along the way. The average of five readings for each one of these thermocouples is taken and recorded every minute.

7.3.5 Electrical and Electromagnetic Noise Considerations

Electrical and electromagnetic noise considerations are important when dealing with thermocouple signals and efforts to reduce these, where possible, should be made. Thermocouple signals can be under 1 mV, making them extremely susceptible to noise.

In order to remove as much of the 50 Hz noise produced by the generator rotating at 1500 rpm, a low-pass filter stage is introduced in the rotor thermocouple reading PCB. Furthermore, to minimise the effects of the radiated electromagnetic noise, twisted pair, screened coaxial cables are used for both of the PCB signal cables at the important output channels. Twisting the cables ensures both signals are affected by noise in an equal manner, whilst the grounded cable screening attempts to shield the signals carried from corrupting noise. In addition to this, the actual data acquisition equipment itself is enclosed in a shielding grounded metallic box, as shown in Figure 7.22. The combination of these measures increases the smoothness of heat curves recorded significantly and should be unquestionably implemented for similar investigations.

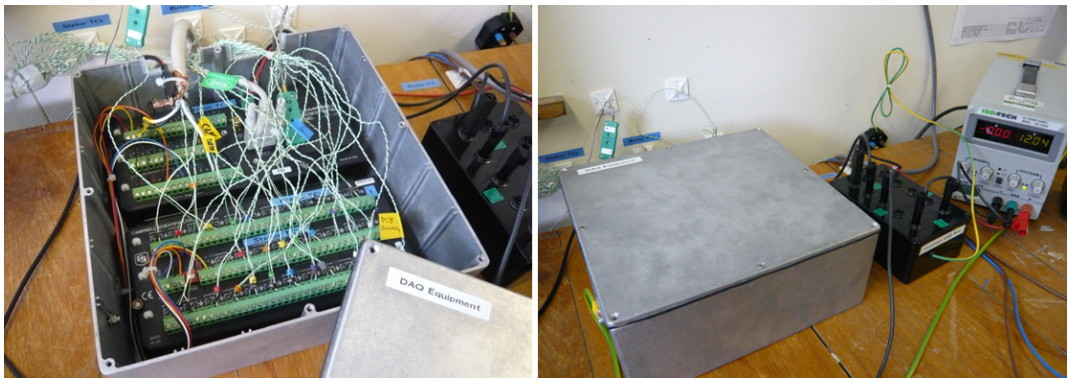

Figure 7.22: *Data acquisition equipment shielding box and cabling arrangements.*

Even though these efforts successfully reduce the effect of the unavoidable noise on the system, noise is always present and awareness of its presence and effects is important.

The fact that, as explained in Section 7.3.3, digital signals are utilised for the PCB driving channels, means that noise can be accepted to a certain extent by the signals. Figure 7.24 shows the logic data and clock PCB signals and the effect that noise has on them after all the noise shielding measures have been implemented. This can be compared with the clean logic signals shown in Figure 7.23. As shown, a very small distortion by the noise is observed, credited to the measures taken. Due to the digital nature of these signals, the system runs smoothly, with the correct multiplexer channels being recorded at the right time, even in the nosier scenario.

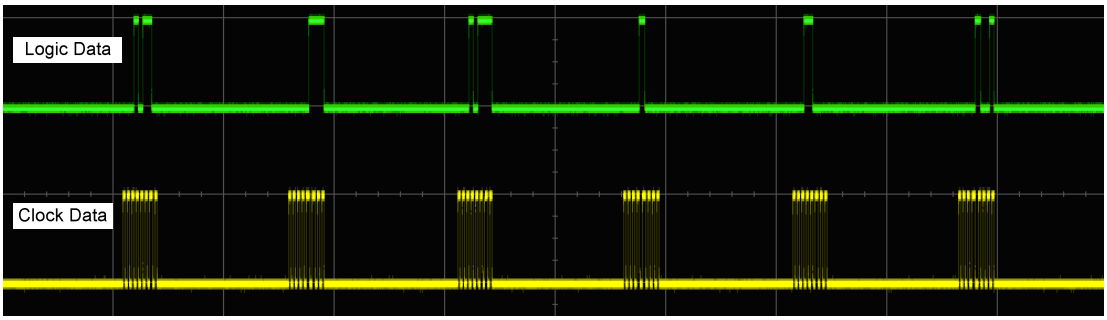

Figure 7.23: *Clean logic data (top) and clock (bottom) signals.*

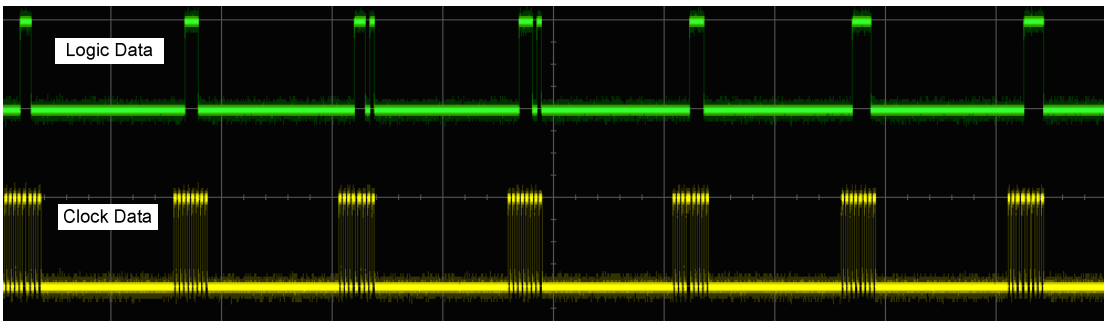

Figure 7.24: *Logic data (top) and clock (bottom) signals slightly affected by noise in final set-up.*

Prior to all the grounding and screening work described the logic data and clock signals were excessively affected by noise, with a very high risk of incorrect

multiplexer channels being read and data greatly corrupted throughout the experiment. A capture of the digital logic and clock signals prior to the anti-noise measures implemented is shown in Figure 7.25.

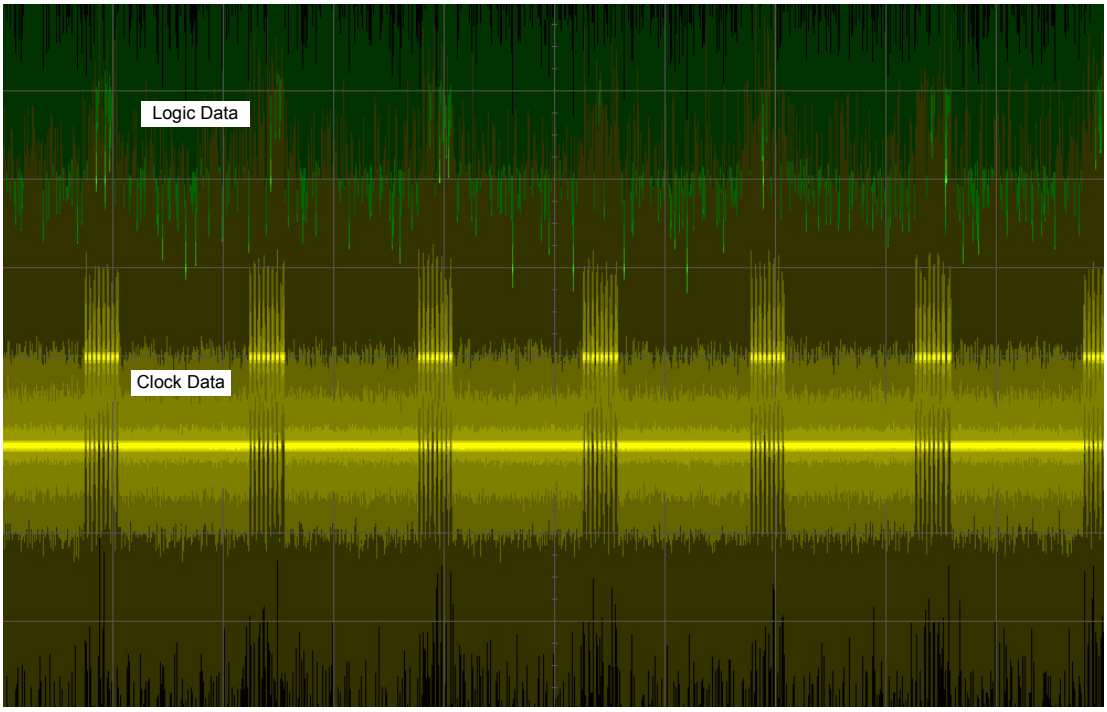

Figure 7.25: *Initial logic data (top) and clock (bottom) signals very affected by noise.*

It should be noted that an additional source of noise in the test rig set-up is the inverter drive that runs the induction machine. It introduces noise to the system when running, but the methods described in this section also help to reduce its effect.

7.3.6 PCB Surface 'Temperature Gradient' Interference

The original PCB design presented shows a slight, but significant, malfunction. This is worth explaining and noting for future designs, since it highlights the sensitivity of thermocouple systems. As shown in the PCB design in Section 7.3.3, originally all rotor thermocouples are soldered straight on to the far left end of the input PCB. The problem appears in the form of a temperature gradient across the PCBs when these are powered up, due to specific ICs heating up. The voltage regulators on the PCB

are located within a few millimetres of each other and across the sensitive thermocouple junctions. As a result of this, these junctions are heated up by the regulators in an unpredictable and uneven manner. Figure 7.25 illustrates the effect of this temperature gradient on the rotor winding thermocouple readings, when the system is simply reading a rotor thermocouple for a room temperature stationary machine.

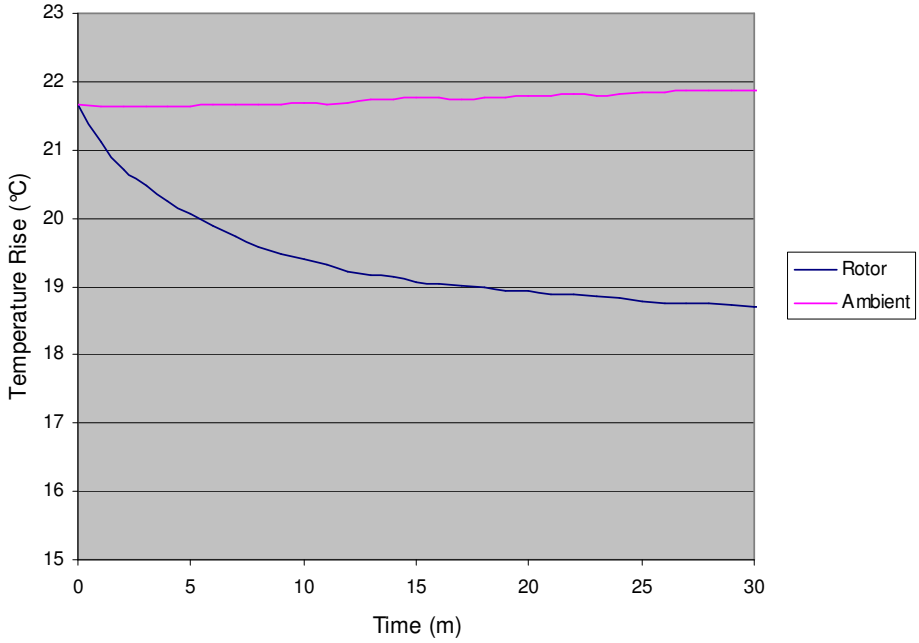

Figure 7.25: *PCB surface 'temperature gradient' problem.*

As soon as the PCB is powered, a thermal gradient develops across the PCB. The rotor thermocouple readings start exhibiting an offset. In order to firstly reduce the presented effect and secondly to account for it, the rotor thermocouple to PCB connections are modified. As shown in Figure 7.26, the final set-up has the problematic rotor thermocouple to copper solder junctions moved away from the PCB and out of the slip-rings shaft. The junctions are now collected together as shown, with a thermocouple (Junction reference thermocouple) placed in the middle of the junction bunch. By collecting all junctions together and with the additional thermocouple, the temperature of these junctions can be kept relatively constant and precisely monitored. Furthermore, a strong centrifugal fan is placed in front of the junctions, with the objective of keeping the junctions at a constant temperature as close to room temperature as possible in order to prevent unwanted unexpected

thermal junctions forming. Additionally, the centrifugal fan serves as an additional PCB precautionary cooling method.

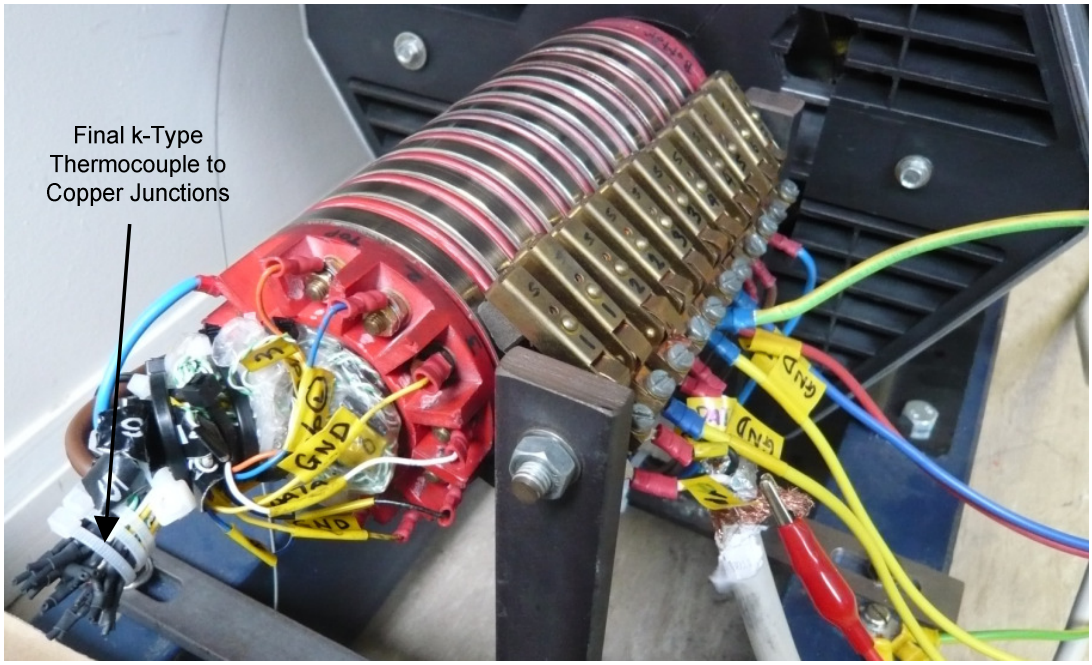

Figure 7.26: *Final thermocouple k-type material to copper junctions.*

An alternative to the approach described is to redesign the PCB layout making sure that no chips are near the thermocouple material to copper solder junctions. This applies in particular to those ICs generating the most heat, such as the voltage regulators. In this particular case this would be challenging given the reduced area available for the PCB and it would be difficult to make sure that a uniform temperature across all junctions is actually achieved.

After this final set-up modification, the data acquisition equipment code was modified to accommodate for the system alteration, with rotor thermocouple readings no longer being taken directly unprocessed, but using Equation 7.7.

$$V_{Rotor\ Absolute} = V_{Rotor} - V_{Junction\ Reference} + V_{Ambient} \tag{7.7}$$

where $V_{Ambient}$ is the voltage resulting from a thermocouple at ambient temperature, $V_{Junction\ Reference}$ from the PCB reference thermocouple, V_{Rotor} from the specific rotor

thermocouple and $V_{Rotor\ Absolute}$ is the resulting voltage that is used for determining actual rotor temperatures.

By accommodating this alteration, the unpredictable effect of the thermally uneven junctions is removed and hence the rotor thermocouple reading accuracy increases.

The final data acquisition code utilised during the experimental validation stage is presented in Appendix F.

7.3.7 Test Rig Earthing and Grounding Critical Issues

Test rig earthing and grounding issues are crucial. Ground loops and floating points need to be avoided, since all data acquisition equipment readings can be greatly affected by an earthing or grounding problem. In the occurrence of an earthing or grounding system set-up error, data is not corrupted in a regular predictable manner, making a post-testing correction impossible. For this reason, these issues should be tackled very carefully before the testing program commences.

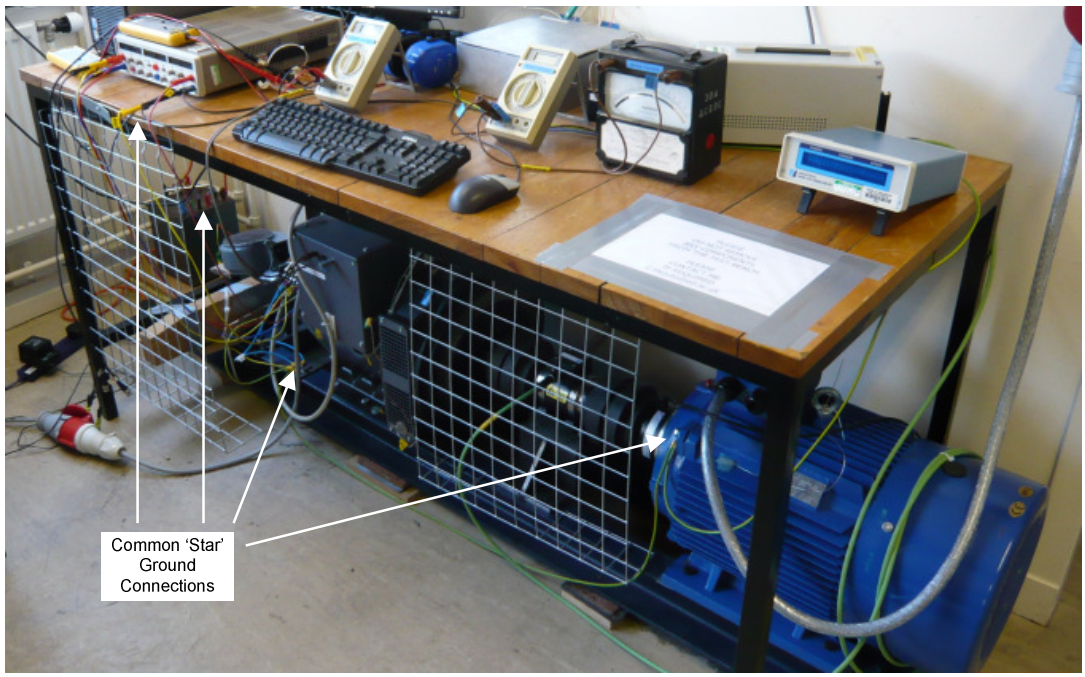

Figure 7.27: *Important machine earth and ground connections.*

The first action required in order to achieve a reliable common ground set-up is to connect the PCB, power supply and DAQ equipment grounds to the machine earth at several points, at both ends of the test rig, as shown in Figure 7.27. This provides a star ground connection system with all grounds coming back to a common point and connected to the 3-phase ground, being a consistent common ground. To make sure the system is completely immune to noise from other ground/earth paths and that no parallel ground paths resulted, an isolating transformer is placed between all test rig electronic equipment and the mains power supply.

7.3.8 Vibrating Effect of Slip-Ring Brushes

As a result of loading the synchronous generator the test rig inevitably vibrates, even when securely supported. This is specially the case for the higher end of the loading range considered in this investigation, where both the generator and motor are working the hardest. As a result of this, there is a higher chance of the slip-ring brushes momentarily not being in perfect contact with the slip-rings themselves. Consequently, a small number of readings could be affected and, even though these would be easily singled out during the analysis of the data collected or removed with the data acquisition code additions described in Section 7.3.4, it is worth taking measures to avoid this problem. With this in mind a 1 μF polyester capacitor is connected between each PCB output slip-ring and ground. Hence, if the vibrations do cause the brushes to lose contact at the time of a particular reading the capacitors prevent the data transferred from being corrupted. This final set-up addition is shown in Figure 7.28, with the introduced 1 μF capacitors clearly marked.

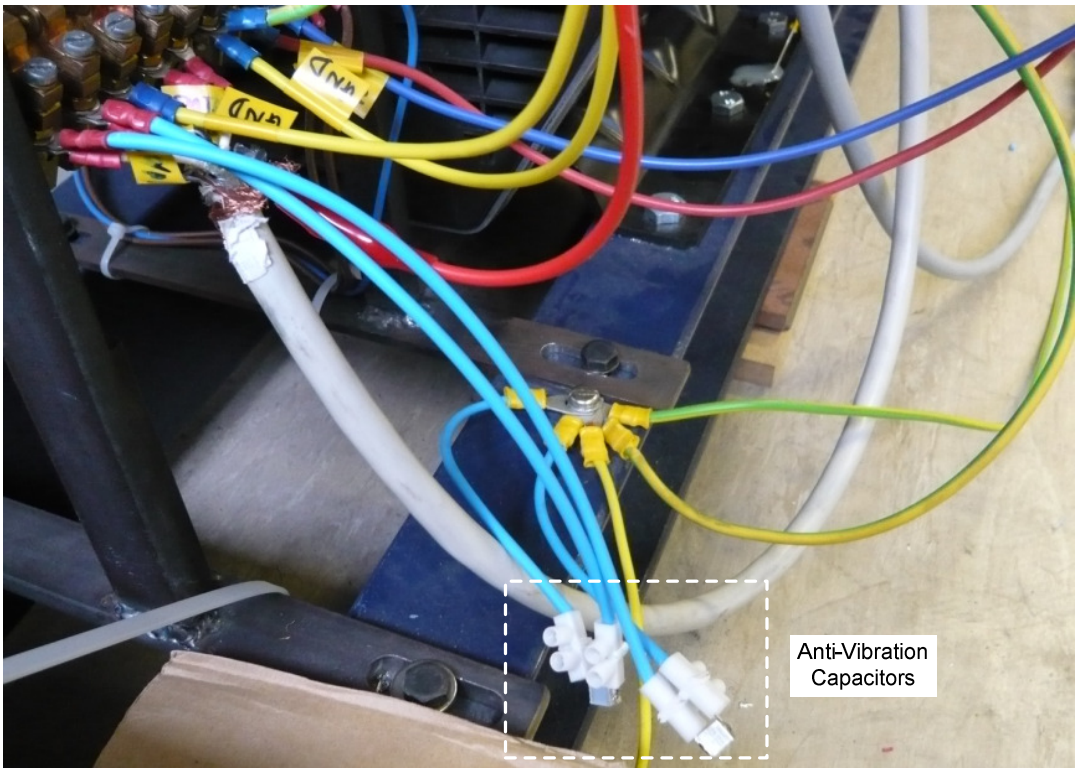

Figure 7.28: *'Anti-vibration' capacitor placed between PCB slip-rings and ground.*

7.3.9 Thermocouple Reading Consistency Test

In order to be confident that all thermocouples are being recorded in a reliable consistent manner, all sensors are monitored for a significantly long period of time - 3 hours in this case - to identify any thermal junction related anomalies.

Figure 7.29 shows the temperature variation of all machine thermocouples with room temperature, as the laboratory's ambient temperature increases. All measured electrical machine thermocouples vary in accordance with room temperature and no anomalies are noticed.

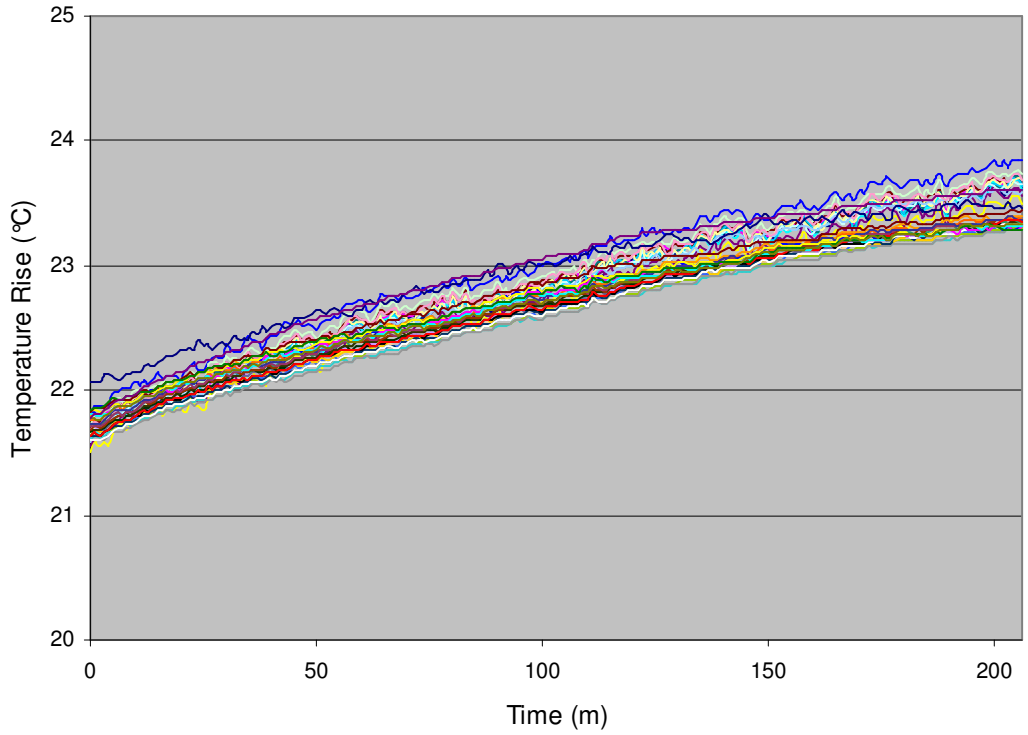

Figure 7.29: *Machine's thermocouple room temperature 2.5 hour tracking consistency test.*

A second validation test is performed in which the cooling curve is monitored after a heat-run. Correct operation sees thermocouples cool down eventually to approximately the same temperature, namely ambient temperature. After two short heat-runs, the cooling curves presented in Figures 7.30 and 7.31 show that both the stator and rotor TCs converge, after a period of 3 to 5 hours.

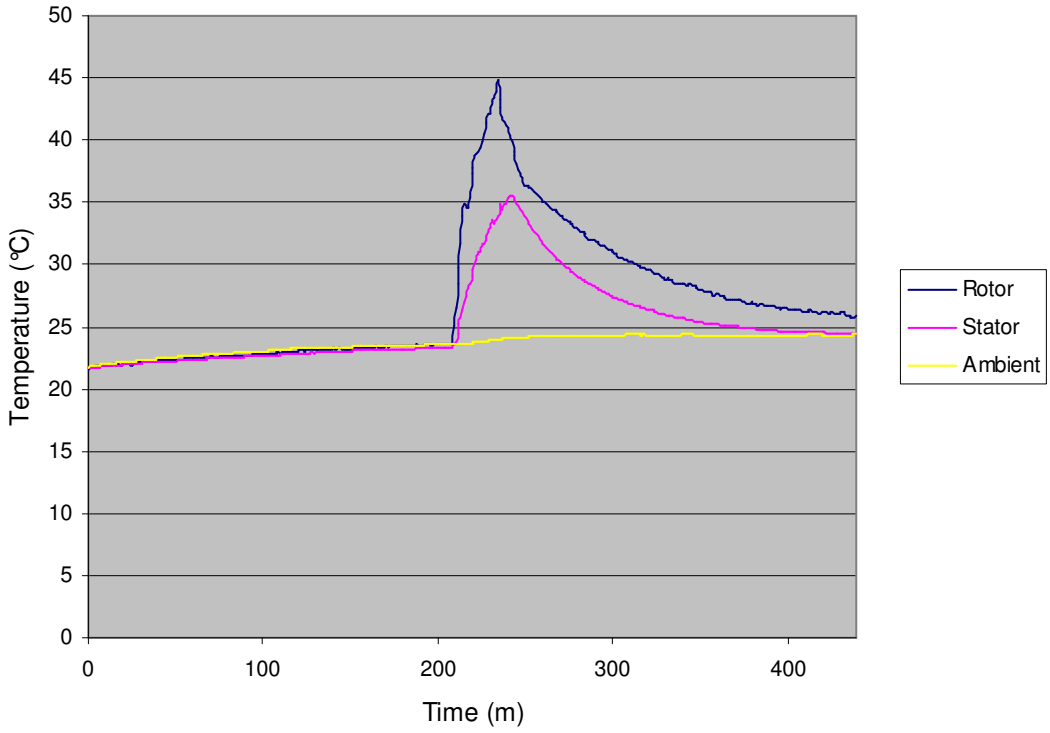

Figure 7.30: *First TC validating cool-down curve.*

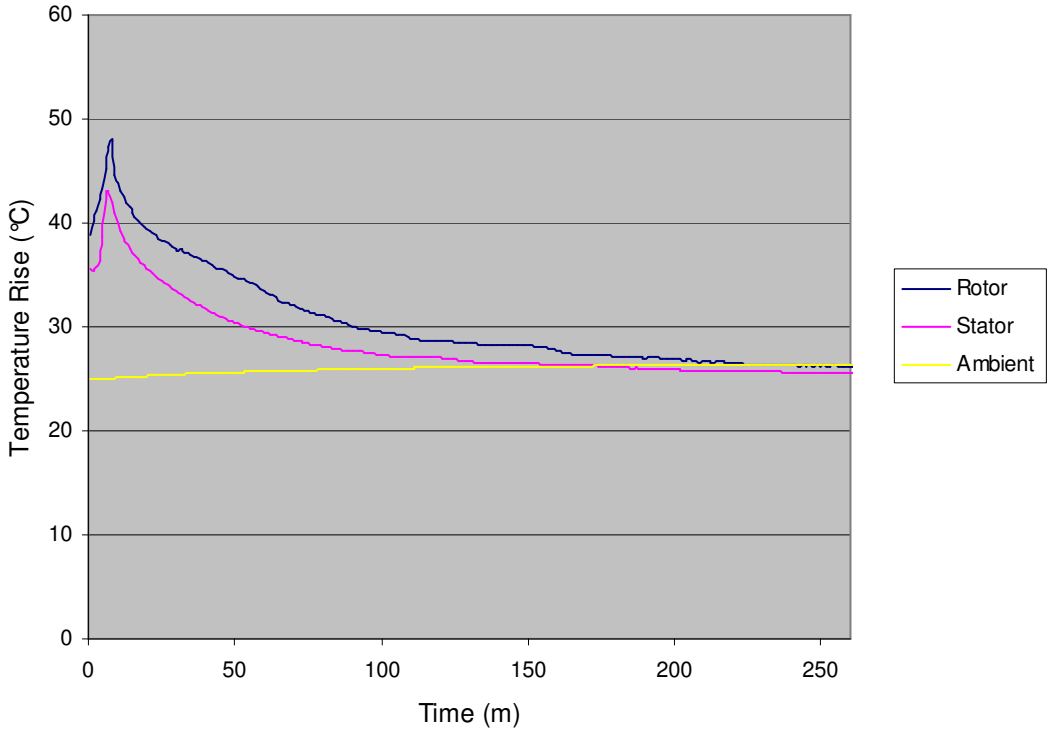

Figure 7.31: *Second TC validating cool-down curve.*

It should be noted that rotor TCs recorded through the PCB do not exhibit as smooth a heat curve as the stator and frame TCs. This is to be expected given that rotor TC signals are amplified, filtered and passed through the slip-rings and several types of wiring. Regardless, a very good level of accuracy is achieved. The results presented and analysed in Chapter 8 show the correct operation of the system presented in this chapter.

7.4 Experimental Limitations

Several experimental limitations and reasonable assumptions are associated with the experimental stage presented. Due to the test installation and equipment available, these are unavoidable, but do not jeopardise or alter the objective of the experiments executed. However, they do need to be noted by the reader when utilising and interpreting the presented results.

The main experimental limitations relate to the monitoring of the generator's cooling airflow. Detailed airflow considerations and results are out with the scope of the thermal study performed. Due to the complicated nature of the through ventilating airflow this is an area that requires further work in the future. As presented and explained in Chapter 8, an uneven flow of air through the electrical machine, and particularly around the winding overhangs, is identified. This is an expected occurrence due to the non-symmetrical nature of the airflow inlets, the internal obstructions to this airflow and the effects that the revolving rotor has on the airflow. The data collected is sufficient for the purpose of this thermal investigation, but the use of airflow measuring equipment monitoring the air entering and leaving the generator vents would increase the information collected regarding this topic. Furthermore, detailed computational fluid dynamics could be used to understand the abnormalities of the airflow along the axial length of the generator.

An additional source of limitations relates to the measuring equipment and methods implemented. As detailed in Chapter 3, MySolver machine operational losses are calculated utilising the rotor and stator winding data collected during the heat-runs. Hence, it is important to make sure that this data is reliable and as accurate as allowed by the measuring equipment available to the user. The necessary field current and voltage are accurately monitored utilising the multimeter indicated in Section 7.2.6. These readings are further validated by the use of a power analyser. This is similarly performed for the armature current, but the armature resistance per phase needed to calculate stator copper losses is more complicated to obtain. Also using a multimeter, a stator phase resistance reading is taken from the machine's armature as soon as the machine is turned off after each one of the heat-runs performed, to ensure that the steady-state machine temperature does not fall. In order to increase confidence in the data collected, these readings were repeated a number of times. The resulting data, used in the thermal modelling, is presented in Section 7.5. Other necessary readings during the investigation, for kW loading, machine rpm and torque are accurately collected by the torque transducer and power analyser used.

Finally, the operational scenarios available for MySolver validation are restricted by the operational range of the induction motor drive system. The availability of a higher rated induction motor would allow for overload heat-runs to be investigated and the use of an inductive load bank for the analysis of non-unity power factor operational conditions. These are both out with the scope of the work performed, but are areas in which future work on this topic could focus.

7.5 Experimental Test Rig Operation Validation Run

Validation runs are carried at three kW loadings, 5 kW, 12 kW and 18 kW, in order to evaluate the performance of the experimental test rig layout described in this chapter and to ensure the repeatability of results. As shown in Table 7.2, very close agreement is observed for the three validation runs performed. The results presented indicate a consistent test rig heat-run operation and highlight the validity of the

results obtained to thermally characterise the synchronous generator analysed and validate the MySolver thermal modelling tool. These results are presented and analysed in Chapter 8.

	Stator Temperature Rise (°C)		Rotor Temperature Rise (°C)	
Loading (kW)	Average	Peak	Average	Peak
5.25	18.08	21.61	18.34	20.95
5.24	18.39	21.89	18.51	20.88
12.26	35.69	44.61	29.26	32.68
12.67	38.00	46.75	29.95	33.40
18.38	73.47	90.59	51.01	56.88
18.49	73.60	90.46	50.99	56.47

Table 7.2: *5 kW, 12 kW and 18 kW validation heat-run results.*

7.6 Chapter Summary

The experimental test rig constructed for the thermal analysis of the Cummins Generator Technologies synchronous machine is presented in this chapter, along with the equipment required to perform the investigation. The complications in setting up the test rig, particularly regarding the extraction of the thermal data collected from the rotor, are presented and analysed in detail. The necessary rotor thermocouple reading PCB is presented and the details of its design, manufacture and test rig integration are covered. Finally, the correct operation of the assembled test rig is illustrated and the system is shown to be appropriate for the thermal study to be undertaken.

CHAPTER 8

Experimental Validation Results

8.1 Experimental Synchronous Generator Thermal Results

Utilising the test rig setup and experimental instrumentation presented in Chapter 7 the Cummins Generator Technologies BCI184E synchronous generator is tested for a wide range of operational loads, ranging from 5kW to 20kW. The heat-run results obtained are presented in this chapter. These results provide detailed insight into the thermal distribution of the electrical machine and serve as a way to validate the lumped parameter models utilised by MySolver, presented in the Chapter 6. Steady-state temperature results are presented in detail in Section 8.1.1, which are very important for a machine designer. All machine steady-state temperatures need to be well understood so that the thermal limit of important machine components is not exceeded. In particular, the winding insulation thermal limits should be very carefully considered, and the thermocouples located within the stator and rotor windings provide the information required. Furthermore, the complete transient heat curve results are presented in Section 8.1.2. Actual experimental kW loading values for each test performed and winding meter readings are tabulated in Table 8.1.

Test loading (kW)	Armature V (V)	Armature I (A)	Field V (V)	Field I (A)
5.25	416.3	7.1	10.5	13.8
8.20	415.7	11.0	11.8	15.3
10.28	415.2	14.1	12.9	16.6
12.26	415.0	16.6	14.6	18.2
14.17	414.8	19.7	15.8	19.5
16.52	415.2	23.0	18.2	21.8
18.38	415.1	25.8	20.4	23.2
23.67	414.8	28.7	22.1	25.0

Table 8.1: *Experimental kW loadings and winding voltage/current information.*

8.1.1 Steady-State Temperature Rise Results and Analysis

The steady-state temperature rise results presented in this section are taken with respect to the laboratory's ambient temperature. Results are divided into the specific machine sections examined to ease thermal comparison between the range of loads applied to the synchronous generator. The highest winding temperature rise is recorded for the stator overhangs, due to the elevated armature current resulting in high losses and the lack of an effective conduction heat transfer mechanism. The rotor winding higher temperatures are observed at the lagging pole half side of the lamination. These results are presented and detailed in this section.

Stator Winding Overhangs

The stator drive-end (DE) and non-drive-end (NDE) winding overhang temperatures are monitored and the results for the loadings considered are presented in Table 8.2. The key included indicates the precise location of the thermocouples, presented in detail in Chapter 7.

It is worth noting the uneven nature of the temperature distribution around the stator winding overhangs. This is most likely caused by the fact that the airflow entering the machine's inlet does so in an uneven manner, with some sections of the overhangs experiencing better cooling than others. Due to the stationary nature of the stator windings, this uneven temperature distribution remains consistent throughout the range of kW loadings considered.

Stator TC	Stator TC steady-state temperature rise for specific kW loading (°C)							
	5.25 kW	8.20 kW	10.28 kW	12.26 kW	14.17 kW	16.43 kW	18.38 kW	23.67 kW
S1	17.0	22.2	27.4	33.7	42.0	56.6	68.8	86.1
S2	19.2	25.2	31.2	38.5	47.8	64.3	77.9	96.8
S3	17.6	22.7	27.5	33.6	41.4	55.3	66.7	82.6
S4	22.2	29.6	36.7	45.4	56.3	74.7	90.4	111.9
S5	20.1	26.5	32.6	39.9	49.3	65.9	79.7	98.7
S6	20.4	26.9	33.2	40.7	50.4	67.2	81.1	100.4
DE average	19.4	25.5	31.4	38.7	47.8	64.0	77.4	96.1
S7	14.1	18.4	22.7	27.9	34.7	47.2	57.3	72.0
S8	13.6	17.6	21.6	26.4	33.1	44.7	55.2	69.8
S9	17.9	23.8	29.4	36.5	45.6	61.3	74.7	93.1
S10	20.1	27.5	34.5	43.0	53.8	72.0	87.6	109.0
S11	19.2	25.6	31.8	39.2	48.7	65.7	79.6	98.9
S12	18.2	24.5	30.5	37.9	47.3	63.9	77.6	96.7
NDE average	17.2	22.9	28.4	35.2	43.8	59.1	72.0	89.9
Key:	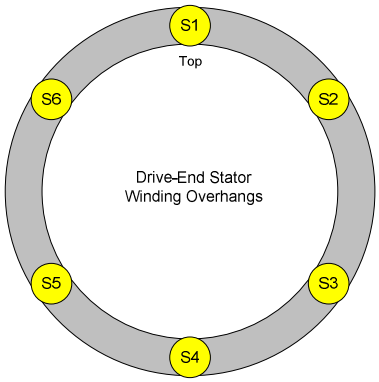 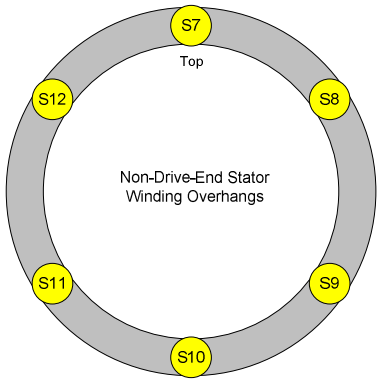							

Table 8.2: *Stator windings overhang steady-state temperature rise results.*

The average drive-end and non-drive-end stator winding overhang results are graphed in Figure 8.1. As shown, an ascending relationship is exhibited by the stator winding overhang temperature rise, with respect to the machine loading. As expected, the stator winding overhangs at the DE of the synchronous generator is consistently at a higher temperature than the NDE overhangs. The difference in average temperature between the two machine stator winding overhangs is 4.0 °C on average, but peaks at 6.2 °C for the highest loading tested. The higher DE overhang temperatures can be explained by the fact the NDE overhangs are exposed to the cooler air entering the machine air inlets. Although the DE overhangs are also cooled by this air flow, the air is warmer by the time it reaches the DE of the machine and is, therefore, less effective at cooling the DE overhangs. This is accentuated at the higher machine loads, where the cooling air flow warms up the most as it ventilates

the core length of the generator. This is further highlighted by the air flow thermocouple results presented later in this section.

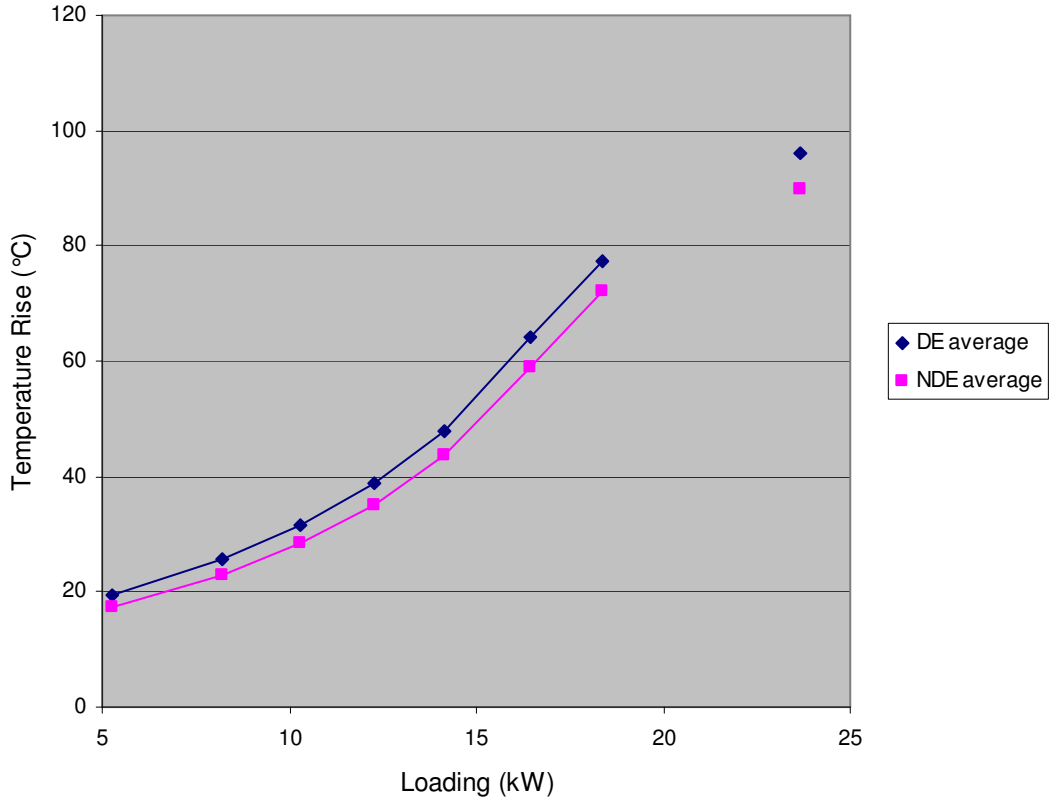

Figure 8.1: *Stator winding overhang DE and NDE average temperature rise.*

It is important to note that a clear problem is identified with the highest loading result presented in Figure 8.1, and in subsequent Figures 8.2, 8.5, 8.6, 8.11, 8.12 and 8.14 in this chapter, where an unexpectedly low temperature rise is recorded. This is most likely caused by the failure of the induction motor, shown in Section 7.2, before the end of the mentioned heat-run. It was not possible to repeat a heat-run at this loading. For this reason, the results are presented in this chapter, but excluded from the relevant result curves in the mentioned figures.

Stator Winding Slot Axial Core Length

The temperature rise information recorded by the stator winding slot thermocouples is presented in Table 8.3. Averages for the complete slot at a particular kW loading and for each specific thermocouple across the complete kW loading range are also calculated and presented in the table.

	Stator TC steady-state temperature rise for specific kW loading (°C)								
Stator TC	5.25 kW	8.20 kW	10.28 kW	12.26 kW	14.17 kW	16.43 kW	18.38 kW	23.67 kW	TC Average
S13 (DE)	19.2	24.6	29.9	36.4	44.6	59.5	71.6	88.6	46.8
S14	19.2	24.5	29.7	36.1	44.3	59.0	70.9	87.7	46.4
S15	18.9	24.0	29.0	35.2	43.0	57.3	68.7	85.0	45.1
S16	18.3	23.3	28.2	34.2	41.9	55.8	67.0	82.9	44.0
S17 (NDE)	17.5	22.3	27.1	33.0	40.4	54.1	65.0	80.6	42.5
kW Average	18.6	23.7	28.8	35.0	42.8	57.1	68.6	85.0	-

Key:

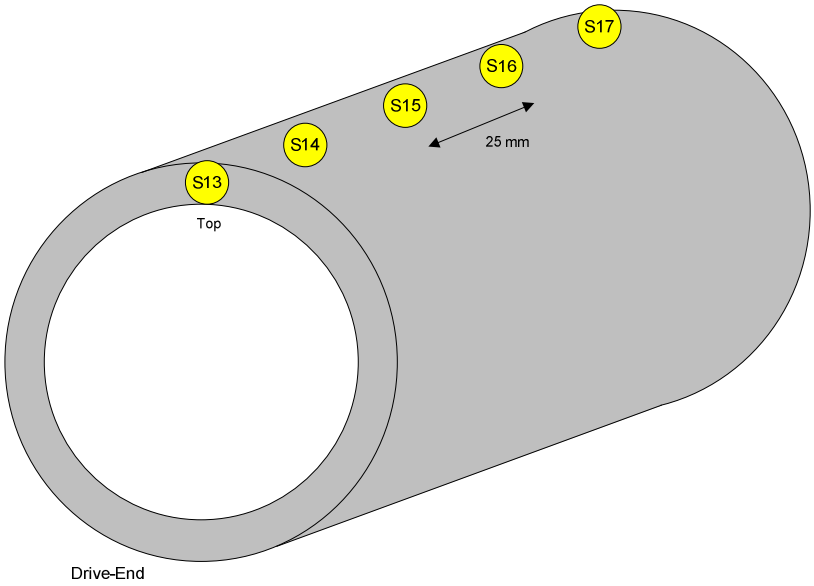

Table 8.3: *Stator winding slot steady-state temperature rise along axial core length.*

The average stator winding slot temperatures are graphed in Figure 8.2 with respect to the machine's kW loading. Similarly to the results obtained for the stator winding overhangs, an ascending relationship is observed. It is interesting to note that the temperature rise recorded for all the thermocouples in the slots is lower than the winding overhang temperature rise average, for each specific loading test. This is explained by the fact that, when in the slot, the heat can be transferred away from the

winding by conduction through the stator laminations, as well as by convection to the ventilating airflow. On the other hand, overhangs can transfer heat by convection to the surrounding airflow and, more significantly, by conduction along the copper winding in the axial direction.

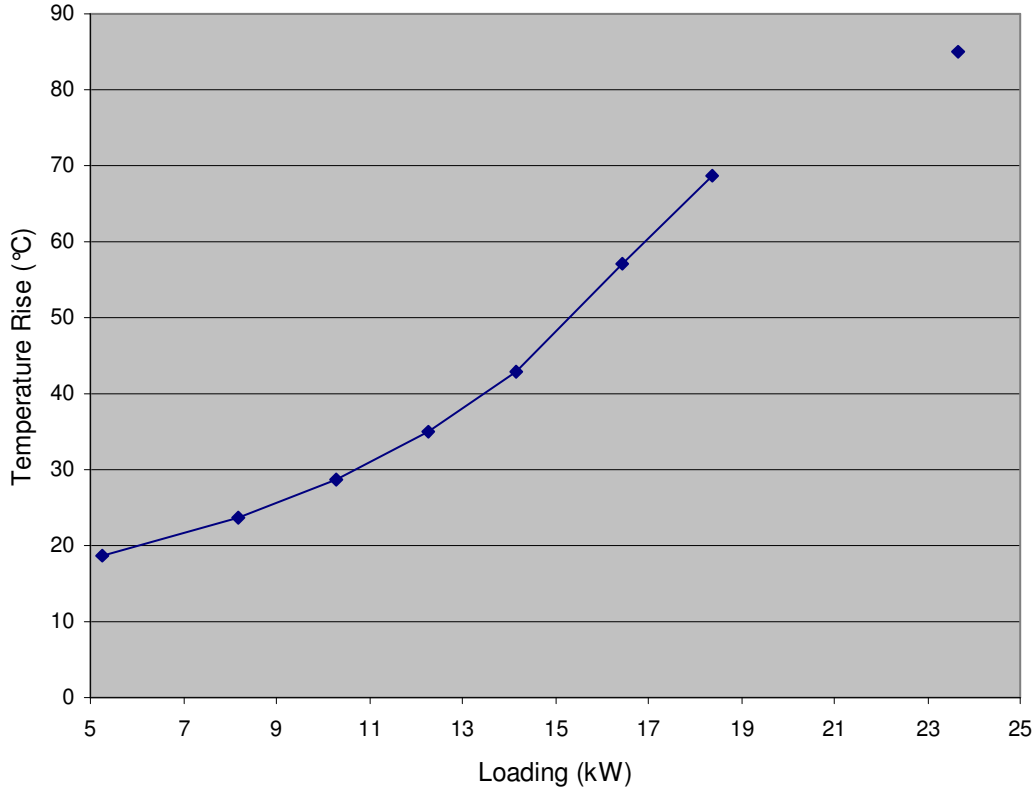

Figure 8.2: *Average stator winding slot temperature rise.*

Another interesting result extracted from the test is the temperature distribution along the axial core length of the stator winding slot. For this, the five stator winding slot thermocouples averages are calculated across the complete kW loading range considered. These results are shown in Figure 8.3, with the stator thermocouple TC numbers referring to the thermocouple axial positions along the stator slot length displayed in Table 8.3.

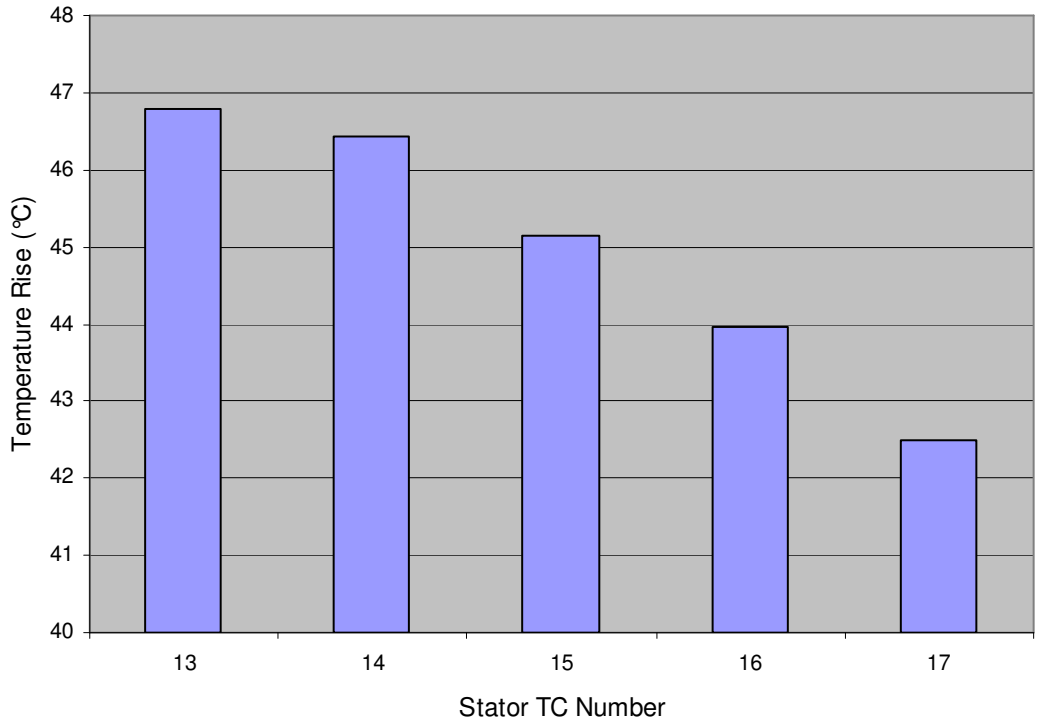

Figure 8.3: *Average stator winding slot thermocouple temperatures.*

As expected, the DE (TC 13) edge of the stator winding in the slot has a significantly higher temperature than the NDE. On average, this temperature difference is 4.3 °C in magnitude, as shown in Figure 8.3. This axial length thermal gradient peaks at the highest kW load tested, with a value of 8.0 °C. As with the stator winding overhang, this thermal difference along the core length of the synchronous machine is due to the fact that the NDE of the machine experiences a better cooling than the DE side which, as a results, exhibits higher temperatures.

Stator Winding Slot Mid-Core Length Circumference

The thermal results for the four thermocouples placed around the circumference of the stator lamination, within the winding stator slots in steps of 90°, are presented in the Table 8.4.

	Stator TC steady-state temperature rise for specific kW loading (°C)							
Stator TC	5.25 kW	8.20 kW	10.28 kW	12.26 kW	14.17 kW	16.43 kW	18.38 kW	23.67 kW
S15	18.9	24.0	29.0	35.2	43.0	57.3	68.7	85.0
S18	19.3	24.7	30.0	36.5	44.8	59.6	71.8	88.8
S19	22.0	28.7	34.9	42.5	52.1	68.9	82.6	101.7
S20	20.6	26.9	32.9	40.2	49.4	65.7	79.0	97.6
Average	20.2	26.1	31.7	38.6	47.3	62.9	75.5	93.3

Key:

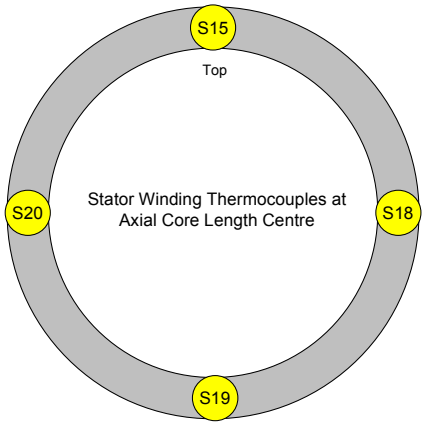

Table 8.4: *Stator windings slot steady-state temperature rise around lamination circumference.*

The average temperature results tabulated in Table 8.4 show a very similar variation with kW loading as those presented in Figure 8.1 for the overhang temperature distribution. Similarly to what is observed with the stator winding overhang, the results presented in Table 8.4 show an uneven temperature distribution around the circumference of the stator lamination at the axial centre of the machine's core length. Again, this is explained by the uneven airflow paths, resulting in different cooling efficiencies, flowing through the machine along the laminations and windings.

Rotor Winding

The rotor winding thermocouple temperature rise results are shown in Table 8.5. The analysis of the rotor winding results performed in this section is split into the four rotor winding areas illustrated in Figure 8.4, to ease the presentation of the results. Areas 1 and 2 are the rotor winding areas along the rotor lamination core length, with Area 1 located in the lagging half of the rotor pole and Area 2 in the leading half of the pole. Furthermore, Areas 1 and 2 are analysed along the two thermal paths shown in the radial and axial directions, Area 3 covers the DE end rotor winding endwinding section and Area 4 the NDE endwinding segment.

Figure 8.4: *Rotor winding Area divisions to ease thermal analysis.*

It is crucial to acknowledge the direction of rotation, since this has a significant effect on the cooling of particular rotor sections and on the operational losses generated within the rotor, as shown later in this section and explained in Chapter 4. Figure 8.4 shows the direction of rotation for the particular case analysed.

	Rotor TC steady-state temperature rise for specific kW loading (°C)								
Rotor TC	5.25 kW	8.20 kW	10.28 kW	12.26 kW	14.17 kW	16.43 kW	18.38 kW	23.67 kW	TC Average
R1	21.0	24.6	27.9	32.7	38.7	48.3	56.9	65.0	39.4
R2	19.9	23.8	27.1	31.3	37.3	46.8	55.1	63.1	38.1
R3	19.5	23.1	26.4	31.1	36.5	45.4	53.7	61.8	37.2
Average	20.1	23.8	27.1	31.7	37.5	46.8	55.2	63.3	38.2
R4	17.3	20.6	23.4	27.5	32.5	40.9	48.1	54.9	33.2
R2	19.9	23.8	27.1	31.3	37.3	46.8	55.1	63.1	38.1
R5	17.1	20.2	22.9	26.5	31.3	39.1	46.0	52.2	31.9
Average	18.1	21.5	24.5	28.5	33.7	42.3	49.7	56.7	34.4
R6	19.0	22.9	26.1	30.9	36.1	45.4	53.5	62.4	37.0
R7	20.4	24.0	27.5	31.9	37.7	47.3	55.6	64.0	38.6
R8	18.2	21.8	25.3	29.8	35.2	43.9	51.6	60.4	35.8
Average	19.2	22.9	26.3	30.9	36.4	45.5	53.6	62.3	37.1
R9	17.7	20.9	24.0	27.8	33.0	41.5	48.9	56.4	33.8
R7	20.4	24.0	27.5	31.9	37.7	47.3	55.6	64.0	38.6
R10	15.9	18.8	21.4	25.5	30.2	37.8	44.3	51.3	30.7
Average	18.0	21.2	24.3	28.4	33.6	42.2	49.6	57.3	34.3
R11	18.1	21.8	24.8	28.9	34.6	43.6	51.3	60.0	35.4
R12	18.6	22.8	26.0	30.7	36.1	45.4	53.2	62.2	36.9
Average	18.4	22.3	25.4	29.8	35.4	44.5	52.3	61.1	36.1
R13	18.3	22.1	25.1	29.1	34.9	43.8	51.3	59.7	35.5
R14	15.6	18.9	21.6	25.7	30.2	38.2	44.7	52.5	30.9
Average	17.0	20.5	23.4	27.4	32.6	41.0	48.0	56.1	33.2
Winding Average	18.6	22.1	25.3	29.5	35.0	43.8	51.6	59.6	-
Key: 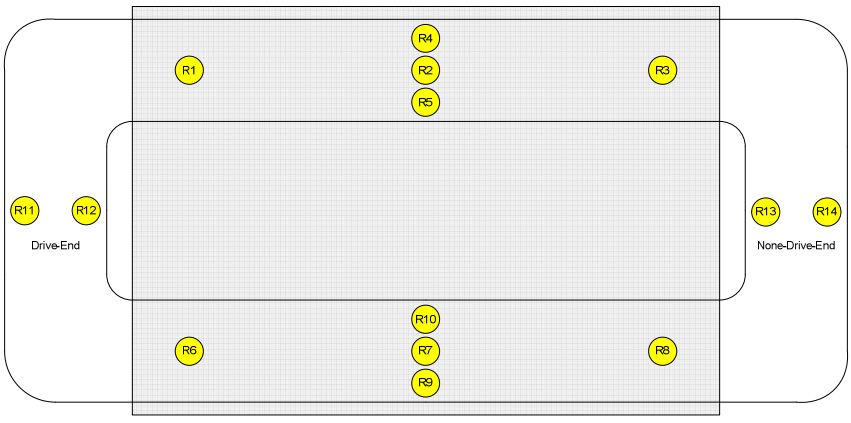									

Table 8.5: *Rotor windings steady-state temperature rise results.*

Rotor Winding Areas 1 and 2 (Adjacent to Lamination Segments)

Rotor winding temperature rise averages for thermocouples 1-3 and 6-8 are used to evaluate the effect on the temperature of the core length sections of the rotor winding with increasing kW load. The results are graphed in Figure 8.5. The previously established ascending relationship between winding temperature rise and kW loading is also observed here, but what is interesting is the consistent difference between the leading and lagging rotor winding sections. This temperature difference is on average 1.1 °C in magnitude. Even though not a major temperature difference, this disparity highlights the importance of considering the rotational direction when performing machine thermal analysis. The thermal disparity between rotor winding Areas 1 and 2 is accounted for by the fact that the leading half of the rotor pole experiences a better airflow exposure and hence a better cooling. Furthermore, as presented in Chapter 4, more machine operational losses are generated in the lagging half of the rotor pole lamination, which also contributes to this temperature difference.

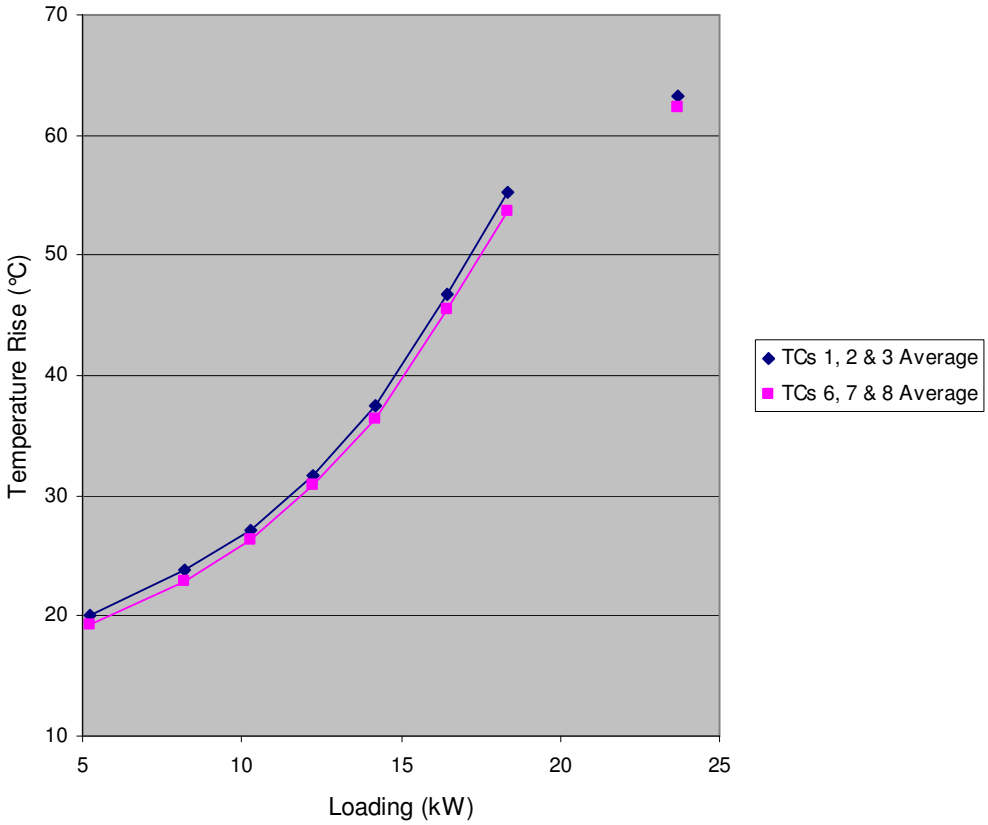

Figure 8.5: *Rotor winding average temperature variation with kW loading.*

Rotor Winding Areas 3 and 4 (Endwinding Sections)

The temperature rise results for the rotor endwinding, encapsulated in Areas 3 and 4 from Figure 8.4, are presented in Figure 8.6. The variation of the rotor endwinding temperatures with kW loading is very similar to that observed for the stator winding overhangs, shown in Figure 8.1. Figure 8.6 shows a significantly higher average temperature rise for the DE rotor endwinding. This thermal difference is on average 2.9 °C, peaking at 5.0 °C for the highest kW loading tested. The reason for this thermal discrepancy is again the uneven airflow characteristics experienced by the two endwindings. The cooler, more direct, airflow hitting the NDE rotor endwinding, results in lower temperatures. This effect is apparent when focusing solely on Area 4, the NDE rotor endwinding. The two thermocouples placed in this section illustrate the effect of the direct cool airflow hitting the NDE endwinding.

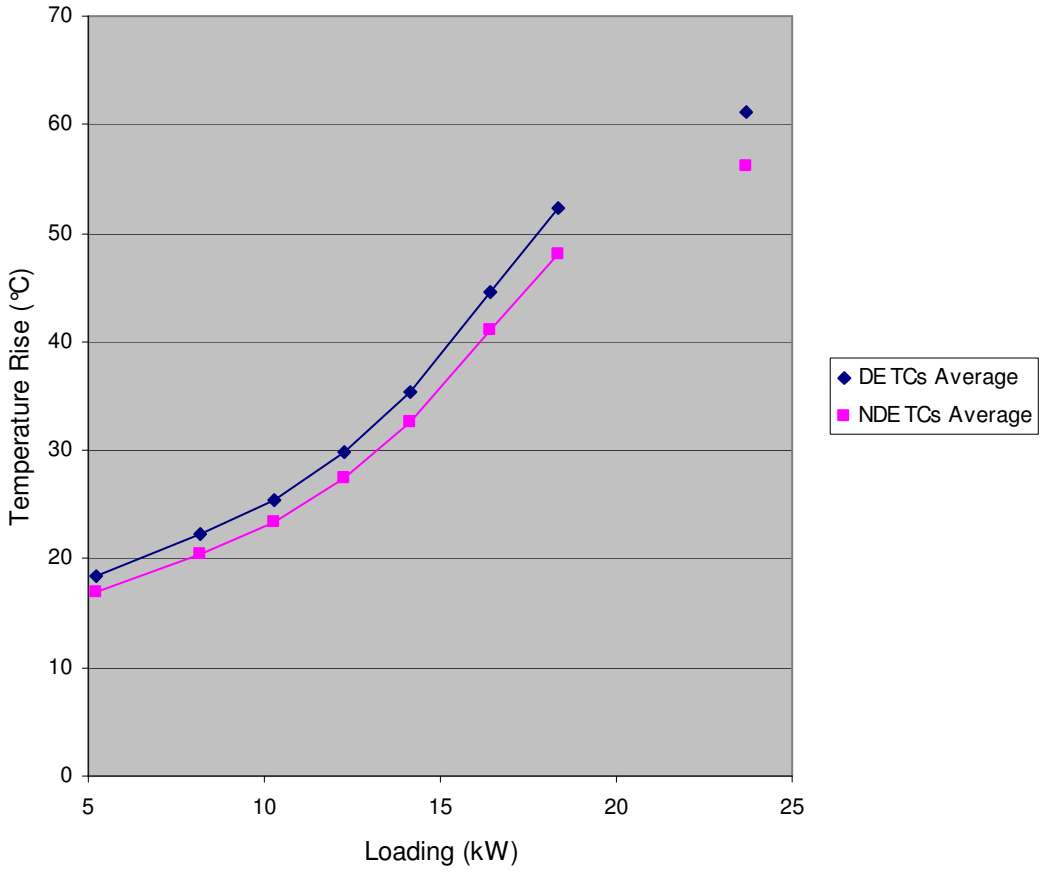

Figure 8.6: *Rotor DE and NDE endwinding average temperature variation with kW loading.*

Thermocouple R14, closest to the air inlet, records significantly lower temperatures than R13, which is just a few millimetres deeper in the rotor endwinding. This difference in temperature between the two thermal sensors is 4.6 °C on average, with a maximum of 7.2 °C. In fact, the inner NDE rotor endwinding thermocouple reads temperatures that are very close to the DE rotor endwinding temperature average, as shown in Table 8.5. These results highlight the effect and importance of airflow on the machine sections directly in the flow path.

Rotor Winding Area 1 (Lagging Rotor Pole Half)

Both rotor winding sections along the generator's core length have four thermocouples located within the winding. This allows for an evaluation of the temperature distribution across this winding section both in the axial and radial directions. Shown in Figure 8.7 is the full kW loading range average temperature distribution along the axial length of the lagging rotor pole half of the rotor winding. The information, collected by rotor thermocouples R1 to R3 shows a thermal gradient between the DE and NDE sides of the rotor winding, which is on average 2.2 °C. These thermal gradient results show the decreasing effectiveness of the cooling along the axial length of the winding from the NDE to the DE of the electrical machine.

Analysing the average thermal distribution in the segment in the radial direction yields Figure 8.8. Rotor thermocouples R4, R2 and R5, shown in Figure 8.4, are utilised for this. It is interesting to note that the hottest point along a cross-section of the rotor winding at this axial core slice is at the centre of the winding, at R2's location. This is due to the fact that the areas around rotor thermocouples R4 and R5 can transfer heat away from the rotor winding through convection to the airflow and conduction to the rotor lamination respectively. The central fragments of the winding do not have these heat transfer mechanisms available and hence are at a higher temperature during machine operation.

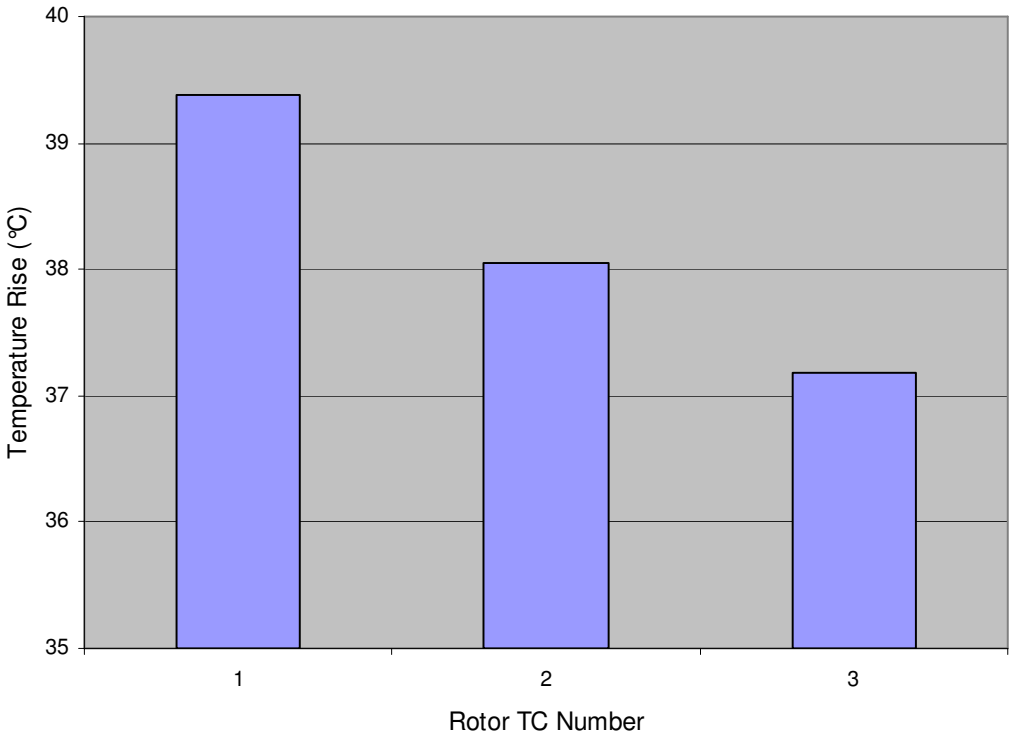

Figure 8.7: *Average temperature distribution along axial length of rotor Area 1.*

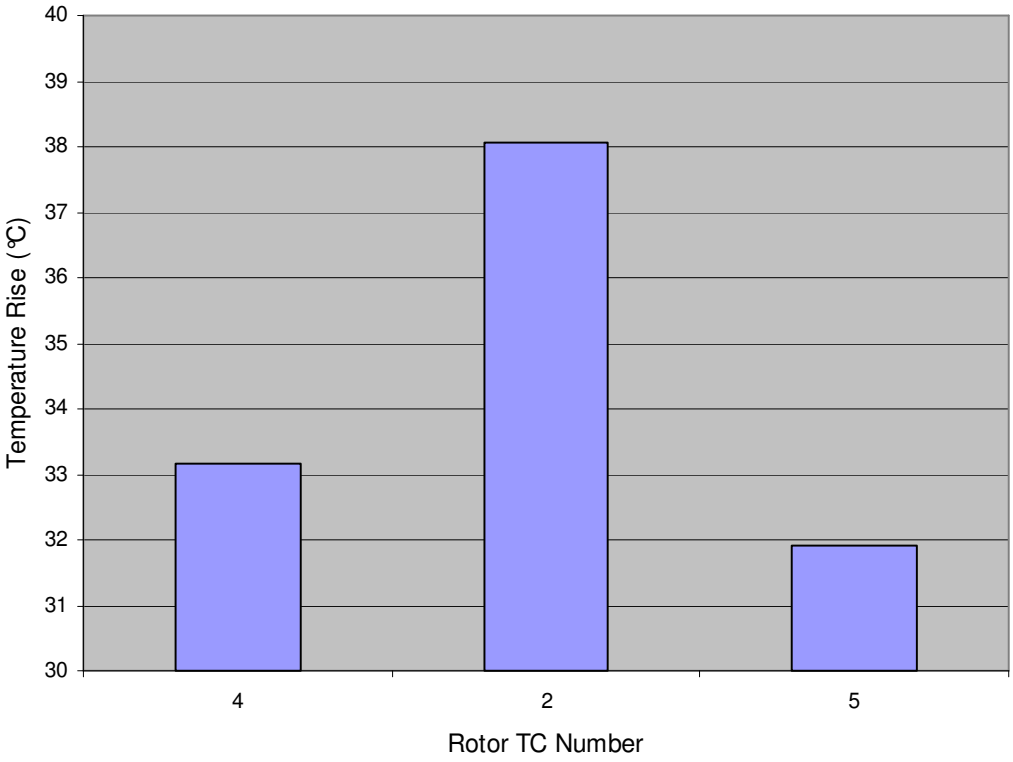

Figure 8.8: *Average temperature distribution along radial length of rotor Area 1.*

Rotor Winding Area 2 (Leading Rotor Pole Half)

A similar study is performed on the leading rotor pole half of the rotor winding, covered by Area 2. The axial complete kW range average temperature distribution along Area 2 is presented in Figure 8.9. A temperature gradient along the axial length of Area 2 is also observed, but differently to the thermal distribution illustrated in Figure 8.7, this is not as close to a linear relationship and the hottest axial position is around the axial centre of the rotor winding. This is the leading side of the rotor pole, which is highly influenced by the airflow. As a result of this, lower winding average temperatures result, but also, uneven airflow paths cool the leading half of the rotor pole winding in an irregular non-linear way, as shown in Figure 8.9. This uneven airflow cooling is also observed around the rotor and stator endwindings, as previously shown in this section.

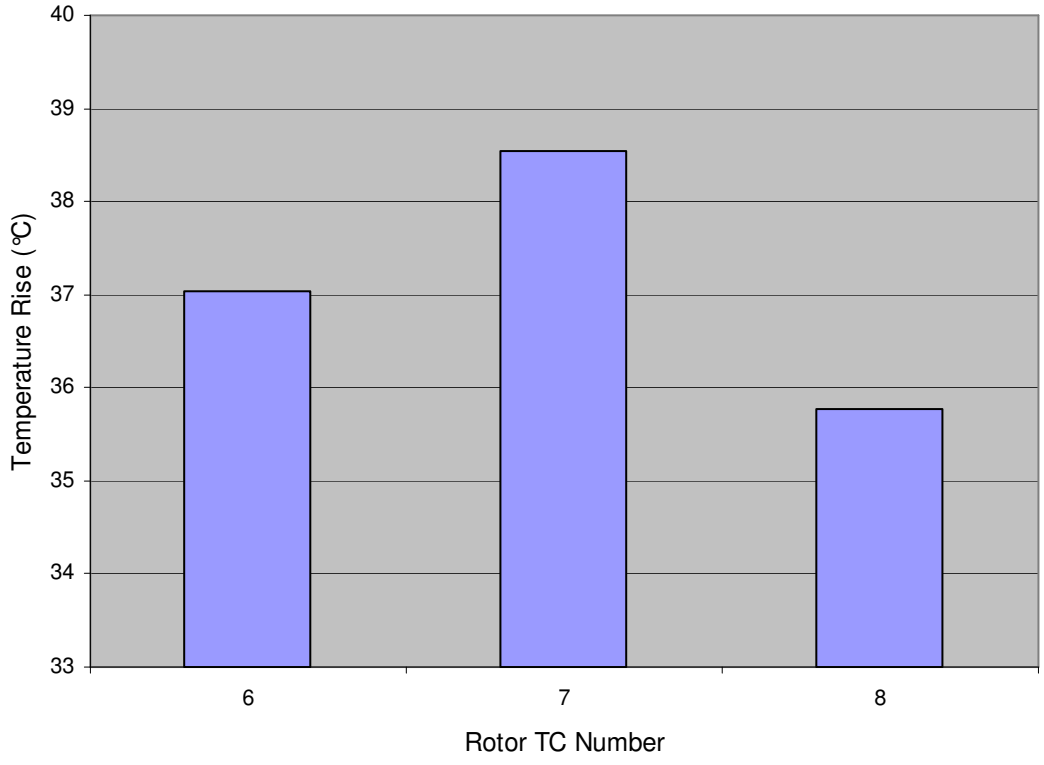

Figure 8.9: *Average temperature distribution along axial length of rotor Area 2.*

The analysis in the radial direction of Area 2 is presented in Figure 8.10, utilising thermocouples R9, R7 and R10 shown in Figure 8.4. Mirroring the radial temperature distribution of the lagging rotor winding section presented in Figure 8.8, the cooler rotor winding sections in Area 2 are also around the winding edges. Again, this is attributed to convection to airflow and conduction to rotor lamination heat transfer paths that exist around R9 and R10 respectively, but not at the central location of R7.

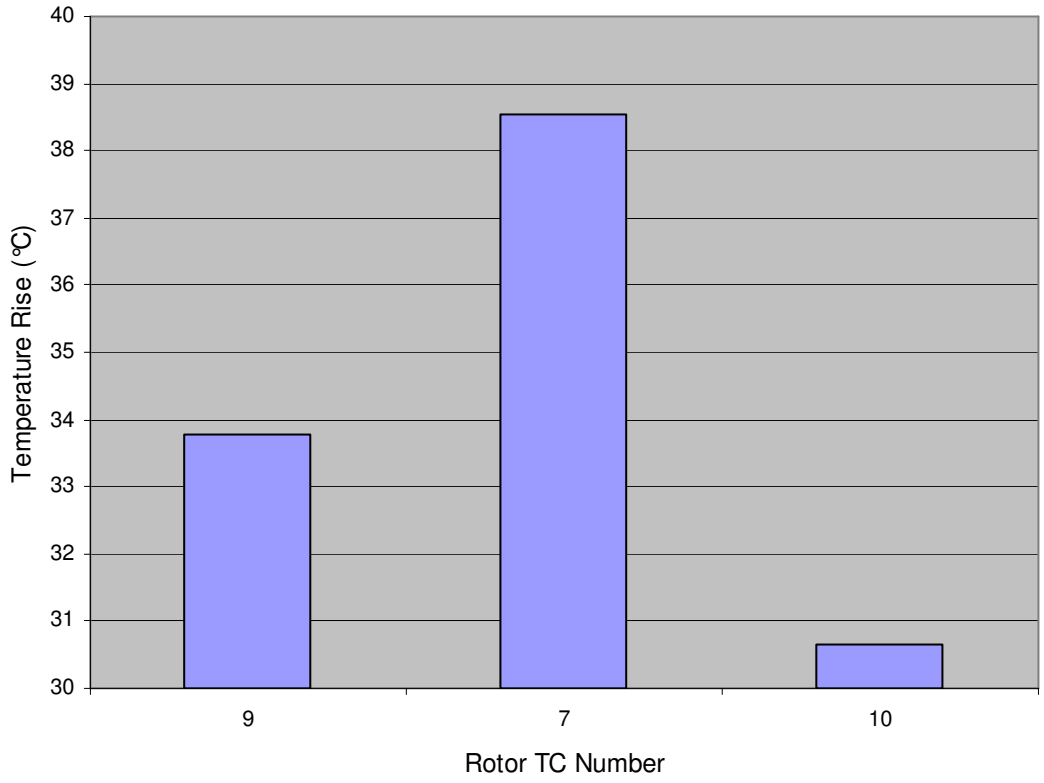

Figure 8.10: *Average temperature distribution along radial length of rotor Area 2.*

Rotor Winding Average

Finally, the overall rotor winding average temperature variation with respect to generator kW loading is presented in Figure 8.11. As with the stator winding temperature variation with kW loading, shown in Figure 8.2, a rising relationship is observed. Higher kW loadings result in increased machine losses which are harder to transfer away from the machine through conduction, convection and radiation, resulting in the higher winding temperatures.

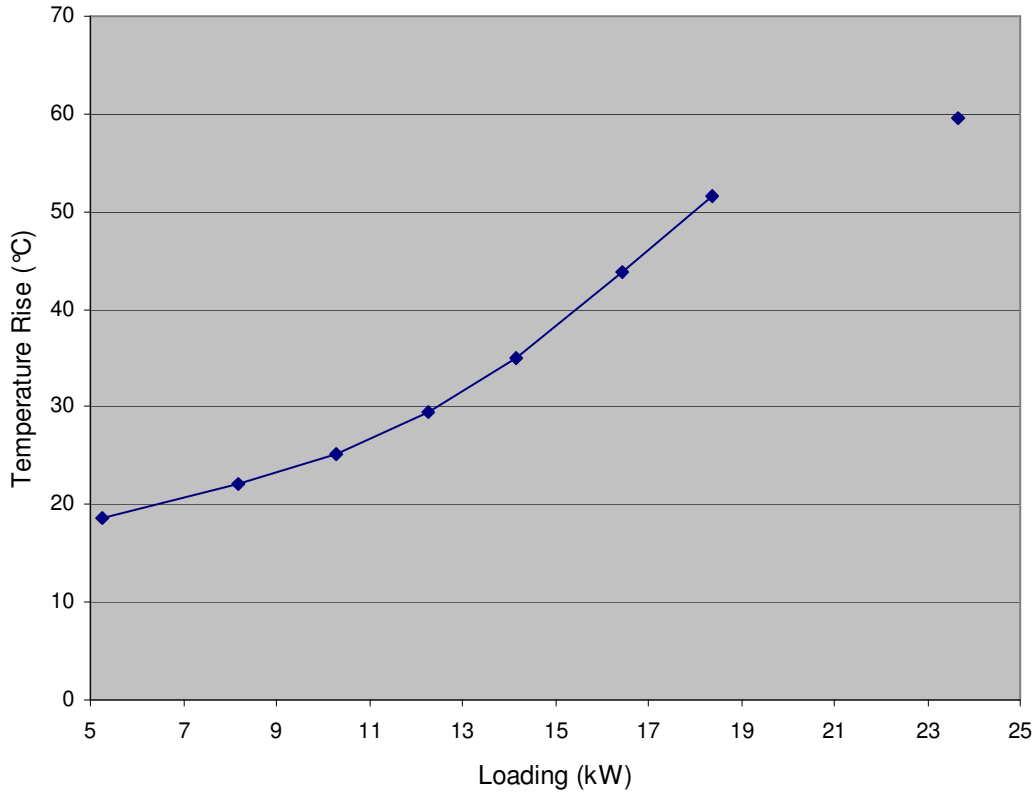

Figure 8.11: *Average rotor winding temperature rise.*

External Thermocouple

The external thermocouples presented in Chapter 7, Figure 7.8, are monitored and the results are displayed in Table 8.6. These cover the thermocouples placed along the axial length of the generator frame, the feet, the AVR box and the through ventilating air temperature rise.

	External TC steady-state temperature rise for specific kW loading (°C)								
Frame TC	5.25 kW	8.20 kW	10.28 kW	12.26 kW	14.17 kW	16.43 kW	18.38 kW	23.67 kW	TC Average
F1	5.9	6.2	6.4	6.5	7.0	8.4	9.1	11.1	7.6
F2	6.0	6.5	6.7	7.0	7.6	9.2	10.2	12.5	8.2
F3	5.8	6.4	6.7	7.0	7.7	9.7	10.6	13.0	8.4
F4	6.7	7.3	7.8	8.3	9.2	11.9	12.7	15.2	9.9
Average	6.1	6.6	6.9	7.2	7.9	9.8	10.7	13.0	-
F5	4.3	4.6	4.9	5.1	5.5	7.4	7.8	9.8	6.2
F6	4.6	4.9	5.2	5.5	6.0	7.8	8.4	10.3	6.6
F7	4.7	5.0	4.7	4.6	4.8	6.0	6.5	10.2	-
F8	10.3	11.6	12.2	13.4	15.1	18.8	21.9	27.8	-
Air temp. rise	5.6	6.6	7.5	8.8	10.3	12.8	15.4	17.6	10.6
Key:	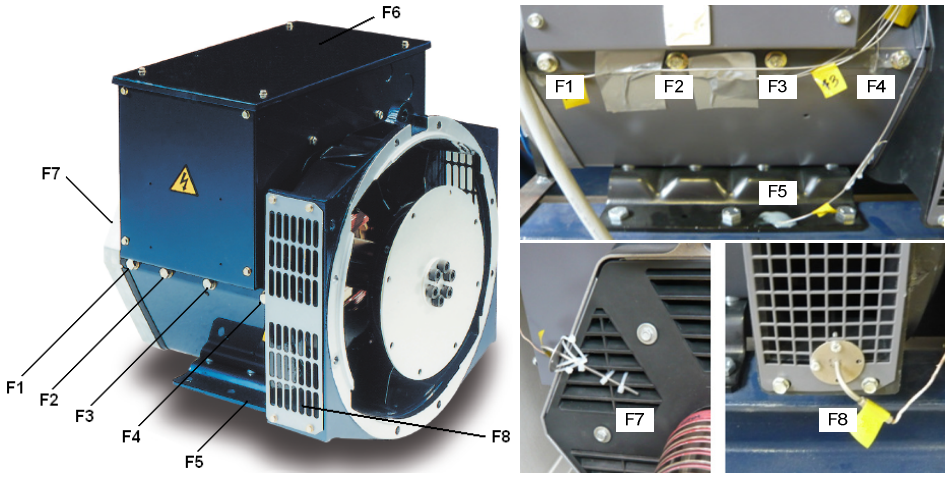								

Table 8.6: *External thermocouple steady-state temperature rise results.*

Frame Axial Length

The four thermocouples placed along the axial length of the generator, displayed in Table 8.6, are monitored. The variation in steady-state average temperature of external thermocouples F1 to F4, with respect to kW loading of the generator, is shown in Figure 8.12. As expected, the higher kW loadings yield higher average frame temperatures. These results are in agreement with the results obtained from the internal winding thermocouples presented in this chapter. The frame average temperature rise across the kW loadings considered is 8.5 °C.

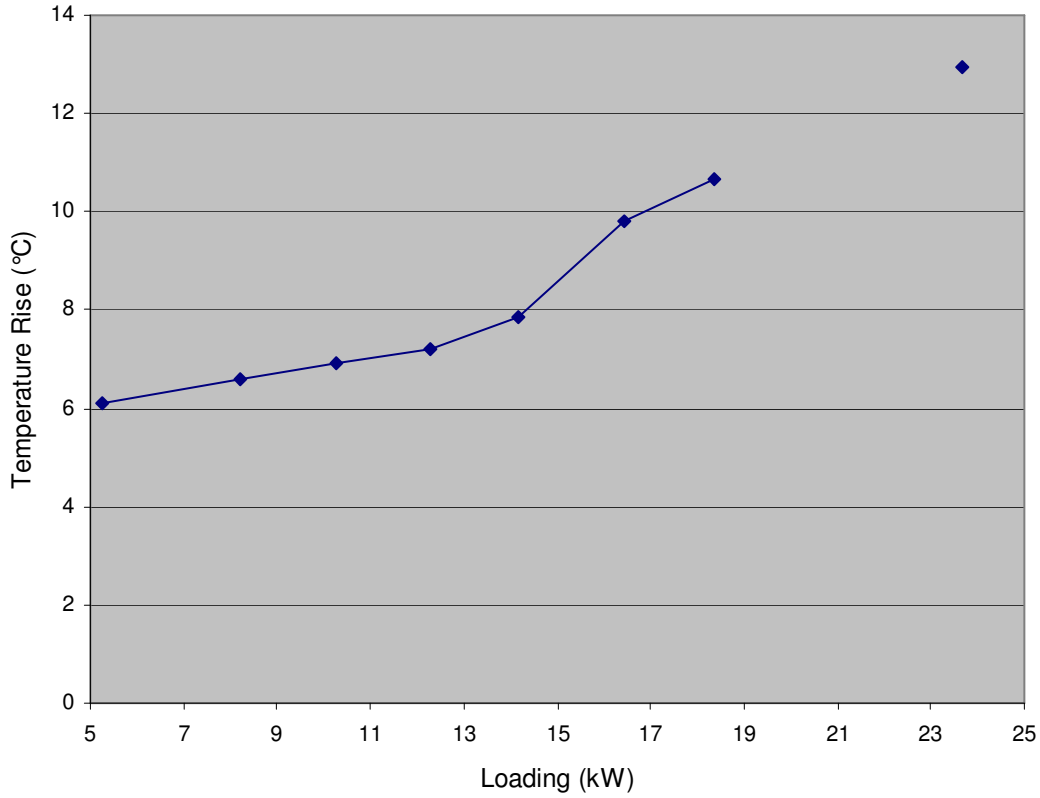

Figure 8.12: *Average generator frame temperature rise.*

Another important result to be extracted from this set of frame thermocouples is the actual frame thermal variation along the axial length of the generator frame. Temperature averages for the four thermocouples are calculated for this, for the complete kW loadings considered. These results are presented in Figure 8.13. The chart presents a temperature gradient of 2.3 °C, with a maximum difference between

F1 and F4 of 4.1 °C being recorded for the 20 kW heat-run. As shown, the two middle thermocouples exhibit a very similar average temperature. On the other hand, similarly to the previously examined generator winding overhangs, the NDE F1 has a lower than average temperature of 7.6 °C and the DE F4 a noticeably higher than average temperature of 9.9 °C.

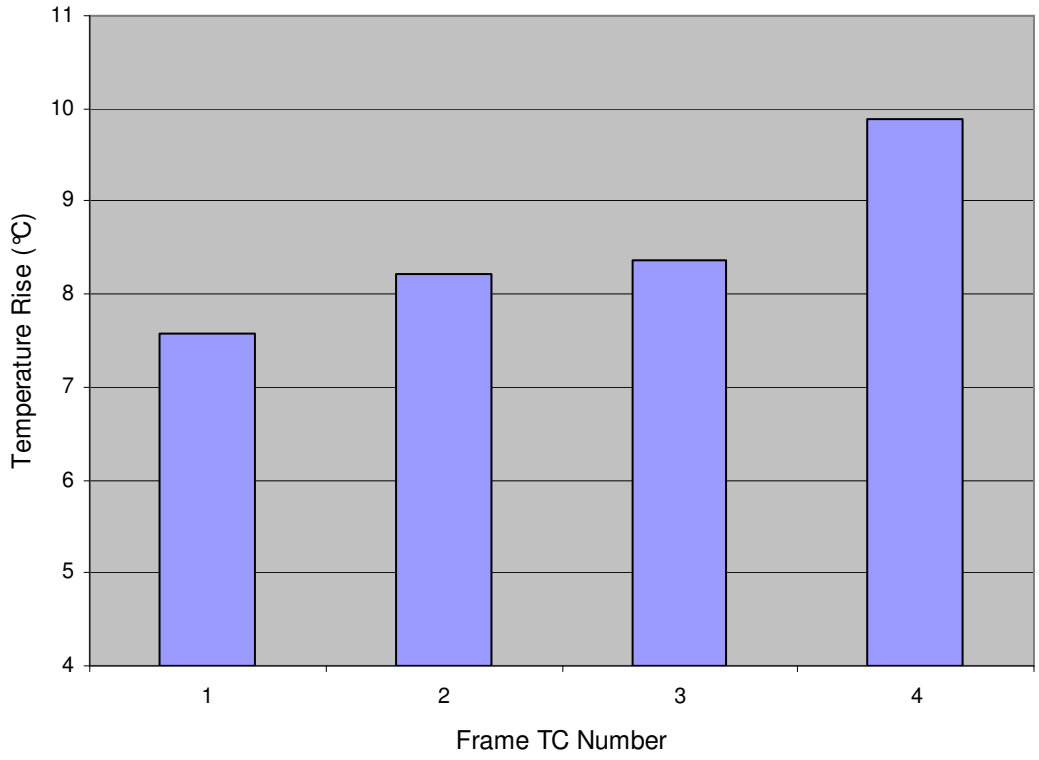

Figure 8.13: *Frame average temperature distribution along the axial length.*

Feet and AVR Box

The generator feet (F5) and AVR box (F6) thermocouple temperature monitoring results are presented in Table 8.6. They present similar thermal characteristics, with average temperature rises of 6.2 °C and 6.6 °C respectively, and maximum temperature rises of 9.8 °C and 10.3 °C respectively.

Through Ventilation Airflow temperature Rise

Using the generator air inlet and outlet thermocouples, F7 and F8, the through ventilation airflow temperature rise is determined for all kW loadings tested. These results are presented in Figure 8.14. The results reveal a significant increase in through ventilation airflow temperature rise with increasing kW loading. An average airflow temperature rise of 10.6 °C is recorded, ranging from a 5.6 °C for the lowest 5 kW loading tested to 17.6 °C for the highest 20 kW loading. Figure 8.14 reveals a rising relationship between through ventilation airflow temperature rise and kW loading.

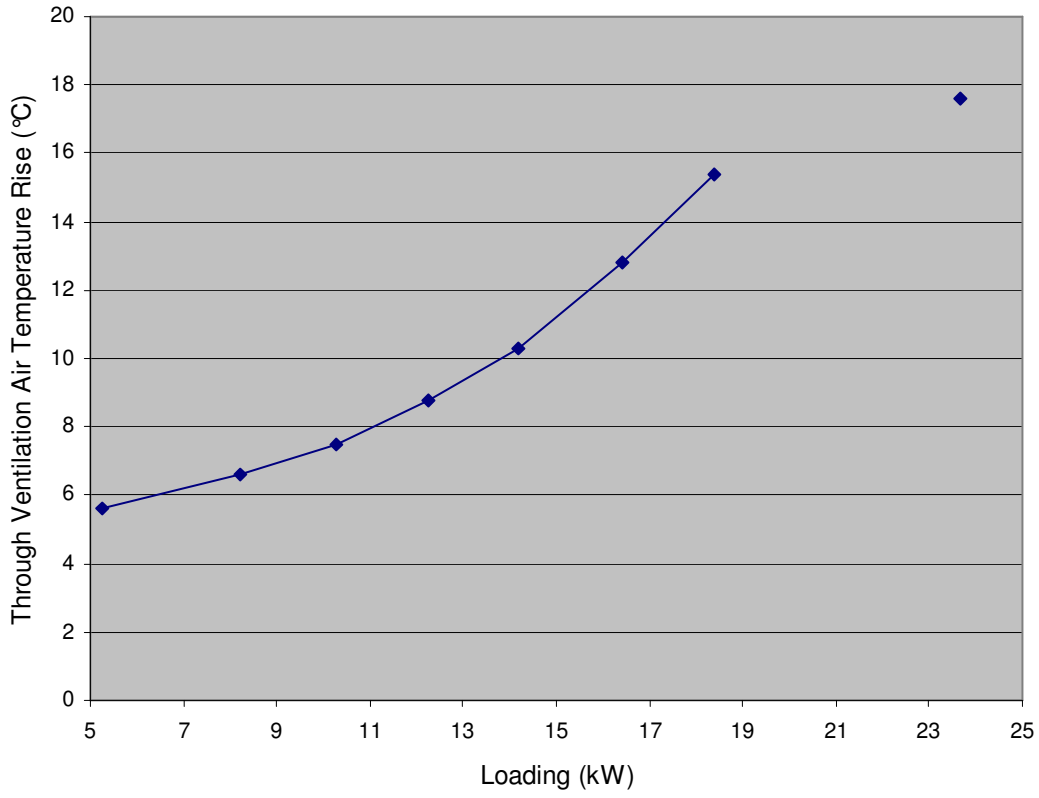

Figure 8.14: *Through ventilation airflow temperature rise.*

The results presented in this section provide detailed insight on the thermal distribution across the most important parts of the synchronous generator once thermal steady-state is reached. These results are important to consider when designing an electrical machine, since they pinpoint the hotter sections of the

machine which are most likely to have an impact on the insulation. The results allow machine thermal designers to focus their efforts on these areas to try and reduce component temperatures where and when necessary, depending on specific machine operation and demand. In addition to this, the results presented serve as an ideal method to validate the models utilised in the MySolver thermal modelling package. This validation process is presented in Section 8.2.

8.1.2 Transient Temperature Rise Results and Analysis

The full heat curve transient results for the 18kW load test are presented in this section, because it is a realistic loading at which the generator could be run for a significant amount of time in industrial operations. Furthermore, as explained in Section 7.4, the induction motor in the experimental test rig does not allow for higher loadings to be tested for extended periods of time. In addition to this, machine losses and airflow implications are most significant at the higher end of the loading scale. The important steady-state temperature results are fully presented and analysed in Section 8.1.1 and the purpose of this section is to present the transient progression of the generator thermocouples as they reach steady-state temperature. Rotor winding and stator winding transient temperature results for the 18kW heat-run are presented in Figures 8.15 to 8.20.

The thermal time constant, for both the rotor and the stator, can also be extracted from the information presented in Figures 8.15 to 8.20. It is interesting to note that the rotor time constant - 20 minutes - is noticeably longer than the stator time constant -12 minutes. In order for a thermal modelling package to perform transient simulations accurately, specific rotor and stator time constants need to be considered and relevant specific heat capacity data adjusted and validated, as explained in Section 3.8.

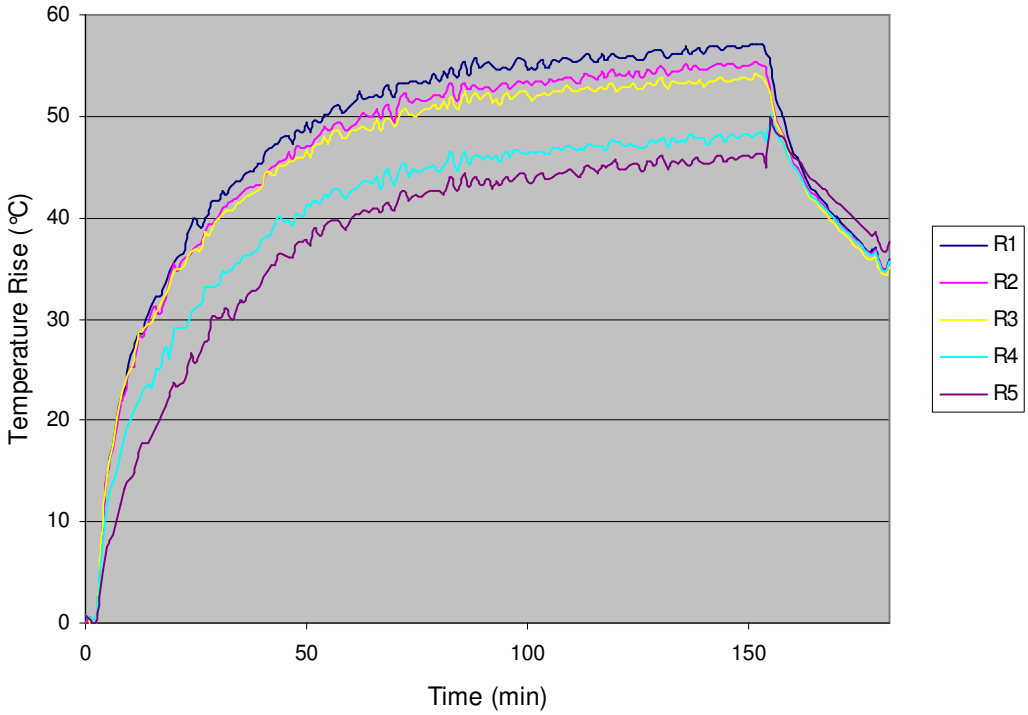

Figure 8.15: *18kW load rotor thermocouples 1 to 5 transient results.*

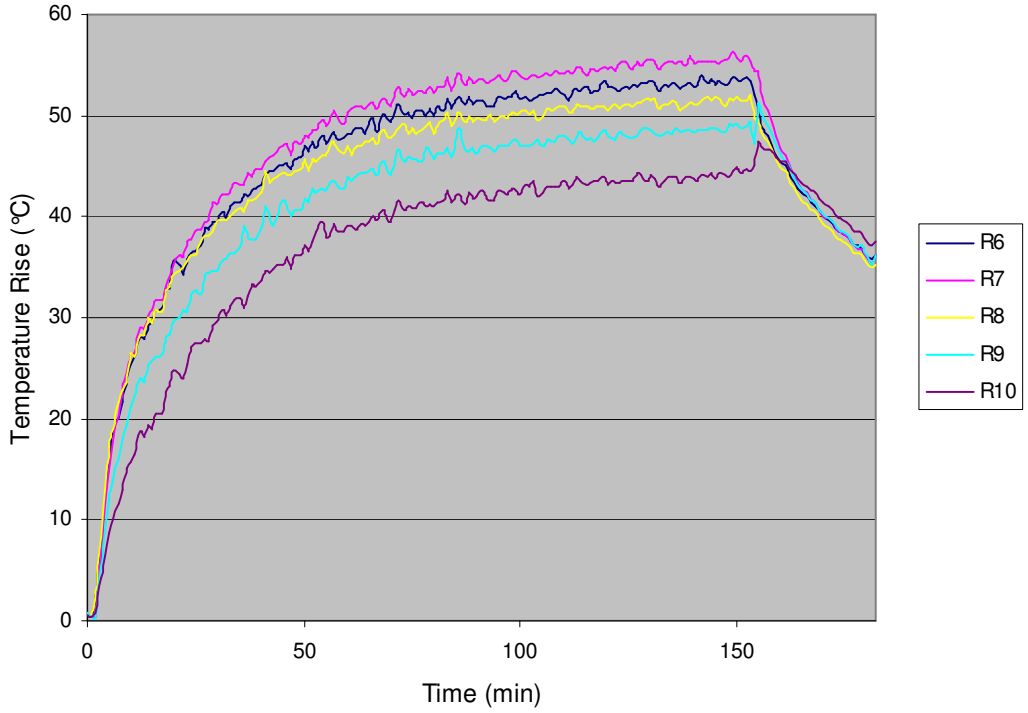

Figure 8.16: *18kW load rotor thermocouples 6 to 10 transient results.*

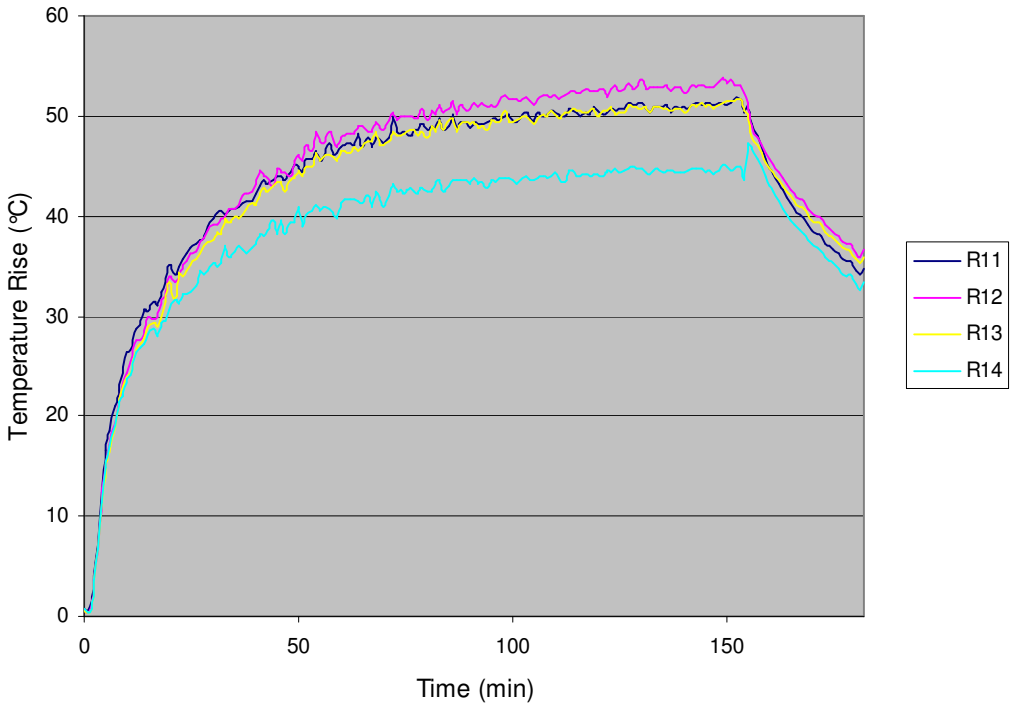

Figure 8.17: *18kW load rotor thermocouples 11 to 14 transient results.*

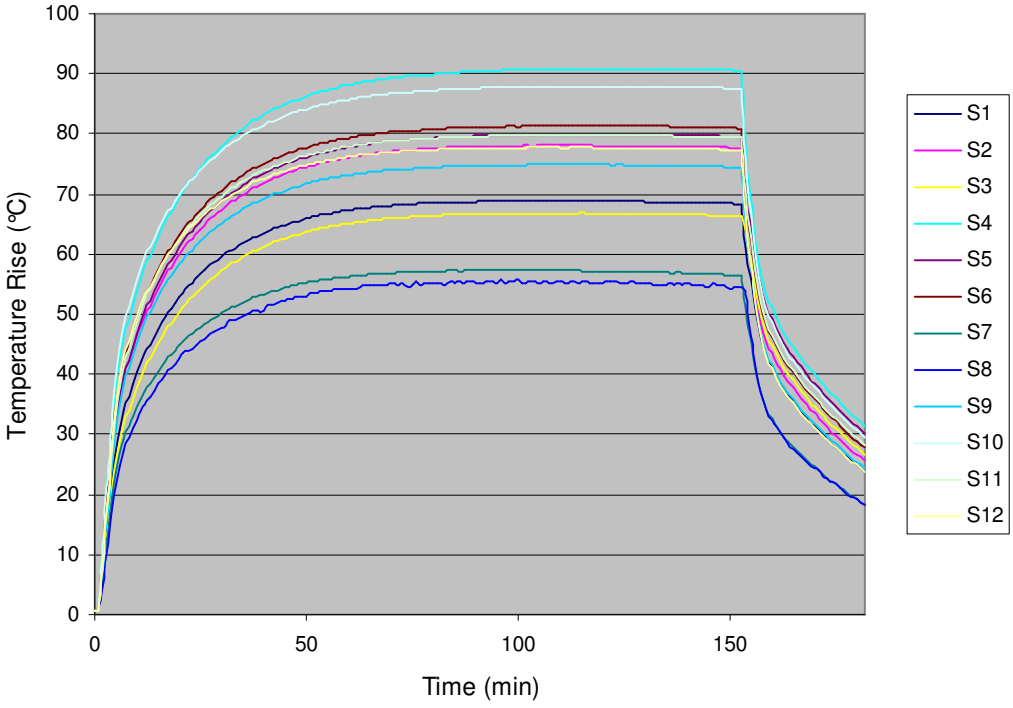

Figure 8.18: *18kW load stator thermocouples 1 to 12 transient results.*

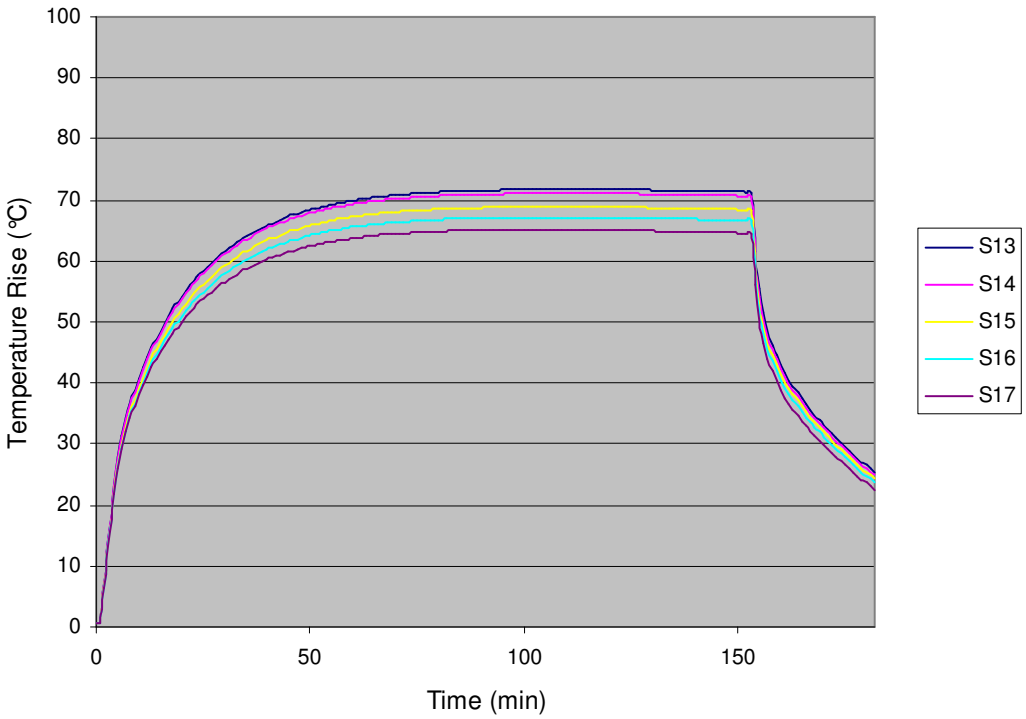

Figure 8.19: *18kW load stator thermocouples 13 to 17 transient results.*

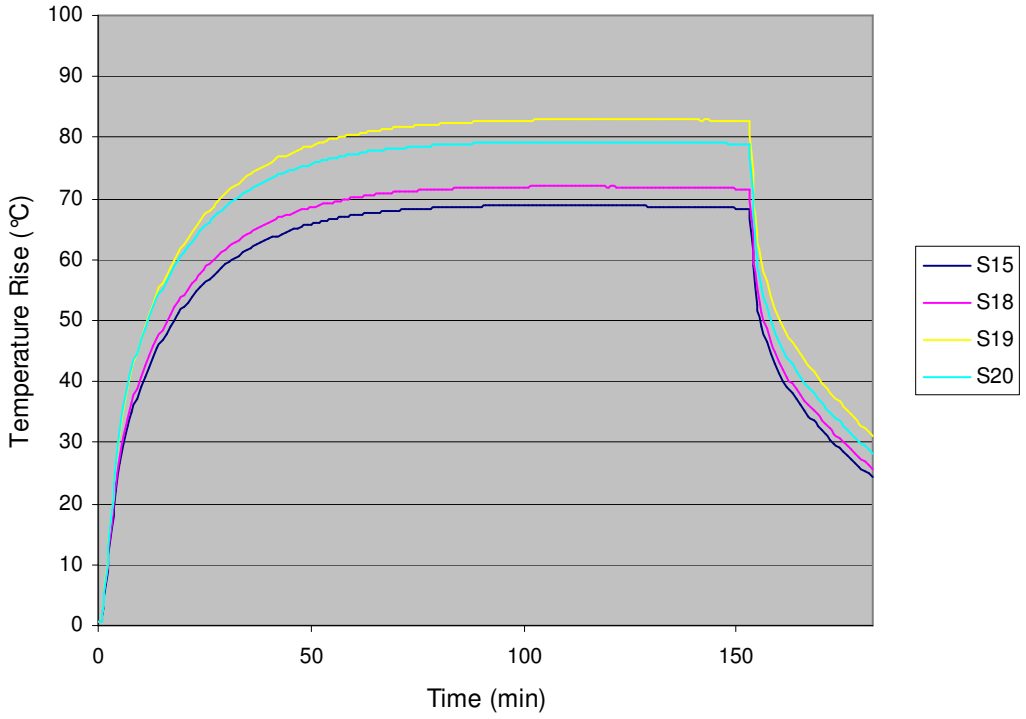

Figure 8.20: *18kW load stator thermocouples 15 and 18 to 20 transient results.*

8.1.3 Thermal Camera Verification

A Cepid Titanium DCO19U-B thermal camera was used as an additional method to verify the external thermocouple frame results collected. Figure 8.21 shows the steady-state thermal distribution of the synchronous generator when running a 20 kW load, at a laboratory room temperature of 24.9 °C. As shown the thermal capture results obtained agree closely with the thermocouple data tabulated in Table 8.6, with temperature along the axial length covered by frame thermocouples F1 to F4 ranging from 36.0 °C to 40.1 °C absolute temperature. Additionally, Figure 8.21 identifies the generator's drive-end end-cap as being the hottest external section, which a temperature of over 50 °C.

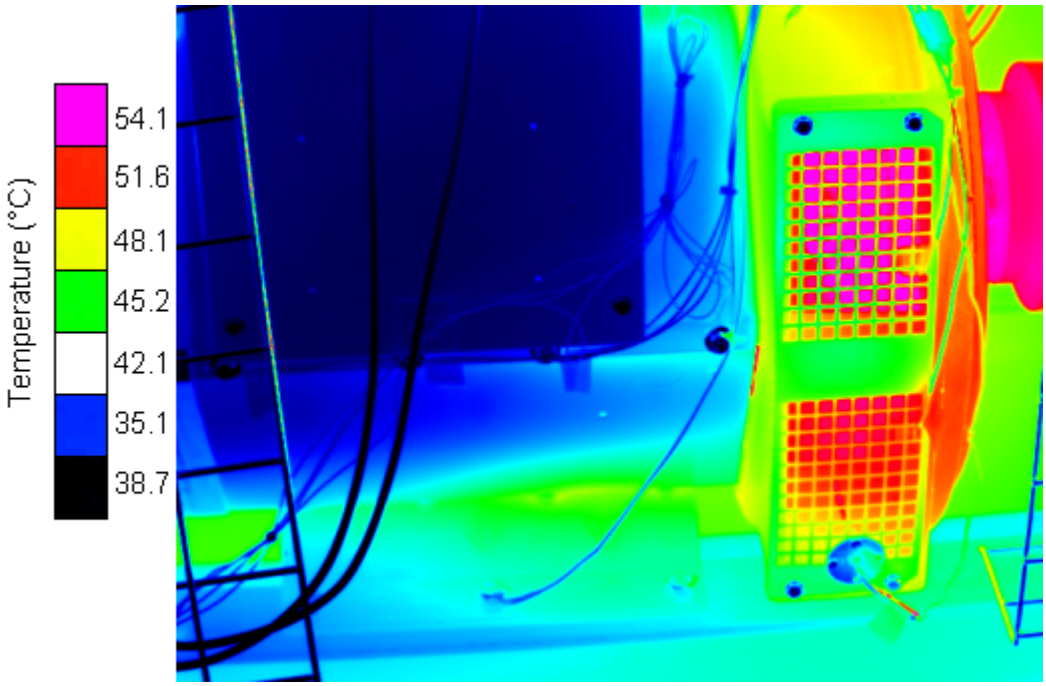

Figure 8.21: *Generator thermal camera 20 kW steady-state temperature capture.*

8.2 Validation of MySolver Thermal Models

The steady-state and transient temperature results presented in Section 8.1 are used to validate the MySolver thermal analysis tool presented in Chapter 6. This validation process is detailed in this section.

8.2.1 Steady-State MySolver Performance Validation

The thermocouples used to match MySolver lumped parameter thermal nodes are illustrated in Table 8.7 for the rotor and the stator. Rotor MySolver lumped parameter thermal network nodes a presented in Figures 3.3 (Section 3.3) and 3.14 (Section 3.5.1) and machine rotor winding TC locations are illustrated in Figure 7.6 in Section 7.2.1. Similarly, Stator MySolver lumped parameter thermal network nodes are presented in Figures 3.7 (Section 3.4) and 3.17 (Section 3.5.2) and machine stator winding TC locations are illustrated in Figures 7.3 and 7.5 in Section 7.2.1.

Rotor	
MySolver node	Machine TC
a1	R3
b1	R2
c1	R1
d1	R13 & R14
e1	R11 & R12
a3	R8
b3	R7
c3	R6

Stator	
MySolver node	Machine TC
a1	S17
b1	S15
c1	S13
d1	S7 to S12
e1	S1 to S6
a2	S17
b2	S15
c2	S13

Table 8.7: *MySolver node to machine thermocouple matching.*

Tables 8.8 to 8.11 compare the steady-state temperature predictions obtained using MySolver with the experimentally obtained data presented in Chapter 8. Rotor and stator MySolver generated machine temperatures are compared with the experimental values and magnitude errors (°C) are calculated for each MySolver thermal network node presented. Tables 8.8 and 8.9 focus on the 18 kW heat-run performed, looking at all possible lumped parameter thermal network and experimental thermocouple reading comparisons. Similar tables for all ratings tested are collected in Appendix G. Results for the complete kW load testing range are summarised in Table 8.10 for the rotor and 8.11 for the stator.

Average errors are graphed in Figures 8.22 and 8.23, illustrating MySolver's accuracy level across the complete kW loading range, for both the rotor and stator.

It is important to note that when making rotor and stator endwinding temperature comparisons, all available endwinding experimental thermocouples are averaged for the DE and NDE areas separately and used in the validation process.

		Actual kW load tested:	18.38 kW
MySolver Node	MySolver (°C)	Experimental (°C)	Error (°C)
a1	50.28	53.71	- 3.43
b1	51.34	55.06	- 3.72
c1	53.05	56.88	- 3.83
d1	51.25	47.99	+ 3.26
e1	56.46	52.25	+ 4.21
a3	50.05	51.58	- 1.53
b3	51.06	55.61	- 4.55
c3	52.80	53.47	- 0.67
Average (°C)	52.04	53.32	- 1.28

Table 8.8: *18 kW loading MySolver rotor thermal network validation.*

		Actual kW load tested:	18.38 kW
MySolver Node	MySolver (°C)	Experimental (°C)	Error (°C)
a1	66.83	65.02	+ 1.81
b1	67.83	68.74	- 0.91
c1	69.20	71.56	- 2.36
d1	69.10	71.98	- 2.88
e1	71.92	77.41	- 5.49
a2	71.05	65.02	+ 6.03
b2	72.31	68.74	+ 3.57
c2	72.70	71.56	+ 1.14
Average (°C)	70.12	70.00	+ 0.12

Table 8.9: *18 kW loading MySolver stator thermal network validation.*

Loading (kW)	MySolver (°C)	Experimental (°C)	Error (°C)
5.25	19.32	19.17	+ 0.15
8.20	22.87	22.88	- 0.01
10.28	26.25	26.13	+ 0.12
12.26	31.28	31.27	+ 0.01
14.17	35.61	36.17	- 0.56
16.52	44.35	45.32	- 0.97
18.38	52.04	53.32	- 1.28
20.39	60.11	61.74	- 1.63

Table 8.10: *Rotor MySolver thermal network steady-state average temperature validation.*

Loading (kW)	MySolver (°C)	Experimental (°C)	Error (°C)
5.25	18.59	18.46	+ 0.13
8.20	24.07	23.80	+ 0.27
10.28	29.66	28.99	+ 0.67
12.26	35.52	35.35	+ 0.17
14.17	44.42	43.49	+ 0.93
16.52	56.73	58.11	- 1.38
18.38	70.12	70.00	+ 0.12
20.39	86.68	86.80	- 0.12

Table 8.11: *Stator MySolver thermal network steady-state average temperature validation.*

As shown in Tables 8.8 to 8.11, a very acceptable level of agreement is achieved between MySolver and experimental results. For the complete kW loading range analysed, the vast majority of the nodal comparisons are within ± 5 °C, with only 6 of the 128 nodal comparisons being slightly over this limit. Rotor MySolver thermal predictions have an error of ± 1.96 °C on average, whilst the stator has an error of ± 2.27 °C, giving an overall °C error of ± 2.12 °C. Five out of the six of the temperature comparisons over ± 5 °C relate to the modelling of the stator overhang section, which is modelled slightly less accurately by the MySolver modelling tool. As shown in the stator winding overhang results for the stator in this chapter, this is a very difficult area to model accurately with a lumped parameter network, given the wide range of temperatures recorded by the overhang thermocouples and the uneven airflow through the machine. With regards to modelling the rotor, the endwinding segment is also the hardest area to achieve a high accuracy in, due to the irregular airflow mentioned.

Figures 8.22 and 8.23 show good correlation between MySolver and the experimental results across the whole ranges of machine loads considered.

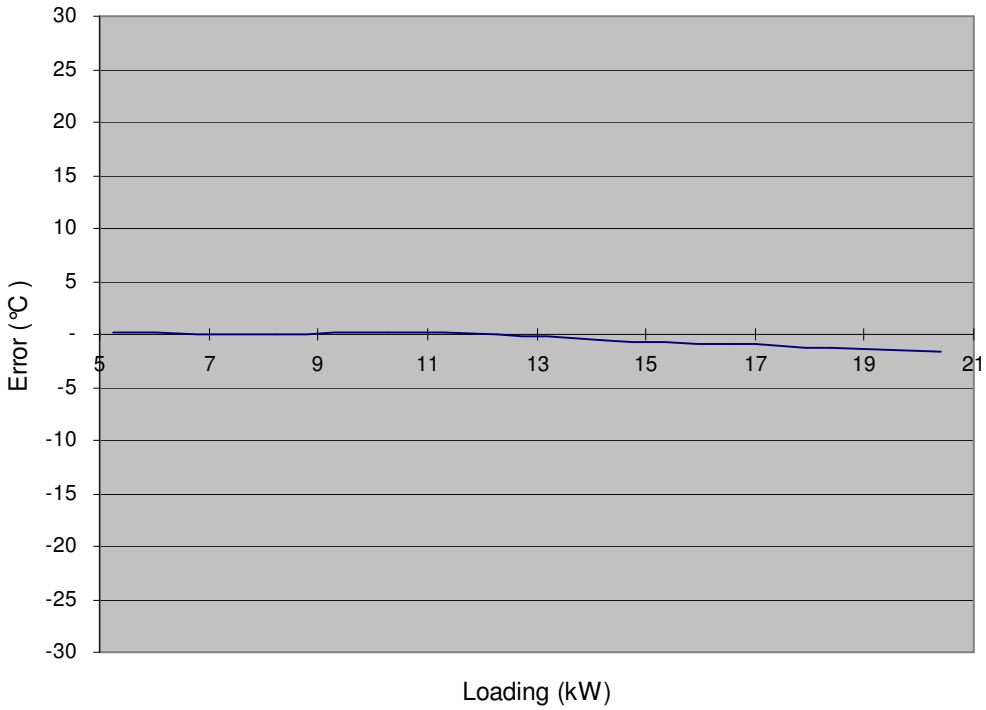

Figure 8.22: *MySolver steady-state rotor lumped parameter network average °C error.*

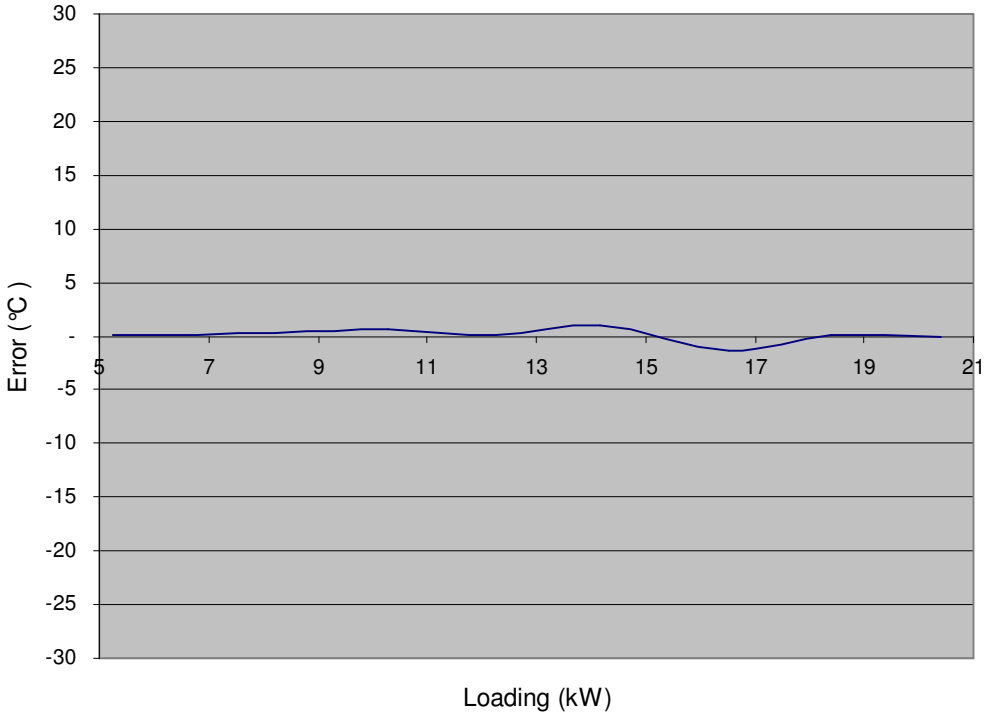

Figure 8.23: *MySolver steady-state stator lumped parameter network average °C error.*

8.2.2 Transient MySolver Performance Validation

In order to evaluate the transient performance of MySolver, temperature comparisons are made between MySolver predictions and experimental data 30 minutes into each heat-run. The results obtained are summarised for the rotor and stator in Tables 8.12 and 8.13 respectively. Results are graphed in Figures 8.24 and 8.25. Furthermore, to compare predictions along the complete heat up curve, a full transient graphical comparison between MySolver predictions and experimental data for the 18 kW loading is presented in Figures 8.26 to 8.31. Full transient results for the complete kW loading range are collected in Appendix G.

Loading (kW)	MySolver (°C)	Experimental (°C)	Error (°C)
5.25	14.51	15.15	- 0.64
8.20	17.36	17.62	- 0.26
10.28	20.06	20.02	+ 0.04
12.26	24.14	24.51	- 0.37
14.17	27.57	28.19	- 0.62
16.52	34.33	34.03	+ 0.30
18.38	40.42	39.70	+ 0.72
20.39	46.77	46.20	+ 0.57

Table 8.12: *Rotor MySolver thermal network transient average temperature validation.*

Loading (kW)	MySolver (°C)	Experimental (°C)	Error (°C)
5.25	15.87	15.65	+ 0.22
8.20	20.85	20.59	+ 0.26
10.28	25.70	25.30	+ 0.40
12.26	31.27	31.39	- 0.12
14.17	39.41	38.53	+ 0.88
16.52	50.20	50.72	- 0.52
18.38	62.39	60.58	+ 1.81
20.39	76.86	74.66	+ 2.20

Table 8.13: *Stator MySolver thermal network transient average temperature validation.*

Across the complete kW loading range considered, an overall average error of ± 1.92 °C is obtained for these temperature comparisons. In this case, the rotor results show an average ± 1.72 °C error (± 1.96 °C at steady-state), whilst the stator results show a ± 2.12 °C average error (± 2.27 °C at steady-state). These results give confidence in

the use of MySolver across the complete kW loading range, in both steady-state and transient mode operation.

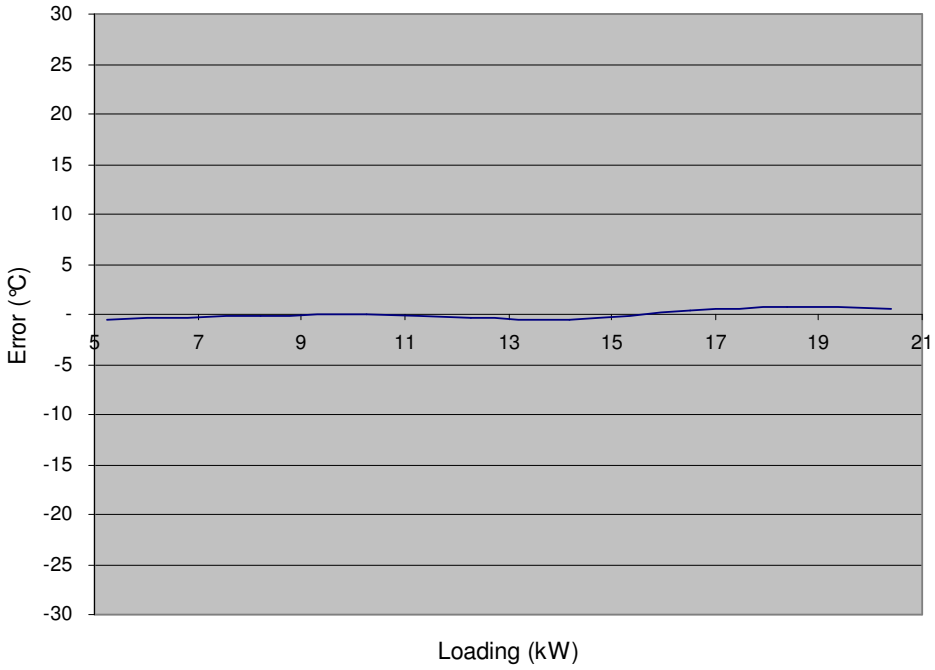

Figure 8.24: *MySolver transient rotor lumped parameter network average °C error.*

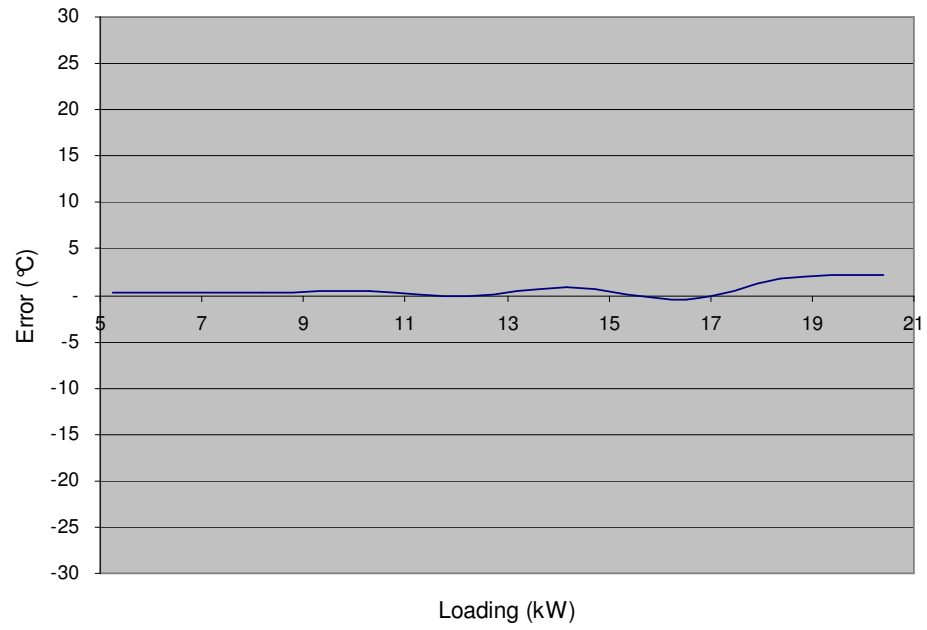

Figure 8.25: *MySolver transient stator lumped parameter network average °C error.*

Figures 8.26 to 8.31 display the rotor and stator complete heat curve temperature comparison between MySolver predictions and experimental data for the 18 kW heat-run performed.

With respect to the rotor, as shown in Figure 8.26, a very good average temperature agreement is achieved by MySolver, in comparison with experimental results. As shown in Table 8.8, an acceptable rotor steady-state temperature difference of 1.28 °C results between experimental and calculated results, but also a close correlation is observed for the 2.5 hours monitored. However, shown in Figure 8.27, MySolver's rotor node b1 transient thermal variation has a final discrepancy of 3.72 °C, but the agreement along the heat curve is sufficiently close. Also, shown in Figure 8.28, are the results for MySolver node a3 at the other end and at a different depth within the rotor winding analysed and, as shown, good results are also obtained.

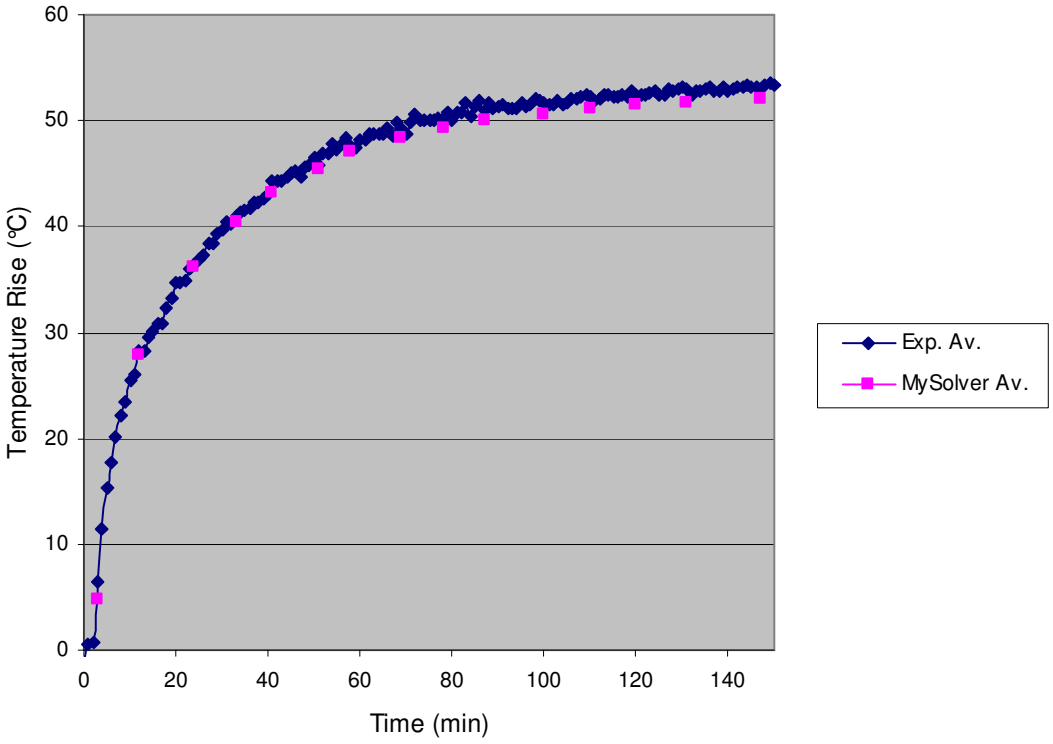

Figure 8.26: *18 kW heat-run rotor average temperature rise complete transient comparison.*

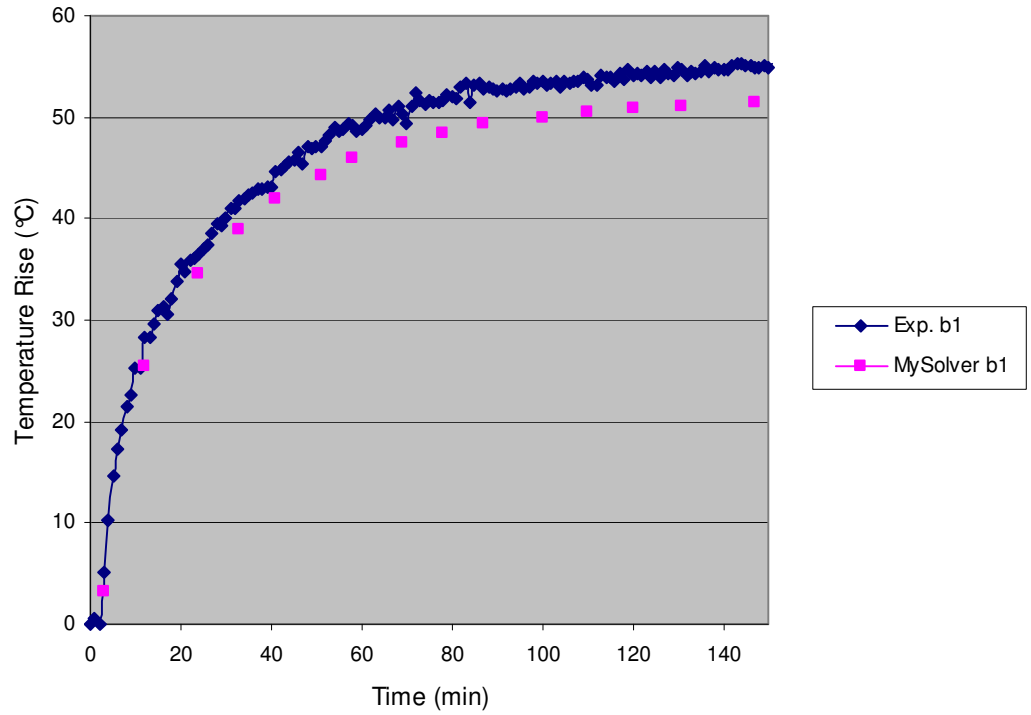

Figure 8.27: *18 kW heat-run rotor b1 node temperature rise complete transient comparison.*

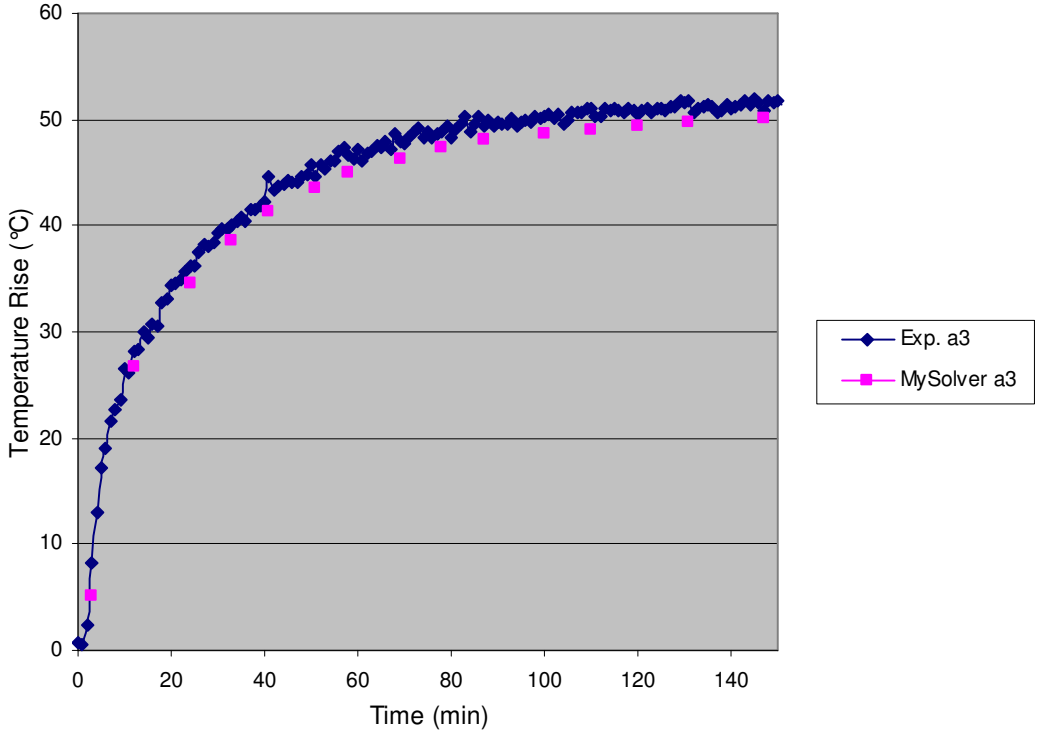

Figure 8.28: *18 kW heat-run rotor a3 node temperature rise complete transient comparison.*

Figures 8.29 to 8.31 focus on the stator 18 kW heat-run transient agreement. As with the rotor results, a very good level of agreement is presented, both for the average temperature predictions computed and for the individual node results presented. The important aspect is that transient results do not reveal any simulation problems that are undetected by the steady-state thermal study. The stator transient simulations presented show an agreement level on a par with the steady-state results obtained, presented in Table 8.13.

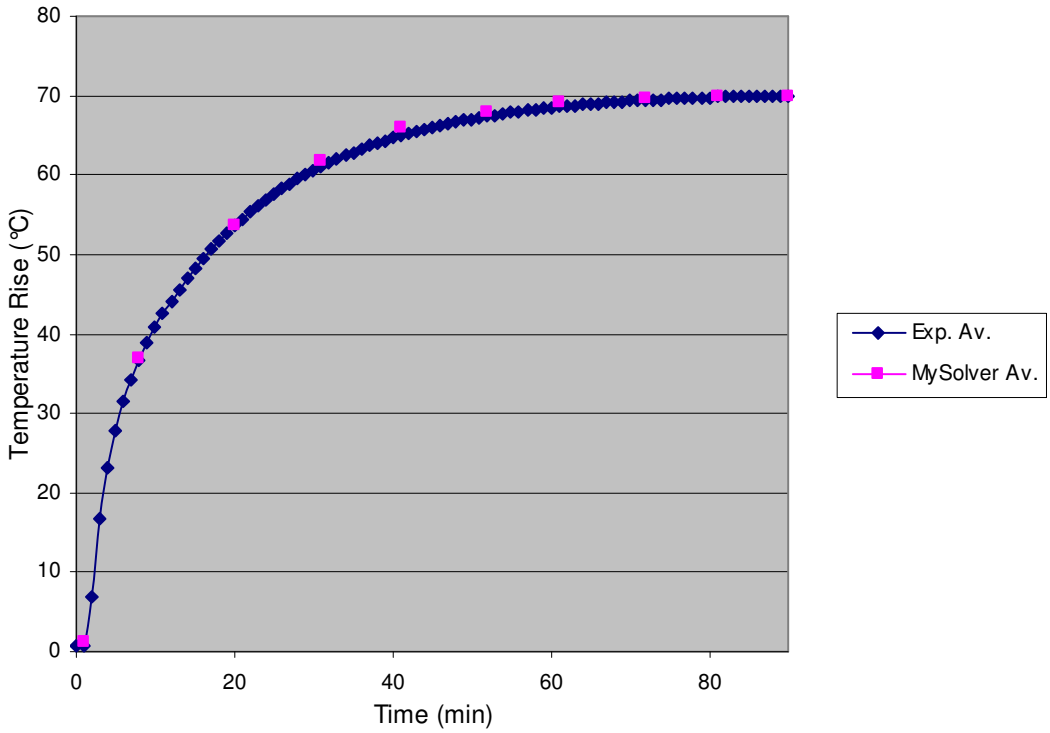

Figure 8.29: *18 kW heat-run stator average temperature rise complete transient comparison.*

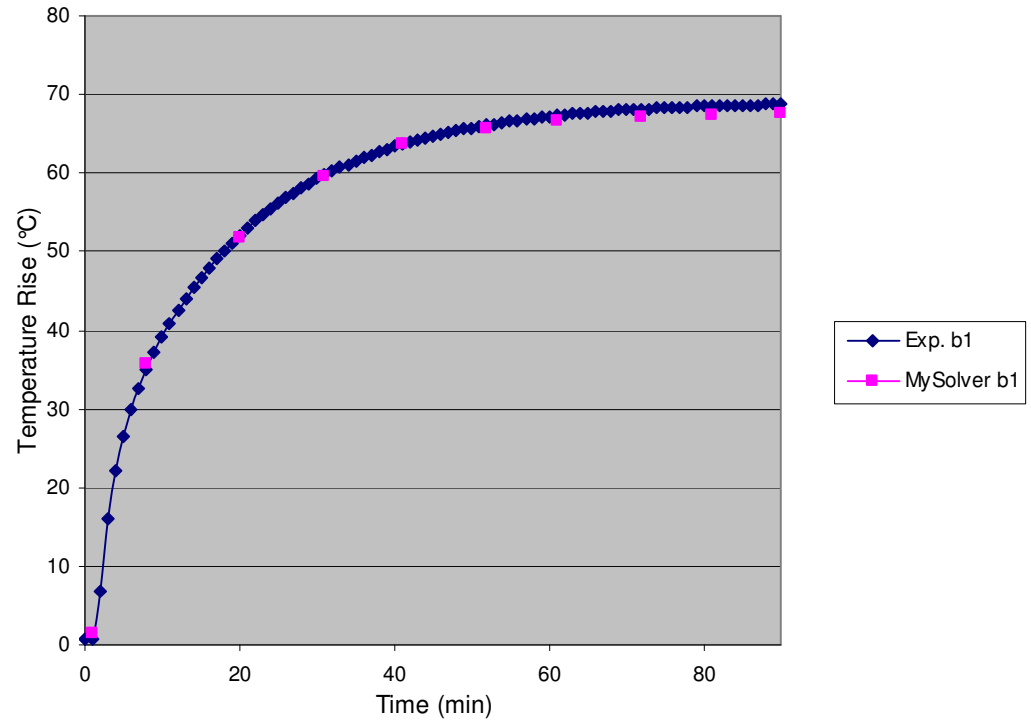

Figure 8.30: *18 kW heat-run stator b1 temperature rise complete transient comparison.*

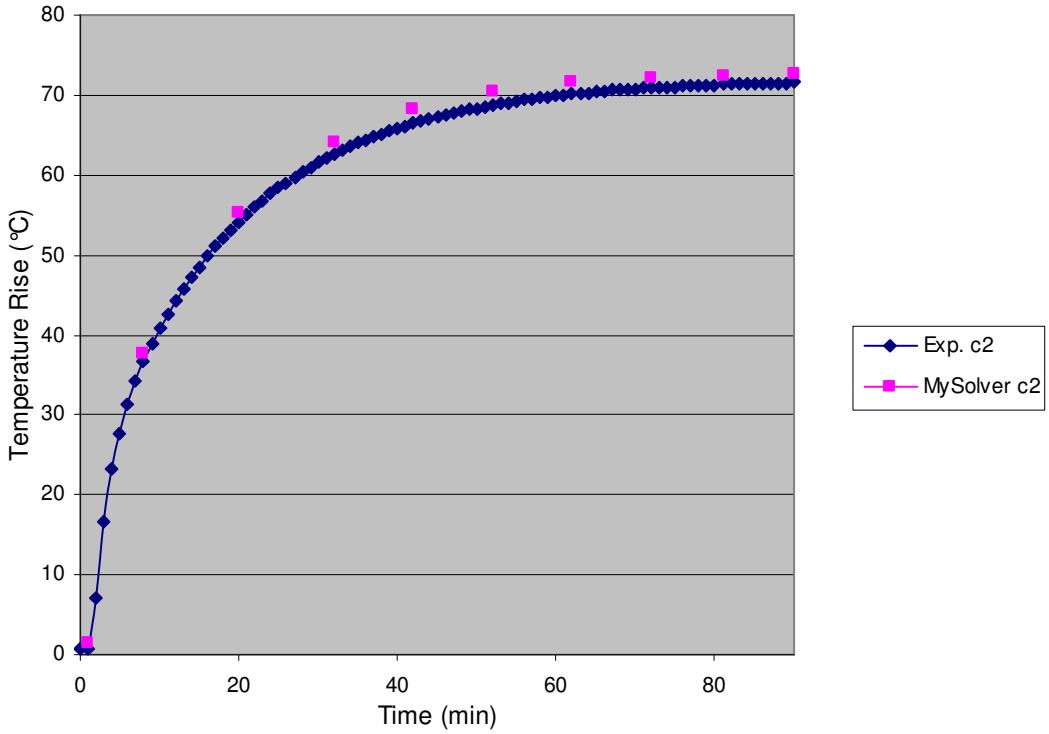

Figure 8.31: *18 kW heat-run stator c2 temperature rise complete transient comparison.*

8.2.3 Duty-Cycle Performance Validation

Duty-cycle simulations are also carried out and MySolver temperature predictions compared with experimentally obtained data. Three-step duty-cycle tests are performed, running three kW loadings for periods of 45 minutes. These simulations are very important in order to evaluate MySolver transient performance. An inaccurate transient operation results in errors accumulating along the different stages of the duty-cycle simulation, resulting in an accentuated final error. On the other hand, if the transient operation of the MySolver models is correct and the model time constants and structures are accurate, final duty cycle temperatures will be in agreement with the standard heat-run steady-state results presented in this chapter. The results for the 5 kW-10 kW-16 kW, the 16 kW-10 kW-5 kW and the 12 kW-5 kW-10 kW duty cycle tests are presented in this section. Two additional duty-cycle test results (5 kW-12 kW-10 kW and 12 kW-8 kW -12 kW) are included in Appendix I.

5 kW – 10 kW – 16 kW Duty Cycle

Results for the rotor are presented in Table 8.14 and for the stator in Table 8.15. Both sets of results are illustrated in Figure 8.32. As shown, good agreement between MySolver with experimental data is recorded for both the rotor and stator thermal predictions throughout the complete duty-cycle. No significant differences between the presented duty-cycle results and the previously analysed steady-state and transient thermal modelling results are observed.

Rotor Temperature Rise (°C)				
Time (m)	Loading (kW)	MySolver	Experimental	Error (°C)
45	5.25	16.16	16.59	- 0.43
90	10.31	24.37	25.46	- 1.09
135	16.39	41.39	40.99	+ 0.40

Table 8.14: *5kW-10kW-16kW duty-cycle MySolver rotor validation results.*

Stator Temperature Rise (°C)				
Time (m)	Loading (kW)	MySolver	Experimental	Error (°C)
45	5.25	17.62	17.15	+ 0.47
90	10.31	29.17	29.02	+ 0.15
135	16.39	55.69	55.14	+ 0.55

Table 8.15: *5kW-10kW-16kW duty-cycle MySolver stator validation results.*

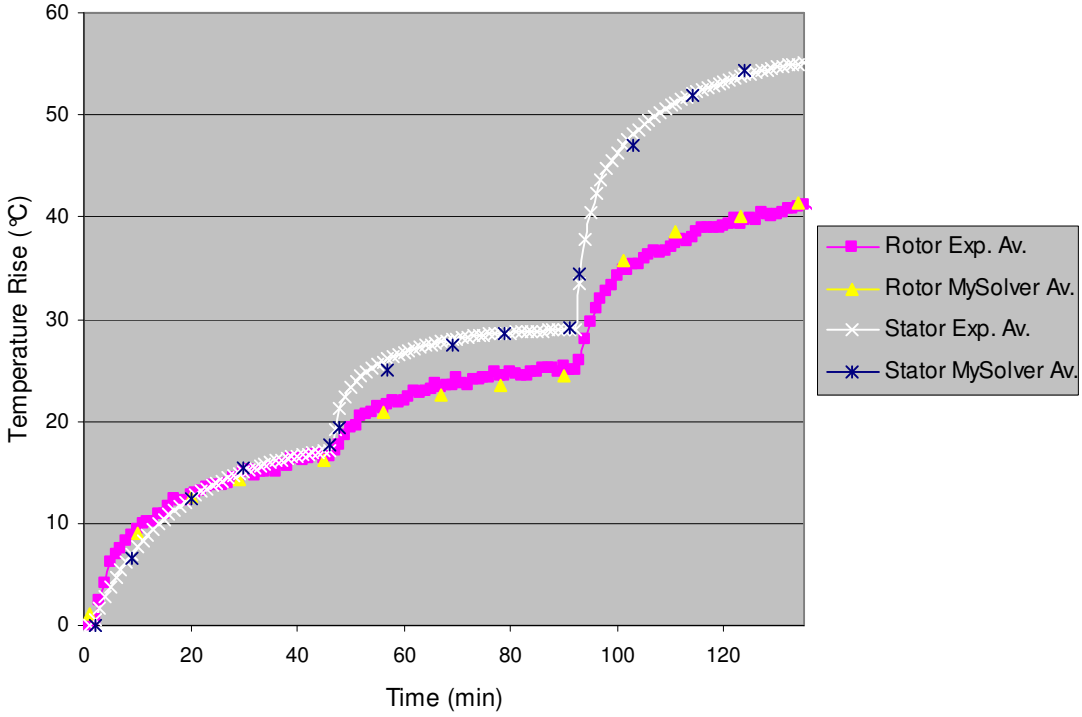

Figure 8.32: *5kW-10kW-16kW duty-cycle MySolver rotor and stator validation results.*

16 kW – 10 kW – 5 kW Duty Cycle

The results for the 16 kW-10 kW-5 kW duty-cycle test are presented in Tables 8.16 and 8.17 and illustrated in Figure 8.33. As with the previous duty-cycle run presented, a good agreement between MySolver predictions and experimental data is observed.

Rotor Temperature Rise (°C)				
Time (m)	Loading (kW)	MySolver	Experimental	Error (°C)
45	16.42	37.76	37.79	- 0.03
90	10.29	26.61	26.80	- 0.19
135	5.24	20.38	20.09	+ 0.29

Table 8.16: *16kW-10kW-5kW duty-cycle MySolver rotor validation results.*

Stator Temperature Rise (°C)				
Time (m)	Loading (kW)	MySolver	Experimental	Error (°C)
45	16.42	54.41	53.54	+ 0.87
90	10.29	30.43	30.46	- 0.03
135	5.24	19.01	18.35	+ 0.66

Table 8.17: *16kW-10kW-5kW duty-cycle MySolver stator validation results.*

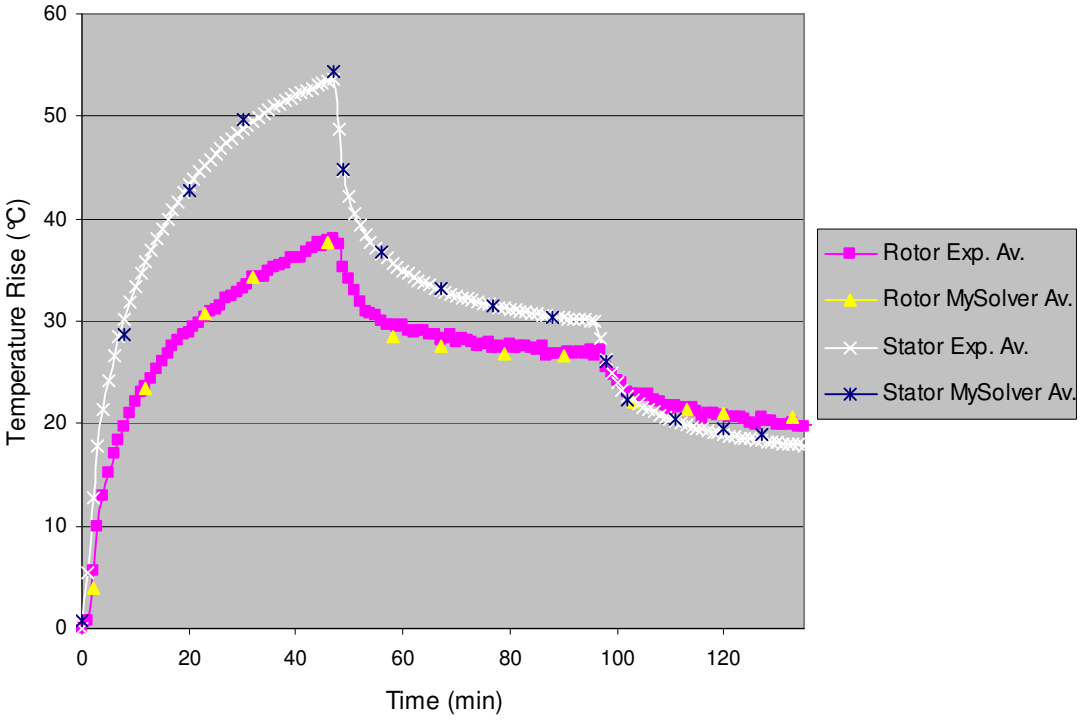

Figure 8.33: *16kW-10kW-5kW duty-cycle MySolver rotor and stator validation results.*

12 kW – 5 kW – 10 kW Duty Cycle

Finally, the results for the 12 kW-5 kW-10 kW duty-cycle test are presented in Tables 8.18 and 8.19 and illustrated in Figure 8.34.

Rotor Temperature Rise (°C)				
Time (m)	Loading (kW)	MySolver	Experimental	Error (°C)
45	12.28	26.45	26.68	- 0.23
90	5.25	19.40	19.31	+ 0.09
135	10.30	25.39	25.42	+ 0.03

Table 8.18: *12kW-5kW-10kW duty-cycle MySolver rotor validation results.*

Stator Temperature Rise (°C)				
Time (m)	Loading (kW)	MySolver	Experimental	Error (°C)
45	12.28	33.90	34.66	- 0.76
90	5.25	19.10	19.08	+ 0.02
135	10.30	29.24	28.58	+ 0.66

Table 8.19: *12kW-5kW-10kW duty-cycle MySolver stator validation results.*

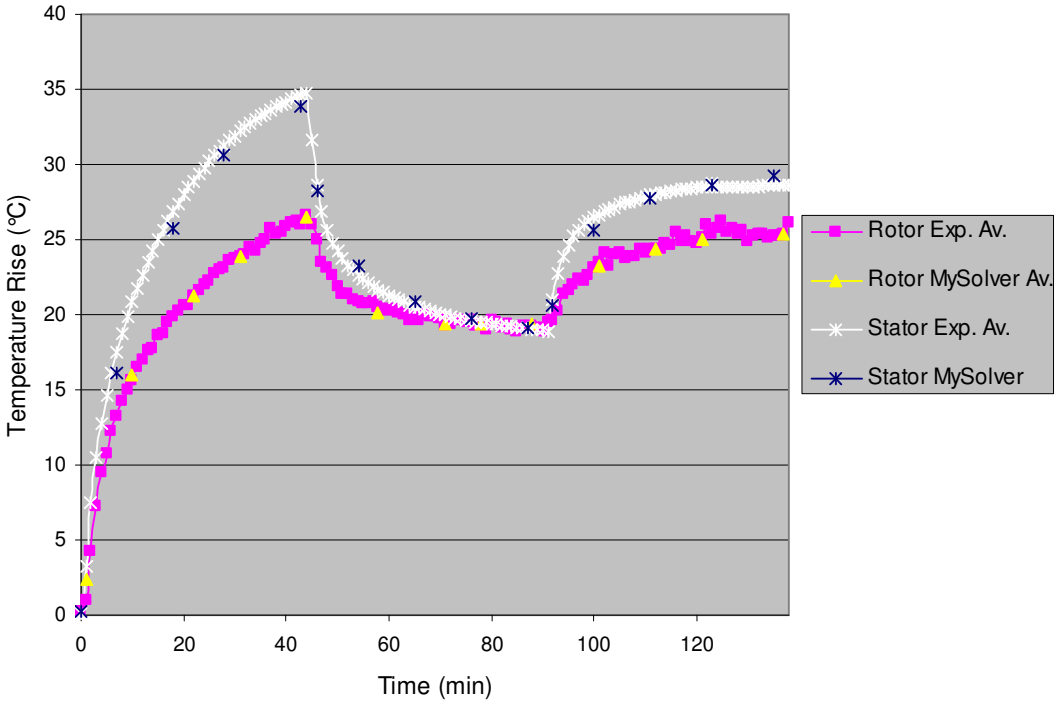

Figure 8.34: *12kW-5kW-10kW duty-cycle MySolver rotor and stator validation results.*

8.3 Chapter Summary

The thermal results obtained during the experimental stage have been presented in this chapter. The full thermal characterisation of the Cummins Generator Technologies BCI184E machine is presented, using the multiple thermocouples placed within the rotor and stator windings and around the external sections of the generator. The stator winding overhang is identified as being the hottest section of the machine, with the non-symmetrical natural of the rotor thermal distribution highlighted. The through ventilating airflow cooling implications and its effect on the heat transfer mechanisms of the different machine segments are discussed and its effect of the thermal distribution across these segments presented.

The application of the thermal steady-state and transient results obtained to validate the MySolver thermal models presented in Chapter 3 is covered. A very close agreement is observed between the two sets of results, with the majority of nodal temperature comparisons under ± 5 °C absolute temperature error. As presented, this is the case for steady-state, transient and for the duty-cycle simulations executed. Full details on how the validation process is carried out are covered in this chapter. Concluding the analysis of the results is the identification of the MySolver modelling package as an adequate synchronous machine thermal modelling tool, with satisfactory results exhibited throughout all validated simulations covered.

CHAPTER 9

Evaluation and Discussion

9.1 Introduction

The performance of the newly developed lumped parameter thermal modelling tool, MySolver, is analysed in Chapter 8, with both steady-state and transient results presented and examined. The results established in the mentioned chapter and all other relevant aspects examined in this thesis are brought together in this chapter and assessed collectively, with the objective of evaluating lumped parameter thermal modelling as an appropriate synchronous generator thermal modelling tool, highlighting and discussing its current weaknesses.

9.2 Lumped Parameter Thermal Modelling Evaluation

The results presented in Section 8.1 illustrate the experimentally obtained, real thermal characteristics of a synchronous generator for a wide range of loading scenarios. In Section 8.2, these results are subsequently utilised to evaluate in detail MySolver's performance as a thermal modelling tool, with thermocouple readings compared with lumped parameter network nodal temperature predictions. In this section, specific aspects of MySolver's lumped parameter thermal modelling technique for particular machine parts are discussed and results are evaluated. These help to reach the conclusions on MySolver's performance, as an electrical machine thermal modelling tool, presented in the concluding thesis Chapter 10. Evaluations made in this chapter mainly utilise the steady-state temperature results, but the issues raised apply to lumped parameter transient thermal modelling in an equal manner.

It should be noted that, from the experimental validation results in Chapter 8, problematic aspects needing further evaluating and discussion are covered in this section. However, detailed analysis of the CGT synchronous generator's temperature distribution and MySolver's full thermal prediction performance, particularly those showing a good agreement, are only covered in Chapters 7 and 8, and not in this chapter.

It is important to note that the conclusions drawn in this thesis are based on MySolver's ability to model synchronous generators accurately. As explained in this thesis, the lumped parameter thermal modelling principles presented are applicable to other machine types, from other manufacturers, and MySolver has the flexibility to accommodate the geometric, power loss and airflow related alterations required for this.

9.2.1 Uneven Airflow Effects on Lumped Parameter Thermal Modelling

A very interesting result affecting lumped parameter thermal modelling is shown in Table 8.2 (Section 8.1.1), where the uneven nature of the airflow cooling the electrical machine investigated is apparent. The stator overhangs results in Table 8.2 show significantly different steady-state temperatures along the radial circumference of the stator lamination, clearly highlighting the presence of through ventilating airflow obstructions and uneven cooling airflow paths along the axial length of the electrical machine. For example, for the 18.38 kW loading test an average drive-end stator winding overhang temperature rise of 77.4 °C is recorded, but individual thermocouple readings of 66.7 °C and 90.4 °C are monitored, illustrating the range of resulting temperatures mentioned. This behaviour is observed for the complete range of kW loadings considered during the experimental stage. In a similar way, such a disturbed airflow pattern will also be affecting the rotor endwindings for the same reasons, complicating its thermal modelling equally.

The findings presented in Table 8.2 indicate that the stator winding overhangs and rotor endwinding are the hardest machine parts to model using MySolver, since

clearly severe complications exist when trying to model these sections utilising a lumped parameter thermal network. As a result, as shown in Tables 8.8 and 8.9 (Section 8.2.1), MySolver in not very accurate when predicting average temperatures for these electrical machine segments, over-predicting rotor endwinding temperatures and under-predicting stator overhang temperatures, although mostly of these temperature errors are under ± 5 °C (see Appendix G). The problem described is particularly significant when modelling industry standard electrical machines that are not fitted with winding thermocouples, which can serve as a calibrating device to account for the previously mentioned unknown uneven airflow paths. Even if such thermal sensors are present in the windings, a complicated calibrating process to achieve a high winding overhang/endwinding accuracy level would defeat the objective of a lumped parameter thermal modelling tool, where a user friendly quick feedback package is desired. It must be noted that the results extracted from Section 8.1 apply exclusively to the CGT BCI184E specially modified prototype alternator investigated in this thesis. Therefore, it is probable that this obvious uneven airflow through this particular synchronous machine is not as significant in other electrical machines, removing or reducing the problems associated with modelling the stator winding overhangs and rotor endwinding machine parts using lumped parameter thermal networks.

Evaluating the relevant results obtained and the discussion presented in this section, it is recommended for the current lumped parameter thermal network stator winding overhangs and rotor endwinding temperature predictions to include a safety margin which, as the selected results at the start of this section show, might need to be as high as approximately ± 10 % of the computed temperature, to account for the highest and lowest temperatures presented in Table 8.2. For electrical machines proven to not have through ventilation airflow obstructions this safety margin can be greatly reduced or even completely removed.

9.2.2 Lumped Parameter Thermal Modelling Airflow Aspects

Further to the points raised in the previous section and for the same reasons, issues related to the prediction of the electrical machine to airflow heat transfer coefficients should be considered. As presented in Section 3.6, the required heat transfer coefficients are calculated utilising well established correlations and data provided by the synchronous machine supplier. Unfortunately, these heat transfer coefficients do not account for the uneven airflow that exists and will, therefore, have an error associated with them. As outlined in the future work section in Chapter 10, further work on these through ventilating airflow paths will provide the necessary insight to compute the synchronous machine airflow heat transfer coefficients more accurately and remove any adjusting coefficients, such as the X_{hc} coefficient presented in Section 3.6.

9.2.3 Electrical Machine Core Length Segments Thermal Modelling

The uneven airflow issue mentioned in the previous sections in this chapter will inevitably have an effect on all electrical machine segment temperatures and their modelling. This is highlighted by the results shown in Table 8.4 (Section 8.1.1), where stator winding slot temperatures at four equally spaced points along the circumference of the stator lamination at the middle of the machine's core length, show a range of steady-state temperatures. Even though the temperature range recorded is considerably smaller than that mentioned in Section 9.2.1, its effects will still have an impact on the machine thermal modelling and should be noted. Again, these results are attributed to the irregular airflow along the machine's axial length, resulting in uneven stator lamination and winding cooling efficiencies. Such issues will also affect rotor lamination and winding temperatures. This effect is significantly less important in these sections along the core length, since the exposure to the airflow is smaller and, hence, its effect is reduced.

From the results in Tables 8.8 and 8.9 (Section 8.2.1), and Appendix G, an acceptable agreement is observed between experimental data and lumped parameter

thermal modelling temperature results for the mentioned core length nodes. For the wide load range considered the error is less than ± 5 °C, indicating an acceptable agreement. For this reason, other than the suggested measures described in the previous sections, no other modifications are recommended to the lumped parameter thermal modelling technique.

9.2.4 Modelling of the Rotor's Non-Symmetrical Temperature Distribution

As shown by the finite element analysis simulations presented in Chapter 4 and supported by the experimental results in Table 8.5 and Figure 8.5, in Section 8.1.1, a non-symmetrical temperature distribution exists across the rotor during the operation of a synchronous machine. As explained in Section 8.1.1 this is due to the fact that losses, mainly iron losses as reasoned in Chapter 4, are not generated uniformly across the rotor lamination and also due to the better cooling efficiency experienced by the leading half of the rotor pole. Thanks to the use of LCCs, developed in Chapter 4, MySolver correctly models the non-symmetrical nature of the temperature distribution across the rotor. As shown in Table 8.8, MySolver correctly predicts the lagging half of the rotor pole winding at a higher temperature than the leading half of the rotor pole winding. Furthermore, lumped parameter thermal network temperature predictions for rotor nodes four and six, shown in Figure 3.3 (Section 3.3), also agree with the mentioned non-symmetrical temperature distribution.

As shown in Table 8.8, the difference in temperature between the leading and lagging rotor poles halves predicted by MySolver is smaller than that obtained experimentally via thermocouples. This is again linked to airflow modelling deficiencies, which have already been identified as the main area where further work is required. A better detailed understanding of exactly how much better the cooling experienced by the leading rotor pole half with respect to the lagging rotor pole half, would allow the heat transfer coefficients utilised by MySolver to account for this and, hence, improve the temperature predictions generated by the lumped parameter thermal models.

9.2.5 Armature Winding Double Layer Lumped Parameter Thermal Modelling

As the results presented in Table 8.9 (Section 8.2.1) show, MySolver appears to struggle modelling the temperature difference that might exist between the two stator winding layers implemented in the CGT synchronous generator modelled. The lack of two thermocouples, one within each of the two stator winding layers, makes a true temperature comparison between the two winding temperatures predicted by MySolver and experimental readings not possible. This temperature comparison can only be made using the thermocouple placed between the two stator winding layers. For this reason, MySolver seems to be slightly under-predicting the temperature of the lower stator winding layer and over-predicting the upper winding layer, but that might not be the case, or not by the margin shown in Table 8.9, since the comparison is made against a thermocouple reading taken between the two stator winding layers. Hence, this is simply an area where, if required, further testing could be done with the addition of a second stator winding thermocouple and should not necessarily be seen as a weakness in the MySolver thermal modelling tool.

9.2.6 Lumped Parameter Thermal Modelling Machine Average Temperatures

The results presented in Tables 8.10 and 8.11 (Section 8.2.1) display the rotor and stator average steady-state temperature comparisons between MySolver predictions and experimentally obtained measurements. These are important results as they illustrate the overall effectiveness of MySolver when thermal modelling synchronous generators. Unless a generator needs to be pushed to its thermal limit, machine average temperatures can be utilised to determine if a machine is thermally appropriate for a particular task. An electrical machine supplier can utilise this information to provide quick reliable customer feedback on specific operational scenarios raised by the machine user. For specific, specially sensitive, electrical machines or particularly delicate operational conditions, machine manufacturers can choose to implement safety margins on top of MySolver temperature predictions.

Average temperature predictions generated by MySolver are within ± 3 °C of the measured temperatures, which indicates that MySolver is an ideal tool to obtain the described thermal information. As shown in Figures 8.22 and 8.23 for steady-state temperature predictions and in Figures 8.24 and 8.25 for transient simulations, an acceptably uniform agreement is observed throughout the complete kW loading range considered.

9.3 Possible Thermal Modelling Alternatives

As explained in Chapter 2, there are a number of possible thermal modelling techniques that can be considered in order to predict the thermal characteristics of a synchronous generator [14]. The analytical approach, utilising lumped parameter thermal models, has been evaluated in this thesis with positive results, but the problems faced, presented in this thesis and overviewed in this chapter, could be solved by the use of a numerical analysis tool. As reasoned in the pros and cons associated with analytical and numerical thermal analysis methods in Chapter 2, introducing a numerical analysis step into the thermal modelling procedure would eliminate the greatest benefit associated with lumped parameter thermal modelling; the quick computing time. Furthermore, this would significantly complicate the setup of the thermal models, their processing and the analysis of the eventual results. Nevertheless, for the particular electrical machine analysed in this thesis and given the previously unknown uneven nature of the through ventilating airflow, numerical methods such as CFD [7] & [98] could be a very appropriate addition to the thermal modelling process, if permitted by the thermal modelling process time constraints. As explained in the suggested future work in Section 10.3, understanding the airflow along the axial length of a through ventilated synchronous generator and electrical machines in general is imperative, and incorporating this step into the actual thermal modelling package would increase accuracy, without the need of any safety margins, such as that described in Section 9.2.6.

With regards to the development of the MySolver lumped parameter thermal modelling tool presented in this thesis, the addition of a numerical analysis stage in the modelling process is disregarded. The clear objectives in the development of MySolver, stated in Section 1.3, highlight the importance in creating a user friendly thermal modelling tool for non-specialist engineers, which can supply electrical machine customers immediate in situ feedback. Furthermore, as explained in Chapter 6, where MySolver is introduced, the developed thermal tool allows for modifications to the rotor and stator thermal networks to be implemented with ease by simple alterations to the lumped parameter thermal resistive structures. This allows for straightforward improvements to the current thermal models in the future and for the addition of new models representing other electrical machine types of interest. If, on the other hand, a numerical tool was utilised, changes to the model would not be as simple to execute and the computing time would certainly be significantly higher, greatly jeopardising the achievement of the objectives established in Chapter 1.

9.4 MySolver Limitations

The developed lumped parameter thermal analysis tool MySolver has a number of limitations associated to it. Some of these limitations are inherited by the analytical lumped parameter nature of the models used, some are due to areas that require further work and others are due to limitations in the quality of the information supplied by the user to MySolver. Such MySolver limitations are listed in this section.

- The MySolver version described in this thesis does not accommodate an airflow solver. Airflow related heat transfer coefficients, computed in Chapter 3, are obtained using information from an internal Cummins Generator Technologies flow solver. Following the completion of the future airflow work described in Section 10.3 and the development of a synchronous

generator flow solver, MySolver could be transformed into a fully independent thermal modelling package.

- The current version of MySolver presented in this thesis, is limited to three core length radial lumped parameter planes in the axial direction and two additional planes to represent drive-end and non-drive-end endwindings, as presented in Sections 3.5.1 and 3.5.2. The need for a higher discretisation level along the axial length of the electrical machine would require modifications to be made to the thermal models presented.

- Furthermore, on the same lines as the previous limitation, MySolver thermal networks represent the rotor with seven lumped parameter nodes and the stator with five, as shown in Sections 3.3 and 3.4. This nodal discretisation level is sufficient for the current MySolver requirements, but if the user wishes a higher level of accuracy with a more complete electrical machine temperature distribution picture, modifications to the rotor and stator thermal models, to raise the number of lumped parameter rotor and stator nodes, would be required.

- With regards to the actual components of the lumped parameter thermal modelling networks created in this thesis, as explained, thermal resistances are computed utilising reliable machine geometric information and material properties. Even so, there are a number of issues a lumped parameter thermal modelling user should be aware of relating to the accuracy of the thermal network components. The contact between two adjacent machine segments and, therefore, the heat transferred between the two will be dependant on how smooth this contact is. Studies have been performed on this issue [99]-[101], although the exact prediction of these parameters for specific electrical machines will always be complicated. Furthermore, the actual manufacturing process and machine assembly could have an effect on the mentioned heat transfer path, making feedback from experienced machine manufacturers very useful.

- MySolver will never provide the same high level of detail as a numerical analysis package, such as FEA, can supply, as discussed in Chapter 2. This is simply due to the analytical lumped parameter nature of MySolver, and users requiring FEA-like levels of thermal accuracy and detail should select numerical thermal analysis tools for the modelling of electrical machines.

- As is clear from the rotor and stator lumped parameter models developed in Chapter 3, the presented MySolver version is specifically designed to model a synchronous generator. In order to model other machine types that might be of interest, such as a permanent magnet machine, modifications to the mentioned thermal models would be needed.

- Some of the information supplied by the MySolver user, such as the machine material BH curves, thermal material properties, armature and field winding information and the magnitude of some operational losses might have to be unavoidably estimated if experimentally obtained reliable data is not available, as explained in the relevant sections in this thesis. This will inevitably lead to inaccuracies in the final results. As explained in Section 10.3, future versions of MySolver could incorporate extensive thermal related information databases, keeping the estimations made by MySolver users to a minimum.

- As highlighted in the MySolver operation outline in Chapter 6, system analysis tool Portunus is called from the main MySolver Excel spreadsheet to execute the thermal analysis of the machine lumped parameter networks. A limitation exhibited by MySolver at this stage is the requirement to repeat any modifications made on the spreadsheet side of MySolver, where network thermal resistances are computed, a second time in Portunus. This slows down MySolver alterations, but does not compromise the accuracy of the results generated.

- MySolver's results output interface could be seen as a limitation by the user, with respect to other numerical analysis solutions, since results are presented in numerical tables and graphical illustrations. Ideally, the user might prefer MySolver output temperature predictions to be presented in a more user friendly manner, colour coding the resulting temperatures across the diagram of the electrical machine to ease understanding. As pointed out in Section 10.3, this is something to consider in future MySolver versions.

9.5 Synchronous Generator Possible Optimisation Using MySolver

MySolver can be utilised for the optimisation of the electrical machines analysed, once the user is confident that these are being modelled to the desired level of accuracy. Thermally relevant rotor and stator machine geometric parameters, presented in Chapter 3, can be varied within realistic limits to improve thermal performance, reducing component steady-state temperatures by promoting a better heat transfer away from the electrical machine.

Illustrated in Figures 9.1 and 9.2 are possible rotor and stator geometric optimisation areas, with some examples shown in the tables included. These examples demonstrate the effect that alterations to the geometric variables listed, Δ Parameter, have on the overall rotor and stator steady-state temperature, Δ T, for an 18kW loading of the CGT alternator investigated in this thesis. On these lines, MySolver can serve as an optimisation tool for electrical machine designers and also provide immediate thermal related feedback to any related relevant customer queries.

For the optimisation process, a sensitivity analysis stage could be utilised to determine the more thermally relevant machine geometric parameters. Once identified, these could be optimised as outlined in Figures 9.1 and 9.2. For this process, performing thermal modelling exclusively would be incorrect, since both the electrical machine's electromagnetic and structural design would have to be carefully considered and approve any thermal optimisation changes suggested.

Rotor optimisation outline:

Parameter	Δ Parameter	Δ T (°C)
p	+ 10 % - 10 %	- 1.19 + 1.30
y	+ 10 % - 10 %	- 1.20 + 1.29
w	+ 10 % - 10 %	- 0.09 + 0.12
x	+ 10 % - 10 %	- 1.42 + 1.50
z	+ 10 % - 10 %	- 0.51 + 0.56
Core length	+ 10 % - 10 %	- 1.96 + 2.25

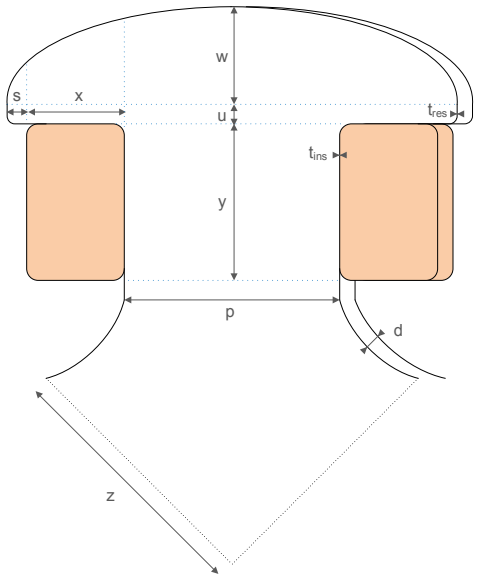

Figure 9.1: *CGT BCI184E alternator rotor optimisation outline illustration.*

Stator optimisation outline:

Parameter	Δ Parameter	Δ T (°C)
u	+ 10 % - 10 %	- 0.07 + 0.07
x	+ 10 % - 10 %	- 0.04 + 0.04

Parameter	Δ Parameter	Δ T (°C)
Lam. inner diameter	+ 10 % - 10 %	- 2.17 + 2.37
Lam. outer diameter	+ 10 % - 10 %	- 4.08 + 4.47

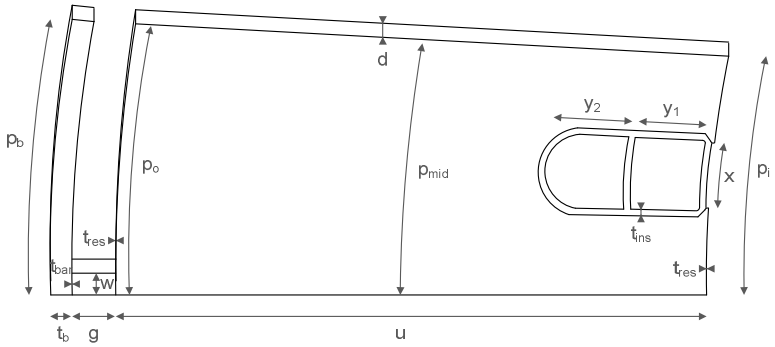

Figure 9.2: *CGT BCI184E alternator stator optimisation outline illustration.*

As shown in Figures 9.1 and 9.2, in general, making machine segments wider in size results in reduced overall temperatures. This is to be expected, since the increase in section size results in more effective thermal paths away from the machine and, hence, better cooling. Clearly, a link between the thermal and electromagnetic design procedures is essential at this stage, since any geometrical optimisation

modifications, such as the ones described in Figures 9.1 and 9.2, need to be electromagnetically validated. Restrictions to the synchronous generator's size imposed by either the manufacturer or the customer might exist, making the thermal optimisation described impossible or greatly limited. Wherever possible and required, such a geometric parameter optimisation process can be carried out in order to reduce overall rotor and stator temperatures with the associated benefits to the electrical machine.

9.6 Further Insight Provided by Additional Experiments

Utilising the test bench developed, presented in Chapter 7, additional experiments are carried out with the objective of supplying further insight on how the thermal characteristics of a synchronous generator are affected by external factors, as opposed to the internal machine aspects such as operational power losses or through ventilating airflow, already covered in this thesis. A more detailed understanding of these issues can be translated into more accurate lumped parameter thermal models. Results on the investigation of the effect of increased generator frame insulation, of the thermal consequences of different moderate ambient temperatures and of the result of a fan modification, are analysed in this section.

9.6.1 Effect of Insulating the Generator Frame on Thermal Distribution

The CGT synchronous generator investigated in this thesis is insulated around the complete circumference of the frame, as shown in Figure 9.3, with the objective of removing all radiation from the machine frame and any heat convection to the surrounding airflow.

Heat-runs are performed under loads of 10 kW and 14 kW, with the steady-state temperatures recorded compared to the non-insulated generator results examined in Chapter 8 and shown in Appendix G. The comparisons between insulated and non-insulated frame thermocouple results are presented in Table 9.1, with the average

temperature rise of all stator/rotor thermocouple readings and the maximum thermocouple reading tabulated.

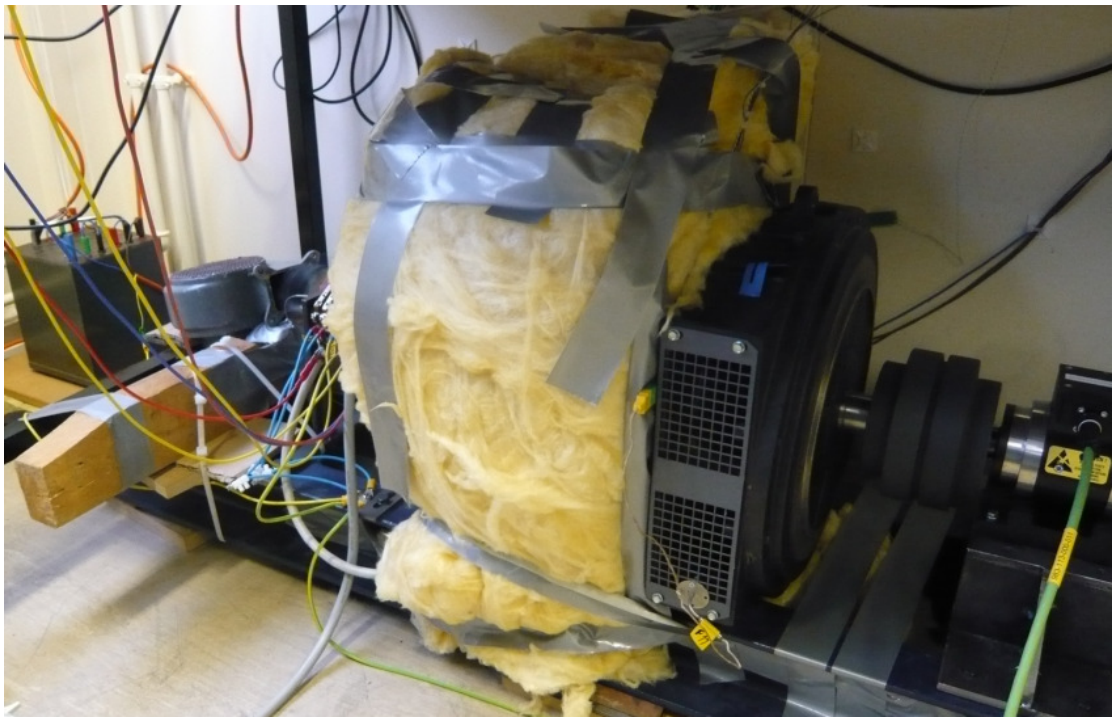

Figure 9.3: *Frame Insulated Cummins Generator Technologies BCI184E Generator.*

Non-insulated frame:	10 kW loading	14 kW loading
Stator average temperature rise (°C)	29.12	44.69
Stator maximum temperature rise (°C)	35.96	55.60
Rotor average temperature rise (°C)	24.97	34.59
Rotor maximum temperature rise (°C)	27.89	38.65

Insulated frame:	10 kW loading	14 kW loading
Stator average temperature rise (°C)	30.07	46.34
Stator maximum temperature rise (°C)	36.45	57.80
Rotor average temperature rise (°C)	25.81	36.37
Rotor maximum temperature rise (°C)	28.48	40.09

Table 9.1: *Non-insulated and insulated frame steady-state temperature rise comparison.*

As shown in Table 9.1, there is not a significant difference in the average and maximum temperature rise values between the insulated and non-insulated frame scenarios considered. This is to be expected, since the majority of heat transfer from

the CGT alternator tested takes place via the through ventilating airflow. This is up to 95 % according to the electrical machine manufacturer. The difference in temperatures observed in Table 9.1 could simply be due to the inevitable differences that exist between two practical experiments, where 100 % agreement is impossible, and not due to the frame insulation wrapping the frame of the generator. Therefore, with regards to the lumped parameter modelling performed by MySolver, this highlights the importance of simulating the machine to airflow heat transfer that takes place inside the frame and reduces the significance of the frame to ambient heat exchange that exists. For electrical machines that are not through ventilated, the removal of the frame to surrounding air heat transfer mechanisms will have a more significant effect on machine temperatures and other results would be obtained.

9.6.2 Effect of Ambient Temperature on Machine Thermal Distribution

Three heat-runs supplying a 12 kW load are executed at three different ambient temperatures, at a cold 10 °C, at 20 °C and at a warm 30 °C, investigating the possible effect that this might have on the synchronous generator's temperature rise and the implications this could have on the lumped parameter thermal modelling. Machine material properties could be sensitive to the temperature range tested, altering operational machine losses, and the study performed should show this. Results are illustrated in Table 9.2.

'Cold' ambient (~ 10 °C):	12 kW loading
Stator average temperature rise (°C)	35.76
Stator maximum temperature rise (°C)	44.27
Rotor average temperature rise (°C)	28.53
Rotor maximum temperature rise (°C)	31.28

'Normal' ambient (~ 20 °C):	12 kW loading
Stator average temperature rise (°C)	35.69
Stator maximum temperature rise (°C)	44.61
Rotor average temperature rise (°C)	29.26
Rotor maximum temperature rise (°C)	32.68

'Hot' ambient (~ 30 °C):	12 kW loading
Stator average temperature rise (°C)	38.12
Stator maximum temperature rise (°C)	47.12
Rotor average temperature rise (°C)	31.49
Rotor maximum temperature rise (°C)	35.62

Table 9.2: *'Cold', 'normal' and 'hot' ambient steady-state temperature rise comparison.*

As shown in Table 9.2, there are no major differences between the steady-state temperature rise magnitudes monitored for the three ambient temperature scenarios considered. Electrical machine material properties will indeed by affected by ambient temperatures, hence the purpose of the investigation, but the temperature range allowed by the testing installations available does not permit for this to be shown. Therefore, for lumped parameter simulations around the ambient temperatures investigated, not too much importance should be given to determining exact ambient temperatures for the modelling. Testing the generator under extreme temperatures, say ~ 0 °C or ~ + 60 °C, would be of great help to explore the effects on the thermal behaviour of the synchronous generator and is something to consider in future investigations.

9.6.3 Effect of Fan Change on the Generator's Thermal Behaviour

Finally, the original synchronous generator shaft mounted fan is substituted by a newer, smaller, Cummins Generator Technologies fan. The new fan has a slightly reduced outer diameter, with shorter blades, resulting in a diminished through

ventilating airflow and is intended for the latest, smaller sized, CGT synchronous generators. The original and new alternator fans are illustrated in Figure 9.4.

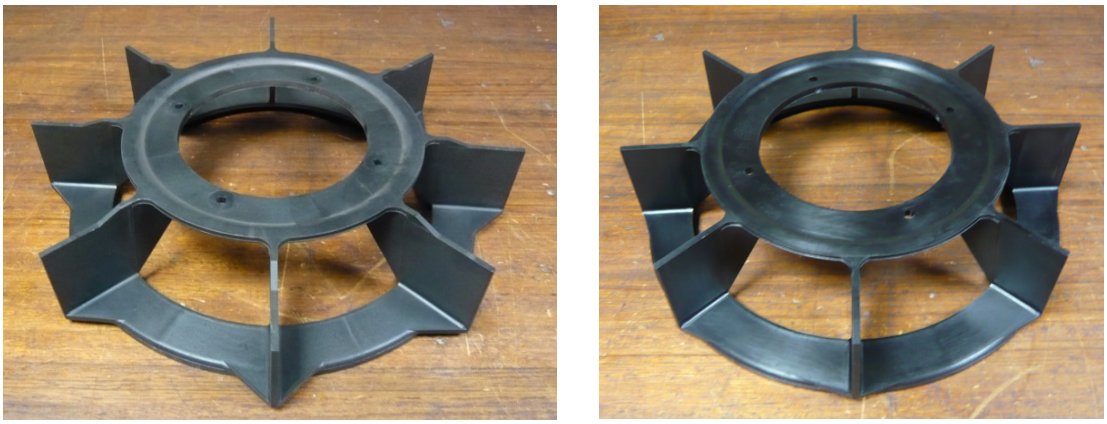

Figure 9.4: *Original (left) and new (right) synchronous generator fans.*

The investigation intends to show the effect that a small alteration to the CGT machine's airflow has on steady-state generator temperatures, for a constant kW loading, and their lumped parameter thermal modelling. Results obtained are presented in Table 9.3.

Original fan:	10 kW loading	14 kW loading
Stator average temperature rise (°C)	29.12	44.69
Stator maximum temperature rise (°C)	35.96	55.60
Rotor average temperature rise (°C)	24.97	34.59
Rotor maximum temperature rise (°C)	27.89	38.65

New fan:	10 kW loading	14 kW loading
Stator average temperature rise (°C)	31.57	48.99
Stator maximum temperature rise (°C)	38.50	60.12
Rotor average temperature rise (°C)	27.40	37.77
Rotor maximum temperature rise (°C)	30.99	42.41

Table 9.3: *Original and new fan steady-state temperature rise comparison.*

As shown in Table 9.3, a slight alteration to the machine's through ventilating airflow has a noticeable effect in the resulting stator and rotor steady-state temperatures. This is a crude investigation, since ideally the original and new airflows should be measured and precise heat transfer coefficients determined as a result. Nevertheless, the investigation highlights the importance of precise through

ventilating airflow modelling and the need for further work in this area, as detailed in Section 10.3, to increase the lumped parameter modelling accuracy of all machine areas exposed to this airflow.

9.7 Chapter Summary

The developed MySolver lumped parameter thermal modelling tool presented in this thesis is evaluated and discussed in this chapter. The main controversial areas, such as the airflow related modelling deficiencies, the non-symmetrical temperature distribution across the radial length of machine sections and limitations to the current lumped parameter models are covered. The limitations listed serve as a way to point out the areas where future work is required and are important information for the MySolver user to be aware of. Furthermore, as shown in this chapter, MySolver can be used to optimise the geometric features of an electrical machine where possible and the approach for this is outlined. To conclude the chapter, additional tests utilising the CGT synchronous generator enhance the understanding of the alternator's thermal behaviour, with frame to surrounding airflow heat exchange, ambient temperature and fan generated airflow implications examined and their relevance to lumped parameter thermal modelling discussed.

CHAPTER 10

Conclusions

10.1 Introduction

Given the wide range of thermal modelling options available to electrical machine designers it is fundamental to objectively reach a conclusion on the true potential that lumped parameter thermal modelling has, given the discussions and evaluations put forward in this thesis. Numerical and analytical thermal modelling techniques offer the user different advantages, which in some cases might leave no room for possible alternatives, if specific requirements need to be met. A numerical analysis tool will never have the computational speed of an analytical solver, whilst an analytical solution will not reach numerical analysis accuracy levels. It is as an everyday thermal modelling package where lumped parameter thermal analysis tools, such as MySolver, can thrive. This is because, in addition to the inherent quick feedback property, lumped parameter thermal models can be further developed to provide reasonably high levels of accuracy by tackling the limitations that exist, as shown in this thesis.

The project detailed in this thesis develops a novel synchronous generator lumped parameter thermal modelling tool, MySolver. Explanations on the development of the rotor and stator thermal networks are given, with examples on the calculation of the network components given. With the objective of making MySolver more accurate, FEA is utilised to predict the distribution of iron losses across the machine laminations and the findings accommodated into the lumped parameter thermal networks. In addition to this, the discretisation levels utilised by MySolver to model the synchronous generator are discussed, with an emphasis on the windings due to their particular sensitivity to this. MySolver's satisfactory operation is verified using

experimentally obtained data from a heavily thermocoupled CGT synchronous generator. In turn, the experimental information provides a good insight into the temperature distribution of the alternator.

The aim of the research performed is to evaluate whether standalone lumped parameter based thermal modelling, as demonstrated by the tool developed in this thesis, MySolver, is an appropriate technique for modelling synchronous generators. Additionally, the work performed further develops areas where additional work is needed and thermal modelling issues that require further progress are identified.

10.2 Conclusion

Lumped parameter thermal modelling is a reliable, precise method to predict synchronous generator component temperatures. Accuracy limitations, which should be clear to the user, still exist compared to numerical analysis techniques, but the objectives established at the start of the project are successfully accomplished using lumped parameter thermal modelling. A user friendly, versatile, quick feedback thermal prediction tool, MySolver, is created and it can go alongside electromagnetic design programs in the designer's work book in an iterative manner. MySolver can consistently serve as a fast consultation instrument for electrical machine designers exploring the thermal limits of new generator designs. It serves as a method to provide electrical machine customer's quick feedback on particular operational scenarios, where thermal considerations might be necessary, making sure that machine thermal limits are not surpassed and the machine's integrity put at risk. Furthermore, where needed, MySolver can be used as a way of improving generator designs to channel operational losses away from the machine more effectively. Geometric machine features can be optimised and, as a consequence, lower temperature generators with extended lifetimes result. These optimised generators can therefore be used for a wider range of operations, increasing customer satisfaction on the generators and relieving stress on the original machine thermal

limits. Therefore, the work presented in this thesis is a significant contribution to the lumped parameter thermal modelling field of study.

The concluding statements in this section are supported by the experimental validation stage performed, confirming an adequate MySolver operation. Specific electrical machine areas where the correlation between simulated and recorded temperatures is not as good are highlighted in the thesis. These relate primarily to the stator winding overhangs and rotor endwindings and are mainly due to the experimentally identified complex non-uniform airflow paths through the synchronous generator. Causes for these limitations, immediate related measures to be taken and further work to solve these deficiencies are covered in this thesis.

Overall, the results provided by MySolver are very good throughout the wide range of operational conditions considered, and average temperatures computed show very good agreement with experimental data. MySolver results are clearly within an error of ± 5 °C for both steady-state and transient simulations. These reliable generator average temperatures serve as a good general indicator for a machine's suitability for a specific task.

Looking ahead into how electrical machine thermal modelling might be performed in the future, the availability of more powerful computing systems that will reduce the disadvantages linked with numerical thermal modelling techniques, might make these more attractive to machine designers. Such techniques have clear accuracy level advantages which might be necessary for some studies, but there will always be a need for quick feedback user friendly thermal modelling methods. A reliable lumped parameter thermal modelling tools, such as MySolver, enhanced by as many numerical analysis studies as possible, holds the key for this.

10.3 Future Work

As mentioned throughout the thesis, there are numerous additional investigations that could be executed in the future to extend the work presented. As shown, the lumped parameter thermal models implemented by MySolver produce good results, but the further work described in this section would increase the modelling accuracy associated with particular machine parts and, hence, the overall MySolver performance.

The need for further airflow related work is clear from the discussions covered in this thesis. The main limitations related to the lumped parameter thermal modelling tool developed are caused by the lack of understanding of the cooling airflow, flowing from the non-drive-end to the drive-end of the machine, making this work the primary target in future investigations. To a certain extent, an even airflow characteristic is assumed across the complete circumference of the through ventilating paths of the synchronous generator investigated. Unfortunately, as the thermocouple experimental results obtained show, this is most certainly not the case and further work is required to add to the work already performed in this area [102]-[104].

Therefore, it would be of great interest to perform a detailed airflow study to fully understand how the air behaves as it travels through the synchronous generator from the non-drive-end to the drive-end of the machine. This could be done both through simulations and with some experimental work to validate the results obtained, much like the thermocouples currently embedded in the synchronous generator verify the resulting temperature predictions generated by MySolver for the different machine parts. Hence, an experimentally validated detailed CFD simulation of the synchronous generator is recommended. As with the FEA work covered in this thesis, detailed machine geometries and reliable component information will be required for this. For the experimental verification, airflow sensors should be placed in as many positions as possible along the airflow paths, both at external locations and inside the generator. In order not to compromise the investigation, these sensors

should be very small in size so that no airflow is impeded. A matrix of airflow sensors could be placed at the generator air inlets and outlets, monitoring how effective these are and potentially highlighting possible improvements in their shape and/or location. To a certain extent, a similar setup could be implemented within the machine, with sensors placed around the circumference of both stator endwindings and around as many lamination and winding segments as realistically possible. From the CFD and experimental information obtained a more accurate representation of the airflow through the synchronous generator could be deduced and consequently more precise convective heat transfer coefficients computed. Potentially, this would lead to novel airflow heat transfer correlations that, once accommodated into the lumped parameter thermal modelling tool, would improve temperature predictions. This would particularly be the case for the machine sections more exposed to the airflow, as explained in this thesis. It is important to note that airflow and therefore the resulting heat transfer coefficients, will be greatly dependent on specific machine geometries and the ventilation system implemented. Hence, it is highly unlikely that findings for a particular machine, from a specific manufacturer, will be transferrable to other machine designs. A number of general conclusions, applying to electrical machines in general, are likely to be drawn from such studies, but how much of the information obtained is exclusive to the particular machine being investigated will only be clear once a wide range of airflow investigations has been carried out.

Another phase of further work that could be considered relates to the user interface and additional operations of the MySolver thermal modelling tool. Currently, in order to truly recreate a specific experimental heat-run, armature and field winding current and voltage magnitudes are input by the user to generate realistic operational power losses. This should always remain a feature of MySolver, but for majority of situations where experimental readings are not available, MySolver could incorporate a parameter estimation feature. Based on the information recorded for a number of electrical machines, MySolver could estimate the necessary armature and field information derived from the machine operational conditions. As a result, this could yield a lumped parameter modelling package a lot more universal and less dependent on user knowledge or information available. Similarly, material databases

could be integrated into MySolver, encapsulating all required machine component information for as wide a range of machine types as possible. This could include material thermal conductivities, densities, specific heat capacities and even a collection of BH curves for possible FEA loss related simulations. For this MySolver addition, the required wide range of information would have to be obtained from electrical machine manufacturers and material suppliers. This has proved challenging in the past, with some information related to specific machine parts and/or operating conditions hard to acquire, which could complicate the described MySolver development. Finally regarding MySolver's user interface, a visually more effective results delivery method could be employed. As mentioned in the thesis, MySolver generates temperature tables and graphical illustrations of the simulations executed, but a better approach could be to add a more FEA-like output technique, such as that illustrated for the rotor lamination example in Figure 10.1, based on 14 kW loading steady-state results. As shown, a temperature dependant colour coded scheme over the relevant electrical machine component diagrams clearly illustrates the temperature of each machine part, making the information easier to comprehend.

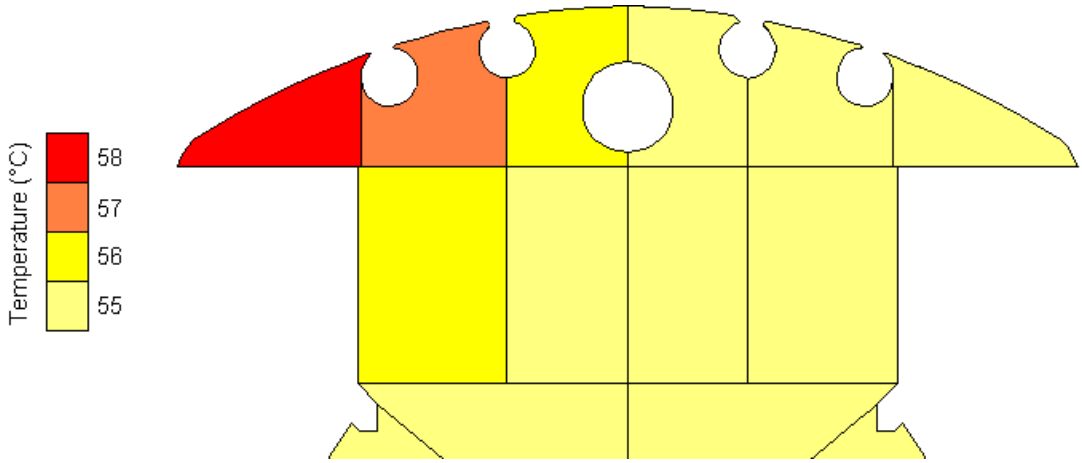

Figure 10.1: *Improved MySolver component temperature output interface rotor lamination example.*

Additionally, current MySolver lumped parameter thermal models could be extended to a more discretised format, both in the radial and axial direction. This would be done by increasing the number of nodes radially representing specific machine parts and including extra axial planes. Such a development was not necessary for this

project, but some applications might require users to obtain more detailed information and this development would allow for it.

To conclude, final further work areas could include expansion of the experiments presented in this thesis. The use of an inductive load could allow MySolver to be validated for a wide range of non-unity power factor conditions. Also, using a higher rated induction motor to drive the synchronous generator would permit for overload MySolver simulations to be verified, either as standalone heat-runs or as part of duty-cycle runs. Finally, after such additions, MySolver could be used to explore other machine types and sizes. MySolver currently gives the user the flexibility to make the geometric, power loss and airflow changes to allow for this and, this way, MySolver's true ability as a universal thermal modelling tool could be determined.

In order to aid all of the further work described in this section, the addition of supplementary thermocouples to unexplored machine segments or around areas where further information would be advantageous. As the results collected in this thesis show, the temperature distribution of a synchronous generator is far from uniform and straightforward to predict, encouraging the use of as many machine thermocouples and temperature sensors as possible.

Appendix A

CGT BCI184E Synchronous Generator Data Sheets

A.1 CGT BCI184E – Product Profile

product profile

BC184 RANGE

TYPICAL APPLICATIONS:

Combined Heat & Power
Parallel Operation
Base Load Prime
Standby
Rental
Telecommunication
Marine/Offshore

Standard Winding (311)

3 Phase Ratings for STAMFORD BC184 Generators

	50Hz (1500 rpm)									60Hz (1800 rpm)								
Rating/Ambient	Base 40ºC			Peak 40ºC			Peak 27ºC			Base 40ºC			Peak 40ºC			Peak 27ºC		
Application/Temp Rise	Continuous 125ºC			Standby 150ºC			Standby 163ºC			Continuous 125ºC			Standby 150ºC			Standby 163ºC		
Voltage	380	400	415	380	400	415	380	400	415	416	440	480	416	440	480	416	440	480
BCI 184E kVA	22.5	22.5	22.5	NA	NA	NA	NA	NA	NA	27.5	28.8	30.0	NA	NA	NA	NA	NA	NA
kW	18.0	18.0	18.0	NA	NA	NA	NA	NA	NA	22.0	23.0	24.0	NA	NA	NA	NA	NA	NA
BCI 184F kVA	27.5	27.5	27.5	29.0	29.0	29.0	30.0	30.0	30.0	32.5	34.4	35.0	33.8	35.0	37.5	34.4	35.6	38.8
kW	22.0	22.0	22.0	23.2	23.2	23.2	24.0	24.0	24.0	26.0	27.5	28.0	27.0	28.0	30.0	27.5	28.5	31.0
BCI 184G kVA	31.3	31.3	31.3	32.5	32.5	32.5	33.0	33.0	33.0	35.0	37.5	37.5	36.3	38.3	38.8	36.9	40.0	40.0
kW	25.0	25.0	25.0	26.0	26.0	26.0	26.4	26.4	26.4	28.0	30.0	30.0	29.0	31.0	31.0	29.5	32.0	32.0
BCI 184H kVA	37.5	37.5	37.5	39.0	39.0	39.0	40.0	40.0	40.0	44.3	46.9	46.9	45.9	48.5	48.5	47.3	50.0	50.0
kW	30.0	30.0	30.0	31.2	31.2	31.2	32.0	32.0	32.0	35.4	37.5	37.5	36.7	38.8	38.8	37.8	40.0	40.0
BCI 184J kVA	40.0	42.5	40.0	41.5	44.0	41.5	42.5	45.0	42.5	47.3	50.0	50.0	49.2	52.0	52.0	50.6	53.5	53.5
kW	32.0	34.0	32.0	33.2	35.2	33.2	34.0	36.0	34.0	37.8	40.0	40.0	39.4	41.6	41.6	40.5	42.8	42.8

1 Phase Ratings for STAMFORD BC184 Generators

	50Hz (1500 rpm)									60Hz (1800 rpm)								
Rating/Ambient	Base 40ºC			Peak 40ºC			Peak 27ºC			Base 40ºC			Peak 40ºC			Peak 27ºC		
Application/Temp Rise	Continuous 125ºC			Standby 150ºC			Standby 163ºC			Continuous 125ºC			Standby 150ºC			Standby 163ºC		
Voltage	220	230	240	220	230	240	220	230	240	220	230	240	220	230	240	220	230	240
BCI 184E kVA	13.0	13.0	13.0	NA	NA	NA	NA	NA	NA	14.6	15.3	16.0	NA	NA	NA	NA	NA	NA
kW	10.4	10.4	10.4	NA	NA	NA	NA	NA	NA	11.7	12.2	12.8	NA	NA	NA	NA	NA	NA
BCI 184F kVA	16.0	16.0	16.0	NA	NA	NA	NA	NA	NA	17.2	18.0	18.8	NA	NA	NA	NA	NA	NA
kW	12.8	12.8	12.8	NA	NA	NA	NA	NA	NA	13.8	14.4	15.0	NA	NA	NA	NA	NA	NA
BCI 184G kVA	18.1	18.1	18.1	NA	NA	NA	NA	NA	NA	18.7	19.5	20.3	NA	NA	NA	NA	NA	NA
kW	14.5	14.5	14.5	NA	NA	NA	NA	NA	NA	15.0	15.6	16.2	NA	NA	NA	NA	NA	NA
BCI 184H kVA	21.7	21.7	21.7	NA	NA	NA	NA	NA	NA	23.6	24.6	25.7	NA	NA	NA	NA	NA	NA
kW	17.4	17.4	17.4	NA	NA	NA	NA	NA	NA	18.9	19.7	20.6	NA	NA	NA	NA	NA	NA
BCI 184J kVA	23.2	23.2	23.2	NA	NA	NA	NA	NA	NA	25.0	26.3	27.4	NA	NA	NA	NA	NA	NA
kW	18.6	18.6	18.6	NA	NA	NA	NA	NA	NA	20.0	21.0	21.9	NA	NA	NA	NA	NA	NA

Due to our policy of continuous improvement, details in this leaflet which were correct at time of printing may now be due for amendment. Information included must therefore not be regarded as binding

PML_BC184 PP GB_11.02_02_GB

NEWAGE International Limited PO Box 17 · Barnack Road · Stamford Lincolnshire · PE9 2NB · England
Tel.: +44 (0) 17 80 48 40 00 · Fax: + 44 (0) 17 80 48 41 00 e-mail: info@newage-avkseg.com · internet: www.newage-avkseg.com

NEWAGE AVK SEG

A.2 CGT BCI184E – Technical Data Sheet

BCI184E
SPECIFICATIONS & OPTIONS

STAMFORD power generation

STANDARDS

Newage Stamford industrial generators meet the requirements of BS EN 60034 and the relevant section of other international standards such as BS5000, VDE 0530, NEMA MG1-32, IEC34, CSA C22.2-100, AS1359.
Other standards and certifications can be considered on request.

VOLTAGE REGULATORS

SX460 AVR - STANDARD

With this self excited control system the main stator supplies power via the Automatic Voltage Regulator (AVR) to the exciter stator. The high efficiency semiconductors of the AVR ensure positive build-up from initial low levels of residual voltage.
The exciter rotor output is fed to the main rotor through a three phase full wave bridge rectifier. This rectifier is protected by a surge suppressor against surges caused, for example, by short circuit.

SA465 AVR

The SA465 shares all the features of the SX460, but additionally will support a range of electronic accessories, such as a 'droop' Current Transformer (CT) to permit parallel operation with other ac generators.
Voltage regulation is improved by use of this AVR.

SX421 AVR

When the SX421 AVR is supplied for use with a BC generator, it will be supplied loose for fitting in the set builder's control panel.
This AVR also operates in a self-excited system. It combines all the features of the SA465 with, additionally, three-phase rms sensing for improved regulation and performance. Over voltage protection is provided via a separate circuit breaker. An engine relief load acceptance feature is built in as standard.

WINDINGS & ELECTRICAL PERFORMANCE

All generator stators are wound to 2/3 pitch. This eliminates triplen (3rd, 9th, 15th …) harmonics on the voltage waveform and is found to be the optimum design for trouble-free supply of non-linear loads. The 2/3 pitch design avoids excessive neutral currents sometimes seen with higher winding pitches, when in parallel with the mains. A fully connected damper winding reduces oscillations during paralleling. This winding, with the 2/3 pitch and carefully selected pole and tooth designs, ensures very low waveform distortion.

TERMINALS & TERMINAL BOX

Standard generators are 3-phase reconnectable with 12 ends brought out to the terminals, which are mounted on a cover at the non-drive end of the generator. A sheet steel terminal box contains the AVR and provides ample space for the customers' wiring and gland arrangements. It has removable panels for easy access.

SHAFT & KEYS

All generator rotors are dynamically balanced to better than BS6861:Part 1 Grade 2.5 for minimum vibration in operation. Two bearing generators are balanced with a half key.

INSULATION/IMPREGNATION

The insulation system is class 'H'.
All wound components are impregnated with materials and processes designed specifically to provide the high build required for static windings and the high mechanical strength required for rotating components.

QUALITY ASSURANCE

Generators are manufactured using production procedures having a quality assurance level to BS EN ISO 9001.

The stated voltage regulation may not be maintained in the presence of certain radio transmitted signals. Any change in performance will fall within the limits of Criteria 'B' of EN 61000-6-2:2001. At no time will the steady-state voltage regulation exceed 2%.

NB Continuous development of our products entitles us to change specification details without notice, therefore they must not be regarded as binding.

Front cover drawing typical of product range.

STAMFORD power generation

BCI184E
WINDING 311

CONTROL SYSTEM	SELF EXCITED		
A.V.R.	STANDARD SX460	OPTIONAL SA465	SX421 (SUPPLIED LOOSE)
VOLTAGE REGULATION	± 1.5 %	± 1.0 %	± 0.5 %
SUSTAINED SHORT CIRCUIT	SELF EXCITED MACHINES DO NOT SUSTAIN A SHORT CIRCUIT CURRENT		

INSULATION SYSTEM	CLASS H							
PROTECTION	IP23							
RATED POWER FACTOR	0.8							
STATOR WINDING	DOUBLE LAYER CONCENTRIC							
WINDING PITCH	TWO THIRDS							
WINDING LEADS	12							
STATOR WDG. RESISTANCE	0.354 Ohms PER PHASE AT 22°C SERIES STAR CONNECTED							
ROTOR WDG. RESISTANCE	0.64 Ohms at 22°C							
R.F.I. SUPPRESSION	BS EN 61000-6-2 & BS EN 61000-6-4,VDE 0875G, VDE 0875N. refer to factory for others							
WAVEFORM DISTORTION	NO LOAD < 1.5% NON-DISTORTING BALANCED LINEAR LOAD < 5.0%							
MAXIMUM OVERSPEED	2250 Rev/Min							
BEARING DRIVE END	BALL. 6309 - 2RS. (ISO)							
BEARING NON-DRIVE END	BALL. 6306 - 2RS. (ISO)							
	1 BEARING				2 BEARING			
WEIGHT COMP. GENERATOR	128 kg				131 kg			
WEIGHT WOUND STATOR	43.6 kg				43.6 kg			
WEIGHT WOUND ROTOR	40.69 kg				41.47 kg			
WR² INERTIA	0.1568 kgm^2				0.1568 kgm^2			
SHIPPING WEIGHTS in a crate	133 kg				141 kg			
PACKING CRATE SIZE	84 x 59 x 75 (cm)				84 x 59 x 75 (cm)			
	50 Hz				60 Hz			
TELEPHONE INTERFERENCE	THF<2%				TIF<50			
COOLING AIR	0.095 m³/sec 200 cfm				0.119 m³/sec 250 cfm			
VOLTAGE SERIES STAR	380/220	400/231	415/240	440/254	416/240	440/254	460/266	480/277
VOLTAGE PARALLEL STAR	190/110	200/115	208/120	220/127	208/120	220/127	230/133	240/138
VOLTAGE SERIES DELTA	220/110	230/115	240/120	254/127	240/120	254/127	266/133	277/138
kVA BASE RATING FOR REACTANCE VALUES	22.5	22.5	22.5	17.5	27.5	28.8	28.8	30
Xd DIR. AXIS SYNCHRONOUS	1.873	1.690	1.570	1.796	2.294	2.148	1.965	1.880
X'd DIR. AXIS TRANSIENT	0.188	0.170	0.158	0.180	0.232	0.217	0.199	0.190
X"d DIR. AXIS SUBTRANSIENT	0.122	0.110	0.102	0.117	0.146	0.137	0.125	0.120
Xq QUAD. AXIS REACTANCE	0.931	0.840	0.780	0.892	1.135	1.063	0.972	0.930
X"q QUAD. AXIS SUBTRANSIENT	0.211	0.190	0.177	0.202	0.256	0.240	0.220	0.210
XL LEAKAGE REACTANCE	0.075	0.068	0.063	0.072	0.093	0.087	0.079	0.076
X2 NEGATIVE SEQUENCE	0.177	0.160	0.149	0.170	0.207	0.194	0.178	0.170
X0 ZERO SEQUENCE	0.081	0.073	0.068	0.077	0.099	0.093	0.085	0.081
REACTANCES ARE SATURATED	VALUES ARE PER UNIT AT RATING AND VOLTAGE INDICATED							
T'd TRANSIENT TIME CONST.	0.02 s							
T"d SUB-TRANSTIME CONST.	0.005 s							
T'do O.C. FIELD TIME CONST.	0.4 s							
Ta ARMATURE TIME CONST.	0.006 s							
SHORT CIRCUIT RATIO	1/Xd							

50 Hz

BCI184E
Winding 311

STAMFORD power generation

THREE PHASE EFFICIENCY CURVES

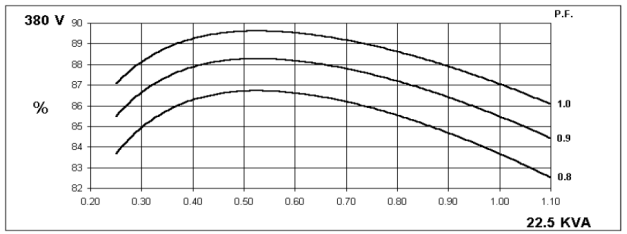

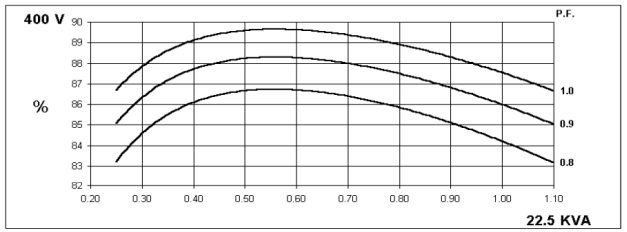

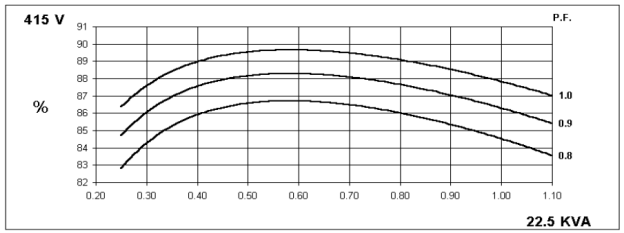

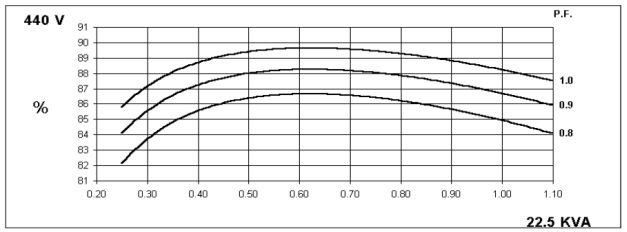

STAMFORD power generation

BCI184E
Winding 311

60 Hz

THREE PHASE EFFICIENCY CURVES

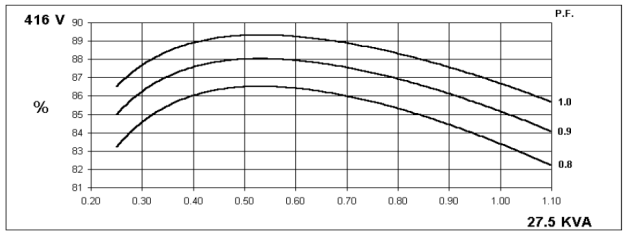

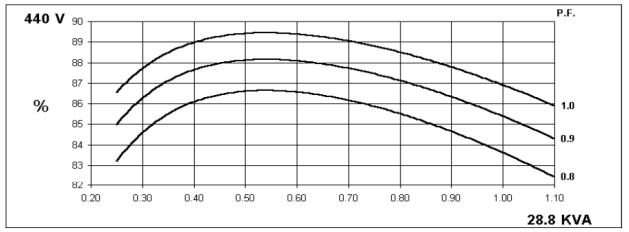

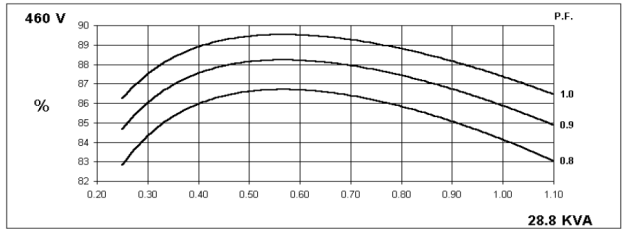

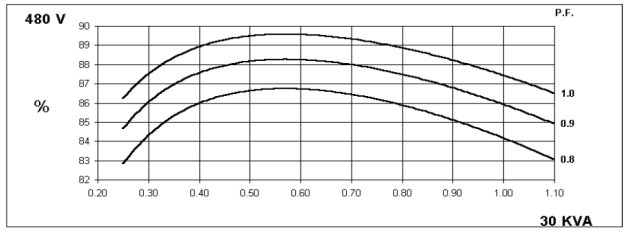

BCI184E
Winding 311

STAMFORD power generation

Locked Rotor Motor Starting Curve

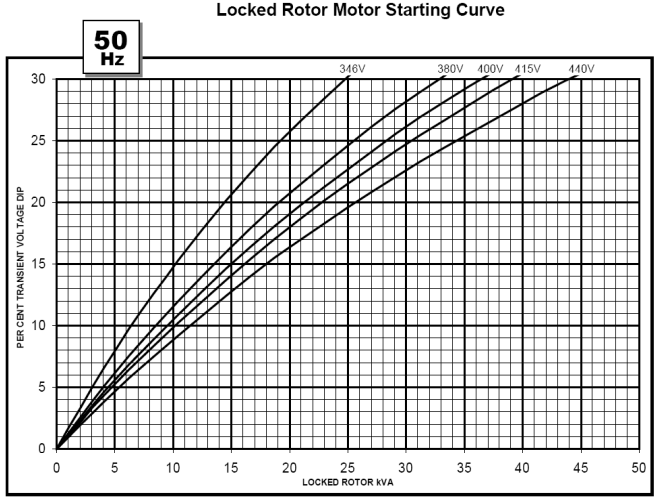

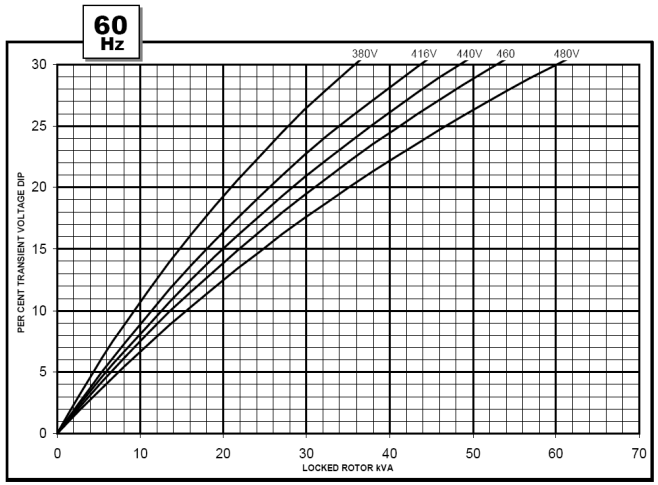

BCI184E
Winding 311 / 0.8 Power Factor

STAMFORD power generation

RATINGS

	Class - Temp Rise	Cont. F - 105/40°C				Cont. H - 125/40°C				Standby - 150/40°C				Standby - 163/27°C			
50 Hz	Series Star (V)	380	400	415	440	380	400	415	440	380	400	415	440	380	400	415	440
	Parallel Star (V)	190	200	208	220	190	200	208	220	190	200	208	220	190	200	208	220
	Series Delta (V)	220	230	240	254	220	230	240	254	220	230	240	254	220	230	240	254
	kVA	20.0	20.0	20.0	15.6	22.5	22.5	22.5	17.5	N/A				N/A			
	kW	16.0	16.0	16.0	12.5	18.0	18.0	18.0	14.0								
	Efficiency (%)	84.8	85.2	85.4	85.7	83.7	84.2	84.5	84.9								
	kW Input	18.9	18.8	18.7	18.7	21.5	21.4	21.3	21.2								
60 Hz	Series Star (V)	416	440	460	480	416	440	460	480	416	440	460	480	416	440	460	480
	Parallel Star (V)	208	220	230	240	208	220	230	240	208	220	230	240	208	220	230	240
	Series Delta (V)	240	254	266	277	240	254	266	277	240	254	266	277	240	254	266	277
	kVA	25.0	26.3	26.3	28.1	27.5	28.8	28.8	30.0	N/A				N/A			
	kW	20.0	21.0	21.0	22.5	22.0	23.0	23.0	24.0								
	Efficiency (%)	84.4	84.5	85.0	84.8	83.4	83.6	84.1	84.2								
	kW Input	23.7	24.9	24.8	26.5	26.4	27.6	27.4	28.5								

DIMENSIONS

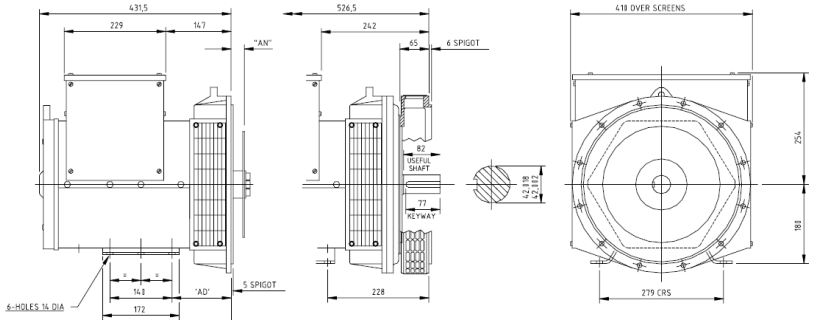

COUPLING DISC	"AN"
SAE 7,5	31,16
SAE 8	61,9
SAE 18	53,98

ADAPTOR	"AD"
SAE 2	172
SAE 3	145
SAE 4	133
SAE 5	133
SAE 6	164,7

8 HOLES SPACED AS 12

ACHIEVED WITH SPACER PLATE 31,7mm THICK

Appendix B

CGT BCI184E Armature Winding Details

B.1 CGT BCI184E Individual Phase Armature Winding Information

Three-phase details of the Cummins Generator Technologies BCI184E synchronous generator armature windings are presented in Tables C.1 to C.3. These are utilised for the FEA work covered in Chapter 4 and provide insight into the armature star winding configuration information illustrated in Figure 4.7 (Section 4.3.1).

Note: CC stands for clock-wise winding direction and CCC stands for counter clock-wise winding direction. Wire diameter is measured in millimetres.

U-Phase							
	End Lead	G0 Slot	Return Slot	Turns	// Wires in Hand	Wire Diameter	Direction
Start	U1	1					
			9	17	3	0.8	CC
		2					
			8	16	3	0.8	CC
		3					
Finish	U2		7	16	3	0.8	CC
Start	U5	18					
			10	17	3	0.8	CCC
		17					
			11	16	3	0.8	CCC
		16					
Finish	U6		12	16	3	0.8	CCC
Start	U1	19					
			27	17	3	0.8	CC
		20					
			26	16	3	0.8	CC
		21					
Finish	U2		25	16	3	0.8	CC
Start	U5	36					
			28	17	3	0.8	CCC
		35					
			29	16	3	0.8	CCC
		34					
Finish	U6		30	16	3	0.8	CCC

Table B.1: *BCI184E generator stator winding U-phase details.*

V-Phase							
	End Lead	G0 Slot	Return Slot	Turns	// Wires in Hand	Wire Diameter	Direction
Start	V1	7					
			15	17	3	0.8	CC
		8					
			14	16	3	0.8	CC
		9					
Finish	V2		13	16	3	0.8	CC
Start	V5	24					
			16	17	3	0.8	CCC
		23					
			17	16	3	0.8	CCC
		22					
Finish	V6		18	16	3	0.8	CCC
Start	V1	25					
			33	17	3	0.8	CC
		26					
			32	16	3	0.8	CC
		27					
Finish	V2		31	16	3	0.8	CC
Start	V5	6					
			34	17	3	0.8	CCC
		5					
			35	16	3	0.8	CCC
		4					
Finish	V6		36	16	3	0.8	CCC

Table B.2: *BCI184E generator stator winding V-phase details.*

W-Phase							
	End Lead	G0 Slot	Return Slot	Turns	// Wires in Hand	Wire Diameter	Direction
Start	W1	13					
			21	17	3	0.8	CC
		14					
			20	16	3	0.8	CC
		15					
Finish	W2		19	16	3	0.8	CC
Start	W5	30					
			22	17	3	0.8	CCC
		29					
			23	16	3	0.8	CCC
		28					
Finish	W6		24	16	3	0.8	CCC
Start	W1	31					
			3	17	3	0.8	CC
		32					
			2	16	3	0.8	CC
		33					
Finish	W2		1	16	3	0.8	CC
Start	W5	12					
			4	17	3	0.8	CCC
		11					
			5	16	3	0.8	CCC
		10					
Finish	W6		6	16	3	0.8	CCC

Table B.3: *BCI184E generator stator winding W-phase details.*

Appendix C

FEA Iron Loss Calculating Command File by Vector Fields

C.1 Iron Loss Calculating Code

The command file presented is provided by Vector Fields and is utilised for the calculation of iron losses across electrical machine laminations. Vector Fields has used and validated the command file for a wide range of machine types. The default command file provided is modified to model the CGT synchronous generator analysed, by altering the machine material properties.

```
This command file calculates the Fourier series expansion for the components of
the flux density at all element centroids (or for the STATOR and ROTOR groups in
LM & RM solutions)

The harmonics are saved in the EXTRA TABLE format in files BXA0.TABLE,
BYA0.TABLE, BXB0.TABLE, BYB0.TABLE..... BYBn.TABLE

$os del *.table

/  Number of harmonics
$CONST #Nhar 5
/  Case number for the start of the period
$CONST #START 221
/  Number of cases in a period
$CONST #NCASES 240
/ Number of region groups to be analysed - ONLY FOR RM AND LM Solutions
$CONST #NGROUP 2
/ For RM or LM models the stationary lossy parts should be labelled STATOR and
the moving lossy parts should be labelled ROTOR
$STRING Group1 'STATOR'
$STRING Group2 'ROTOR'
$IF #NGROUP EQ 2
  $ASK #PERIOD 'For RM and LM : Enter the angular extent of a period'
$END IF

/ Create a set of tables for store the harmonic components of the Flux density at
the centre of each element in the model
$do #n 0 #NHAR 1
  EXTRA
  TABLE REG1=1 Reg2=* TYPE=ELEM MATE=ALL NOT=ANY COMP=0.0
NAME=BXA%INT(#N) UNIT=FLUXU OPTI=NEW NUMB=1
  Y
  TABLE REG1=1 Reg2=* TYPE=ELEM MATE=ALL NOT=ANY COMP=0.0
NAME=BXB%INT(#N) UNIT=FLUXU OPTI=NEW NUMB=2
  Y
  TABLE REG1=1 Reg2=* TYPE=ELEM MATE=ALL NOT=ANY COMP=0.0
NAME=BYA%INT(#N) UNIT=FLUXU OPTI=NEW NUMB=3
  Y
  TABLE REG1=1 Reg2=* TYPE=ELEM MATE=ALL NOT=ANY COMP=0.0
NAME=BYB%INT(#N) UNIT=FLUXU OPTI=NEW NUMB=4
  Y
  SAVE BXA%INT(#N).table BXA%INT(#N)
  SAVE BXB%INT(#N).table BXB%INT(#N)
  SAVE BYA%INT(#N).table BYA%INT(#N)
  SAVE BYB%INT(#N).table BYB%INT(#N)
```

```
  QUIT
$END DO

/ Now calculate the integral of the Bx.Cos(nTheta), Bx.Sin(nTheta), etc., where theta
varies from 0 to 2Pi from case 1 to ncases+1

$Do #case #START #NCASES 1
  Read case=%int(#case) geom=no
  $DO #n 0 #NHAR 1
    $CONST #ANGLE 2.0*pi/((#NCASES-#START)+1)*((#CASE-#START)-1)
    $IF #N EQ 0
      $CONST #SCALE 1.0/(2.0*PI)
    $ELSE
    $CONST #SCALE 1.0/(PI)
    $END IF
    $CONST #SINA SIN(#ANGLE*#N)*(2.0*PI)/((#NCASES-#START)+1)*#SCALE
    $CONST #COSA COS(#ANGLE*#N)*(2.0*PI)/((#NCASES-#START)+1)*#SCALE
    EXTRA

 / Clear tables if needed
      $if #N gt 0
      DELETE TABLE 1 *
      $end if

    LOAD BXA%INT(#N).table
    LOAD BXB%INT(#N).table
    LOAD BYA%INT(#N).table
    LOAD BYB%INT(#N).table
    $IF #NGROUP Eq 0
      TABLE REG1=1 Reg2=* TYPE=ELEM MATE=ALL NOT=ANY,
           COMP=BX*#COSA NAME=BXA%INT(#N) UNIT=FLUXU OPTI=ADD NUMB=1
      TABLE REG1=1 Reg2=* TYPE=ELEM MATE=ALL NOT=ANY,
           COMP=BX*#SINA NAME=BXB%INT(#N) UNIT=FLUXU OPTI=ADD NUMB=2
      TABLE REG1=1 Reg2=* TYPE=ELEM MATE=ALL NOT=ANY,
           COMP=BY*#COSA NAME=BYA%INT(#N) UNIT=FLUXU OPTI=ADD NUMB=3
      TABLE REG1=1 Reg2=* TYPE=ELEM MATE=ALL NOT=ANY,
           COMP=BY*#SINA NAME=BYB%INT(#N) UNIT=FLUXU OPTI=ADD NUMB=4
    $ELSE
      $DO #GROUP 1 #NGROUP 1
       $IF #GROUP EQ 2

/ For Rm and LM models the field must be in the 'Rotor' frame of reference
        $CONST #RMANGLE (#PERIOD/((#NCASES-#START)+1)*((#CASE-#START)-1))
        $PARA #BX BX*COS(#RMANGLE)+BY*SIN(#RMANGLE)
        $PARA #BY -BX*SIN(#RMANGLE)+BY*COS(#RMANGLE)
      $ELSE
        $PARA #BX BX
        $PARA #BY BY
      $END IF
      TABLE REG1=&GROUP%INT(#GROUP)& TYPE=ELEM MATE=ALL NOT=ANY,
           COMP=#BX*#COSA NAME=BXA%INT(#N) UNIT=FLUXU OPTI=ADD NUMB=1
      TABLE REG1=&GROUP%INT(#GROUP)& TYPE=ELEM MATE=ALL NOT=ANY,
           COMP=#BX*#SINA NAME=BXB%INT(#N) UNIT=FLUXU OPTI=ADD NUMB=2
      TABLE REG1=&GROUP%INT(#GROUP)& TYPE=ELEM MATE=ALL NOT=ANY,
           COMP=#BY*#COSA NAME=BYA%INT(#N) UNIT=FLUXU OPTI=ADD NUMB=3
      TABLE REG1=&GROUP%INT(#GROUP)& TYPE=ELEM MATE=ALL NOT=ANY,
           COMP=#BY*#SINA NAME=BYB%INT(#N) UNIT=FLUXU OPTI=ADD NUMB=4
    $END DO
  $END IF
  SAVE BXA%INT(#N).table BXA%INT(#N)
  Y
  SAVE BXB%INT(#N).table BXB%INT(#N)
  Y
  SAVE BYA%INT(#N).table BYA%INT(#N)
  Y
  SAVE BYB%INT(#N).table BYB%INT(#N)
  Y
  QUIT
 $END DO
$END DO

/ Complete : The files created contain
/ BXA0.Table      Constant Bx
/ BYA0.Table      Constant By
/ BXA1.Table      First order Cosine Fourier coefficient for Bx
/ BXB1.Table      First order Sine Fourier coefficient for Bx
/ BYA1.Table      First order Cosine Fourier coefficient for By
/ BYB1.Table      First order Sine Fourier coefficient for By
/ BXA2.Table      Second order Cosine Fourier coefficient for Bx
/.....up to BYB for the nth harmonic

////////////////////////////////////////////////////////////////
GROUP ACTION=CREATE NAME=ALLIRON
GROUP ACTION=ADD NAME=ALLIRON REG1=ROTOR REG2=* MATERIAL=ALL
NOT=ANY
GROUP ACTION=ADD NAME=ALLIRON REG1=STATOR REG2=* MATERIAL=ALL
NOT=ANY
```

```
////////////////////////////////////////////////////////////////

/ Number of poles in machine
$cons #numpoles 4

/ Frequency
$cons #revm 1500
$cons #rads #revm*2*3.1415/60
$cons #freq (#rads*#numpoles)/(2*2*3.1415)

/ Material information

/ Hysteresis loss constant
$cons #Kh 485

/ Eddy current loss constant
$cons #Ke 1.6

/ Computing np using constants associated with a particular steel type
$cons #fac1 -0.205
$cons #fac2 0.875
$cons #fac3 1.31

/ Establish number of harmonics to consider

$cons #modes 5
/ Set accumulator
$CONST #Ironlosses 0

/ Create HEAT table
  EXTRA
  TABLE REG1=1 Reg2=* TYPE=ELEM MATE=ALL NOT=ANY COMP=0.0
NAME=HEAT UNIT=POWEU/LENGU**3 OPTI=NEW NUMB=5
  SAVE HEAT.table 5
  QUIT
$do #i 0 #modes

  EXTRA
  DELETE TABLE 1 4
  LOAD FILE=BXA%int(#i).table
  LOAD FILE=BXB%int(#i).table
  LOAD FILE=BYA%int(#i).table
  LOAD FILE=BYB%int(#i).table
  QUIT

  / Setup harmonics
  $para #h sqrt(bxa%int(#i)**2+bya%int(#i)**2+bxb%int(#i)**2+byb%int(#i)**2)

  / Compute the n factor
  $para #np  #fac1*#h**2+#fac2*#h+#fac3

  / Computing hysteresis loss based on #np and maximum flux density of a section
  $para #PHyst #Kh*(#i*#freq)*#h**#np

  / Computing eddy current loss based on frequency and maximum flux density of a
section
  $para #Peddy #Ke*(#i*#freq)**2*#h**2

  / Compute total iron loss
  $para #Ptotal #Physt+#Peddy

/ Update HEAT table with Peddy value
    EXTRA
    TABLE REG1=1 Reg2=* TYPE=ELEM MATE=ALL NOT=ANY COMP=#Peddy
NAME=HEAT UNIT=POWEU/LENGU**3 OPTI=ADD NUMB=5
    SAVE HEAT.table 5
    Y
    QUIT

  INTA reg1=alliron comp=#ptotal

/ Accumulator of Iron loss
 $CONST #Ironlosses #Ironlosses+INTEGRAL

$end do
```

Appendix D

ThyssenKrupp Stahl, PowerCore® M 800-65 A, Lamination Information

D.1 CGT BCI184E Rotor and Stator Lamination Data

ThyssenKrupp Stahl
- Produktion Elektroband Bochum - Division Industrie -
- Production Electrical Steel Bochum - Industry Division -

PowerCore® M 800-65 A

f = 400 Hz				
$\hat{J}$ T	$\hat{H}$ A/m 0°/90°	μ_a 0°/90°	P_s W/kg 0°/90°	S_s VA/kg 0°/90°
0,2	116	1378	2,66	3,86
0,3	142	1680	5,57	7,24
0,4	169	1890	9,27	11,37
0,5	200	1993	13,89	16,56
0,6	236	2023	19,64	23,03
0,7	278	2004	26,68	31,02
0,8	326	1956	35,23	40,78
0,9	379	1889	45,64	52,75
1,0	**439**	**1813**	**57,85**	**66,85**
1,1	503	1740	72,17	83,44
1,2	576	1659	88,98	103,34
1,3	653	1585	108,39	126,64
1,4	737	1514	130,23	154,30
1,5				
1,6				

f = 500 Hz				
$\hat{J}$ T	$\hat{H}$ A/m 0°/90°	μ_a 0°/90°	P_s W/kg 0°/90°	S_s VA/kg 0°/90°
0,2	119	1340	3,56	4,96
0,3	148	1614	7,44	9,40
0,4	179	1784	12,51	15,04
0,5	215	1848	18,86	22,15
0,6	259	1846	26,91	31,23
0,7	309	1804	36,96	42,63
0,8	366	1740	49,28	56,68
0,9	431	1664	64,33	73,91
1,0	**503**	**1582**	**82,56**	**94,96**
1,1	583	1503	103,89	119,77
1,2	668	1430	128,34	148,45
1,3	760	1362	156,92	182,51
1,4	859	1298	188,96	222,16
1,5				
1,6				

f = 1000 Hz				
$\hat{J}$ T	$\hat{H}$ A/m 0°/90°	μ_a 0°/90°	P_s W/kg 0°/90°	S_s VA/kg 0°/90°
0,2	144	1105	9,81	12,17
0,3	186	1281	20,09	23,58
0,4	240	1326	34,50	39,60
0,5	306	1300	53,61	61,10
0,6	385	1240	79,11	89,98
0,7	478	1165	112,71	128,10
0,8	585	1089	154,69	176,16
0,9	704	1019	206,05	235,18
1,0				
1,1				
1,2				
1,3				
1,4				
1,5				
1,6				

f = 2000 Hz				
$\hat{J}$ T	$\hat{H}$ A/m 0°/90°	μ_a 0°/90°	P_s W/kg 0°/90°	S_s VA/kg 0°/90°
0,2	186	428	27,30	31,76
0,3	261	610	57,13	64,82
0,4	361	663	101,61	114,82
0,5	486	656	166,74	188,35
0,6				
0,7				
0,8				
0,9				
1,0				
1,1				
1,2				
1,3				
1,4				
1,5				
1,6				

Appendix E

Rotor Thermocouple Winding Reading PCB Schematic

Note: *Two decoupling capacitors (2.2 μF and 0.01 μF) are used for every schematic IC, with only one shown in Figure E.1 for circuit clarity.*

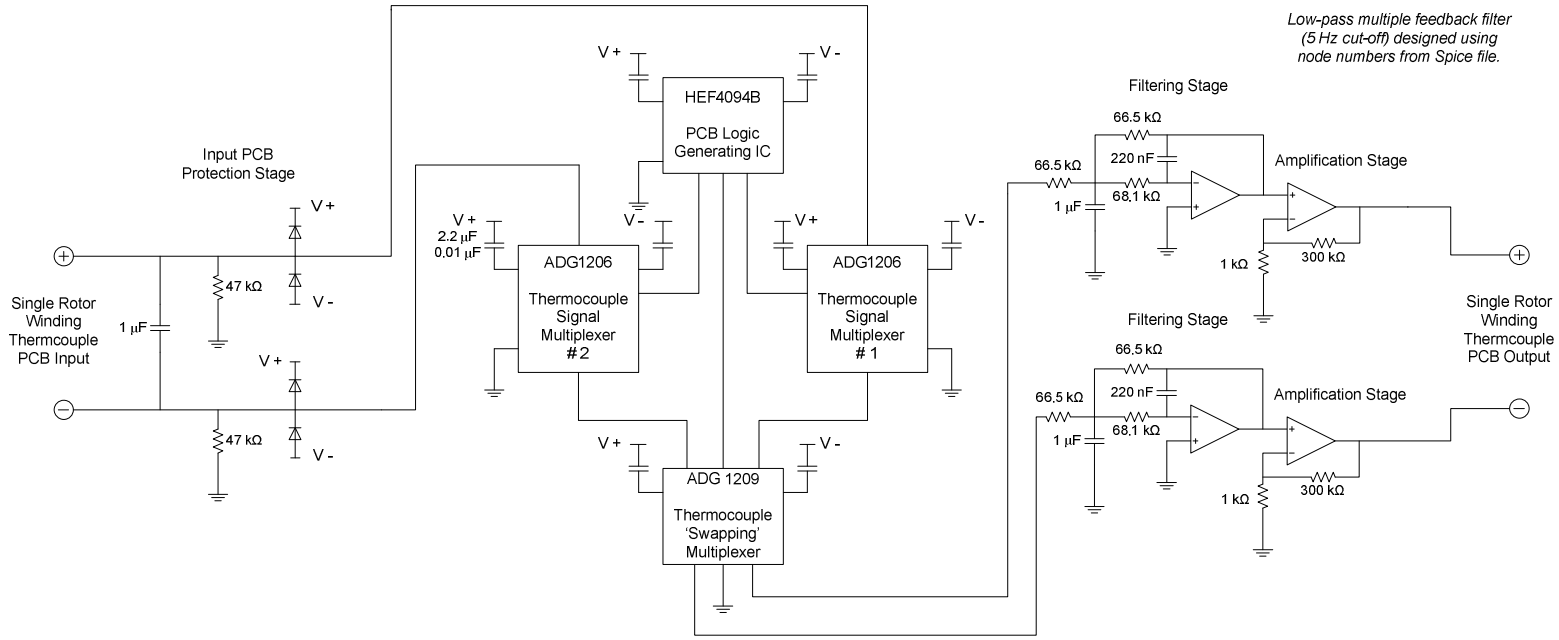

Figure E.1: *Rotor thermocouple winding reading PCB schematic.*

Appendix F

Campbell Scientific CR1000 - Data Acquisition Driving Code

F.1 Data Acquisition Driving Code

```
'CR1000 DAQ code for Cummins Generator Technologies BCI184E synchronous generator thermal analysis

' Declare Variables and Units
Dim LCount_4
Dim LCount_6
Public Batt_Volt
Public PTemp_C

' Temp_C variables used to average 5 stator, frame etc. readings
Public Temp_C(32)
Public Temp_C1(32)
Public Temp_C2(32)
Public Temp_C3(32)
Public Temp_C4(32)
Public Temp_C5(32)
Public StatorAvCounter

'2 off measurements of each of the 16 PCB TCs
Public Temp_C_mV(32)
Public Pre_AvTemp_C_mV(15)
Public AvTemp_C_mV(16)
Public Rise_AvTemp_C_mV(14)
Public RiseTemp_C(32)
Public Binary_Counter

' 100 reading average + error reading removal variables
Public TempTemp_C(100)
Public TempTemp_Counter
Public TempTempSum
Public TempTempAv
Public TempTempAvHigh
Public TempTempAvLow

Public TempTemp_Counter_02
Public TempTempSum_02
Public AvCounter
Public TempTempAvFinal

' y = mx + c variables and offset
Public m
Public c
Public offset

' Variable Units
Units Batt_Volt=Volts
Units PTemp_C=Deg C
Units Temp_C=Deg C
Units Temp_C_mV=Deg C

'Define Data Tables
DataTable(NOV10,True,-1)
  DataInterval(0,60,Sec,10)
  ' Rotor TCs
  Sample (1,AvTemp_C_mV(1),FP2)
  Sample (1,AvTemp_C_mV(2),FP2)
  Sample (1,AvTemp_C_mV(3),FP2)
  Sample (1,AvTemp_C_mV(4),FP2)
  Sample (1,AvTemp_C_mV(5),FP2)
  Sample (1,AvTemp_C_mV(6),FP2)
  Sample (1,AvTemp_C_mV(7),FP2)
  Sample (1,AvTemp_C_mV(8),FP2)
  Sample (1,AvTemp_C_mV(9),FP2)
  Sample (1,AvTemp_C_mV(10),FP2)
  Sample (1,AvTemp_C_mV(11),FP2)
  Sample (1,AvTemp_C_mV(12),FP2)
  Sample (1,AvTemp_C_mV(13),FP2)
  Sample (1,AvTemp_C_mV(14),FP2)
  Sample (1,AvTemp_C_mV(15),FP2)
  Sample (1,AvTemp_C_mV(16),FP2)

' Stator TC readings
  Sample (1,Temp_C(12),FP2)
  Sample (1,Temp_C(13),FP2)
  Sample (1,Temp_C(14),FP2)
  Sample (1,Temp_C(15),FP2)
  Sample (1,Temp_C(16),FP2)
  Sample (1,Temp_C(17),FP2)
  Sample (1,Temp_C(18),FP2)
  Sample (1,Temp_C(19),FP2)
  Sample (1,Temp_C(20),FP2)
  Sample (1,Temp_C(21),FP2)
  Sample (1,Temp_C(22),FP2)
  Sample (1,Temp_C(23),FP2)
  Sample (1,Temp_C(24),FP2)
  Sample (1,Temp_C(25),FP2)
  Sample (1,Temp_C(26),FP2)
  Sample (1,Temp_C(27),FP2)
  Sample (1,Temp_C(28),FP2)
  Sample (1,Temp_C(29),FP2)
  Sample (1,Temp_C(30),FP2)
  Sample (1,Temp_C(31),FP2)
```

```
  ' PCB Fan TC
  Sample (1,Temp_C(32),FP2)

' Frame TC readings
  Sample (1,Temp_C(1),FP2)
  Sample (1,Temp_C(2),FP2)
  Sample (1,Temp_C(3),FP2)
  Sample (1,Temp_C(4),FP2)

' AVR box TC reading
  Sample (1,Temp_C(5),FP2)

' Feet TC reading
  Sample (1,Temp_C(6),FP2)

' Induction machine TC
  Sample (1,Temp_C(7),FP2)

' Air inlet and outlet TC readings
  Sample (1,Temp_C(10),FP2)
  Sample (1,Temp_C(11),FP2)

' DAQ board (i.e. ambient) temperature reading
  Sample (1,PTemp_C,FP2)

' Temperature rises

' Rotor TCs
  Sample (1,Rise_AvTemp_C_mV(1),FP2)
  Sample (1,Rise_AvTemp_C_mV(2),FP2)
  Sample (1,Rise_AvTemp_C_mV(3),FP2)
  Sample (1,Rise_AvTemp_C_mV(4),FP2)
  Sample (1,Rise_AvTemp_C_mV(5),FP2)
  Sample (1,Rise_AvTemp_C_mV(6),FP2)
  Sample (1,Rise_AvTemp_C_mV(7),FP2)
  Sample (1,Rise_AvTemp_C_mV(8),FP2)
  Sample (1,Rise_AvTemp_C_mV(9),FP2)
  Sample (1,Rise_AvTemp_C_mV(10),FP2)
  Sample (1,Rise_AvTemp_C_mV(11),FP2)
  Sample (1,Rise_AvTemp_C_mV(12),FP2)
  Sample (1,Rise_AvTemp_C_mV(13),FP2)
  Sample (1,Rise_AvTemp_C_mV(14),FP2)

' Stator TCs
  Sample (1,RiseTemp_C(12),FP2)
  Sample (1,RiseTemp_C(13),FP2)
  Sample (1,RiseTemp_C(14),FP2)
  Sample (1,RiseTemp_C(15),FP2)
  Sample (1,RiseTemp_C(16),FP2)
  Sample (1,RiseTemp_C(17),FP2)
  Sample (1,RiseTemp_C(18),FP2)
  Sample (1,RiseTemp_C(19),FP2)
  Sample (1,RiseTemp_C(20),FP2)
  Sample (1,RiseTemp_C(21),FP2)
  Sample (1,RiseTemp_C(22),FP2)
  Sample (1,RiseTemp_C(23),FP2)
  Sample (1,RiseTemp_C(24),FP2)
  Sample (1,RiseTemp_C(25),FP2)
  Sample (1,RiseTemp_C(26),FP2)
  Sample (1,RiseTemp_C(27),FP2)
  Sample (1,RiseTemp_C(28),FP2)
  Sample (1,RiseTemp_C(29),FP2)
  Sample (1,RiseTemp_C(30),FP2)
  Sample (1,RiseTemp_C(31),FP2)

  ' Frame TCs
  Sample (1,RiseTemp_C(1),FP2)
  Sample (1,RiseTemp_C(2),FP2)
  Sample (1,RiseTemp_C(3),FP2)
  Sample (1,RiseTemp_C(4),FP2)

' AVR box TC
  Sample (1,RiseTemp_C(5),FP2)

' Feet TC
  Sample (1,RiseTemp_C(6),FP2)

' Induction machine TC
  Sample (1,RiseTemp_C(7),FP2)

' Air inlet and outlet TCs
  Sample (1,RiseTemp_C(10),FP2)
  Sample (1,RiseTemp_C(11),FP2)

EndTable

' Main Program
BeginProg

  Scan(60,Sec,1,0)
' Default Datalogger Battery Voltage measurement
Batt_Volt:
    Battery(Batt_Volt)

' Run Loop to generate LOGIC and measure the 16 rotor
PCB TCs
' Loop will run from Binary_Counter=0 until
Binary_Counter > 31
' Measurements will be stored in Temp_C_mV(1) to
Temp_C_mV(16)
    LCount_6=1
    Binary_Counter = 0
    Do
      ' C5 is the data channel, D. Initially set to LOW.
      PortSet (5,0)
      ' C8 is the CP o/p.
      ' 1 STAGE
      PortSet (8,1 )
      Delay (1,20,mSec)
      ' 2 STAGE
      PortSet (8,0)
      Delay (1,20,mSec)
      ' 3 STAGE
      PortSet (8,1 )
      Delay (1,20,mSec)
      ' 4 STAGE
      PortSet (8,0)
      Delay (1,20,mSec)
      ' 5 STAGE
      PortSet (8,1 )
      Delay (1,20,mSec)
      ' 6 STAGE
      ' If Binary_Counter is 1 go HIGH
      If Binary_Counter = 1 Then
        PortSet (5,1)
      EndIf
      ' If Binary_Counter is 3 go HIGH
      If Binary_Counter = 3 Then
        PortSet (5,1)
      EndIf
      ' If Binary_Counter is 5 go HIGH
      If Binary_Counter = 5 Then
        PortSet (5,1)
      EndIf
      ' If Binary_Counter is 7 go HIGH
      If Binary_Counter = 7 Then
        PortSet (5,1)
      EndIf
      ' If Binary_Counter is 9 go HIGH
      If Binary_Counter = 9 Then
        PortSet (5,1)
```

```
EndIf
' If Binary_Counter is 11 go HIGH
If Binary_Counter = 11 Then
  PortSet (5,1)
EndIf
' If Binary_Counter is 13 go HIGH
If Binary_Counter = 13 Then
  PortSet (5,1)
EndIf
' If Binary_Counter is 15 go HIGH
If Binary_Counter = 15 Then
  PortSet (5,1)
EndIf
' If Binary_Counter is 17 go HIGH
If Binary_Counter = 17 Then
  PortSet (5,1)
EndIf
' If Binary_Counter is 19 go HIGH
If Binary_Counter = 19 Then
  PortSet (5,1)
EndIf
' If Binary_Counter is 21 go HIGH
If Binary_Counter = 21 Then
  PortSet (5,1)
EndIf
' If Binary_Counter is 23 go HIGH
If Binary_Counter = 23 Then
  PortSet (5,1)
EndIf
' If Binary_Counter is 25 go HIGH
If Binary_Counter = 25 Then
  PortSet (5,1)
EndIf
' If Binary_Counter is 27 go HIGH
If Binary_Counter = 27 Then
  PortSet (5,1)
EndIf
' If Binary_Counter is 29 go HIGH
If Binary_Counter = 29 Then
  PortSet (5,1)
EndIf
' If Binary_Counter is 31 go HIGH
If Binary_Counter = 31 Then
  PortSet (5,1)
EndIf
PortSet (8,0)
Delay (1,20,mSec)
' 7 STAGE
PortSet (8,1 )
Delay (1,20,mSec)
' 8 STAGE
' If Binary_Counter is 1 go LOW
If Binary_Counter = 1 Then
  PortSet (5,0)
EndIf
' If Binary_Counter is 3 go LOW
If Binary_Counter = 3 Then
  PortSet (5,0)
EndIf
' If Binary_Counter is 5 go LOW
If Binary_Counter = 5 Then
  PortSet (5,0)
EndIf
' If Binary_Counter is 7 go LOW
If Binary_Counter = 7 Then
  PortSet (5,0)
EndIf
' If Binary_Counter is 9 go LOW
If Binary_Counter = 9 Then
  PortSet (5,0)
EndIf
' If Binary_Counter is 11 go LOW
If Binary_Counter = 11 Then
  PortSet (5,0)
EndIf
' If Binary_Counter is 13 go LOW
If Binary_Counter = 13 Then
  PortSet (5,0)
EndIf
' If Binary_Counter is 15 go LOW
If Binary_Counter = 15 Then
  PortSet (5,0)
EndIf
' If Binary_Counter is 16 go HIGH
If Binary_Counter = 16 Then
  PortSet (5,1)
EndIf
' If Binary_Counter is 18 go HIGH
If Binary_Counter = 18 Then
  PortSet (5,1)
EndIf
' If Binary_Counter is 20 go HIGH
If Binary_Counter = 20 Then
  PortSet (5,1)
EndIf
' If Binary_Counter is 22 go HIGH
If Binary_Counter = 22 Then
  PortSet (5,1)
EndIf
' If Binary_Counter is 24 go HIGH
If Binary_Counter = 24 Then
  PortSet (5,1)
EndIf
' If Binary_Counter is 26 go HIGH
If Binary_Counter = 26 Then
  PortSet (5,1)
EndIf
' If Binary_Counter is 28 go HIGH
If Binary_Counter = 28 Then
  PortSet (5,1)
EndIf
' If Binary_Counter is 30 go HIGH
If Binary_Counter = 30 Then
  PortSet (5,1)
EndIf
PortSet (8,0)
Delay (1,20,mSec)
' 9 STAGE
PortSet (8,1 )
Delay (1,20,mSec)
' 10 STAGE
' If Binary_Counter is 8 go HIGH
If Binary_Counter = 8 Then
  PortSet (5,1)
EndIf
' If Binary_Counter is 9 go HIGH
If Binary_Counter = 9 Then
  PortSet (5,1)
EndIf
' If Binary_Counter is 10 go HIGH
If Binary_Counter = 10 Then
  PortSet (5,1)
EndIf
' If Binary_Counter is 11 go HIGH
If Binary_Counter = 11 Then
  PortSet (5,1)
EndIf
' If Binary_Counter is 12 go HIGH
If Binary_Counter = 12 Then
  PortSet (5,1)
EndIf
```

```
' If Binary_Counter is 13 go HIGH
If Binary_Counter = 13 Then
  PortSet (5,1)
EndIf
' If Binary_Counter is 14 go HIGH
If Binary_Counter = 14 Then
  PortSet (5,1)
EndIf
' If Binary_Counter is 15 go HIGH
If Binary_Counter = 15 Then
  PortSet (5,1)
EndIf
' If Binary_Counter is 16 go LOW
If Binary_Counter = 16 Then
  PortSet (5,0)
EndIf
' If Binary_Counter is 17 go LOW
If Binary_Counter = 17 Then
  PortSet (5,0)
EndIf
' If Binary_Counter is 18 go LOW
If Binary_Counter = 18 Then
  PortSet (5,0)
EndIf
' If Binary_Counter is 19 go LOW
If Binary_Counter = 19 Then
  PortSet (5,0)
EndIf
' If Binary_Counter is 20 go LOW
If Binary_Counter = 20 Then
  PortSet (5,0)
EndIf
' If Binary_Counter is 21 go LOW
If Binary_Counter = 21 Then
  PortSet (5,0)
EndIf
' If Binary_Counter is 22 go LOW
If Binary_Counter = 22 Then
  PortSet (5,0)
EndIf
' If Binary_Counter is 23 go LOW
If Binary_Counter = 23 Then
  PortSet (5,0)
EndIf
PortSet (8,0)
Delay (1,20,mSec)
' 11 STAGE
PortSet (8,1 )
Delay (1,20,mSec)
' 12 STAGE
' If Binary_Counter is 4 go HIGH
If Binary_Counter = 4 Then
  PortSet (5,1)
EndIf
' If Binary_Counter is 5 go HIGH
If Binary_Counter = 5 Then
  PortSet (5,1)
EndIf
' If Binary_Counter is 6 go HIGH
If Binary_Counter = 6 Then
  PortSet (5,1)
EndIf
' If Binary_Counter is 7 go HIGH
If Binary_Counter = 7 Then
  PortSet (5,1)
EndIf
' If Binary_Counter is 8 go LOW
If Binary_Counter = 8 Then
  PortSet (5,0)
EndIf
' If Binary_Counter is 9 go LOW
If Binary_Counter = 9 Then
  PortSet (5,0)
EndIf
' If Binary_Counter is 10 go LOW
If Binary_Counter = 10 Then
  PortSet (5,0)
EndIf
' If Binary_Counter is 11 go LOW
If Binary_Counter = 11 Then
  PortSet (5,0)
EndIf
' If Binary_Counter is 20 go HIGH
If Binary_Counter = 20 Then
  PortSet (5,1)
EndIf
' If Binary_Counter is 21 go HIGH
If Binary_Counter = 21 Then
  PortSet (5,1)
EndIf
' If Binary_Counter is 22 go HIGH
If Binary_Counter = 22 Then
  PortSet (5,1)
EndIf
' If Binary_Counter is 23 go HIGH
If Binary_Counter = 23 Then
  PortSet (5,1)
EndIf
' If Binary_Counter is 24 go LOW
If Binary_Counter = 24 Then
  PortSet (5,0)
EndIf
' If Binary_Counter is 25 go LOW
If Binary_Counter = 25 Then
  PortSet (5,0)
EndIf
' If Binary_Counter is 26 go LOW
If Binary_Counter = 26 Then
  PortSet (5,0)
EndIf
' If Binary_Counter is 27 go LOW
If Binary_Counter = 27 Then
  PortSet (5,0)
EndIf
PortSet (8,0)
Delay (1,20,mSec)
' 13 STAGE
PortSet (8,1 )
Delay (1,20,mSec)
' 14 STAGE
' If Binary_Counter is 2 go HIGH
If Binary_Counter = 2 Then
  PortSet (5,1)
EndIf
' If Binary_Counter is 3 go HIGH
If Binary_Counter = 3 Then
  PortSet (5,1)
EndIf
' If Binary_Counter is 4 go LOW
If Binary_Counter = 4 Then
  PortSet (5,0)
EndIf
' If Binary_Counter is 5 go LOW
If Binary_Counter = 5 Then
  PortSet (5,0)
EndIf
' If Binary_Counter is 10 go HIGH
If Binary_Counter = 10 Then
  PortSet (5,1)
EndIf
' If Binary_Counter is 11 go HIGH
```

```
If Binary_Counter = 11 Then
  PortSet (5,1)
EndIf
' If Binary_Counter is 12 go LOW
If Binary_Counter = 12 Then
  PortSet (5,0)
EndIf
' If Binary_Counter is 13 go LOW
If Binary_Counter = 13 Then
  PortSet (5,0)
EndIf
' If Binary_Counter is 18 go HIGH
If Binary_Counter = 18 Then
  PortSet (5,1)
EndIf
' If Binary_Counter is 19 go HIGH
If Binary_Counter = 19 Then
  PortSet (5,1)
EndIf
' If Binary_Counter is 20 go LOW
If Binary_Counter = 20 Then
  PortSet (5,0)
EndIf
' If Binary_Counter is 21 go LOW
If Binary_Counter = 21 Then
  PortSet (5,0)
EndIf
' If Binary_Counter is 26 go HIGH
If Binary_Counter = 26 Then
  PortSet (5,1)
EndIf
' If Binary_Counter is 27 go HIGH
If Binary_Counter = 27 Then
  PortSet (5,1)
EndIf
' If Binary_Counter is 28 go LOW
If Binary_Counter = 28 Then
  PortSet (5,0)
EndIf
' If Binary_Counter is 29 go LOW
If Binary_Counter = 29 Then
  PortSet (5,0)
EndIf
PortSet (8,0)
Delay (1,20,mSec)
' 15 STAGE
PortSet (8,1 )
Delay (1,20,mSec)
' 16 STAGE
' If Binary_Counter is 2 go LOW
If Binary_Counter = 2 Then
  PortSet (5,0)
EndIf
' If Binary_Counter is 3 go LOW
If Binary_Counter = 3 Then
  PortSet (5,0)
EndIf
' If Binary_Counter is 6 go LOW
If Binary_Counter = 6 Then
  PortSet (5,0)
EndIf
' If Binary_Counter is 7 go LOW
If Binary_Counter = 7 Then
  PortSet (5,0)
EndIf
' If Binary_Counter is 10 go LOW
If Binary_Counter = 10 Then
  PortSet (5,0)
EndIf
' If Binary_Counter is 11 go LOW
If Binary_Counter = 11 Then
  PortSet (5,0)
EndIf
' If Binary_Counter is 14 go LOW
If Binary_Counter = 14 Then
  PortSet (5,0)
EndIf
' If Binary_Counter is 15 go LOW
If Binary_Counter = 15 Then
  PortSet (5,0)
EndIf
' If Binary_Counter is 18 go LOW
If Binary_Counter = 18 Then
  PortSet (5,0)
EndIf
' If Binary_Counter is 19 go LOW
If Binary_Counter = 19 Then
  PortSet (5,0)
EndIf
' If Binary_Counter is 22 go LOW
If Binary_Counter = 22 Then
  PortSet (5,0)
EndIf
' If Binary_Counter is 23 go LOW
    If Binary_Counter = 23 Then
      PortSet (5,0)
    EndIf
    ' If Binary_Counter is 26 go LOW
    If Binary_Counter = 26 Then
      PortSet (5,0)
    EndIf
    ' If Binary_Counter is 27 go LOW
    If Binary_Counter = 27 Then
      PortSet (5,0)
    EndIf
    ' If Binary_Counter is 30 go LOW
    If Binary_Counter = 30 Then
      PortSet (5,0)
    EndIf
    ' If Binary_Counter is 31 go LOW
    If Binary_Counter = 31 Then
      PortSet (5,0)
    EndIf
    PortSet (8,0)

    ' Delay long enough to allow logic setting to settle
    Delay (1,333,mSec)

' Take 100 readings for each rotor TC 'position' and
average out
    TempTemp_Counter = 1
    TempTempSum = 0

    Do While TempTemp_Counter < 101
    VoltDiff
(TempTemp_C(TempTemp_Counter),1,mV5000,2,False,0,
250,1.0,0)
    TempTempSum = TempTempSum +
TempTemp_C(TempTemp_Counter)
    TempTemp_Counter = TempTemp_Counter + 1
    Loop

    TempTempAv = TempTempSum / 100

' Use the average, take another 100 readings removing
those above (1.10*average) and under (0.90*average)
' Average out the readings within the range.
    TempTempAvHigh = TempTempAv * 1.10
    TempTempAvLow = TempTempAv * 0.90

    TempTemp_Counter_02 = 1
```

```
    AvCounter = 0
    TempTempSum_02 = 0

    Do While TempTemp_Counter_02 < 101

    VoltDiff
(TempTemp_C(TempTemp_Counter_02),1,mV5000,2,Fals
e,0,250,1.0,0)

    If (TempTemp_C(TempTemp_Counter_02) >
TempTempAvLow)
    TempTempSum_02 = TempTempSum_02 +
TempTemp_C(TempTemp_Counter_02)
    AvCounter = AvCounter + 1
    EndIf

    If (TempTemp_C(TempTemp_Counter_02) >
TempTempAvHigh)
    TempTempSum_02 = TempTempSum_02 -
TempTemp_C(TempTemp_Counter_02)
    AvCounter = AvCounter - 1
    EndIf

    TempTemp_Counter_02 = TempTemp_Counter_02 + 1
    Loop

    If (AvCounter = 0)
    AvCounter = 1
    Else
    AvCounter = AvCounter
    EndIf

    TempTempAvFinal = TempTempSum_02 / AvCounter

    Temp_C_mV(LCount_6) = TempTempAvFinal

    LCount_6=LCount_6+1
    Binary_Counter = Binary_Counter + 1
    If Binary_Counter>31 Then ExitDo
    Delay (1,20,mSec)

  Loop

' Wiring Panel Temperature measurement PTemp_C:
  PanelTemp(PTemp_C,_60Hz)

' Turn AM16/32 Multiplexer On to measure 31
thermocouples stored in Temp_C(1) to Temp_C (31)
' PCB junction temperature recorded (32th reading)
  PortSet(1,1)

' 5 readings (ONE to FIVE) are taken for every stator,
frame, etc TC
  LCount_4=1
  SubScan(0,uSec,32)
    ' Switch to next AM16/32 Multiplexer channel
    PulsePort(2,10000)
    ' ONE: Type K (chromel-alumel) Thermocouple
measurements Temp_C on the AM16/32 Multiplexer:

TCDiff(Temp_C1(LCount_4),1,mV7_5C,1,TypeK,PTemp_C,
True,0,_50Hz,1,0)

    LCount_4=LCount_4+1

  NextSubScan

  LCount_4=1

  SubScan(0,uSec,32)
    'Switch to next AM16/32 Multiplexer channel
    PulsePort(2,10000)
    ' TWO: Type K (chromel-alumel) Thermocouple
measurements Temp_C on the AM16/32 Multiplexer:

TCDiff(Temp_C2(LCount_4),1,mV7_5C,1,TypeK,PTemp_C,
True,0,_50Hz,1,0)

    LCount_4=LCount_4+1

  NextSubScan

  LCount_4=1

  SubScan(0,uSec,32)
    ' Switch to next AM16/32 Multiplexer channel
    PulsePort(2,10000)
    ' THREE: Type K (chromel-alumel) Thermocouple
measurements Temp_C on the AM16/32 Multiplexer:

TCDiff(Temp_C3(LCount_4),1,mV7_5C,1,TypeK,PTemp_C,
True,0,_50Hz,1,0)

    LCount_4=LCount_4+1

  NextSubScan

  LCount_4=1

  SubScan(0,uSec,32)
    ' Switch to next AM16/32 Multiplexer channel
    PulsePort(2,10000)
    ' FOUR: Type K (chromel-alumel) Thermocouple
measurements Temp_C on the AM16/32 Multiplexer:

TCDiff(Temp_C4(LCount_4),1,mV7_5C,1,TypeK,PTemp_C,
True,0,_50Hz,1,0)

    LCount_4=LCount_4+1

  NextSubScan

  LCount_4=1

  SubScan(0,uSec,32)
    ' Switch to next AM16/32 Multiplexer channel
    PulsePort(2,10000)
    ' FIVE: Type K (chromel-alumel) Thermocouple
measurements Temp_C on the AM16/32 Multiplexer:

TCDiff(Temp_C5(LCount_4),1,mV7_5C,1,TypeK,PTemp_C,
True,0,_50Hz,1,0)

    LCount_4=LCount_4+1

  NextSubScan

' 5 stator, frame, etc readings are averaged
  StatorAvCounter = 1

  Do While StatorAvCounter < 33

  Temp_C(StatorAvCounter) =
(Temp_C1(StatorAvCounter) + Temp_C2(StatorAvCounter)
+ Temp_C3(StatorAvCounter) +
Temp_C4(StatorAvCounter) + Temp_C5(StatorAvCounter))
/ 5
  StatorAvCounter = StatorAvCounter + 1

  Loop
```

```
    ' Turn AM16/32 Multiplexer Off
    PortSet(1,0)

' After all measurements are taken subtract readings
and divide by 2 to give average of 2 sequential readings
' y = mx + c applied for amplifier conversion
' Correct DAQ ordering applied (note: a soldering error
means TCs 6 and 9 were swapped in the DAQ code)
   ' y = mx + c values for amplifier conversion
   m = 12.18
   c = -262

' Calculate AvTemp_C_mv first since it is used for the
rest
   AvTemp_C_mV(16)=(((Temp_C_mV(31)-
Temp_C_mV(32))/2)-(c))/(m)

' Rotor TCs

' Pre-junction correction
   Pre_AvTemp_C_mV(1)=(((Temp_C_mV(1)-
Temp_C_mV(2))/2)-(c))/(m)
   Pre_AvTemp_C_mV(2)=(((Temp_C_mV(3)-
Temp_C_mV(4))/2)-(c))/(m)
   Pre_AvTemp_C_mV(3)=(((Temp_C_mV(5)-
Temp_C_mV(6))/2)-(c))/(m)
   Pre_AvTemp_C_mV(4)=(((Temp_C_mV(7)-
Temp_C_mV(8))/2)-(c))/(m)
   Pre_AvTemp_C_mV(5)=(((Temp_C_mV(9)-
Temp_C_mV(10))/2)-(c))/(m)

   Pre_AvTemp_C_mV(6)=(((Temp_C_mV(25)-
Temp_C_mV(26))/2)-(c))/(m)
   Pre_AvTemp_C_mV(7)=(((Temp_C_mV(13)-
Temp_C_mV(14))/2)-(c))/(m)
   Pre_AvTemp_C_mV(8)=(((Temp_C_mV(27)-
Temp_C_mV(28))/2)-(c))/(m)
   Pre_AvTemp_C_mV(9)=(((Temp_C_mV(11)-
Temp_C_mV(12))/2)-(c))/(m)
   Pre_AvTemp_C_mV(10)=(((Temp_C_mV(23)-
Temp_C_mV(24))/2)-(c))/(m)

   Pre_AvTemp_C_mV(11)=(((Temp_C_mV(21)-
Temp_C_mV(22))/2)-(c))/(m)
   Pre_AvTemp_C_mV(12)=(((Temp_C_mV(19)-
Temp_C_mV(20))/2)-(c))/(m)
   Pre_AvTemp_C_mV(13)=(((Temp_C_mV(17)-
Temp_C_mV(18))/2)-(c))/(m)
   Pre_AvTemp_C_mV(14)=(((Temp_C_mV(15)-
Temp_C_mV(16))/2)-(c))/(m)

' Slight offset from isolated PCB tests. Offset validated
pre and post heat-runs. Use IF NEEDED.
   offset = 0

' Junction correction
   AvTemp_C_mV(1)=((Pre_AvTemp_C_mV(1)) -
(AvTemp_C_mV(16)) + (PTemp_C)) + offset
   AvTemp_C_mV(2)=((Pre_AvTemp_C_mV(2)) -
(AvTemp_C_mV(16)) + (PTemp_C)) + offset
   AvTemp_C_mV(3)=((Pre_AvTemp_C_mV(3)) -
(AvTemp_C_mV(16)) + (PTemp_C)) + offset
   AvTemp_C_mV(4)=((Pre_AvTemp_C_mV(4)) -
(AvTemp_C_mV(16)) + (PTemp_C)) + offset
   AvTemp_C_mV(5)=((Pre_AvTemp_C_mV(5)) -
(AvTemp_C_mV(16)) + (PTemp_C)) + offset

   AvTemp_C_mV(6)=((Pre_AvTemp_C_mV(6)) -
(AvTemp_C_mV(16)) + (PTemp_C)) + offset
   AvTemp_C_mV(7)=((Pre_AvTemp_C_mV(7)) -
(AvTemp_C_mV(16)) + (PTemp_C)) + offset
   AvTemp_C_mV(8)=((Pre_AvTemp_C_mV(8)) -
(AvTemp_C_mV(16)) + (PTemp_C)) + offset
   AvTemp_C_mV(9)=((Pre_AvTemp_C_mV(9)) -
(AvTemp_C_mV(16)) + (PTemp_C)) + offset
   AvTemp_C_mV(10)=((Pre_AvTemp_C_mV(10)) -
(AvTemp_C_mV(16)) + (PTemp_C)) + offset

   AvTemp_C_mV(11)=((Pre_AvTemp_C_mV(11)) -
(AvTemp_C_mV(16)) + (PTemp_C)) + offset
   AvTemp_C_mV(12)=((Pre_AvTemp_C_mV(12)) -
(AvTemp_C_mV(16)) + (PTemp_C)) + offset
   AvTemp_C_mV(13)=((Pre_AvTemp_C_mV(13)) -
(AvTemp_C_mV(16)) + (PTemp_C)) + offset
   AvTemp_C_mV(14)=((Pre_AvTemp_C_mV(14)) -
(AvTemp_C_mV(16)) + (PTemp_C)) + offset

' PCB short-circuited channel
   Pre_AvTemp_C_mV(15)=(((Temp_C_mV(29)-
Temp_C_mV(30))/2)-(c))/(m)

   AvTemp_C_mV(15)=((Pre_AvTemp_C_mV(15)) -
(AvTemp_C_mV(16)) + (PTemp_C)) + offset

' Calculate the temperature rises for all USEFUL stator,
rotor and external TCs

' Rotor TCs
   Rise_AvTemp_C_mV(1) = AvTemp_C_mV(1) - PTemp_C
   Rise_AvTemp_C_mV(2) = AvTemp_C_mV(2) - PTemp_C
   Rise_AvTemp_C_mV(3) = AvTemp_C_mV(3) - PTemp_C
   Rise_AvTemp_C_mV(4) = AvTemp_C_mV(4) - PTemp_C
   Rise_AvTemp_C_mV(5) = AvTemp_C_mV(5) - PTemp_C
   Rise_AvTemp_C_mV(6) = AvTemp_C_mV(6) - PTemp_C
   Rise_AvTemp_C_mV(7) = AvTemp_C_mV(7) - PTemp_C
   Rise_AvTemp_C_mV(8) = AvTemp_C_mV(8) - PTemp_C
   Rise_AvTemp_C_mV(9) = AvTemp_C_mV(9) - PTemp_C
   Rise_AvTemp_C_mV(10) = AvTemp_C_mV(10) -
PTemp_C
   Rise_AvTemp_C_mV(11) = AvTemp_C_mV(11) -
PTemp_C
   Rise_AvTemp_C_mV(12) = AvTemp_C_mV(12) -
PTemp_C
   Rise_AvTemp_C_mV(13) = AvTemp_C_mV(13) -
PTemp_C
   Rise_AvTemp_C_mV(14) = AvTemp_C_mV(14) -
PTemp_C
   ' Stator TCs
   RiseTemp_C(12) = Temp_C(12) - PTemp_C
   RiseTemp_C(13) = Temp_C(13) - PTemp_C
   RiseTemp_C(14) = Temp_C(14) - PTemp_C
   RiseTemp_C(15) = Temp_C(15) - PTemp_C
   RiseTemp_C(16) = Temp_C(16) - PTemp_C
   RiseTemp_C(17) = Temp_C(17) - PTemp_C
   RiseTemp_C(18) = Temp_C(18) - PTemp_C
   RiseTemp_C(19) = Temp_C(19) - PTemp_C
   RiseTemp_C(20) = Temp_C(20) - PTemp_C
   RiseTemp_C(21) = Temp_C(21) - PTemp_C
   RiseTemp_C(22) = Temp_C(22) - PTemp_C
   RiseTemp_C(23) = Temp_C(23) - PTemp_C
   RiseTemp_C(24) = Temp_C(24) - PTemp_C
   RiseTemp_C(25) = Temp_C(25) - PTemp_C
   RiseTemp_C(26) = Temp_C(26) - PTemp_C
   RiseTemp_C(27) = Temp_C(27) - PTemp_C
   RiseTemp_C(28) = Temp_C(28) - PTemp_C
   RiseTemp_C(29) = Temp_C(29) - PTemp_C
   RiseTemp_C(30) = Temp_C(30) - PTemp_C
   RiseTemp_C(31) = Temp_C(31) - PTemp_C

   ' Frame TCs
   RiseTemp_C(1) = Temp_C(1) - PTemp_C
```

```
  RiseTemp_C(2) = Temp_C(2) - PTemp_C
  RiseTemp_C(3) = Temp_C(3) - PTemp_C
  RiseTemp_C(4) = Temp_C(4) - PTemp_C

' AVR box TC
  RiseTemp_C(5) = Temp_C(5) - PTemp_C

' Feet TC
  RiseTemp_C(6) = Temp_C(6) - PTemp_C

' Induction machine TC
  RiseTemp_C(7) = Temp_C(7) - PTemp_C

' Air inlet and outlet TCs
  RiseTemp_C(10) = Temp_C(10) - PTemp_C
  RiseTemp_C(11) = Temp_C(11) - PTemp_C

'Call Data Tables and Store Data
    CallTable(NOV10)
  NextScan
EndProg
```

Appendix G

Full MySolver Steady-State & Transient Validation against Experimental Data

Note: The thermocouples used to validate MySolver are illustrated in Table 8.7 (Section 8.2.1). Rotor MySolver lumped parameter thermal network nodes a shown in Figures 3.3 (Section 3.3) and 3.14 (Section 3.5.1) and rotor winding thermocouple locations in Figure 7.6 (Section 7.2.1). Stator MySolver lumped parameter thermal network nodes a presented in Figures 3.7 (Section 3.4) and 3.17 (Section 3.5.2) and stator winding thermocouple locations are in Figures 7.3 and 7.5 (Section 7.2.1).

G.1 Steady-State MySolver Validation

5 kW loading

		Actual kW load tested:	5.25 kW
Node	MySolver (°C)	Experimental (°C)	Error (°C)
a1	18.85	19.53	- 0.68
b1	19.43	19.91	- 0.48
c1	19.96	20.96	- 1.00
d1	18.38	16.98	+ 1.40
e1	20.41	18.39	+ 2.02
a3	18.62	18.20	+ 0.42
b3	19.15	20.43	- 1.28
c3	19.72	18.97	+ 0.75
Average (°C)	19.32	19.17	+ 0.15

Table G.1: *5 kW loading MySolver rotor thermal network steady-state validation.*

		Actual kW load tested:	5.25 kW
Node	MySolver (°C)	Experimental (°C)	Error (°C)
a1	18.07	17.46	+ 0.61
b1	19.01	18.86	+ 0.15
c1	18.90	19.24	- 0.34
d1	15.77	17.20	- 1.43
e1	16.75	19.40	- 2.65
a2	19.51	17.46	+ 2.05
b2	20.57	18.86	+ 1.71
c2	20.12	19.24	+ 0.88
Average (°C)	18.59	18.46	+ 0.13

Table G.2: *5kW loading MySolver stator thermal network steady-state validation.*

8 kW loading

Actual kW load tested: 8.20 kW

Node	MySolver (°C)	Experimental (°C)	Error (°C)
a1	22.26	23.12	- 0.86
b1	22.90	23.78	- 0.88
c1	23.56	24.62	- 1.06
d1	21.95	20.50	+ 1.45
e1	24.33	22.30	+ 2.03
a3	22.03	21.80	+ 0.23
b3	22.62	24.04	- 1.42
c3	23.31	22.86	+ 0.45
Average (°C)	22.87	22.88	- 0.01

Table G.3: *8 kW loading MySolver rotor thermal network steady-state validation.*

Actual kW load tested: 8.20 kW

Node	MySolver (°C)	Experimental (°C)	Error (°C)
a1	23.29	22.34	+ 0.95
b1	24.29	24.01	+ 0.28
c1	24.29	24.63	- 0.34
d1	21.25	22.89	- 1.64
e1	22.44	25.52	- 3.08
a2	25.05	22.34	+ 2.71
b2	26.19	24.01	+ 2.18
c2	25.79	24.63	+ 1.16
Average (°C)	24.07	23.80	+ 0.27

Table G.4: *8 kW loading MySolver stator thermal network steady-state validation.*

10 kW loading

Actual kW load tested: 10.28 kW

Node	MySolver (°C)	Experimental (°C)	Error (°C)
a1	25.51	26.44	- 0.93
b1	26.20	27.05	- 0.85
c1	26.98	27.89	- 0.91
d1	25.34	23.37	+ 1.97
e1	28.06	25.41	+ 2.65
a3	25.28	25.28	0.00
b3	25.92	27.53	- 1.61
c3	26.74	26.10	+ 0.64
Average (°C)	26.25	26.13	+ 0.12

Table G.5: *10 kW loading MySolver rotor thermal network steady-state validation.*

Actual kW load tested: 10.28 kW

Node	MySolver (°C)	Experimental (°C)	Error (°C)
a1	28.58	27.11	+ 1.47
b1	29.61	29.03	+ 0.58
c1	29.75	29.89	- 0.14
d1	26.95	28.42	- 1.47
e1	28.34	31.42	- 3.08
a2	30.66	27.11	+ 3.55
b2	31.84	29.03	+ 2.81
c2	31.51	29.89	+ 1.62
Average (°C)	29.66	28.99	+ 0.67

Table G.6: *10 kW loading MySolver stator thermal network steady-state validation.*

12 kW loading

Actual kW load tested: 12.26 kW

Node	MySolver (°C)	Experimental (°C)	Error (°C)
a1	30.34	31.42	- 1.08
b1	31.09	32.38	- 1.29
c1	32.05	33.40	- 1.35
d1	30.41	28.16	+ 2.25
e1	33.58	30.54	+ 3.04
a3	30.11	30.05	+ 0.06
b3	30.81	32.89	- 2.08
c3	31.81	31.36	+ 0.45
Average (°C)	31.28	31.27	+ 0.01

Table G.7: *12 kW loading MySolver rotor thermal network steady-state validation.*

Actual kW load tested: 12.26 kW

Node	MySolver (°C)	Experimental (°C)	Error (°C)
a1	34.14	32.96	+ 1.18
b1	35.20	35.17	+ 0.03
c1	35.50	36.38	- 0.88
d1	32.95	35.16	- 2.21
e1	34.56	38.65	- 4.09
a2	36.54	32.96	+ 3.58
b2	37.76	35.17	+ 2.59
c2	37.51	36.38	+ 1.13
Average (°C)	35.52	35.35	+ 0.17

Table G.8: *12 kW loading MySolver stator thermal network steady-state validation.*

14 kW loading

Actual kW load tested: 14.17 kW

Node	MySolver (°C)	Experimental (°C)	Error (°C)
a1	34.50	36.47	- 1.97
b1	35.32	37.28	- 1.96
c1	36.45	38.65	- 2.20
d1	34.75	32.55	+ 2.20
e1	38.37	35.35	+ 3.02
a3	34.27	35.20	-0.93
b3	35.05	37.72	- 2.67
c3	36.20	36.13	+0.07
Average (°C)	35.61	36.17	- 0.56

Table G.9: *14 kW loading MySolver rotor thermal network steady-state validation.*

Actual kW load tested: 14.17 kW

Node	MySolver (°C)	Experimental (°C)	Error (°C)
a1	42.55	40.43	+ 2.12
b1	43.59	43.04	+ 0.55
c1	44.16	44.64	- 0.48
d1	42.23	43.84	- 1.61
e1	44.15	47.83	- 3.69
a2	45.43	40.43	+ 5.00
b2	46.67	43.04	+ 3.63
c2	46.58	44.64	+ 1.94
Average (°C)	44.42	43.49	+ 0.93

Table G.10: *14 kW loading MySolver stator thermal network steady-state validation.*

16 kW loading

Actual kW load tested: 16.52 kW

Node	MySolver (°C)	Experimental (°C)	Error (°C)
a1	42.90	45.43	- 2.53
b1	43.84	46.81	- 2.97
c1	45.27	48.25	- 2.98
d1	43.55	40.97	+ 2.58
e1	47.99	44.51	+ 3.48
a3	42.67	43.87	- 1.20
b3	43.57	47.30	- 3.73
c3	45.03	45.41	- 0.38
Average (°C)	44.35	45.32	- 0.97

Table G.11: *16 kW loading MySolver rotor thermal network steady-state validation.*

Actual kW load tested: 16.52 kW

Node	MySolver (°C)	Experimental (°C)	Error (°C)
a1	54.19	54.10	+ 0.09
b1	55.23	57.29	- 2.06
c1	56.18	59.50	- 3.32
d1	55.06	59.13	- 4.07
e1	57.42	63.99	- 6.57
a2	57.71	54.10	+ 3.61
b2	58.97	57.29	+ 1.68
c2	59.11	59.50	- 0.39
Average (°C)	56.73	58.11	- 1.38

Table G.12: *16 kW loading MySolver stator thermal network steady-state validation.*

18 kW loading

Actual kW load tested: 18.38 kW

Node	MySolver (°C)	Experimental (°C)	Error (°C)
a1	50.28	53.71	- 3.43
b1	51.34	55.06	- 3.72
c1	53.05	56.88	- 3.83
d1	51.25	47.99	+ 3.26
e1	56.46	52.25	+ 4.21
a3	50.05	51.58	- 1.53
b3	51.06	55.61	- 4.55
c3	52.80	53.47	- 0.67
Average (°C)	52.04	53.32	- 1.28

Table G.13: *18 kW loading MySolver rotor thermal network steady-state validation.*

Actual kW load tested: 18.38 kW

Node	MySolver (°C)	Experimental (°C)	Error (°C)
a1	66.83	65.02	+ 1.81
b1	67.83	68.74	- 0.91
c1	69.20	71.56	- 2.36
d1	69.10	71.98	- 2.88
e1	71.92	77.41	- 5.49
a2	71.05	65.02	+ 6.03
b2	72.31	68.74	+ 3.57
c2	72.70	71.56	+ 1.14
Average (°C)	70.12	70.00	+ 0.12

Table G.14: *18 kW loading MySolver stator thermal network steady-state validation.*

20 kW loading

Actual kW load tested: 20.39 kW

Node	MySolver (°C)	Experimental (°C)	Error (°C)
a1	58.03	61.81	- 3.78
b1	59.22	63.10	- 3.88
c1	61.23	65.00	- 3.77
d1	59.32	56.08	+ 3.24
e1	65.37	61.12	+ 4.25
a3	57.80	60.37	- 2.57
b3	58.95	64.03	- 5.08
c3	60.99	62.43	- 1.44
Average (°C)	60.11	61.74	- 1.63

Table G.15: *20 kW loading MySolver rotor thermal network steady-state validation.*

Actual kW load tested: 20.39 kW

Node	MySolver (°C)	Experimental (°C)	Error (°C)
a1	82.47	80.60	+ 1.87
b1	83.40	85.00	- 1.60
c1	85.29	88.60	- 3.31
d1	86.53	89.92	- 3.39
e1	89.90	96.08	- 6.18
a2	87.54	80.60	+ 6.94
b2	88.79	85.00	+ 3.79
c2	89.52	88.60	+ 0.92
Average (°C)	86.68	86.80	- 0.12

Table G.16: *20 kW loading MySolver stator thermal network steady-state validation.*

G.2 Transient MySolver Validation

5 kW loading

Actual kW load tested: 5.25 kW

Node	MySolver (°C)	Experimental (°C)	Error (°C)
a1	14.09	15.58	- 1.49
b1	14.31	15.23	- 0.92
c1	14.82	16.36	- 1.54
d1	14.43	13.61	+ 0.82
e1	15.76	14.82	+ 0.94
a3	13.92	14.80	- 0.88
b3	14.14	16.19	- 2.05
c3	14.63	14.57	+ 0.06
Average (°C)	14.51	15.15	- 0.64

Table G.17: *5 kW loading MySolver rotor thermal network transient validation.*

Actual kW load tested: 5.25 kW

Node	MySolver (°C)	Experimental (°C)	Error (°C)
a1	15.51	14.89	+ 0.62
b1	16.38	15.96	+ 0.42
c1	16.20	16.21	- 0.01
d1	13.17	14.76	- 1.59
e1	13.96	16.34	- 2.38
a2	16.75	14.89	+ 1.86
b2	17.72	15.96	+ 1.76
c2	17.25	16.21	+ 1.04
Average (°C)	15.87	15.65	+ 0.22

Table G.18: *5 kW loading MySolver stator thermal network transient validation.*

8 kW loading

Actual kW load tested: 8.20 kW

Node	MySolver (°C)	Experimental (°C)	Error (°C)
a1	16.81	18.03	- 1.22
b1	17.02	18.31	- 1.29
c1	17.66	19.07	- 1.41
d1	17.43	16.12	+ 1.31
e1	18.99	17.11	+ 1.88
a3	16.64	17.11	- 0.47
b3	16.88	17.88	- 1.00
c3	17.48	17.34	+ 0.14
Average (°C)	17.36	17.62	- 0.26

Table G.19: *8 kW loading MySolver rotor thermal network transient validation.*

Actual kW load tested: 8.20 kW

Node	MySolver (°C)	Experimental (°C)	Error (°C)
a1	20.25	19.42	+ 0.83
b1	21.17	20.70	+ 0.47
c1	21.09	21.18	- 0.09
d1	18.16	20.11	- 1.95
e1	19.13	22.03	- 2.90
a2	21.78	19.42	+ 2.36
b2	22.82	20.70	+ 2.12
c2	22.39	21.18	+ 1.21
Average (°C)	20.85	20.59	+ 0.26

Table G.20: *8 kW loading MySolver stator thermal network transient validation.*

10 kW loading

Actual kW load tested: 10.28 kW

Node	MySolver (°C)	Experimental (°C)	Error (°C)
a1	19.38	20.30	- 0.92
b1	19.60	20.12	- 0.52
c1	20.35	21.04	- 0.69
d1	20.26	17.83	+ 2.43
e1	22.06	19.72	+ 2.34
a3	19.22	20.00	- 0.78
b3	19.47	20.90	- 1.43
c3	20.18	20.26	- 0.08
Average (°C)	20.06	20.02	+ 0.04

Table G.21: *10 kW loading MySolver rotor thermal network transient validation.*

Actual kW load tested: 10.28 kW

Node	MySolver (°C)	Experimental (°C)	Error (°C)
a1	24.85	23.76	+ 1.09
b1	25.77	25.22	+ 0.55
c1	25.83	25.92	- 0.09
d1	23.17	25.20	- 2.03
e1	24.29	27.39	- 3.10
a2	26.65	23.76	+ 2.89
b2	27.70	25.22	+ 2.48
c2	27.34	25.92	+ 1.42
Average (°C)	25.70	25.30	+ 0.40

Table G.22: *10 kW loading MySolver stator thermal network transient validation.*

12 kW loading

Actual kW load tested: 12.26 kW

Node	MySolver (°C)	Experimental (°C)	Error (°C)
a1	23.27	24.99	- 1.72
b1	23.48	24.66	- 1.18
c1	24.41	25.76	- 1.35
d1	24.55	22.36	+ 2.19
e1	26.67	23.98	+ 2.69
a3	23.13	23.92	- 0.79
b3	23.37	25.64	- 2.27
c3	24.25	24.81	- 0.56
Average (°C)	24.14	24.51	- 0.37

Table G.23: *12 kW loading MySolver rotor thermal network transient validation.*

Actual kW load tested: 12.26 kW

Node	MySolver (°C)	Experimental (°C)	Error (°C)
a1	30.13	29.39	+ 0.74
b1	31.08	31.11	- 0.03
c1	31.28	32.10	- 0.82
d1	28.89	31.68	- 2.79
e1	30.21	34.27	- 4.06
a2	32.23	29.39	+ 2.84
b2	33.31	31.11	+ 2.20
c2	33.03	32.10	+ 0.93
Average (°C)	31.27	31.39	- 0.12

Table G.24: *12 kW loading MySolver stator thermal network transient validation.*

14 kW loading

Actual kW load tested: 14.17 kW

Node	MySolver (°C)	Experimental (°C)	Error (°C)
a1	26.54	28.53	- 1.99
b1	26.75	28.54	- 1.79
c1	27.83	29.52	- 1.69
d1	28.14	25.67	+ 2.47
e1	30.57	27.74	+ 2.83
a3	26.40	28.21	- 1.81
b3	26.66	29.39	- 2.73
c3	27.68	27.91	- 0.23
Average (°C)	25.57	28.19	- 0.62

Table G.25: *14 kW loading MySolver rotor thermal network transient validation.*

Actual kW load tested: 14.17 kW

Node	MySolver (°C)	Experimental (°C)	Error (°C)
a1	37.82	35.98	+ 1.84
b1	38.73	37.97	+ 0.76
c1	39.18	39.30	- 0.12
d1	37.43	39.42	- 1.99
e1	39.01	42.35	- 3.34
a2	40.35	35.98	+ 4.37
b2	41.43	37.97	+ 3.46
c2	41.30	39.30	+ 2.00
Average (°C)	39.41	38.53	+0.88

Table G.26: *14 kW loading MySolver stator thermal network transient validation.*

16 kW loading

Actual kW load tested: 16.52 kW

Node	MySolver (°C)	Experimental (°C)	Error (°C)
a1	32.98	34.50	- 1.52
b1	33.16	34.76	- 1.60
c1	34.54	35.40	- 0.86
d1	35.31	31.37	+ 3.94
e1	38.27	33.77	+ 4.50
a3	32.87	33.48	- 0.61
b3	33.12	35.08	- 1.96
c3	34.42	33.90	+ 0.52
Average (°C)	34.33	34.03	+ 0.30

Table G.27: *16 kW loading MySolver rotor thermal network transient validation.*

Actual kW load tested: 16.52 kW

Node	MySolver (°C)	Experimental (°C)	Error (°C)
a1	48.04	47.37	+ 0.67
b1	48.90	49.80	- 0.90
c1	49.69	51.64	- 1.95
d1	48.81	52.30	- 3.49
e1	50.72	55.83	- 5.11
a2	51.09	47.37	+ 3.72
b2	52.15	49.80	+ 2.35
c2	52.23	51.64	+ 0.59
Average (°C)	50.20	50.72	- 0.52

Table G.28: *16 kW loading MySolver stator thermal network transient validation.*

18 kW loading

Actual kW load tested: 18.38 kW

Node	MySolver (°C)	Experimental (°C)	Error (°C)
a1	38.78	40.00	- 1.22
b1	38.95	40.07	- 1.12
c1	40.60	41.70	- 1.10
d1	41.71	36.41	+ 5.30
e1	45.18	39.47	+ 5.71
a3	38.69	39.41	- 0.72
b3	38.96	41.13	- 2.17
c3	40.50	39.39	+ 1.11
Average (°C)	40.42	39.70	+ 0.72

Table G.29: *18 kW loading MySolver rotor thermal network transient validation.*

Actual kW load tested: 18.38 kW

Node	MySolver (°C)	Experimental (°C)	Error (°C)
a1	59.54	56.49	+ 3.05
b1	60.34	59.23	+ 1.11
c1	61.53	61.56	- 0.03
d1	61.70	63.13	- 1.43
e1	64.00	66.96	- 2.96
a2	63.21	56.49	+ 6.72
b2	64.23	59.23	+ 5.00
c2	64.57	61.56	+ 3.01
Average (°C)	62.39	60.58	+ 1.81

Table G.30: *18 kW loading MySolver stator thermal network transient validation.*

20 kW loading

Actual kW load tested: 20.39 kW

Node	MySolver (°C)	Experimental (°C)	Error (°C)
a1	44.82	46.28	- 1.46
b1	45.00	46.84	- 1.84
c1	46.93	48.42	- 1.49
d1	48.37	42.64	+ 5.73
e1	52.41	45.84	+ 6.57
a3	44.75	45.60	- 0.85
b3	45.05	47.57	- 2.52
c3	46.86	46.38	+ 0.48
Average (°C)	46.77	46.20	+ 0.57

Table G.31: *20 kW loading MySolver rotor thermal network transient validation.*

Actual kW load tested: 20.39 kW

Node	MySolver (°C)	Experimental (°C)	Error (°C)
a1	73.20	69.58	+ 3.62
b1	73.88	72.79	+ 1.09
c1	75.54	75.77	- 0.23
d1	77.12	78.33	- 1.21
e1	79.83	82.69	- 2.86
a2	77.58	69.58	+ 8.00
b2	78.52	72.79	+ 5.73
c2	79.17	75.77	+ 3.40
Average (°C)	76.86	74.66	+ 2.20

Table G.32: *20 kW loading MySolver stator thermal network transient validation.*

Appendix H

Additional Duty Cycle Simulations

5 kW – 12 kW – 10 kW Duty Cycle

Rotor Temperature Rise (°C)				
Time (m)	Loading (kW)	MySolver	Experimental	Error (°C)
45	5.24	16.07	17.12	- 1.05
90	12.27	28.73	29.02	- 0.29
135	10.30	26.14	26.32	- 0.18

Table H.1: *5kW-12kW-10kW duty-cycle MySolver rotor validation results.*

Stator Temperature Rise (°C)				
Time (m)	Loading (kW)	MySolver	Experimental	Error (°C)
45	5.24	17.55	17.12	+ 0.43
90	12.27	34.80	35.39	- 0.59
135	10.30	29.78	29.06	+ 0.72

Table H.2: *5kW-12kW-10kW duty-cycle MySolver stator validation results.*

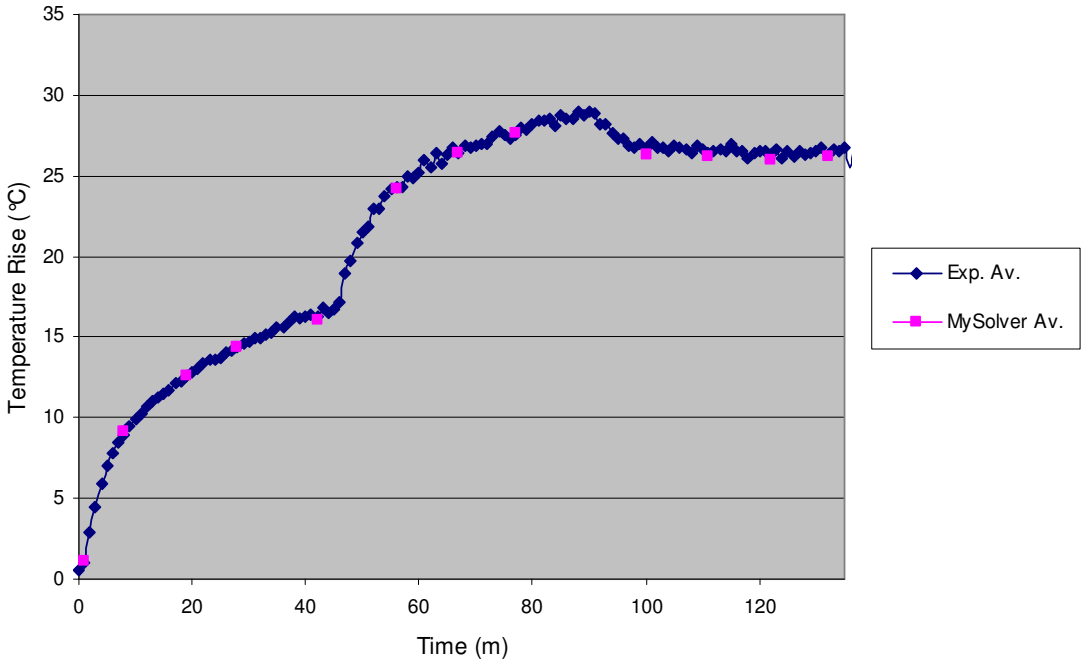

Figure H.1: *5kW-12kW-10kW duty-cycle MySolver rotor and validation results.*

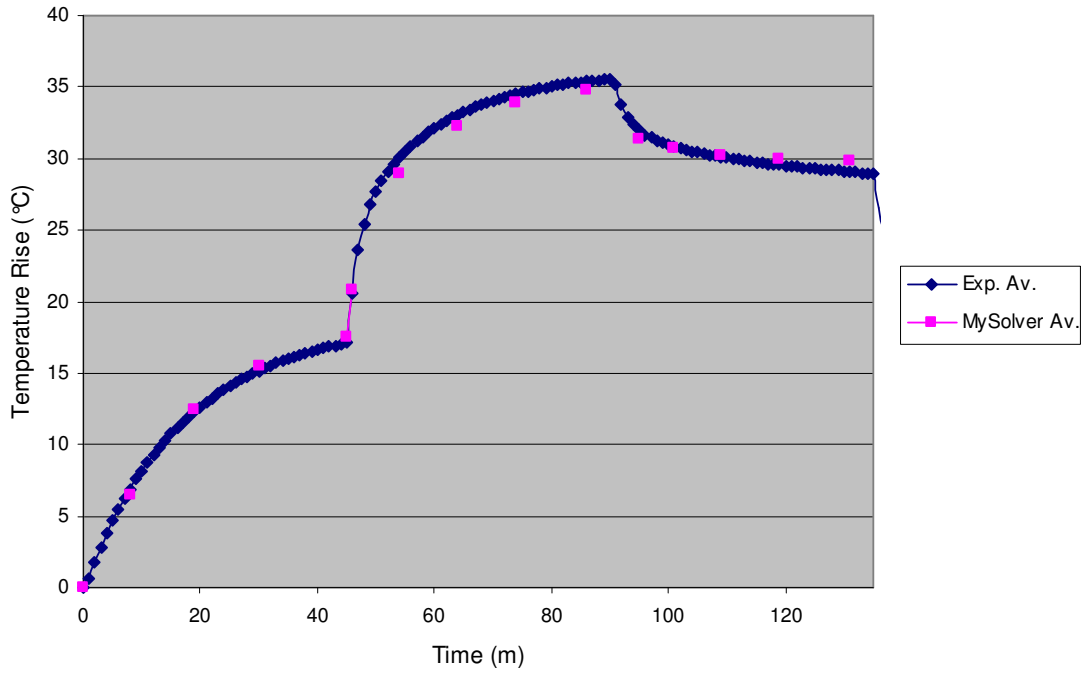

Figure H.2: *5kW-12kW-10kW duty-cycle MySolver stator and validation results.*

12 kW – 8 kW – 12 kW Duty Cycle

Rotor Temperature Rise (°C)				
Time (m)	Loading (kW)	MySolver	Experimental	Error (°C)
45	12.29	26.45	26.98	- 0.53
90	8.21	22.49	22.62	- 0.13
135	12.27	30.10	30.13	- 0.03

Table H.3: *12kW-8kW-12kW duty-cycle MySolver rotor validation results.*

Stator Temperature Rise (°C)				
Time (m)	Loading (kW)	MySolver	Experimental	Error (°C)
45	12.29	33.90	34.13	- 0.23
90	8.21	24.37	23.72	+ 0.65
135	12.27	35.07	35.10	- 0.03

Table H.4: *12kW-8kW-12kW duty-cycle MySolver stator validation results.*

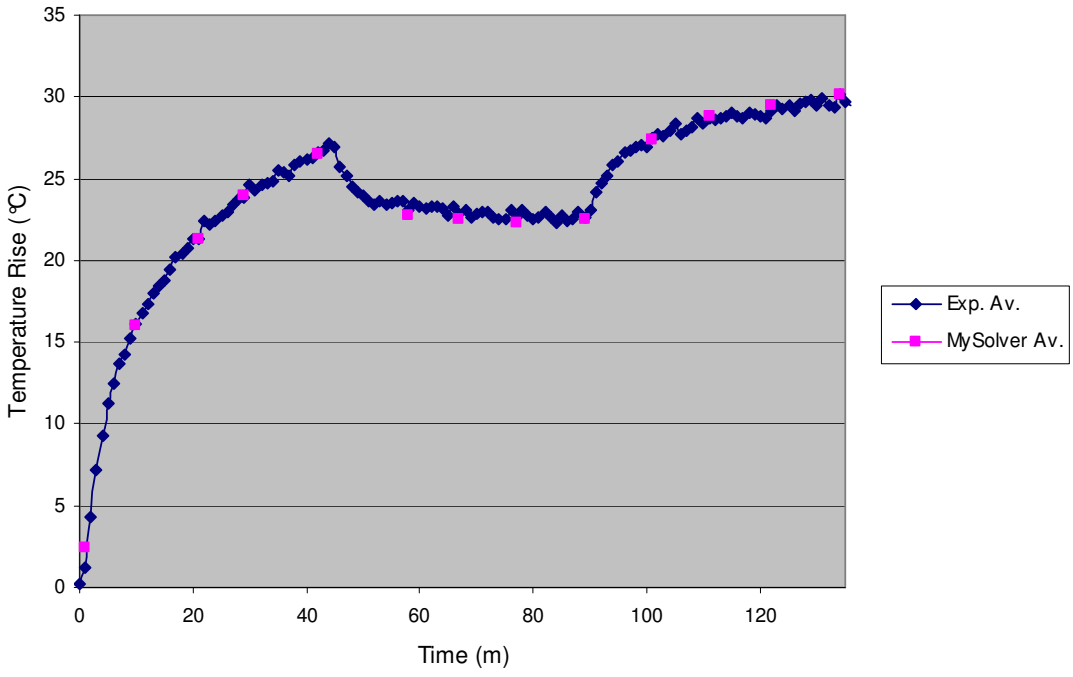

Figure H.3: *12kW-8kW-12kW duty-cycle MySolver rotor and validation results.*

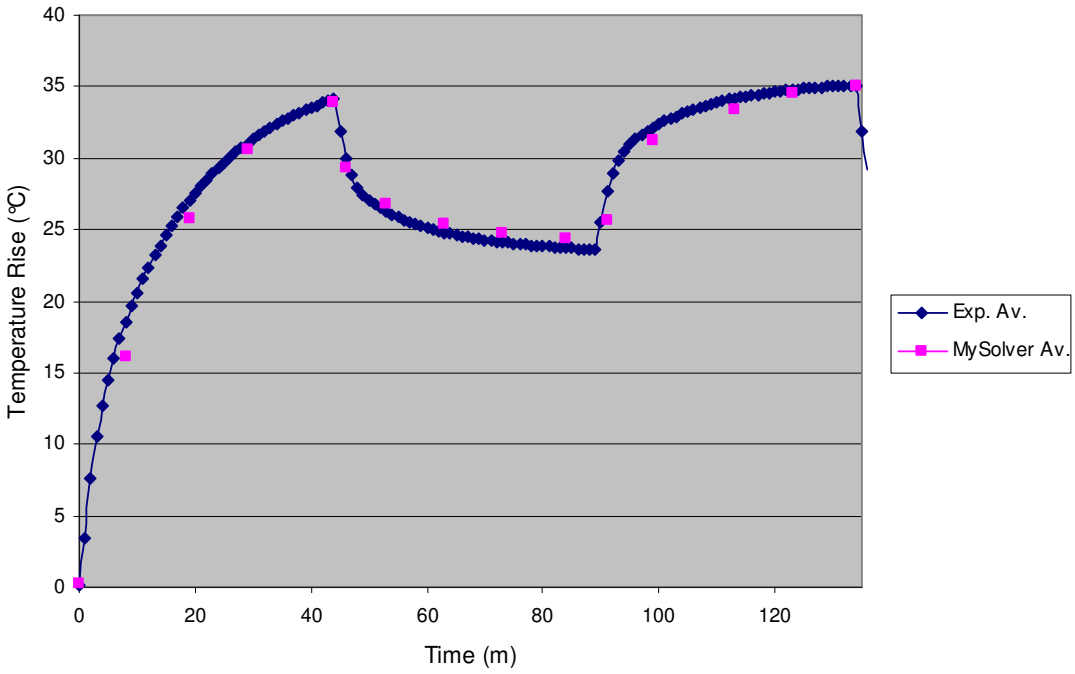

Figure H.4: *12kW-8kW-12kW duty-cycle MySolver stator and validation results.*

Appendix I

Publications

I.1 Details of Published Papers

Boglietti, A.; Cavagnino, A.; Staton, D.; Shanel, M.; Mueller, M. and Mejuto, C., "Evolution and Modern Approaches for Thermal Analysis of Electrical Machines", *Industry Electronics, IEEE Transactions on*, Volume: 56, Issue: 3, Page(s): 871-882, March 2009.

Mejuto, C.; Mueller, M.; Shanel, M.; Mebarki, A.; Reekie, M. and Staton, D., "Improved synchronous machine thermal modelling", presented at 18th International Conference on Electrical Machines, September 2008.

Mejuto, C.; Mueller, M.; Shanel, M.; Mebarki, A. and Staton, D., "Thermal modelling investigation of heat paths due to iron losses in synchronous machines", presented at IET Conference on Power Electronics, Machines and Drives, Page(s): 225-229, April 2008.

Mejuto, C.; Mueller, M.; Staton, D.; Mebarki, S. and Al-Khayat, N., "Thermal Modelling of TEFC Alternators", presented at 32nd Conference of the IEEE Industrial Electronics Society (IECON), Page(s): 4813-4818, November 2006.

IEEE TRANSACTIONS ON INDUSTRIAL ELECTRONICS, VOL. 56, NO. 3, MARCH 2009

Evolution and Modern Approaches for Thermal Analysis of Electrical Machines

Aldo Boglietti, *Senior Member, IEEE*, Andrea Cavagnino, *Member, IEEE*, David Staton, Martin Shanel, Markus Mueller, and Carlos Mejuto

***Abstract*—In this paper, the authors present an extended survey on the evolution and the modern approaches in the thermal analysis of electrical machines. The improvements and the new techniques proposed in the last decade are analyzed in depth and compared in order to highlight the qualities and defects of each. In particular, thermal analysis based on lumped-parameter thermal network, finite-element analysis, and computational fluid dynamics are considered in this paper. In addition, an overview of the problems linked to the thermal parameter determination and computation is proposed and discussed. Taking into account the aims of this paper, a detailed list of books and papers is reported in the references to help researchers interested in these topics.**

***Index Terms*—Computed fluid dynamic, electrical machines, finite-element analysis (FEA), lumped-parameter thermal network (LPTN), thermal model, thermal parameter identification.**

I. Introduction

IN THE PAST, the thermal analysis of electric machines has received less attention than electromagnetic analysis. This is clear from the number of technical papers published relating to each of these particular subjects. This inequality is particularly true for small- and medium-sized motors. Traditionally, for such machines, motor designers have only superficially dealt with the thermal design aspects, maybe by specifying a limiting value of current density or some other rudimentary sizing variable. The problem with such sizing methods is that they do not give an indication of how the design may be improved to reduce temperatures.

With the increasing requirements for miniaturization, energy efficiency, and cost reduction, as well as the imperative to fully exploit new topologies and materials, it is now necessary to analyze the thermal circuit to the same extent as the electromagnetic design.

Manuscript received January 28, 2008; revised December 1, 2008. Current version published February 27, 2009.

A. Boglietti and A. Cavagnino are with the Department of Electrical Engineering, Politecnico di Torino, 10129 Turin, Italy (e-mail: aldo.boglietti@polito.it; andrea.cavagnino@polito.it).

D. Staton is with Motor Design Ltd., Ellesmere, SY12 OEG, U.K. (e-mail: dave.staton@motor-design.com).

M. Shanel is with Cummins Generator Technologies, Stamford, PE9 2NB, U.K. (e-mail: martin.shanel@cummins.com).

M. Mueller and C. Mejuto are with the Institute for Energy Systems, University of Edinburgh, Edinburgh, EH9 3JL, U.K. (e-mail: markus.mueller@ed.ac.uk; carlosmejuto@hotmail.com).

Color versions of one or more of the figures in this paper are available online at http://ieeexplore.ieee.org.

Digital Object Identifier 10.1109/TIE.2008.2011622

In fact, there should be a strong interaction between the electromagnetic and thermal designs as it is impossible to accurately analyze one without the other, i.e., the losses are critically dependent upon the temperature and vice versa.

Currently, the interest in thermal analysis involves not only the electrical machine but also the drive and power converter design [1], [2]. A possible reason why thermal analysis has received less attention than electromagnetic analysis is that electric-motor designers usually have an electrical engineering background, while thermal analysis is a mechanical engineering discipline.

Electric-motor thermal analysis can be divided into two basic types: analytical lumped-circuit and numerical methods. The analytical approach has the advantage of being very fast to calculate; however, the developer of the network model must invest effort in defining a circuit that accurately models the main heat-transfer paths [3]–[6].

In its most basic form, the heat-transfer network is analogous to an electrical network, and the analysis consists of the calculation of conduction, convection, and radiation resistances for different parts of the motor construction. The formulations for such resistances are really quite simple. The conduction resistance is equal to the path length divided by the product of the path area and the materials' thermal conductivity. The convection and radiation resistances are equal to one divided by the product of the surface area and the heat-transfer coefficient. The radiation-heat-transfer coefficient is simply a function of the surface properties, i.e., the emissivity and the view factor. The emissivity is known for different types of surface, and the view factor can be calculated based on the geometry. The convection-heat-transfer coefficient is most often based on empirical formulations based on convection correlations which are readily available in the heat-transfer literature. Fortunately, there is a wealth of convection correlations for most of the basic geometric shapes used in electrical machines, both for natural and forced convection cooling (i.e., cylindrical surfaces, flat plates, open- and closed-fin channels, etc.). The most common and useful convection correlations are even available in undergraduate textbooks on heat transfer [7]–[12].

The main strength of numerical analysis is that any device geometry can be modeled. However, it is very demanding in terms of model setup and computational time. There are two types of numerical analysis: finite-element analysis (FEA) and computational fluid dynamics (CFD). CFD has the advantage that it can be used to predict flow in complex regions, such as around the motor end windings [13], [14]. FEA can only be used to model conduction heat transfer in solid components.

For convection boundaries, the same analytical/empirical algorithms used in the lumped-circuit analysis must be adopted (i.e., convection correlations).

Taking into account the survey approach of this paper, a short historical evolution on electrical-machine thermal analysis is hereafter included.

Before the advent of computers, motor sizing was traditionally made using the so-called D^2L, D^3L, and D^xL sizing equations, where the designer provided limiting values of specific magnetic and electric loadings and/or current density from past experience [15]. This method of sizing does not involve thermal analysis directly, the specific magnetic loading and current density being limited to prevent overheating. At this time, simple thermal-network analysis based on lumped parameters were also used by some designers to perform rudimentary thermal analysis; however, the thermal networks were kept as simple as possible so they could be calculated by hand, e.g., maybe just one thermal resistances to calculate the steady-state temperature rise of the winding. With the introduction of computers to motor design, the complexity of the thermal networks increased. A reference paper highlighting the introduction of more complex thermal networks calculated using computers was published in 1991 by Mellor *et al.* [3]. Thermal-network analysis has become the main tool used by many researchers involved in thermal analysis of electrical machines, both for steady-state and transient analyses [16]. A further factor that has led to increased interest in thermal-network analysis was the introduction of induction motor inverter supplies. Several authors have studied the effect of increased losses, resulting from six-step and pulsewidth-modulation voltages, on motor temperatures [17], [18].

Thermal analysis has always received less attention than electromagnetic design. However, in the new century, the topic had started to receive more importance due to market globalization and the requirement for smaller, cheaper, and more efficient electric motors. In many cases, the software used for the design of electric machines has now adopted improved thermal modeling capabilities and features enabling better integration between the electromagnetic and the thermal designs [19], [20].

Several interesting papers have been published in recent years on thermal analysis of electric machines. References [19] and [20] deal with coupled electromagnetic and thermal analysis with the thermal network solved using network analysis. In [20], the losses are calculated using analytical methods [21], while in [19], electromagnetic FEA is used. In [22], a thermal-network method is proposed to account for combined air flow and heat transfer, i.e., for forced air cooling in stator and rotor core ducts in this case. In [23], a combined network and CFD method is used to model the machine. Network analysis is used to calculate conduction through the electromagnetic structure while CFD is used for convection at the surface. The use of CFD for prediction of convective heat transfer is expanded in Section VI. Calibration with measured data is typically used to calibrate thermal resistances that are influenced by the motor manufacturing process [4], [6], [24]. An example is the thermal interface resistance between stator lamination and housing, which is influenced by the method used to insert the stator in the frame.

II. Thermal Network Based on Lumped Parameters

This section details the main concerns relating to lumped-parameter thermal-network (LPTN) analysis. Analytical thermal-network analysis can be subdivided into two main calculation types: heat-transfer and flow-network analyses. Heat-transfer analysis is the thermal counterpart to electrical-network analysis with the following equivalences: temperature to voltage, power to current, and thermal resistance to electrical resistance. Flow-network analysis is the fluid mechanics counterpart to electrical-network analysis with the following equivalences: pressure to voltage, volume flow rate to current, and flow resistance to electrical resistance. In the heat-transfer network, a thermal resistance circuit describes the main paths for power flow, enabling the temperatures of the main components within the machine to be predicted for a given loss distribution.

As is well known, in a thermal network, it is possible to lump together components that have similar temperatures and to represent each as a single node in the network. Nodes are separated by thermal resistances that represent the heat transfer between components. Inside the machine, a set of conduction thermal resistances represents the main heat-transfer paths, such as from the winding copper to the stator tooth and back iron (in this case, the heat transfer is through the winding insulation consisting of a combination of enamel, impregnation, and slot-liner materials), from the tooth and stator back iron nodes to the stator bore and housing interface, etc. In addition, internal convection and radiation resistances are used for heat transfer across the air gap and from the end windings to the endcaps and housing. External convection and radiation resistances are used for heat transfer from the outside of the machine to ambient. In the past, due to limited computational capabilities, simple thermal networks with few thermal resistances, capacitances, and sources were adopted. Nowadays, much more detailed thermal and flow networks can be quickly solved, including a high number of thermal and flow elements. An example of a detailed heat-transfer network is shown in Fig. 1. Detailed information on this thermal network can be found in [35].

Lumped-circuit thermal models have been extensively utilized and validated on numerous machine types and operating points. Such a wide range of studies has increased confidence in such thermal models.

As an example of this approach, the thermal model shown in Fig. 1 has been used to analyze a 22.5-kVA synchronous machine, shown in Fig. 2.

The model calculates both the air flow and heat transfer in the machine. Air flow and temperature rise for all stator and rotor nodes were within 10% of the measured values [25].

Analytical lumped-circuit techniques are also very useful in determining the thermal model's required discretization level. This refers to the number of sections used to model the electrical machine as a whole, or some of the more critical components, both in the axial and radial directions. In [25], studies have been performed to determine the required discretization level for a synchronous generator, with particular attention being given to the winding area. Due to its low thermal

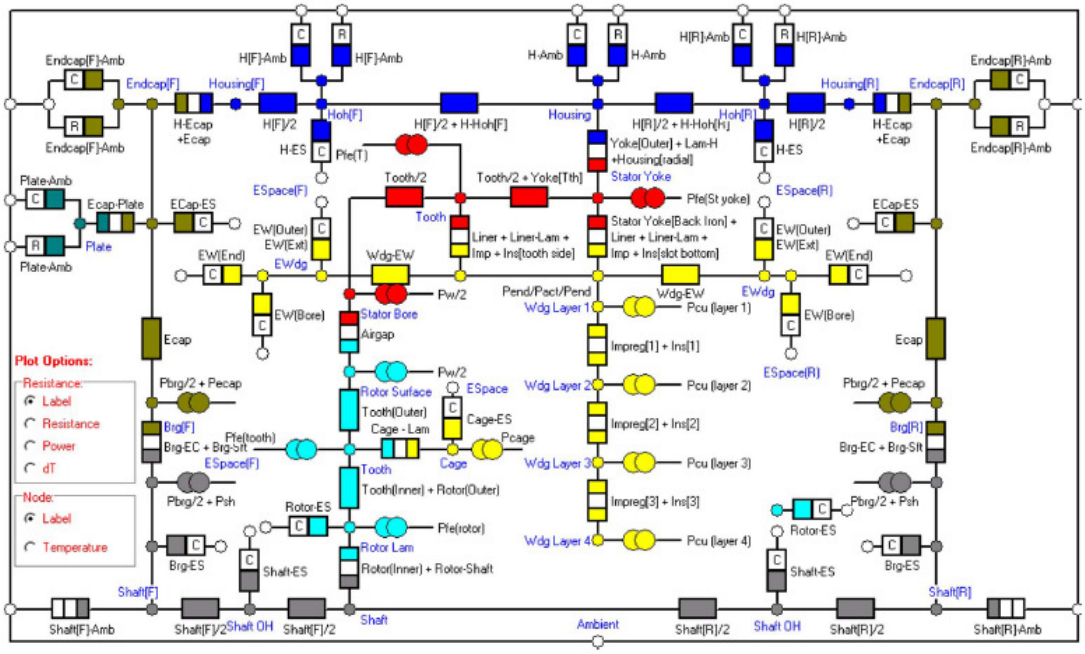

Fig. 1. Example of heat-transfer network for an electric motor.

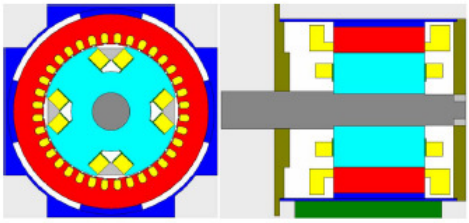

Fig. 2. Radial and axial cross sections of the modeled alternator.

conductivity [2–3 $W/(m \cdot °C)$], this area is of great thermal significance and has to be analyzed with care.

In the real winding, the heat generation is distributed over the section, and this paper highlights the impact upon accuracy of specifying such a loss in the discrete nodes. A number of rotor winding models were used, ranging from a "single-block" (1×1) representation to a rotor winding represented by 100 smaller sections (10×10). These two models are shown in Fig. 3.

In Fig. 4, the trend of the predicted averaged node temperatures as a function of the number of network nodes per section is shown. Concentrating all loss in one node in the 1×1 network results in an unrealistic gradient between the wall and the winding center. Thus, a suitable formula must be used to derive the average section temperature (20.2 °C) from a single-node temperature and wall temperatures; otherwise, it could be wrongly interpreted as the whole winding section being at 60.5 °C. The winding discretization level of 10×10 yields more accurate predictions (average 17.7 °C, peak 35.8 °C) without the need for the formula when compared

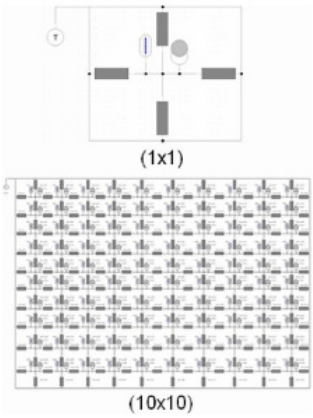

Fig. 3. Rotor winding models of (top) 1×1 and (bottom) 10×10.

with FEA results (average 17.0 °C, peak 37.2 °C). To sum up, using lower levels of discretization reduces the accuracy of the results, while increasing the node numbers unnecessarily complicates the thermal model.

As previously reported, lumped thermal parameters analysis involves the determination of thermal resistances. The main methods used for the calculation of conduction, radiation, and convection thermal resistances are hereafter summarized.

It is important to remark that these methods for the thermal resistance determination have general validity and they are not linked to the thermal-network complexity.

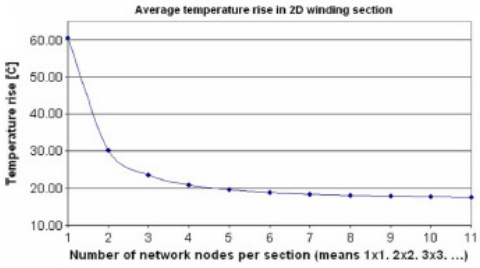

Fig. 4. Rotor winding discretization results up to 11×11.

A. Conduction Heat Transfer

Conduction thermal resistances can be simply calculated using the following:

$$R = \frac{L}{kA} \tag{1}$$

where L (in meters) is the path length, A (in square meters) is the path area, and k (in watt per meter degree Celsius) is the thermal conductivity of the material. In most cases, L and A can simply be gained from the components' geometry. The only complication is in assigning a correct value to L for thermal resistances due to the interface gap between components. As discussed in [24] and [26], experience factors are very important for a correct prediction of this thermal resistance. Commercial software packages typically provide details on various types of material with different roughness and manufacturing techniques to aid the user to set such interface gaps. Sensitivity analysis with values between the minimum and maximum expected values is always useful to gain a thorough understanding of the problem.

B. Radiation Heat Transfer

Radiation thermal resistances for a given surface can be simply calculated using

$$R = \frac{1}{h_R A} \tag{2}$$

where A (in square meters) is the surface area and h_R (in watt per square meter degree Celsius) is the heat-transfer coefficient. The surface area is easily calculated from the surface geometry. The radiation-heat-transfer coefficient can be calculated using the following:

$$h_R = \sigma \varepsilon F_{1-2} \frac{(T_1^4 - T_2^4)}{(T_1 - T_2)} \tag{3}$$

where $\sigma = 5.669 \times 10^{-8}$ W/(m$^2 \cdot$ K^4), ε is the emissivity of the surface, F_{1-2} is the view factor for dissipating surface 1 to the absorbing surface 2 (the ambient temperature for external radiation), and T_1 and T_2 are, respectively, the temperatures of surfaces 1 and 2, in units of kelvin. The emissivity is a function of the surface material and finish, for which data are given in most engineering textbooks [7]–[12]. The view factor can easily be calculated for simple geometric surfaces, such as cylinders and flat plates; however, it is a little more difficult for complex geometries, such as open-fin channels. In these cases, books are available to help with the calculation of the view factor [27], [28].

C. Convection Heat Transfer

Convection is the transfer process due to fluid motion. In natural convection, the fluid motion is due entirely to buoyancy forces arising from density variations in the fluid. In a forced convection system, movement of fluid is by an external force, e.g., fan, blower, or pump. If the fluid velocity is high, then turbulence is induced. In such cases, the mixing of hot and cold air is more efficient, and there is an increase in heat transfer. The turbulent flow will, however, result in a larger pressure drop; as a consequence, with a given fan/pump, the fluid volume flow rate will be reduced. Convection thermal resistances for a given surface can be simply calculated using

$$R = \frac{1}{h_C A}. \tag{4}$$

The previous equation is basically the same equation as for radiation but with the radiation-heat-transfer coefficient replaced by the convection-heat-transfer coefficient h_C (in watt per square meter degree Celsius). Proven empirical heat-transfer correlations based on dimensionless analysis are used to predict h_C for all convection surfaces in the machine [3]–[12], [24], [29].

D. Flow-Network Analysis

Forced convection heat transfer from a given surface is a function of the local flow velocity. In order to predict the local velocity, a flow-network analysis is performed to calculate the fluid flow (air or liquid) through the machine. Empirical dimensionless analysis formulations are used to predict pressure drops for flow restrictions, such as vents, bends, contractions, and expansions [24], [29]–[34]. The governing equation that relates the pressure drop (P, in pascal, equivalent to an electrical voltage) to the volume flow rate (Q, in cubic meters per second, equivalent to electrical current) and fluid-dynamic resistance (R, in kg/m^7) is

$$P = RQ^2. \tag{5}$$

In (5), the formulation is in terms of Q^2 rather than Q due to the turbulent nature of the flow. Two types of flow resistance exist. The first exists where there is a change in the flow condition, such as expansions, contractions and bends. The second is due to fluid friction at the duct wall surface; in electrical machines, this is usually negligible compared with the first resistance type due to the comparatively short flow paths. The flow resistance is calculated for all changes in the flow path using

$$R = \frac{k\rho}{2A^2} \tag{6}$$

where ρ (in kilograms per cubic meter) is the air density (depending on the temperature), A (in square meters) is the flow area, and k is the dimensionless coefficient of local fluid resistance whose value depends upon the local flow condition (obstruction, expansion, contraction, etc).

Many empirical formulations are available in the technical literature to calculate the k factor for all changes in the flow section within the motor. A merit of thermal tool [35] is to automatically select the most appropriate formulation for all the flow paths involved (i.e., a sudden contraction when air enters the stator/rotor ducts, a 90° bend where the air passes around the end winding, etc.).

III. Analytical Thermal-Network Analysis Software

The main characteristics of analytical software packages used in thermal analysis of electrical machines are discussed in this section. Analytical thermal-network analysis software packages can be subdivided into three types, namely, dedicated software for thermal analysis of electric motors, general-purpose network solvers with library components that can be used for thermal analysis, and custom packages written by the electrical-machine designers for a particular machine type. There are very few commercial software packages for electric-motor thermal analysis. One of the most widely used tools is given in [35]. The main advantage of the package is that the user needs only to input details of geometry, winding, and materials used, and the software automatically sets up the thermal network and selects the most appropriate analytical formulations for each of the circuit components. Thus, the user need not be an expert in heat-transfer analysis in order to use the software. The main limitation of such dedicated software is that the geometry is based on a fixed set of topologies (i.e., preparameterized models). If the user's geometry is not similar to any of the built-in topologies, then a model cannot be implemented. Ideally, such packages should have some advanced features such that the user can edit the thermal circuit to model minor modifications to the geometry [35]. It is important to underline that most motor topologies are relatively standard from the thermal point of view.

If a totally new type of structure is being analyzed, then there can be advantages in the user developing a completely new thermal network in a simulation tool. Such packages usually have powerful network editors with drag-and-drop interfaces. An example of this type of package is given in [36]. This tool has features to help the user set up thermal networks in terms of thermal libraries. In particular, powerful "wizard" dialogs are used to select geometry and material data from which the most appropriate analytical mathematical formulations are automatically selected. Thus, the user sets up the thermal circuit from a geometric point of view rather than spending time researching heat-transfer formulations. This is also the typical approach used by a motor designer when developing thermal-analysis software for their own company use. For established machine topologies for which design evolves slowly, impressive user interfaces and topology flexibility can be replaced by available measured results, allowing for the validation and fine tuning of such in-house software. Simultaneous iterative solutions of heat generation; fan and flow circuit parameters; surface heat transfer; and conduction in solid material can be carried out for both steady-state and transient simulations. In addition to geometry and material changes, effects, such as varied load, ambient conditions, filter, or blockage effects, can be studied with the package.

A further advantage of commercial packages used for thermal analysis is that they can be programmed to use sophisticated integration techniques that are tolerant of stiff sets of equations and nonlinearities [38]. Stiffness can be a major problem when calculating the thermal transient response of motors, which are constructed with parts having very different mass values. For example, as the air-gap thermal capacity is much less than that of the winding, the air-gap thermal capacity will influence the integration step length but have little influence on the thermal response of the machine [50]. Moreover, network-based solvers that represent the system in terms of differential algebraic equations rather than ordinary differential equations have advantages in terms of stability for very nonlinear systems [36].

It is important to highlight that, in order to obtain an accurate thermal model for an electrical machine, both analytical formulation and numerical method benefit from the previous experience of the designer. As discussed in Section VI, this is due to some thermal phenomena being dependent upon the component manufacturing process.

IV. Thermal Analysis Using FEM

FEA is now a standard tool for electromagnetic analysis. Both 2- and 3-D models are used (see Section VII). Often, software packages for electromagnetic analysis also include a module for thermal analysis [39]. At first glance, FEA seems more accurate than thermal-network analysis. However, FEA suffers from the same problems previously described, with uncertainty in the computation of thermal resistances due to interfaces and convection.

In fact, an accurate FEA solution requires the knowledge of the same thermal parameters discussed in Section II. A superficial knowledge of the geometrical and material properties used in a machine construction is often not sufficient to give an accurate prediction of the thermal performances.

The main role of FEA is in the accurate calculation of conduction heat transfer in complex geometric shapes, such as heat transfer through strands of copper in a slot. For this problem, FEA analysis can be used to calculate the equivalent thermal conductivity that can then be used in the network analysis [40].

One problem with this calculation is that some assumptions must be made regarding the randomness of the conductor placement, the impregnation goodness, and any gaps between the slot liner and the stator lamination. This approach is much easier for winding types that have a known conductor placement, i.e., for wound or precision windings.

In Fig. 5 a steady-state thermal 2-D FEA solution of a set of rectangular-shaped copper conductors in a slot is shown [26]. A fixed temperature boundary condition is applied to the outer

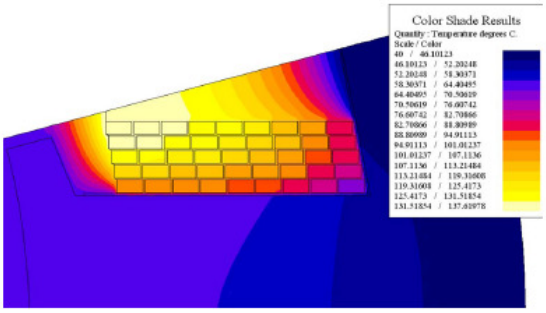

Fig. 5. Steady-state 2-D FEA of the temperature rise in a slot with rectangular copper conductors.

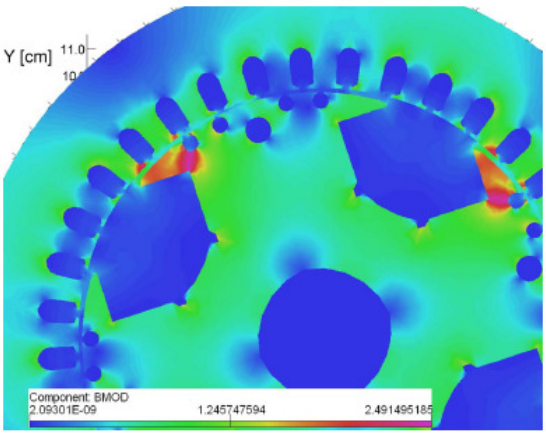

Fig. 6. Magnetic flux distribution across machine radial cross-section.

surface of the stator lamination, and a fixed amount of copper loss is applied to the problem. This simple boundary condition is possible, as the designer is only interested in calculating the temperature difference between the winding hotspot and tooth/stator back iron.

It is important to underline that simple thermal resistances in the lumped circuit can then be calibrated and used to give the same temperature rise, avoiding time-consuming tasks, such as mesh definition and heat-field computations [24].

FEA can be used to modify thermal networks to take into account a specific loss distribution. In many LPTNs, it is assumed that the loss distribution across the electrical machine is uniform; however, FEA results clearly illustrate the nonsymmetrical nature of the operational flux density and related power loss distribution inside the machine, as shown in Fig. 6 for a salient pole synchronous machine [25].

As a consequence, FEA results can be used to define the thermal-network discretization level and a more realistic injection of the losses in the network nodes. It is important to underline that FEA applications are very time consuming for the actual geometry discretization and modification, even if a parametric approach for the geometry definition is used. As a consequence, considering that the majority of FEA electromagnetic packages include finite-element thermal-analysis facilities, FEA can be considered a convenient solution in a very complex geometry not approachable with lumped parameters.

V. Thermal Analysis Using CFD

CFD applied to the design of an electrical machine primarily aims to determine coolant flow rate, velocity, and pressure distribution in the cooling passages or around the machine, as well as the levels of surface heat transfer for subsequent analysis of temperature in the active material and remaining solid structures. This method can replace the combination of traditional 1-D ventilation resistance networks, based on correlations for pressure drops across local and friction resistances, and correlations for surface-heat-transfer coefficients. The history of CFD use for studying aspects of electrical machines spans more than two decades, back to the days of simple purpose written CFD codes and early days of commercial codes. The limitations of the software and hardware of this age meant steep calculation costs and only a little practical benefit for the industry. The industry benefited more by engaging in university research projects that evaluated the capability of CFD as physical models for phenomena such as turbulence or rotation effects, which could lead to a variation in results [41]. Numerous papers were published, which dealt with the comparison of predicted surface-heat-transfer coefficients with those measured experimentally or determined by established correlations [42]. In the 1990s, the confidence in CFD and the evidence of its practical use in the design of machines started to emerge. Coolant flow optimization studies and isolated fan design were the most common examples. Computer hardware limitations still meant heavy use of periodic assumptions and coarse computational meshes, unless parallel computing was available.

With the recent arrival of affordable 64-b computing power, the investment in CFD capability guarantees a good return even with a single license on a dedicated workstation.

Without proper understanding of fluid flow in or around the machines, continuation in the trend of increasing the power density will not be possible. Modern CFD codes are mostly based on the finite-volume technique solving Navier–Stokes equations complimented by a selection of validated and proven physical models to solve 3-D laminar or turbulent flow and heat transfer to a high degree of accuracy. Major challenges for CFD vendors now lie in bringing the codes to a wider engineering community [43]. Experts on CFD are not as much segregated from other engineers due to the in-depth knowledge of the underlying fundamental physics but due to the skills it takes to convert geometry into a discretized mesh (or grid). The complexity of the meshing process lies in reducing the amount of detail in the machine without impacting on the accuracy of the solution. In most cases today, CFD analysis would start with some form of 3-D native model produced in a CAD package. The deciding factor for choosing a CFD package is how tolerant it is to deficiencies in the particular geometry meshing software. Many CFD users, including those working with the leading commercial codes, have experienced periods of frustration when dealing with real geometry. When meshing

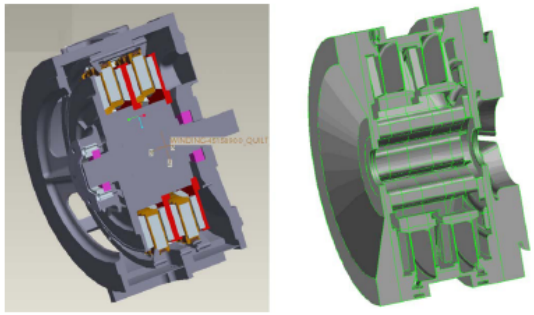

Fig. 7. CAD model in preparation for analysis of ventilation in a 60-kW axial flux generator. Picture on the right shows the fluid region (inverted volume).

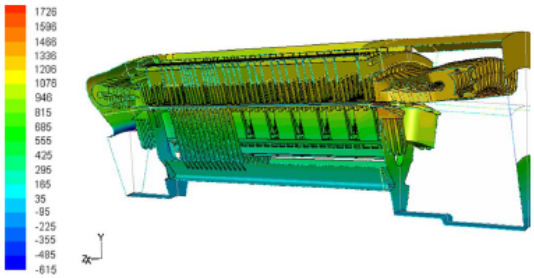

Fig. 8. Static pressure (in pascal) distribution in a generator ventilation circuit. Increased complexity of model leads to only one-pole periodicity modeling.

internal volumes of electrical machines, one has to observe certain rules to avoid excessive numbers of cells in the mesh. Very narrow gaps between rotor and stator or in radial channels require high aspect ratio hexahedral elements, which usually rule out automated meshing techniques. A very good practice, often unavoidable, is subdividing the whole domain to volumes that are easier to mesh (Fig. 7). The splitting is required by some CFD codes also to separate domains with rotation associated with rotating and stationary parts.

To provide a rough guide on the size of models and required computer power, a 64-b workstation with 8 GB of RAM is a recommended minimum industry standard, typically needed to perform an analysis of air flow and convective heat transfer for a 180° periodic or full model, depending on the level of details, for internal flow. This corresponds to the discretization of the fluid region to approximately eight million cells.

In case of machines with many internal cooling ducts, one-pole periodicity may result in consuming the same resource.

The types of CFD analysis for an electrical machine can be divided into the following.

1) Internal flow—either in a through-ventilated machine, where ventilation is driven by a fan (Fig. 8) or self-pumping effect of rotor, or in a totally enclosed fan-cooled (TEFC) motor/generator to assess the air movements that exchange heat from winding overhangs to frame.
2) External flow—flow around the enclosure of a TEFC motor/generator (Fig. 9).

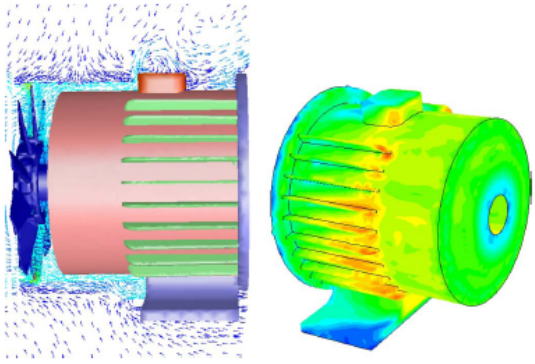

Fig. 9. Velocity vectors around TEFC generator (cowling not depicted) and resulting contours of frame surface-heat-transfer coefficients.

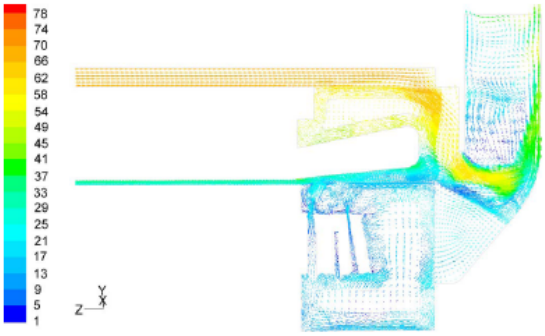

Fig. 10. Velocity vectors (relative to rotor) through fan, showing how the position of the fan results in only 20% of fan passage having radial flow out, with the rest filled with recirculation.

3) Fan design and performance studies—due to cost of material, manufacturing processes, space, or access constraints, fans employed in electrical machines often have a very poor aerodynamic efficiency (Fig. 10). In the case of radial fans, there are rarely any means of pressure recovery at exit. CFD offers a great deal of help in improving fan design and its interaction with the cooling circuit.
4) Supporting analysis—water flow in cooling jackets and cooling of associated power electronics (Fig. 11).

Using an example of rotating machine analysis, CFD takes inputs in the form of realistic geometry and boundary conditions. The geometry defines lengths and cross-sectional areas for passages of flow, which are the most decisive for pressure drops in the system. As boundary conditions, coolant mass flow rate or total pressure at inlet, static pressure at outlet, and rotating speed are used. For the energy equation, the surface heat flux or presumed temperatures of surfaces must be given. For the latter, predicted surface-heat-transfer coefficients are not a function of temperature itself if the flow is turbulent, as it is in the majority of cases. Analysis results are verified easiest for the flow rate where measurements are frequently carried on prototype machines by traversing with a velocity probe in a duct

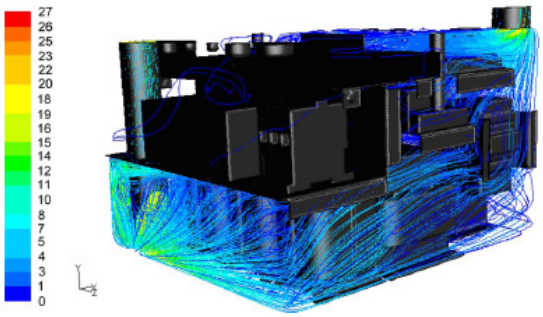

Fig. 11. Air flow path lines inside a power electronics enclosure, colored by velocity magnitude (in meters per second).

with a known cross-sectional area mounted to a machine inlet. Surface-heat-transfer predictions are often not verified directly but the agreement of subsequent thermal-network modeling is compared with heat runs on machines instrumented with resistance temperature detectors or thermocouples.

The secondary function of CFD can be to solve heat flow paths all the way into the regions of their origin by means of conduction. This is essentially extending the CFD capability by FEA thermal solution, often referred to as conjugate heat-transfer modeling [44]. In an R&D environment, it may be useful in prototype design work for validating lumped-parameter thermal models; otherwise, in most cases, it devalues the primary objective of CFD by introducing additional assumptions related to manufacturing processes and material properties. A link between CFD and a lumped thermal parameter circuit is much more meaningful for a design engineer wishing to perform analysis of a number of design iterations and settings. It has been proven in the design office environment that including solid regions in a CFD analysis prolonged preparation by increasing the complexity of setup, with little appreciable benefit. On the other hand, the conduction modeling capability of CFD can be used separately by disabling flow equations (leaving just one equation for energy) to undertake studies, such as detailed temperature distribution in stator slots (Fig. 12).

While attempting the CFD analysis for an electrical machine, the most common assumptions or simplifications are as follows.

1) Periodicity: Depending on the position of inlets and outlets, terminal connections, etc., in the case of internal flow or orientation in the environment for external flow, this may impact upon the accuracy of results and requires good judgment on the part of the analyst.
2) Steadiness of flow and heat transfer with rotation: Transient flow solutions are, in most cases, unnecessary, as time-averaging models give close results at a fraction of time. Some heat-transfer augmentation due to pressure waves from rotor onto stator and back in salient pole machines was reported in [38]; however, such differences are small and local.
3) Surface roughness: Data for surface roughness are very difficult to obtain and particularly difficult to input, as many surfaces have a specific type of roughness, such as one-directional roughness (back of laminated core), or some surfaces are more uneven, in flatness, rather than rough.
4) Geometry of complex structures can be simplified, e.g., porosity model can be applied to simplify the geometry of bar-wound overhangs.

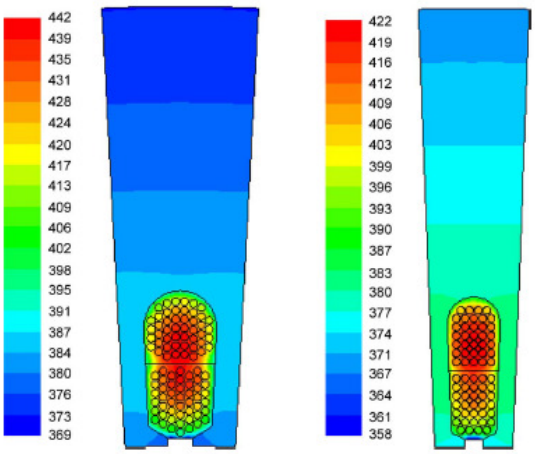

Fig. 12. Temperature (in kelvin) prediction on two lamination designs with windings at the same current density.

The following most common mistakes are made when attempting a CFD analysis.

1) Not allocating sufficient computer resource, resulting in too coarse a computational mesh.
2) Deficiencies in computational mesh (highly skewed cells) can vary, in effect, from the inability to obtain a solution to large local errors in the flow field and heat transfer.
3) Unsuitable type of cells resulting in excessive mesh size, often due to automated meshing, e.g., using tetrahedral cells in rotor–stator air gap instead of high aspect ratio hexahedral cells.
4) Poor definition of boundary conditions, where results of any analysis can be only as good as the input data.

There are multiple ways of looking at the role of CFD in the future. There is no doubt that CFD, as a discipline, will become more popular and widespread — a cost-effective tool for innovation. The vendors and academic circles will continue to enhance the capability of commercial codes for more complex physics phenomena; this is, however, unlikely to influence accuracy of solutions for electrical machines as achieved today. From the industrial viewpoint, CFD can be used to identify possibilities for segmentation of product ranges, e.g., for high-efficiency continuous operation or low-cost standby units. It is within the scope of CFD to evaluate efficiency improvements in electric machines, which can be translated to cost savings during operation.

VI. Thermal Parameter Determination

As discussed in the previous sections, the accuracy of both sophisticated and simple thermal networks is dependent upon

several parameters for which reliable data may be difficult to find. In fact, many of the complex thermal phenomena inside electric machines cannot be solved by pure mathematical approaches using a closed relationship. Designers with extensive working experience on similar designs using comparable manufacturing processes can make a correct choice of such parameter values. For designers approaching their first thermal analysis, these choices are more difficult. It is particularly important for the user to have available reasonable starting values for the less well known and defined parameters. The authors have researched reliable relationships to be used in the determination of the more complex thermal parameters [4], [24], [26], [45]–[47]. From the sensitivity point of view, the weight of these parameters on the thermal-analysis results has been investigated in [47]. Such information can be used successfully to set default parameters in thermal-analysis software to give reasonably accurate predictions at the start of the design process before manufacturing methods and tolerances have been fully thought out [24], [35]. Expected upper and low limits of such parameters, based on experience, can be built into automated sensitivity analysis so that the designer can quickly access the main constraints to cooling and quantify the effects of manufacturing options and tolerances. In the following, a summary of the obtained results is reported.

A. Equivalent Thermal Resistance Between External Frame and Ambient Due to Natural Convection

In totally enclosed machines with no fan or with a shaft-mounted fan operating at slow speed, the thermal resistance R_0 (in degree Celsius per watt) between the housing and ambient is often the largest single resistance between winding and ambient. When the total area A of the external frame is known, (7) can be initially used, taking into account both convection and radiation heat transfers

$$R_0 = 0.167A^{1.039}. \tag{7}$$

An alternative is to make a first estimate of the convection and radiation-heat-transfer coefficients and then calculate R_0 using (2) and (4). Typically, the combined natural convection and radiation-heat-transfer coefficient lies in the range 12–14 W/(m^2 ·°C) for simple geometric shapes [49].

An interesting experimental method can be found in [48].

B. Equivalent Thermal Conductivity Between Winding and Lamination

It is widely recognized that the thermal behavior of the wires inside the slot is very complex. The thermal resistance can be computed using (1); however, the value of the thermal conductivity k is not easily defined. A possible approach to simplify the thermal resistance computation is to use an equivalent thermal conductivity of the system winding impregnation and insulation ($k_{\mathrm{cu,ir}}$). This equivalent thermal conductivity depends on several factors, such as material and quality of the impregnation, residual air quantity after the impregnation process, and so on. If the equivalent thermal conductivity $k_{\mathrm{cu,ir}}$ is known, the thermal resistance between the winding and the stator lamination can be easily computed. When the slot fill factor K_f, the slot area A_{slot}, and the axial core length L_{core} are known, (8) can be used as a rough guide

$$k_{\mathrm{cu,ir}} = 0.2749\left[(1-k_f)A_{\mathrm{slot}}L_{\mathrm{core}}\right]^{-0.4471}. \tag{8}$$

The quantity inside the square bracket represents the available net volume for the wire/slot insulation and the impregnation inside the slot.

An alternative approach is to subdivide the winding in the slot into a number of thermal resistances from the slot center to the slot wall. The resistance values can be calculated from the knowledge of the slot shape, slot fill, and impregnation goodness. Full details of the resulting model are given in [49].

C. Forced Convection-Heat-Transfer Coefficient Between End Winding and Endcaps

The thermal resistance between winding and endcaps due to force convection can be evaluated by (4). Again, the value of h_C is not simple to define. For totally enclosed machines, the value of h_C can be evaluated by (9) as a function of the air speed inside the motor endcaps

$$h_C = 6.22v \tag{9}$$

or by (10) to account for combined natural and forced convection

$$h = 41.4 + 6.22v. \tag{10}$$

Other alternative relationships are also available [24], [29], [45], [49] and give similar results.

D. Radiation-Heat-Transfer Coefficients

The thermal resistance for radiation can be evaluated using (2) when h_R is available. Inside and outside the motor, several parts exchange heat by radiation. In some cases, such as aerospace applications, all the heat transfer is due to radiation. The following values of the radiation-heat-transfer coefficients can be initially used [46]:

8.5 W/(m^2 ·°C) between copper–iron lamination;
6.9 W/(m^2 ·°C) between end winding–external cage;
5.7 W/(m^2 ·°C) between external cage–ambient.

E. Interface Gap Between Lamination and External Frame

The interface gap between the lamination and the external frame is due to imperfections in the touching surfaces, and it is a complex function of material hardness, interface pressure, smoothness of the surfaces, and air pressure. The interface gap between stator lamination and external frame is very important because most of the motor losses cross this surface. For industrial induction motors, interface gap values between 0.01 and 0.08 mm have been found. As the interface gap between the lamination and the external frame is not only dependent on the frame material but is also strongly influenced by the stator core

assembly and by the core–external frame inserting process, it is not possible to compute its value. A value of 0.03 mm can be considered a reasonable value to be used as a default at the start of the design process. Sensitivity analysis, with the interface gap varied between 0.01 and 0.08 mm, gives a quick evaluation of its importance on the design under consideration. In many cases, it is not that important. However, in highly rated machines, such as those with housing water jackets, it can be significant.

VII. Final Remarks

In the previous sections, an overview of the most used techniques for the electrical-machine thermal analysis has been reported. Hereafter, a critical discussion on these approaches is included.

The LPTN is the most used and friendly solution for a fast- and low-computation time-consuming thermal analysis. The accuracy of this method is strongly dependent on the thermal parameters, particularly the heat-transfer coefficients.

It is important to underline that an accurate prediction of the electric machine thermal performances is not a simple task, even if the machine geometry and the properties of the used materials are well known. This is because many of the complex thermal phenomena that occur in electric machines cannot be solved by pure mathematical approaches. In most cases, empirical data must be used to calibrate analytical models in order to get acceptable results from the accuracy point of view. The high calculation speed is one of the major advantages of the thermal-network analysis, particularly when a large number of calculations are required, for example, when a parameter sensitivity analysis of the thermal network has to be performed [47]. In addition, the LPTN is surely the approach that allows for the development of self-made thermal-analysis tools.

The finite-element method (FEM) thermal analysis is often used because this tool is available together with the electromagnetic one; in fact, the most important software tools for FEM electromagnetic studies have embedded the FEM thermal analysis. The FEM approach requires a quite long "preprocessing" time to input the machine geometry under study, and the computation time is longer with respect to the thermal network. In fact, FEM suffers from long model setup and computation times. From this point of view, the FEM approach is quite interesting when a "parametric model" facility is available. In this case, the software changes, in an automatic way, the model dimensions and/or the material property in defined ranges, allowing one to analyze the influence of these variations on the overall thermal performance.

In addition, the most important limitation of the FEM solution is that the software uses analytical/empirical-based algorithms for convection boundaries, exactly as in the lumped-circuit analysis. As a consequence, the result accuracy is dependent on the same factors previously described for the thermal network. For these reasons, the only advantage of the FEM method is that it can model solid component conduction more accurately than the thermal network. The 3-D FEM thermal analysis presents the same advantage and disadvantage for the 2-D approach, with very high long model setup and computation times. Obviously, the 3-D approach is required when the problem cannot be reduced in an equivalent 2-D problem (i.e., to study both the radial and axial heat fluxes).

The main strength of the numerical CFD approach is that is can be used to predict the flow in complex regions, such as around the end windings. Both 2- and 3-D models can be used depending on the geometry under analysis. The 3-D model suffers from very long model setup and computation times. Hence, its use is devoted and recommended when sophisticated simulations are imposed by the high costs of the prototypes; the typical cases are big motors or generators. It is important to underline that the data obtained using CFD are useful for improving the analytical algorithms used in the FEM model or in the thermal networks.

In conclusion, several approaches are available to develop a thermal analysis of electrical machines. All these approaches have both advantages and disadvantages, as largely discussed in this paper. As a consequence, the methodology selection is in the hands of the designers, which have to take into account the project development costs (i.e., time, result accuracy, and available resources) and the product marked value.

About the future expectations on the use of the thermal network, FEM, and CFD approaches, it is the authors' opinion that the CFD methods will be more and more attractive due to the increase of the PC computational speed and the availability of more friendly pre- and postprocessing software. In addition, a cost reduction of the CFD software can be expected, together with the availability of specific tools and libraries devoted to electrical machines.

As a final comment, the authors want to underline that this paper has to be considered as a survey work concerning the most used approaches for the electrical-machine thermal analysis. Examples of the described techniques for specific applications can be found in the papers [51]–[64] recently published in the Special Section "Thermal Issues in Electrical Machines and Drives" by the IEEE Transaction on Industrial Electronics, vol. 55, no. 10, October 2008.

VIII. Conclusion

In this paper, a summary of the evolution of thermal analysis of electrical machines was given. The most common methods used for thermal analysis were compared, and their strengths and weaknesses are discussed. This paper has given constructive suggestions for researchers involved in thermal analysis of power electronics and power converters, as well as electrical machines. A useful list of books and papers was given for designers wishing to carry out further electric-motor thermal-analysis research.

References

[1] J. J. Nelson, G. Venkataramanan, and A. M. El-Refaie, "Fast thermal profiling of power semiconductor devices using Fourier techniques," *IEEE Trans. Ind. Electron.*, vol. 53, no. 2, pp. 521–529, Apr. 2006.

[2] Z. Gao, T. G. Habetler, R. G. Harley, and R. S. Colby, "A sensorless rotor temperature estimator for induction machines based on a current harmonic spectral estimation scheme," *IEEE Trans. Ind. Electron.*, vol. 55, no. 1, pp. 407–416, Jan. 2008.

[3] P. Mellor, D. Roberts, and D. Turner, "Lumped parameter thermal model for electrical machines of TEFC design," *Proc. Inst. Elect. Eng.*, vol. 138, no. 5, pp. 205–218, Sep. 1991.

[4] A. Boglietti, A. Cavagnino, M. Lazzari, and M. Pastorelli, "A simplified thermal model for variable-speed self-cooled industrial induction motor," *IEEE Trans. Ind. Appl.*, vol. 39, no. 4, pp. 945–952, Jul./Aug. 2003.

[5] G. Kylander, "Temperature simulation of a 15 kW induction machine operated at variable speed," in *Proc. ICEM*, Manchester, U.K., Sep. 15–17, 1992, pp. 943–947.

[6] D. A. Staton, "Thermal computer aided design—Advancing the revolution in compact motors," in *Proc. IEEE IEMDC*, Boston, MA, Jun. 2001, pp. 858–863.

[7] J. P. Holman, *Heat Transfer*. New York: McGraw-Hill, 1997.

[8] A. F. Mills, *Heat Transfer*. Englewood Cliffs, NJ: Prentice-Hall, 1999.

[9] J. R. Simonson, *Engineering Heat Transfer*, 2nd ed. New York: MacMillan, 1998.

[10] A. Bejan, *Heat Transfer*. Hoboken, NJ: Wiley, 1993.

[11] W. S. Janna, *Engineering Heat Transfer*. New York: Van Nostrand-Reinhold, 1988.

[12] F. P. Incropera and D. P. De Witt, *Introduction to Heat Transfer*. Hoboken, NJ: Wiley, 1990.

[13] J. Mugglestone, S. J. Pickering, and D. Lampard, "Effect of geometric changes on the flow and heat transfer in the end region of a TEFC induction motor," in *Proc. 9th IEEE Int. Conf. Elect. Mach. Drives*, Canterbury, U.K., Sep. 1999, pp. 40–44.

[14] D. Staton, S. J. Pickering, and D. Lampard, "Recent advancement in the thermal design of electric motors," in *Proc. SMMA—Fall Tech. Conf.*, Durham, NC, Oct. 3–5, 2001.

[15] R. E. Steven, *Electrical Machines and Power Electronics*. New York: Van Nostrand-Reinhold, 1983.

[16] M. S. Rajagopal, K. N. Seetharamu, and P. A. Aswathnarayana, "Transient thermal analysis of induction motors," *IEEE Trans. Energy Convers.*, vol. 13, no. 1, pp. 62–69, Mar. 1998.

[17] G. Champenois, D. Roye, and D. S. Zhu, "Electrical and thermal performance predictions in inverter-fed squirrel-cage induction motor drives," *Elect. Mach. Power Syst.*, vol. 22, no. 3, pp. 335–370, 1994.

[18] J. T. Boys and M. J. Miles, "Empirical thermal model for inverter-driven cage induction machines," *Proc. Inst. Elect. Eng.—Elect. Power Appl.*, vol. 141, no. 6, pp. 360–372, Nov. 1995.

[19] S. Mezani, N. Takorabet, and B. Laporte, "A combined electromagnetic and thermal analysis of induction motors," *IEEE Trans. Magn.*, vol. 41, no. 5, pp. 1572–1575, May 2005.

[20] D. G. Dorrell, D. A. Staton, J. Hahout, D. Hawkins, and M. I. McGilp, "Linked electromagnetic and thermal modelling of a permanent magnet motor," in *Proc. IEEE PEMD*, Dublin, Ireland, Apr. 2006, pp. 536–540.

[21] J. R. Hendershot and T. J. E. Miller, *Design of Brushless Permanent-Magnet Motors*. Oxford, U.K.: Clarendon, 1994.

[22] Y. See, S. Hahn, and S. Kauh, "Thermal analysis of induction motor with forced cooling channels," *IEEE Trans. Magn.*, vol. 36, no. 4, pp. 1398–1402, Jul. 2000.

[23] J. F. Trigeol, Y. Bertin, and P. Lagonotte, "Thermal modeling of an induction machine through the association of two numerical approaches," *IEEE Trans. Energy Convers.*, vol. 21, no. 2, pp. 314–323, Jun. 2006.

[24] D. Staton, A. Boglietti, and A. Cavagnino, "Solving the more difficult aspects of electric motor thermal analysis in small and medium size industrial induction motors," *IEEE Trans. Energy Convers.*, vol. 20, no. 3, pp. 620–628, Sep. 2005.

[25] C. Mejuto, M. Mueller, M. Shanel, A. Mebarki, and D. Staton, "Thermal modelling investigation of heat paths due to iron losses in synchronous machines," in *Proc. IEEE PEMD*, Apr. 2008, pp. 225–229. CD-ROM.

[26] A. Boglietti, A. Cavagnino, and D. Staton, "Determination of critical parameters in electrical machine thermal models," in *Conf. Rec. IEEE IAS Annu. Meeting*, New Orleans, LA, Sep. 2007, pp. 73–90.

[27] S. N. Rea and S. E. West, "Thermal radiation from finned heat sinks," *IEEE Trans. Parts, Hybrids, Packag.*, vol. PHP-12, no. 2, pp. 115–117, Jun. 1976.

[28] M. F. Modest, *Radiative Heat Transfer*. New York: Academic, 2003.

[29] A. Cavagnino and D. Staton, "Convection heat transfer and flow calculations suitable for analytical modelling of electric machines," in *Proc. IEEE IECON*, Paris, France, Nov. 2006, pp. 4841–4846.

[30] R. W. Fox, A. T. McDonald, and P. J. Pritchard, *Introduction to Fluid Mechanics*. Hoboken, NJ: Wiley, 2004.

[31] I. E. Idlechik, *Handbook of Hydraulic Resistance—Coefficients of Local Resistance and of Friction*, 3rd ed. CRC Begell House, 1994. [Online]. Available: www.engr.iupui.edu/me/courses/hydraulicresistance.pdf

[32] *Woods Practical Guide to Fan Engineering*, Woods of Colchester Ltd., Colchester, U.K., Jun. 1960. [Online]. Available: www.flaktwoods.com

[33] D. A. Lightband and D. A. Bicknell, *The Direct Current Traction Motor: Its Design and Characteristics*. London, U.K.: Business Books, 1970.

[34] J. L. Taylor, *Calculating Air Flow Through Electrical Machines*, 1960, Kent, U.K.: Elect. Times. [Online]. Available: http://www.electricaltimes.co.uk

[35] Motor-CAD. [Online]. Available: www.motor-design.com

[36] Portunus. [Online]. Available: www.adapted-solutions.com

[37] Cummins Generator Technologies. [Online]. Available: www.cumminsgeneratortechnologies.com

[38] W. L. Miranker, *Numerical Methods for Stiff Equations and Singular Perturbation Problems*. Amsterdam, The Netherlands: Reidel, 1979.

[39] *FLUX*. [Online]. Available: www.cedrat.com

[40] D. J. Powell, "Modelling of high power density electrical machines for aerospace," Ph.D. dissertation, Univ. Sheffield, Sheffield, U.K., May 2003.

[41] M. Shanel, S. J. Pickering, and D. Lampard, "Application of computational fluid dynamics to the cooling of salient pole electrical machines," in *Proc. ICEM*, Espoo, Finland, Aug. 2000, vol. 1, pp. 338–342.

[42] S. J. Pickering, D. Lampard, and M. Shanel, "Modelling ventilation and cooling of the rotors of salient pole machines," in *Proc. IEEE-IEMDC*, Cambridge, MA, Jun. 2001, pp. 806–808.

[43] *Fluent 6.3 User Guide*. [Online]. Available: www.fluent.com

[44] M. Shanel, S. J. Pickering, and D. Lampard, "Conjugate heat transfer analysis of a salient pole rotor in an air cooled synchronous generator," in *Proc. IEEE-IEMDC*, Madison, WI, Jun. 2003, pp. 737–741.

[45] A. Boglietti and A. Cavagnino, "Analysis of the endwinding cooling effects in TEFC induction motors," *IEEE Trans. Ind. Appl.*, vol. 43, no. 5, pp. 1214–1222, Sep./Oct. 2007.

[46] A. Boglietti, A. Cavagnino, M. Parvis, and A. Vallan, "Evaluation of radiation thermal resistances in industrial motors," *IEEE Trans. Ind. Appl.*, vol. 42, no. 3, pp. 688–693, May/Jun. 2006.

[47] A. Boglietti, A. Cavagnino, and D. Staton, "TEFC induction motors thermal models: A parameter sensitivity analysis," *IEEE Trans. Ind. Appl.*, vol. 41, no. 3, pp. 756–763, May/Jun. 2005.

[48] A. Valenzuela and J. A. Tapia, "Heat transfer and thermal design of finned frames for TEFC variable speed motors," in *Proc. IEEE IECON*, Paris, France, Nov. 2006, pp. 4835–4840.

[49] D. Staton, "Thermal analysis of electric motors and generators," in *Conf. Rec. IEEE IAS Annu. Meeting*, Chicago, IL, 2001. Tutorial Course Notes.

[50] I. J. Perez and J. K. Kassakian, "A stationary thermal model for smooth air-gap rotating electric machines," *Elect. Power Compon. Syst.*, vol. 3, no. 3/4, pp. 285–303, Apr. 1979.

[51] M. A. Valenzuela and J. A. Tapia, "Heat transfer and thermal design of finned frames for TEFC variable-speed motors," *IEEE Trans. Ind. Electron.*, vol. 55, no. 10, pp. 3500–3508, Oct. 2008.

[52] D. A. Staton and A. Cavagnino, "Convection heat transfer and flow calculations suitable for electric machines thermal models," *IEEE Trans. Ind. Electron.*, vol. 55, no. 10, pp. 3509–3516, Oct. 2008.

[53] C. Micallef, S. J. Pickering, K. A. Simmons, and K. J. Bradley, "Improved cooling in the end region of a strip-wound totally enclosed fan-cooled induction electric machine," *IEEE Trans. Ind. Electron.*, vol. 55, no. 10, pp. 3517–3524, Oct. 2008.

[54] Z. Gao, R. S. Colby, T. G. Habetler, and R. G. Harley, "A model reduction perspective on thermal models for induction machine overload relays," *IEEE Trans. Ind. Electron.*, vol. 55, no. 10, pp. 3525–3534, Oct. 2008.

[55] N. Jaljal, J. F. Trigeol, and P. Lagonotte, "Reduced thermal model of an induction machine for real-time thermal monitoring," *IEEE Trans. Ind. Electron.*, vol. 55, no. 10, pp. 3535–3542, Oct. 2008.

[56] J. Nerg, M. Rilla, and J. Pyrhönen, "Thermal analysis of radial-flux electrical machines with a high power density," *IEEE Trans. Ind. Electron.*, vol. 55, no. 10, pp. 3543–3554, Oct. 2008.

[57] C. Kral, A. Haumer, and T. Bäuml, "Thermal model and behavior of a totally-enclosed-water-cooled squirrel-cage induction machine for traction applications," *IEEE Trans. Ind. Electron.*, vol. 55, no. 10, pp. 3555–3565, Oct. 2008.

[58] D. G. Dorrell, "Combined thermal and electromagnetic analysis of permanent-magnet and induction machines to aid calculation," *IEEE Trans. Ind. Electron.*, vol. 55, no. 10, pp. 3566–3574, Oct. 2008.

[59] L. Alberti and N. Bianchi, "A coupled thermal-electromagnetic analysis for a rapid and accurate prediction of IM performance," *IEEE Trans. Ind. Electron.*, vol. 55, no. 10, pp. 3575–3582, Oct. 2008.

[60] C. Cecati and F. de Monte, "A coupled electrothermal model for planar transformer temperature distribution computation," *IEEE Trans. Ind. Electron.*, vol. 55, no. 10, pp. 3583–3590, Oct. 2008.

[61] F. Marignetti, V. Delli Colli, and Y. Coia, "Design of axial flux PM synchronous machines through 3-D coupled electromagnetic thermal and fluid-dynamical finite-element analysis," *IEEE Trans. Ind. Electron.*, vol. 55, no. 10, pp. 3591–3601, Oct. 2008.
[62] A. Di Gerlando, G. Foglia, and R. Perini, "Permanent magnet machines for modulated damping of seismic vibrations: Electrical and thermal modeling," *IEEE Trans. Ind. Electron.*, vol. 55, no. 10, pp. 3602–3610, Oct. 2008.
[63] P. Zhang, B. Lu, and T. G. Habetler, "A remote and sensorless stator winding resistance estimation method for thermal protection of soft-starter-connected induction machines," *IEEE Trans. Ind. Electron.*, vol. 55, no. 10, pp. 3611–3618, Oct. 2008.
[64] A. Tenconi, F. Profumo, S. E. Bauer, and M. D. Hennen, "Temperatures evaluation in an integrated motor drive for traction applications," *IEEE Trans. Ind. Electron.*, vol. 55, no. 10, pp. 3619–3626, Oct. 2008.

Aldo Boglietti (M'04–SM'06) was born in Rome, Italy, in 1957. He received the Laurea degree in electrical engineering from the Politecnico di Torino, Turin, Italy, in 1981.

Since 1984, he has been with the Department of Electrical Engineering, Politecnico di Torino, first as a Researcher in electrical machines; then, he became an Associate Professor of electrical machines in 1992. He has been a Full Professor since November 2000 and is currently the Head of the Department of Electrical Engineering. He is the author of about 100 papers. His research interests include energetic problems in electrical machines and drives, high-efficiency industrial motors, magnetic materials, and their applications in electrical machines, electrical machine and drive models, and thermal problems in electrical machines.

Prof. Boglietti is an Associate Editor for the IEEE TRANSACTIONS ON INDUSTRIAL ELECTRONICS, the Secretary of the Electric Machines Committee of the IEEE Industry Applications Society and the Chair of the Electrical Machine Committee of the IEEE Industrial Electronics Society.

Andrea Cavagnino (M'04) was born in Asti, Italy, in 1970. He received the M.Sc. and Ph.D. degrees in electrical engineering from the Politecnico di Torino, Turin, Italy, in 1995 and 1999, respectively.

Since 1997, he has been with the Electrical Machines Laboratory, Department of Electrical Engineering, Politecnico di Torino, where he is currently an Assistant Professor. His research interests include electromagnetic design, thermal design, and energetic behaviors of electric machines. He is the author of more than 60 papers published in technical journals and conference proceedings.

Dr. Cavagnino is an Associate Editor for the Electric Machines Committee of the IEEE TRANSACTIONS ON INDUSTRY APPLICATIONS.

David Staton received the Ph.D. degree in computer-aided design of electrical machines from Sheffield University, Sheffield, U.K., in 1988.

Since then, he has worked on motor design and, in particular, the development of motor design software with Thorn EMI; the SPEED Laboratory, Glasgow University, Glasgow, U.K.; and Control Techniques. Since 1999, he has been with Motor Design Ltd., Ellesmere, U.K., a company which he set up to develop thermal-analysis software for electrical machines.

Martin Shanel received the Master's degree from the Mechanical Engineering Faculty, Technical University of Ostrava, Ostrava, Czech Republic, in 1996, and the Ph.D. degree from the University of Nottingham, Nottingham, U.K., in 2002, where he was involved in research on cooling of electrical machines.

For a period of three years, he was with Siemens Industrial Turbomachinery, Lincoln, U.K., dealing with the thermal design of gas turbine components, until an opportunity came, in 2005, to return to cooling of generators; since 2005, he has been with Cummins Generator Technologies, Stamford, U.K., formerly known as Newage International, where he is responsible for thermal design discipline, and is engaged in product development and numerous university research activities.

Dr. Shanel is a Chartered Engineer Member of the Institution of Mechanical Engineers.

Markus Mueller received the Ph.D. degree from the University of Cambridge, Cambridge, U.K., in 1991.

He was with the University of Cambridge, for three years, as a Postdoctoral Researcher, working on a project sponsored by Brook Crompton. He was with Brook Crompton for six months. In January 1995, he was with SR Drives Ltd., as a Senior Development Engineer. He decided to return to academia, and in 1997, he became a Lecturer with the University of Durham, Durham, U.K., where he spent seven years working on direct-drive machines for wind and wave energy converters. Since 2004, he has been with the Institute for Energy Systems, University of Edinburgh, Edinburgh, U.K., where he was first appointed to a lectureship position and, where, since 2006, he has been a Senior Lecturer. He is building a research group specializing in the development of integrated electrical, mechanical, and thermal design tools for electrical machines for renewable energy applications, with a focus on optimized lightweight machines for direct-drive systems.

Dr. Mueller was the recipient of the Donald Julius Groen Prize, awarded by the Institution of Mechanical Engineers in recognition of his work on linear generators for direct-drive wave energy converters. He is a Chartered Engineer, and as an active member of The Institution of Engineering and Technology, he is a Technical Advisor for the Power Conversion and Applications Network.

Carlos Mejuto received the B.S. degree and the M.Eng. Honors degree in electrical engineering, with a master's project for Cummins Generator Technologies, from the University of Edinburgh, Edinburgh, U.K., where he received the Ph.D. degree from the Institute for Energy Systems.

He is currently with the Institute for Energy Systems, University of Edinburgh, working with Markus Mueller (from the Univeristy of Edinburgh), Martin Shanel (of Cummins Generator Technologies), and Dave Staton (of Motor Design Ltd.) in designing improved thermal models for synchronous machines.

Proceedings of the 2008 International Conference on Electrical Machines Author ID 608 / Paper ID 812

Improved Synchronous Machine Thermal Modelling

Carlos Mejuto *; Markus Mueller *; Martin Shanel °; Adbeslam Mebarki °; Martin Reekie *; Dave Staton †
* The University of Edinburgh, School of Engineering and Electronics; ° Cummins Generator Technologies; † Motor Design Ltd.
* C.Mejuto@ed.ac.uk; ° Martin.Shanel@Cummins.com; † Dave.Staton@Motor-Design.com

***Abstract* - It is well accepted nowadays that in synchronous machine design procedures thermal aspects should be weighed equally with electromagnetic issues and considered in an iterative manner. Synchronous machine thermal models are being constantly optimised and improved, and many design areas are well understood and documented. Even so, there are a number of thermal model design aspects that require significant further study and analysis. These aspects include accurate machine operational loss prediction, precise loss distribution, thermal model discretisation level issues and cooling air flow implications. They will be analysed in the paper, with future related investigations being identified.**

I. Introduction

The traditional use of raw spread sheet, equivalent circuit based, thermal modelling packages is giving way to more accurate and reliable thermal modelling techniques. These techniques make use of powerful numerical analysis methods such as computational fluid dynamics (CFD) and finite element analysis (FEA), combining them with the fast computation times linked with analytical lumped circuit analysis. Extensive studies using CFD [1] and FEA [2] on numerous machine types and operating conditions have generated a high level of insight regarding the thermal behaviour of electrical machines, which is now taken into account in the creation of modern machine thermal models.

In practice, exclusive use of these accurate numerical design tools for all design queries and customer design checks would be impossible due to the tedious calibration and lengthy computing times required. This makes the need for precise analytically based thermal models even more pressing.

There are numerous benefits to be obtained from improved thermal models, ranging from the economical to the ecological. They will allow the rapid design of smaller, cooler, more efficient machines with a better overload capability, reduced running costs and a lesser environmental impact due to the associated reduction in operational losses. In addition, machines designed in this way will have significantly longer lifetimes, which will also bring obvious benefits to customers and manufacturers alike [3, 4].

II. Iron Loss Lamination Distribution

FEA is a powerful tool that can help designers model the magnetic flux distribution in machines more accurately. Iron losses and their distribution can then be calculated from such solutions. In order to predict these losses in an effective and reliable manner, harmonic evaluation of the flux density waveform in each FEA model element for the time cycle under investigation is required. Hence, the end result is a decomposition of the magnetic flux waveform per element into its constituent parts (fundamental, 1st order, 2nd order, 3rd order, etc.).

For ferrite materials, this is then used to compute the loss per harmonic using the well-known Steinmetz formulae [5], shown in Equation 1.

$$\textit{Iron Loss}, \quad P_t = C_m f^{\alpha} B_m^{\beta} \tag{1}$$

where P_t is the total iron loss, and C_m, α and β are empirical parameters obtained from experimental measurement under sinusoidal conditions. B_m represents the peak magnetic flux density and f represents frequency.

More generally, total iron loss is the sum of the hysteresis and eddy current components, with the addition of an excess loss component due to domain wall effects, which should be taken into account for non-ferrite materials [6, 7, 8].

$$\textit{Iron Loss}, \quad P_t = P_h + P_e + P_x \tag{2}$$

$$= k_h f B_m^{\beta} + k_c (f B_m)^2 + k_e (f B_m)^{1.5} \tag{3}$$

where P_h is the hysteresis component, P_e the eddy-current component and P_x the excess loss. The constants k_h, k_c, k_e and β, are the respective loss constants and are determined by curve fitting to measured iron loss data.

Using FEA and iron loss equation (3) provides accurate predictions of losses, together with their distribution across the machine's cross-section [9]. An example for a 22.5 kVA, 31.3 A, 415 V, 50 Hz clockwise rotating machine is shown in Figure 1. This displays the magnetic flux distribution across the synchronous machine, which is closely linked iron loss magnitude and distribution.

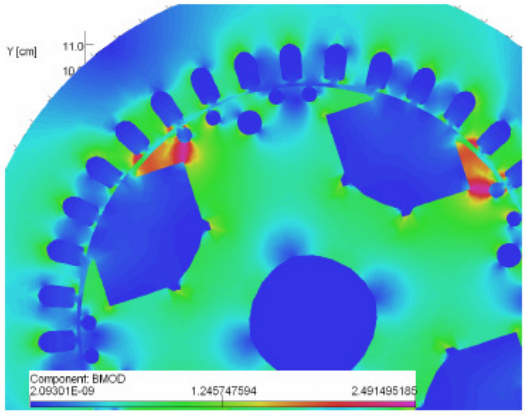

Figure 1: Alternator's magnetic flux density distribution.

978-1-4244-1736-0/08/$25.00 ©2008 IEEE

The application of these losses to the generator's thermal model results in a much more realistic temperature distribution.

Lumped thermal network coefficients can be derived by using the calculated loss data and comparing the iron loss concentration distribution across the machine. These coefficients have been called Lumped Circuit Coefficients (LCCs) and they greatly assist in the generation of a lumped circuit thermal model that is truly representative of the synchronous generator's rotor and stator loss distribution. They are presented in the Figures 2 and 3.

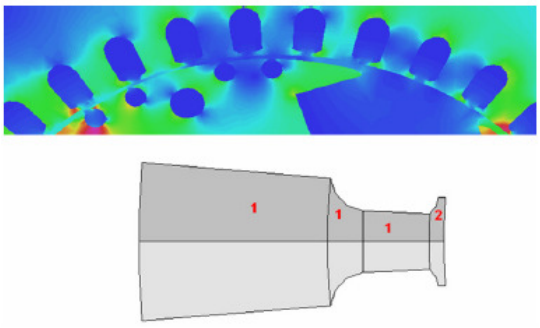

Figure 2: Stator loss coefficient distribution [10].

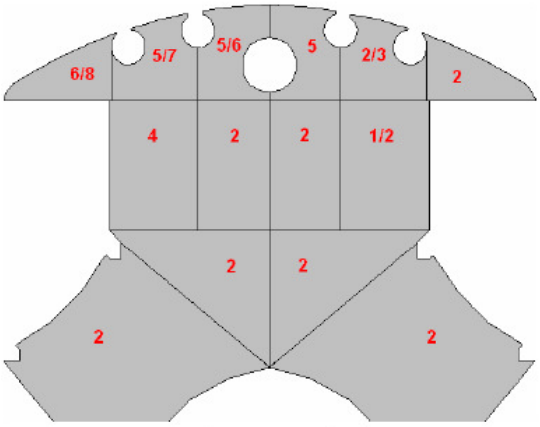

Figure 3: Rotor loss coefficient distribution [10].

The coefficients presented in Figure 3 are for the machine's rotor lamination. They can be applied to the machine's thermal model reluctance network as weighing factors, resulting in an improved synchronous generator thermal model that simulates the iron loss distribution of the alternator in a more realistic manner [10].

As well as giving the level and distribution of the iron losses, FEA can provide the total iron loss stator to rotor split ratio. Evaluation of a wide range of operating points reveal a stator:rotor iron loss split ratio of 85:15. This is a useful result for machine designers as it allows a quick loss evaluation from overall loss figures.

III. Iterative Iron Loss Calibration

A fundamental aspect of iron loss modelling involves the prediction of temperature variations at specific locations within a machine. In addition to the increase in accuracy achieved by using radial LCCs, the iron loss axial length distribution must also be considered. Machine losses will be more highly concentrated at the hotter sections of the generator and a reliable modelling package should take this into account. To achieve this, an iterative process was developed that updates iron losses with local component temperatures. Using this technique, a more realistic distribution of axial and radial temperatures is found. This method was applied to for the rotor and stator laminations models shown in Figure 4 and the results are presented in Reference [10].

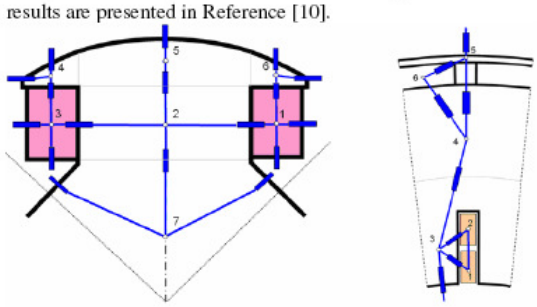

Figure 4: Rotor (left) & stator (right) lamination lumped networks.

A. *Rotor lamination iron loss re-distribution*

In the rotor a lumped parameter circuit is used. Iron losses are added at nodes 2, 4, 5, 6 and 7, shown in Figure 4, but only copper losses are fed into nodes 1 and 3. The iterative process utilises local temperatures in axial planes A, B and C (see Figure 6) to update iron losses.

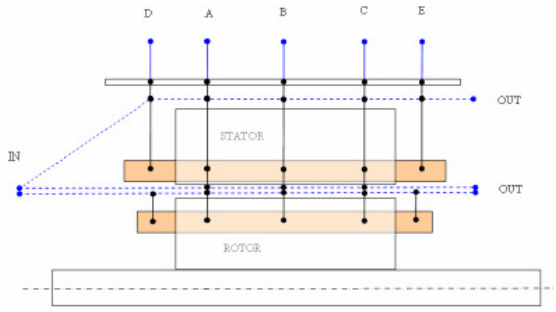

Figure 5: Axial planes in lumped parameter network.

These are updated according to a temperature ratio, which is initially assumed to be equally distributed between the three planes in Figure 5 (1/3 in each plane). The iterative process

proceeds until the change between updated input iron loss powers is less than 0.0001W between iterations. This can be adjusted depending on the level of accuracy desired. At this point a true axial temperature dependent iron loss rotor lamination distribution is achieved.

LCC results presented in Section 2 were combined with the axial temperature dependent iron loss iterative process and results for a full-load 22.5 kVA synchronous machine are shown in Figure 6. Series numbers 1 to 7 refer to rotor lamination nodes 1 to 7 in Figure 4. The results show that the application of LCCs allows for a realistic radial temperature distribution, which agrees with the FEA simulations that were also performed. Furthermore, in the axial direction, the iterative process yields hotter temperature spots towards the drive-end of the machine, as would be expected.

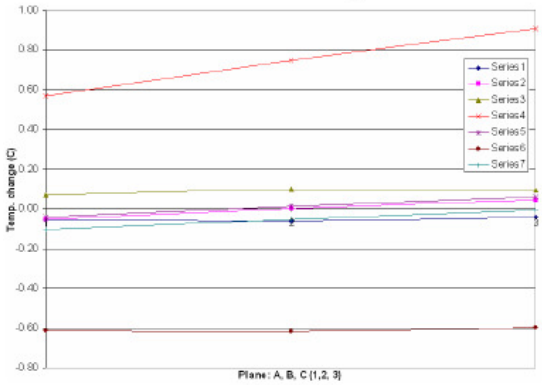

Fig. 6: Temperature dependent iron loss rotor lamination re-distribution results.

As can be seen, temperature changes within the rotor laminations of this machine are very small in magnitude. Even so, this is a useful step towards a more reliable thermal model and should be adopted. Furthermore, for bigger machines with higher kVA ratings, the temperature changes presented are significantly higher and so are more important if accurate predictions are required.

B. Stator lamination iron loss re-distribution

A similar method was applied to the stator lamination. In the stator a lumped parameter circuit is used and iron losses are only added to node 3, shown in Figure 4. Copper losses are fed into nodes 1 and 2. As before, the iterative process utilises local temperatures in axial planes A, B and C (see Figure 5) to update the iron losses. These are updated according to a temperature ratio, which is initially assumed to by equally distributed between the three planes (1/3 in each plane). The iterative process proceeds until the change between updated input iron loss powers is less than 0.0001W between iterations. At the completion of the iterative process a true axial temperature dependent iron loss stator lamination distribution is achieved.

Results are presented in Figure 7. Clearly temperature fluctuations in the axial direction are smaller than in the rotor lamination and are therefore of a lesser importance. As with the rotor lamination simulation, results presented are for a full-load 22.5 kVA synchronous machine. Series numbers 1 to 6 refer to stator lamination nodes 1 to 6 in Figure 4.

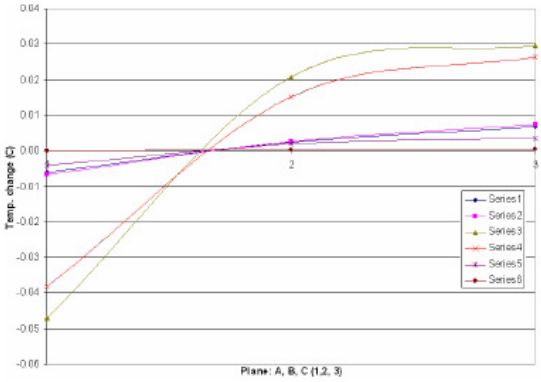

Fig. 7: Temperature dependent iron loss stator lamination re-distribution results.

IV. Rotor Winding Discretisation Study

A thermal model's discretisation level refers to the sections that are used to model the electrical machine, both in the axial and radial directions. The machine may be modelled as a whole, or only some of its more critical components may be involved. The level of discretisation employed in a thermal model is of great importance. An excessively crude model with too low a discretisation level will prove simple to create and fast to analyse, but will lack accuracy. On the other hand, increasing the discretisation level unjustifiably will complicate the model's analysis without yielding better, more accurate results. Hence, it is critical that an acceptable discretisation level is identified, both in terms of accuracy and computing time.

The component's thermal conductivity is the most important factor when determining discretisation levels for a thermal model. Structures made exclusively from components such as copper or steel would require very low discretisations due to their high thermal conductivities (around 400 $Wm^{-1}K^{-1}$ and 40 $Wm^{-1}K^{-1}$, respectively). Therefore, for example, heavily discretising a machine's rotor lamination in the axial direction will bring little advantage, since heat travels with little obstruction in this direction. It is in the electrical machine's windings where the use of a high discretisation level is very important. In the windings the conductivity is dramatically reduced by the presence of insulating resins (~0.25 $Wm^{-1}K^{-1}$) and trapped air pockets (~0.03 $Wm^{-1}K^{-1}$). Therefore, winding thermal conductivities fall to around 2-3 $Wm^{-1}K^{-1}$.

A study was performed in order to determine a reasonable axial discretisation level of a synchronous generator's rotor and stator windings. To do this a number of rotor winding models were used, ranging from a 'single block' (1x1) representation to a detailed rotor winding model represented by 100 smaller

sections (10x10). The 1x1 and 10x10 models are illustrated in Figure 8.

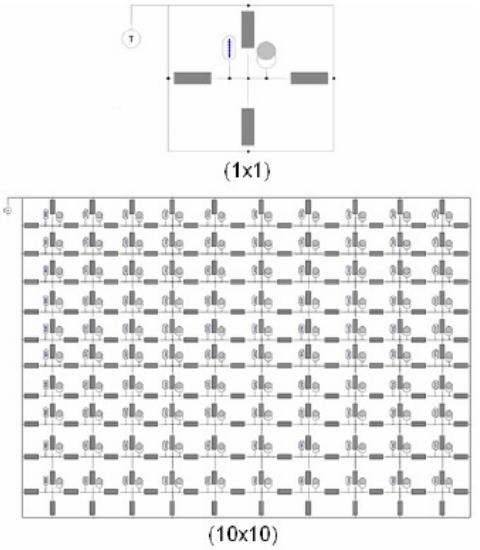

Figure 8: 1x1 (top) & 10x10 (bottom) rotor winding models.

An algorithm, to supply each discretisation model with the correct machine loss, was applied to each of the models considered. Algorithms were exposed to an identical loss scenario, with 1500 Watts of loss being divided between the power nodes making up the model, and the results obtained were graphed in Figure 9. At the same time FE thermal analysis (using CFD code Fluent) was used to analyse the winding under investigation, outputting an average winding stable state temperature of 17.07 °C. This temperature is the reference value used for the study in Figure 9.

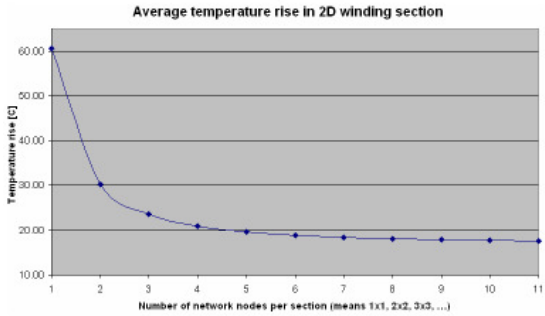

Figure 9: Rotor winding discretisation results up to 11x11.

As shown by the results, which were validated for a wide range of input loses, winding thermal conductivities and winding geometries, a rotor winding discretisation level of 10x10 yields very accurate results (17.71 °C) in comparison with the CFD results obtained. Using lower levels of discretisation reduces the accuracy of the results, whilst increasing discretisation unnecessarily complicates the thermal model.

V. Experimental Validation Stage

Experimental work is required to shine some light on the thermal model ambiguities described in this paper. A synchronous generator will be fully thermally characterised in order to achieve an improved thermal model. To achieve this, an industry standard 22.5 kVA alternator has been fully equipped with numerous thermocouples along all thermally significant components (see Figure 10). Closely monitoring the generator heat runs for numerous operational conditions will provide a high level of insight on the machine's thermal behaviour.

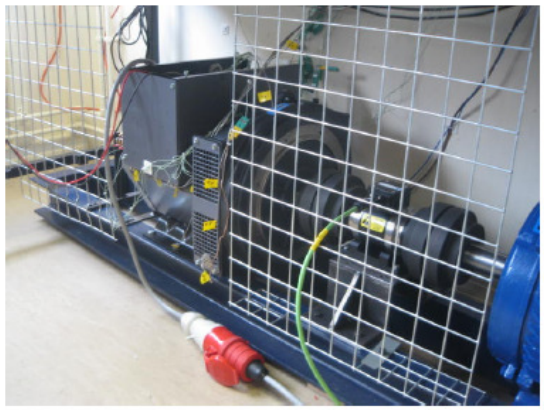

Figure 10: Alternator thermal analysis test-rig set-up.

VI. Rotor Thermocouple Reading Through Slip-Rings

The most challenging experimental section involves reading and processing the data from rotor thermocouples via shaft mounted bronze 11 brush slip-rings (see Figure 11). The main difficulty arises in the form of unintended thermocouple junctions. These can be reduced by ensuring that the correct thermocouple material wiring is utilised between the thermocouple sensors and the data acquisition system, but the junction located between the wiring and the slip-rings connections cannot be removed.

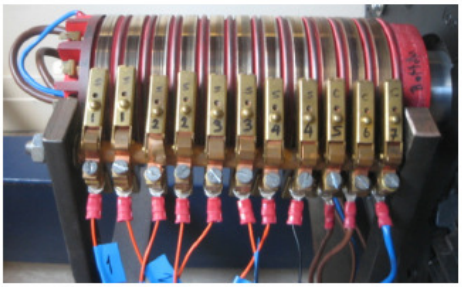

Figure 11: Shaft mounted bronze 11 brush slip-rings.

Furthermore, as the synchronous machine rotates at 1500rpm, the low voltage thermocouple readings (~0.8mV at 20 °C) can easily be swamped by electrical noise. Hence, it is vital that these signals are amplified as close to the source as possible and certainly prior to the slip-rings.

The material junction problem appears to be due to the frictional heat generated as the machine rotates, which causes the slip-rings to reach a temperature of ~60°C. The temperature difference between this junction and the temperature at the data acquisition end results in inaccurate results being collected. Although this junction cannot be removed since slip-rings are required, collecting, processing and amplifying the thermocouple voltages prior to the slip-rings will diminish the problem significantly, resulting in an acceptable level of accuracy.

To accomplish this, a small electronics PCB will be placed inside the slip-ring shaft. The PCB will read all 14 rotor winding thermocouples and process them through several multiplexers. In addition to this, an amplification stage will also be incorporated. A flow diagram of the electronics is shown in Figure 12.

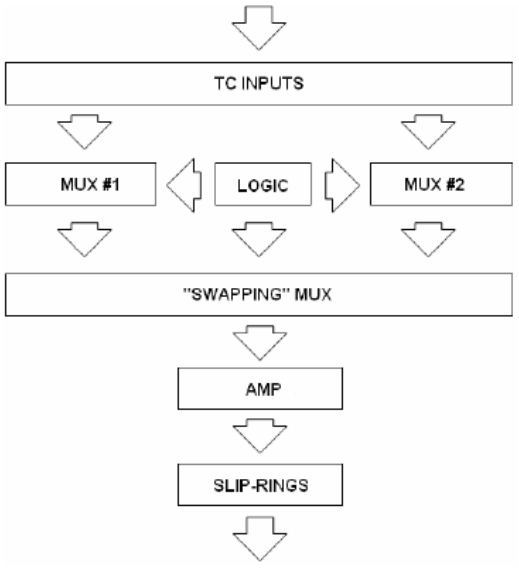

Figure 12: Flow diagram of rotor TC reading electronics.

The multiplexers (MUX), controlled by the logic stage will read each of the 14 rotor thermocouples in turn, whilst the amplification stage will increase the magnitude of the resulting multiplexer differential voltage before it is sent though the slip-ring to the data acquisition system. Though the output signal will still be susceptible to noise, the signal to noise ratio will be significantly increased. Protection circuitry will stop voltage spikes from saturating or damaging the multiplexers, and the inevitable 50 Hz noise will be cancelled and any remnants filtered out.

A crucial function of the electronics stage is performed by the "swapping" multiplexer. In order to remove slip-ring related temperature offsets, the following operation, outlined in Figure 13, is performed for every thermocouple reading. Two rings are allocated data output and these remain unchanged through the experimental stage to avoid introducing further offsets.

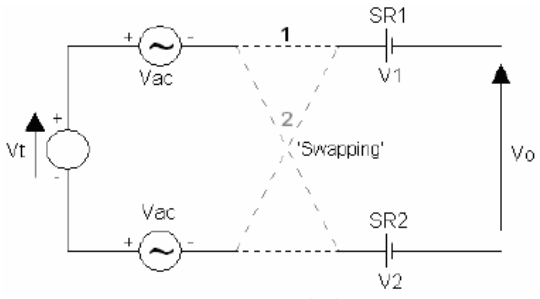

Figure 13: "Swapping" multiplexer operation.

where V_t is the thermocouple voltage, V_{ac} is the resulting ac voltage that generates on the thermocouple wires, V_1 is the voltage drop/offset through slip-ring 1 (SR1), V_2 is the voltage drop/offset through slip-ring 2 (SR2) and V_o is the resulting output voltage.

The 'swapping' dotted lines represent the possible reading paths allowed by the "swapping" MUX in Figure 13, paths 1 and 2. The "swapping" multiplexer takes one reading through path 1 and another through path 2 for every thermocouple measurement.

The 'swapping' procedure operates as follows. In general, analysing the circuit in Figure 13:

$$V_o = V_2 + V_{ac} + V_t - V_{ac} - V_1 \tag{4}$$

$$V_o = (V_2 - V_1) + V_t \tag{5}$$

Hence, V_o is obtained by the "swapping" multiplexer for the two positions shown in Figure 13. This yields V_{o1} and V_{o2} as shown.

$$V_{o1} = V_t + (V_2 - V_1) \tag{6}$$

$$V_{o2} = -V_t + (V_2 - V_1) \tag{7}$$

Therefore, a simple multiplexer subtraction of (6) and (7) removes the unwanted voltage offset introduced by the slip-rings.

$$V_{o1} - V_{o2} = 2V_t \tag{8}$$

Consideration was given to other data transmission systems, notably digitisation and radio transmission of the data, but that

would still require a scheme very similar to that outlined here to perform the necessary signal conditioning before digitisation and transmission. As the available space was extremely limited, this simpler system was used and found to be entirely adequate.

VII. Frame & External Thermal Captures

In addition to the described work, an accurate thermal camera was used to obtain the machine's exterior thermal distribution. The comparison between the no-load and full-load machine external temperature distribution is shown in Figures 14 and 15. Agreeing with the results presented in Section 3, the drive-end of the machine is clearly at a higher temperature, with the drive-end end-caps and couplings the hottest.

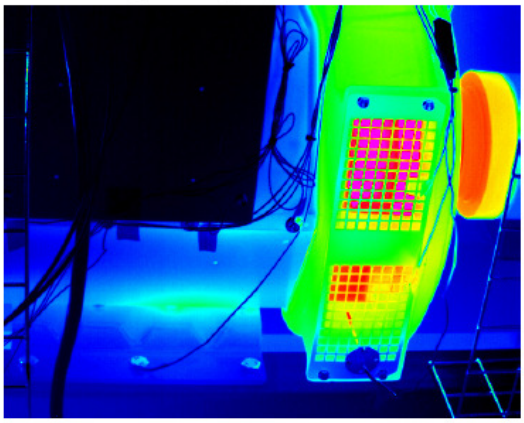

Figure 14: Alternator no-load thermal capture.

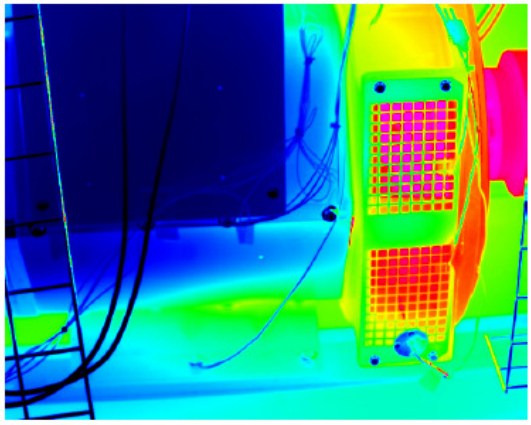

Figure 15: Alternator full-load thermal capture.

In Figures 14 and 15, the cooler blue shade of the non-drive-end of the machine is at ~38°C, the warmer green/yellow drive-end is at ~48°C and the hottest end-cap sections are at ~55°C.

VIII. Further Work

The method described in Section 6 allows for accurate thermal characterisation of the rotor winding. This, combined with the information collected from stator winding and frame thermocouples, will provide the complete machine thermal model desired. Initial simulations will then be confirmed, and the resulting thermal models will be validated over a wide range of operational conditions.

IX. Conclusions

The combined application of the thermal modelling improvements described in the paper has proven to result in more accurate and reliable synchronous machine thermal models. Additional experimental findings will further advance the current models, increasing accuracy and reliability. The models are applicable to a wide range of machines and ratings, aiding rapid effective operational consultations and easing new machine designs.

Acknowledgment

The authors thank The University of Edinburgh and Cummins Generator Technologies, as well as Motor Design Ltd. and Adapted Solutions for their aid and support.

References

[1] Maynes, B.D.J.; Kee, R.J.; Tindall, C.E.; Kenny, R.G.; "Simulation of airflow and heat transfer in small alternators using CFD", *Electric Power Applications, IEE Proceedings, Vol.150, No.2,* March '03 Page(s): 146–152.

[2] Salon, S.J.; "Finite Element Analysis of Electrical Machines", *Rensselaer Polythechin Institute, Kluwer Academic Publishers.*

[3] Staton, D.; Pickering, S.J.; Lampard, D.; "Recent advancement in the thermal design of electric motors", *Paper presented at the SMMA 2001 Fall Technical Conference, Emerging Technologies for Electric Motion Industry,* Durham, North Carolina, USA, 3 -5 October, 2001.

[4] AlAkayshee, Q.; Staton, D.A.; "1150hp Motor Design, Electromagnetic & Thermal Analysis", *ICEM,* Brugge, Belgium, 25-28 August, 2002.

[5] Lin, D.; Zhou, P.; Fu, W. N.; Badics, Z.; Cendes, Z. J.; "A dynamic core loss model for soft ferromagnetic and power ferrite materials in transient finite element analysis", *IEEE Transactions on Magnetics, Vol.40, No. 2,* March 2004.

[6] Mueller, M.A.; Williamson, S.; Flack, T.J.; Atallah, K.; Baholo, B.; Howe, D.; Mellor, P.H.; "Calculation or iron losses from time-stepped finite-element models of cage induction machines", *Electrical Machines and Drives, 1995. Seventh International Conference on (Conf. Publ. No. 412),* 11-13 Sep. 1995, Page(s): 88.

[7] Novinschi, A.; Brown, N.L.; Mebarki, A.; Haydock, L.; "The development of an FEA design environment model and comparison with traditional design and test data for the design of electrical machine", *IEE Conference on Power Electronics and Machines, pp 574-572,* 16-18 April 2002.

[8] Brown, N.L.; Mebarki, A.; Hydock, L.; "Design aspect of a 200KW, 3600 rpm, permanent magnet generator for use in variable speed integrated generator", *IEE International Conference on Power Electronics and Machines, pp 574-579,* 16-18 April 2002.

[9] Mueller, M.A.; Williamson, S.; McClay, C.I.; "Calculation of high-frequency losses in closed-slot induction motor rotors".

[10] Mejuto, C.; Mueller, M.; Shanel, M.; Mebarki, A.; Staton, D.; "Thermal modelling investigation of heat paths due to iron losses in synchronous machines", *4th International Conference on Power Electronics, Machines and Drives,* - 4 April 2008, York St John University College, York, UK.

Thermal Modelling Investigation of Heat Paths due to Iron Losses in Synchronous Machines

C. Mejuto [*], M. Mueller [*], M. Shanel [†], A. Mebarki [†], D. Staton [◦]

[*] The University of Edinburgh, Institute for Energy Systems, The King's Buildings, Mayfield Road, EH9 3JL, Scotland
[†] Cummins Generator Technologies, Barnack Road, Stamford, Lincolnshire, PE9 2NB, England
[◦] Motor Design Ltd., Lloyds Bank Chambers, 4 Scotland Street, Ellesmere, Shropshire, SY12 0EG, England

Keywords: Synchronous machine, Finite element analysis, Iron loss, Loss and Thermal distribution, Lumped circuit.

Abstract

The prediction and distribution of operational iron losses in synchronous machines are of great importance in order to improve the design procedure and yield more efficient generators. To achieve this, finite element analysis was utilised to analyse a Cummins Generator Technologies alternator and, using the required test data and material properties, the iron loss distribution across the machine's cross-section was established. From this, Lumped Circuit Coefficients (LCCs) were created. LCCs are used to translate the generator's thermal model to a lumped circuit thermal network.

1 Introduction

The prediction and exact distribution of iron losses under transient conditions across a synchronous machine's lamination has proven to be a challenging area. In the past, several methods have been applied in the frequency domain, but analysis in the time domain still requires significant work [1]. Therefore, the objective of the study was to utilise finite element analysis (FEA) to determine iron losses in the time domain.

FEA is a powerful design tool that allows mirroring electrical machine tests and extracting important electromagnetic and thermal information, with a high degree of accuracy. Once precise geometries of the machine under investigation have been established, feeding experimentally obtained data related to the field and armature of the machine permits for the determination of useful data such as the vector potential, current density, magnetic flux density and magnetic field strength distribution. Therefore, FEA provides a level of insight and detail of the machine's inner behaviour otherwise unattainable by experimental methods, at the expense of meticulous model calibration and extensive computing times.

Modelling synchronous generators using FEA carries a number of differences with regards to motor simulations. The main machine characterising parameters required for a synchronous machine model relate to the rotor, where the field voltage and winding impedance are required as an input. On the other hand, no voltage input settings are required for the armature winding, since these will be generated by the simulation itself. Only the armature winding resistance and inductance are required for the stator settings.

Magnetisation properties of the rotor and stator lamination materials, as well as the shaft, are of vital importance and need to be accurately established. Furthermore, boundary conditions (fixed potential edges) around particular machine components need to be carefully considered. [2]

2 Model Development

The geometries of the generator windings, shaft, laminations and other design components need to be precisely extracted from reliable machine drawings. From them, the 2-dimensional cross-section of the alternator can be created as shown in Figure 1.

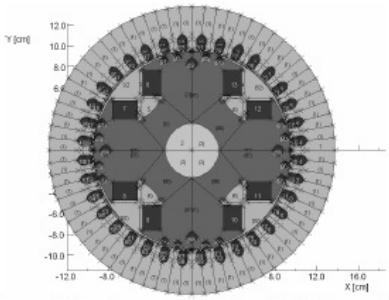

Figure 1: Synchronous machine 2D FEA model.

The model presented is that of the Cummins Generator Technologies (CGT) BCI184E 4-pole synchronous generator. It is composed of 36 stator slots, in which a 2/3 pitched double layer concentric winding is used. There are 3 slots per pole per phase and 98 turns per phase. The generator's armature is series star wound and machine rotation is in the clockwise direction. The particular alternator operating point considered in the analysis is 22.5 kVA, 31.3 A, 415 V, 50 Hz. It is important to note that for the CGT alternator model shown, fixed potential boundaries are exclusively utilised around the stator lamination.

Rotor and stator lamination properties are set in accordance with material suppliers data. However, in the study, lamination suppliers lack or are unable to provide certain material data for particular operating conditions. In these

situations reasonable approximations, from BH curves for similar materials on comparable machines, need to be made. In the study, the crucial fragment of the BH curve, the point at which the 'knee' occurs (see BH curves in Figures 2 and 3), was provided by the material supplier and the graph was extrapolated further to achieve the required complete BH curve. The 'knee' section of the BH curve characterises the saturation region. Curve points below the BH curve 'knee' are normally not critical for the simulation's outcome. In the study, the BH curves used for the synchronous machine laminations, Figure 2, and for the steel shaft, Figure 3, are displayed below. These were extracted from data provided by material suppliers, but had to be slightly approximated due to limited information being available for the desired frequency range and operational condition. Selected BH curves were validated by comparing them with previously utilised CGT BH curves for the same machine range.

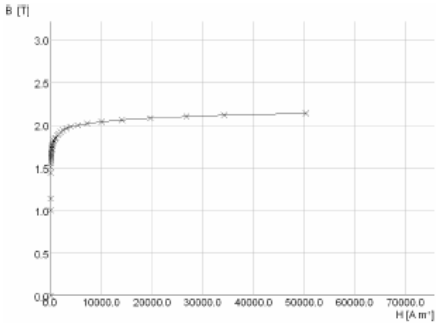

Figure 2: BH curve for alternator's rotor lamination.

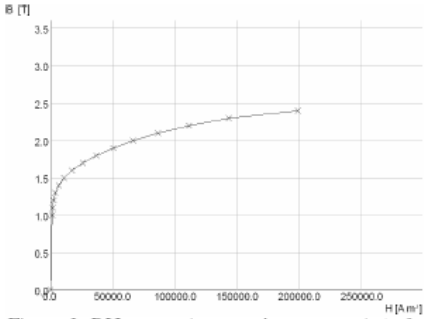

Figure 3: BH curve alternator's rotor steel shaft.

Once material geometries and properties have been successfully logged into the FEA model, the designer's attention shifts to the characterisation of the particular alternator operating point being analysed. At this stage, the armature wiring configuration needs to be confirmed. For this particular machine, the stator is wound in a series star configuration, with a double layer concentric winding layout of 2/3 pitch and 98 turns per phase. Once the electrical machine's armature winding details are established, FEA external circuit simulation settings can be determined. For this machine utilising 6 external circuits, with 2 external circuits per phase, is appropriate as illustrated in Figure 4.

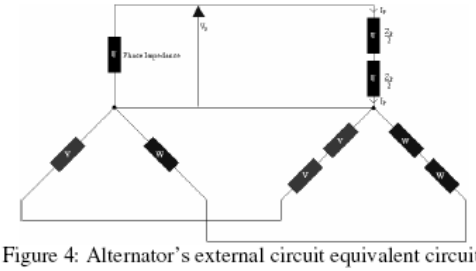

Figure 4: Alternator's external circuit equivalent circuit.

At this point, rotor field and stator armature simulation settings need to be fed into the simulator. For a synchronous generator this refers to the field voltage, field resistance, armature resistance and armature inductance. These are computed using the CGT test data provided.

Operating conditions: 22.5 kVA, 31.3 A, 415 V, 50 Hz

Rotor Field Settings:

Field current, I_F = 35 A
Field resistance, R_F = 0.863 Ω
Field voltage, V_F = 30.205 V

Stator Armature Settings:

Armature line voltage, V_L = 415 V
Armature current, I_A = 31.3 A
Armature resistance, R_A = 0.8896 Ω
Armature phase voltage, V_P = 239.6 V
Armature phase load, X_P = 6.12397 + 4.59298 Ω
External R per external circuit = 3.506785 Ω
External L per external circuit = 7.30995 mH

2.1 Simulation Results Validation

Once the synchronous generator material properties have been established and the simulation settings adjusted, the FEA simulator can be initialised. A reasonable simulation tolerance and time step for the simulation are required. Setting an adaptive time step manages the simulators computing time effectively, focusing on the most sensitive simulation segments. The desired output times, at which the simulator will subsequently generate data, also needs to be determined.

The initial task, once the simulation has terminated and the results are unveiled, is to validate the data obtained. In order to do this, experimental test data supplied by CGT for the particular operation model under consideration is required. In particular, field and armature currents need to be carefully examined. The graphical data displayed in Figures 5 and 6 confirms an acceptable level of agreement between the FEA simulation results and the experimentally obtained information supplied. Firstly, the rotor's field current variation with time is presented in Figure 5, followed by the 3-phase stator armature current distribution, in Figure 6.

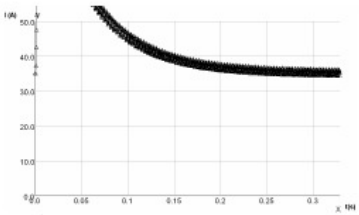

Figure 5: Rotor field current variation with time.

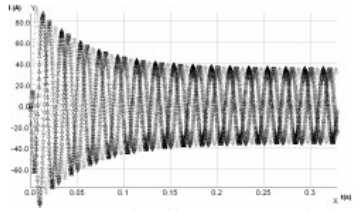

Figure 6: Stator armature 3-phase current variation with time.

Both graphs exhibit an acceptable stable state condition agreement with the experimental data supplied by CGT. Rotor field current results fully agree with the experimental data. Stator armature current results show an error of just over 10% with respect to the test measurements. This is an acceptable mismatch given the enforced BH curve related assumptions made during the generator's model setup. Furthermore, there are numerous factors that could lead to a discrepancy between simulation and practical results. Apart from the mentioned material properties related data, machine manufacturing techniques can have a significant effect on the resulting armature current, since the high pressures exerted on the laminations, or the turning process, can considerably alter their electromagnetic behaviour.

3 Iron Loss determination & distribution

The main objective of the FEA Rotating Machine (RM) [3] simulation work regards the prediction of iron losses and, in particular, the distribution of these across the CGT electrical machine. For this reason, it is necessary to dissect the rotor and stator section of the model as shown in Figure 7.

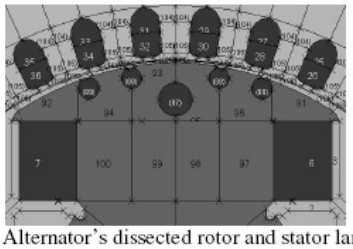

Figure 7: Alternator's dissected rotor and stator lamination.

This modification allows for the evaluation of each individual rotor/stator section presented separately and is of great aid in order to transfer the eventual power loss information discoveries made, to a lumped circuit thermal network representation of the electrical synchronous machine. From this, the thermal model for ¼ of the rotor can be represented by up to 13 individual segments. Similarly, this applies to the stator, where a discretisation of up to 4 sectors is possible to represent 1/72 of the lamination.

In order to correctly understand and predict the occurrence and allocation of power losses during synchronous generator operation, it is fundamental to analyse the magnetic flux distribution across the electrical machine. The magnetic flux density plot for the alternator is displayed in Figure 8.

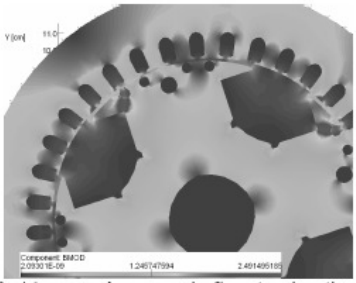

Figure 8: Alternator's magnetic flux density distribution.

It is important to note that the rotor turns in a clockwise direction. The presented magnetic flux distribution clearly illustrates the non-symmetrical nature of the operational power losses that occur during synchronous machine rotation. The most concentrated losses are situated at the 'lagging' half of the rotor pole, with flux densities of over 2T in particular areas. Interestingly, a relatively low magnetic flux density is identified at the 'leading' half of the rotor pole, which due to armature reaction.

4 Analysis and Results

Operational iron losses for each rotor and stator sections can be easily extracted from the FEA RM [3] results, via a specially designed command file. The command file performs a harmonic evaluation of the flux density waveform in each model element for the time cycle under investigation (one rotor rotation). Hence, the end result is a decomposition of the magnetic flux waveform per element into its constituent parts (fundamental, 1st order, 2nd order, 3rd order, etc.). It is important to note that the described method considers iron losses exclusively and excludes stray losses from consideration, since these should be dealt with independently.

For ferrite materials, this is then used to compute the loss per harmonic using the well-known Steinmetz formulae [1].

$$Iron\ Loss, \quad P_t = C_m f^{\alpha} B_m^{\beta} \tag{1}$$

C_m, α and β are empirical parameters obtained from experimental measurement under sinusoidal condition. B_m represents the peak magnetic flux density and f represents frequency.

This is applied in the iron loss calculating command file by the following equation [4].

$$\text{Iron Loss}, \quad P_t = P_h + P_e = k_h B^n f + k_e B^2 f^2 \tag{2}$$

P_t is the total iron loss, P_h the hysteresis component, P_e the eddy-current component and P_x the excess loss. k_h and k_e represent the hysteresis and eddy current iron loss coefficients respectively.

As a more general approach, total iron loss is the sum of the hysteresis and eddy current components, with the addition of an excess loss component due to domain wall effects that should be taken into account for non-ferrite materials [5].

4.1 Hysteresis and Eddy Current Coefficients

In order to calculate the essential hysteresis, k_h, and eddy current, k_e, iron loss coefficients the following technique should be employed. The Steinmetz related equation displayed below, together with the generator's PowerCore® M 800-65 A 0.65 mm ThyssenKrupp Stahl lamination material information are required for this [6].

$$\text{Iron Loss}, \quad P_t = P_h + P_e = k_h B^n \frac{f}{density} + k_e B^2 \frac{f^2}{density} \tag{3}$$

$$\text{Hence}, \quad P_t = k_h \frac{f}{density} + k_e \frac{f^2}{density} \tag{4}$$

Using Equations 3 and 4 and the alternator's PowerCore® M 800-65 A 0.65 mm ThyssenKrupp Stahl lamination material information the following hysteresis and eddy current coefficients can be calculated [7].

$k_e = 1.59861 \qquad k_h = 488.631$

4.2 Calculating Coefficient *n*

As presented in Equation 2, *n* coefficients (*a*, *b* and *c*) are used as a calibrating mechanism for the iron loss calculation process, as outlined below.

$$n = a + b \cdot B + c \cdot B^2 \tag{5}$$

As a standard industry practical level, *n* should equal around 1.5 at B=0T and 2.5 at B=2T, but specific lamination material *n* values will vary.

4.3 Lumped Circuit Coefficients

Utilising the loss data calculated, lumped thermal network coefficients can be derived by comparing the iron loss concentration distribution across the machine. These coefficients are of great aid in order to generate a lumped circuit thermal model truly representative of the synchronous generator's rotor and stator loss distribution. The generated coefficients will be called Lumped Circuit Coefficients (LCCs) and are obtained by combining electromagnetic coefficients (EMCs) and thermal coefficients (TempCs).

Electromagnetic Iron Loss Coefficients (EMCs)

Rotor electromagnetic iron loss coefficients (EMCs) evaluate the concentration of the magnetic flux density at specific rotor lamination sections. Rotor EMC values for the top and middle sections are illustrated in the Figure 9. For instance, the top left rotor pole section receives an EMC value with is 4 to 8 time the base lamination value.

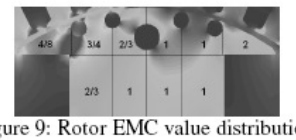

Figure 9: Rotor EMC value distribution.

EMC values for the rotor lamination sections not displayed in Figure 9 are set to 1, due to their low magnetic flux density. Critical rotor lamination sections, mainly located at the 'lagging half', have a range related to their EMC values. This is because magnetic flux density pattern may vary slightly depending on machine operational conditions and on design issues such as damper bars.

Transient Thermal Iron Loss Coefficients (TempCs)

Using the FEA thermal transient results, TempC values can be established, depending on the temperature distribution of specific rotor lamination areas. The TempC layout is displayed below for total iron losses in Figures 10.

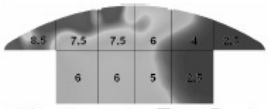

Figure 10: Total iron loss rotor TempC value distribution.

Default Lumped Circuit Coefficients (LCCs)

The two sets of coefficients (EMCs, TempCs) are weighed and averaged to generate the general Lumped Circuit Coefficients (LCCs). These general default settings can effectively be used to create a truly representative thermal model. Established LCC values are illustrated in Figure 11. For example, LCCs between 6 and 8 should be used for Section 92.

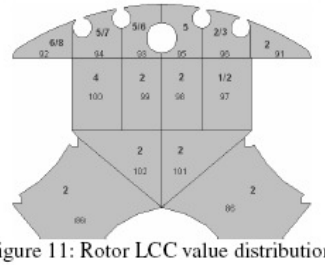

Figure 11: Rotor LCC value distribution.

A section with an LCC value of 2 has approximately twice the iron loss concentration as one with an LCC value of 1. Figure 11 indicates that, across the rotor, the main thermal sources concentrated at the top left corner (rotating 'lagging' half) of the rotor pole. LCC's of 8 to 5 for sections 92 to 95 signify this. Adjacent sections 96 and 100 also exhibit a significant thermal concentration and hence receive LCC values of 2 to 4. With the exception of section 97, which could exhibit an LCC of 1, the rest of the rotor dissections have a LCC value of 2, denoting a low temperature in these areas.

4.4 Stator Section

Stator sections are simpler to model thermally, due to their non-rotating nature. A similar process to that performed on the rotor was executed. LCC values for stator sections are presented in Figure 12.

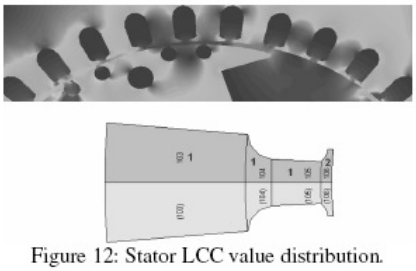

Figure 12: Stator LCC value distribution.

Figure 12 shows that, as expected, the highest concentration of iron losses, and hence highest temperature, across the stator lamination is located at the bottom of the stator lamination tooth. For this reason, section 106 has an LCC value of 2, whilst the remaining stator sections have a value of 1, indicating a low iron loss concentration.

Confirmation runs performed at other operational conditions validate the information presented.

5 Results

The presented findings have been effectively applied to the synchronous machine's lumped circuit thermal networks, shown in Figure 13. By accommodating the LCCs in the thermal model, the impact of and true distribution of iron losses and their thermal effect is achieved, allowing for an accurate representative electrical machine thermal model.

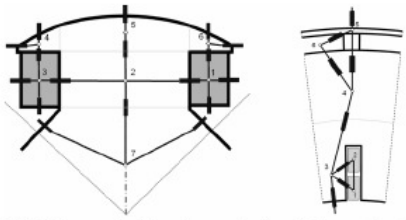

Figure 13: Rotor and stator lumped circuit thermal networks.

LCCs were applied to the reluctance network (Figure 13) in terms of the weighing factors presented in this paper and resulted in an improved synchronous generator thermal model, which mimics the true iron loss distribution of the alternator in a more realistic manner. As shown in Figure 14 the application of LCCs to the top rotor pole section (nodes 4, 5 and 6 of Figure 13) affects the temperature distribution across the rotor lamination is achieved.

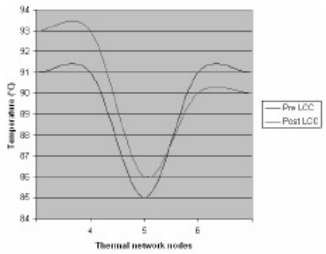

Figure 14: Rotor LCC application results for pole top section.

6 Conclusions

It is important for modern generator design methods to take into account precise iron loss magnitudes and distributions. FEA is a powerful tool and was utilised to determine iron losses and their location along the cross-section. From these results, LCCs were calculated by considering electromagnetic distributions and the resulting thermal effects. Application of LCCs to the alternator's reluctance thermal model yielded a truly reliable representation of the electrical machine. This method was implemented on a range of CGT machines for a number of operation conditions with satisfactory results.

Acknowledgements

The authors would like to thank The University of Edinburgh and Cummins Generator Technologies, as well as Motor Design Ltd. and Adapted Solutions for their aid and support.

References

[4] A. Novinschi, N.L. Brown, A. Mebarki, et al. *"The development of an FEA design environment model and comparison with traditional design and test data for the design of electrical machine"*, IEE Conference on Power Electronics and Machines, pages 574 – 572 (16-18 April 2002).

[1] D. Lin, P. Zhou, et. al. "A Dynamic Core Loss Model for Soft Ferromagnetic and Power Ferrite Materials in Transient Finite Element Analysis", *IEEE Transactions on Magnetics*, Vol. 40, No. 2, (March, 2004).

[7] L. Ma, M. Sanada, et. al. "Iron loss prediction considering the rotational field and flux harmonics in IPMSM and SynRM", *IEE Proc.-Electr. Power Appl.*, Vol. 150, No. 6, (November 2003).

[5] M. A. Mueller, S. Williamson, et. al. "Calculation of Iron Losses from Time-Stepped Finite-Element Models of Cage Induction Machines", *IEE Electrical Machines and Drives*, Conference Publication No. 412, (1995).

[2] S. J. Salon. "Finite Element Analysis of Electrical Machines", *Kluwer Academic Publisher*, (1995).

[6] ThyssenKrupp Stahl. PowerCore® M 800-65 A 0.65 mm lamination material information (2007).

[3] Vector Fields, Opera 2-d software manual (V.12), 2007.

Thermal Modelling of TEFC Alternators

Carlos Mejuto & Markus Mueller
University of Edinburgh
The Kings Buildings
Mayfield Road
Edinburgh, EH9 3JL
Markus.Mueller@ed.ac.uk

Dave Staton
Motor Design Ltd
1 Eaton Court, Tetchill, Ellesmere
Ellesmere, Shropshire
SY12 9DA, UK
dave.staton@motor-design.com

Salem Mebarki & Nazar Al-Khayat
Newage International Ltd
Barnack Road
Stamford, Lincolnshire
PE9 2NB
salem.mebarki@newage-avkseg.com

Abstract* – *The importance and necessity for an electrical machine design process where thermal and electromagnetic issues are considered in an iterative manner is clear today. A commercially available thermal modelling package is used to investigate the design of a TEFC synchronous machine for a mobile refrigeration application, which imposes significant demands on the thermal performance of the machine. Experimental results of a fully instrumented machine have been used to show that the software package predicts the thermal performance of the machine to a high degree of accuracy. Sensitivity analysis was used to optimise the machine for the required application.

I. INTRODUCTION

It is clear today that in order for a new breed of higher efficiency electric machines to emerge, electromagnetic analysis and thermal modelling need to be carried out in an iterative manner from the beginning of the design process. By doing so, losses in the machine have the potential of being greatly reduced and channelled through components that provide the fastest and most efficient path away from the machine.

In the past many experienced synchronous generator manufacturing companies have used spread sheet calculations, based on equivalent circuits, to predict the thermal performance. An available alternative is Computational Fluid Dynamics (CFD). While the CFD can provide accurate flow and heat transfer results, the method is expensive in terms of time to produce a model and computing time. Designers are therefore in need of a faster modelling technique that does not compromise on accuracy and allows thermal trends and critical machine parameters to be identified in a cost efficient manner. Lumped-circuit analysis promises to be a good solution. Its ability to instantaneously calculate component temperatures makes it ideal for inexpensive machine designing. Furthermore, definition and processing times are reduced considerably. As a consequence of this, improved electric machines with a longer lifetime will be designed, leading to more efficient gensets (generator sets, including prime mover), which will be adapted to customer demands with a greater ease. In addition to this, reduced temperatures will improve the generator's overload capability, increasing reliability.

II. MODERN THERMAL DESIGN

Modern computer aided design packages can now be used to design the thermally relevant features of electric machines in an iterative manner to the electromagnetic design. These software tools achieve a model which is true to the specific machine under investigation. Optimum characteristics, in terms of size, weight, output, efficiency, cost and lifetime can be achieved with them. Development times and prototype costs are greatly reduced as a consequence of this. It is fundamental for designers to be aware of the effect, if any, that machine parameters will have on thermal performance and thermal analysis software tools allow this. At first, a designer may not be aware of the most significant design variables affecting thermal performance and might be concentrating efforts on areas of the machine that have no significant thermal importance. This is where sensitivity analysis becomes fundamental, allowing engineers to identify crucial design areas and machine parameters. Modern thermal design tools also allow customer wishes to be evaluated nearly instantly, as the designer will immediately gain feedback on whether the electric machine analysed is suitable for the required task. In the same way, if a change in a machine component material or in the manufacturing procedure is suggested in order to improve performance or productivity, thermal analysis packages allow for a quick quantification of the implications that such changes could have. Advantages and deficiencies of the proposed alterations will be easily highlighted.

Today's thermal design techniques can be divided into two groups: Analytical Lumped Circuit Analysis (Motor-CAD) and Numerical Analysis. Numerical Analysis can be sub divided into Finite Element Analysis and Computational Fluid Dynamics [1]. In the last few years, there has been a growing awareness on the fact that thermal considerations are essential when designing electric machines. Many papers have been published, discussing methods to improve understanding, modelling and approach to the thermal distribution within a machine. One of the main issues under investigation is the debate between CFD techniques and the latest lumped circuit analysis methods. Many papers seem to conclude that in most cases lumped circuit tools are the most popular due to their speed advantage, removing the other option from the designing procedure completely. The flow diagram displayed in Fig 1 outlines the designing process that could lead to an ideal optimised machine.

1-4244-0136-4/06/$20.00 ©2006 IEEE

The iterative presence of analytical and numerical design steps in order to account for electromagnetic and thermal factors is presented as the correct approach. The emphasis here is in proposing that analytical and numerical modelling techniques should not compete against each other, but be merged in the same designing process. The speed calculation advantage characterising analytical tools should be combined with the greater accuracy provided by numerical methods. CFD techniques are excellent for predicting flow in complex areas of the design, such as the open fin leakage. This method should be implemented to model difficult sections of the thermal design and develop functional relationships that can be used in the faster lumped circuit analysis. As a result of this effective combination, machine parameters optimisation will be possible and uncomplicated. In particular, a considerable reduction in machine size will be facilitated [2,3].

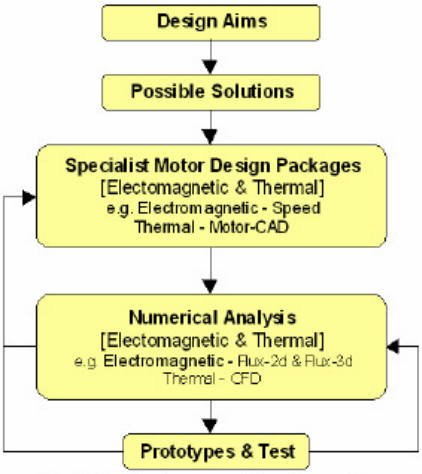

Fig 1: Ideal design process flow diagram [2].

III. MOTOR-CAD:

Motor-CAD is a novel lumped-circuit based computer aided design software package dedicated to thermal analysis of rotating machines. The software has already been tested in a wide range of scenarios, such as in automotive, aerospace and industrial areas. Motor-CAD provides instantaneous calculation speeds, taking into account heat transfer paths through conduction, convection and radiation mechanisms. Cooling methods, such as water jackets, spray cooling and fan ventilation, are incorporated in the package. By establishing machine geometric dimensions and material composition, a network comprising of thermal resistances, power sources, thermal capacitances and nodal temperatures is created. From this the designer receives a combination of numerical and graphical outputs that facilitate the designing procedure and assist result interpretation greatly. Alterations to machine features are visualised by the user, reducing the chance of errors occurring when inputting relevant data. The lumped-circuit resembles an electrical network with ohmic resistors, capacitors and current sources, being easily comprehended by engineers. The use of Motor-CAD promises to be a very useful tool in generator design and optimisation, with the corresponding benefits in efficiency and overall cost [4]. Motor-CAD allows a wide range of motor/generator types to be thermo-modelled, including the synchronous generators under investigation.

IV. THE TEFC ALTERNATOR

The totally enclosed fan cooled (TEFC) alternator investigated was required by an American truck company in order to power large refrigerator containers. These containers are subjected to extreme climatic conditions and therefore the generator needs to be isolated from the surrounding atmosphere [5]. To try and avoid the alternator from overheating, a fan, mounted on the truck engine driven shaft is be used to ventilate the enclosing frame. The TEFC arrangement is presented in Fig 2. An Ingress Protection (IP) level of 54 is desired by the customer, meaning protection against harmful levels of dust and water sprayed from any direction [6]. This can only be achieved by utilising the illustrated totally enclosed arrangement.

Fig 2: TEFC UC22 generator.

V. TESTING THE ALTERNATOR

The first set of thermo-modelling results was obtained by running the generator on a test bench. By carefully locating thermocouples and search coils on relevant machine components, the machine's temperature distribution was monitored. Up to 52 sensors were used. A selection of these are shown on Figs 3 and 4.

The totally enclosed alternator was exhaustively tested in order to achieve a full thermal characterisation of the machine. Tests were performed on the generator both for the totally enclosed non-ventilated (TENV) and TEFC operational modes. The airflow generated in the fan cooled investigations was also carefully monitored and air velocity measurements around the generator's

circumference were taken. These tests are fundamental in order to evaluate and validate the software before it can be confidently used for design purposes.

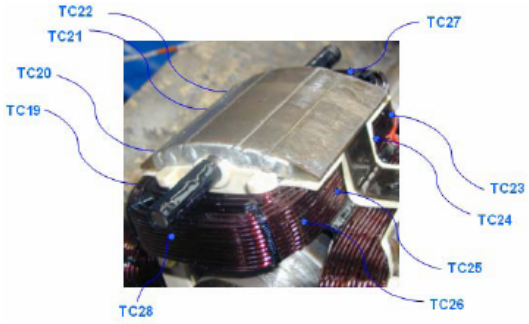

Fig 3: Location of rotor thermocouples.

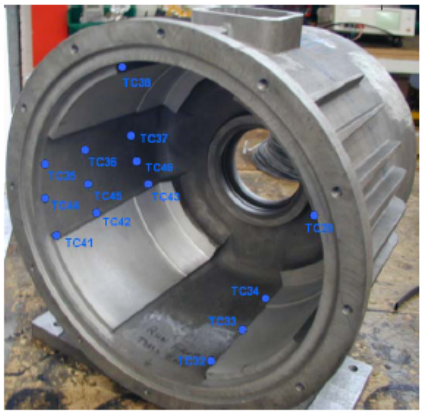

Fig 4: Location of frame thermocouples.

The alternator was driven until components reached steady-state temperatures for a wide kVA range. Firstly, tests were carried out without a fan (TENV). Subsequently, an axial fan was mounted on the generator's shaft and the tests repeated (TEFC). Since Motor-CAD is based on a lumped parameter model, it is necessary for the thermocouples used in the tests to be grouped according to the generators physical component. By doing this, experimental temperature averages for the most important machine elements were calculated. TENV results are displayed on Table 1. TEFC results are displayed on Table 2.

Tables 1 and 2 will be used to calibrate and validate Motor-CAD. When analysing the TENV machines the model complexities introduced by the cooling air flow are eliminated, but since the ultimate aim is to generate the thermal in-house capability design of a TEFC alternator air flow consideration will be of great importance and the air flow measurements taken during testing need to be processed.

	kVA Rating			
Component	**4.38**	**6.42**	**8.6**	**10.64**
Housing – Front	68.1	69.9	80.7	94.3
Housing – Active	68	69.6	79.6	92.6
Housing – Rear	64.8	66.4	75.6	87.8
Bearing – Front	68.3	69.6	80.6	94.5
Bearing – Rear	61.5	63.2	70.5	81.7
Stator Winding	74.1	76.6	86.8	101
Rotor Winding	83.7	88.1	103	124.5
Winding Av.	76.15	79.5	91.3	107.5
EndWinding – Front	76.7	80.6	93.3	110.8
EndWinding – Rear	75.5	79.3	91.7	108.7

Table 1: TENV component temperature averages (°C)

	kVA Rating			
Component	**9**	**13.5**	**18**	**23.6**
Housing – Front	40	45.7	55.9	78.1
Housing – Active	38.2	43	51.5	70.7
Housing – Rear	35.8	40.2	48.1	66
Bearing – Front	42.4	47.3	56.5	77.8
Bearing – Rear	38.5	42.9	51.4	70.2
Stator Winding	48	56	69.2	96.8
Rotor Winding	58	74.1	98.4	149.8
Winding Av.	51.4	62.7	81.8	120.1
EndWinding – Front	54.1	67.5	90	135.7
EndWinding – Rear	52.8	66	88.3	132.7

Table 2: TEFC component temperature averages (°C)

VI. AIR FLOW EXAMINATION

Air velocity readings were taken at four points along the generator's axial frame length, A, B, C and D as shown on Fig 5. Each of these points is a fixed distance from the end of the cowling, as shown on Table 3.

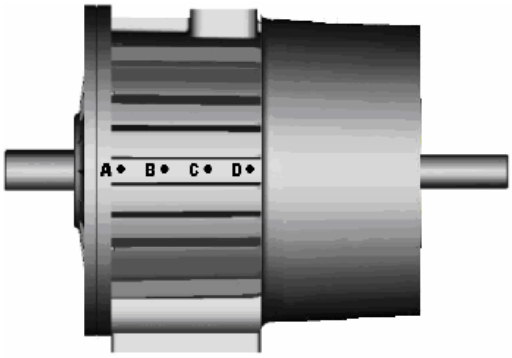

Fig 5: Air flow measuring points of the UC22B frame.

Air flow reading point	**Distance from cowling end**
A	24 mm
B	71 mm
C	119 mm
D	166 mm

Table 3: Distance from the cowling end to reading points.

These four readings were repeated around the circumference of the frame and average air velocities as a function of the distance from the end of the cowling were calculated. Table 4 shows the average readings. At this stage Motor-CAD models were validated using geometric, air flow and loss related information.

Location (Distance from cowling)	A	B	C	D
Air Speed (m/s)	15.2	8.5	8.3	7.2

Table 4: Average air velocity readings

VII. EXPERIMENTAL VS. MOTOR-CAD THERMAL PREDICTIONS

Once confident with all Motor-CAD input parameters, lumped circuit simulations were carried out. By comparing component temperature predictions with those measured during the alternator heat runs, the software's ability to model the thermal capability of a totally enclosed synchronous generator can be evaluated. The schematic output for the TEFC 18 kVA model is displayed in Fig 6. From the schematic of each model, temperature predictions were recorded and compared with those measured on the alternator.

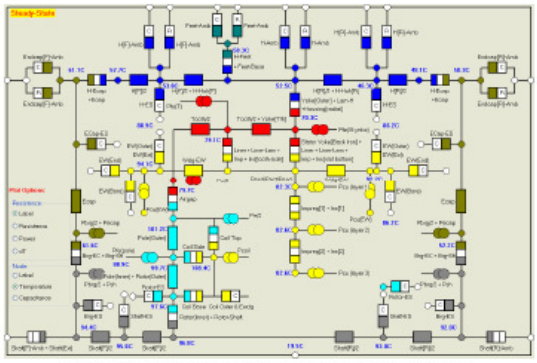

Fig 6: Schematic output for the TEFC 18 kVA generator.

Experimental results are compared with predictions from Motor-CAD in Tables 5 (TENV) and 6 (TEFC). Differences between experimental and simulated temperatures are displayed both in terms of magnitude and percentage error. Average winding and end-winding temperature information refer to the stator. The version of the software used had a very crude model for the rotor winding (this has been improved in the latest version of the software). The overall percentage errors obtained, 5.88 % for the TENV models and 6.50 % for the TEFC, are very satisfactory. Thermal predictions for specific generator components is very challenging and percentage errors of up to 20 % can be acceptable in some situations. Table 7 looks at the percentage errors associated with particular machine parts.

4.38 kVA	O/p Parameter	Exp. o/p (°C)	Motor-CAD o/p (°C)	ΔT (°C) [Exp. - Mot.]	% Error
	Housing - Front	68.1	67.51	0.59	0.87
	Housing - Active	68	66.05	1.95	2.87
	Housing - Rear	64.8	63.94	0.86	1.33
	Bearing - Front	68.3	68.75	-0.45	-0.66
	Bearing - Rear	61.5	64.47	-2.97	-4.83
	Stator Winding	74.1	74.86	-0.76	-1.03
	Rotor Winding	83.7	82.05	1.65	1.97
	Winding Average	76.15	73.93	2.22	2.92
	EndWinding (F)	76.7	69.9	6.8	8.87
	EndWinding (R)	76.5	68.85	6.65	8.81
				Average % Error	3.42
6.42 kVA	O/p Parameter	Exp. o/p (°C)	Motor-CAD o/p (°C)	ΔT (°C) [Exp. - Mot.]	% Error
	Housing - Front	69.9	71.71	-1.81	-2.59
	Housing - Active	69.6	70.19	-0.59	-0.85
	Housing - Rear	66.4	68.22	-1.82	-2.74
	Bearing - Front	69.6	72.97	-3.37	-4.84
	Bearing - Rear	63.2	68.82	-5.62	-8.89
	Stator Winding	76.6	79.84	-3.24	-4.23
	Rotor Winding	88.1	81.35	6.75	7.66
	Winding Average	79.5	79.41	0.09	0.11
	EndWinding (F)	80.6	76.1	4.5	5.58
	EndWinding (R)	79.3	75.09	4.21	5.31
				Average % Error	4.28
8.6 kVA	O/p Parameter	Exp. o/p (°C)	Motor-CAD o/p (°C)	ΔT (°C) [Exp. - Mot.]	% Error
	Housing - Front	80.7	77.25	3.45	4.28
	Housing - Active	79.6	75.77	3.83	4.81
	Housing - Rear	76.6	73.84	1.76	2.33
	Bearing - Front	80.6	78.53	2.07	2.57
	Bearing - Rear	70.5	74.54	-4.04	-5.73
	Stator Winding	86.9	86.78	0.02	0.02
	Rotor Winding	103	89.78	13.22	12.83
	Winding Average	91.3	86.99	4.31	4.72
	EndWinding (F)	93.3	84.39	8.91	9.55
	EndWinding (R)	91.7	83.3	8.4	9.16
				Average % Error	5.60
10.64 kVA	O/p Parameter	Exp. o/p (°C)	Motor-CAD o/p (°C)	ΔT (°C) [Exp. - Mot.]	% Error
	Housing - Front	94.3	84.8	9.5	10.07
	Housing - Active	92.6	82.6	10	10.80
	Housing - Rear	87.8	80.77	7.03	8.01
	Bearing - Front	94.5	85.44	9.06	9.59
	Bearing - Rear	81.7	81.66	0.04	0.05
	Stator Winding	101	95.19	5.81	5.75
	Rotor Winding	124.5	100.7	23.8	19.12
	Winding Average	107.5	96.28	11.22	10.44
	EndWinding (F)	110.8	94.85	15.95	14.40
	EndWinding (R)	108.7	93.68	15.02	13.82
	OVERALL TENV % ERROR: 5.88 %			Average % Error	10.20

Table 5: TENV experimental against Motor-CAD temperature prediction comparison.

Examining the results tabulated in Table 7 reveals that in general housing temperature predictions are very satisfactory. The front of the housing shows a higher percentage error than the active and rear sections. This can be explained by the fact that Motor-CAD only models the generator part of the genset. During the alternator experiments, the generator was driven as a complete genset. This results in the front area of the alternator being heated by the losses in the engine, especially at high kVA's. When operating at a lower kVA a reverse effect is observed. In this situation, the presence of the attached engine can provide an extra heat conduction path away from the generator's housing, resulting in an overestimate from the model in Motor-CAD. A similar explanation can be given for the difference in percentage error between front and rear bearings, since the former will be vulnerable to heat conducted from the engine for high kVA operation. Stator temperature predictions are generally very good. This is to be expected as the software allows for the stator to be characterised with great detail. Similarly stator winding average percentage errors are also very satisfying. On the other hand, the rotor model used lacks detail and accuracy and requires development (the latest release of the software does have an improved rotor winding model but has not been evaluated yet). The end-winding section of the stator windings is a challenging area which needs further research. Further in depth understanding of this would allow for percentage error

offsets to be reduced to the active winding percentage error levels.

9 kVA	O/p Parameter	Exp. o/p (°C)	Motor-CAD o/p (°C)	ΔT (°C) [Exp. - Mot.]	% Error
	Housing - Front	40	44.11	-4.11	-10.28
	Housing - Active	38.2	40.21	-2.01	-5.26
	Housing - Rear	35.8	36.78	-0.98	-2.74
	Bearing - Front	42.4	46.95	-4.55	-10.73
	Bearing - Rear	38.5	39.31	-0.81	-2.10
	Stator Winding	48	54.06	-6.06	-12.63
	Rotor Winding	58	66.74	-8.74	-15.07
	Winding Av.	51.4	56.39	-4.99	-9.71
	EndWinding (F)	54.1	59.48	-5.38	-9.94
	EndWinding (R)	52.8	58.28	-5.48	-10.38
				Average % Error	8.89
13.5 kVA	O/p Parameter	Exp. o/p (°C)	Motor-CAD o/p (°C)	ΔT (°C) [Exp. - Mot.]	% Error
	Housing - Front	45.7	50	-4.3	-9.41
	Housing - Active	43	45.54	-2.54	-5.91
	Housing - Rear	40.2	41.69	-1.49	-3.71
	Bearing - Front	47.3	53.29	-5.99	-12.66
	Bearing - Rear	42.9	44.89	-1.99	-4.64
	Stator Winding	56	63.07	-7.07	-12.63
	Rotor Winding	74.1	81.6	-7.5	-10.12
	Winding Av.	62.7	67.6	-4.9	-7.81
	EndWinding (F)	67.5	74.1	-6.6	-9.78
	EndWinding (R)	66	72.63	-6.63	-10.06
				Average % Error	8.67
18 kVA	O/p Parameter	Exp. o/p (°C)	Motor-CAD o/p (°C)	ΔT (°C) [Exp. - Mot.]	% Error
	Housing - Front	55.9	57.74	-1.84	-3.29
	Housing - Active	51.5	52.49	-0.99	-1.92
	Housing - Rear	48.1	48.14	-0.04	-0.08
	Bearing - Front	56.5	61.64	-5.14	-9.10
	Bearing - Rear	51.4	52.25	-0.85	-1.65
	Stator Winding	69.2	74.68	-5.48	-7.92
	Rotor Winding	98.4	101.2	-2.8	-2.85
	Winding Av.	81.8	82.45	-0.65	-0.79
	EndWinding (F)	90	94.07	-4.07	-4.52
	EndWinding (R)	88.3	92.21	-3.91	-4.43
				Average % Error	3.66
23.6 kVA	O/p Parameter	Exp. o/p (°C)	Motor-CAD o/p (°C)	ΔT (°C) [Exp. - Mot.]	% Error
	Housing - Front	78.1	72.61	5.49	7.03
	Housing - Active	70.7	65.52	5.18	7.33
	Housing - Rear	66	60.56	5.44	8.24
	Bearing - Front	77.8	77.78	0.02	0.03
	Bearing - Rear	70.2	66.54	3.66	5.21
	Stator Winding	86.8	96.03	0.77	0.80
	Rotor Winding	149.8	140.5	9.3	6.21
	Winding Av.	120.1	110.1	10	8.33
	EndWinding (F)	135.7	132.2	3.5	2.68
	EndWinding (R)	132.7	129.7	3	2.26
	OVERALL TEFC % ERROR: 6.50 %			Average % Error	4.80

Table 6: TEFC experimental against Motor-CAD temperature prediction comparison.

Generator Part	Temp. Prediction % Error
Housing – Front	5.98
Housing – Active	4.97
Housing – Rear	3.65
Bearing – Front	6.27
Bearing – Rear	4.14
Stator Winding	5.63
Rotor Winding	9.48
Winding Average	5.60
End-Winding – Front	8.15
End-Winding – Rear	8.03

Table 7: Temp. prediction % errors for specific generator parts.

Analysing the percentage errors for the TENV 10.64 kVA machine (Table 5) relatively high offset errors are observed. The overall average error of 10.2 % is nearly twice the average TENV percentage error and crucial component predictions such as the rotor present individual errors for up to 19.12 %. Motivated and encouraged by this problem, higher kVA rated machines (3000 kVA to 3300 kVA) were analysed and modelled using Motor-CAD. Confidence in Motor-CAD's capability to predict high kVA rated machines was restored as acceptable results were obtained.

VIII. ALTERNATOR OPTIMISATION

Once Motor-CAD was carefully validated and labelled as a reliable alternator thermo-modelling tool, it was utilised to optimise the TEFC alternator in order for it to satisfy the American truck company's geometric specifications. The main geometric alteration required was a 23 mm bearing-to-bearing length reduction.

In order to reduce the generator's length without resulting in a significant increase in component temperature, the machine's geometric features were individually thermally optimised forcing individual temperatures to fall. Achieving a significant temperature drop will permit the designer to reduce the generator's core length sufficiently as required for the application. Subsequent to optimisation, the required 23 mm reduction in machine length will elevate component temperatures once again. Ideally, this increase in temperature will be less than or equal to the temperature drop achieved through optimisation. If this is so, generator performance will not be jeopardised and the shortening of the machine will suit specifications. During the optimisation stage it was essential for the electromagnetic aspects of the generator to remain unaltered in order to reduce manufacturing costs. Hence, the thermal side of the machine can and must be fully optimised to achieve the established aim. The two main areas of thermal optimisation are the frame and the cooling system.

Motor-CAD was used to optimise the frame related sections of the generator. Up to 38 distinct tests were carried out regarding issues such as fin extension, fin thickness, number of fins, fin arrangement type, feet width, feet length, frame width, endcap dimensions, base width, base thickness, stator duct gap width, frame material properties and cowling issues. The optimisation stage yielded the required TEFC generator needed and all the specifications demanded by the customer were efficiently met.

XI. DISCUSSION

Motor-CAD has proven to be a very useful modelling tool in the thermo-modelling of TEFC synchronous generators. As promised, its Lumped Circuit nature simplified the thermal characterisation of the generator effectively and resulted in near-instantaneous component temperature predictions. This highly contrasts with Numerical Analysis methods, such as Finite Element Analysis or Computational Fluid Dynamics, since they are both have long and tedious computing and processing times. In fact, CFD was utilised to analyse the TEFC alternator in parallel with the Motor-CAD simulations and feared complexities associated with Numerical Analysis methods were confirmed. The CFD results obtained agreed with those provided by Motor-CAD and, even though a higher degree of accuracy was provided by the CFD analysis, such as the detailed air flow illustrated in Fig 7, complications in meshing and analysing the alternator do not justify this thermal analysis method for

most engineering purposes.

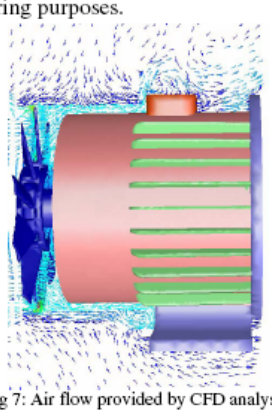

Fig 7: Air flow provided by CFD analysis.

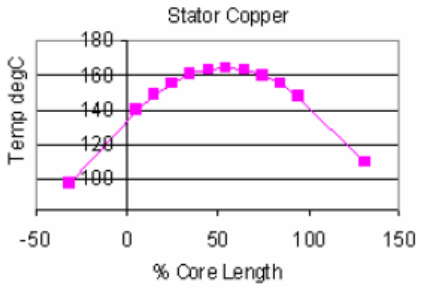

Fig 8: Stator copper thermal predictions.

Numerical Analysis techniques do provide a degree of accuracy that can be very attractive in some cases, especially when it comes to analysing the generator's core thermal distribution. Their thermal predictions (Fig 8) can be very helpful for machine developers. Motor-CAD only provides an average temperature for the mentioned components, which excludes the possibility of identifying the hotter sections of the core and pinpointing specific hotspots. In order to allow for this degree of accuracy, Motor-CAD could include some Numerical Analysis techniques for specific critical parts of the machine under investigation, while the rest of the machine could be lump-circuited and analysed in the traditional analytical way. This will clearly not be a simple addition to the software and processing times could be unacceptably increased. An alternative way of increasing Motor-CAD's accuracy, without making use of Numerical Analysis techniques, would be to divide critical components into smaller sections. They would then form part of the overall lumped circuit analysis and extended details for the selected generator components would be provided. Hence, the alternator's core or winding could be divided into a dozen different sections, allowing for a more detailed thermal characterisation of the mentioned components. Thermal progression graphs, such as the one displayed in Fig 8, could be derived from these. A more accurate modelling of the hottest alternator components would allow for current hot spot margins to be greatly reduced, resulting in more economical generators that could be reduced in size further.

X. CONCLUSION

Results presented in the paper validate the thermal model developed for a TEFC synchronous machine to a high degree of accuracy. A lumped parameter model can therefore be used with confidence for the design of electrical machines for applications to be used in extreme environments. The authors do also acknowledge the limitations of such models and have briefly discussed solutions for further work.

XI. ACKNOWLEDGMENT

The author would like to thank the following colleagues at Newage AVK SEG for their advice and encouragement Dr. Anca Novinski, Dr. Shamas Bokhari, Mr. Cleveland Mills, Mr. Paul Marshall, Mr. Steve Allen, Dr. Nigel Jakeman and Dr. Chris Maddison

XII. REFERENCES

[1] Motor-CAD v3.1 Manual, April 2006.

[2] Staton, D.; Pickering, S.J.; Lampard, D.; "Recent advancement in the thermal design of electric motors", *Paper presented at the SMMA 2001 Fall Technical Conference, Emerging Technologies for Electric Motion Industry*, Durham, North Carolina, USA, 3 -5 October, 2001.

[3] Al'Akayshee, Q.; Staton, D.A.; "1150hp Motor Design, Electromagnetic & Thermal Analysis", *ICEM*, Brugge, Belgium, 25-28 August, 2002.

[4] Staton, D.A.; "Thermal computer aided design-advancing the revolution in compact motors", *Electric Machines and Drives Conference, 2001. IEMDC 2001. IEEE International*, Page(s): 858 – 863, 2001.

[5] Mesrobian, A.; Hudson, J.A.; "Comparative performance of open and totally enclosed machines", *Industry Applications, IEEE Transactions on*, Volume 33, Issue 1, Page(s): 154 – 159 January – February, 1997.

[6] Ingress Protection Ratings, European Committee for Electro Technical Standardization, CENELEC, described IEC/EN 60529.

References

[1] Staton, D.; Boglietti, A. and Cavagnino, A., "Solving the More Difficult Aspects of Electric Motor Thermal Analysis in Small and Medium Size Industrial Induction Motors", *Energy conversion, IEEE transactions on*, Volume: 20, Issue: 3, Page(s): 620-628, September 2005.

[2] Mezani, S.; Takorabet, N. and Laporte, B., "A combined electromagnetic and thermal analysis of induction motors", *Magnetics, IEEE Transactions on*, Volume: 41, Issue: 5, Page(s): 1572-1575, May 2005.

[3] Thermo King [Online] Available: www.thermoking.com

[4] Airbus [Online] Available: www.airbus.com

[5] Hyundai Heavy Industries [Online] Available: www.english.hhi.co.kr

[6] IET Fact file, Standards for Energy Efficient Motors [Online] Available: www.theiet.org/factfiles

[7] The European Motor Challenge Programme, promoted by the European Commission, detailed in "Energy Efficient Motor Driven System", published by the European Copper Institute, Tervurenlaan, Brussels, Belgium, February, 2003.

[8] Dorrell, D. G.; Staton, D. A.; Kahout, J.; Hawkins, D. and McGilp, M. I., "Linked Electromagnetic and Thermal Modelling of a Permanent Magnet Motor", presented at Third Conference on Power Electronics, Machines and Drives, Page(s): 536-540, March 2006.

[9] Emerson Motor Technologies, Product data sheet, Horizontal A.C. Motors, Unimount 125®, Totally enclosed fan cooled, 2003.

[10] Staton, D., "Thermal analysis of electric motors and generators", presented at 32nd Conference of the IEEE Industrial Electronics Society (IECON), November 2006.

[11] Staton, D.; Pickering, S.J. and Lampard, D., "Recent advancement in the thermal design of electric motors", presented at SMMA Fall Technical Conference, October 2001.

[12] Mellor, P.H.; Roberts, D.; Turner, D.R., "Lumped parameter thermal model for electrical machines of TEFC design", *Electric Power Applications, IEE Proceedings*, Volume: 138, Issue: 5, Page(s): 205-218, September, 1991.

[13] Ibtiouen, R.; Mezani, S.; Touhami, O.; Nouali, N. and Benhaddadi, M., "Application of lumped parameters and finite element methods to the thermal modelling of an induction motor", presented at International Conference on Electric Machines and Drives, Page(s): 505-507, 2001.

[14] Boglietti, A.; Cavagnino, A.; Staton, D.; Shanel, M.; Mueller, M. and Mejuto, C., "Evolution and Modern Approaches for Thermal Analysis of Electrical Machines", *Industry Electronics, IEEE Transactions on*, Volume: 56, Issue: 3, Page(s): 871-882, March 2009.

[15] Steven, R. E., *Electrical Machines and Power Electronics*. New York: Van Nostrand-Reinhold, 1983.

[16] Underwriters Laboratories Inc. [Online] Available: www.ul.com

[17] Dorrell, D.G., "Combined Thermal and Electromagnetic Analysis of Permanent-Magnet and Induction Machines to Aid Calculation", *Industry Electronics, IEEE Transactions on*, Volume: 55, Issue: 10, Page(s): 3566-3574, October 2008.

[18] Chin, Y.K.; Nordland, E. and Staton, D.A., "Thermal analysis – lumped-circuit model and finite element analysis", presented at 6th International Power Engineering Conference (IPEC), Page(s): 952-957, November 2003.

[19] Staton, D.A., "Thermal computer aided design-advancing the revolution in compact motors", presented at International Electric Machines and Drives Conference, Page(s): 858-863, June 2001.

[20] Mejuto, C.; Mueller, M.; Staton, D.; Mebarki, S. and Al-Khayat, N., "Thermal Modelling of TEFC Alternators", presented at 32nd Conference of the IEEE Industrial Electronics Society (IECON), Page(s): 4813-4818, November 2006.

[21] Mejuto, C.; Mueller, M.; Shanel, M.; Mebarki, A.; Reekie, M. and Staton, D., "Improved synchronous machine thermal modelling", presented at 18th International Conference on Electrical Machines, September 2008.

[22] Chin, Y.K. and Staton, D.A., "Transient thermal analysis using both lumped-circuit approach and finite element method of a permanent magnet traction motor", presented at 7th AFRICON Conference, Volume: 2, Page(s): 1027-1035, September 2004.

[23] Al'Akayshee, Q. and Staton, D.A., "1150 hp motor design, electromagnetic and thermal analysis", presented at 12th International Conference on Electrical Machines, August 2002.

[24] Rajagopal, M. S.; Seetharamu, K. N. and Aswathnarayana, P. A., "Transient thermal analysis of induction motors," *Energy Conversion, IEEE Transactions on.*, Volume: 13, Issue: 1, Page(s): 62-69, March 1998.

[25] Trigeol, J. F.; Bertin ,Y. and Lagonotte, P., "Thermal modeling of an induction machine through the association of two numerical approaches," *Energy Conversion, IEEE Transactions on*, Volume: 21, Issue: 2, Page(s): 314-323, June 2006.

[26] Boglietti, A.; Cavagnino, A.; Lazzari, M. and Pastorelli, M., "A simplified thermal model for variable-speed self-cooled industrial induction motor", *Industry Applications, IEEE Transactions on*, Volume: 39, Issue: 4, Page(s): 945-952, July-August 2003.

[27] Powell, D.J, "Modelling of high power density electrical machines for aerospace," PhD Dissertation, University of Sheffield, Sheffield, United Kingdom, May 2003.

[28] Alberti, L. and Bianchi, N., "Thermal assisted finite element analysis of electrical machines", presented at 18th International Conference on Electrical Machines, September 2008.

[29] Glises, R.; Chamagne, D. and Kauffmann, J.M., "3D thermal behaviour computation by F.E. method of a 4 kW asynchronous motor. Effect of the rotation speed on thermal parameters", presented at 12th International Conference on Electrical Machines, September 2002.

[30] S.J. Salon, *Finite Element Analysis of Electrical Machines*, 2nd Edition, Kluwer Academic Publisher, 1995.

[31] Boglietti, A.; Cavagnino, A. and Staton, D., "Determination of critical parameters in electrical machine thermal models," presented at International Industry Applications Society Conference, Page(s): 73-90, September 2007.

[32] Maynes, B.D.J.; Kee, R.J.; Tindall, C.E. and Kenny, R.G., "Simulation of airflow and heat transfer in small alternators using CFD", *Electric Power Applications, IEE Proceedings* -, Volume: 150, Issue: 2, Page(s): 146-152, March 2003.

[33] Puranen, J. and Pyrhonen, J., "Optimization of the loadability of an induction servomotor with a coupled electromagnetic-thermal model", International Symposium on Power Electronics, Electrical Drives, Automation and Motion (SPEEDAM), Page(s): 153-158, May 2006.

[34] Gerling, D. and Dajaku, G., "Novel lumped-parameter thermal model for electrical systems", presented at European Conference on Power Electronics and Applications, Page(s): 10, 2005.

[35] Duran, M.J. and Fernandez, J., "Lumped-parameter thermal model for induction machines", *Energy Conversion, IEEE Transactions on*, Volume: 19, Issue: 4, Page(s): 791-792, December 2004.

[36] Mukosiej, J., "Measurements of thermal resistance on ready-made induction motors", presented at 16th International Conference on Electrical Machines, September 2006.

[37] EL-Refaie, A.M.; Harris, N.C.; Jahns, T.M. and Rahman, K.M., "Thermal analysis of multibarrier interior PM synchronous Machine using lumped parameter model", *Energy Conversion, IEEE Transactions on*, Volume: 19, Issue: 2, Page(s): 303-309, June 2004.

[38] Junak, J.; Ombach, G. and Staton, D., " Permanent magnet DC motor brush transient thermal analysis", presented at 18th International Conference on Electrical Machines, September 2008.

[39] Staton, D.; Popescu, M.; Cossar, C.; McGlip, M.; Omori, S. and Kurimoto, T., "Analytical thermal models for small induction motors", presented at 18th International Conference on Electrical Machines, September 2008.

[40] Pal, S.K., *Heat transfer in electrical machines – A critical machines*, ERA Technology Ltd., 1987.

[41] Hay, N.; Lampard, D.; Pickering, S.J. and Roylance, T.F., *A review of airflow and heat transfer for ribbed surfaces, end-windings, ducts and airgaps in electrical machines*, ERA Technology Ltd., August 1990.

[42] Leinhard IV, J.H. and Leinhard V, J.H., *A Heat Transfer Textbook*, 3rd Edition, Phlogiston Press, Cambridge, Massachusetts, 2005.

[43] Holman, J.P., *Heat Transfer*, McGraw-Hill, New York, 1997.

[44] Mills, A.F., *Heat Transfer*, Prentice-Hall, Englewood Cliffs, NJ, 1999.

[45] Trigkidis, G.; Bousbaine, A. and Thorn, R., "Thermal Modelling of IGBT Devices", presented at Universities Power Engineering Conference (UPEC), Page(s): 584-588, September 2006.

[46] Cavagnino, A. and Staton, D., "Convection heat transfer and flow calculations suitable for analytical modelling of electric machines," presented at 32nd Conference of the IEEE Industrial Electronics Society (IECON), Page(s): 4841-4846, November 2006.

[47] Dhinsa, K.K.; Bailey, C.J. and Pericleous, K.A.; **"**Turbulence modelling and it's impact on CFD predictions for cooling of electronic components", presented at 9th Intersociety Conference on Thermal and Thermomechanical Phenomena in Electronic Systems (ITHERM), Volume: 1, Page(s): 487-494, June 2004.

[48] Manglik, R., *Heat Transfer - Data Book*, General Electric Company, Corporate Research and Development, Schenectady, New York.

[49] Gerling, D. and Dajaku, G., "An improved lumped parameter thermal model for electrical machines", Institute for Electrical Drives, University of Federal Defence Munich, Neubiberg, Germany.

[50] Junak, J.; Ombach, G. and Staton, D.; "Permanent magnet DC motor brush transient thermal analysis", presented at 18th International Conference on Electrical Machines, September 2008.

[51] Pickering, S.J.; Lampard, D.; Hay, N. and Roylance, T.F., "Heat transfer from the stator end-windings of a low voltage concentric-wound induction motor", presented at Seventh International Conference on Electrical Machines and Drives, Page(s): 477-481, Conference publication number: 412, September 1995.

[52] Pickering, S.J.; Lampard, D.; Hay, N. and Roylance, T.F., "Heat transfer in a through-ventilated induction motor", *Electric Power Applications, IEE Proceedings* -, Volume: 145, Issue: 5, Page(s): 429-433, September 1998.

[53] Yangsoo Lee; Song-Yop Hahn and Kauh, S.K., "Thermal analysis of induction motor with forced cooling channels", *Magnetics, IEEE Transactions on*, Volume: 36, Issue: 4, Page(s): 1398-1402, July 2000.

[54] Jokinen, T. and Saari, J., "Modelling of the coolant flow with heat flow controlled temperature sources in thermal networks (in induction motors)", *Electric Power Applications, IEE Proceedings* -, Volume: 144, Issue: 5, Page(s): 338-342, September 1997.

[55] Manglik, R., *Fluid Flow - Data Book*, General Electric Company, Corporate Research and Development, Schenectady, New York.

[56] Idelchik, I.E., *Handbook of hydraulic resistance*, Begell House, 2001.

[57] Fox, R.W.; McDonald, A.T. and Pritchard, P.J., *Introduction to Fluid Mechanics*, 6th Edition, John Wiley & Sons Inc., 2004.

[58] Young, D.F.; Munson, B.R. and Okiishi, T.H., *A Brief Introduction to Fluid Mechanics*, 3rd Edition, John Wiley & Sons Inc., 2004.

[59] Shaughnessy, E.J.; Katz, I.M. and Schaffer, J.P., *Introduction to Fluid Mechanics*, Oxford University Press, 2005.

[60] Greer, A.R. and Tindall, C.E.; "Loss evaluation in genset alternators", supported by Moteurs Leroy Somer (France) and FG Wilson Engineering Ltd., The Queen's University of Belfast, 1998.

[61] Ionel, D.M.; Popescu, M.; Dellinger, S.J.; Miller, T.J.E.; Heideman, R.J. and McGilp, M.I., "On the variation with flux and frequency of the core loss coefficients in electrical machines", *Industry Applications, IEEE Transactions on*, Volume: 42, Issue: 3, Page(s): 658-667, May-June 2006.

[62] Gieras, J.F.; Koenig, A.C. and Vanek, L.D., "Calculation of eddy current losses in conductive sleeves of synchronous machines", presented at 18th International Conference on Electrical Machines, September 2008.

[63] Valenzuela, M.A.; Tapia, J.A. and Rooks, J.A.; "Thermal evaluation of TEFC induction motors operating on frequency-controlled variable-speed drives", *Industry Applications, IEEE Transactions on*, Volume: 40, Issue: 2, Page(s): 692-698, March-April, 2004.

[64] Aglen, O., "Loss calculation and thermal analysis of a high-speed generator", presented at International Conference on Electric Machines and Drives Conference, Volume: 2, Page(s): 1117-1123, June 2003.

[65] Karmaker, H.C., "Stray losses in large synchronous machines", *Energy Conversion, IEEE Transactions on*, Volume: 7, Issue: 1, Page(s): 148-153, March 1992.

[66] Nailen, R.L., *Stray load loss: What's it all about?*, Electrical Apparatus, Barks Publications, 1997.

[67] Aoulkadi, M. and Binder, A., "Evaluation of different measurement methods to determine stray load losses in induction machines", presented at International Symposium on Power Electronics, Electrical Drives, Automation and Motion (SPEEDAM), Page(s): 949-954, May 2006.

[68] Hagen, A.R.; Binder, A.; Aoulkadi, M.; Knopik, T. and Bradley, K., "Comparison of measured and analytically calculated stray load losses in standard cage induction machines", presented at 18th International Conference on Electrical Machines, September 2008.

[69] R.L. Nailen, "Energy efficient motors - myths vs. reality", presented at International Textile, Fiber and Film Industry Technical Conference, Page(s): 1/1-1/5, 1993.

[70] Levi, E.; Lamine, A. and Cavagnino, A., "Impact of stray load losses on vector control accuracy in current-fed induction motor drives", *Energy Conversion, IEEE Transactions on*, Volume: 21, Issue: 2, Page(s): 442-450, June 2006.

[71] Lamine, A.; Levi, E. and Cavagnino, A., "Compensation of Stray Load Loss Induced Detuning in Rotor Flux Oriented Induction Machines", presented at International Universities Power Engineering Conference (UPEC), Volume: 2, Page(s): 685-689, September 2006.

[72] Cummins Generator Technologies [Online] Available: www.cummins.com

[73] Mueller, M.A.; Williamson, S.; Flack, T.J.; Atallah, K.; Baholo, B.; Howe, D. and Mellor, P.H, "Calculation of iron losses from time-stepped finite-element models of cage induction machines", presented at Seventh International Conference on Electrical Machines and Drives, Page(s): 88, September 1995.

[74] Lin, D.; Zhou, P.; Fu, W.N.; Badics, Z. and Cendes, Z.J., "A dynamic core loss model for soft ferromagnetic and power ferrite materials in transient finite element analysis", *Magnetics, IEEE Transactions on*, Volume: 40, Issue: 2, Page(s): 1318-1321, March 2004.

[75] Yamazaki, K., "Harmonic copper and iron losses calculation of induction motor using nonlinear time-stepping finite element method", presented at International Electric Machines and Drives Conference, Page(s): 551-553, 2001.

[76] Righi, L.A.; Sadowski, N.; Carlson, R.; Bastos, J.P.A. and Batislsla, N.J, "A new approach for iron losses calculation in voltage fed time stepping finite elements", *Magnetics, IEEE Transactions on*, Volume: 37, Issue: 5, Page(s): 3353-3356, September 2001.

[77] Vector Fields [Online] Available: www.vectorfields.com

[78] Domeki, H.; Ishihara, Y.; Kaido, C.; Kawase, Y.; Kitamura, S.; Shimomura, T.; Takahashi, N.; Yamada, T. and Yamazaki, K., "Investigation of benchmark model for estimating iron loss in rotating machine", *Magnetics, IEEE Transactions on*, Volume: 40, Issue: 2, Page(s): 794-797, March 2004.

[79] Chunting Mi; Slemon, G.R. and Bonert, R., "Modeling of iron losses of permanent-magnet synchronous motors", *Industry Applications, IEEE Transactions on*, Volume: 39, Issue: 3, Page(s): 734-742, May-June 2003.

[80] Dupre, L.R.; Van Keer, R. and Melkebeek, J.A.A., "An iron loss model for electrical machines using the Preisach theory", *Magnetics, IEEE Transactions on*, Volume: 33, Issue: 5, Page(s): 4158-4160, September 1997.

[81] Ma, L., Sanada, M., Morimoto, S. and Takeda, Y., "Iron loss prediction considering the rotational field and flux density harmonics in IPMSM and SynRM", *Electric Power Applications, IEE Proceedings* -, Volume: 150, Issue: 6, Page(s): 747-751, November 2003.

[82] Venkatachalam, K.; Sullivan, C.R.; Abdallah, T. and Tacca, H., "Accurate prediction of ferrite core loss with nonsinusoidal waveforms using only Steinmetz parameters", presented at Workshop on Computers in Power Electronics, Page(s): 36-41, June 2002.

[83] Amara, Y.; Jiabin Wang and Howe, D., "Stator iron loss of tubular permanent-magnet machines", *Industry Applications, IEEE Transactions on*, Volume: 41, Issue: 4, Page(s): 989-995, July-August 2005.

[84] Stumberger, B.; Hamler, A. and Hribernik, B., "Analysis of iron loss in interior permanent magnet synchronous motor over a wide-speed range of constant output power operation", *Magnetics, IEEE Transactions on*, Volume: 36, Issue: 4, Page(s): 1846-1849, July 2000.

[85] Mi, C.C.; Slemon, G.R. and Bonert, R., "Minimization of iron losses of permanent magnet synchronous machines", Energy conversion, IEEE transactions on, Volume: 20, Issue: 1, Page(s): 121-127, March 2005.

[86] Atallah, K.; Zhu, Z.Q. and Howe, D., "An improved method for predicting iron losses in brushless permanent magnet DC drives", Magnetics, IEEE Transactions on, Volume: 28, Issue: 5, Page(s): 2997-2999, September 1992.

[87] Roshen, W., "Iron loss model for PM synchronous motors in transportation", presented at Conference on Vehicle Power and Propulsion, Page(s): 4, September 2005.

[88] Hippner, M.; Yamada, H. and Mizuno, T., "Iron loss analysis in linear DC motor: laminated vs. solid core", *Magnetics, IEEE Transactions on*, Volume: 35, Issue: 5, Page(s): 3715-3717, September 1999.

[89] Leonardi, F.; Matsuo, T. and Lipo, T.A., "Iron loss calculation for synchronous reluctance machines", presented at International Conference on Power Electronics, Drives and Energy Systems for Industrial Growth, Volume: 1, Page(s): 307-312, 1996.

[90] Novinschi, A.; Brown, N.L.; Mebarki, A. and Haydock, L., "The development of an FEA design environment model and comparison with traditional design and test data for the design of electrical machine", presented at International Conference on Power Electronics, Machines and Drives, Page(s): 574-579, Conference publication number: 487, 2002.

[91] Nailen, R.L., "Can field tests prove motor efficiency?", presented at Industrial and Commercial Power Systems Technical Conference, Page(s): 110-116, May 1988.
[92] Opera-2d, Software for Electromagnetic Design Manual, from Vector Fields, February 2004.
[93] Jian Guo Zhu and Ramsden, V.S, "Improved formulations for rotational core losses in rotating electrical machines", *Magnetics, IEEE Transactions on*, Volume: 34, Issue: 4, Page(s): 2234-2242, July 1998.
[94] Smith, A.C. and Edey, K., "Influence of manufacturing processes on iron losses", presented at Seventh International Conference on Electrical Machines and Drives, Page(s): 77-81, September 1995.
[95] Walters, D.G., Williams, I.J. and Jackson, D.C., "The case for a new generation of high efficiency motors-someproblems and solutions", presented at Seventh International Conference on Electrical Machines and Drives, Page(s): 26-31, September 1995.
[96] Mejuto, C.; Mueller, M.; Shanel, M.; Mebarki, A. and Staton, D., "Thermal modelling investigation of heat paths due to iron losses in synchronous machines", presented at IET Conference on Power Electronics, Machines and Drives, Page(s): 225-229, April 2008.
[97] Adapted Solutions [Online] Available: www.adapted-solutions.com
[98] Mugglestone, J.; Pickering, S.J. and Lampard, D., "Effect of geometric changes on the flow and heat transfer in the end region of a TEFC induction motor", presented at International Electric Machines and Drives Conference, Page(s): 40-44, September 1999.
[99] Boglietti, A. and Cavagnino, A., "Analysis of the endwinding cooling effects in TEFC induction motors", *Industry Applications, IEEE Transactions on*, Volume: 43, Issue: 5, Page(s): 1214-1222, September-October 2007.
[100] Boglietti, A.; Cavagnino, A.; Parvis, M. and Vallan, A., "Evaluation of radiation thermal resistances in industrial motors", *Industry Applications, IEEE Transactions on*, Volume: 42, Issue: 3, Page(s): 688-693, May-June 2006.
[101] Boglietti, A.; Cavagnino, A. and Staton, D., "TEFC induction motors thermal models: A parameter sensitivity analysis", *Industry Applications, IEEE Transactions on*, Volume: 41, Issue: 3, Page(s): 756-763, May-June 2005.
[102] Micallef, C.; Pickering, S.J.; Simmons, K. and Bradley, K., "Improvements in Air Flow in the End Region of a Large Totally Enclosed Fan Cooled Induction Motor", presented at International Electric Machines and Drives Conference, Page(s): 579-584, May 2005.
[103] Pickering, S.J.; Lampard, D. and Shanel, M., "Modelling ventilation and cooling of the rotors of salient pole machines", presented at International Conference on Electric Machines and Drives, Page(s): 806-808, 2001.
[104] Boglietti, A.; Cavagnino, A.; Staton, D.A.; Popescu, M.; Cossar, C. and McGilp, M.I., "End Space Heat Transfer Coefficient Determination for Different Induction Motor Enclosure Types", presented at Industry Applications Society Annual Meeting, Page(s): 1-8, October 2008.